Composition-structure-activity relations in Cu-Sn and Cu-S based electrocatalysts for CO_2 conversion

Inaugural-Dissertation
to obtain the academic degree
Doctor rerum naturalium (Dr. rer. nat.)

submitted to the Department of Biology, Chemistry, Pharmacy
of Freie Universität Berlin

by

Sasho Stojkovikj

June 2022

Time period for conducting the doctoral studies:

08.01.2018 - 01.07.2022

Supervisor:

Dr. Matthew Mayer

Young Investigator Group Electrochemical Conversion, Helmholtz-Zentrum Berlin für Materialen und Energie GmbH, Hahn-Meitner-Platz 1, 14109 Berlin, Germany

Institute where the doctoral research was conducted:

Helmholtz-Zentrum Berlin für Materialen und Energie GmbH, Hahn-Meitner-Platz 1, 14109 Berlin, Germany

1st reviewer:

Dr. Matthew Mayer

Young Investigator Group Electrochemical Conversion, Helmholtz-Zentrum Berlin für Materialen und Energie GmbH, Hahn-Meitner-Platz 1, 14109 Berlin, Germany

2nd reviewer:

Prof. Dr. Beate Paulus

Theoretical Chemistry, Institut für Chemie und Biochemie, Freie Universität Berlin, Arnimallee 22, 14195 Berlin, Germany

Date of defense: 13.09.2022

Acknowledgments

The period during the doctoral research is definitely different than the time passed in school or during the undergraduate of master studies. The doctoral research is rather a journey that leaves great impact on the way of life… or maybe this several years are kind of a way of life that has the potential to shape the future of the person going through it. One cannot succeed finishing this process without the support of family, friends, colleagues, collaborators… Therefore, I fully acknowledge everyone that gave me the smallest, even the most indirect support. Most of them did it even without being aware of that. Maybe some of them helped me without myself being aware of that. Thus, I will apologize that I would not be able to mention everyone's name in these acknowledgements, the number of pages will go over the limit, still I will try my best to acknowledge every person, institution, project funding, that contributed even slightly to reach the end of this process.

I would like to express my gratitude to my supervisor Dr. Matthew Mayer for accepting me as a member of his research group, and for his support and guidance throughout the doctoral research. I specially thank him for the discussions, motivation, encouragement and above all for ensuring we have a great time being part of his team. Looking forward for to future collaborations! Next, I would like to deeply acknowledge my current and former group/institute colleagues and friends: Dr. Laura Pardo Pérez, Alexander Arndt, Veronica Davies, Frederik Firschke, Theocharis Tzanoudakis, Jana Rehm, Dr. Philipp Gotico, Flora Haun, Dr. Mahsa Barzgarvishlaghi, Zora Chalkley, Dr. Ibbi Ahmet, Dr. Peter Bogdanoff, Denis Antipin, Dr. Prince Saurabh Bassi, Dr. Joachim Breternitz, Yulin Tsai, Dilan Aksoy, Zhaoli Zhu, Álvaro Díaz Duque, Ahmad Alsawaf, Dr. Utam Gupta and many others, and special thanks to Dr. Gumaa El-Nagar and Siddharth Gupta for the fruitful collaboration and above all, our friendship. Once more I would like to thank my friend Jana Rehm for her help in proper translation of the summary in German language. I acknowledge Prof. Dr. Roel van de Krol and Prof. Dr. Beate Paulus as members of my research progress committee, for the very useful discussions and feedbacks, Dr. Gabrielle Lampert and Prof. Dr. Susan Schorr for organizing the doctoral graduate school research progress colloquiums. In addition, I would like to thank all collaborators from different groups, institutes, universities and research facilities from Germany and abroad: Dr. Ronny Golnak, Prof. Dr. Christina Roth, Dr. Falk Münch, Dr. Tim Böttcher, Dr. Philip Tockhorn, Dr. Eike Köhnen, Dr. Jie Xiao, Prof. Dr. Metodija Najdoski, Dr. Léo Choubrack, Dr. Götz Schuck, Dr. Martin Radtke, Prof. Dr. Violeta Koleva, Dr. Prashant Khadke, Dr. Ana Guilherme Buzanich and others. I am very grateful to Dr. Réne Gunder, Christian Höhn, Dr. Daniel Abou-Ras, Ursula Michalczik, Holger Kropf, Lars Steinkopf, Claudia Leistner, Max Rieckert, Karsten Harbauer, Dr. Michael Tovar, Dr. Lifei Xi, and members of the workshops at Helmholtz-Zentrum Berlin for providing trainings, experimental and technical support without which this work would not have been possible.

Last but not least I would like to express my highest acknowledgement to my wife Irena Stojkovikj, my parents, my siblings, other family members, relatives and close friends from my homeland for their support and belief in me.

This work was funded by the Helmholtz Association's Initiative and Networking Fund via the Helmholtz Young Investigators Group award (VH-NG-1225) and the Helmholtz-Climate-Initiative (HI-CAM). Instrumentation provided by the Helmholtz Energy Materials Foundry (HEMF) laboratories was used in the scope of this work. Additional financial support came from the European Union project FlowPhotoChem Grant Agreement No. 862453.

Declaration of Independence

Herewith, I certify that I have prepared and written my thesis independently, and that I have not used any sources and aids other than those indicated by me.

Permission was requested and granted for all data, figures and schematics reproduced from the literature except where no copyright permission was required. In all cases the source of reproduced data, figures and schematics is cited.

Sasho Stojkovikj,
Berlin, June 2022

Outline

➢ **Chapter 1** presents an introduction of the thesis and is divided in three sections. The first section discusses general aspects regarding the development of the human society in all sectors with the start of the industrial revolution, the continuous increase in the demand for energy, materials and various commodities, pollution of the environment, greenhouse gases, extraction of natural resources and the climate change consequences from the greenhouse gas CO_2 that is emitted during fossil fuels combustion for production of energy. The second section is dedicated to the CO_2 capture and conversion concepts, briefly discussing the approaches for these purposes. The third section is dedicated to the electrochemical approach for CO_2 conversion, discussing the relevant subjects in this field of research related to the advantages of this approach, catalyst materials, conditions and parameters that affect the conversion selectivity from which various challenges arise and still hinder the industrial application of this concept targeting production of hydrocarbons, alcohols and other products, valuable as fuels and chemical feedstocks.

➢ **Chapter 2** represents the methods section of this thesis. The first part of this chapter discusses the synthesis methods for preparation of Cu-Sn and Cu-S electrocatalyst materials, that are investigated in the scope of this thesis, via two-step electrochemical/chemical approach for the CO selective Cu rich (Sn poor) Cu-Sn nanowires and $HCOO^-$ selective Sn-rich (high) Cu-Sn nanowires and Cu_xS foam, or only single electrochemical step for the CO selective Cu rich Cu-Sn foam, derived from waste bronze. The second part of this chapter discusses the characterization methods used in this work together with their basic principles.

➢ **Chapter 3** presents discussion and summary of the most important findings regarding the Cu-Sn and Cu-S based electrocatalyst materials for CO_2 conversion. The full studies are presented as publications and manuscript, embedded in the thesis as Chapters 4-6.

➢ **Chapter 4** represents a publication dedicated to study of the composition-structure relations with the CO_2 reduction activity for CO and $HCOO^-$ production on Cu-Sn nanowires with low and high Sn content, from which the optimal composition and surface speciation of Cu and Sn were revealed using x-ray spectroscopy supported by microscopy and electron diffraction. Moreover, computational method was used for modeling the key intermediate binding modes to correlate the experimentally observed behavior for favoring the $HCOO^-$ over CO selectivity with an increase of the Sn content and its metallic fraction under more negative potentials.

➢ **Chapter 5** is a publication that describes repurposing/recycling waste bronze alloy to derive CO_2 conversion Cu rich Cu-Sn foam electrocatalysts with high selectivity for CO via facile one-step electrochemical method. Cu and Sn are endangered elements with future risk of supply, hence application of recycling concept for preparation of catalyst materials, ultimately without utilization of natural raw materials and for solving environmentally important issues such as mitigation of the CO_2 concentration in the atmosphere via its conversion into valuable products, is essential precondition for building sustainable society.

➢ **Chapter 6** describes a study of composition-structure relations with the activity for CO_2 conversion into $HCOO^-$ on Cu-S foam electrocatalysts. The electrocatalyst surface speciation was examined using *quasi in-situ* XPS and is found that Cu is present in oxidation state +1, stabilized by residual sulfur species under all examined potentials. Cu^+ favorably binds the *OCHO* intermediate which undergoes further conversion into $HCOO^-$. Besides this, it is found that the $HCOO^-$ selectivity is dependent on other factors such as electrochemical activation of the electrocatalyst that is related to the Cu:S composition and electrode-electrolyte interface effects (local pH changes). The latter effects are not fully understood which is motivating for further studies. Finally, for the purpose of this study, simple, cheap and fast room temperature method was developed for sulfidation of Cu foam with elemental sulfur dissolved in toluene.

➢ **Chapter 7** is the last chapter of this thesis, summarizing the advantages, challenges and view of future perspectives of the electrochemical conversion of CO_2 and the Cu-Sn and Cu-S based electrocatalysts intended for this purpose. Finally, a brief discussion is given to emphasize the importance of other electrochemical conversion concepts such as the research in the field of ammonia and urea electrosynthesis, as crucial chemicals for supporting the food production on our planet.

Summary

The development of our society relying on utilization of raw materials from Earth has left unprecedented marks on our planet's environment. A key issue is the climate change phenomenon caused by the continuous increase in the atmospheric concentration of the greenhouse gas CO_2 due to combustion of fossil fuels as main energy source. The mitigation of the CO_2 emissions via its capture and conversion, increase in the utilization of renewable energy and recycling technologies, and eliminating the dependence from fossil fuels is a strategy for building sustainable society. A promising concept for tackling the CO_2 emission via its conversion into valuable products (hydrocarbons and alcohols etc.) is the electrochemical reduction of CO_2 (CO_2ER), that has many advantages over the other conversion concepts. Cu is unique in terms of material that can intrinsically catalyze CO_2 reduction into hydrocarbons and alcohols. However, there are many Cu catalyst/experimental conditions/engineering - related challenges and other issues of various nature that affect the product selectivity and therefore still hinder the large-scale application of the CO_2ER. Regarding the catalyst and experimental conditions challenges, possible alternative for overcoming the selectivity issues is step-wise CO_2ER i.e., two-electron electrochemical reduction of CO_2 into CO and subsequent conversion of CO into hydrocarbons, alcohols and other valuable products. Furthermore, another two-electron product, that is formic acid (HCOOH) or formate ($HCOO^-$) that find various industrial applications and are also promising alternative as fuel in fuel cells, together with CO can be produced with high selectivity on various cheap and abundant electrocatalysts. Namely, the Cu rich Cu-Sn materials appear to be promising catalysts for CO_2ER into CO, while Sn rich Cu-Sn and Cu-S for production of $HCOO^-$, and therefore they are worth and inspiring to be more thoroughly studied in terms of their composition-structure relations with the catalytic activity for electrochemical conversion of CO_2.

Hence, the first main goal of this thesis is dedicated to study of the composition-structure-CO_2ER activity relations in the Cu-Sn and Cu-S based electrocatalyst materials. On the other hand, the second main goal encompasses providing simple, cheap and fast synthesis methods for both Cu-Sn and Cu-S based materials, and moreover, including a successful proof-of-concept for recycling/repurposing waste for deriving CO selective Cu-Sn electrocatalyst, which are prerequisites toward possible application of these materials for large-scale conversion of CO_2 and building a sustainable society based on recycling in order to mitigate and finally cease the extraction of natural resources.

The thesis is divided into three studies, from which the first study represents determination of the composition and speciation of Cu and Sn in Cu-Sn electrocatalysts under CO_2 electrolysis in order to reveal the relationship between these parameters and the CO_2ER selectivity alteration between CO and $HCOO^-$ at various applied potentials. For the purpose of this study, SnO_2 functionalized CuO nanowires with varying thickness of surface SnO_2 layers (low and high Sn), were synthesized. The CO_2ER product quantification was performed using chromatography, while the material characterization methods comprised of mainly spectroscopy-based techniques including *ex-situ* soft x-ray XAS, *in-situ* hard x-ray XAS and *quasi in-situ* XPS, supported by microscopy/electron diffraction (EF-TEM, HR-TEM and SAED) and computational modeling (DFT). The results show that thin layer of SnO_2 (low Sn) functionalized CuO nanowires electrocatalysts that are selective for CO_2ER into CO, reaching maximal FE of ~80% at

–0.7 V, undergo surface transformation generating Cu^0 and SnO_x ($Sn^{\delta+}$) species under all examined potentials. The presence of $Sn^{\delta+}$ is supporting the Sn to Cu charge redistribution mechanism and therefore promoting desorption of the Cu bound *CO intermediate, leading to significantly higher CO evolution, compared to the activity of pristine Cu. On the other hand, the results show that the increase in the surface Sn content is beneficial for CO_2ER into $HCOO^-$, achieving the highest FE (80%) at –0.9 V for the catalyst with highest Sn content. Altering the potential toward more negative values is leading to increase in the surface fraction of metallic Sn specie that readily bind the *OCHO* intermediate following the $HCOO^-$ pathway, accompanied with significant suppression of the competitive hydrogen evolution reaction (HER) due to weak binding of the *H intermediate. Even though these Cu-Sn materials can reach very high selectivity for both CO and $HCOO^-$ in dependence of the surface Sn content, sophisticated, expensive and time-consuming approach, that includes atomic layer deposition (ALD) of SnO_2, was used for their synthesis.

An important requirement for future practical application of the CO_2ER catalysts is definitely simple, cheap and fast synthesis. Therefore, in the scope of the second study, facile one-step electrochemical method was developed for deriving Cu-Sn foam with low Sn content from waste bronze. The bronze derived Cu-Sn foam reached 80% FE for CO at –0.8 V, competing with the best catalysts for this purpose, which makes it promising for future large-scale application. This study is showing that recycling/repurposing waste material for CO_2ER catalyst synthesis is achievable, which is an important step towards sustainable supply of materials for this purpose.

The third study is based on investigation of the composition-structure relations in Cu-S catalysts selective for CO_2ER into $HCOO^-$, and moreover presenting a facile method for synthesis of these materials based on direct reaction between elemental Cu and S dissolved in toluene, hence avoiding usage of expensive and extremely toxic precursors. The most important finding in this study, based on examination of the Cu-S catalysts with *quasi in-situ* XPS, reveals that under CO_2 electrolysis the materials do not undergo complete reduction and Cu^+ surface species persist at all examined potentials (–0.5 to –0.9 V), compared to pristine Cu which is completely reduced to metallic under identical conditions. The presence of residual surface sulfur species is most probably stabilizing the Cu^+ with oxophilic nature on which the *OCHO* intermediate favorably binds and further converts into $HCOO^-$. However, the $HCOO^-$ selectivity that can reach up to 70-75% is dependent on activation of the electrocatalyst that is related to the Cu:S surface composition and various electrode-electrolyte interface effects. Namely, besides the S^{2-}, presence of unexpected SO_4^{2-} specie is found on the surface of the electrocatalysts that are subjected to applied potential of –0.9 V, most probably due to local pH increase effects. These local effects are not fully understood from this study which is inspiring for further research that involve probing the electrode-electrolyte interface with other surface sensitive methods under *in-situ* conditions such as Raman and infrared spectroscopy.

Finally, the future challenges include an adaptation of the facile synthesis methods developed in this work to prepare gas-diffusion electrodes loaded with Cu-Sn and Cu-S catalysts. Examining their CO_2ER activity in gas-diffusion electrolyzers is important to achieve high current densities and, hence, industrial relevant conversion rates that are required for future large-scale applications.

Zusammenfassung

Die stetige Weiterentwicklung unserer Gesellschaft auf Grundlage der Nutzung natürlicher Ressourcen hat beispiellose Spuren in der Umwelt unseres Planeten hinterlassen. Ein zentrales Problem ist dabei der globale Klimawandel, der durch den kontinuierlichen Anstieg der CO_2 Konzentrationen in der Erdatmosphäre infolge der Verbrennung fossiler Brennstoffe als Hauptenergiequelle verursacht wird. Insbesondere das Erreichen einer Unabhängigkeit von fossilen Brennstoffen durch die verstärkte Nutzung erneuerbarer Energien, die Eindämmung der CO_2 Emissionen durch Abscheidung und Umwandlung, sowie das Verwenden von Recyclingtechnologien bilden zentrale Strategien für den Aufbau einer nachhaltig lebenden Gesellschaft. Die elektrochemische Umwandlung von CO_2 (CO_2ER) in verwertbare Produkte wie Kohlenwasserstoffe, Alkohole etc. stellt einen vielversprechenden Ansatz zur Bekämpfung der globalen CO_2 Emissionen dar und bietet viele Vorteile gegenüber anderen CO_2 Umwandlungskonzepten. Insbesondere Cu erweist sich als geeignetes Katalysatormaterial für die CO_2ER, da es intrinsisch CO_2 zu Kohlenwasserstoffen und Alkoholen umwandeln kann. Die mangelnde Produktselektivität dieses Katalysators, sowie weitere Versuchs- und Ingenieurtechnische Probleme, machen eine großtechnische Anwendung zum jetzigen Zeitpunkt jedoch noch nicht möglich. Die schrittweise durchgeführte CO_2ER, in der zunächst eine zwei Elektronen elektrochemische Reduktion von CO_2 zu CO und anschließend die Umwandlung von CO in Kohlenwasserstoffe, Alkohole und andere Produkte stattfindet, bildet eine mögliche Lösung zur Überwindung des Selektivitätsproblems. Darüber hinaus können bei diesem Prozess neben CO weitere zwei-Elektronen-Umwandlungsprodukte wie Ameisensäure (HCOOH) und Formiate ($HCOO^-$) unter der Verwendung billiger und im Überfluss vorhandener Elektrokatalysatormaterialien mit hoher Selektivität gewonnen werden. Ameisensäure und Formiate finden verschiedenste industrielle Anwendungen und bilden des weiteren eine vielversprechende Alternative zu herkömmlichen verwendeten Brennstoffen in BrennstoffzellenInsbesondere Cu-reiche Cu-Sn-materialen scheinen sich als vielversprechende Katalysatoren für die Umwandlung von CO_2 in CO zu erweisen, während Sn-reiche Cu-Sn und Cu-S Katalysatoren eher für die Herstellung von $HCOO^-$ geeignet sind.

Diese Beobachtungen bilden die Grundlage dieser Arbeit zur Untersuchung der katalytischen Aktivität von Cu-Sn und Cu-S Verbindungen gegenüber bestimmten CO_2 Umwandlungsprodukten. Das Hauptziel der Arbeit besteht dabei insbesondere darin, Verständnis über das Zusammenspiel und den Einfluss von Zusammensetzung und Struktur auf die CO_2ER Aktivität und Selektivität dieser Elektrokatalysatormaterialien zu gewinnen. Des weiteren ist das Ziel der Arbeit, einfache, billige und schnelle Synthesemethoden zur Herstellung von Cu-Sn und Cu-S basierten Materialien vorzustellen, wobei dabei ein erfolgreiches Proof-of-Concept für das Recycling und die Wiederverwendung von Abfallmaterialien zur Gewinnung eines CO-selektiven Cu-Sn Elektrokatalysators impliziert wird. Einfache Synthesemethoden und das Wiederverwenden von Materialien bilden die Grundlage für eine mögliche großtechnische Umwandlung von CO_2 und den Aufbau einer nachhaltigen Gesellschaft. Letztere setzt dabei insbesondere auf das Recycling von Materialien, was zu einer Verringerung des mineralischen Rohstoffabbaus und zu einem umweltschonenderen Umgang mit natürlichen Ressourcen führt.

Die Arbeit ist insgesamt in drei Studien unterteilt. Die erste Studie befasst sich dabei mit der Bestimmung der Zusammensetzung und Speziation von Cu und Sn in Cu-Sn Elektrokatalysatoren während der CO_2 Elektrolyse, um die Beziehung zwischen diesen Parametern und der CO_2ER Selektivitätsänderung zwischen CO und $HCOO^-$ bei verschiedenen angelegten Potentialen aufzuzeigen. Dafür wurden mit SnO_2 funktionalisierte CuO-Nanodrähte mit unterschiedlich dicken SnO_2-Oberflächenschichten (mit niedrigem und hohem Sn-Gehalt) synthetisiert. Die CO_2ER-Produktquantifizierung wurde mittels Chromatographie durchgeführt. Die Materialcharakterisierung erfolgte hauptsächlich mit Hilfe von spektroskopischen Methoden wie *ex-situ* weiche Röntgen-XAS, *in-situ* harte Röntgen-XAS und *quasi in-situ* XPS. welche zudem durch Mikroskopie/Elektronenbeugung (EF-TEM, HR-TEM und SAED) und rechnergestützten Modellierungen (DFT) unterstützt wurde. Die Ergebnisse zeigen, dass die mit dünnen SnO_2 Schichten (low Sn/geringer Sn-Gehalt) funktionalisierten CuO-Nanodrähte CO-selektive CO_2ER Elektrokatalysatoren sind, die eine maximale FE ~80% bei –0.7 V erreichen und aufgrund ihrer Oberflächenumwandlung unter allen untersuchten Potentialen Cu^0 and SnO_x ($Sn^{\delta+}$) Spezies erzeugen. Das Vorhandensein von $Sn^{\delta+}$ unterstützt die Ladungsumverteilung von Sn zu Cu und fördert somit die Desorption des an Cu gebundenen *CO-Zwischenprodukts, was im Vergleich zur Aktivität von unbehandelten Cu, zu eine signifikant hoher Bildung von CO führt. Im Gegensatz dazu zeigen die Ergebnisse, dass die Erhöhung des Sn-Gehalts an der Oberfläche für die Umwandlung von CO_2 in $HCOO^-$ vorteilhaft ist, wobei die höchste FE (80%) bei –0.9 V für den Katalysator mit dem höchsten Sn-Gehalt erreicht wird. Die Änderung des Potenzials in Richtung negativerer Werte führt zu einer Erhöhung des Oberflächenanteils metallischer Sn-Spezies, die die *OCHO*-Zwischenprodukte auf dem $HCOO^-$-Umwandlungspfad leicht binden und wird aufgrund der schwachen Bindung des *H- Zwischenprodukts von einer erheblichen Unterdrückung der kompetitiven Wasserstoffentwicklungsreaktion (HER) begleitet. Obwohl die Cu-Sn-Materialien in Abhängigkeit vom Sn-Gehalt an der Oberfläche eine sehr hohe Selektivität sowohl für CO als auch für $HCOO^-$ zeigen, basierte die Synthese dieser CO_2ER Katalysatoren auf einem zeitaufwendigen, teuren und komplizierten Herstellungsverfahren. Insbesondere die Abscheidung der SnO2 Schichten mit dem Atomlagenabscheidung (ALD) Verfahren machen eine spätere industrielle Anwendung dieser Synthesemethode eher unwahrscheinlich.

Eine wichtige Voraussetzung für die künftige praktische Anwendung von CO_2ER-Katalysatoren besteht zweifelsohne in einer einfachen, billigen und schnellen Materialsynthese. Daher wurde im Rahmen der zweiten Studie der Arbeit eine einfache elektrochemische Ein-Schritt-Methode zur Gewinnung von Cu-Sn-Schäumen mit niedrigem Sn-Gehalt aus Altbronze entwickelt. Der aus Bronze gewonnene Cu-Sn-Schaum erreichte 80% FE für CO bei –0.8 V und kann damit mit den besten CO_2ER erprobten Katalysatoren konkurrieren. Die Ergebnisse bilden eine vielsprechende Basis für eine künftige großtechnische Anwendung und zeigen, dass die Wiederverwendung von Abfallmaterialen für die Synthese von CO_2ER-Katalysatoren möglich ist.

Die dritte Studie der Arbeit basiert auf der Untersuchung der Zusammensetzungs-Struktur-Beziehungen in Cu-S-Katalysatoren, die eine Selektivität für CO_2ER zu $HCOO^-$ aufweisen. Darüber hinaus wird eine einfache Katalysatorsynthesemethode vorgestellt, die auf einer direkten Reaktion zwischen elementarem Cu und in Toluen gelöstem S basiert, wodurch die Verwendung von teuren und

toxischen chemischen Ausgangsstoffen vermieden werden kann. Dabei zeigen die Ergebnisse der *quasi in-situ* XPS Untersuchungen, dass die Cu-S Materialien bei der CO_2-Elektolyse keine vollständige Reduktion durchlaufen und Cu^+-Oberflächenspezies bei allen angelegten Potentialen (–0.5 bis –0.9 V) erhalten bleiben. Im Vergleich dazu, werden reine Cu-Katalysatoren unter identischen Bedingungen vollständig zu metallischem Cu reduziert. Das Vorhandensein von Schwefelresten an der Oberfläche stabilisiert dabei wahrscheinlich das $Cu^{+,}$ dass aufgrund seiner oxophilen Natur die Bindung dess *OCHO*- Zwischenprodukts begünstig und weiter in $HCOO^-$ umwandelt. Die Selektivität von $HCOO^-$, die bis zu 70-75% erreichen kann, hängt jedoch von der Aktivierung des Elektrokatalysators ab, welche mit der Cu:S-Oberflächenzusammensetzung und verschiedenen Elektroden-Elektrolyt-Grenzflächeneffekten zusammenhängt. Auf der Oberfläche der Elektrokatalysatoren, an die ein Potenzial von –0.9 V angelegt wird, findet sich neben S^{2-} auch eine unerwartete SO_4^{2-} -Spezies, dessen Auftreten wahrscheinlich auf lokale pH-Erhöhungseffekte zurückzuführen ist. Diese lokalen Effekte werden in dieser Studie nicht vollständig verstanden und regen an, die Elektroden-Elektrolyt-Grenzfläche mit anderen oberflächensensitiven Methoden wie Raman- und Infrarotspektroskopie unter *In-situ*-Bedingungen näher zu untersuchen.

Zu den künftigen Herausforderungen gehören schließlich die Anpassung der in dieser Arbeit entwickelten Synthesemethoden, um eine Herstellung von, mit Cu-Sn und Cu-S-Elektrokatalysatoren beladenen Gasdiffusionselektroden, zu ermöglichen. Die Untersuchung ihrer CO_2ER Aktivität in Gasdiffusionselektrolyseuren ist wichtig, um hohe Stromdichten damit, industriell relevante Umwandlungsraten zu erzielen, die für eine großtechnische Anwendung erforderlich sind.

Table of content

CHAPTER 1. Introduction **20**
1.1 Global society, environmental issues, greenhouse gases, CO_2 emission **20**
1.2. Capture and conversion of CO_2 ..... **25**
Capture of CO_2 26
Conversion of CO_2 27
1.3. Electrochemical conversion of CO_2 ..... **35**
Introduction to electrochemical reduction of CO_2 35
Intermediates and pathways in electrochemical reduction of CO_2 40
Challenges originating from the parameters and experimental conditions that affect the CO_2ER selectivity on Cu catalysts 45
Electrochemical rection of CO_2 into CO and HCOOH/$HCOO^-$, are these products valuable and which catalyst materials are optimal for this purpose? 58
Composition-structure-activity relations in CO and $HCOO^-$ selective Cu-Sn and $HCOO^-$ selective Cu-S electrocatalyst materials as topic of this thesis 59
CHAPTER 2. Methods section **61**
2.1. Methods for synthesis of the CO_2ER catalysts **61**
General description of the synthesis approaches 61
Preparation and subsequent anodization of Cu layers for synthesis of $Cu(OH)_2$ nanowires 61
Functionalization of the CuO_x nanowires with deposition of SnO_2 62
Dynamic H_2 bubble template electrodeposition for synthesis of Cu and Cu-Sn foams 63
Facile method for sulfidation of DHBT electrodeposited Cu foam 64
2.2. Characterization methods **65**
X-ray diffraction analysis (XRD) 66
Inductively coupled plasma-optical emission spectrometry (ICP-OES) 68
In-situ thermogravimetric analysis coupled with mass spectrometry (TGA-MS) and differential scanning calorimetry (DSC) 70
Electron microscopy (SEM and TEM), energy dispersive x-ray (EDX) spectroscopy and electron diffraction methods 71
X-ray fluorescence spectrometry (XRF) 73
X-ray photoelectron spectroscopy (XPS) 74
Ex-situ and in-situ x-ray absorption spectroscopy (XAS) 77
2.3. Electrochemical setups, experimental conditions and methods for qualitative and quantitative analysis of electrolysis products **81**
Gas chromatography for quantification of gaseous and volatile liquid products 83
Hight performance liquid chromatography (HPLC) 85
In-situ mass spectrometry coupled with electrolysis (EC-MS) 85
Estimation of the relative surface roughness factor (RSRF) 86
CHAPTER 3. Discussion of publications and manuscript included in the thesis **89**
3.1. General discussion of the electrochemical conversion of CO_2, and Cu-Sn and Cu-S electrocatalysts **89**
3.2. Composition-structure-activity relations in Cu-Sn catalysts **92**
3.3. Deriving CO selective Cu-Sn electrocatalyst from waste bronze alloy **105**

3.4. Composition-structure-activity relations in Cu-S electrocatalysts prepared via facile synthesis method.....110
CHAPTER 4. Determining structure-activity relationships in oxide derived Cu–Sn catalysts during CO_2 electroreduction using x-ray spectroscopy.....125
CHAPTER 5. Electrocatalyst derived from waste Cu-Sn bronze for CO_2 conversion into CO.....177
CHAPTER 6. Facile method for synthesis of Cu_xS catalysts and study of various effects on the selectivity for electrochemical conversion of CO_2 into formate.....234
CHAPTER 7. Outlook and future perspectives.....324
List of abbreviations in alphabetical order..... 329
List of published papers included in the thesis..... 332
Manuscript in preparation included in the thesis..... 333
List of publications from the Doctoral period that are not in the scope of the thesis..... 334
Curriculum Vitae..... 335
Bibliography.....345

Table of figures

Figure 1.1. Mean concentration of CO_2 in the time period between 1959 and 2021. The data used in the graph is credited to: Dr. Pieter Tans, NOAA/GML (https://gml.noaa.gov/ccgg/trends/) and Dr. Ralph Keeling, Scripps Institution of Oceanography (https://scrippsco2.ucsd.edu). 22
Figure 1.2. Schematic representation of water, oxygen, carbon and nitrogen cycles in nature. These cyclic processes do not occur in one direction or subsequently, but rather in both directions with interconnected mediums where water, oxygen, carbon and nitrogen are distributed. 23
Figure 1.3. Schematic representation of the CO_2 capture, conversion, storage and utilization technology concept. 25
Figure 1.4. Schematic representation of the CO_2 capture possibilities divided in three groups. 26
Figure 1.5. Schematic representation of the CO_2 conversion approaches. 28
Figure 1.6. Schematic representation of a strategy for closing the carbon cycle and achieving sustainable energy concept via CO_2 capture, its renewable energy driven electrochemical conversion to fuels and chemical feedstocks that can be either stored or subjected to immediate usage. Reproduced from Garg et al.[121] with permission from the Royal Society of Chemistry. 36
Figure 1.7. Schematic representation of typical setup (electrochemical cell) for electrochemical reduction of CO_2. The cathodic process is depicting the general CO_2ER process presented with **Equation 1.27**. More information regarding the actual electrochemical setups used in this work can be found in **Chapter 2**. 37
Figure 1.8. Modified periodic table of d and p block elements classified by their electrocatalytic selectivity towards H_2 from the HER and towards CO, HCOOH and products obtained via CO_2ER beyond CO. Reproduced with permission from Bagger et al.[146] – Copyright 2017 John Wiley and Sons Inc. (license number 5313691341868). 40
Figure 1.9. Binding energies of *H, *COOH and *OCHO intermediates on the elements that are highlighted in **Figure 1.8**: 3-D plot of *OCHO* vs. *COOH vs. *H **(a)**; *OCHO* vs. *COOH **(b)**; *COOH vs. *H **(c)** and *OCHO* vs. H* **(d)**. Reproduced with permission from Bagger et al.[146] – Copyright 2017 John Wiley and Sons Inc. (license number 5314711215146). 42
Figure 1.10. Binding energies of *H, *COOH and *OCHO intermediates on the surface of the elements that are highlighted in **Figure 1.8**: *CO vs. *H binding energy plot. Reproduced with permission from Bagger et al.[146] – Copyright 2017 John Wiley and Sons Inc. (license number 5313691341868). 43
Figure 1.11. Mechanistic CO_2ER and HER reaction pathways involving two and multi electron/H^+ steps. Black-carbon, red-oxygen and white-hydrogen spheres stand for atoms of the various reactants, intermediates and products in the CO_2ER/HER pathways, while the light blue spheres stand for the atoms from the surface of the electrocatalyst. Reprinted by permission from Springer Nature: Nature Energy, Birdja et al.[130] Copyright 2019. .. 44
Figure 1.12. Faradaic efficiency (current efficiency in the original publication) distribution of 15 CO_2ER products and H_2 in the range of applied potentials between −0.6 and −1.2 V vs. RHE on polycrystalline Cu catalyst. Reproduced from Kuhl et al.[123] with permission from the Royal Society of Chemistry. 47
Figure 1.13. Schematic representation of the parameters and conditions affecting the CO_2ER selectivity. Reprinted by permission from Springer Nature: Nature Energy, Birdja et al.[130] Copyright 2019. 48
Figure 1.14. Schematic representation of gas-diffusion electrode. The figure is reproduced from Luo et al.[159] This work is licensed under a Creative Commons Attribution 4.0 International license (CC-BY 4.0, credit to the authors). Link to license: https://creativecommons.org/licenses/by/4.0/ 51
Figure 1.15. Schematic representation of CO_2ER product distribution and reaction pathways on the surface of pure Cu and Cu-M electrocatalysts: pure Cu, CO_2ER into various products **(a)**; Cu-rich Cu-Sn(In), CO_2ER into CO **(b)**; Sn(In) rich/intermediate Cu-Sn(In) **(c)** and Cu-S **(d)** favoring CO_2ER into $HCOO^-$. Reproduced from Stojkovikj et al.[178] and edited via adding one more layer illustrating the Cu-S surface CO_2 to $HCOO^-$ conversion. This work is

licensed under a Creative Commons Attribution 4.0 International license (CC-BY 4.0, credit to the authors). Link to license: 57
Figure 2.1. Schematic presentation of the $Cu(OH)_2$ nanowires synthesis procedure via electrochemical anodization of Cu layers in alkaline environment (**Chapter 4**). 62
Figure 2.2. Schematic representation of the dehydration of $Cu(OH)_2$ to CuO and subsequent functionalization with thin layers of SnO_2 (**Chapter 4**). 63
Figure 2.3. Schematic representation of the DHBT electrodeposition of bimetallic Cu-Sn or pure Cu foams. M^{x+} represent Cu^{2+} or Sn^{2+}/Sn^{4+} cations. In the case of bimetallic Cu-Sn foam electrodeposition via transfer of these elements from waste bronze alloy, another identical bronze alloy electrode was used as an anode (**Chapter 5**), while in the case of pure Cu foam, high purity Cu foil anode was used instead (**Chapter 6**). 64
Figure 2.4. Schematic representation of the facile and fast method for sulfidation of the DHBT electrodeposited Cu foam via its immersion in sulfur/toluene solution (**Chapter 6**). 65
Figure 2.5. Schematic illustration of Bragg's law and the difference between Brag-Brentano and GI-XRD configuration. 68
Figure 2.6. Schematic representation of the ICP-OES technique and simplified principle on which it is based. ... 69
Figure 2.7. Schematic representation of the in-situ TGA-MS and DSC techniques. 71
Figure 2.8. Schematic representation of the interaction volume/simplified summary of electron-sample interactions as basis for the SEM/TEM and EDX techniques and example of FIB ablation of metallic foam/cross-section SEM for thickness estimation. 73
Figure 2.9. Photo of waste bronze anode used for DHBT electrodeposition of Cu-Sn foams (**Chapters 3** and **5**) and simple schematic representation of the fluorescence principle. The Cu and Sn bulk elemental distribution and quantification covering the whole area of the bronze anode was conducted via XRF spectrometry. 74
Figure 2.10. Schematic presentation of the quasi in-situ XPS approach. The electrolysis is conducted in a glovebox under inert conditions. After the electrolysis the electrocatalysts are transferred from the glovebox into the XPS analyzer via the sample transfer arm (vessel) under vacuum. This approach is beneficial for preservation of electrocatalysts' surface element(s) oxidation states. The H-type electrochemical cell is depicted in **Figure 2.14** and more information is provided in section 2.3 of this chapter. This setup was used for the research described in **Chapters 4** and **6**. 75
Figure 2.11. Schematic representation of x-rays interaction with the sample via photoelectron (left side) and Auger electron emission in the case of KL_1L_2 transition as an example (right side). During this transition an incident x-ray ejects electron from the K shell (secondary electron -SE) hence hole is being created **(a)**. This hole is filled with outer shell (L_1) electron accompanied with secondary photon emission **(b)**. The secondary photon has sufficient energy to eject another electron from outer shell (L_2) known as Auger electron creating second hole **(c)**. 76
Figure 2.12. Schematic representation of x-ray absorption and electron transitions for corresponding edges. 79
Figure 2.13. Schematic representation of the BESSY II synchrotron radiation source operated by Helmhotz-Zentrum Berlin GmbH, beamlines and end-stations for XAS measurements and experimental setups used in this research. 81
Figure 2.14. Schematic representation of the electrolysis experiment depicting the H-type electrochemical cell, WE - working electrode (electrocatalyst), RE - reference electrode, CE - counter electrode, cation exchange nafion membrane and product quantification using gas chromatography (GC) for the gaseous and volatile liquid products (headspace sampling) and high-performance liquid chromatography (HPLC) for the non-volatile liquid products ($HCOO^-$). Helium as a carrier gas and pulse discharge and flame ionization detectors (PDD and FID) were used in the GC setup. The HPLC operates with H_2SO_4(aq) as eluent and ultraviolet light detector. 82
Figure 2.15. Schematic representation of the in-situ EC-MS setup used for tracking of H_2S evolution as product from electroreduction of the Cu_xS catalysts. 86

Figure 2.16. Schematic representation of the electrode-electrolyte interface (double layer). The positive charges represent solvated cations with dipole molecules from the solvent. 88
Figure 3.1. Schematic illustration of the reaction pathways on the surface of pure Cu on which various CO_2ER products can be obtained **(a)**, Cu rich Cu-Sn favoring CO_2ER to CO **(b)**, Sn rich Cu-Sn **(c)** and Cu-S **(d)**, favoring CO_2ER into $HCOO^-$. 91
Figure 3.2. Schematic representation of the synthesis approach CuNW-Sn **(a)**, SEM images of CuNW-Sn15c **(b, c)**, Cross-section SEM of CuNW-Sn15c **(d)**, and GI-XRD patterns of as-prepared bare CuNW, CuNW-Sn15c and CuNW-Sn182c **(e)**. 93
Figure 3.3. CO_2ER activity results: Faradaic efficiency (FE) and total current density distribution of various products for bare and SnO_2 modified CuNW with various ALD cycles **(a)**, Partial current density distribution of various products on bare and SnO_2 modified CuNW with various ALD cycles **(b)**, FE and partial current density distribution of H_2, CO and $HCOO^-$ at various potentials on CuNW-Sn_{LOW} **(c)** and CuNW-Sn_{HIGH} electrocatalyst **(d)**. The electrocatalytic activity is studied in CO_2 saturated 0.1 mol·dm^{-3} $KHCO_3$(aq) as electrolyte. 95
Figure 3.4. Cu L **(a)** and Sn M **(b)** edge soft x-rays XAS spectra recorded ex-situ for: bare CuNW, CuNW-Sn_{LOW} and CuNW-Sn_{HIGH} under as-synthesized, pre-reduced with chronopotentiometry (CP) at –2 mA·cm^{-2} and 2 h CO_2 electrolysis conditions at –0.7 V. Additional Cu L and Sn M XAS spectra were recorded for Cu- **(c)** and Sn- **(d)** based reference materials, respectively. 97
Figure 3.5. Cu K edge XANES spectra of bare Cu NW, CuNW-Sn_{LOW}, CuNW-Sn_{HIGH} and reference materials, recorded ex-situ for the as-synthesized samples and reference materials and in-situ during the chronopotentiometry (CP) pre-reduction at fixed current density of –0.2 mA·cm^{-2} **(a)** and during CO_2 electrolysis at –0.1 V **(c)**. The CP pre-reduction time regions **(b)** are color coded with the XANES spectra presented on **(a)**. FT-EXAFS of bare Cu NW, CuNW-Sn_{LOW}, CuNW-Sn_{HIGH} and reference materials generated from EXAFS spectra **(d)**. The EXAFS spectra were recorded ex-situ for the as-prepared and reference materials and in-situ during CO_2 electrolysis at –0.1 V. The XANES and EXAFS spectra were collected at –0.1 V after decreasing the potential from –0.4 V due to noise caused by bubbles formation. 99
Figure 3.6. Sn K edge XANES spectra of CuNW-Sn_{LOW}, CuNW-Sn_{HIGH} and Sn reference materials, recorded ex-situ for the as-synthesized (AS) samples and reference materials and in-situ for the CuNW-Sn_{LOW} **(a)** and CuNW-Sn_{HIGH} **(b)** during CO_2 electrolysis in the range of applied potentials between –0.5 and –0.9 V. Linear combination (fitting) analysis (LCF or LCA) generated from the Sn K edge XANES spectra **(c)**. 101
Figure 3.7. Results from the quasi in-situ XPS quantification of the surface species in the as-synthesized (AS), and post-electrolysis CuNW-Sn_{LOW} **(a)** and CuNW-Sn_{HIGH} **(b)** samples. The CO_2 electrolysis was conducted in the range of potentials between –0.5 and –0.9 V. The highest FE for CO is obtained at –0.7 V on the CuNW-Sn_{LOW} corresponding to total Sn fraction of ~13 at.%, while the highest FE for $HCOO^-$ at –0.9 V, on the CuNW-Sn_{HIGH} electrocatalyst (total Sn fraction of ~70 at.%). 103
Figure 3.8. Schematic summary of the composition-speciation transformation results for the CO selective CuNW-Sn_{LOW} **(a)** and for the $HCOO^-$ selective CuNW-Sn_{HIGH} **(b)** electrocatalysts, at various potentials. 104
Figure 3.9. Schematic illustration of the electrochemical approach for deriving Cu-Sn foam catalyst from waste bronze alloy. The anodic processes resemble Cu and Sn oxidation into Cu^{2+} and Sn^{4+} and their dissolving in H_2SO_4(aq) as medium. The dissolved Cu and Sn are simultaneously electrodeposited on the cathode using HER generated H_2 bubbles as templates around which Cu-Sn foam microstructures are formed. Both anode and cathode (substrate) are made from the waste bronze. The surface compositions of the waste bronze ($Cu_{14}Sn$) and Cu-Sn foam ($Cu_{10}Sn$) are estimated from XPS. 106
Figure 3.10. GI-XRD patterns of Cu foil, Sn foil, waste bronze, Cu foam and Cu-Sn foam **(a)**. SEM images revealing the foam-like morphology that is composed of dendrite microstructures for Cu-Sn foam derived from bronze **(b, c)** and pure Cu foam derived from Cu foil **(d, e)**. 107

Figure 3.11. Faradaic efficiency (FE) and partial and total current density distribution for CO, H_2, $HCOO^-$ and C_2H_4 on waste bronze alloy **(a, b)** and Cu-Sn foam electrocatalyst **(c, d)** in the range of potentials between –0.5 and –1.0 V. The electrocatalytic activity for both materials, is studied in CO_2 saturated 0.1 mol·dm^{-3} $KHCO_3$(aq) as electrolyte. 108
Figure 3.12. Comparison of the faradaic efficiency (FE), partial and total current density distribution for CO, H_2, $HCOO^-$ and C_2H_4 on Cu and Sn foils, waste bronze alloy, pure Cu foam and Cu-Sn foam **(a, b)**, FE for CO and H_2 and total current density during 15 h continuous electrolysis at –0.8 V on the waste bronze derived Cu-Sn foam electrocatalyst **(c)**, SEM images of the Cu-Sn foam after 2 **(d, e)** and 15 h electrolysis **(f, g)**. The electrocatalytic activity is studied in CO_2 saturated 0.1 mol·dm^{-3} $KHCO_3$(aq) as electrolyte. 109
Figure 3.13. Schematic representation of dynamic hydrogen bubble template (DHBT) electrodeposition of Cu foam on Cu mesh as a substrate in a two-electrode setup. Cathode - Cu mesh, anode - Cu foil, duration of electrodeposition 9.5 s under geometric current density of 5 mA·cm^{-2}. 111
Figure 3.14. Schematic representation of the procedure for sulfidation of Cu foam. The Cu foam was subsequently immersed in each of the beakers under constant stirring and at room temperature, for amount of time presented in the scheme. The sulfidation is observable by instantaneous color change of the Cu foam from metallic Cu-like into bluish. 112
Figure 3.15. SEM images of pristine **(a)** and sulfidated Cu foam **(b)**. XRD patterns of pristine Cu foam, and sulfidated Cu foam, examined as-prepared and post-electrolysis **(c)**. D and R stand for Digenite ($Cu_{1.765}S$) and Roxbyite (Cu_7S_4) phases, respectively. The digenite is a major phase with fraction of ~70 wt.%. 113
Figure 3.16. Faradaic efficiency (FE) and total current density distribution for various products on $Cu_{1.8}S$/Cu foam **(a-c)** and pristine Cu foam **(d-f)**. The arrows show the direction of ramping the applied potential i.e., ramping in less negative direction (RLN) from –0.9 to –0.5 V vs. RHE **(a, d)** and ramping in more negative direction (RMN) from –0.5 to –0.9 V vs. RHE **(b, e)**. During altering in both directions, each applied potential was kept constant for 1 h. The solid line on **(c, f)** represent the total current density when altering the potential in RLN, while the dotted line - in RMN direction. The electrocatalytic activity is studied in CO_2 saturated 0.1 mol·dm^{-3} $KHCO_3$(aq) as electrolyte. 114
Figure 3.17. In-situ EC-MS tracking of the H_2S evolution from $Cu_{1.8}S$/Cu foam electrocatalysts via altering the applied potential in RLN direction (–0.9 to –0.5 V). Potential (E) in linear sweep voltammetry (LSV) and chronoamperometry (CA) modes **(a)** and mass vs. charge signal (m/z) of various species **(b)** plotted vs. time. Each applied potential was kept constant for 30 min. The tracking of the H_2S evolution is studied in CO_2 saturated 0.1 mol·dm^{-3} $KHCO_3$(aq) as electrolyte. 116
Figure 3.18. In-situ EC-MS tracking of the H_2S evolution on $Cu_{1.8}S$/Cu foam electrocatalysts via altering the applied potential in RMN direction (–0.5 to –0.5 9). Potential (E) in linear sweep voltammetry (LSV) and chronoamperometry (CA) modes **(a)** and mass signal vs. charge (m/z) of various species **(b)** plotted vs. time. Each applied potential was kept constant for 30 min. The tracking of the H_2S evolution is studied in CO_2 saturated 0.1 mol·dm^{-3} $KHCO_3$(aq) as electrolyte. 117
Figure 3.19. Comparison of the electrocatalytic activity for all examined catalyst materials: FE distribution of various products and total current density at –0.9 V **(a, b)** and at –0.7 V **(c, d)**. The electrocatalytic activity is studied in CO_2 saturated 0.1 mol·dm^{-3} $KHCO_3$(aq) as electrolyte. 119
Figure 3.20. Post-electrolysis results from the inductively coupled plasma – optical emission spectrometry (ICP-OES) analysis of the concentration of sulfur in the electrolyte under various conditions. 120
Figure 3.21. Quasi in-situ XPS quantification results: Surface fractions of various Cu species obtained from the Cu $L_3M_{4,5}M_{4,5}$ Auger spectra **(a)** and of total Cu and S^{2-}/SO_4^{2-} surface species obtained from Cu 2p and S 2p core levels spectra, respectively **(b)**. In the case of the $Cu_{1.8}S$/Cu foam-inert sample, it was not possible to quantify the fraction of the SO_4^{2-} surface due to high noisiness in the S 2p spectra (data showed in **Chapter 6**). 121

Figure 3.22. Summary of the composition-structure-activity relations in the Cu-S electrocatalyst materials and conclusion of the research and findings in this study. 123

CHAPTER 1. Introduction

1.1 Global society, environmental issues, greenhouse gases, CO_2 emission

The rapid and comprehensive scientific, technological, educational, economic, social, cultural and political development of the global society since the start of the Industrial revolution, have caused various benefits for the human population thus leading to economic progress and substantial improvement of average quality and quantity of life. For example, the human population and average lifetime have increased, the standard and comfort of life have dramatically improved, many diseases have been eradicated or controlled, literacy have increased, geographical distances became relative with the new means of transport, society became globalized, interconnected etc. All of this is based on, and therefore can be described with, one simple chemical equation representing the process of combustion of organic material (**Equation 1.1**), for producing most of the energy demanded for the aforementioned achievements and benefits. The human society did know how to burn wood for ~1 million years, maybe even more, but it was from the invention of the steam machine that we learned how to utilize the energy more efficiently and thus besides using it only for heating, we learned how to convert the thermal energy to mechanical, then electrical… and that is how our modern society started.

Equation 1.1: $C_xH_yO_z + (x + {}^{y}/_{4} - {}^{z}/_{2})O_2 \rightarrow xCO_2 + {}^{y}/_{2}H_2O$ + energy (heat)

Various technological, economic, social and many others information and statistics regarding the direct or indirect effects of the continuous development in different aspects of the human society can be found elsewhere.[1-12] We ourselves are witnessing the rapid technological development especially in the last 20-30 years with the massive expansion of the electronic devices and the internet for example, or even in a more short-term period of ~2 years since the start of the Covid 19 pandemic when we have swiftly learned and managed to transform many of our daily activities on-line.[13, 14] All of this would have not happened without the start of the Industrial revolution that paved the way towards the development from which large part of the human population is able to benefit nowadays. However, these anthropogenic activities associated with the massive development of the human society in the last ~250 years have generated tremendous changes that affect every pore of the environment of our planet. Namely, the global industrialization has caused continuous increase in the energy demand,[9, 15-18] enormous extraction of minerals[12, 19-24] and fossil fuels (coal, oil, gas etc.)[16, 24-26] from Earth's crust utilized for of various industrial, energy, transport, livestock and other purposes,

consequently leading to emissions of various waste substances in the environment.[12, 27, 28] Moreover, the construction of homes and various large infrastructures and facilities and the extraction and processing of materials needed to do so, according to the human civilisation requirements, besides waste emission, have affected the landscape, biodiversity etc.,[29-32] thus irrevocably impacting various ecosystems. Furthermore, the environmental impact caused by the global conflicts,[33] closely connected to the technological development should not be neglected. With other words, we evolved as humans in both positive and negative direction. We did, and still attempting to improve our life, but `we paid`, `still paying` and in future `will have to pay the price` of the massive damage caused to the environment i.e., ecosystem in which we live, since the natural recovery is a long-term process. The global waste emissions in our environment per year are calculated in hundreds of millions up to a billion tons,[27] from which around 3-60% of solid waste for various countries is recycled.[34, 35] A rising issue of concern are the chemical elements with risk of supply in the future due to their either low abundance and/or enormous extraction for various purposes.[19-23] An example is the sudden increase of lithium extraction used for production of batteries due to the higher demand and policies for transition towards electric vehicles.[36, 37] Large and rather very significant fraction of the waste emissions are the pollutants emitted in the atmosphere. Among them, the major concern are the hazardous substances with acute, relatively short or mid-term health effects like various aromatic, heterocyclic, polycyclic, and halogenated hydrocarbons, HCHO, SO_2, SO_3, lower-atmosphere O_3, NO_x, CO, heavy metals (Pb, Ni, Mn, Cd, Hg, Cr) and their compounds, microparticulate matter (PM_{10} and $PM_{2.5}$), nanoparticles, asbestos, various forms of dust, radioactive isotopes, etc.[38-41] Some of these pollutants (halogenated hydrocarbons, N_2O, O_3) together with CO_2, CH_4, water vapor, well-known as greenhouse gases,[26, 40, 42, 43] have serious and already threatening effects on our environment. These gases are responsible for the `greenhouse phenomenon`,[40, 44-49] that causes increase of the average temperature on our planet (global warming or climate change[42, 43, 47]), thus leading to heating of oceans, melting of snow, ice, glaciers and permafrost in the polar and subpolar regions and ultimately rise of the sea level. Some statistics show that the average temperature increased >1 °C since the pre-industrial era,[50] and that ~2 billion tons of ice are melted per day contributing to the rise of sea level to almost 27 cm net value since 1900.[12] Among the greenhouse gases, CO_2 is the targeted one since it represents the highest fraction (~65%) of the total greenhouse gas emissions in the atmosphere[26, 51] and moreover due to its thermal radiation absorption nature. Namely, it should be noted that water vapor is the most potent greenhouse substance because its infrared light absorption bands cover very broad range of the thermal radiation spectra, with two major transparency windows, one between ~3 and ~5 the other between ~7 and ~20 μm.[52] Unfortunately, the CO_2 infrared light absorption bands, one centered at ~4.5 and the broadest one at ~15 μm are matching certain parts of these water vapor transparency windows.[52] Hence,

the synergy between the highest abundance of CO_2 in the emitted greenhouse gases and its infrared light absorption nature is effectively preventing the transmission of Earth's thermal radiation into space. On the other hand, the molecules of the major atmosphere components, N_2 and O_2 do not have dipole moments thus being transparent for infrared light.[52] The CO_2 emissions are continuously increasing,[50] since the start of the industrial revolution, thus the concentration of this gas in the atmosphere has reached ~420 ppm in 2022.[53] **Figure 1.1** shows the increase in the atmospheric concentration of CO_2 in the time period between 1959 and 2021. According to some statistics, more than 100 million tons of anthropogenic CO_2 are emitted on a daily basis,[12] mainly originating from fossil fuels combustion and industrial processes. Regarding the industrial processes, besides the energy production required for the industry itself, CO_2 is also emitted as a by-product from process chemical reactions during the production of steel, aluminium, cement, ammonia, polymers etc.[54, 55]

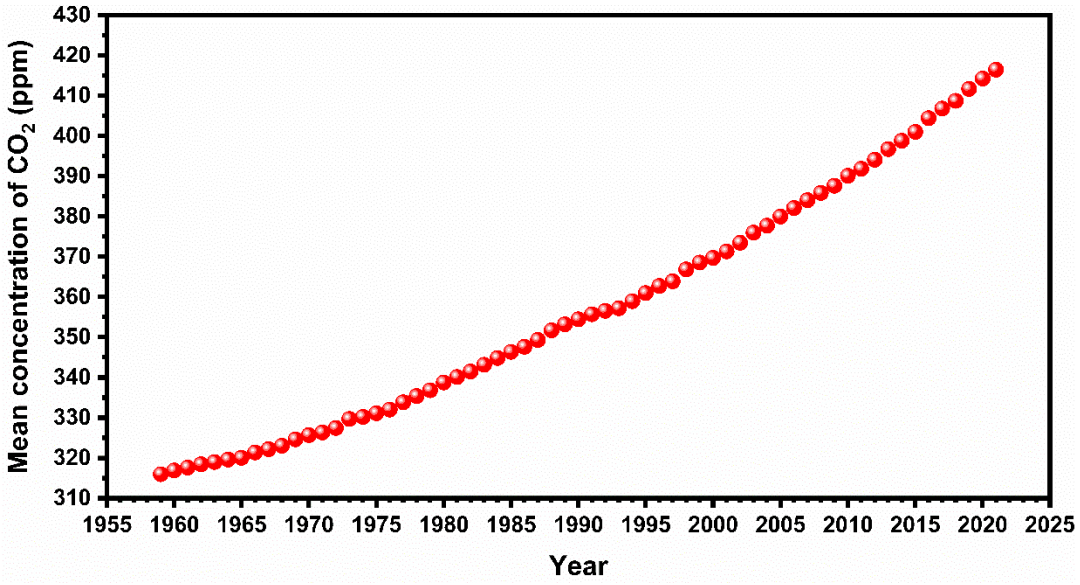

Figure 1.1. Mean concentration of CO_2 in the time period between 1959 and 2021. The data used in the graph is credited to: Dr. Pieter Tans, NOAA/GML (https://gml.noaa.gov/ccgg/trends/) and Dr. Ralph Keeling, Scripps Institution of Oceanography (https://scrippsco2.ucsd.edu).

Water, oxygen, carbon, nitrogen cycles encompass main cyclic processes in nature (**Figure 1.2**) via various chemical reactions, transport and distribution between the gaseous, liquid and solid part of our planet i.e., the atmosphere, oceans/seas/rivers/ice on the south and north pole and soil/inner crust of the Earth. These cyclic processes are known as biogeochemical cycles.[56, 57] These cyclic processes are relatively slow and were relatively under equilibrium i.e., steady-state condition in the pre-industrial era. The natural balance of the carbon cycle has been seriously distorted via the anthropogenic activities such as the

aforementioned extraction of fossil fuels from Earth's crust, their combustion and emissions of CO_2 in the atmosphere,[58] on a far faster timescale than the accumulation of the fossil carbon over millions of years. These anthropogenic distortions have led to the aforementioned increase of the CO_2 concentration in the atmosphere (**Figure 1.1**), even though the process of photosynthesis (discussed in the next section - 1.2.) together with many other processes, as part of this cycle have the capacity to achieve fixation of significantly higher amount of CO_2 compared to the anthropogenic emissions.[54, 59]

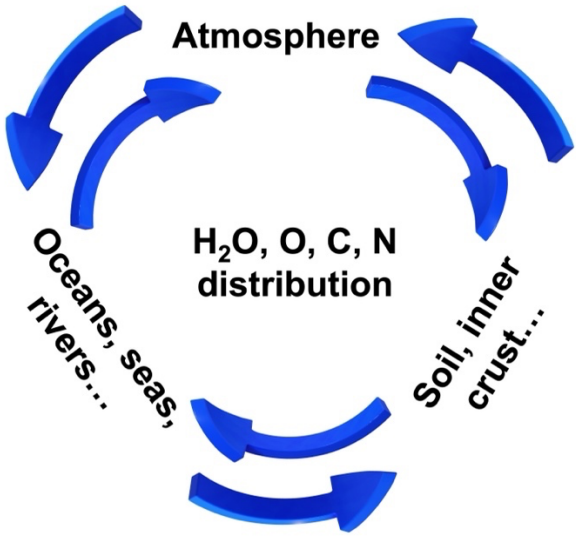

Figure 1.2. Schematic representation of water, oxygen, carbon and nitrogen cycles in nature. These cyclic processes do not occur in one direction or subsequently, but rather in both directions with interconnected mediums where water, oxygen, carbon and nitrogen are distributed.

However, the CO_2 emission/fixation processes as part of the carbon cycle are not that simple.[58, 60, 61] Namely, the photosynthesis processes do not occur throughout 24 hours since they need sunlight, also not during all seasons of the year, for example during the cold months of the year some threes do not have leaves, the photosynthesis capable organisms (phototrophs) are not equally distributed on the Earth's surface and these organisms also emit CO_2 during in the process of cellular respiration.[60, 61] Furthermore, the continuous deforestation for providing land fields for agricultural and other purposes already destroyed large part of the rain forests,[62] thus under the current circumstances it is predicted that they will disappear in approximately 80 years,[12] therefore affecting Earth's photosynthesis capacity.

Since the anthropogenic CO_2 emissions and their environmental impact on our planet have been caused by the anthropogenic activities, it is a `right approach` that they should be solved by the humans. The results from the vast scientific research efforts over several decades regarding the significance and negative effects of the greenhouse gas emissions

causing global warming and the massive exploitation of the natural resources have provided various potential solutions for tackling these issues.[42-45, 54, 55, 63-66] In a simple manner the ideal concept for solving these problems is achieving nett zero anthropogenic CO_2 emissions,[55, 63, 64, 67] and ideally bringing down the concentration of this gas in the atmosphere to the preindustrial levels. In order to accomplish these goals, besides mitigation of the emissions via transition from fossil fuels to renewable energy production, the utilization of renewable energy driven technologies based on CO_2 capture and conversion into valuable products are highly demandable. The simple reasons for this are that, besides as fuels, the fossil oil and natural gas are also used as feedstocks in the petrochemical, chemical, pharmaceutical industry etc. and additionally, as previously mentioned, there are other important industrial processes where CO_2 is a byproduct,[54, 55] and for which it is very challenging to find alternatives in the near future. Therefore, capturing CO_2 from point sources (cement, ammonia, fertilizers or metallurgical industry…) and atmosphere and then subsequently converting it, in the best case on-site, into chemicals that can be used as feedstocks and fuels is of great importance. The approaches and processes regarding CO_2 capture and conversion will be more thoroughly discussed in the next section of this chapter (1.2.). However, this concept will not be completely achieved without recycling the waste materials to minimize and ultimately terminate the extraction of natural resources thus achieving sustainable energy and resources circulation.[68-70] The efforts for mitigation of greenhouse gas emissions and complete transition of the human society towards full utilization of renewable energies and recycling of waste materials would most probably symbolize the 21th century. This is a global necessity that affects everyone on the planet Earth, thus the involvement of various sectors of the society is of high significance. We are witnessing promising examples of the already implemented measures via adopting national and international policies, regulations and agreements.[42, 43, 55, 71] These examples include limitations of the CO_2 emissions from industry and transport,[72] increase in the utilization of solar, wind, hydropower and other renewable energy sources,[73, 74] transitioning towards use of electric vehicles,[37] implementation of CO_2 taxes,[75] increased recycling of waste materials,[35, 69] providing more funding for research and development of alternative carbon neutral technologies etc. Furthermore, the most important policies are achieving net zero CO_2 emissions to keep the average temperature increase below 1.5-2 °C,[43, 55, 63, 64, 67] and targeting >50% average waste reutilization by 2050.[69] Unfortunately, it is still uncertain and debatable whether the 2050 goals are achievable in reality,[64, 67] yet the human society has consciousness and is aware that there is no alternative planet.

1.2. Capture and conversion of CO_2

In order to tackle the global warming and climate change issues caused by the continuous increase of the average CO_2 concentration in the atmosphere, besides policy-based limitation of the emissions, efficient CO_2 capture, storage and conversion technologies,* are required.[63, 65, 76-79] As briefly mentioned in the previous section of this chapter (1.1.), these technologies include capture of CO_2[63, 65, 76-81] from the atmosphere and from industrial process that produce this gas as a byproduct,[54, 55, 79] and for which there are not so many promising alternatives to be implemented in the near future. The captured CO_2 could be either stored or directly converted into existing industry/transport required valuable products such as chemical feedstocks and fuels,[48, 82] via integrated capture-conversion-utilization-storage systems.[63, 65, 77-79] Thus, these products could be immediately utilized on-site or be stored until their usage in the industry is required. A simple illustration of the CO_2 capture, storage, conversion and utilization technology concept is depicted in **Figure 1.3**.

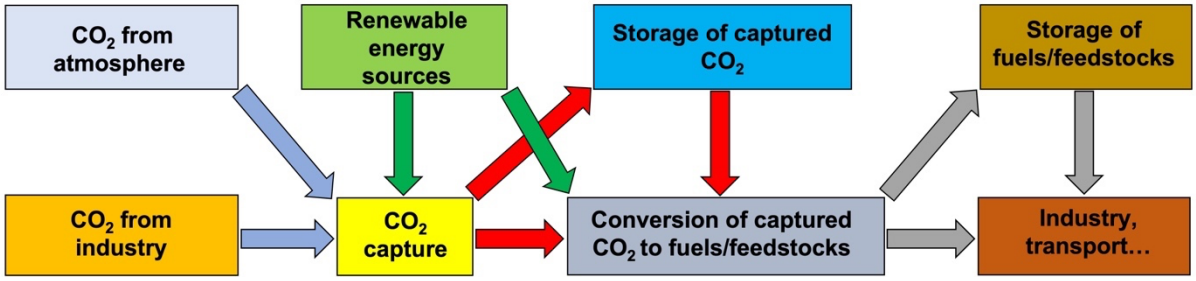

Figure 1.3. Schematic representation of the CO_2 capture, conversion, storage and utilization technology concept.

* Regarding these concepts, it is useful to note that in the literature the terms *capture*, and/or *storage* are sometimes referred to *sequestration*, and some of the capture processes involve chemical reactions, thus CO_2 undergoes chemical conversion. The purpose of such conversion is for capturing and subsequent storage purposes and not a conversion to final CO_2 derived products to be further utilized as fuels or feedstock chemicals. Moreover, sometimes in the literature all three terms *capture*, *storage* and *conversion* can be referred to *sequestration* and so on… None of this is wrong and there are precise definitions as to which concepts involve which approaches e.g., in terms of long or short term efficiency etc., but in order to avoid confusion, in this thesis the process of *capture* refers to `taking` the CO_2 from the atmosphere or from point sources, *storage* refers to storing the physically or chemically captured CO_2 and *conversion* refers to the chemical processes where CO_2 is transformed into products that can be either stored or further utilized as fuels or feedstock chemicals.

Capture of CO_2

Regarding the CO_2 capture possibilities and approaches, various literature sources use similar or different ways for their classification,[65, 77-80] however they can simply be classified into three groups as physical, physico-chemical and chemical (or inorganic reactions based) methods (**Figure 1.4**). The simplest physical methods involve CO_2 capture from the atmosphere and from CO_2 rich flue gases from industrial point sources via its absorption or dissolving into various organic solvents such as alcohols, ethers, etc.[63, 65, 77] Among the physico-chemical methods literature sources report processes based on CO_2 adsorption or chemisorption. CO_2 adsorption approaches involve using porous materials with high active surface area such as molecular sieves, activated carbon, carbon nanomaterials, metal organic frameworks (MOF) and various polymers whereas chemisorption approaches use amines, ammonia, amino acid salts, ionic liquids, aminosilanes, lactams etc.[65, 76-78, 80, 83] The group of chemical capture methods encompasses inorganic carbonation reactions between CO_2 and alkaline or alkaline earth metal oxides, hydroxides and salts to form metal carbonates, and even possibilities for mineralization of compressed or supercritical CO_2 transported at the bottom of oceans. [65, 77, 78, 81]

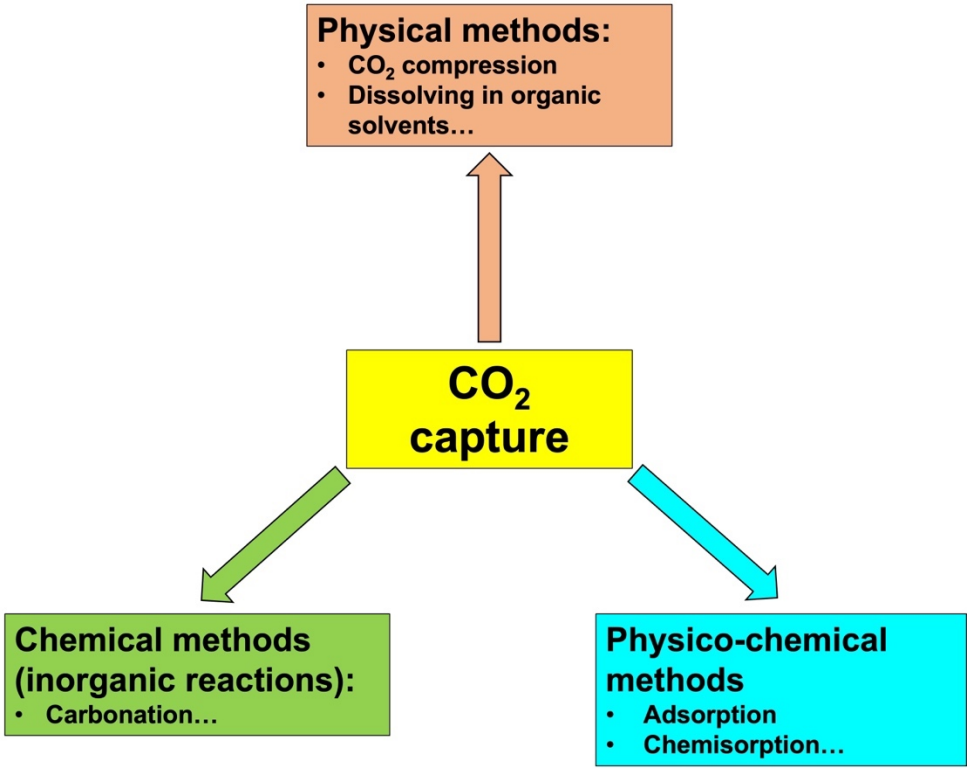

Figure 1.4. Schematic representation of the CO_2 capture possibilities divided in three groups.

However, besides CO_2 the flue gases contain many other components such as dust particles, CO, water vapor, NO_x, SO_2 etc.[84, 85] Therefore, CO_2 purification or separation from the other components is necessary. The purification or separation processes are an integrated part in all capture approaches when flue gases are used as source of CO_2. These methods are based on purification of the flue gases before or after the process of combustion or pre-processing the fuel/oxidant mixture thus CO_2 with decent purity will be emitted.[65, 77, 78] Moreover, there are research efforts in developing technologies based on fuel combustion using solid oxidizers instead of air (chemical loop combustion).[65, 77, 78] The pre-combustion fuel reprocessing involves partial oxidation of carbon (gasification) or hydrocarbons generating syngas (mixture of H_2 and CO), based on approaches for industrial production of H_2[86-88] presented with **Equations 1.25** and **1.26**, and discussed later in the CO_2 conversion subsection. Complete combustion of syngas produces CO_2 and water vapor which can be relatively easily separated. Another pre-combustion method involves enriching the fuel/oxidant mixture with pure O_2[65, 77] for the same purpose of complete fuel combustion. The post combustion purification methods are based on physical filtration or electrostatic charge assisted removal of the physical impurities such as dust particles,[85] and subsequent CO_2 separation via selective gas permeable membranes, cryogenic distillation etc.[65, 77, 78] Direct capture of CO_2 from air requires processing of huge amounts of ambient air in order to achieve considerable efficiency for CO_2 removal, having in mind that the average atmospheric concentration of this gas is around 420 ppm.[53] These processes involve the already discussed absorption, chemisorption or carbonation approaches.[65, 76-78, 81] Various information can be found in the literature regarding progress, perspectives, commercialization and technology readiness levels of different CO_2 capture systems,[63, 65, 76-81, 89] yet many more efforts are required for their massive industrial scale application. The CO_2 purification/separation, capture methods and processes of CO_2 recovery prior to conversion are energy demanding, and according to the sustainable energy requirements[68-70] this energy should be provided from renewable sources[73, 74, 79] as illustrated in **Figure 1.3**. The methods for CO_2 capture, and later in this section CO_2 conversion mimic the natural carbon cycle on our planet (**Figure 1.2**) i.e., redistributing the carbon from the atmosphere or waste gas emissions via its capture and subsequent storage to be further converted into valuable products.

Conversion of CO_2

As stated in the previous subsection the concepts of CO_2 capture and conversion mimic the natural carbon cycle. The processes of CO_2 conversion represent chemical reactions which fundamentally can be described as reversing the organic material combustion reaction

presented with **Equation 1.1**. Carbon in the CO_2 molecule is in its highest oxidation state and bound to the electronegative O atom thus, this compound is thermodynamically ($\Delta_f G^\circ$ = −394.4 kJ·mol^{-1} at 25 °C) and kinetically stable,[54, 86, 90, 91] Therefore, subjecting this molecule in chemical reactions is energy demanding, particularly for formation of the reactive *CO_2 intermediates ($CO_2^{\bullet -}$, *COOH and *OCHO* - that are discussed later) and this energy should be provided from renewable sources for achieving an energy sustainable society.[68-70, 79]

The CO_2 conversion approaches, or concepts can be simply divided in several groups based on chemical conversion (carbonation), photocatalysis, photoelectrocatalysis (photoelectrochemical reduction), electrocatalysis (electrochemical reduction), thermochemical catalysis, homogeneous catalysis and biochemical (non-photosynthesis) conversion, as depicted in **Figure 1.5**.

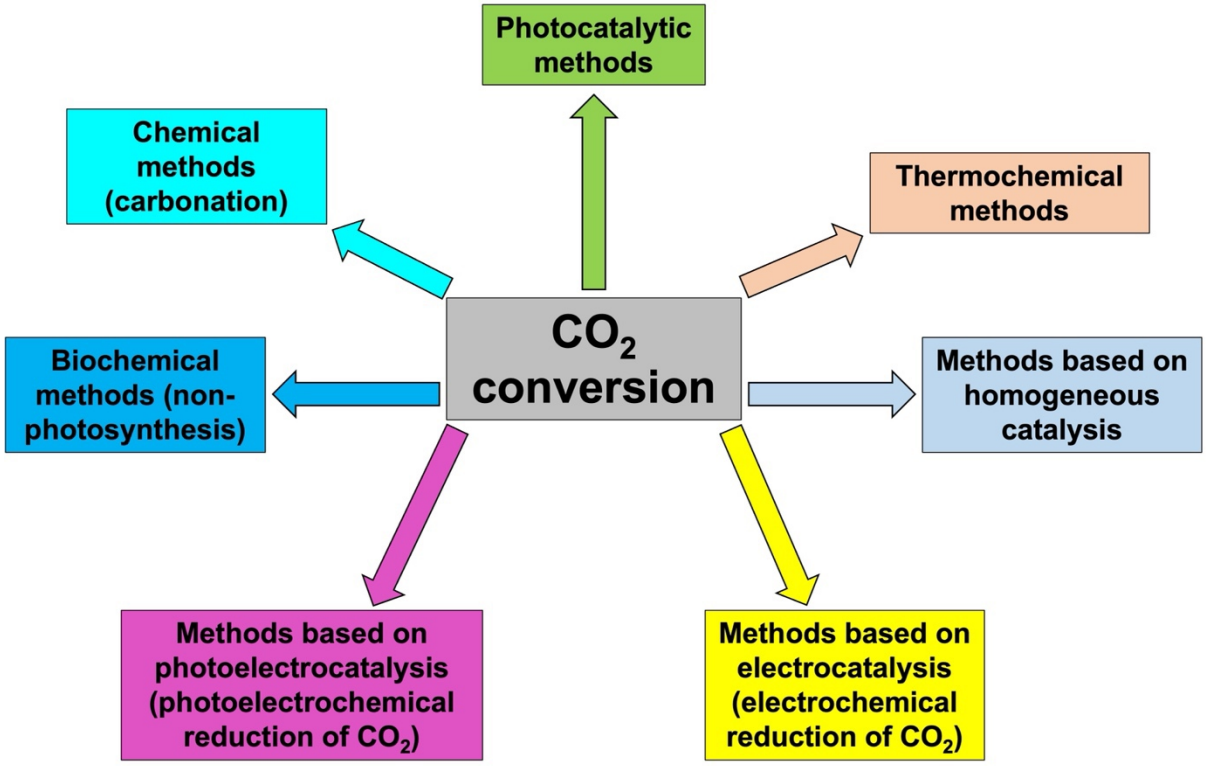

Figure 1.5. Schematic representation of the CO_2 conversion approaches.

Chemical methods for CO_2 conversion

The chemical methods based on inorganic carbonation reactions between CO_2 and alkaline (K and Na) or alkaline earth (Ca and Mg) metal hydroxides to form metal (hydrogen)carbonates, as presented with **Equations 1.2-1.9** are the simplest and most basic ones for CO_2 conversion. These reactions are a part of the natural CO_2 mineralization process

in the carbon cycle,[65, 77, 78, 81] and as mentioned before, they find application in direct capture of CO_2 from air in integrated CO_2 capture-conversion-storage methodologies.[65, 76-78, 81]

Equation 1.2: $KOH + CO_2 \rightleftarrows KHCO_3$
Equation 1.3: $2KOH + CO_2 \rightleftarrows K_2CO_3 + H_2O$

Equation 1.4: $NaOH + CO_2 \rightleftarrows NaHCO_3$
Equation 1.5: $2NaOH + CO_2 \rightleftarrows Na_2CO_3 + H_2O$

Equation 1.6: $Ca(OH)_2 + 2CO_2 \rightleftarrows Ca(HCO_3)_2$
Equation 1.7: $Ca(OH)_2 + CO_2 \rightleftarrows CaCO_3 + H_2O$

Equation 1.8: $Mg(OH)_2 + 2CO_2 \rightleftarrows Mg(HCO_3)_2$
Equation 1.9: $Mg(OH)_2 + CO_2 \rightleftarrows MgCO_3 + H_2O$

Photocatalytic CO_2 conversion

The next group of CO_2 conversion methods to be discussed are the ones based on photocatalytical processes. It can be expected that this discussion will start with one of the most important parts of the natural carbon cycle i.e., the process of photosynthesis.[44, 59, 92-95] Photosynthesis can be defined as the process that is responsible for converting solar into chemical energy stored in various organic compounds such as basic carbohydrates - $(CH_2O)_n$, for example glucose ($C_6H_{12}O_6$). Some of these basic carbohydrates undergo further conversion into polysaccharides, proteins, lipids and other chemical energy carriers via various biochemical processes. The carbohydrates and the other substances produced from them are the basic source of nutrition in the ecosystem's food chain i.e., their biochemical conversion leads to energy production that is essential for all vital functions in the living organisms from the simplest to the most complex ones. The photosynthesis process that can be generally described with **Equation 1.10**, occurs in the cells of the phototropic organisms (plants, threes, algae, cyanobacteria etc.) via two coupled processes. In the first process, photon is adsorbed by the chlorophyl or other chromophores that are part of the photosystems in these organisms hence, reduction of the $NADP^{+}$[†] and ADP[‡] occurs accompanied by a water splitting reaction leading to production of the energy carriers NADPH[§] and ATP[**] and additionally evolution of O_2 as a by-product.[44, 95] The seconds step, known as the Calvin cycle,[44, 59, 96] occurs in absence

[†] $NADP^{+}$: nicotinamide adenine dinucleotide phosphate in oxidized form.
[‡] ADP: adenosine diphosphate.
[§] NADPH: nicotinamide adenine dinucleotide phosphate in reduced form.
[**] ATP: adenosine triphosphate.

of light i.e., dark mode. These processes involve CO_2 reduction by the NADPH and ATP, synthesized in the first photocatalytic step, producing carbohydrates, ADP and $NADP^+$. The ADP and $NADP^+$ are then reutilized in the first step.

Equation 1.10: $nCO_2 + nH_2O + h \cdot \nu \rightarrow (CH_2O)_n + nO_2$ Photosynthesis – general equation

Nevertheless, as already mentioned, the photosynthesis process produces O_2 that through the cellular respiration processes,[97, 98] is stipulating the life conditions for many living organisms including the human beings. Cellular respiration is a reverse process of the photosynthesis where the energy carriers undergo oxidation accompanied with release of the stored energy and CO_2 production. In the case of phototropic organisms this happens in the absence of sunlight i.e., during the night. The photosynthesis and cellular respiration, coupled with various other biochemical processes responsible for all vital functions in the living organisms, are more complex and possibly not fully understood by the scientific communities, than how they are explained in this paragraph. Hence, for simplicity purposes, these processes are presented as general as possible. More information regarding the photosynthesis, cellular respiration and other conjugated biochemical processes can be found elsewhere.[59, 92-98] It is useful to be mentioned again that the natural photosynthesis has the capacity for converting higher amount of CO_2 than the anthropogenic emissions,[54, 59] yet the CO_2 concentrations in the atmosphere are continuously rising[53] due to several factors:[60, 61] day/night, year seasons and geographical location availability of sunlight, non-equal distribution of the phototrophs, continuous deforestation, agricultural activities etc. Therefore, a possible solution is indeed utilization of bigger land area for growing plants that can capture and convert CO_2 into biomass and its subsequent conversion via fermentation into CH_4, alcohols etc.[54, 63, 77, 78] that are valuable as biofuels and feedstock chemicals for industrial and transport purposes. However, with the rising population on our planet,[5, 10] it seems more reasonable to utilize vast land areas for production of food, than for fuels and industrial feedstocks.[54] Therefore, the research and development focus is rather placed on developing different concepts for CO_2 conversion in which there is no requirement for occupying large areas of land tentative to the food production requirements.

Regarding synthetic photocatalytic processes for CO_2 conversion, there is certain research progress thus various photocatalysts are proposed for CO_2 conversion into CO, syngas, CH_4, CH_3OH, HCHO, organic acids such as HCOOH and CH_3COOH etc. under ultraviolet or visible light irradiation.[44, 99, 100] The photocatalyst materials used for this purpose are based on semiconductors such as metallic oxides, sulfides, complex compounds etc.[44, 99, 101] When a photocatalyst is irradiated with light, an internal photoelectric effect occurs i.e., an electron is being excited from the valence (VB) into the conduction band (CB).[44, 90, 99-101] The

energy of the photon must be at least equal to, or higher than, the energy of the bandgap (the energy difference between the CB and VB).[90, 100, 101] This process results in a formation of electron(e^-)-hole(h^+) pair,[44, 90, 99-101] as described with **Equation 1.11**. Therefore, the photogenerated electrons can reduce the CO_2 molecule into CO, for example[99, 100] (**Equation 1.12**) and additionally reduce H^+ into H_2 as a competitive hydrogen evolution reaction (HER) in aqueous system (**Equation 1.13**),[90] while the photogenerated holes can cause oxidation of e.g., water, as a counter reaction[99, 100] (**Equation 1.14**). The overall reaction resembles CO_2 conversion combined with water splitting which can be defined as artificial photosynthesis.[79]

Equation 1.11: Photocatalyst + $h \cdot \nu \rightarrow e^- + h^+$

Equation 1.12: $CO_2 + 2H^+ + 2e^- \rightarrow CO + 2H_2O$ $\quad E^{\circ}_{vs.\ RHE} = -0.10$ V[54]

Equation 1.13: $2H^+ + 2e^- \rightarrow H_2$

Equation 1.14: $2H_2O \rightarrow 4H^+ + O_2 + 4e^-$ $\quad E^{\circ}_{vs.\ SHE} = +1.23$ V[54]

Photoelectrocatalytic (photoelectrochemical) CO_2 conversion

If system consisting of a semiconductor working electrode and a metallic counter electrode is immersed in an electrolyte and the semiconductor is irradiated with light, the photogenerated electrons (holes) migrate in opposite directions thus drive the reduction (oxidation) reaction on the working electrode while the counter reaction will occur on the counter electrode.[100, 101] This concept is referred to photoelectrocatalysis,[44, 100] and in the case when the intention is to convert CO_2 into product it is referred to photoelectrocatalytic or photoelectrochemical conversion of CO_2. Depending on the nature of the semiconductor it can act as a photocathode thus the CO_2 reduction process will occur on this electrode while the oxidation process on the counter electrode or vice versa in the case when the semiconductor has a role of photoanode. Another possibility is to construct a system where two photoelectrodes are immersed in electrolyte from which simultaneously on the first one, the photogenerated electrons will drive the reduction, while on the second one the holes will drive the oxidation reaction. In this case a bridging or mediator redox couple is required to consume the holes from the photocathode and the electrons from the photoanode.[44, 101] Both photocatalytic and photoelectrocatalytic CO_2 conversion approaches share the same concept as the natural photosynthesis, but since this process is conducted synthetically it can be referred to artificial photosynthesis. When instead of irradiation with light, the energy for driving the CO_2 conversion is provided by electricity, the concept refers to electrochemical conversion of CO_2 which is in the scope of this thesis and will be discussed thoroughly in the next section of this chapter (1.3.). Basic thermodynamical and kinetical requirements for driving the

photocatalytic or photoelectrocatalytic reactions is the bandgap energy of the semiconductor.[44, 90, 100, 101] Namely, the bandgap must be sufficiently large so that the standard equilibrium potentials for both CO_2 reduction (**Equation 1.12**) and water oxidation (**Equation 1.14**), or any other oxidation counter reaction process, fall in this range. Or with another explanation, the CB should be above the standard equilibrium potential for the formation of $CO_2^{\bullet -}$ radical anion (**Equation 1.15**) as the first reduction single-electron step and the VB to be below the standard equilibrium potential for the oxidation reaction.[44, 90, 100, 101] This can be solved using the aforementioned two photoelectrodes approach when one is typically involved in CO_2 reduction and the other one in oxidation process.[44] The formation and further transformation of the $CO_2^{\bullet -}$ radical anion and other intermediate species (*COOH and *OCHO*) into products is further discussed in the paragraph for thermocatalytic CO_2 conversion in this section and additionally in section 1.3 of this chapter, dedicated to the electrochemical conversion of CO_2.

Equation 1.15: $CO_2 + e^- \rightleftarrows CO_2^{\bullet -}$ radical anion $E^{\circ}_{vs.\ SHE} = -1.9$ V[44]

There are many other parameters affecting the semiconductor properties and consequently, the kinetics and thermodynamics of the reactions driven by light. Hence, more information regarding the photocatalytical and photoelectrocatalytical CO_2 conversion methods and research efforts in these fields can be found in the literature.[44, 68, 79, 90, 99-104]

Biochemical methods for CO_2 conversion

In this paragraph the non-photosynthetic biochemical CO_2 conversion methods are briefly discussed. These methods are based on complex enzymatic processes that involve CO_2 conversion in heterotrophic aerobic or anaerobic microorganisms.[105, 106] Some of these microorganisms are able to convert CO_2 into CH_4 and such non-photosynthetic processes are part of the natural carbon cycle under dark conditions i.e., soil or deep in the oceans where the sunlight is not able to penetrate.[105] The research efforts in the field of biotechnology strive towards improving the efficiency of such microbial conversion of CO_2 via metabolic and genetic engineering approaches.[105, 107] An example for such microorganisms are the chemolithotrophs that are fed by inorganic materials and therefore provide energy for synthesis of ATP and NADPH,[106] that can subsequently reduce CO_2 via the Calvin cycle[44, 59, 96] (the second step of the overall photosynthesis process that occurs under dark mode). Additional subsequent complex biochemical processes can lead to final production of CH_3COOH, C_2H_5OH and other alcohols.[106] Another example involves study of genetically engineered *Escherichia coli* bacteria for the purpose of converging CO_2 into carbohydrates.[107] Furthermore, a very interesting study

is based combined solar electricity driven electrochemical/biochemical two-step CO_2 conversion approach.[108] In a first step, CO_2 and H_2O are electrochemically converted into syngas which undergoes reaction with unreacted CO_2 from the electrolysis process in a bioreactor containing anaerobic bacteria. In dependance of the type of bacteria used, either CH_3COOH, C_2H_5OH or butanol and hexanol can be produced. This research is part of the Rheticus project under which a test pilot-plant for CO_2 conversion was constructed in Marl, Germany.[109] This is a good example for combining two groups of methods, i.e. electrochemical and biochemical for a step-wise synthesis of long carbon chain compounds which is rather challenging to be achieved only by single conversion step e.g., only electrochemical conversion of CO_2 (as discussed in section 1.3 of this chapter).

Thermochemical methods for CO_2 conversion

Another methodology for CO_2 conversion is based on heterogeneous catalytic processes that in most cases require relatively high temperatures. Therefore, these methods are referred to thermochemical or thermocatalytic CO_2 conversion reactions. Namely, CO_2 can be converted into CO, CH_4 or solid C via the reactions, described with **Equations 1.16**-**1.19**. These reactions occur in the presence of Ni, Ru, Al, Fe, Co, Cu, Zn, Pt, Pd etc. based catalysts under elevated temperatures and pressures.[54, 86, 110-112]

Equation 1.16: $CO_2 + H_2 \rightarrow CO + H_2O$ Reverse water – gas shift reaction[54, 86, 111]

Equation 1.17: $CO_2 + 4H_2 \rightarrow CH_4 + 2H_2O$ Sabatier reaction[111, 112]

Equation 1.18: $CO_2 + 2H_2 \rightarrow C + 2H_2O$ Bosch reaction[113]

Equation 1.19: $CO_2 + CH_4 \rightarrow 2CO + 2H_2$ CH_4/CO_2 reforming[86]

The reaction mechanism of these processes involves adsorption and bending of the linear CO_2 molecule on the surface of the catalysts thus thermal and rather energy demanding driven formation of the $*CO_2^{\bullet -}$ radical anion occurs via electron transfer from the surface of the catalyst into the electrophilic carbon atom in the adsorbed CO_2 molecule.[90] The reaction for the $*CO_2^{\bullet -}$ radical anion formation is presented in the previous subsection with **Equation 1.15**. In the next step, the radical anion can dissociate into *CO and $*O^{\bullet}$, thus in the case of weak binding between the *CO intermediate and the surface of the catalyst it can desorb as CO.[91] This mechanism is typical for the reverse water – gas shift reaction (**Equation 1.16**). On the other side, if the *CO intermediate is bound stronger it can be subjected to further dissociation to *C and *O intermediates where *C is subsequently hydrogenated to CH_4[91, 112] – Sabatier reaction (**Equation 1.17**). In other mechanisms the $*CO_2^{\bullet -}$ radical anion follows the formate

and carboxylate pathways leading to production of CH_3OH. [91] These pathways involve steps than can also lead to production of CH_4 as final product.[91] On the other side, the CO produced from the reverse water – gas shift and/or the CH_4/CO_2 reforming reactions (**Equations 1.16** and **1.19**) can additionally react with H_2 and thus be further converted into hydrocarbons or CH_3OH according to the hydrogenation reactions, described with **Equations 1.20** and **1.21**, respectively. In the case when C_{2+} hydrocarbons are produced via the Fischer – Tropsch synthesis method, the reaction mechanisms involve C-C coupling step(s).[114]

Equation 1.20: $nCO + (2n+1)H_2 \rightarrow C_nH_{2n+2} + nH_2O$ Fischer – Tropsch synthesis[54, 110, 112]

Equation 1.21: $CO + 2H_2 \rightarrow CH_3OH$ Reverse water – gas shift/CH_3OH synthesis[54, 112]

Similarly, as in the case of the thermal CO_2 to $CO/CH_4/C$ conversion, the Fischer – Tropsch and Reverse – water gas shift/CH_3OH synthesis processes are energy demanding and therefore, operating at relatively high temperatures and pressures in the presence of various catalyst materials (listed above in this text). Moreover, the H_2 required as a reactant is still majorly produced via the reactions described with **Equations 1.22-1.26**. These reactions require hydrocarbons and natural gas of fossil origin thus CO_2 is generated as a by-product.[115] Therefore, increase and domination of the `green` H_2 production approaches,[115] utilizing renewable energy sources is an important part of the overall energy and resources sustainability concept.

Equation 1.22: $CO + H_2O \rightarrow CO_2 + H_2$ Water – gas shift reaction[86-88]

Equation 1.23: $CH_4 + H_2O \rightarrow CO_2 + 3H_2$ Steam reforming of CH_4[87, 88]

Equation 1.24: $CH_4 \rightarrow C + 2H_2$ Pyrolysis of CH_4[86]

Equation 1.25: $C_nH_m + {}^n/_2O_2 \rightarrow nCO + {}^m/_2H_2$ Partial oxidation of hydrocarbons[87, 88]

Equation 1.26: $3C + H_2O + O_2 \rightarrow 3CO + 3H_2$ Coal partial oxidation/gasification[86, 87]

Besides converting CO_2 into CO, hydrocarbons and CH_3OH via the aforementioned approaches, there are many (thermo)catalytic hydrogenation and other processes that can utilize CO_2 as reactant for synthesis of various organic compounds.[48, 86, 112, 116, 117] However, not so many of them are widely industrialized. Typical examples are the synthesis of salicylic acid (Kolbe-Schmitt reaction), urea (Bosch-Meiser process) and synthesis of some heterocyclic and polymer compounds.[48, 86, 112, 116, 117]

CO_2 conversion methods based on homogeneous catalysis

The group of CO_2 conversion methods where the catalyst is in the same phase as the reactants and reaction medium can be classified as homogeneous catalysts. This paragraph refers to catalysts which operate under elevated temperatures etc. and where the catalytic conversion of CO_2 is not driven by electrical energy, light irradiation etc. Some literature sources report studies of various catalysts based on d or p – block element complexes with organic ligands intended for CO_2 conversion into HCOOH/$HCOO^-$,[112] CO_2 and CH_3OH reaction to produce dimethyl/other dialkyl carbonates[116, 118] and other compounds. Besides the already cited publications, more information regarding CO_2 conversion based on homogenous catalysis can be found elsewhere.[119, 120]

1.3. Electrochemical conversion of CO_2

Introduction to electrochemical reduction of CO_2

The conversion of CO_2 via electrocatalytic or electrochemical reduction (CO_2ER) which can be generally described with **Equation 1.27**, is a promising heterogeneous catalysis strategy for transformation of this greenhouse gas into existing industry and transport desired chemicals and fuels[48, 82] via utilization of electricity provided by an external source in comparison with the photoelectrochemical concept discussed in the previous section (1.2.), when the electrons are photogenerated.

Equation 1.27: $xCO_2 + yH^+ + ye^- \rightarrow C,H,(O)\text{-product} + zH_2O$

As mentioned before in the previous sections of this chapter (1.1. and 1.2.), for achieving sustainable energy concept,[68-70] the electrical energy for driving the CO_2ER should be provided from renewable sources.[73, 74] In terms of practical application the electrochemical concept has advantage over the photoelectrochemical which is constrained to, and limited by amount of available sunlight during different year seasons or parts of the day. On the other hand, the electrochemical concept does not depend on the type of renewable electricity source. Additionally, the electrochemical concept can be superior to the thermochemical one since the electrical energy is directly utilized to drive the CO_2 conversion readily under ambient conditions, without the prerequisite to be transformed in thermal and there is no requirement for gaseous H_2 which, as mentioned above, its production is presently dependent on fossil oil and natural gas. The strategy for closing the carbon cycle and achieving sustainable energy

concept via CO_2 capture and utilization of renewable energy driven CO_2ER to fuels and chemical feedstocks, their storage or immediate usage is illustrated in **Figure 1.6** - adopted from Garg et al.[121]

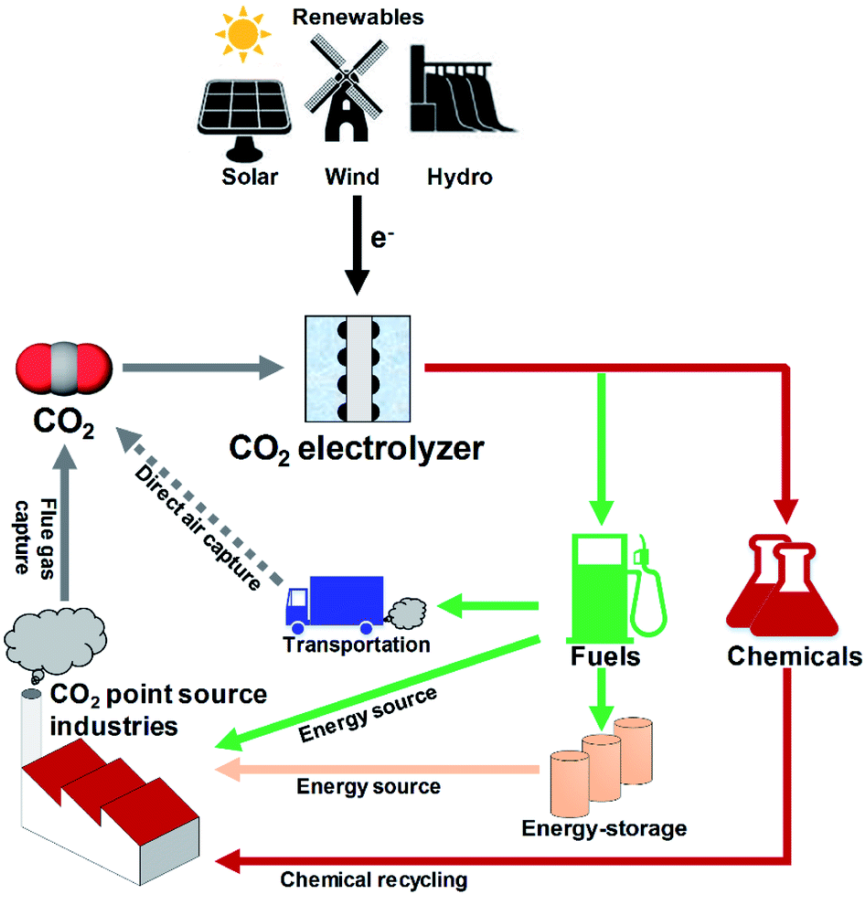

Figure 1.6. Schematic representation of a strategy for closing the carbon cycle and achieving sustainable energy concept via CO_2 capture, its renewable energy driven electrochemical conversion to fuels and chemical feedstocks that can be either stored or subjected to immediate usage. Reproduced from Garg et al.[121] with permission from the Royal Society of Chemistry.

The most common and simplest CO_2ER electrochemical setup (**Figure 1.7**) is utilizing aqueous electrolytes thus the hydrogen i.e., H^+ ions required in the CO_2ER reaction (**Equation 1.27**) are provided from water.[90, 122] This setup is identical as in the case of the previously discussed photoelectrochemical i.e., consists of cathode and anode immersed in electrolyte in which CO_2 is purged,[90, 122] except there are no requirements for semiconductor-based electrodes and light source for the aforementioned reason that the CO_2 reduction is driven by an external source of electricity.

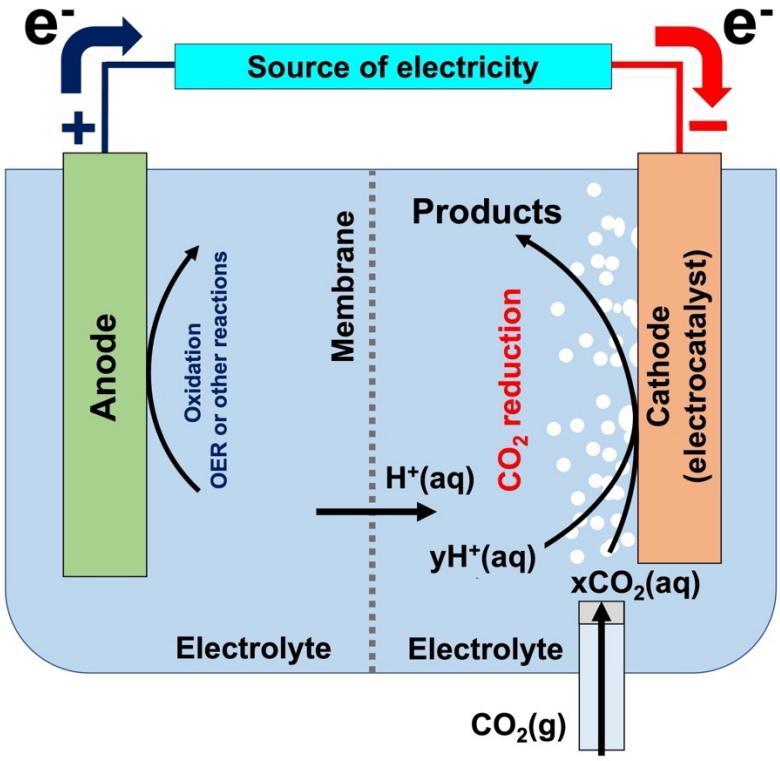

Figure 1.7. Schematic representation of typical setup (electrochemical cell) for electrochemical reduction of CO_2. The cathodic process is depicting the general CO_2ER process presented with **Equation 1.27**. More information regarding the actual electrochemical setups used in this work can be found in **Chapter 2**.

Various possible products can be obtained from the CO_2ER involving two- or multiple electron/H^+ processes, thus the reactions for the most important ones are presented with **Equations 1.28-1.44** (arranged in ascending order in terms of the required electron/H^+). The standard equilibrium potential values for each of these reactions in aqueous electrolyte at pH = 7 are adopted from the literature as calculated from thermodynamical data.[54, 123] The cathodic and anodic compartment in the electrochemical cell (**Figure 1.7**) in the most common experimental setups are separated with cation exchange membrane that allows transfer of H^+ from the anodic to the cathodic,[122] but prevents transfer of the dissolved CO_2ER products from the cathodic to the anodic compartment that can lead to their reoxidation on the anode.[123, 124] More information regarding various membranes and electrochemical cell designs can be found in the literature.[122]

Equation 1.28: $CO_2 + 2H^+ + 2e^- \rightleftarrows HCOOH$ formic acid/formate $E^{\circ}_{vs.\ RHE} = -0.12$ V[54]

Equation 1.29: $CO_2 + 2H^+ + 2e^- \rightleftarrows CO + H_2O$ carbon monoxide $E^{\circ}_{vs.\ RHE} = -0.10$ V[54]

Equation 1.30: $CO_2 + 6H^+ + 6e^- \rightleftarrows CH_3OH + H_2O$ methanol $E^{\circ}_{vs.\ RHE} = +0.03$ V[54]

Equation 1.31: $2CO_2 + 6H^+ + 6e^- \rightleftarrows (CHO)_2 + 2H_2O$ glyoxal $E^\circ_{vs.\ RHE} = -0.16$ V[123]

Equation 1.32: $CO_2 + 8H^+ + 8e^- \rightleftarrows CH_4 + 2H_2O$ methane $E^\circ_{vs.\ RHE} = -0.17$ V[54]

Equation 1.33: $2CO_2 + 8H^+ + 8e^- \rightleftarrows CH_3COOH + 2H_2O$ acetic acid/acetate $E^\circ_{vs.\ RHE} = +0.11$ V[54]

Equation 1.34: $2CO_2 + 8H^+ + 8e^- \rightleftarrows CH_2OHCHO + 2H_2O$ glycol aldehyde $E^\circ_{vs.\ RHE} = -0.03$ V[123]

Equation 1.35: $2CO_2 + 10H^+ + 10e^- \rightleftarrows (CH_2)_2(OH)_2 + 2H_2O$ ethylene glycol $E^\circ_{vs.\ RHE} = +0.2$ V[123]

Equation 1.36: $2CO_2 + 10H^+ + 10e^- \rightleftarrows CH_3CHO + 3H_2O$ acetaldehyde $E^\circ_{vs.\ RHE} = +0.06$ V[54]

Equation 1.37: $2CO_2 + 12H^+ + 12e^- \rightleftarrows C_2H_4 + 4H_2O$ ethylene $E^\circ_{vs.\ RHE} = +0.08$ V[54]

Equation 1.38: $2CO_2 + 12H^+ + 12e^- \rightleftarrows C_2H_5OH + 3H_2O$ ethanol $E^\circ_{vs.\ RHE} = +0.09$ V[54]

Equation 1.39: $2CO_2 + 14H^+ + 14e^- \rightleftarrows C_2H_6 + 4H_2O$ ethane $E^\circ_{vs.\ RHE} = +0.14$ V[54]

Equation 1.40: $3CO_2 + 14H^+ + 14e^- \rightleftarrows CH_3COCH_2OH + 4H_2O$ hydroxy acetone $E^\circ_{vs.\ RHE} = +0.46$ V[123]

Equation 1.41: $3CO_2 + 16H^+ + 16e^- \rightleftarrows C_2H_5CHO + 5H_2O$ propionaldehyde $E^\circ_{vs.\ RHE} = +0.09$ V[54]

Equation 1.42: $3CO_2 + 16H^+ + 16e^- \rightleftarrows (CH_3)_2CO + 5H_2O$ acetone $E^\circ_{vs.\ RHE} = -0.14$ V[123]

Equation 1.43: $3CO_2 + 16H^+ + 16e^- \rightleftarrows CH_2CHCH_2OH + 5H_2O$ allyl alcohol $E^\circ_{vs.\ RHE} = +0.11$ V[123]

Equation 1.44: $3CO_2 + 18H^+ + 18e^- \rightleftarrows C_3H_7OH + 5H_2O$ n-propanol $E^\circ_{vs.\ RHE} = +0.10$ V[54]

However, as already mentioned above when discussing the photo(electro)catalytic concepts, in aqueous electrolytes, the hydrogen evolution reaction (HER) described with **Equation 1.45**[††], is a competitive process.[54, 68, 90, 125-129] The values of the standard equilibrium potentials for the CO_2ER reactions described with **Equations 1.28**-**1.44** are not significantly more positive or negative than 0 V vs. RHE for HER. Yet, the standard equilibrium potential for the energy demanding formation[90] of the $CO_2^{\bullet -}$ radical anion in a single electron step without a catalyst[124] is −1.49 V vs. RHE (**Equation 1.46**[‡‡]), which is much more negative than in the case of HER. However, it is important to note that the presence of proper electrocatalyst reduces the energetical barrier for formation of the $CO_2^{\bullet -}$ radical anion thus in this case less negative potential is required.[130] Namely, it can be simply stated that, if this is not the case, no CO_2ER products should be theoretically observed at potentials that are less negative than −1.49 V vs. RHE. Yet, the competition between CO_2ER and HER remains one of the key challenges in this research field.[121]

Equation 1.45: $2H^+ + 2e^- \rightarrow H_2$ (cathode) HER $E^\circ_{vs.\ RHE} = 0$ V[54]

Equation 1.46: $CO_2 + e^- \rightleftarrows CO_2^{\bullet -}$ $E^\circ_{vs.\ SHE} = -1.9$ V at pH = 7[44, 124] or $E^\circ_{vs.\ RHE} = -1.49$ V[§§]

[††] **Equation 1.45** is identical to **Equation 1.13** (HER).
[‡‡] **Equation 1.46** is identical to **Equation 1.15** (formation of the $CO_2^{\bullet -}$ radical anion).
[§§] Converted from $E^\circ_{vs.\ SHE}$ to $E^\circ_{vs.\ RHE}$ using the equation $E^\circ_{vs.\ RHE} = E^\circ_{vs.\ \mathrm{SHE}} + 0.059 \cdot \mathrm{pH}$

Regarding the anodic, i.e., oxidation counter reaction, the most utilized one in laboratory scale research is the water oxidation i.e., oxygen evolution reaction (OER) presented with **Equation 1.47**[***], using anode made of Pt, or other electrocatalysts active for OER. The role of the oxidation reaction is providing electrons and H^+ and, as mentioned above, the H^+ can simultaneously cross the cation exchange membrane and supply the cathodic CO_2 conversion processes.

Equation 1.47: $2H_2O \rightarrow 4H^+ + O_2 + 4e^-$ (anode) $E^{\circ}_{vs.\ RHE} = +1.23$ V[54]

Having an overall reaction where CO_2 and $H^+(H_2O)$ are converted into C,H,(O)-products (CO, hydrocarbons, alcohols, carboxylic acids etc.) is basically reversing the general combustion reaction presented with **Equation 1.1**. Moreover, driving coupled CO_2ER and OER via solar energy generated electricity[131] is indeed mimicking nature and, as mentioned in the previous text, can be referred to artificial photosynthesis.[132] However, it is well known from the literature that the OER has a sluggish kinetics originating from its mechanism thus high overpotential is required.[133] Therefore, for achieving energy efficient artificial photosynthesis coupling CO_2ER with OER, the research efforts and advancements in the OER field are of great importance.[134] Furthermore, alternative oxidation reactions can be coupled with CO_2ER for the purpose of electrosynthesis of various valuable compounds.[135-137]

From a historical point of view, the first known report regarding electrochemical reduction of CO_2 in aqueous electrolytes goes back to the 19th century. Namely, there are publications in the literature[44] that cite a 1870 report, from a French chemist named M. E. Royer, in which CO_2ER to HCOOH or $HCOO^-$ on Zn cathode is described.[138] In the 1950s another publication appeared reporting CO_2ER to HCOOH or $HCOO^-$ using Hg as cathode.[139] Additionally, that publication cites several other papers from which one from 1930, that is easily accessible, reports that HCOOH/$HCOO^-$ was obtained on various amalgams-based cathodes.[140] There are some other publications from the 1970s claiming similar results in terms of HCOOH/$HCOO^-$ production on cathodes made of Au, Pb, Zn, Cd, Sn, and In[141] and an additional one reporting production of CO, CH_4 and CH_3OH on Ru cathodes.[141, 142] In 1985 Hori et al.[141] re-examined the CO_2ER performance on cathodes made of most of the elements reported in the previous publications and some additional ones (Cu, Ag, Ni and Fe) in aqueous $KHCO_3$ as a supporting electrolyte and successfully achieved quantification of the electrolysis products for which the faradaic efficiencies (FE, **Equation 1.48**) were practically adding up to 100%. It was found that Cd, Sn, Pb and In, predominantly produce HCOOH/$HCOO^-$, Ag, Au and Zn produce CO as a main product, Ni and Fe favour the HER, while Cu is the only one

[***]**Equation 1.47** is identical to **Equation 1.14** (water oxidation)

that besides all previous CO_2ER products and H_2 from the HER is able to achieve CO_2 reduction to CH_4 with significant faradaic efficiency.[141]

Equation 1.48: $FE_{electrolysis\ product-i}\ (\%) = \frac{q_i \cdot 100\%}{q_{total}}$ where q_i and q_{total} are partial, for electrolysis product - i and total passed charge, respectively. Namely, the FE can be defined as fraction of electrical charge contributing to the generation rate of a given product.

In two other publications Hori and his co-workers[143, 144] reported that besides CH_4, other hydrocarbons (C_2H_4) and additionally alcohols (C_2H_5OH and *n*-C_3H_7OH) can be produced during CO_2ER using polycrystalline Cu as cathode. The performance of the examined elements for electrochemical reduction of CO_2 (or HER) on cathodes made of the above listed elements and some additional ones examined under the same conditions, presented in Hori[145] and Nitopi et. al.[54] (Ti, Pt, Pd, Ga and Tl), is illustrated in **Figure 1.8** as a modified periodic table showing the major CO_2ER products and H_2 from HER for electrodes made of several d and p block elements - reproduced from the Bagger et al.[146]

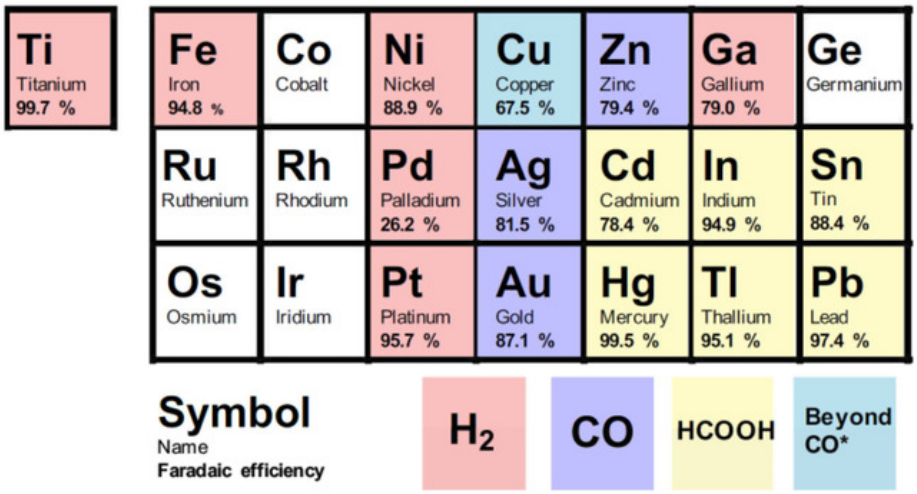

Figure 1.8. Modified periodic table of d and p block elements classified by their electrocatalytic selectivity towards H_2 from the HER and towards CO, HCOOH and products obtained via CO_2ER beyond CO. Reproduced with permission from Bagger et al.[146] – Copyright 2017 John Wiley and Sons Inc. (license number 5313691341868-old, 5390340393537-new).

Intermediates and pathways in electrochemical reduction of CO_2

Further studies showed that on Cu electrocatalyst, CO_2 can be reduced to additional compounds different than the ones mentioned in the previous subsection, thus leading to 17 different CO_2ER products in which CO, carboxyl acids, hydrocarbons, aldehydes, ketones etc.

are included.[54, 123] The reactions for CO_2ER into these products are already presented above with **Equations 1.28-1.44**. Therefore, it can be assumed that the capability of the Cu electrocatalyst to reduce CO_2 beyond CO in multi electron/H^+ steps can be defined as its intrinsic property.[54] On the other hand, the electrocatalysts made of the elements highlighted in violet and yellow in **Figure 1.8** intrinsically reduce CO_2 to CO and HCOOH/$HCOO^-$, respectively. These intrinsic properties originate from the binding energies of the key intermediates involved in the reaction pathways for both CO_2ER and HER. The basic intermediates for CO_2ER to HCOOH/$HCOO^-$ are C bound *COOH (sometimes bidentate C and O bound - *CO*OH[146]) and O bound *OCHO*, while only the C bound *COOH is involved in the CO pathway.[146, 147] In the case of the HER, the key intermediate is the adsorbed hydrogen atom (*H).[130, 146, 147] It can be stated that the *COOH represents a `protonated form` of the $CO_2^{\bullet -}$ radical anion assuming that the first electron step also involves protonation thus the as formed intermediate is bound on the surface of the of the catalyst through the carbon atom. Moreover, Birdja et al.[130] suggested that the *OCHO* intermediate can be formed via nucleophilic attack on the C atom in the CO_2 molecule from adsorbed hydride anion intermediate (*H^-). On the other side, it can be presumed that the formation of the O bound *OCHO* intermediate does not occur via radical formation mechanism. In the publication from Bagger et al.[146], the binding energies of the three intermediates are plotted one versus another for all elements that are highlighted in the modified periodic table in **Figure 1.8**. These plots are presented in **Figure 1.9** and the simplest trend for observation and discussion is showed in **Figure 1.9c**. The elements forming a cluster in the bottom-left part of the graph in **Figure 1.9c,** that are supporting the HER (as presented in **Figure 1.8**), bind the *COOH intermediate much stronger compared to the other ones in the same graph, thus inhibiting the CO_2ER. In contrast, the elements in the upper-right corner of **Figure 1.9c**, highlighted in purple and yellow, bind the *COOH much weaker compared to the other ones, allowing transformation of this intermediate in second electron/H^+ step into CO and HCOOH/$HCOO^-$ as products which desorb from the surface. Moreover, the CO producing elements bind the *COOH intermediate stronger than *H, while the HCOOH/$HCOO^-$ producing elements bind the *H intermediate slightly weaker than the CO producing ones. **Figure 1.9d** shows that the HCOOH/$HCOO^-$ producing elements through the *OCHO* display much stronger binding of this intermediate compared to *H, except for Hg where the *OCHO* binding energy is slightly stronger than the case of *H. The experimental results presented in Hori[145] and Nitopi et. al.[54] are in agreement with the findings by Bagger et al.[146] i.e., the elements Ag, Au and Zn resemble CO as a main CO_2ER product while the elements Hg, Cd, Sn, Pb and In, intrinsically reduce CO_2 to HCOOH/$HCOO^-$ with very high FE, while the FE for the HER are typically low. Cu is the only one that shows neither to strong nor to weak binding energy for the *COOH intermediate

compared with the elements that are clustering in the bottom-left and top-right corners in the graph in **Figure 1.9c.** Yet, this discussion is simplified with the graph plotting the binding energies of *CO vs. *H intermediate, presented in **Figure 1.10** - adopted from Bagger et al.[146] The *CO is formed in second electron/H^+ step via conversion of the *COOH intermediate.

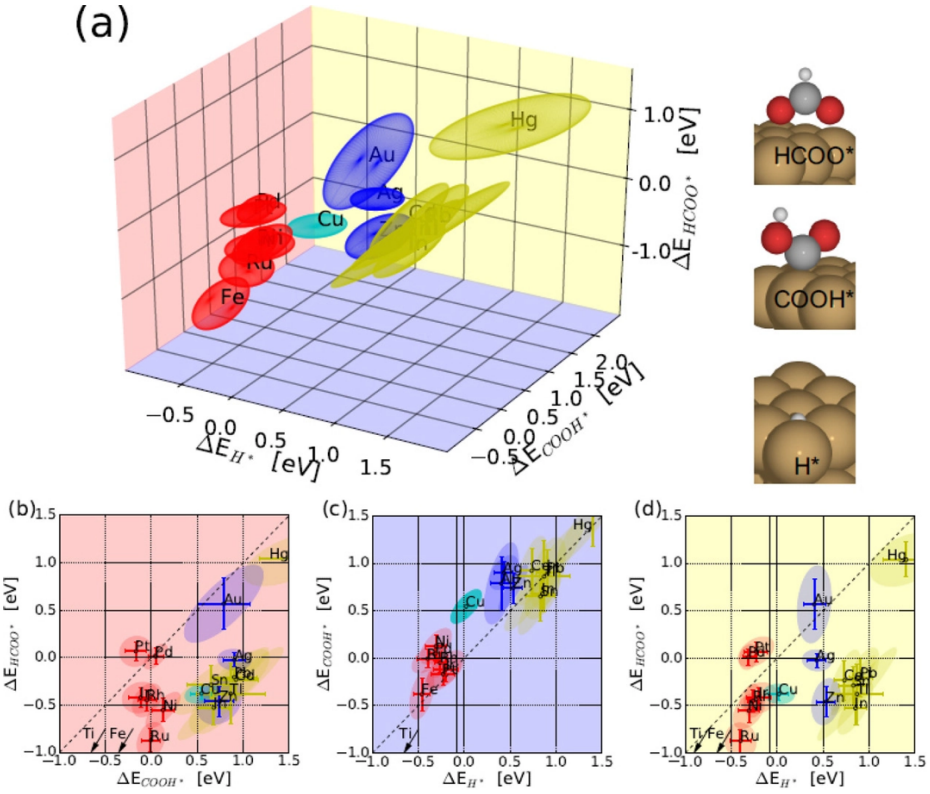

Figure 1.9. Binding energies of *H, *COOH and *OCHO intermediates on the elements that are highlighted in **Figure 1.8**: 3-D plot of *OCHO* vs. *COOH vs. *H **(a)**; *OCHO* vs. *COOH **(b)**; *COOH vs. *H **(c)** and *OCHO* vs. H* **(d)**. Reproduced with permission from Bagger et al.[146] – Copyright 2017 John Wiley and Sons Inc. (license number 5314711215146-old, 5391820629839-new).

From **Figure 1.10** it is obvious that the binding energy of the *CO intermediate on Cu is somewhat optimal i.e., neither to high, nor to low, from which can be assumed that *CO will not desorb completely from the surface as CO product but on the other side will also not be completely inhibited towards further reduction, as mentioned before discussing the *COOH intermediate. Additionally, the binding energy for *H has a value that is slightly higher than zero,[54, 146] which makes the HER theoretically not favourable, yet still possible to occur. On the other hand, the *CO binding energies for Ni, Fe, Ti, Pt, Pd and Ga concentrate on the left-bottom corner of the graph in **Figure 1.10** suggesting stronger binding and inhibition of this intermediate in comparison with *H and therefore favouring the HER over CO_2ER as their intrinsic property. Similarly as in the case of the graph in **Figure 1.9c,** the top-right corner on

the graph in **Figure 1.10** shows two clusters of elements for which the *CO intermediate binding energies do not significantly differ and both clusters of elements have weaker binding energy for the *CO intermediate than Cu which makes *CO more prone to desorb from the surface as CO product.

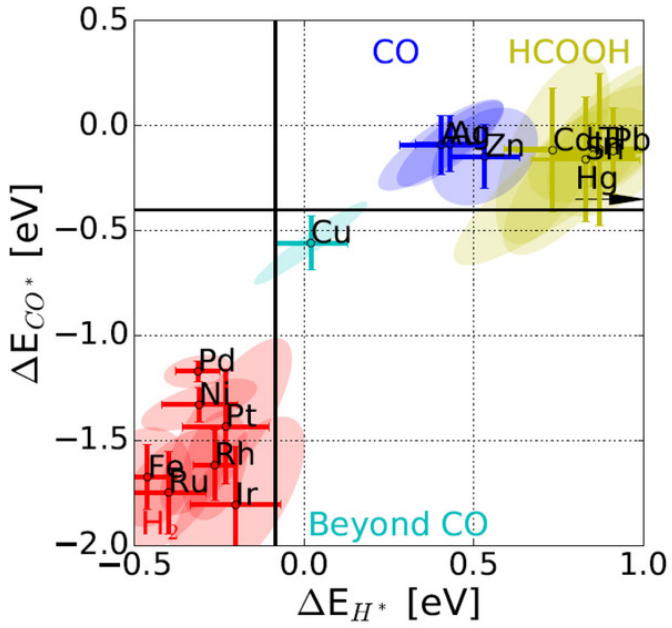

Figure 1.10. Binding energies of *H, *COOH and *OCHO intermediates on the surface of the elements that are highlighted in **Figure 1.8**: *CO vs. *H binding energy plot. Reproduced with permission from Bagger et al.[146] – Copyright 2017 John Wiley and Sons Inc. (license number 5313691341868-old, 5390340393537-new).

In the case of Cu, the *CO intermediate can undergo, as mentioned above, further multielectron/H^+ reduction. The reduction of *CO is following complex mechanistic pathways that involve *CO hydrogenation to produce CH_4 and CH_3OH, C-C dimerization or coupling and other transformations towards C_2 hydrocarbons, C_2H_5OH, CH_3COOH/CH_3COO^- and other C_2 products, trimerization towards production of C_3 compounds etc.[123, 130, 148-150] The C-C coupling appears to be an important step towards CO_2ER to C_{2+} products.[130, 150, 151] Some of these mechanistic pathways are presented in **Figure 1.11**, adopted from Birdja et al.[130] More comprehensive schematic regarding the reaction mechanism pathways involving two and multi multielectron/H^+ steps and the rate determining steps (RDS) can be found in the comprehensive review publication from Nitopi et. al.[54] An actual experimental evidence that *CO is essential intermediate for further reduction towards multi-electron/H^+ products are the experiments involving electrochemical reduction of CO (COER) as a starting point instead of CO_2.[54, 152, 153] The reactions for COER to CH_4, C_2H_4, C_2H_5OH and CH_3COO^- are presented with **Equations 1.49-1.53** The reactions described with **Equations 1.52** and **1.53** are conducted in

strongly alkaline electrolyte[153] and in such case the source of hydrogen is water. However, there are claims that the C-C coupling is not the RDS on Cu electrocatalysts but rather the water hydrogenation of CO due to mass-transport limitations and lack of correlation between the partial pressure and CO coverage.[154]

Equation 1.49: $CO + 6H^+ + 6e^- \rightleftarrows CH_4 + H_2O$ methane $E^\circ_{vs.\ RHE} = +0.26$ V[54]

Equation 1.50: $2CO + 8H^+ + 8e^- \rightleftarrows C_2H_4 + 2H_2O$ ethylene $E^\circ_{vs.\ RHE} = +0.17$ V[54]

Equation 1.51: $2CO + 8H^+ + 8e^- \rightleftarrows C_2H_5OH + H_2O$ ethanol $E^\circ_{vs.\ RHE} = +0.19$ V[54]

Equation 1.52: $2CO + 7H_2O + 8e^- \rightleftarrows C_2H_5OH + 8OH^-$ ethanol $E^\circ_{vs.\ RHE} = +0.18$ V[153]

Equation 1.53: $2CO + 3H_2O + 4e^- \rightleftarrows CH_3COO^- + 3OH^-$ acetate $E^\circ_{vs.\ RHE} = +0.50$ V[153]

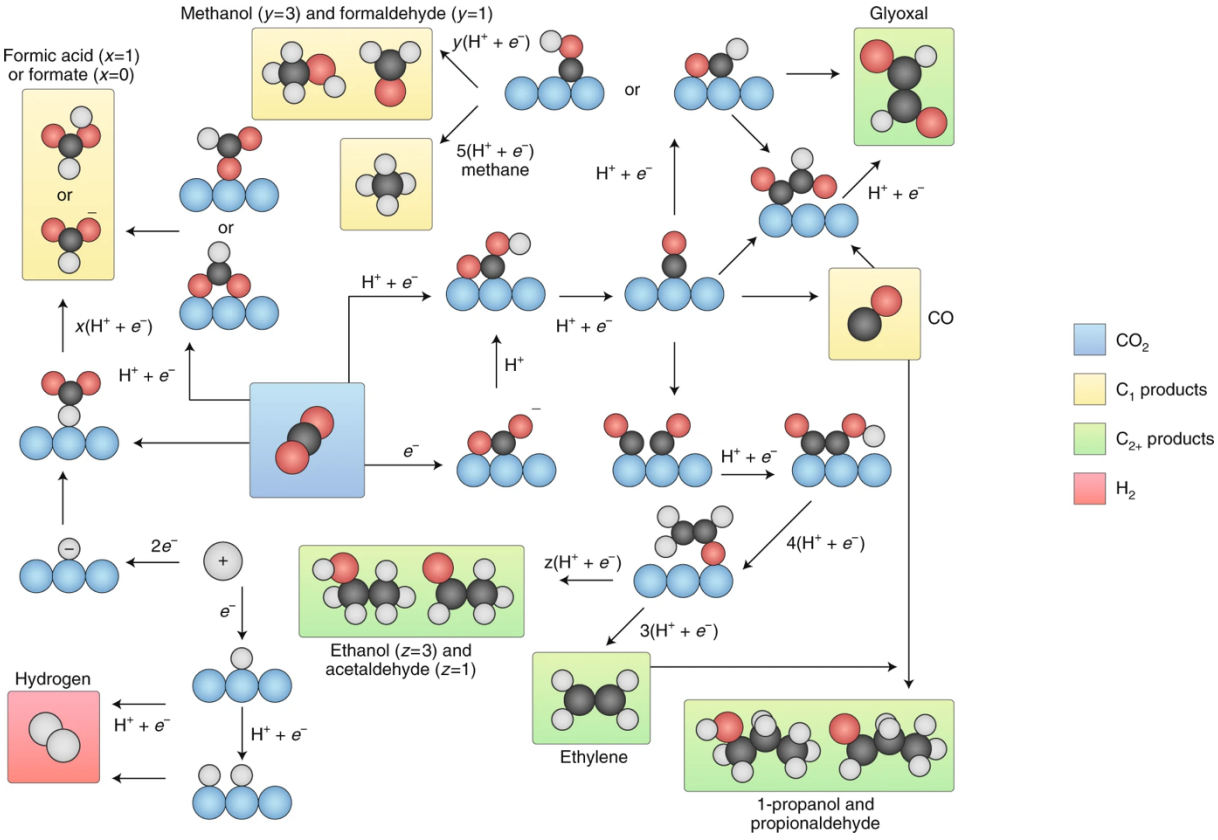

Figure 1.11. Mechanistic CO_2ER and HER reaction pathways involving two and multi electron/H^+ steps. Black-carbon, red-oxygen and white-hydrogen spheres stand for atoms of the various reactants, intermediates and products in the CO_2ER/HER pathways, while the light blue spheres stand for the atoms from the surface of the electrocatalyst. Reprinted by permission from Springer Nature: Nature Energy, Birdja et al.[130] Copyright 2019.

Challenges originating from the parameters and experimental conditions that affect the CO_2ER selectivity on Cu catalysts

Even though the electrochemical reduction represents a promising strategy for the CO_2 emissions mitigation via conversion of this greenhouse gas with direct utilization of electricity that can be supplied from renewable energy sources, the application of this concept in industrial scale facilities is hampered by many challenges of various nature that are mainly affected by the parameters and experimental conditions during the process of electrolysis. As already stated before, Cu is unique electrocatalyst capable of intrinsically converting CO_2 into multi electron/H^+ products such as hydrocarbons, alcohols etc. that are valuable both as fuels and chemical feedstocks[48, 82] The fuels and chemical feedstocks are conventionally obtained from fossil crude oil, coal and natural gas derivates in the petrochemical industry hence, the outcome of the general efficiency and cost effectiveness of the CO_2ER approach must be competitive with the conventional technologies in order to mitigate the utilization of these fossil raw materials. Therefore, it is anticipated that the research efforts have been indeed concentrated on Cu and Cu based catalyst materials. However, before moving towards a more thorough discussion of the parameters and experimental conditions related to various challenges in the CO_2ER approach, a somewhat detailed discussion of the electrocatalytic performance and product distribution on planar Cu electrode is necessary.

Namely, the CO_2ER on Cu can lead to production of 15 products involving more than two-electron/H^+ steps, presented with **Equations 1.30**-**1.44**. The FE for most of these products when polycrystalline planar Cu electrode is examined in the range of potentials between −0.6 and −1.2 V vs. RHE using aqueous $KHCO_3$ as electrolyte, are presented in **Figure 1.12** - reproduced from Kuhl et al.[123] The electrochemical cell used in this experiment, consists of two-compartments that are separated with a membrane and where CO_2 is purged into the cathodic compartment.[123] Namely, this is the most common laboratory scale electrochemical setup that is conceptually identical to the one presented in **Figure 1.7**. The CO_2ER products and H_2 from the HER are classified in three groups in **Figure 1.12**, based on the maximal FE values that can be reached in the aforementioned range of potentials. Namely, the group of 5 products in the top graph in **Figure 1.12** are listed as major products[123] that can reach maximal FE values between 20 and 80%. At less negative potentials (−0.7 and −0.8 V vs. RHE), H_2, CO and HCOOH/$HCOO^-$ can be observed and this is expected since only 2 electrons and $2H^+$ are required for their production. At around −0.8 V vs. RHE, very small FE values for CH_4 and C_2H_4 can be observed requiring 8 and 14 electrons/H^+, respectively. The FE for these products increases with a decrease in the H_2 and CO production involving CO protonation/hydrogenation and C-C coupling pathways for CH_4 and C_2H_4, respectively (**Figure**

1.11). On the other hand, the FE for HCOOH/$HCOO^-$ production following the *COOH or *OCHO* intermediate formate pathways is peaking at around −0.85 V vs. RHE, then decreasing at more negative potentials. The FE for CO and HCOOH/$HCOO^-$ significantly decrease and reach steady-state more negative than −1 V vs. RHE and around the same potential the FE for the HER reaches its minimal, while C_2H_4, its maximal value. The FE for H_2 increases again more negative than −1.1 V vs. RHE and this effect comes from CO_2 mass transport limitations that will be discussed later in the text. More negative than −0.85 V vs. RHE, when the FE for C_2H_4 starts to increase, the production of 3 intermediate[123] and 8 minor[123] products with FE efficiency values up to 10 and 1%, respectively, start to emerge. The intermediate products (middle graph in **Figure 1.12**) resemble C_2H_5OH and C_3 products such as *n*-propanol and allyl alcohol generated from *CO following the C-C coupling and hydrogenation/protonation for C_2H_5OH and *CO trimerization and hydrogenation/protonation pathways for the C_3 products (**Figure 1.11**). The FE for C_2H_5OH is peaking at around −1.05 V vs. RHE and for the C_3 products at around −1 V vs. RHE. The minor products (bottom graph in **Figure 1.12**) resemble a mixture of C_1-C_3 compounds and all of them appear in the same range of potentials as in the case of the intermediate products, that is between −0.9 and −1.15 V vs. RHE. From this group of products, the highest FE (0.5-0.6%) are reached for the glycolaldehyde and propionaldehyde, lower (0.3-0.4%) for CH_3COOH/CH_3COO^- and acetaldehyde and the lowest (<0.2%) for all other quantified products. It is useful to note that under local pH increase in the electrode-electrolyte interface (double layer) under high overpotentials (which will be discussed later), alkaline catalyzed transformation of some aldehydes into carboxylic acids and alcohols could occur,[54, 130] suggesting that maybe not all observed products are generated from the CO_2ER.

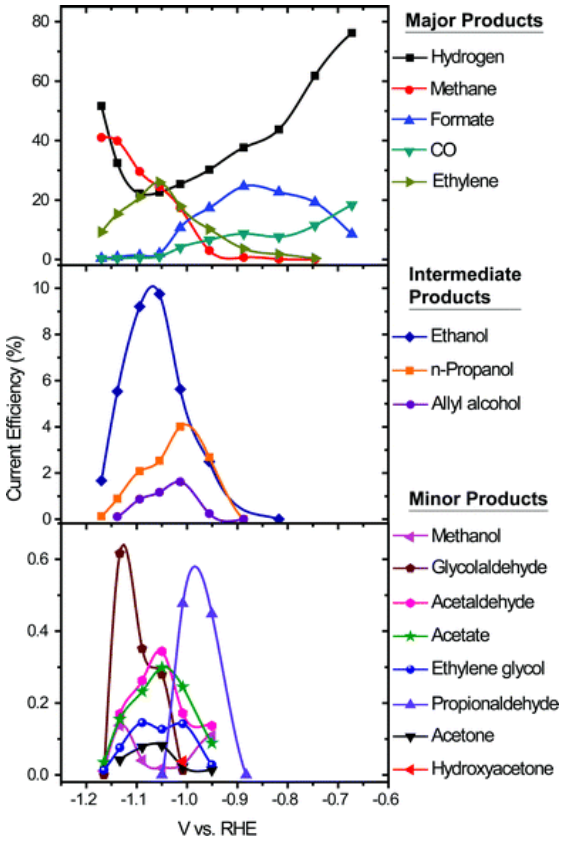

Figure 1.12. Faradaic efficiency (current efficiency in the original publication) distribution of 15 CO_2ER products and H_2 in the range of applied potentials between –0.6 and –1.2 V vs. RHE on polycrystalline Cu catalyst. Reproduced from Kuhl et al.[123] with permission from the Royal Society of Chemistry.

From the discussion of the CO_2ER product distribution on planar polycrystalline Cu electrocatalys, it is obvious that even though industrially valuable products can be produced, besides competition with HER, there is a competition between various CO_2ER reaction pathways.[130] Moreover, as observed from **Figure 1.12**, the potentials under which significant FE for the CO_2ER products are achieved, are significantly higher than the thermodynamic equilibrium potentials for all reactions presented with **Equations 1.28-1.44**, referring to large required overpotentials. The large overpotentials are most probably associated with sluggish reaction kinetics hence, triggering various reaction pathways. However, it appears that the planar Cu electrocatalyst is far from selective towards single CO_2ER product. One possibility is to include a product separation step, yet this requires higher energy consumption and will add up to the overall cost for practical application.[155] Therefore, controlling the selectivity towards obtaining a single product from CO_2 and hindering the competitive HER are among the many challenges that still need to be tackled for large-scale application of the CO_2ER approach. The most important parameters and experimental conditions that are affecting these challenges include various effects of the electrolyte, effects of local (double layer) pH and other

changes, cation and anion effects, effects of electrocatalyst's facets, defects, grain boundaries, morphology, particle sizes, distances, effects of other elements, effects of impurities, stability of the electrocatalyst, electrochemical setup, configuration and designs, temperature, pressure etc. Most of these effects are discussed in the following subsections, and additionally some of them are illustrated in **Figure 1.13.** More detailed information can be found in several review publications.[54, 121, 130, 132, 151, 156, 157]

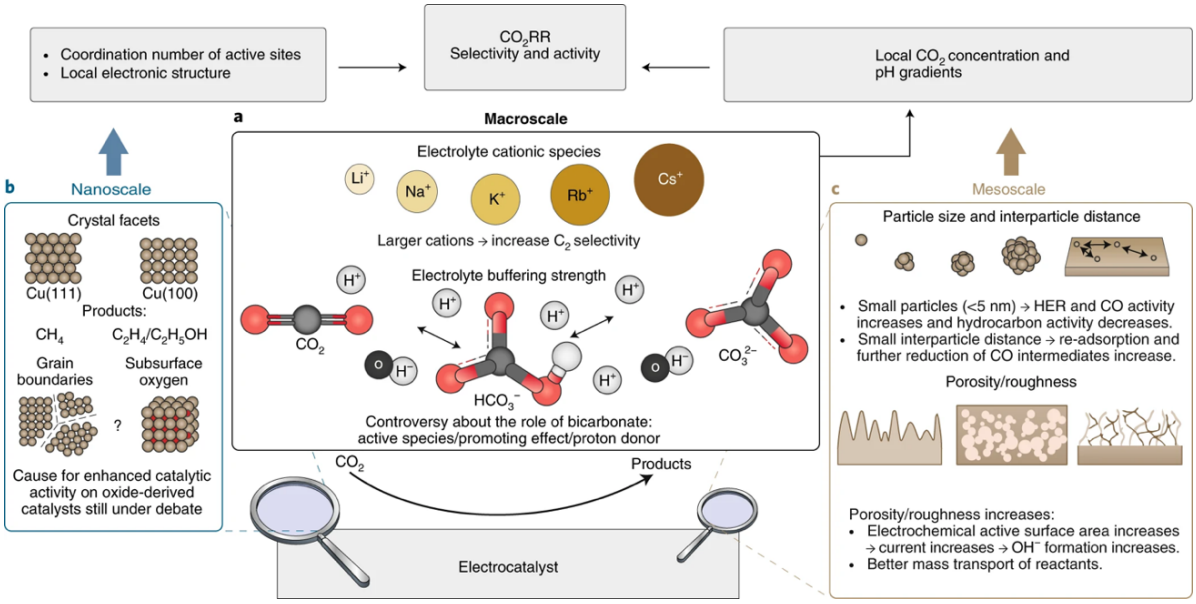

Figure 1.13. Schematic representation of the parameters and conditions affecting the CO_2ER selectivity. Reprinted by permission from Springer Nature: Nature Energy, Birdja et al.[130] Copyright 2019.

Electrolyte, pH effects and electrochemical setup configurations

As presented in **Figure 1.13** the electrolyte effects including changes in the local CO_2 concentration and pH, driven by the processes in the electrode-electrolyte interface (double layer), can directly affect the CO_2ER product selectivity. The typical research approaches when screening materials or studying various properties of known CO_2ER catalysts involve electrolysis using the previously described common electrochemical setup i.e., using aqueous electrolytes that are saturated with CO_2 in a two-compartment cell (**Figure 1.7**). Namely, in aqueous electrolyte the CO_2 dissolves (**Equation 1.54**) and when the solubility is defined by Henry's law (**Equation 1.55**) at ambient conditions, it can achieve around 30 mmol·dm^{-3}.

Equation 1.54: $CO_2(g) \rightleftarrows CO_2(aq)$

Equation 1.55: $c_{CO_2} = H_{CO_2} \cdot p_{CO_2}$ where c_{CO_2} is the concentration of dissolved CO_2, H_{CO_2} is Henry's constant for CO_2 which is 30 mmol·bar·dm^{-3},[54] and p_{CO_2} is the partial pressure of CO_2 above the solution.

Yet, CO_2 not only dissolves but also reacts with the water forming the very weak carbonic acid (**Equation 1.56**). This acid dissociates in two steps according to the reactions described with **Equations 1.57-1.59**. The equilibrium constants for these reactions are adopted from Nitopi et al.[54]

Equation 1.56: $CO_2(g) + H_2O(l) \rightleftarrows H_2CO_3(aq)$ K_{eq}~10^{-3}

Equation 1.57: $H_2CO_3(aq) \rightleftarrows H^+(aq) + HCO_3^-(aq)$ K_{a_1}~10^{-4}

Equation 1.58: $CO_2(g) + H_2O(l) \rightleftarrows H^+(aq) + HCO_3^-(aq)$ K_h~10^{-7}

Equation 1.59: $HCO_3^-(aq) \rightleftarrows H^+(aq) + CO_3^{2-}(aq)$ K_{a_2}~10^{-11}

Thus, as discussed in the previous text and observed in **Figure 1.12**, higher overpotentials, compared to the equilibrium ones, are required for production of hydrocarbons, alcohols etc. with meaningful FE, on planar polycrystalline Cu. Therefore, if the applied potential is significantly increased (more negative) than the thermodynamical equilibrium potential, the current density will also increase according to the Butler-Volmer equation for cathodic process (**Equation 1.60**). Namely, this equation shows that the current density is a natural exponential function of the overpotential and moreover proportional to the CO_2 concentration on the surface or near the electrode. Higher current densities will increase the reaction rate according to **Equation 1.61** and lead to depletion of CO_2 in the electrolyte-electrode interface (double layer) that cannot be sufficiently compensated with mass transport from the bulk electrolyte into the double layer. More information regarding the equations and their derivations can be found in the electrochemical literature.[158]

Equation 1.60: $j_{cathodic\ process} = -j_0 \cdot \frac{c_{CO_2(0,\ t)}}{c^*_{CO_2}} \cdot EXP\left[-\frac{a \cdot z \cdot F \cdot \eta}{R \cdot T}\right]$

Equation 1.61: $\vartheta_{cathodic\ process} = k \cdot c^*_{CO_2} = \frac{j_{cathodic\ process}}{z \cdot F}$

Where $j_{cathodic\ process}$ is the current density, j_0 is the exchange current density, $c_{CO_2(0,\ t)}$ is a time dependent concentration of CO_2 at a distance zero from the electrode's surface, $c^*_{CO_2}$ is the CO_2 equilibrium concentration, a is charge transfer coefficient (symmetry factor), z is number of electrons, F is Faraday constant (96485.3 C·mol^{-1}), η is overpotential, R is the universal or ideal gas constant (8.314 Pa·m^3·mol^{-1}·K^{-1}), T is temperature, $\vartheta_{cathodic\ process}$ is reaction rate and k is the rate constant.

Therefore, when CO_2 is depleted in the double layer under high overpotentials the FE for HER increases, while the FE for all CO_2ER products except CH_4 are decreasing, as observed in

Figure 1.12. The consumption of H^+ is leading to increase in the local pH value i.e., increase of the concentration of OH^- ions. The OH^- ions react with both dissolved CO_2 and HCO_3^- leading to formation of HCO_3^- and CO_3^{2-} according to **Equations 1.62** and **1.63**, respectively. Thus, the H^+ and CO_2 consumption distorts the equilibrium reactions involving the $CO_2/HCO_3^-/CO_3^{2-}$ species (**Equations 1.56-1.59**) leading to increase in the equilibrium concentrations of the HCO_3^-/CO_3^{2-} species. These species are not considered to be species involved in the first electron/H^+ step of the CO_2ER, but rather the dissolved CO_2 is considered as the real active specie.[130] However, there are still controversies and ongoing debates regarding which specie(s) from the $CO_2/HCO_3^-/CO_3^{2-}$ equilibrium is/are directly involved in the reduction reactions.

Equation 1.62: $CO_2(g) + OH^-(aq) \rightleftarrows HCO_3^-(aq)$

Equation 1.63: $HCO_3^-(aq) + OH^-(aq) \rightleftarrows CO_3^{2-}(aq) + H_2O(l)$

Additionally, the HCO_3^- ions are more prone proton donors than water[54, 130], which can also contribute towards favoring of the HER. Moreover, in alkaline conditions the water reduction dominates over the H^+ reduction[54] i.e., over the HER. Regarding the observed increase of FE for CH_4 at the most negative potentials in **Figure 1.12**, it can be attributed to increased surface coverage of the *H and decreased for *CO, leading to hydrogenation of the *CO intermediates, thus hindering the C-C coupling towards production of C_{2+} CO_2ER products.[54] On the other hand, there are claims that the CO_2ER selectivity towards production of C_2 hydrocarbons can be increased in electrolytes with lower buffer capacity or with increase of the CO_2 pressure.[130] In the review publication by Nitopi et al,[54] it is stated that the rate determining step (RDS) in the C_{2+} products pathway when performing COR on Cu is independent of pH on the SHE scale, but not in the case of CH_4 where the RDS involves H^+ transfer, thus being pH dependent. However, the effect of pH on the CO_2ER selectivity especially for production of products that are reduced beyond CO is rather complex and more research is required to be fully understood. Additional discussion regarding the effect of buffering and non-buffering anions on the CO_2ER towards C_1 and C_{2+} products and HER selectivity is provided in the following subsection, thus more comprehensive information can be found in literature.[54, 121, 130, 151]

One of the solutions for overcoming the mass transport limitations and CO_2 depletion in the double layer encompasses utilization of a gas-diffusion electrochemical configuration. This cell design is different than the typical concept schematically presented in **Figure 1.7** and which is more suitable for laboratory scale electrocatalytic activity screening of materials[124] The CO_2ER in the gas-diffusion cells or setups occurs in the interface between the gas-liquid-solid phase (triple phase interface).[124, 159] The gas-diffusion cell consists of porous gas-

diffusion electrode (GDE), that is loaded with electrocatalyst as presented in **Figure 1.14** - adopted from Luo et al.[159] The GDE and the anolyte are separated with ion exchange membrane, yet if the design consists of thin electrolyte layer flowing between the GDE and the membrane, it is known as catholyte configuration or liquid fed electrolyzer, while if the membrane is placed directly on the GDE it resembles zero-gap configuration cell which can achieve higher energy efficiency due to the lowered ohmic resistance[157] in the absence of catholyte. The zero-gap configuration electrolyzers are fed with humidified CO_2, thus the water vapor acts as source of hydrogen required in the CO_2ER reactions. Besides these configurations, many other electrolyzer designs are described in the literature.[121, 124, 157, 159] The GDE based electrolyzers can achieve >10 times higher current densities i.e., industrial relevant current densities[54, 121, 124, 151] thus attaining industrially meaningful rate of CO_2 conversion, compared to the typical lab-scale cells, due to overcoming of the CO_2 mass transport limitation discussed before, which makes them applicable for large-scale CO_2ER. The local pH effect on the GDE suppresses the HER hence, CO_2ER to C_{2+} products with high FE can be achieved because the C_{2+} pathway RDS, as discussed before, is not depended of pH, while the production of CH_4 is not favorable in highly alkaline conditions since the RDS involves hydrogenation.[54, 159] With other words, preventing the local CO_2 depletion on GDE most probably increases the *CO coverage that facilitates the C-C coupling over the *CO hydrogenation pathway under increased local pH conditions, favoring the C_{2+} over CH_4 production. However, there are various other challenges that can affect the selectivity and therefore significant part of the CO_2ER scientific and industrial communities are dedicated on resolving many issues associated with the GDE based electrolyzers in order to improve their efficiency. More information regarding CO_2ER in GDE based electrolyzers performances, progress and challenges can be found in recent literature sources.[157, 159, 160]

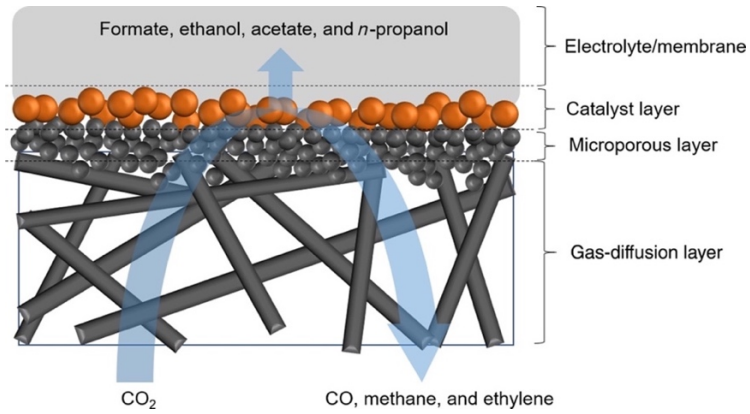

Figure 1.14. Schematic representation of gas-diffusion electrode. The figure is reproduced from Luo et al.[159] This work is licensed under a Creative Commons Attribution 4.0 International license (CC-BY 4.0, credit to the authors). Link to license: https://creativecommons.org/licenses/by/4.0/

Besides performing CO_2ER in aqueous electrolytes, there are research efforts for conducting electrolysis in non-aqueous electrolytes based on organic solvents such as CH_3OH, acetonitrile, dimethylformamide, dimethyl sulfoxide, propylene carbonate and others, where CO_2 is significantly more soluble compared to water.[121] The higher CO_2 solubility can prevent its local depletion and moreover, the absence of water i.e., H^+ prevents the HER. Therefore, higher current densities and better product selectivity can be achieved even in typical two-compartment electrolyzers.[121] Additionally, there are reports about performing CO_2 electrolysis in miscible water/organic solvent electrolytes which provides a possibility for altering the H^+ concentration hence, the product selectivity.[121] Nevertheless, many organic solvents could be expensive and/or toxic, yet there are possibilities to be recycled and reused for the same purpose.[121] Moreover, utilization of ionic liquids (ILs) as electrolytes or electrolyte additives are reported to stabilize the $CO_2^{\bullet -}$ radical anion intermediate via formation of adduct compounds, that can lead to lower overpotential requirements, improved product selectivity and higher current densities.[121, 161] Finally, the organic solvents and ILs need to be stable in the corresponding electrochemical window for both cathodic and anodic processes etc. Therefore, more research and comprehensive assessments of the utilization of organic, mixed aqueous/organic and ILs based electrolytes regarding their advantages and disadvantages including the possibilities for large-scale CO_2ER application are required.

Cation and anion effects

Even though the typical electrolytes utilized in the CO_2ER research are based on CO_2 saturated aqueous $KHCO_3$ (bicarbonate buffer) in order to maintain near neutral pH value,[54] the alkaline metal cation size has effect on the selectivity, as presented in **Figure 1.13** and deliberated in various literature sources.[54, 121, 130, 151] The cation and anion effects are extension of the previous discussion regarding the electrolyte effects. Namely, cations with larger radius drive the CO_2ER selectivity towards production of C_{2+} products and can contribute towards suppression of the HER.[54] One possible effect on the selectivity is that the larger cations are prone to hydrolysis in the double layer leading to buffering of the local pH increase and preventing the local CO_2 depletion.[54, 130] Additionally, the larger cations have lower hydration capacity than the smaller ones hence being more prone to adsorb on the surface of the electrode and repel the H^+, and therefore suppress the HER and CH_4 production.[121] Another possible effect could be stabilization of the intermediates involved in the CO_2ER pathways towards C_{2+} products[54, 121, 130, 151] etc. On the other hand, regarding the effect of anions, it was already discussed above that the HCO_3^- ions can be transformed into CO_3^{2-} under highly alkaline local pH (**Equation 1.63**) and moreover can serve as H^+ donors thus favoring the HER

on planar Cu electrodes. Other buffering anions such as $H_2PO_4^{2-}/HPO_4^{2-}$ have similar effect as the HCO_3^- in terms of promoting the HER and CH_4 production over C_{2+} products.[54, 121] Electrolytes based on non-buffering anions in the electrolyte, such as SO_4^{2-} and ClO_4^- suppress the production of products where the RDS in the reaction pathways are pH dependent such as the HER and CO_2ER into CH_4, favoring the CO_2ER into C_{2+} compounds[54, 121] The presence of halide anions in the electrolyte can lead to their adsorption on the surface of Cu, affecting the Cu's electronic structure thus altering and favoring the CO_2ER selectivity over HER.[54, 121, 130]

Effects of electrocatalyst's morphology and particle sizes/interparticle distances

Another important factor, presented in **Figure 1.13**, that can affect the CO_2ER product selectivity is the surface morphology or surface roughness. Morphologically rougher electrocatalyst materials composed of various micro- and nanostructures generally resemble higher electrochemically active surface area compared to the planar ones, and therefore higher number of electrochemically active sites. The current density increases with an increase of the electrochemically active surface area[130] thus, higher conversion rates can be expected on morphologically rougher electrocatalysts. Namely, Dutta et al.[162] reported higher selectivity and higher partial current densities for C_2 hydrocarbons accompanied with suppression of the HER on dynamic H_2 bubble template (DHBT) electrodeposited Cu foams composed of dendrite-like microstructures compared to planar Cu wafer. Moreover, tuning the Cu foam's pore sizes can alter the C_2 hydrocarbons selectivity. According to various literature sources,[163-168] materials composed of pores with interconnected channels can hamper the CO_2 mass transport limitations and suppress the local CO_2 depletion. Regarding the particle size effects (**Figure 1.13**), it is claimed that decrease of Cu nanoparticle sizes increase the current densities[54] and enhances the selectivity for CO and H_2, while suppresses the production of hydrocarbons compared to planar polycrystalline Cu electrode.[130] This effect is attributed to lowering the coordination of the surface atoms with decrease of the particle sizes,[54, 130] which creates difficulties for the *CO intermediate to be further reduced.[130] On the other side, the decrease of the interparticle distances can enhance further reduction of the *CO intermediate due to its re-adsorption.[54, 130] However, these effects are rather complex and more research is required to be fully understood.

In order to deconvolute the morphology from the other CO_2ER selectivity effects, mainly originating from differences in the surface composition, the increase in the electrochemically active surface area should be estimated. The parameter associated with the surface-active sites is the electrochemically active surface area (EASA). However, the accurate experimental

determination of the EASA is challenging since it is not always exactly known which surface species from that surface area and how many of them are involved in the CO_2ER pathways. Therefore, in many cases the relative surface roughness factor (RSRF), assuming being proportional to the EASA, is experimentally estimated instead of the actual EASA from the electrode's double layer capacitance (C_{DL}), as discussed in **Chapter 2** (section 2.3).

Effects of electrocatalyst's facets and defects

Besides the particle sizes and distances, their shapes also have an important effect on the CO_2ER selectivity. Namely, particle shapes resembling Cu (111) crystal facets are selective towards CO_2ER to CH_4, while Cu(100) prefer C-C coupling pathways leading to C_2 products (**Figure 1.13**).[54, 130] However, maintaining the shapes of particles with specific facets during extended electrolysis can be an issue.[54] Creating grain boundaries and other defects in the Cu's structure via electrochemical reduction of copper oxides (oxide-derived or OD-Cu) can increase the surface roughness leading to improved production of CO and HCOOH/$HCOO^-$ compared to planar polycrystalline Cu electrode, while other studies reported CO_2ER to hydrocarbons and alcohols.[54] However, it seems like the selectivity for CO_2ER towards certain products is dependent on the conditions under which the Cu oxides were formed such as thermal oxidation, anodization, oxygen plasma treatment etc.[54, 130] Yet, the real nature of the OD-Cu active sites due to possible presence of surface or subsurface oxygen species and their role on the CO_2ER selectivity is still under debate in the scientific communities.[54, 130]

Effect of second element on the CO_2ER selectivity of Cu

Altering the CO_2ER selectivity on Cu electrocatalysts via their modification with second element is an important effect studied in the scope of this thesis. As already discussed in the previous text, the CO_2ER/HER selectivity on some of the d and p block elements can be divided into four groups i.e., elements on which CO_2 is intrinsically reduced to CO, HCOOH/$HCOO^-$ and beyond CO, and elements on which the HER is dominating over the CO_2ER (**Figure 1.8**). The intrinsic properties are based on the key intermediates binding energies, as presented in **Figures 1.9** and **1.10**. Combining Cu with another element can change the CO_2ER intrinsic properties of only Cu, or both Cu and the second element due to various effects originating from changes in the electronic structure hence, affecting the key CO_2ER/HER intermediates binding modes. This phenomenon can be defined as *synergistic effect* and in general it is

dependent on the Cu:M ratio, where M stands for the second element. Namely, when elements on which the HER is typically dominating over CO_2ER are combined with Cu, such materials generally show CO_2ER catalytic activity similar to the elements that are used to modify the Cu i.e., favouring the HER over CO_2ER[54] On the other hand, Pd intrinsically favours both CO_2ER to CO and HER in FE-wise almost equal manner, however when electrode made of this element is subjected to hydrogen adsorption on its surface the selectivity is altered towards HCOOH/$HCOO^-$ production.[54] When Cu is modified with Pd and subsequently hydrogen is adsorbed on the surface of the Pd, such electrocatalysts favours production of CH_4 and HCOOH/$HCOO^-$.[54] The presence of Pd ions in the electrolyte when performing CO_2ER on OD-Cu can shift the selectivity from C_2H_4, typically produced on Cu, into C_2H_6 via Pd assisted hydrogenation of the C_2H_4.[54, 169] Cu-Pd electrocatalyst materials where Cu and Pd are phase separated or poorly mixed on atomic level (disordered particles) favour production of C_2H_4 and C_2H_5OH in descending order with an increase of the Pd content.[54, 170] In this case CO is most likely produced on the Pd sites, thus undergoes C-C coupling on the Cu sites.[170] On the other side, when both elements are well mixed on atomic level, i.e. the Pd is incorporated into the structure of Cu, CO_2ER to CO is a favourable process.[54, 170]

Modification of Cu with Zn, that intrinsically reduces CO_2 to CO, can lead to production of CO, i.e. cause the selectivity of the bimetallic Cu-Zn system to display Zn-like behaviour, in the case of phase-separated and core-shell structure electrocatalysts.[171] Another study where Zn is electrodeposited on the surface of planar Cu electrode shows enhanced CO_2ER to CH_4.[172] Furthermore, Cu-Zn bimetallic materials are reported as catalysts for significant CO_2ER into C_2H_5OH[173] and *n*-C_3H_7OH.[174] In the latter case,[174] it is suggested that under more negative potentials leading to high local pH the formation of CH_4 is suppressed, while *CH_3-*CO coupling is enhanced, since is does not require proton transfer. The reaction mechanism most probably encompasses formation of *CO intermediates on the Zn sites which couples with the *CH_3 formed on the Cu sites under high overpotentials.[174]

The Au and Ag modified Cu materials in many cases show similar intrinsic activity as the pristine Au and Ag i.e., facilitating CO_2ER into CO, however analogously as in the case of Cu-Zn, the Cu-Au and Cu-Ag electrocatalysts are also able to reduce CO_2 beyond CO towards production of C_{2+} products due to synergistic effects or tandem catalyst mechanisms.[54] Again in analogy to the Cu-Zn system, Au and Ag sites can provide CO_2ER into CO increasing the surface coverage of the *CO intermediate, which is further converted into C_{2+} via the C-C coupling step on the Cu sites.[54]

The discussion moves towards combination between Cu and elements that in pristine form catalyse CO_2ER into HCOOH/$HCOO^-$, such as Sn and In (**Figure 1.8**). Namely, modifying Cu with Sn or In can drive the CO_2ER selectivity towards either CO or HCOOH/$HCOO^-$

production in dependence on the Cu vs. Sn or In composition. Thus, Cu rich bimetallic Cu-Sn(In) electrocatalysts are favouring CO_2ER into CO over the HCOOH/$HCOO^-$, while Sn(In) intermediate and rich ones follow the opposite behaviour.[131, 175-180] Namely, the Cu rich Cu-Sn bimetallic materials have been very extensively studied catalysts for CO_2ER into CO, having in mind the number of reports in the literature.[131, 164, 165, 175-178, 181-187] Furthermore, the modification of Cu with Sn(In) can significantly suppress the competitive HER in comparison with pristine Cu.[176-180, 184, 188, 189] The origin of the enhanced CO and HCOOH/$HCOO^-$ selectivity on these materials compared to pristine Cu, is most probably attributed to the difference in the reaction pathways, schematically illustrated in **Figure 1.15**. Namely, in the case of the Cu-Sn materials, electronic effects take place involving charge redistribution from Sn into Cu, leading to formation of partial positive (δ+) and negative (δ–) charges on the Sn and Cu sites, respectively.[175] The $Cu^{\delta-}$ sites are carbophilic thus supporting binding of the *COOH intermediate, while the $Sn^{\delta+}$ sites that show oxophilic nature favourably bind the *OCHO*,[175] that transforms into CO (**Figure 1.15b**) and HCOOH/$HCOO^-$ (**Figure 1.15c**), respectively in a second electron/H^+ step. Furthermore, density functional theory modelling (DFT), showed that the binding of the *OCHO* becomes stronger with an increase of the Sn content while the binding of the *COOH intermediate is weakening,[175] which is consistent with the observations that the Sn-rich or intermediate Cu-Sn electrocatalysts favour CO_2ER into HCOOH/$HCOO^-$ over CO.[175, 177, 187] As it was already mentioned, the In modified Cu electrocatalysts show similar behaviour in terms of altering the selectivity between CO vs. HCOOH/$HCOO^-$ in dependence of the Cu-In compostion,[179, 180] which most probably originates from identical electronic effects i.e., charge redistribution leading to competition between the *COOH and *OCHO* intermediates in favour of stronger binding of the *OCHO* vs. *COOH intermediate with an increase of the In content (**Figure 1.15b, c**). Besides altering the CO_2ER selectivity towards either CO or HCOOH/$HCOO^-$, as already mentioned above in this subsection, the Cu-Sn(In) electrocatalysts are suppressing the HER, due to weak binding of the *H intermediate.[184, 188, 189] Another study suggests that the presence of Sn atoms on the surface of Cu nanoparticles are occupying the low-coordinated Cu sites that are active for the HER, hence suppressing this process.[190]

When Cu is modified with S, the multiproduct CO_2ER selectivity, typical for pristine Cu, is altered towards HCOOH/$HCOO^-$ production.[191-198] This is interesting having in mind that the elemental sulfur is non-metal, does not conduct electricity and does not reduce CO_2 by itself. However, the presence of sulfur promotes the binding of the *OCHO* on the surface of Cu following the HCOOH/$HCOO^-$ pathway,[193-195] while hindering the binding of the *COOH intermediate that leads to *CO formation[195] The presence of sulfur most probably promotes formation of oxophilic $Cu^{\delta+}$ sites on which the *OCHO* intermediate binds through its O atoms

and undergoes transformation into $HCOO^-$ in a second electron step, as schematically illustrated in **Figure 1.15c**. Yet, it is not experimentally clear whether $Cu^{\delta+}$ sites really exist during CO_2 electrolysis, since to the best of knowledge, there are no literature sources reporting studies of Cu-S electrocatalysts surfaces under *in-situ* or near *in-situ* conditions. On the other hand, based on DFT simulations, Wang et al.[197] suggested that there is a possibility that both *COOH and *OCHO* intermediates participate in the $HCOOH/HCOO^-$ pathway. Additionally, the presence of sulfur in the structure of Cu is suppressing the competitive HER, either because the binding of the *H is weakened or, as claimed by Dou et al.,[192] facilitated compared to its binding energy on pristine Cu which most probably inactivates this intermediate.

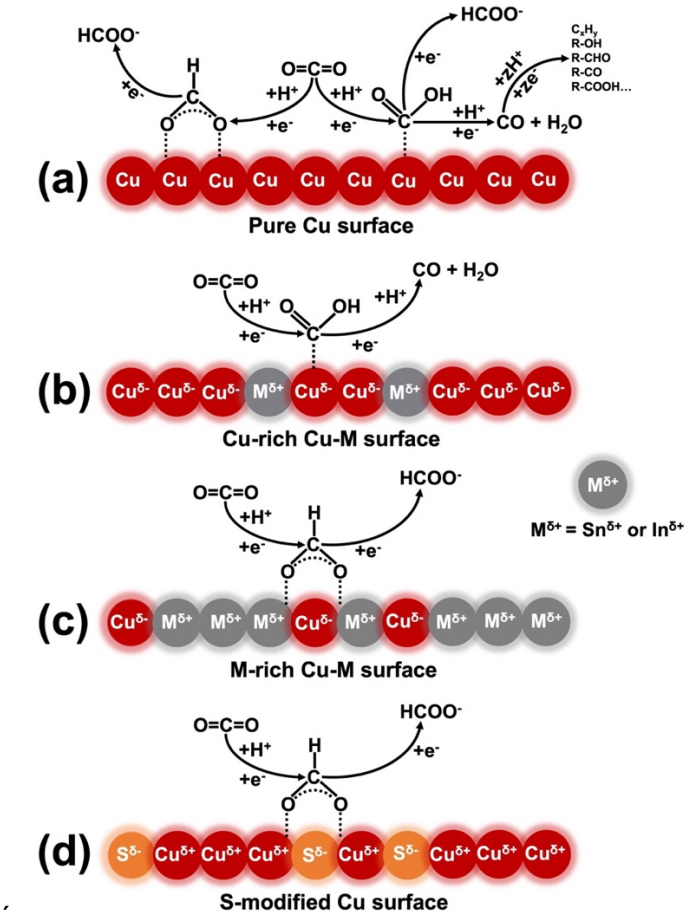

Figure 1.15. Schematic representation of CO_2ER product distribution and reaction pathways on the surface of pure Cu and Cu-M electrocatalysts: pure Cu, CO_2ER into various products **(a)**; Cu-rich Cu-Sn(In), CO_2ER into CO **(b)**; Sn(In) rich/intermediate Cu-Sn(In) **(c)** and Cu-S **(d)** favoring CO_2ER into $HCOO^-$. Reproduced from Stojkovikj et al.[178] and edited via adding one more layer illustrating the Cu-S surface CO_2 to $HCOO^-$ conversion. This work is licensed under a Creative Commons Attribution 4.0 International license (CC-BY 4.0, credit to the authors). Link to license: https://creativecommons.org/licenses/by/4.0/

Besides the above stated, modification of Cu with other HCOOH/$HCOO^-$ producing elements,[146, 199] such as Pb, Cd and Bi can maintain the intrinsic selectivity of the secondary element, i.e., Cu-Pb,[200] Cu-Cd[201] and Cu-Bi[202] combinations are reported as catalysts for CO_2ER into HCOOH/$HCOO^-$. Apart from HCOOH/$HCOO^-$ production, Cu-Bi materials are also reported as very selective catalyst for CO_2ER into CH_4.[203] Based on DFT simulations, it is claimed that modifying Cu with Bi as second element is significantly decreasing the formation energy of the *COH intermediate as RDS in the CH_4 pathway.[203]

Electrochemical rection of CO_2 into CO and HCOOH/$HCOO^-$, are these products valuable and which catalyst materials are optimal for this purpose?

The struggling of the research communities with the challenges affected by the already discussed parameters and experimental conditions, electrolyzer designs etc. to achieve large scale application of CO_2ER targeting hydrocarbons and alcohols on Cu based materials, that can directly be utilized in the existing industry, can raise a question that maybe it is better if alternative ways are more seriously considered. Hence, it appears that single-product selective electrochemical reduction of CO_2 with decent to very high FE appears to be experimentally achievable and reproducible for CO_2 reduction via two electron/H^+ steps into CO and HCOOH/$HCOO^-$. In that context, there are already several projects for CO_2ER pilot plants targeting production of CO (or syngas) and HCOOH/$HCOO^-$, from what is available in the lieterature.[121] One of these projects – the Rheticus project,[109] that was already briefly discussed in section 1.2 of this chapter, involves electrochemical CO_2 and H_2O conversion into syngas on Ag based GDE reaching current densities up to 300 $mA \cdot cm^{-2}$. The syngas together with additional CO_2 is further converted into C_4 and C_6 alcohols in a biochemical step.[108] Other examples of such projects intended to operate under current densities of 100-200 $mA \cdot cm^{-2}$ can be found in Garg et al.[121] Some possibilities include CO_2ER to CO or combined CO_2ER/HER into syngas and further conversion into hydrocarbons and alcohols using the Fischer-Tropsch or reverse water gas-shift/CH_3OH synthesis processes.[54, 82, 110, 112] On the other hand, HCOOH and its salts ($HCOO^-$) are important industrial chemicals finding applications in the textile, leather, rubber, pharmaceutical, agricultural, food and other industries.[204] Moreover, $HCOO^-$ emerged as a fuel alternative for H_2 in the direct formate fuel cells (DFFC).[205, 206] Coupling the CO_2ER with DFFC to achieve double effect of CO_2 conversion and electricity production[207] could be promising and sustainable concept. Furthermore, based on some techno-economic analyses,[82, 208] the CO_2ER into CO and HCOOH/$HCOO^-$ are feasible processes when certain

conditions are fulfilled, thus the answer of the first question in the subsection title is that both CO and HCOOH/$HCOO^-$ appear to be indeed valuable CO_2ER products.

But which catalyst materials are optimal for CO_2 conversion into CO and/or HCOOH/$HCOO^-$? Regarding CO_2ER into CO, besides the best performing Ag/Au-based[44, 209] electrocatalyst, the ones based on Zn/ZnO,[210, 211] Cu rich Cu-Sn[131, 164, 165, 175-178, 181-187] and Cu-rich Cu-In[189, 212] materials are also very selective towards CO_2ER to CO. However, when both Ag and Au are excluded as expensive and moreover considering that Ag, In and Zn are listed as endangered elements with serious risk for future supply,[20-22] the very extensively studied Cu rich Cu-Sn materials appear to be very equitable option for CO_2ER into CO. On the other hand, the CO_2 conversion into HCOOH/$HCOO^-$ can be selectively achieved on Sn/SnO_x,[181, 199, 213] Sn rich and intermediate Cu-Sn,[175, 181-183] In rich Cu-In,[180] Pb-based (Pb with various morphologies, Pb-Sn, Cu-Pb),[200] Cu-Cd,[201] Cu-Bi[202]/other Bi based materials,[199] Cu-S[191-198] etc. However, Pb, Cd and other elements that can also catalyse CO_2ER into HCOOH/$HCOO^-$, such as Hg and Tl are toxic, and probably this is a limiting factor for their possible application in practice. Yet, the other catalysts for CO_2ER into HCOOH/$HCOO^-$ such as Sn/SnO_x, Sn rich Cu-Sn(In), Cu-Bi and other Bi based, and Cu-S materials compete between each other in terms of cost, abundance, future risk of supply etc. Namely, Cu, Sn and Bi are also listed as endangered element for future supply, though not with serious risk like Zn, In and Ag,[20-22] and the future supply of S is currently not under concern.[20-22] However, Bi is significantly less abundant it Earth's crust compared to Cu, Sn and S.[214] Furthermore, Cu, and especially S, are considerably cheaper, based on the current market prices,[215-217] and more abundant compared to Sn.[214] Therefore, the Cu-S based electrocatalysts appear to be cost- and abundance-wise optimal option for CO_2ER to HCOOH/$HCOO^-$.

Composition-structure-activity relations in CO and $HCOO^-$ selective Cu-Sn and $HCOO^-$ selective Cu-S electrocatalyst materials as topic of this thesis

Since it appears that Cu-Sn and Cu-S electrocatalyst materials are promising from various aspects to be possibly utilized in large scale CO_2 conversion into CO and $HCOO^-$, they are certainly motivating and worth to be more thoroughly investigated. Namely, the CO_2ER products distribution on the Cu-Sn and Cu-S materials and the competition with the HER are not only dependent on the Cu vs. Sn or S composition, but also strongly dependent on and/or related with the applied potential for activation of the electrocatalysts, surface morphology (active surface area), Cu, Sn and S surface speciation (oxidation states) and chemical nature, electrolyte species etc. Therefore, understanding and being able to control these composition-

structure-activity relations and experimental conditions that affect the CO_2ER selectivity is of key importance for facing and resolving the challenges in this field toward achieving future large-scale application. Such application of these materials cannot be feasible without employing simple, fast and cheap synthesis routes, and additionally relying on recycling technologies for building a sustainable material circulation process with goal of mitigation the extraction of the natural resources. Therefore, together with investigation of the composition-structure-activity relations in the Cu-Sn and Cu-S electrocatalysts during CO_2ER, a successful approach for recycling/repurposing of waste bronze alloy for deriving Cu-Sn foam-based CO selective electrocatalyst, and simple, fast and cheap synthesis method for preparation of $HCOO^-$ selective Cu-S electrocatalysts were developed as one of the main goals of this thesis.

The investigation of the composition-structure-activity relations, experimental conditions and optimization of the synthesis methods is hardly imaginable without utilization of *in-situ* methods coupled with the CO_2 electrolysis experiment. Besides *in-situ* quantification and tracking of the electrolysis products over time, utilization of methods that are able to probe the electrocatalyst under operating conditions, thus screen its morphological, chemical, structural, electronic and phase changes and the products of these changes, then monitor the electrode-electrolyte interface, including the pH changes, reaction intermediates, mobility of various species etc. are of great importance. Most of these methods involve various spectroscopy, microscopy and diffraction characterization techniques such as Raman, FTIR, XPS, XAS, MS, DEMS, ICP-OES/MS, SEM, TEM, XRD etc.[218-224] Therefore, many of the above stated characterization methods including *in-situ* and *quasi in-situ* approaches coupled with CO_2 electrolysis are utilized in the scope of this thesis for investigating the Cu-Sn and Cu-S based electrocatalysts, their electrochemically driven composition-structure changes and the relation of these changes with the CO_2ER activity. The characterization methods that are used in the scope of for this thesis and their principles, together with the synthesis approaches are discussed in **Chapter 2**, the results from the studies are discussed and summarized in **Chapter 3** and comprehensively presented and discussed in **Chapters 4-6** (publications and manuscripts included in the thesis). Finally, the importance, advantages, challenges and future perspectives of the electrochemical conversion of CO_2, the Cu-Sn and Cu-S electrocatalyst materials and additionally possibilities and importance of other electrochemical conversion concepts such as ammonia and urea electrosynthesis, are summarized in **Chapter 7**.

CHAPTER 2. Methods section

2.1. Methods for synthesis of the CO_2ER catalysts

General description of the synthesis approaches

The methods utilized for synthesis of Cu rich Cu-Sn as CO-, and Sn rich Cu-Sn and Cu-S materials, as $HCOO^-$ selective CO_2 conversion electrocatalysts in this work are either single or two-step procedures from which the first one is electrochemical and the second one a chemical process. The electrochemical step involves several methods which are based on: anodization of Cu layers sputtered on glass substrates (**Chapter 4**), electrodeposition of bimetallic Cu-Sn on planar bronze alloy substrates (**Chapter 5**) and electrodeposition of pure Cu material on Cu mesh substrates (**Chapter 6**). In the first study (**Chapter 4**), electrochemical anodization of Cu layers was utilized for preparation of $Cu(OH)_2$ with nanowires morphology, while in the second (**Chapter 5**) and third study (**Chapter 6**), dynamic hydrogen bubble template (DHBT) electrodeposition technique was applied to prepare Cu-Sn and pure Cu, respectively, with porous (foam-like) morphology. The second chemical step involved functionalization of the nanowires with atomic layer deposition (ALD) of SnO_2 thin layers (**Chapter 4**) or sulfidation of the Cu foam with elemental sulfur dissolved in organic solvent (**Chapter 6**). In the case when the DHBT method was applied for electrodeposition of bimetallic Cn-Sn foam, no second step was involved, thus the as-prepared materials were directly used to study their CO_2ER catalytic activity (**Chapter 5**). A brief discussion of the synthesis methods is presented in the following text and detailed description is given in **Chapters 4-6** and corresponding publications.[177, 178]

Preparation and subsequent anodization of Cu layers for synthesis of $Cu(OH)_2$ nanowires

Cu layers were prepared on glass substrates via sputtering deposition. The synthesis of the nanowires was conducted via anodization of the sputtered Cu layers. The anodization procedure resembles electrochemical oxidation of Cu from metallic into Cu^{2+} in alkaline environment thus the presence of OH^- ions is driving growth of $Cu(OH)_2$ nanowires. The anodization of the Cu layers was conducted galvanostatically until reaching certain charge density threshold. Besides electrochemical anodization, similar nanowires growth effect can be achieved when Cu is oxidized via treatment with strong oxidant (e.g., $S_2O_8^{2-}$) under alkaline

conditions. However, the morphological outcome in such cases, besides nanowires, can lead to formation of other morphological structures such as nanosheets, nanotubes etc., as reported in the literature,[178, 225, 226] and accordingly presented in section S3 of the supporting information in **Chapter 5**. Proposed mechanisms regarding the process and conditions for formation of nanowires and other nanostructures can be found in the literature.[225, 227, 228] **Figure 2.1** illustrates the $Cu(OH)_2$ nanowires synthesis procedure via electrochemical anodization and the detailed description of the experimental conditions utilized in this research can be found in section S1 of the supporting information in **Chapter 4**, i.e. in the corresponding literature report,[177] and additionally in other literature sources from where it was adopted.[131]

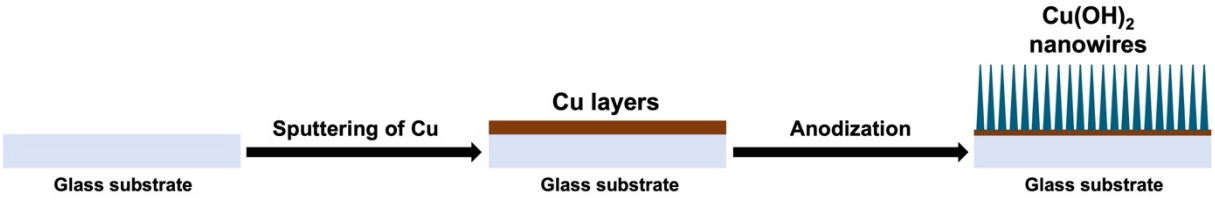

Figure 2.1. Schematic presentation of the $Cu(OH)_2$ nanowires synthesis procedure via electrochemical anodization of Cu layers in alkaline environment (**Chapter 4**).

Functionalization of the CuO_x nanowires with deposition of SnO_2

The $Cu(OH)_2$ nanowires were thermally dehydrated under vacuum conditions into CuO prior to functionalization with SnO_2. The functionalization of the CuO nanowires was conducted using atomic layer deposition (ALD) of thin layers of SnO_2 by altering the amount of deposition cycles (from 1 to 182) to achieve surface that is either poor or rich with Sn, hence synthesizing CO or $HCOO^-$ selective, CO_2ER catalyst, respectively (as discussed in **Chapter 4** – publication reference[177]). The dehydration/ALD functionalization process is depicted in **Figure 2.2**. ALD is a vapor-based deposition technique that when certain temperature/pressure conditions are achieved, reactions between the precursors (in this case metal-organic Sn-complex and water) and the surface of the substrate are triggered, thus the nanowires undergo process of uniform coating with thin layers of SnO_2. The layer thickness can be controlled via the precursor(s) concentration, temperature, pressure, number and duration of the deposition cycles etc. More information regarding this technique can be found elsewhere.[229] The processes of thermal dehydration of the $Cu(OH)_2$ nanowires and SnO_2 functionalization with ALD do not affect the morphology, thus the nanowire structures are preserved.

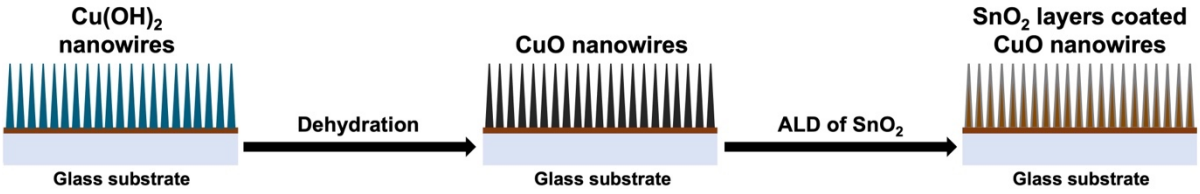

Figure 2.2. Schematic representation of the dehydration of $Cu(OH)_2$ to CuO and subsequent functionalization with thin layers of SnO_2 (**Chapter 4**).

Dynamic H_2 bubble template electrodeposition for synthesis of Cu and Cu-Sn foams

The dynamic H_2 bubble template (DHBT) is relatively simple and fast method that is already reported in the literature for preparation of CO_2ER catalysts.[167] As already mentioned, this method is utilized for electrodeposition of Cu and Cu-Sn foams in the scope of this work. The method is based on formation of H_2 bubbles via electrochemical reduction of H^+ in strongly acidic electrolyte. These bubbles serve as templates around which mutual reduction of Cu^{2+} and Sn^{2+}/Sn^{4+} cations lead to formation of bimetallic Cu-Sn foam (**Chapter 5**), while reduction of only Cu^{2+} is deriving pure Cu foam (**Chapter 6**). The as-synthesized pure Cu and bimetallic Cu-Sn foams resemble porous morphology, as illustrated in **Figure 2.3**, which are composed of dendrite-like microstructures (see SEM images in **Chapters 3, 5** and **6**). The Cu-Sn foam was DHBT electrodeposited potentiostatically in a three-electrode setup using waste Cu-Sn bronze alloy anode as a source of Cu and Sn (**Chapter 5**), while DHBT electrodeposition in a galvanostatic mode and in a two-electrode setup was used for preparation of pure Cu foam from deposition solution containing Cu^{2+} (**Chapter 6**). In both cases the electrodeposition was conducted until certain time threshold was reached. The synthesis optimization was conducted via varying the applied potential, current density and time of electrodeposition. The conditions for formation of metallic porous foams, their pore sizes and thicknesses are dependent on the metals deposition exchange current densities that are associated with their electrocatalytic activities for HER, and furthermore the applied potential or current, time, electrolyte convection, presence of complexing, buffering, surfactant agents etc., during the DHBT electrodeposition process. More information regarding these effects can be found in the literature.[167, 230] Several publications claim that interconnected channel-porous materials, and moreover when composed of dendrite-like microstructures can avoid CO_2 local depletion near the surface of the electrode thus enhancing its mass transport during the electrolysis,[163-168] as already discussed in **Chapter 1** (section 1.3).

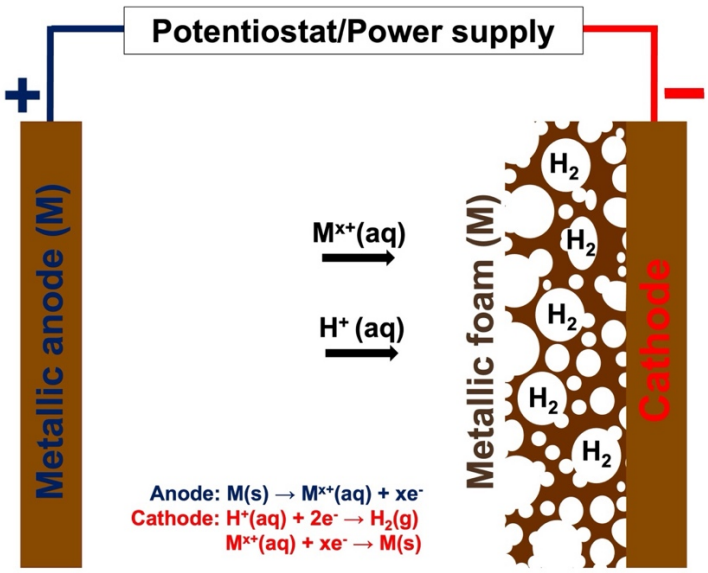

Figure 2.3. Schematic representation of the DHBT electrodeposition of bimetallic Cu-Sn or pure Cu foams. M^{x+} represent Cu^{2+} or Sn^{2+}/Sn^{4+} cations. In the case of bimetallic Cu-Sn foam electrodeposition via transfer of these elements from waste bronze alloy, another identical bronze alloy electrode was used as an anode (**Chapter 5**), while in the case of pure Cu foam, high purity Cu foil anode was used instead (**Chapter 6**).

Facile method for sulfidation of DHBT electrodeposited Cu foam

The sulfidation method for preparation of $HCOO^-$ selective CO_2ER catalysts was conducted via simple immersion of the DHBT electrodeposited Cu foam in solution composed of sulfur dissolved in toluene for several seconds under constant stirring. The sulfidation process does not affect the overall morphology, thus the pore sizes and thickness of the foam are preserved, yet slightly affects the foam constituents, i.e., the dendrite microstructures undergo blunting of their edges (SEM images in **Chapters 3, 5** and **6**). Two possible hypotheses regarding the sulfidation mechanism are discussed in **Chapter 6**, thus one hypothesis is based on a literature report,[231] and the other one inspired by an older publication claiming that the commercial sulfur could contain sulfur species that are more reactive compared to the thermodynamically stable octa-sulfur (S_8).[232] **Figure 2.4** depicts a schematic presentation of the Cu foam sulfidation method. Additionally, sulfidation of Cu foam was also successfully conducted using solution composed of sulfur dissolved in CS_2, which was abandoned to the toxicity of this solvent.

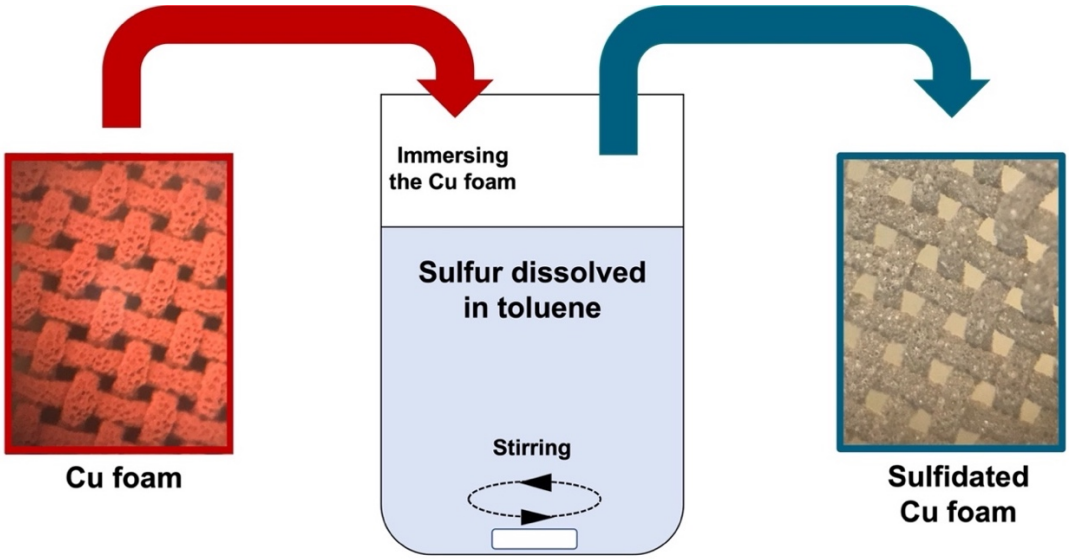

Figure 2.4. Schematic representation of the facile and fast method for sulfidation of the DHBT electrodeposited Cu foam via its immersion in sulfur/toluene solution (**Chapter 6**).

2.2. Characterization methods

The chemical composition, crystal structure, morphology, pore size, thickness, oxidation state speciation, thermal properties of the materials used as electrocatalysts were determined using various methods intended for specific purpose, as presented in the following text. All characterization methods were utilized for study of the as-synthesized materials, while large part of them were used to characterize the materials and electrolytes post-electrolysis. Besides *ex-situ* pre- and post-electrolysis characterization, several methods were applied under *in-situ* conditions including gas chromatography (GC), thermogravimetric analysis (TGA), electrolysis coupled with mass spectrometry (EC-MS) and x-ray absorption spectroscopy (XAS), and under *quasi in-situ* conditions, such as x-ray photoelectron spectroscopy (XPS). The methods that are coupled with electrolysis without bulk/surface characterization of the electrocatalyst itself, such as chromatography and mass spectrometry, are discussed in the next section (2.3) of this chapter. The important principles, on which each technique is based, are depicted in the corresponding subsection where the specific technique is discussed. Furthermore, the experimental results from the characterization studies such as the chemical composition, phase and crystal structure, and surface speciation can be used as parameters in computational modeling methods for various CO_2ER/HER mechanistic predictions. A very common computational method is the density functional theory (DFT) that is used to calculate the binding energies of various intermediate species involved in the catalytic pathways thus to predict possible reaction mechanisms. Namely, the DFT modeling was used for calculating the

binding energies of the *COOH/*CO and *OCHO* intermediates on Cu-Sn surfaces that follow the pathways towards CO_2ER into CO and $HCOO^-$, respectively, and moreover for calculating the binding energies of the *H intermediate that is responsible for the competitive HER. Thus, the DFT results contributed towards understanding the influence of the chemical composition and surface speciation on the electrocatalytic selectivity towards CO, $HCOO^-$ and H_2. More information regarding the DFT modeling details, specifically for studying the Cu-Sn system, can be found in **Chapter 4**, or the corresponding publication.[177]

The following text of this section is dedicated to the experimental characterization methods.

X-ray diffraction analysis (XRD)

X-ray diffraction (XRD), a non-destructive analysis technique, is used to study and reveal the chemical, morphological, phase composition and crystal structure of the solid electrocatalyst materials used in this research. The technique was applied for studying the as-prepared and post-electrolysis electrocatalyst materials. XRD is based on the *diffraction phenomenon* which can be simply defined as interference caused by crystal lattice motifs subjected to x-ray radiation with dimensions comparable to the wavelength of the x-rays. During the diffraction the x-rays are scattered elastically when interacting with the electrons of the atoms, thus no photon energy is being lost. The interference can be of constructive or destructive nature depending on whether the scattered x-ray waves oscillate in- or out of phase, respectively. For constructive interference to occur, the phase difference of the waves must be an integer multiple of the wavelength in order to satisfy the Bragg's law (**Equation 2.1**).

Equation 2.1: $n \cdot \lambda = 2 \cdot d \cdot sin\theta$

where n is an integer number (1, 2, 3…), λ is the x-rays wavelength, d is the spacing between the lattice planes and θ is the angle between the incident or the scattered x-ray and the lattice plane (diffraction angle), as depicted in **Figure 2.5**. The scattered waves are spherical and most of them are oscillating out of phase, thus being canceled out and only few of them undergo constructive interference i.e., the Bragg's law is satisfied. Yet, it is not always the case that the waves that oscillate out of phase have to fully cancel out, that is only the resultant amplitude will be decreased. A full cancelation occurs when a superposition of two waves with the same frequency (coherent waves) have a phase difference which is odd number

multiplying π. A fully amorphous materials due to lack of long-range order arrangement in their structure do not fulfill the Braggs's law hence, no diffraction signals can be observed. In reality, there are no perfect crystals (in theory highest order arrangement is achieved at 0 K i.e., zero entropy as basis for formulation of the Third's law of thermodynamic) thus, one of the reasons for broadening of the diffraction patterns in a diffractogram is presence of fraction(s) of poorly ordered arrangement of the constituents i.e., amorphous phase(s) in the sample of interest. Besides presence of amorphous phase(s), the defects in the structure of various nature are decreasing the ordered arrangement and can also contribute to the aforementioned broadening.

The XRD studies are typically carried out in two configurations, the Bragg-Brentano and the grazing incidence x-ray diffraction (GI-XRD), as depicted in **Figure 2.5**. Powder diffraction analysis is conventionally carried out in Bragg-Brentano configuration, while the GI-XRD is used to probe materials such as films and coatings deposited on substrate in a manner that avoids interference from the substrate itself. This approach uses small angles between the incoming radiation and the surface of the sample (grazing or glancing angle - ω). When this angle is smaller than the critical angle the beam will undergo a total reflection i.e., will be parallel to the surface thus no diffraction will be observed, while if it is higher, the x-rays will penetrate deeper in the sample hence, possible interaction of the substrate can occur. Therefore, intermediate angles are used to achieve probing only from the deposited material but not from the substrate. This is achieved in a configuration where the x-ray source, i.e., the incident angle (ω) is fixed, and the detector can move in comparison with the Bragg-Brentano configuration where both source and detector move with the same rate. Moreover, another reason for using the GI-XRD technique is the possibility for accurate sample height correction. If the height is not corrected properly, peak shifts and misinterpretation of the information can occur, especially when looking for possible alloy formation in the case of the Cu-Sn bimetallic materials studied in the scope of this work. XRD is a simple technique to record diffractograms of solid materials with known crystal structures. However, converting the diffraction signals, data refinement and using this information for resolving unknown crystal structures requires complex mathematical operations (such as Fourier transformations), and experience which is beyond the scope of this thesis. The x-rays used for the XRD analysis techniques are obtained via bombardment of metal target with electrons. Various x-rays are emitted in this process and most of them are of continuum nature coming from *bremsstrahlung* i.e., deceleration of the electrons when interacting with the target. During this process, secondary core electrons (SE) are removed from the target atoms thus leaving holes. These holes are fulfilled by outer shell electrons accompanied with emitting characteristic x-rays with much higher intensity than the continuum rays. Thus, these characteristic x-rays are used for the XRD analysis, most commonly the Kα spectral lines that are obtained via electron bombardment of Cu target (Cu

Kα). The generation of characteristic x-rays via SE emission/electron hole fulfilling and the SE emission itself are typical for the x-ray spectroscopy-based methods (EDX, XRF, XPS, XAS etc.) hence, more discussion is provided in the following text.

The diffractometer instrumental setup, parameters, and the results and discussions from the XRD analysis are presented and discussed in (**Chapters 3-6**) and the corresponding publications.[177, 178] More information regarding the XRD techniques and their applications can be found elsewhere.[233, 234]

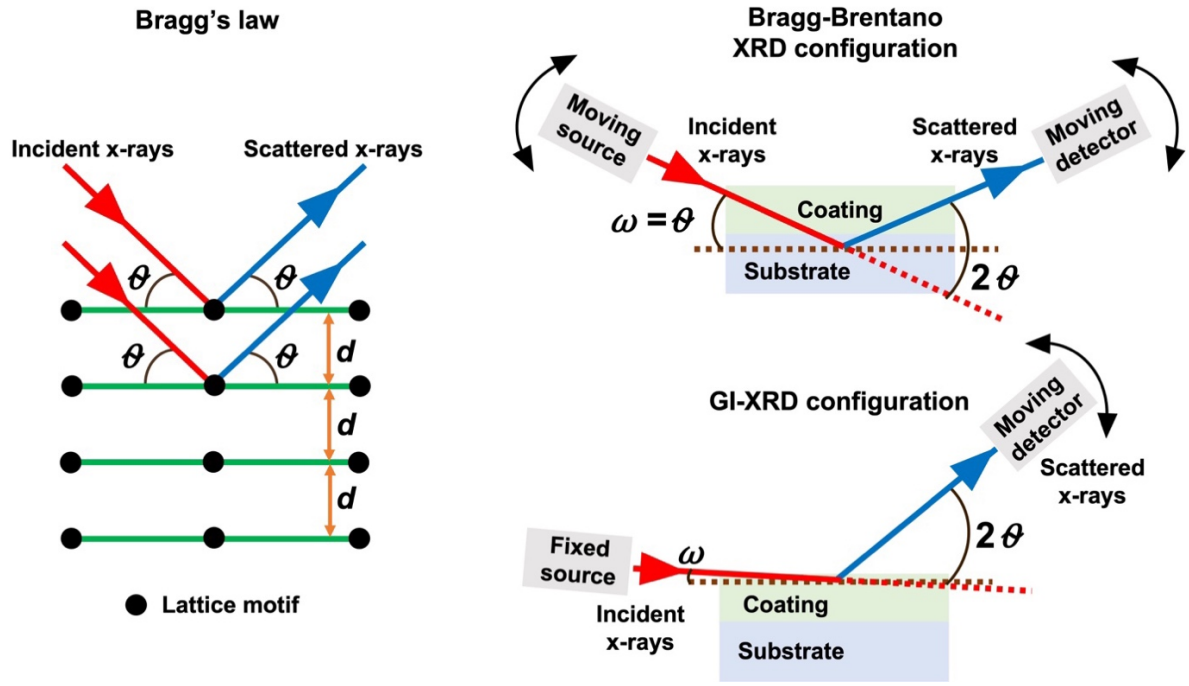

Figure 2.5. Schematic illustration of Bragg's law and the difference between Brag-Brentano and GI-XRD configuration.

Inductively coupled plasma-optical emission spectrometry (ICP-OES)

The quantitative analyses of the bulk composition of the materials used as synthesis precursors, the as-synthesized electrocatalysts and the concentration of various elements in the electrolytes post-CO_2 electrolysis were conducted using inductively couple plasma-optical emission spectrometry (ICP-OES). The sample preparation prior to the analysis is specific for each analyte i.e., the solid materials were dissolved in acids (HNO_3, HCl and their mixtures dependent on the sample/analyte nature), while the electrolytes were analyzed directly or with particular pre-treatment. The utilization of this technique for the aforementioned purposes and the analysis results are discussed in **Chapters 3-6** (and references,[177, 178] for the published work). The ICP-OES is a multielement quantification technique that is based on atomic

emission spectroscopy. The liquid sample (aqueous solution) is sprayed in a nebulizer and transferred in ionized argon plasma under very high temperature (10^3-10^4 K) thus, evaporation and creation of excited atoms and ions from the elements of quantification interest occurs. The argon plasma is created via strong electromagnetic field induced by radio-frequent generator. The de-excitation of the excited/ionized atoms emits radiation that is characteristic for each element (spectral lines), typically in the UV-Vis region of the electromagnetic spectra. However, various factors can cause broadening and shift of the characteristic spectral lines thus leading to overlapping. The intensity of the emitted radiation is proportional to the concentration of a certain element in the sample, following the Beer-Lambert´s law (**Equation 2.2**). Using this technique, quantification with relatively high sensitivity can be achieved.

Equation 2.2: $A = \varepsilon \cdot l \cdot c$, where A is absorbance, ε is absorptivity or extinction coefficient, l is optical path length and c is the concentration of the element of interest.

More information regarding this technique can be found elsewhere.[235, 236] The technique setup and principle on which it is based are schematically depicted in **Figure 2.6**.

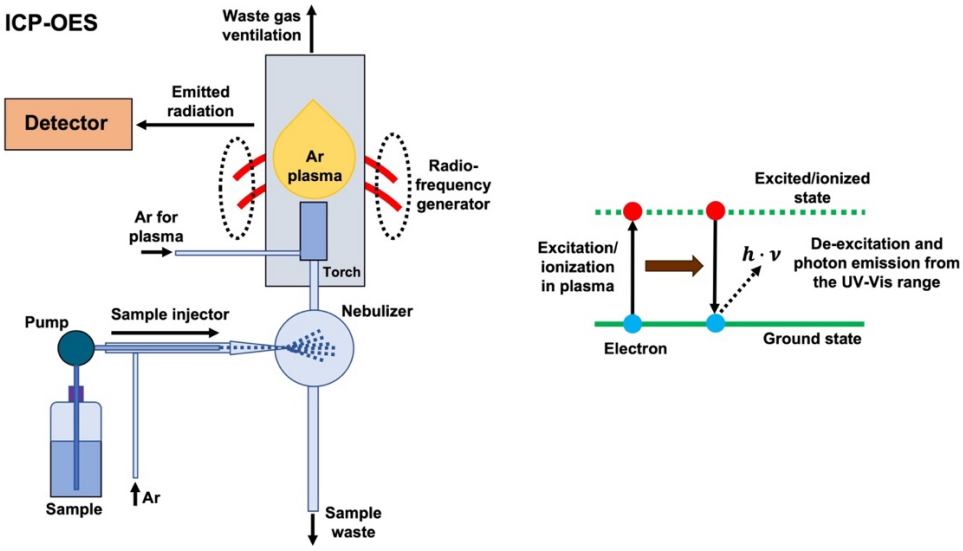

Figure 2.6. Schematic representation of the ICP-OES technique and simplified principle on which it is based.

In-situ thermogravimetric analysis coupled with mass spectrometry (TGA-MS) and differential scanning calorimetry (DSC)

The thermal properties of the copper sulfide materials synthesized via immersing metallic Cu in organic solvent in which sulfur is dissolved were analyzed using thermogravimetric analysis that is *in-situ* coupled with mass spectrometry (TGA-MS) and differential scanning calorimetry (DSC). The instrumental setups and measurement results are presented and discussed in **Chapter 6**. The TGA is based on measurement of the mass loss as a function of the temperature.[237] This technique is often coupled *in-situ* with the very sensitive MS in order to analyze volatile compounds and/or gaseous decomposition products. Thus, the MS technique is utilized as a detector and besides coupling with TGA, it can be coupled with many other techniques such as chromatography, atomic adsorption and emission spectrometry, electrophoresis etc., and in the case of this work, it is coupled with electrochemical techniques for *in-situ* tracking of gaseous products (H_2S) evolved during electrolysis (EC-MS) as presented in the next section (2.3.) of this chapter and discussed in **Chapters 3** and **6**. The mass spectrometry is based on detection of various ion species based on their mass-to-charge (m/z) ratio. The analyte is being ionized with electron bombardment, chemical, photo, plasma, thermal ionization etc., thus transferred in a separation chamber (mass analyzer). The ions are separated and detected based on their behavior in magnetic and/or electric field, time of travel (flight) etc., driven by the differences in the (m/z) ratio. More information about the mass spectrometry techniques and their application can be found in the literature.[238] The DSC is utilized to estimate the *endo*- or *exo*- heat effects attributed to physical, chemical or phase transformation of certain material dependent on the temperature. It is based on controlled applying of heat simultaneously on the sample of interest and a reference material with known heat capacity and measuring the heat absorption or emission at a certain temperature with respect to the reference material. A simplified schematic representation of both TGA-MS and DSC techniques is depicted in **Figure 2.7** and more information can be found elsewhere.[239]

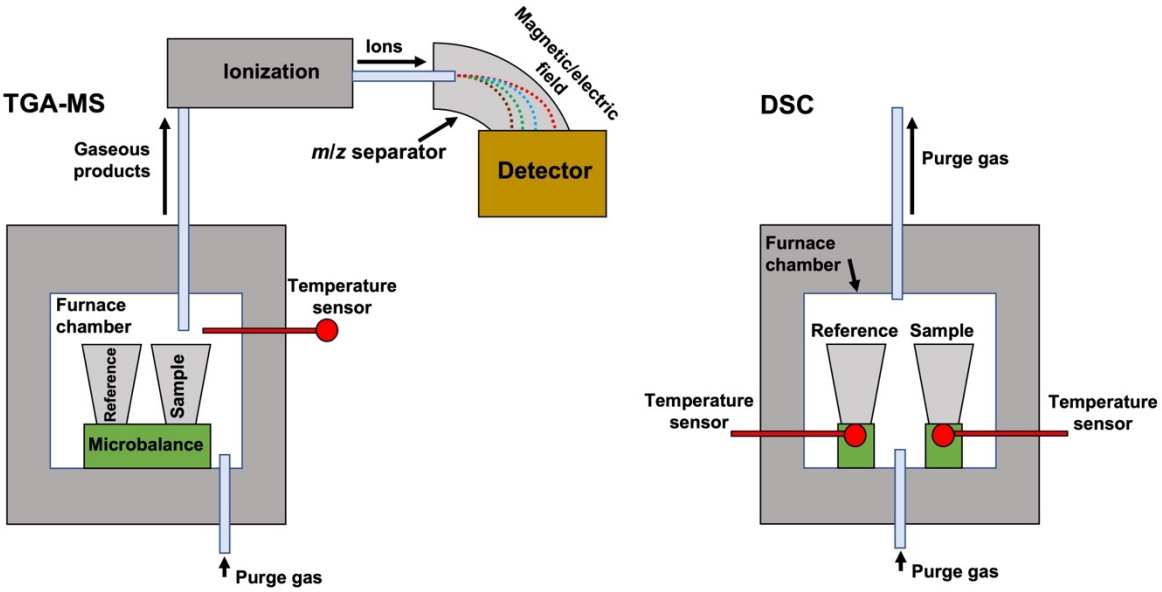

Figure 2.7. Schematic representation of the *in-situ* TGA-MS and DSC techniques.

Electron microscopy (SEM and TEM), energy dispersive x-ray (EDX) spectroscopy and electron diffraction methods

The determination of the surface morphology, thickness and pore sizes of the electrocatalyst materials pre- and post-electrolysis was conducted using scanning electron microscopy (SEM). The method is based on applying electron beam on the solid material in vacuum thus information about the topography is gathered from the signals coming from the interaction between electrons and surface species. When the electron beam (energy order of magnitude ~keV range) interacts the examined probe, Auger and secondary electrons (SE) are emitted from the shallow surface of the material, back-scattered electrons (BSE) are reflected from the surface and the bulk, and additionally characteristic and continuum x-rays (background and fluorescence) are emitted from the bulk of the material. The electrons that have sufficient energy to pass through the material are known as transmitted electrons. The part of the examined material that interacts with the electron beam is known as interaction (sampling) volume that has droplet-like shape (**Figure 2.8**). The size of the interaction volume depends on the energy of the applied electron beam and can reach depth in the order of several micrometers. The SE is core electron that is removed from atom by a primary electron (from the electron beam), thus in the most common instrumental setups, the SE are used for providing high-resolution SEM images. On the other side the hole created when a SE is removed from the atom is fulfilled with an upper shell electron thus characteristic x-ray photon is emitted. The energy of the emitted x-ray photon is equal to the energy difference between

the upper and the shell where the hole is fulfilled. These characteristic x-rays are unique for each element thus being a basis of the energy dispersive (EDX) spectroscopy. The SE generated deeper in the sample (several micrometers) have smaller mean-free path than the characteristic x-rays, hence, are unlikely to be detected. The EDX technique is often combined with the SEM, thus being utilized for bulk quantification and elemental mapping of the electrocatalyst materials. The thickness of the electrocatalysts when deposited on a substrate is estimated from the cross-section SEM after a vertical hole is made using focused ion beam (FIB) ablation or milling. This technique is based on applying beam of metal ions (most commonly Ga^{+}) thus, area and depth-controlled removal of the sample material occurs. The sample in then tilted under specific angle and the cross-section thickness is estimated, as depicted in **Figure 2.8**.

The transmitted electrons illustrated in the interaction volume scheme (**Figure 2.8**) are used in the transmission electron microscopy (TEM) technique for imaging materials yet being limited to nanoscale thicknesses of the analyzed sample. TEM typically requires higher acceleration voltages and therefore higher resolution is achieved than in the case of SEM and moreover the effects of electron interactions with the sample of interest can be utilized to study its chemical and phase composition. Commonly used techniques for this purpose are the energy filtered and high-resolution transmission electron microscopy (EF- and HR-TEM) and selected area electron diffraction (SAED). The EF-TEM is used for elemental mapping i.e., studying the chemical composition while HR-TEM and SAED provide crystallographic information.

More information regarding the SEM, EDX, FIB and TEM instrumental setups used in this research and more general application of these methods can be found in **Chapters 3-6**[177, 178] and various literature sources,[240-244] respectively.

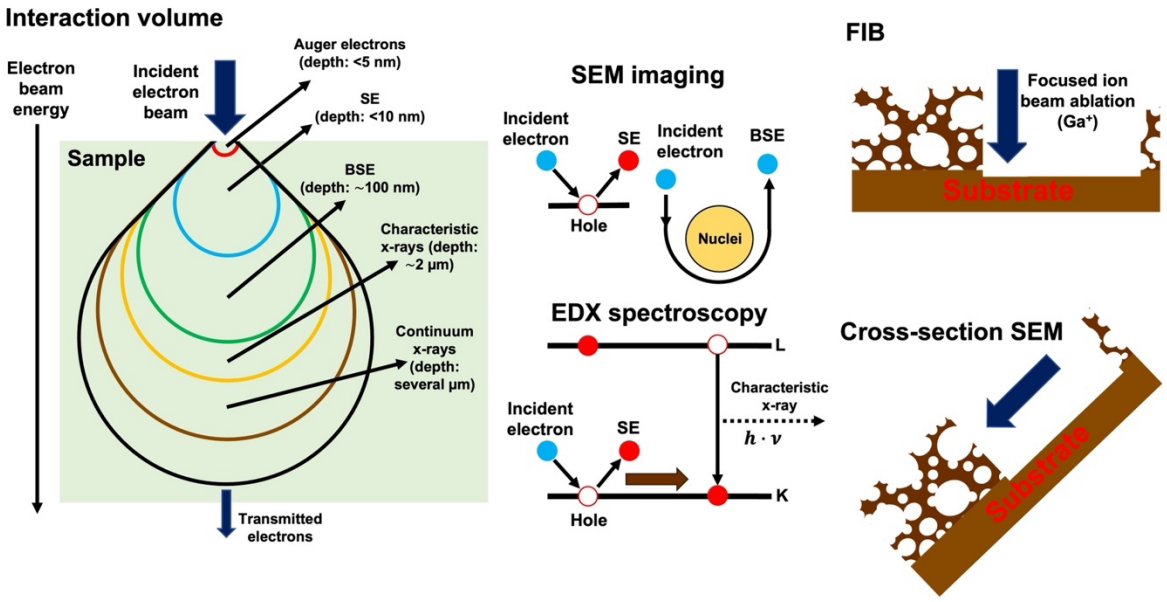

Figure 2.8. Schematic representation of the interaction volume/simplified summary of electron-sample interactions as basis for the SEM/TEM and EDX techniques and example of FIB ablation of metallic foam/cross-section SEM for thickness estimation.

X-ray fluorescence spectrometry (XRF)

When elemental mapping and composition analysis of relatively large samples are required, such as the case of the waste bronze alloy samples depicted in **Figure 2.9**, (pre-cut from casted ingots) that were used as anodes during the DHBT electrodeposition of Cu-Sn foams (**Chapter 5**[178]), the EDX is not practically applicable to completely cover such a big area and the ICP-OES gives average Cu-Sn composition. Thus, x-ray fluorescence (XRF) technique was found to be rather useful for this purpose. The XRF is based on ejection of electron from the inner electron shells of the atom (core electron) with high energy radiation such as the x-rays hence, leaving hole which is subsequently filled with another electron from an outer shell accompanied with emission of characteristic x-ray photon. The energy of the photon corresponds to the energy difference between the outer shell from which the electron `jumped` and the inner one where it filled the hole. Yet, the energy of the emitted x-rays is smaller than the energy that was used to create the hole and this is known as *fluorescence effect* (**Figure 2.9**). Besides deexcitation with radiation emission, an electron from the outer shell can undergo non-radiative transitions (such as vibrations in the case of covalent bond character between the atoms). More information regarding the XRF spectrometry principles and applications and analysis of Cu-Sn bronzes with this technique can be found elsewhere.[245-247]

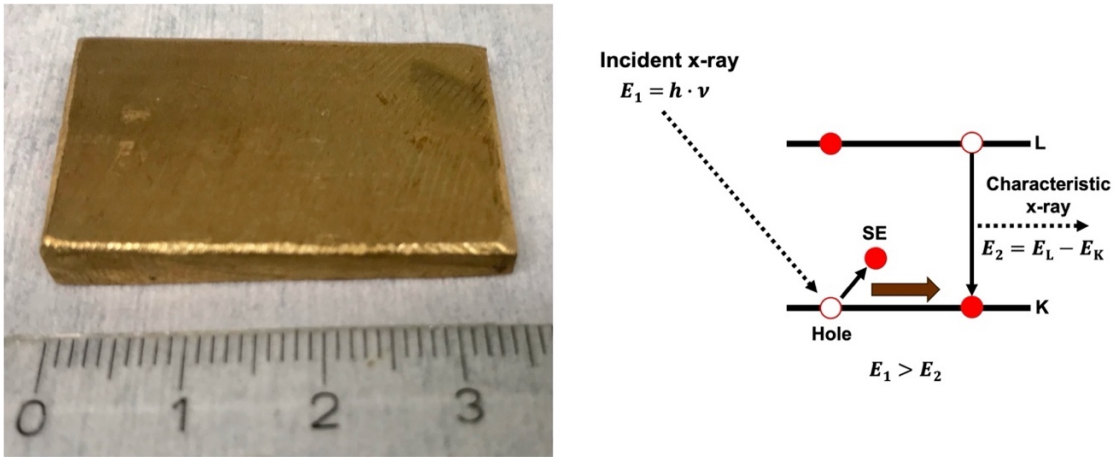

Figure 2.9. Photo of waste bronze anode used for DHBT electrodeposition of Cu-Sn foams (**Chapters 3** and **5**) and simple schematic representation of the fluorescence principle. The Cu and Sn bulk elemental distribution and quantification covering the whole area of the bronze anode was conducted via XRF spectrometry.

X-ray photoelectron spectroscopy (XPS)

As a very surface sensitive method due to relatively small electron mean-free path, the x-ray photoelectron spectroscopy (XPS) is one of the most important techniques for studying the electrocatalysts in terms of their surface composition and speciation (oxidation states and chemical nature), pre- and post-electrolysis (*ex-situ*) and as near *in-situ* as possible using the so called *quasi in-situ* XPS approach[168] (**Figure 2.10**). The reason for utilization of this approach is preservation of the surface elements oxidation states, post-electrolysis, in the case of materials that are prone to oxidation in air. Namely, as presented in **Figure 2.10**, the CO_2 electrolysis experiment is conducted in glovebox under inert atmosphere. After termination of the electrolysis, the samples are transferred into vessel (transfer arm) attached to the glovebox, which is afterwards sealed, evacuated and re-attached to the XPS analyzer. The *quasi in-situ* XPS approach was applied for studying the surface speciation of the Cu-Sn and Cu-S electrocatalysts, as presented and discussed in **Chapters 3, 4** and **6** of the thesis (corresponding references for the published work[177]).

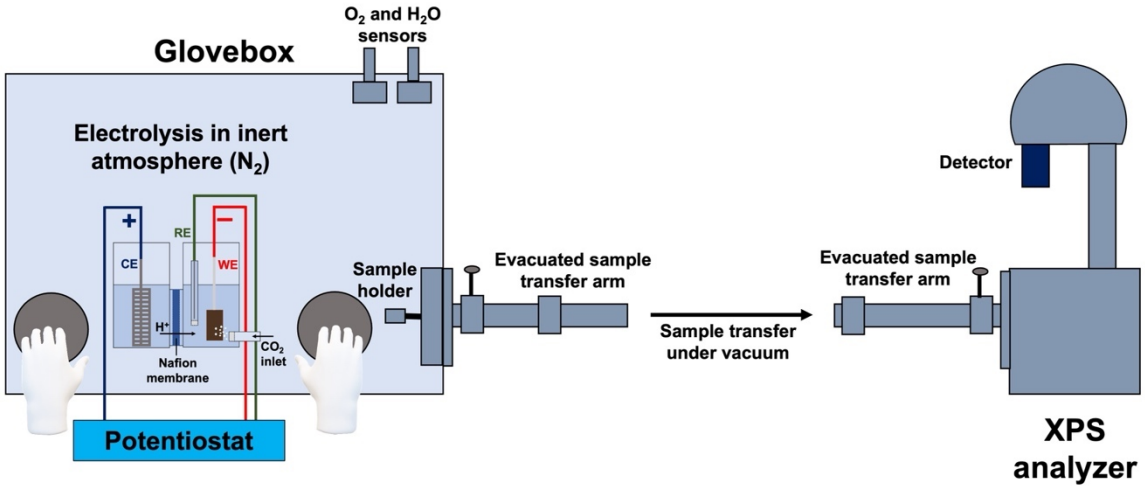

Figure 2.10. Schematic presentation of the *quasi in-situ* XPS approach. The electrolysis is conducted in a glovebox under inert conditions. After the electrolysis the electrocatalysts are transferred from the glovebox into the XPS analyzer via the sample transfer arm (vessel) under vacuum. This approach is beneficial for preservation of electrocatalysts' surface element(s) oxidation states. The H-type electrochemical cell is depicted in **Figure 2.14** and more information is provided in section 2.3 of this chapter. This setup was used for the research described in **Chapters 4** and **6**.

The XPS technique is based on the photoelectric effect i.e., ejection of core level electrons with x-rays range energy photons in vacuum. The photon energy that is required for an electron to be excited from a specific core level into the Fermi level is known as binding energy (BE). The BE is related to the ejected electron kinetic energy (KE) in vacuum and the work function (WF) according to **Equation 2.3**. The WF represents the minimal energy required for the electron to overcome the barrier between the vacuum and the Fermi level i.e., to be ejected into the vacuum (ionize the atom). This ejected electron is known as photoelectron. The basic principle of XPS is schematically depicted in **Figure 2.11** (left side), and information regarding this technique can be found elsewhere.[247] The specific core level BE energy set is unique for particular element, yet in reality certain overlapping can occur due to various factors.[248]

Equation 2.3: $h \cdot \nu = BE + KE + WF$, where $h \cdot \nu$ is the incident x-ray photon energy.

The XPS core levels of interest in this work are the Cu 2p, Sn 3d, O 1s and S 2p and additionally the characteristic Cu $L_3M_{4,5}M_{4,5}$ Auger transition.[249] Where necessary, the spectra were corrected with respect to the C 1s core level attributed to C-C bond at 285 eV.[250] All core level peaks were fitted using fitting software and the fitting parameters are adopted from the literature.[250, 251] The Cu 2p, Cu $L_3M_{4,5}M_{4,5}$ Auger and Sn 3d were used for quantification of the

Cu-Sn based electrocatalysts surface composition and speciation of the constituent elements, as discussed in **Chapters 4** and **5** (and the corresponding references for the published work[177, 178]). On the other hand, in the case of the Cu-S based electrocatalysts, both Cu 2p and S 2p were used for quantification of the Cu:S surface composition, S 2p was additionally used for speciation of the surface sulfur (as S^{2-} and SO_4^{2-}), while the Cu $L_3M_{4,5}M_{4,5}$ Auger transition was used to distinguish and quantify different Cu oxidation states and their chemical nature[251] (such as Cu^+ from Cu_2S vs. from Cu_2O), as discussed in **Chapter 6**.

The Auger effect, depicted on **Figure 2.11** (right side) showing KL_1L_2 transition as a simple example, is a net radiation-less electron emission phenomenon. In the case of the KL_1L_2 Auger transition, an electron is ejected from the K shell with incident photon that has sufficient energy to do so (x-rays) hence, a hole is being created (**Figure 2.11a**). This hole is fulfilled with another electron from the L_1 shell thus secondary x-ray photon is emitted (**Figure 2.11b**). The energy of the secondary photon is the difference between the energy of the corresponding shells (L_1 – K) and this photon has sufficient energy to eject another electron from outer shell or subshell (L_2 in the case of KL_1L_2 transition), known as Auger electron where KE is its kinetic energy, simultaneously creating a second hole (**Figure 2.11c**).

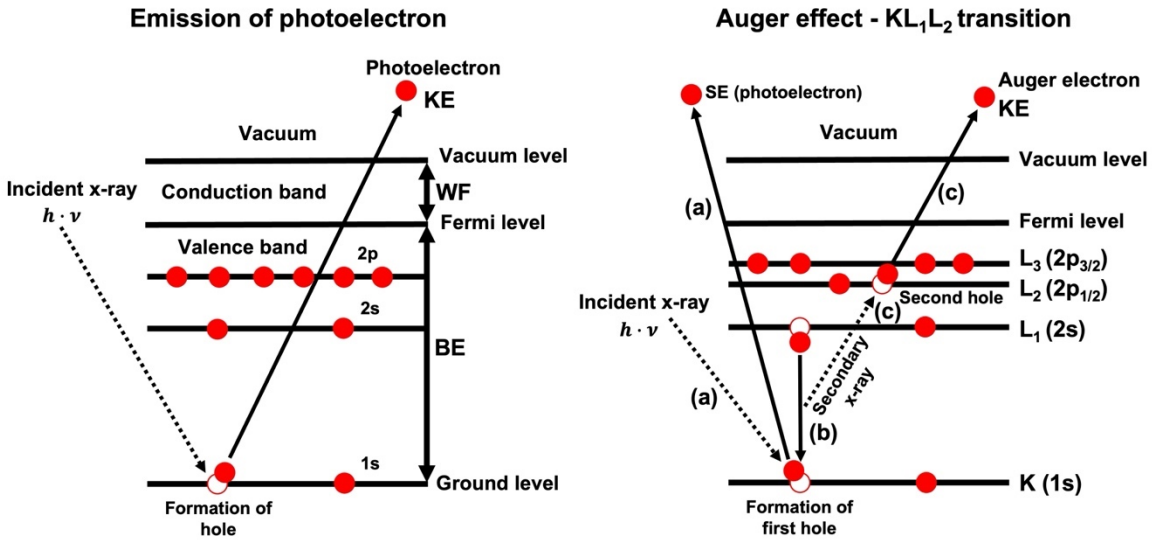

Figure 2.11. Schematic representation of x-rays interaction with the sample via photoelectron (left side) and Auger electron emission in the case of KL_1L_2 transition as an example (right side). During this transition an incident x-ray ejects electron from the K shell (secondary electron -SE) hence hole is being created **(a)**. This hole is filled with outer shell (L_1) electron accompanied with secondary photon emission **(b)**. The secondary photon has sufficient energy to eject another electron from outer shell (L_2) known as Auger electron creating second hole **(c)**.

Regarding the quantification of the Cu and S surface fractions in the Cu-S based electrocatalysts, it is important to emphasize that primarily the peak-areas of the corresponding core levels were normalized with respect to the relative sensitivity factors (RSF) according to **Equation 2.4**. The RSF values depend on the x-ray energy and the angle between the source and the analyzer thus, different values apply for different XPS instrument setups. The RSF factors are associated with the photoionization cross-section which is the probability of a photon to completely remove an electron i.e., to ionize the atom at a given photon energy.[252] This probability is different for different core levels and atoms when interacting with a constant photon energy from a specific x-ray source.

Equation 2.4: $Peak\ area_{corrected\ vs.\ RSF} = \frac{Peak-area\ after\ fitting}{RSF\ for\ specific\ core\ level}$

The RSF correction was not necessary in the case of Cu-Sn due to the similar RSF values for Cu 2p and Sn 3d core levels of these elements.

Ex-situ and in-situ x-ray absorption spectroscopy (XAS)

X-ray absorption spectroscopy (XAS) was used under *ex-situ* (pre- and post-electrolysis) and *in-situ* mode to study the electronic structure of the SnO_2 functionalized CuO nanowires, as described in **Chapters 3** and **4**.[177] The purpose of this study is correlating the Cu and Sn oxidation states with the CO_2ER catalytic activity of the SnO_2 functionalized CuO nanowires at various applied potentials. Synchrotron radiation from BESSY-II (*German:* Berliner Elektronenspeicherring-Gesellschaft für Synchrotronstrahlung, *translated in English*: Berlin electron storage ring – Society for synchrotron radiation) was used as x-rays source.[253] The synchrotron generated x-rays pass through a monochromator prior being utilized for the XAS study of the electronic structure of the materials in the corresponding beamline/end-station. The XAS spectroscopy is based on core electron x-ray absorption which undergoes transition to unoccupied orbitals (conduction band), as depicted in **Figure 2.12**, contrary to XPS where a core electron is being ejected beyond the conduction band i.e., into the vacuum (**Figure 2.11**- left side). The de-excitation process is mainly accompanied by fluorescence (scheme in **Figure 2.9**) hence, in the case of the hard x-rays XAS, characteristic fluorescence photons are being detected. These photons have higher mean-free path which makes this method rather bulk sensitive (hundreds of nanometers). Yet, transitions accompanied with photoelectron i.e., SE emission cannot be fully excluded and moreover electrons can be emitted due to the Auger effect (**Figure 2.11** – right side). These electron emissions are the basis of the total electron

yield (TEY) detectors in the case of the soft x-rays XAS which is rather surface sensitive technique since the emitted electrons resemble significantly smaller mean-free path, compared to the aforementioned fluorescence x-ray photons. The transitions during the x-ray absorption follow the selection rules thus the transitions where the difference in the orbital quantum number (l) is 1 ($\Delta l = \pm 1$) are permitted. Without entering into many details, the allowed transitions from the ground state orbitals of the core electrons to the unoccupied orbitals are s $\rightarrow$ p, p $\rightarrow$ d, p $\rightarrow$ s, d $\rightarrow$ p, while transitions like s $\rightarrow$ s, p $\rightarrow$ p, d $\rightarrow$ d, or s $\rightarrow$ d are forbidden. The x-ray absorption spectrum (intensity vs. energy) can be generally divided into three regions. The first region (pre-edge) involves electron excitation into lower energy bonding orbitals, the second i.e., edge region involves the highest intensity transition of the electron, and the third range that requires higher energy than the edge is known as extended x-ray absorption fine structure (EXAFS). The appearance of pre-edge feature in the spectrum is simply a deviation from the selection rules ($\Delta l = \pm 1$), which in reality does occur. Namely, the x-ray absorption causes an electron to undergo $\Delta l = \pm 2$ transition e.g., s $\rightarrow$ d but however, the intensity of the pre-edge feature is lower compared to the edge. The pre-edge and edge regions belong to a broader region known as x-ray absorption near edge structure (XANES) region. The XANES features in the spectrum give information regarding the oxidation state (e.g., in this research a differentiation between Cu^0, Cu^+ and Cu^{2+} species thus higher energy shift of the edge implicates higher oxidation state, **Chapter 4**[177]). On the other hand, the EXAFS is in a simple way affected by electrons from adjacent atoms and gives information about their identity, coordination number and bond distances (such as Cu-Cu or Cu-O in this research). This information cannot be seen immediately from the EXAFS region of the spectrum, but complex mathematical operations such as Fourier transformations in adequate software (e.g., Athena) are required for processing of the data.

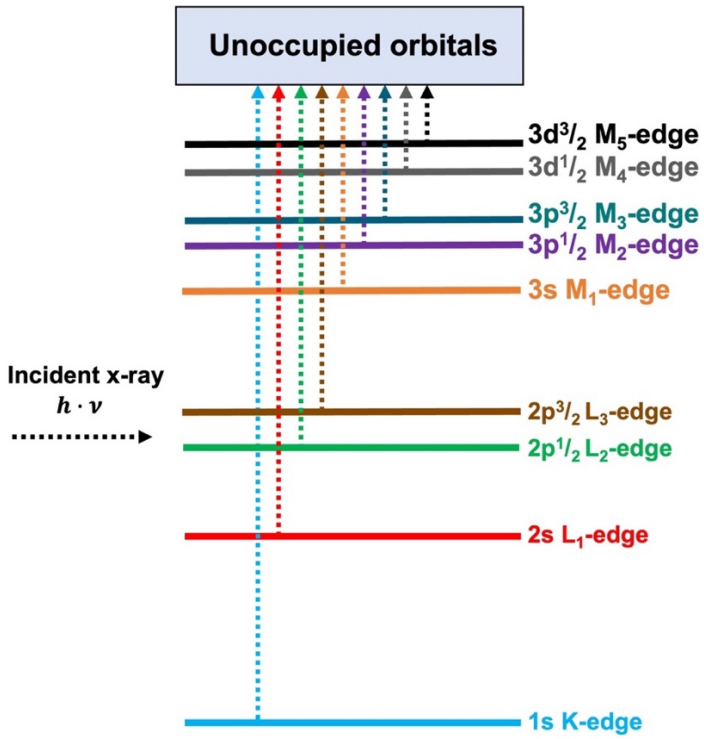

Figure 2.12. Schematic representation of x-ray absorption and electron transitions for corresponding edges.

The *in-situ* XAS measurements were conducted at the KMC-2 (energy range: 4-15 keV)[254, 255] and BAM (energy range: 8-60 keV)[256, 257] beamlines, for probing the Cu and Sn K edges with hard x-rays, respectively. The electrolysis during the *in-situ* XAS experiments was conducted in a three-electrode setup using a single compartment box-like electrochemical cell, placed in an experimental hutch for protection from the high-energy x-rays. The cell was constructed in a way that x-ray permeable window (LDPE or Kapton tape) was facing the WE (electrocatalyst), thus a thin electrolyte layer was present between the window and the WE. The x-rays source and fluorescence detector were placed under angle of 90°. The WE was irradiated from the front side hence, the x-rays were first passing through the thin electrolyte layer. A schematic representation of the experimental setup is depicted in **Figure 2.13**. The utilized fluorescence detector is based on the aforementioned fluorescence effect (XRF, schematically depicted in **Figure 2.9**). Additionally, x-ray transmission detector was used for measuring the powder reference materials (small amount of Cu_2O, CuO, $Cu(OH)_2$, SnO and SnO_2 mixed with cellulose, then wrapped in Kapton tape or compressed as pellets).

The *ex-situ* measurements of the electrocatalyst materials (pre- and post-electrolysis) were conducted at the UE56/2_PGM-2 beamline using the LiXEdrom end-station, for probing the Cu L and Sn M edges with soft x-rays (energy range: 60-1300 eV),[258, 259] as described in **Chapter 4**.[177] For this purpose, the typical H-type cell was placed in a glovebox and the

electrolysis was performed under inert conditions (as the aforementioned case of *quasi in-situ* XPS, **Figure 2.10**), but yet the samples were briefly exposed to air during their loading in the analysis chamber (**Figure 2.13**). This can be characterized as a disadvantage, even though this technique utilizing soft x-rays and as mentioned before, detecting emitted electrons (SE, Auger electrons etc.) with the TEY detector is very surface sensitive with probing depth of several nanometers. The soft x-rays attenuation when passing through a liquid medium (electrolyte layer, like in the case of the hard x-rays *in-situ* XAS) and the surface sensitivity coming from the aforementioned small mean-free path of the emitted electrons are limiting factors that prevent this method to be conducted under *in-situ* conditions. Besides qualitative analysis of the oxidation states for both *ex-situ* soft x-rays and *in-situ* hard x-rays XAS, quantification of the Cu and Sn oxidation states was performed using linear combination analysis or fitting (LCA). The LCA was conducted assuming that the measured XAS spectra ABC is a sum of individual spectra from A, B, and C constituents with a, b and c fractions for each component, respectively. Mathematically, this can be expressed with **Equation 2.5**. These components are actually an element e.g., Cu present in all three oxidation states (0, +1 and +2) and each oxidation state is fraction in the measured sample. Since a, b and c are fractions of a whole, their sum must be equal to 1 (**Equation 2.6**). Plugging both linear equations (**Equations 2.5** and **2.6**) with three variables a, b and c in a mathematical software will generate values of the variables i.e., oxidation state fractions via providing the best fitting between the measured and mathematically synthesized XAS spectra. It is important to note that the individual XAS spectra from the A, B, and C constituents are collected from individual reference materials i.e., high purity Cu and Sn compounds where each of these elements is in the oxidation state of interest.

Equation 2.5: $ABC = a \cdot A + b \cdot B + c \cdot C$
Equation 2.6: $a + b + c = 1$

All data was processed using the Athena software and additionally the LCA for the *ex-situ* Cu L-edge soft x-rays XAS was performed using the Origin2019b software.

The discussion of the results and more information regarding the experimental conditions and parameters can be found in **Chapter 4**.[177] More information regarding the XAS techniques and applications can be found elsewhere.[260-262]

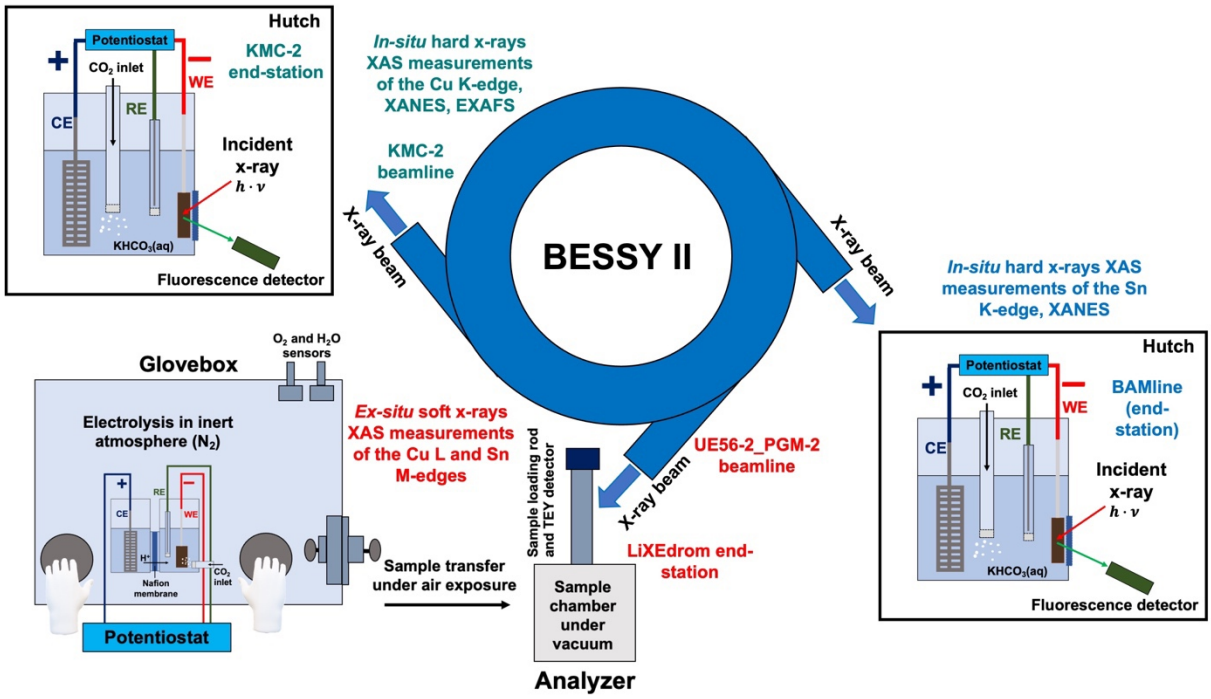

Figure 2.13. Schematic representation of the BESSY II synchrotron radiation source operated by Helmhotz-Zentrum Berlin GmbH, beamlines and end-stations for XAS measurements and experimental setups used in this research.

2.3. Electrochemical setups, experimental conditions and methods for qualitative and quantitative analysis of electrolysis products

The electrocatalytic activity measurements were conducted using conventional H-type two compartment gas-flow cell custom made of glass. Both compartments (cathodic and anodic) were separated with cation exchange Nafion membrane. The procedure for activation of a commercial cation exchange Nafion membrane used in this research is presented in **Chapter 6** (supporting information). Both compartments were filled with 0.1 mol·dm^{-3} $KHCO_3$(aq) and the electrolyte in the cathodic compartment was continuously purged with CO_2. The CO_2 conversion active electrocatalysts were placed in the cathodic, while Pt mesh counter electrode was placed into the anodic compartment. The reference electrode (3 mol·dm^{-3} KCl(aq) filled Ag/AgCl with $E^{\circ}_{Ag/AgCl\ vs.\ SHE}$ = +0.210 V at 25 °C) was placed in the cathodic compartment near the electrocatalyst. The electrochemical cell is depicted in **Figure 2.14**.

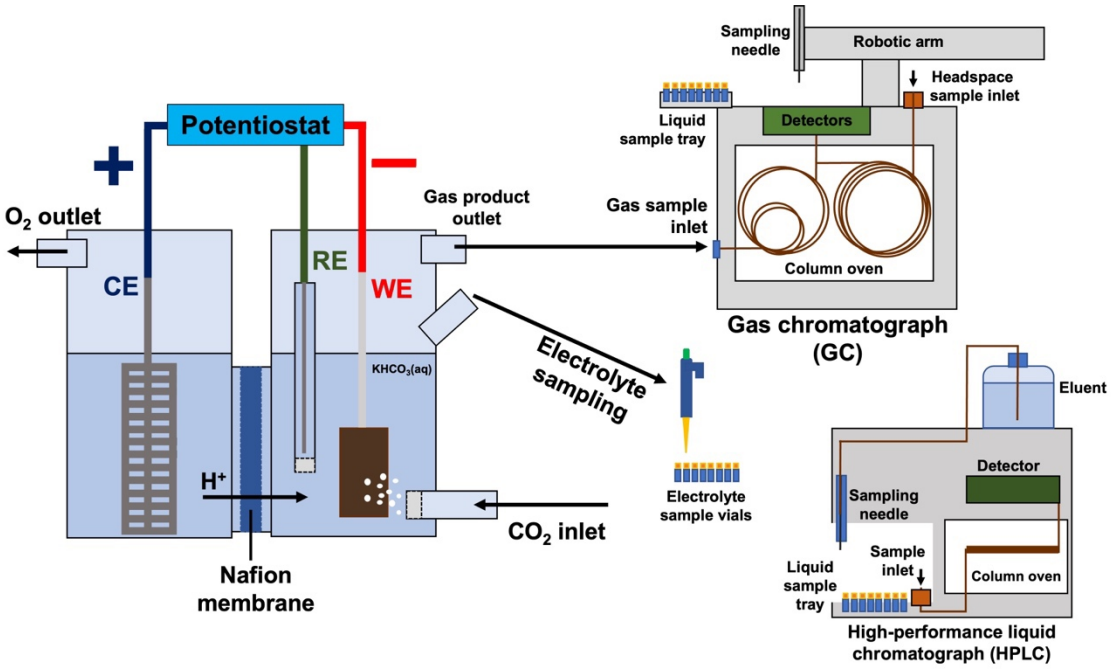

Figure 2.14. Schematic representation of the electrolysis experiment depicting the H-type electrochemical cell, WE - working electrode (electrocatalyst), RE - reference electrode, CE - counter electrode, cation exchange nafion membrane and product quantification using gas chromatography (GC) for the gaseous and volatile liquid products (headspace sampling) and high-performance liquid chromatography (HPLC) for the non-volatile liquid products ($HCOO^-$). Helium as a carrier gas and pulse discharge and flame ionization detectors (PDD and FID) were used in the GC setup. The HPLC operates with H_2SO_4(aq) as eluent and ultraviolet light detector.

The electrochemical bias required for study of the catalytic activity for CO_2ER of all materials included in this work and the bias required for the aforementioned electrochemical synthesis step (see section 2.1 of this chapter) was provided using a potentiotat/galvanostat operating in two- or three-electrode modes. Various electrochemical methods were utilized in dependence of the specific requirements. The methods used for study of the electrocatalytic activity are described in the following text, while the electrochemical synthesis methods via anodization or DHBT electrodeposition are already described in section 2.1 of this chapter.

The electrolysis experiments in all cases when the electrocatalytic activities were studied, were performed in a potentiostatic i.e., chronoamperometry (CA) mode and 85% of the $I \cdot R$ drop was corrected by the potentiostat software. The remaining fraction of the $I \cdot R$ drop is considered negligible when performing electrolysis in H-type cell since relatively low currents were achieved at the applied potentials of interest hence, it was not additionally corrected. In the case when the electrocatalyst was electrochemically activated (pre-reduced), the bias was applied in galvanostatic mode i.e., using chronopotentiometry (CP) **– Chapters 4** and **5**, or linear sweep voltammetry (LSV) – **Chapter 6**. Yet, after the CP or LSV step,

potentiostatic activation at more negative potentials was applied for the electrocatalysts presented and discussed in **Chapters 5**[178] and **6**. Additionally, cyclic voltammetry in a non-faradaic range of potentials was used for estimation of the relative surface roughness factor (RSRF), as discussed in the following text of this section and more information is provided in **Chapters 5**[178] and **6**. All potentials referring to the electrocatalytic activity results were converted with respect to the reversible hydrogen electrode (RHE) using **Equation 2.7**, if not otherwise stated.

Equation 2.7: $E_{vs.\ RHE} = E_{vs.\ Ag/AgCl} + E^{\circ}_{Ag/AgCl\ vs.\ SHE} + 0.059 \cdot pH$

Gas chromatography for quantification of gaseous and volatile liquid products

The gaseous and volatile liquid substances obtained as products from the CO_2ER (CO, CH_4, C_2H_4, C_2H_6, alcohols, aldehydes, ketones, esters etc.) and from the HER (H_2) were quantified with gas chromatography. The technique is based on separation of the components driven by their interaction with the column stationary phase when they pass through the column itself. If the stationary phase consists of polar substances, the non-polar components (H_2, hydrocarbons) will not interact strongly thus their elution from the column will be faster (shorter retention time) in comparison with the polar components (CO, alcohols etc.) that will require longer retention time due to stronger interaction. Even though a single instrument and carrier gas (helium) were used for analysis of both gaseous and volatile liquid products, separate columns and operation modes are utilized for both groups of products i.e., gas and headspace channels. Schematic illustration of the methods for product quantification is presented in **Figure 2.14**. More information regarding the instrumental setup, separation columns, detectors, liquid samples preparation, operation and parameters can be found in **Chapters 4-6** (supporting information of the published[177, 178] and unpublished work). Additionally, the electrochemical cell utilized for electrolysis, instrument, electrolyte sampling and operation of the GC-HS channel are visualized in the Helmholtz-Zentrum Berlin Long Night of Sciences 2021 Virtual Guided Tour.[263] The gaseous products were quantified *in-situ* during the process of electrolysis using the gas channel of the instrument. The quantification results together with other experimental parameters (as described below in this text) are used to calculate the faradaic efficiency (FE) according to **Equation 2.8**:

Equation 2.8: $FE_{gaseous\ product-i}\ (\%) = \frac{z_i \cdot F \cdot x_i \cdot Q_m \cdot 100\%}{I_{total}}$

Where z_i is the number of electrons required for the reduction reaction for production of a certain product - i (see **Equations 1.28-1.44** for number of electrons required for CO_2ER into different products), F is the Faraday constant (96485.3 C·mol^{-1}),[264] x_i is the molar fraction of a certain electrolysis product in the bulk gaseous mixture,[†††] Q_m is the molar gas flow of CO_2 purged into the cathodic compartment of the electrochemical cell. The multiplication product of the parameters in the numerator represents the partial charge - q_i that is passed for production of a certain product - i for a certain amount of time - t, while the denominator is the total exchanged current - I_{total} passed in the electrochemical cell. The quantification results for each gaseous product are presented in ppm, *v* units (volume fraction of specific gas product multiplied by 10^6) and the total gas flow is given as volumetric flow - Q_v (which is 20 cm^3·min^{-1} in all experiments). Under ideal gas conditions assumption for simplification of the calculations, the molar fraction x_i of a component - i in a gas mixture is equal to its volume fraction thus this parameter can be directly incorporated into **Equation 2.8**, while the volumetric flow - Q_v is converted into molar flow - Q_m with **Equation 2.9** derived from the ideal gas law or sometimes known as the Clapeyron equation (**Equation 2.10)** where R is the universal or ideal gas constant (8.314 Pa·m^3·mol^{-1}·K^{-1})[264] under temperature - T of 25 °C (298 K) and atmospheric pressure - P of 101325 Pa, and again under ideal gas conditions approximation for simplification of the calculations.

Equation 2.9: $Q_m = \frac{Q_v \cdot P}{R \cdot T}$

Equation 2.10: $P \cdot V = n \cdot R \cdot T$

On the other hand, the volatile liquid products (alcohols, aldehydes, ketones, esters etc.) were quantified post-electrolysis using gas chromatography coupled with sampling of the vapor phase above the liquid, referred to headspace gas chromatography (GC-HS). The FE for the volatile liquid products are calculated using **Equation 2.11**.

Equation 2.11: $FE_{liquid\ product-i}(\%) = \frac{z_i \cdot c_i \cdot F \cdot V_{catholyte} \cdot 100\%}{I_{total} \cdot t_{electrolysis}}$

Where, in analogy z_i is the number of electrons required for the reduction reaction for production of a certain volatile liquid product - i (the number of electrons for each of these reactions is given in **Equations 1.28-1.44**), F is the Faraday constant, c_i is the molar

[†††] Note: CO_2 is a bulk component in the gas mixture, thus it can be approximated that $n_{\text{total}} = n_i + n_{CO_2} \approx n_{CO_2}$

concentration of a certain electrolysis product and $V_{\mathrm{catholyte}}$ is electrolyte volume in the cathodic compartment of the electrochemical cell.

Hight performance liquid chromatography (HPLC)

The non-volatile CO_2ER liquid products ($HCOO^-$ in this case) are quantified post-electrolysis using high-performance liquid chromatography (HPLC), after sampling electrolyte aliquot from the electrochemical cell (**Figure 2.14**). The separation process is based on the same principle of interaction between the components and the column stationary phase, as previously discussed for the gas chromatography. The instrumental setup and parameters, eluent, separation column, detector can be found in the supporting information of **Chapters 4-6**.[177, 178] The FE of the $HCOO^-$ is estimated identically as in the case of the volatile liquid products using **Equation 2.11**.

In-situ mass spectrometry coupled with electrolysis (EC-MS)

As already mentioned in the previous section (2.2) of this chapter where the TGA-MS and DSC techniques and additionally the principles of MS were discussed, the *in-situ* mass spectrometry coupled with electrochemistry (EC-MS) setup (**Figure 2.15**) was utilized for qualitative real-time tracking of the H_2S evolution during the CO_2 electrolysis process on Cu_xS based electrocatalyst. Moreover, the onset potential of the electrochemical reduction of Cu_xS (with mixed digenite/roxbyite phase composition) was determined using this *in-situ* technique. The experiments were conducted using the typical H-type electrochemical cell, as in the case of the electrocatalytic activity measurements, depicted in **Figure 2.14**. The discussion of the results and the information about the instrumental setup and conditions are presented in **Chapter 6**.

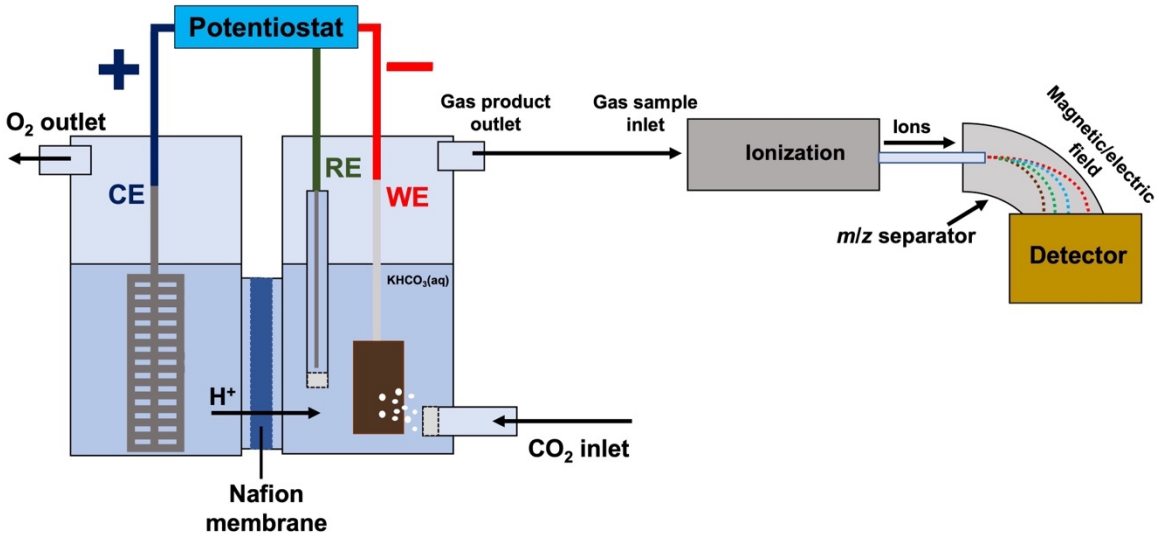

Figure 2.15. Schematic representation of the *in-situ* EC-MS setup used for tracking of H_2S evolution as product from electroreduction of the Cu_xS catalysts.

Estimation of the relative surface roughness factor (RSRF)

The CO_2ER product selectivity and suppression of the HER, and their reaction kinetics could be affected by the electrochemically active surface area (EASA) due to enhanced or hindered CO_2 and H^+ mass transport or other effects, as discussed in section 1.3. of **Chapter 1**. Therefore, this parameter is important for deriving conclusions about the performance of a certain electrocatalyst, i.e., whether the CO_2ER selectivity towards certain product formation is perhaps improved because of surface roughening or maybe change in the composition that affects the intrinsic properties of the electrocatalyst e.g., incorporation of a second element in the structure of Cu. However, the determination of EASA is not straightforward since it is not always known which surface species and how many of them are actually involved in the electrochemical processes. For example, in electrocatalysis, some active surface sites can be blocked due to strong binding adsorbed intermediates, poisoned by certain impurities, presence of inhomogeneities, defects etc. On the other side, the electrode double layer capacitance (C_{DL}) is related to the EASA by assuming that a higher electrode surface i.e., rougher morphology (estimated from SEM imaging) should resemble higher C_{DL}. The capacitance property is associated with the electrode-electrolyte interface (double-layer) being able to store electrical charge. The double layer consists of dipole molecules solvated ions with opposite polarity of the electrode and free solvent dipole molecules. In electrical field the solvent dipole molecules arrange in a layer covering the electrode surface thus creating a border between them and the solvated ions attracted by electrode of opposite polarity, as

depicted in **Figure 2.16**. The surface area of the double-layer interface can naturally increase with increase in the area of the electrode e.g., in the case of rougher surface morphology, as mentioned before. The ratio between the C_{DL} of the electrocatalyst material with certain surface morphology and the C_{DL} of a reference material (**Equation 2.12**), gives the relative surface roughness factor (RSRF). In many cases, including this work, the reference material is a planar or near planar substrate used for deposition/derivation of CO_2ER catalyst material with rougher morphology.

Equation 2.12: $RSRF = \frac{C_{DL-rough\ material}}{C_{DL-reference\ material}}$

When cyclic voltammograms (CV) are recorded at various scan rates (SR) in region of potentials where no faradaic processes occur, the difference in the capacitive current density $\Delta j_{\mathrm{capacitive}}$ at a fixed applied potential is linearly correlated with the SR, where C_{DL} represents the slope (**Equation 2.13**).

Equation 2.13: $\Delta j_{capacitive} = (j_{anodic} - j_{cathodic}) = C_{DL} \cdot SR + intercept$

Even though the RSRF provides, to some extent, satisfactory information regarding the possible origin of the electrocatalytic performance related to the rougher morphology, it is important to note that this factor is not the actual EASA due to the above stated reasons. Therefore, the EASA and RSRF terms should not be interchanged. Moreover, the actual values of the C_{DL} can be subjected to many discrepancies due to various sources such as drifts in the reference electrode (RE) potential (the non-faradaic processes region of applied potentials is rather small thus minor drifts in the RE potential are significant), possible faradaic processes in the particular range of potentials, comparing materials with different composition, different electrical conductivity (conductors vs. semiconductors) etc. Therefore, comparing the C_{DL} order of magnitudes could give more reasonable conclusions than the actual capacitance values, as discussed in supporting information of **Chapter 6**. More information regarding the electrode double layer interface and protocols for accurate determination of the EASA can be found in the literature.[265-268]

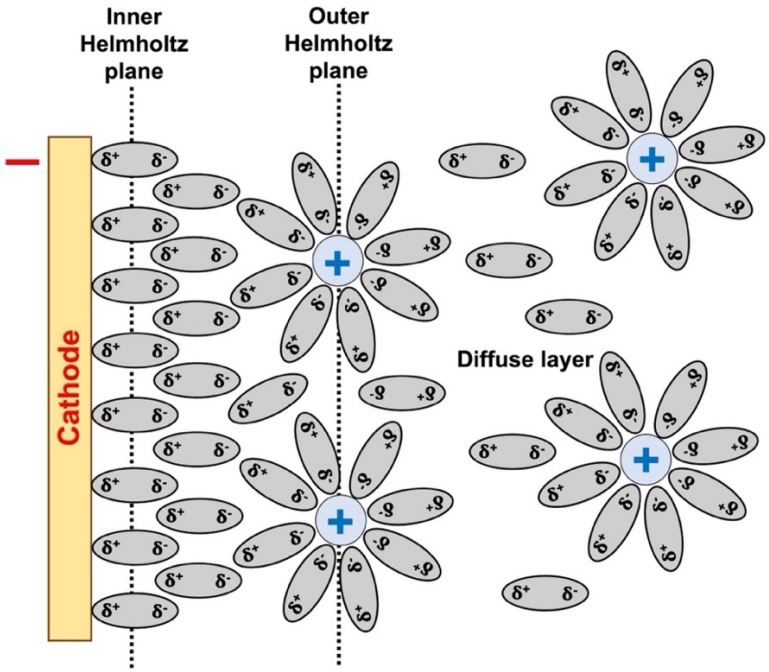

Figure 2.16. Schematic representation of the electrode-electrolyte interface (double layer). The positive charges represent solvated cations with dipole molecules from the solvent.

CHAPTER 3.

Discussion of publications and manuscript included in the thesis

3.1. General discussion of the electrochemical conversion of CO_2, and Cu-Sn and Cu-S electrocatalysts

The necessity for immediate actions to tackle climate change caused by increasing CO_2 concentration in the atmosphere has triggered the scientific communities to focus on studying of various approaches for CO_2 capture and conversion. The ultimate idea is to capture CO_2 directly from air or from point sources of emissions and to convert it into compounds that can be utilized as fuels and chemical feedstocks, which are conventionally produced from fossil raw materials (coal, crude oil, natural gas etc.). CO_2 is stable molecule hence, the first step involving the formation of reactive $*CO_2$ intermediate ($*CO_2^{\bullet -}$, *COOH and/or *OCHO*), which is further converted into products like CO, $HCOOH/HCOO^-$, hydrocarbons, alcohols etc., is an energy demanding process. Most of the global energy requirements are still facilitated by combustion of fossil fuels which are the major source of CO_2 emissions. Yet, to build a sustainable society independent of fossil fuels, renewable sources of energy must be used to power the CO_2 conversion processes. Among the CO_2 conversion methodologies, a promising and extensively studied conversion approach is the electrochemical reduction of CO_2 (CO_2ER). This has many advantages over other conversion approaches the most important being the possibility to perform CO_2ER in aqueous electrolytes, at ambient temperatures and pressures, and to directly store/utilize electricity produced by any renewable energy source. Namely, this makes the renewable energy powered CO_2ER approach independent of the amount of sunlight, wind etc.

Regarding the electrocatalyst materials, Cu is unique terms of its intrinsic ability to convert CO_2 via multi electron/proton steps into hydrocarbons, alcohols etc. which are valuable as fuels and industrial feedstocks. However, even after decades of studying Cu catalysts, it is still very challenging to improve the CO_2ER selectivity towards a single product whilst simultaneously suppressing the competitive hydrogen evolution reaction (HER) in aqueous electrolytes, hence impeding the large-scale application of the electrochemical CO_2 conversion. The challenges originate from various catalysts, experimental conditions and parameters, including electrolytic effects such as double layer changes of pH, effect of cations/anions, effects of surface morphology, facets, defects, particle sizes, inter particle distances, presence of second elements in the catalyst's structure etc., and various engineering challenges in the reactor i.e., electrolyzer designs. Many of these effects are still debated and not fully understood. Various catalyst materials are selective towards two

electron/proton CO_2 reduction into CO and $HCOOH/HCOO^-$ with significant suppression of the HER. Converting CO_2 to CO with high selectivity and its further transformation into valuable hydrocarbons, alcohols etc. via other conversion approaches such as thermocatalytic or biochemical processes appears to be a reasonable strategy. Besides Ag and Au, cheaper and more abundant materials have emerged as suitable electrocatalysts for selective CO_2ER to CO. These include Cu-Sn based materials where Sn shifts the multi product CO_2ER on pristine Cu into a single product (**Figures 3.1a** vs. **b, c**). Modifying Cu with a small amount of Sn can substantially increase the selectivity towards CO, while modification with intermediate and large amounts of Sn results in CO_2ER selectivity towards $HCOO^-$. On the other hand, modification of Cu with S can also alter Cu's selectivity towards $HCOO^-$. In both cases i.e., whether Cu is modified with Sn or S, the HER can be significantly suppressed. The changes in Cu's intrinsic properties by the second element (Sn or S in this work) originate from electronic structure perturbations i.e., charge transfer from one element to the other one, on the surface of the electrocatalysts that affect the binding modes of the *COOH, *OCHO* and *H intermediates following the CO, $HCOO^-$ and HER pathways, respectively. These electronic effects can be referred to as synergistic effects between Cu and the second element and whether one pathway or intermediate binding is preferred over the others is generally dependent on the surface ratio between both elements. In the case of Cu-Sn electrocatalysts, charge is transferred from Sn to Cu creating $Sn^{\delta+}$ and $Cu^{\delta-}$ sites on the surface. The $Cu^{\delta-}$ sites are carbophilic thus preferably bind the *COOH following the CO pathway (**Figure 3.1b**), while the oxophilic $Sn^{\delta+}$ sites bind the *OCHO* intermediate leading to production of $HCOO^-$ as illustrated in **Figure 3.1c**. Hence, the increase in the Sn surface concentration favors binding of the *OCHO* over *COOH intermediate therefore enhancing the $HCOO^-$ selectivity, while increase in the surface Cu favors CO production. On the other hand, when Cu is modified with sulfur, a charge transfer from Cu to S or actual redox process takes place creating positive Cu and negative S sites, thus the oxophilic $Cu^{\delta+}$ (or Cu^+) sites most probably prefer binding of the *OCHO* intermediate following the $HCOO^-$ pathway (**Figure 3.1d**). Yet, to the best of knowledge there is no experimental evidence that $Cu^{\delta+}$ or Cu^+ sites exist on the surface of the electrocatalyst material during CO_2 electrolysis, which is one of the main challenges investigated in the scope of this thesis. However, the CO_2ER selectivity towards both CO and $HCOO^-$ on Cu-Sn and the selectivity towards $HCOO^-$ in the case of Cu-S catalysts is not only dependent on the composition. It can be affected by other factors such as, applied potential, surface morphology, electrochemical activation, local electrolyte species etc. Therefore, studies associated with the influence of these effects on the CO_2ER selectivity and moreover revealing how the surface speciation (oxidation states) of Cu, Sn and S and their chemical nature are related to the selectivity, were performed using various characterization techniques.

Besides utilization of chromatography methods to quantify the CO_2ER products and to estimate their faradaic efficiencies (FE) distribution under different conditions, the other applied methods are intended to characterize the chemical and phase composition, structure, morphology and surface speciation of the electrocatalyst materials. The latter methods involve XRD and several spectroscopy techniques such as *ex-situ* hard x-ray and *in-situ* soft x-ray XAS, *ex-situ*/*quasi in-situ* XPS, *in-situ* EC-MS, ICP-OES, and microscopy techniques such as SEM, TEM etc. Furthermore, studying the possibilities for recycling/repurposing Cu-Sn waste bronze to derive CO selective Cu-Sn and development of facile and fast method for preparation of $HCOO^-$ selective Cu-S electrocatalyst is of great importance towards the sustainable future application of these materials in large-scale CO_2 conversion electrolyzers.

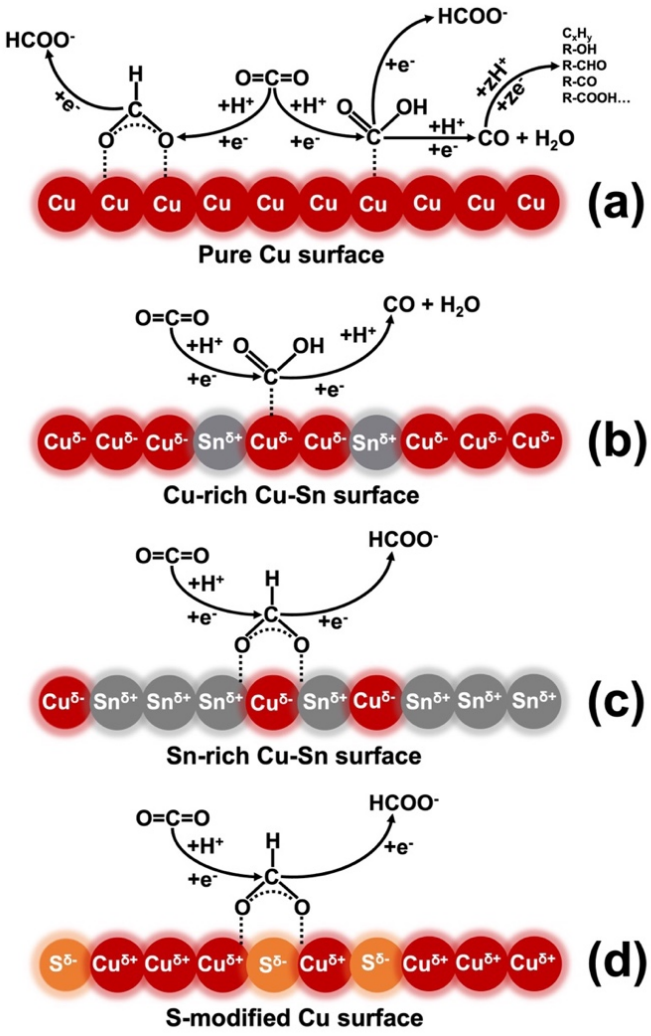

Figure 3.1. Schematic illustration of the reaction pathways on the surface of pure Cu on which various CO_2ER products can be obtained **(a)**, Cu rich Cu-Sn favoring CO_2ER to CO **(b)**, Sn rich Cu-Sn **(c)** and Cu-S **(d)**, favoring CO_2ER into $HCOO^-$.

3.2. Composition-structure-activity relations in Cu-Sn catalysts

In order to reveal the composition-structure-activity relations of the Cu-Sn electrocatalysts during CO_2ER, SnO_2 functionalized CuO nanowires were synthesized. This was done in two steps combining electrochemical anodization of pre-sputtered Cu layers on glass substrates in alkaline medium to grow the nanowire structures and subsequent thermal dehydration/atomic layer deposition (ALD) of ultrathin SnO_2 layers on top of the surface of the CuO nanowires for their functionalization (**Figure 3.2a**). Several different thicknesses of the SnO_2 layers were obtained by varying the number of ALD cycles (between 1 and 182c, corresponding to 0.1-20 nm). The SEM images of CuO nanowires functionalized with 15c of SnO_2 (CuNW-Sn) are presented in **Figures 3.2b, c**. The average length of the nanowires is around 10 μm. The results from the (grazing incidence) GI-XRD characterization in **Figure 3.2e** show that the as-prepared CuNW resemble the XRD pattern of $Cu(OH)_2$. The $Cu(OH)_2$ phase undergoes conversion into CuO during the dehydration/SnO_2 ALD functionalization step, as observed from the diffractograms of both CuNW-Sn samples (15 and 182 cycles). Metallic Cu features can also be observed in the diffractograms for all examined materials i.e., bare CuNW and CuNW-Sn prepared with 15 and 182 ALD cycles, coming from the sputtered Cu layers from which the nanowires grew in the process of anodization. No SnO_2 features can be observed in the CuNW-Sn diffractograms even for the samples with the highest number of ALD cycles (SnO_2 thickness of 20 nm). This could be due to the orientation of the nanowires leading to predominantly probing the bulk $Cu(OH)_2$ structure.

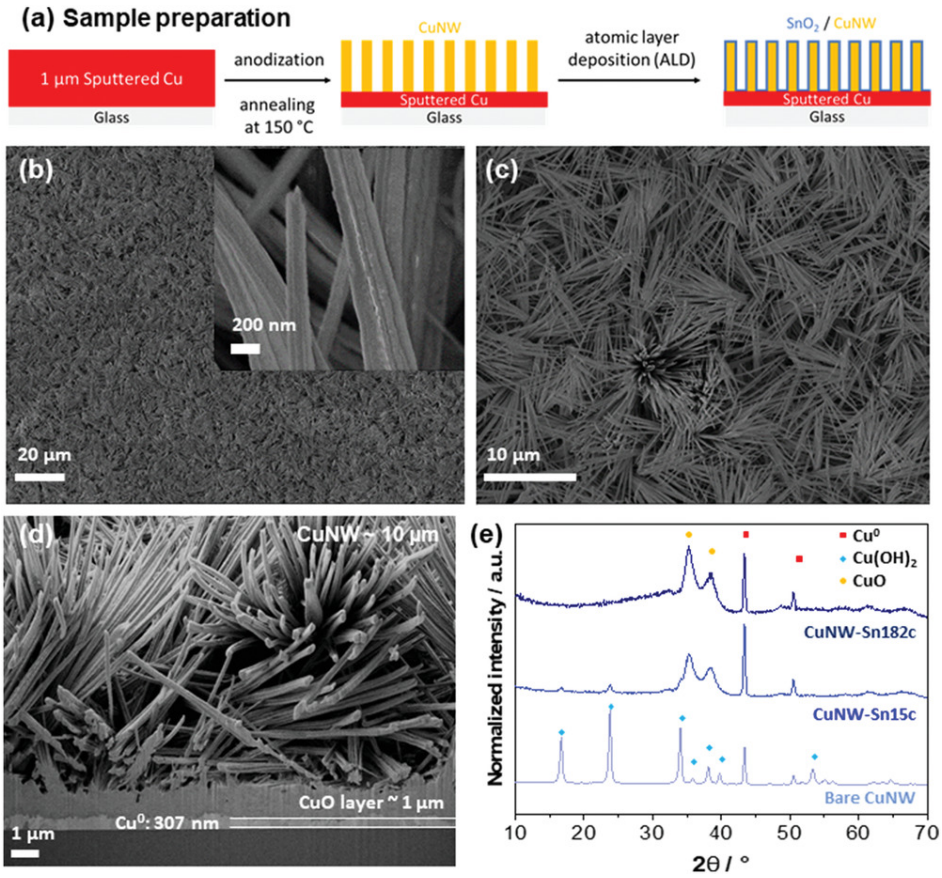

Figure 3.2. Schematic representation of the synthesis approach CuNW-Sn **(a)**, SEM images of CuNW-Sn15c **(b, c)**, Cross-section SEM of CuNW-Sn15c **(d)**, and GI-XRD patterns of as-prepared bare CuNW, CuNW-Sn15c and CuNW-Sn182c **(e)**.

The CuNW-Sn functionalized with various SnO_2 ALD cycles were examined for their CO_2ER electrocatalytic activity in $KHCO_3$(aq) and the results are presented in **Figure 3.3**. Prior to examination of the product selectivity, the electrocatalysts were activated by applying a fixed current density of -2 mA·cm^{-2} until a potential threshold of -0.5 V vs. RHE V is reached. **Figure 3.3a** shows that the CO selectivity increasing with an increase in the amount of surface Sn from 0 to 15 ALD cycles. For 15-25 ALD cycles, a steady state FE of 75-80% was obtained at an applied potential of -0.7 V vs. RHE. Simultaneously, from 0 to 15 ALD cycles the H_2 selectivity decreases and reaches a steady-state FE of 12-14% for 15-25 ALD cycles. Moreover, the production of $HCOO^-$ significantly decreases compared to bare CuNW even with the smallest amount of SnO_2 (1 ALD cycle). Namely, FE values of 6-7% are observable for all CuNW-Sn, except when SnO_2 is deposited with 182 cycles. In the latter case, the FE for $HCOO^-$ and H_2 increase and for CO decreases reaching values that are similar as for the bare CuNW, except no hydrocarbons like CH_4 and C_2H_4 can be observed. From these results, at an applied potential of -0.7 V, it can be summarized that functionalization of the CuNW with small

amounts of SnO_2 (1-25 ALD cycles) typically show synergistic effects between Cu and Sn leading to suppression of the HER and $HCOO^-$ while substantially enhancing the selectivity towards CO. The CuNW-Sn functionalized with 15 and 182 ALD cycles of SnO_2, abbreviated with CuNW-Sn_{LOW} and CuNW-Sn_{HIGH}, respectively, were further studied at various applied potentials. The results from the CO, $HCOO^-$ and H_2 FE distributions at various applied potentials for the CuNW-Sn_{LOW} are presented in **Figure 3.3c**. It can be observed that the presence of $HCOO^-$ production is suppressed in the whole range of potentials, while the HER, even though cannot achieve higher FE values than 30% at all applied potentials, it undergoes the highest suppression at −0.7 V. Simultaneously a maximal CO FE of ~80% is observed. On the other hand, the Sn rich electrocatalyst i.e., CuNW-Sn_{HIGH} typically shows low FE for CO (<15%) in the whole examined range of potentials, yet the $HCOO^-$ production enhances with an increase of the applied potential, while the H_2 production simultaneously decreases from −0.6 to −0.9 V (**Figure 3.3d**). The observed enhancements in CO-, on the Cu-rich (CuNW-Sn_{LOW}), and $HCOO^-$ on the Sn rich (CuNW-Sn_{HIGH}) surface are due to effect coming from the *COOH vs *OCHO* intermediates binding interplay, as discussed in the previous section (3.1.) and presented in **Figure 3.1**. Moreover, it appears that more negative potential is required to reach the highest FE for $HCOO^-$ on the CuNW-Sn_{HIGH} in comparison with the applied potential required for the highest FE for CO in the case of the CuNW-Sn_{LOW} electrocatalyst.

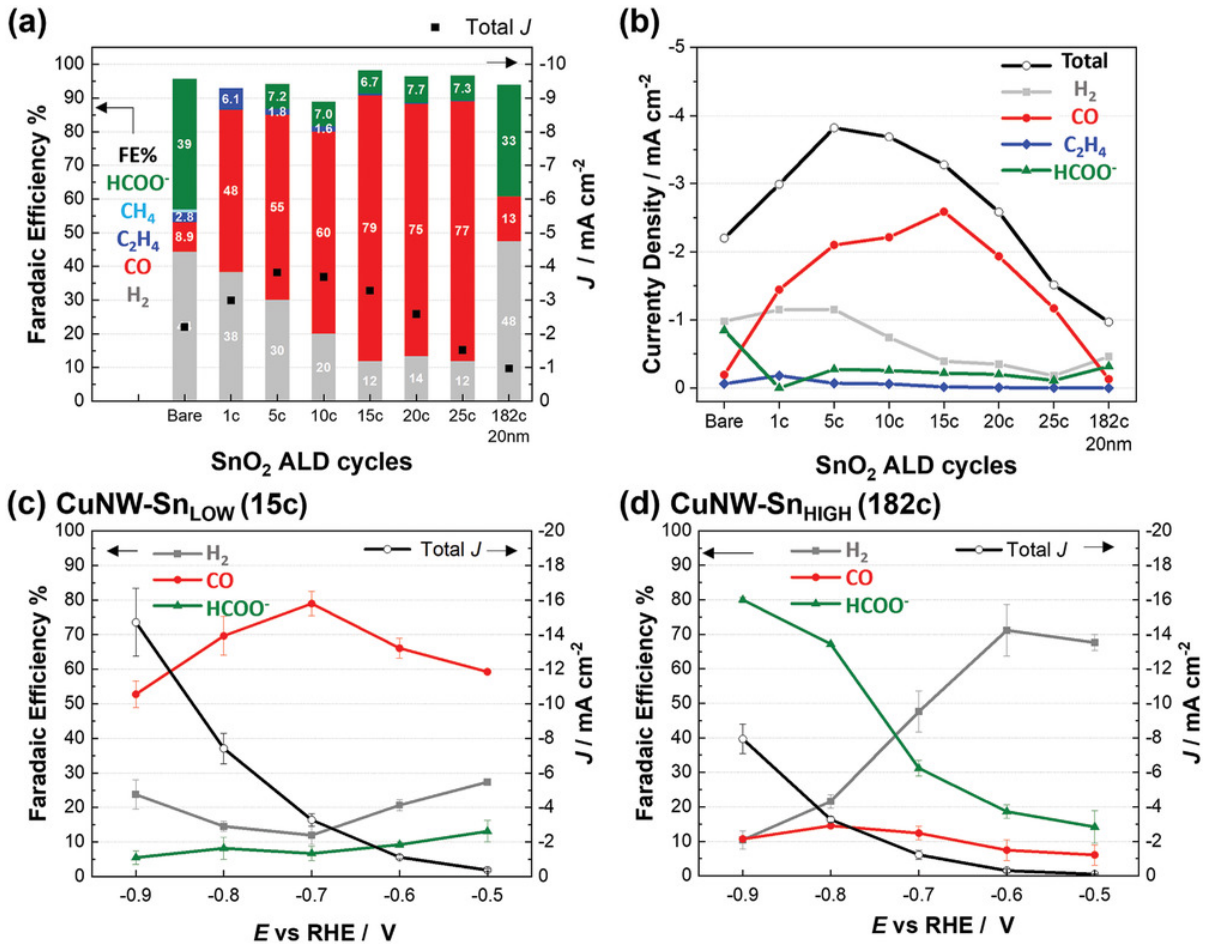

Figure 3.3. CO_2ER activity results: Faradaic efficiency (FE) and total current density distribution of various products for bare and SnO_2 modified CuNW with various ALD cycles **(a)**, Partial current density distribution of various products on bare and SnO_2 modified CuNW with various ALD cycles **(b)**, FE and partial current density distribution of H_2, CO and $HCOO^-$ at various potentials on CuNW-Sn_{LOW} **(c)** and CuNW-Sn_{HIGH} electrocatalyst **(d)**. The electrocatalytic activity is studied in CO_2 saturated 0.1 mol·dm^{-3} $KHCO_3$(aq) as electrolyte.

However, the schematic illustration in **Figures 3.1b, c**, showing the partial charges on Cu and Sn surface atoms formed due to charge redistribution, does not explain the real oxidation states of these elements and moreover how the selectivity is related with the surface speciation. Therefore, several x-ray spectroscopy and other techniques were applied for probing the electrocatalyst's chemical and phase composition and the Cu and Sn oxidation states in the electrocatalyst materials.

The electrocatalytic processes occur on the surface of the catalyst material, therefore a surface sensitive soft x-ray XAS technique was applied to study the Cu L and Sn M edges in bare CuNW and CuNW-Sn electrocatalysts under various conditions. The surface sensitivity of this method is limited by the mean-free path of the x-ray generated photoelectrons thus

constraining the probing depth below 10 nm. Hence, the advantage for surface sensitivity examination, together with the attenuation of the x-rays when passing through a liquid medium (electrolyte) restricts the possibility for *in-situ* studies of the Cu and Sn oxidation states under CO_2 electrolysis conditions. Therefore, the CO_2 electrolysis experiments were first conducted under inert atmosphere (in glovebox) and the samples were subsequently transferred in the XAS analyzer chamber under vacuum. Unfortunately, brief air exposure was unavoidable during the sample transfer process. The results from the Cu L and Sn M edges soft x-ray XAS study of bare CuNW, CuNW-Sn_{LOW} and CuNW-Sn_{HIGH}, as-prepared, after electrochemical activation at a fixed applied current density of -2 mA·cm^{-2} until reaching potential of -0.5 V and after CO_2 electrolysis for 10 min (only for CuNW-Sn_{HIGH}), and 2 h, at applied potential of -0.7 V for all samples, are presented in **Figure 3.4**. Namely, **Figure 3.4a** represents the Cu L edge XAS spectra for the samples examined under the aforementioned conditions and additionally XAS spectra of relevant Cu-based reference materials. The Cu L edge spectra of bare CuNW and CuNW-Sn_{LOW} recorded prior to the electrolysis resemble two peaks that match the L_3 and L_2 peak positions for Cu^{2+} species from $Cu(OH)_2$ and CuO when compared with the reference materials spectra, which is in agreement with the XRD data in terms of the observed phases. On the other hand, the CuNW-Sn_{HIGH} material does not show any Cu L edge signal because the thickness of the SnO_2 functionalization layer (20 nm) is higher than the probing depth of this technique. Identical result for the CuNW-Sn_{HIGH} sample can be observed even after the material was pre-reduced under fixed current. However, the fixed current pre-reduction until -0.5 V of the bare CuNW transforms the Cu^{2+} into Cu^{+} and metallic Cu^{0} surface species, while incomplete transformation can be observed in the case of CuNW-Sn_{LOW} i.e., besides Cu^{+}/Cu^{0}, unreduced Cu^{2+} species are still present. The Cu L edge spectra for the bare CuNW and CuNW-Sn_{LOW} after 2 h electrolysis at -0.7 V does not differ significantly from the pre-reduction spectra of these materials, yet in the case of CuNW-Sn_{HIGH} Cu signal did appear resembling ill-shaped Cu L edge peaks. The appearance of the Cu L signal in the CuNW-Sn_{HIGH} after 2 h electrolysis at -0.7 V suggest that the SnO_2 layer became as thin as the probing depth possibility to be observed. Hence, it appears that significant amount of surface Sn was removed during the electrolysis via possible migration into the bulk or was dissolved in the electrolyte. **Figure 3.4b** shows the Sn M edge spectra where in the case of as-prepared and pre-reduced CuNW-Sn_{LOW} and CuNW-Sn_{HIGH}, features that are attributed to both Sn^{4+} and Sn^{2+} species can be observed when compared with the reference spectra of the SnO_2 and SnO. The Sn M edge signal disappears after 10 min of electrolysis at -0.7 V for the CuNW-Sn_{LOW}, while significantly diminished features in the spectrum are observable after 2 hours electrolysis in the case of CuNW-Sn_{HIGH}. However, the weak features at ~485 and ~493 eV can possibly be attributed to metallic Sn^{0}. The diminishing of the peaks in the CuNW-Sn_{HIGH} material i.e., Sn

removal from the surface after 2 h electrolysis is in agreement with the appearance of the ill-shaped Cu L features (**Figure 3.4a**). The electrolyte was analyzed using ICP-OES confirming the loss of both Cu and Sn, with a more significant loss of Sn in the case of CuNW-Sn_{HIGH}. The deconvolution of the Cu^{+}/Cu^{0} in the Cu L edge and Sn^{4+}/Sn^{2+} species in the Sn M edge spectra is rather challenging. Moreover, possible re-oxidation caused by the short air exposure during sample transfer hampers the providing of clear evidence whether, besides metallic Cu and Sn, Cu^{+} and Sn^{2+} and possibly Cu^{2+} and Sn^{4+} species persist during the electrolysis.

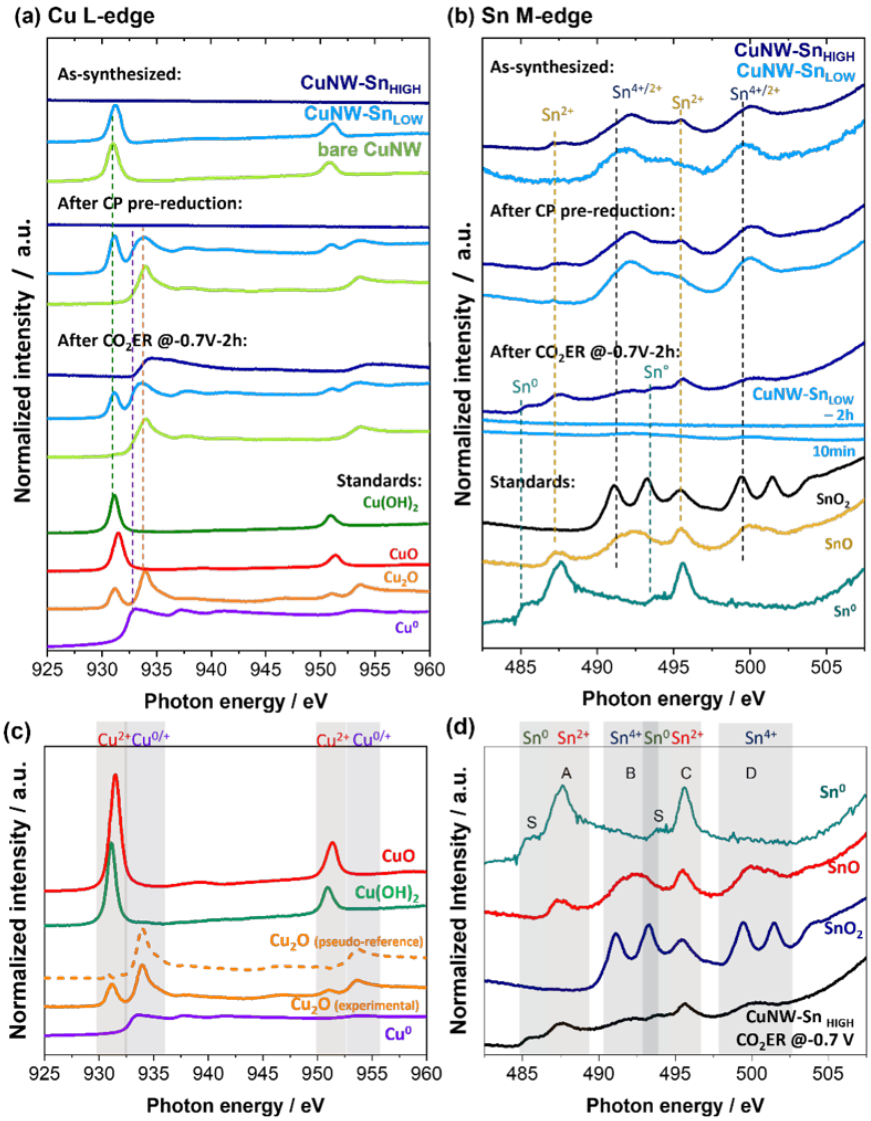

Figure 3.4. Cu L **(a)** and Sn M **(b)** edge soft x-rays XAS spectra recorded *ex-situ* for: bare CuNW, CuNW-Sn_{LOW} and CuNW-Sn_{HIGH} under as-synthesized, pre-reduced with chronopotentiometry (CP) at -2 mA·cm^{-2} and 2 h CO_2 electrolysis conditions at –0.7 V. Additional Cu L and Sn M XAS spectra were recorded for Cu- **(c)** and Sn- **(d)** based reference materials, respectively.

To gain more knowledge about the Cu and Sn electronic structures without air exposure and possible reoxidation of the samples, the bare CuNW and CuNW-Sn materials were investigated *in-situ* during the pre-reduction and during the CO_2 electrolysis using hard x-ray XAS, probing the Cu and Sn K edges. Namely, the penetration depth of the hard x-rays can reach few micrometers in the sample and additionally 1-2 mm in water (electrolyte), which makes this method suitable for *in-situ* characterization of the catalyst materials under CO_2 electrolysis conditions in electrochemical cell with a thin electrolyte layer (~0.5 mm) located between the electrocatalyst (cathode) and x-ray transparent window. The Cu K edge XANES and FT-EXAFS spectra for the bare CuNW and CuNW-Sn materials recorded under various conditions and for the reference materials are presented in **Figure 3.5**, According to the results, the as-synthesized materials resemble Cu^{2+} oxidation state attributed to $Cu(OH)_2$, for the bare CuNW, and to CuO for the CuNW-Sn_{LOW} and CuNW-Sn_{HIGH}, and this is also obvious from the Cu-O bond features with radial distance of ~1.6 Å in the FT-EXAFS (**Figure 3.5d**). Moreover, all as-synthesized samples show features for metallic Cu species (pre-edge shoulder at ~8977 eV) in the XANES spectra and feature at ~2.3 Å attributed to Cu-Cu bond in the FT-EXAFS. The presence of metallic Cu can be attributed to interference from the sputtered Cu layer from which the nanowires grew during the synthesis process. The XANES spectra recorded in several time intervals to follow the transformation of the bare CuNW, CuNW-Sn_{LOW} and CuNW-Sn_{HIGH} materials during electrochemical pre-reduction show that the Cu^{2+} specie gradually transforms into fully metallic Cu (**Figures 3.5a, b**). After the pre-reduction, the electrolysis was performed at applied potential –0.4 V, yet due to noise from bubble formation it was decreased to –0.1 V. Namely, this value is lower than the typical applied potentials where the highest FE for CO and $HCOO^-$ are observed on the CuNW-Sn_{LOW} and CuNW-Sn_{HIGH} electrocatalysts, respectively (**Figures 3.3c, d**), yet it was quite challenging to record EXAFS spectra under more negative potentials. However, only metallic Cu can be observed from both XANES and FT-EXAFS results (**Figure 3.5d**). These results are supporting the previously discussed soft x-rays XAS in terms of reductive transformation of the Cu^{2+} under electrochemical bias and moreover revealing that metallic Cu is rather dominant over the Cu^+ species during the CO_2 electrolysis. In the next step, the Sn speciation in the CuNW-Sn materials was investigated with hard x-ray XAS via probing the Sn K edge.

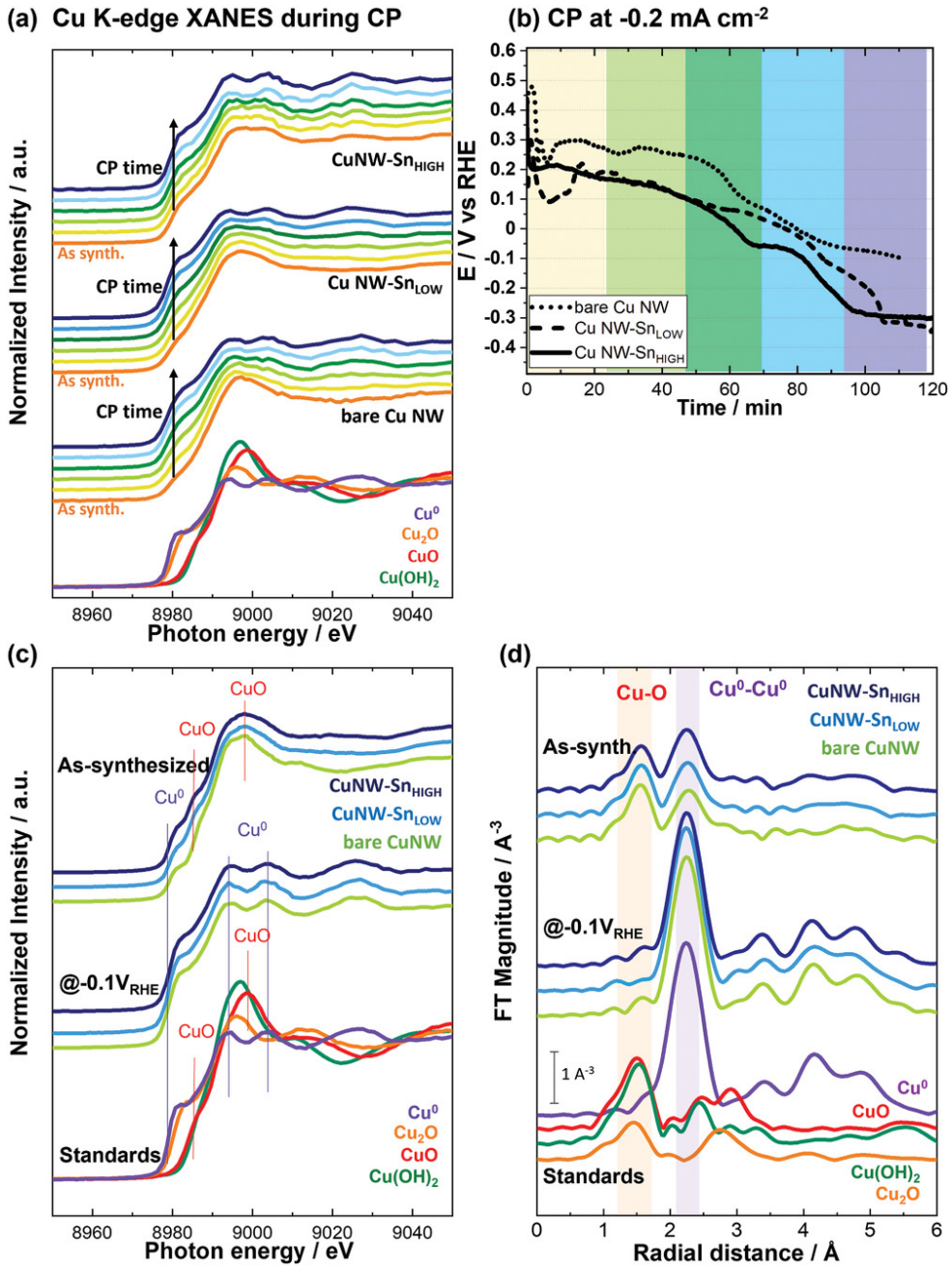

Figure 3.5. Cu K edge XANES spectra of bare Cu NW, CuNW-Sn_{LOW}, CuNW-Sn_{HIGH} and reference materials, recorded *ex-situ* for the as-synthesized samples and reference materials and *in-situ* during the chronopotentiometry (CP) pre-reduction at fixed current density of –0.2 mA·cm^{-2} **(a)** and during CO_2 electrolysis at –0.1 V **(c)**. The CP pre-reduction time regions **(b)** are color coded with the XANES spectra presented on **(a)**. FT-EXAFS of bare Cu NW, CuNW-Sn_{LOW}, CuNW-Sn_{HIGH} and reference materials generated from EXAFS spectra **(d)**. The EXAFS spectra were recorded *ex-situ* for the as-prepared and reference materials and *in-situ* during CO_2 electrolysis at –0.1 V. The XANES and EXAFS spectra were collected at –0.1 V after decreasing the potential from –0.4 V due to noise caused by bubbles formation.

The results from probing the Sn K edge with XAS under *ex-situ* for the as-prepared and *in-situ* conditions during the CO_2 electrolysis are presented in **Figure 3.6**. From these results, it can be observed that the Sn K edge XANES spectra resemble SnO_2 for both as-prepared CuNW-Sn_{LOW} and CuNW-Sn_{HIGH} materials (**Figures 3.6a, b**). The SnO_2 readily reduces into SnO and metallic Sn under negative bias when examined in range of potentials between –0.5 and –0.9 V, for the CuNW-Sn_{HIGH}, and between –0.5 and –0.7 V, for the CuNW-Sn_{LOW} electrocatalysts. However, the SnO_2 reduction into Sn^0 is not complete and both SnO and SnO_2 species are still observable. The linear combination (fitting) analysis (LCF or LCA) results estimated from the CuNW-Sn_{HIGH} XANES spectra (**Figure 3.6c**) show that the Sn oxidation state is dependent on the applied potential. At applied potential of –0.5 V, a mixture of SnO and SnO_2 can be observed, certain SnO fraction transforms into metallic Sn starting from –0.6 V, while the SnO_2 fraction is not affected at both –0.6 and –0.7 V. Yet, at –0.7 V additional SnO fraction undergoes transformation into metallic Sn thus, the metallic fraction surpasses the SnO. Finally, at applied potential of –0.9 V, under which the highest FE for $HCOO^-$ is observed for the CuNW-Sn_{HIGH} electrocatalyst (**Figure 3.3d**), the metallic Sn emerges as the dominant fraction, SnO_2 as secondary and additionally a small fraction of SnO is still present. These observations suggest that besides Sn^0, Sn can indeed persist in +4 and traces of +2 oxidation states which is challenging to resolve from the Sn M edge soft x-ray XAS spectra due to the sample transfer air exposure, as discussed above in this section (**Figure 3.4b**). However, the hard x-ray XAS is more bulk than surface sensitive, as obvious when observing metallic Cu in the as-prepared materials (**Figures 3.5a, c, d**) originating from the sputtered layer from which the wires grew during the synthesis. Furthermore, it cannot be excluded that the reduction of the CuO/Cu_2O and SnO/SnO_2 into metallic Cu and Sn, respectively during the electrolysis is attributed to reduction of subsurface oxides, which presence in the case of oxide-derived Cu catalysts is debated in the scientific communities.

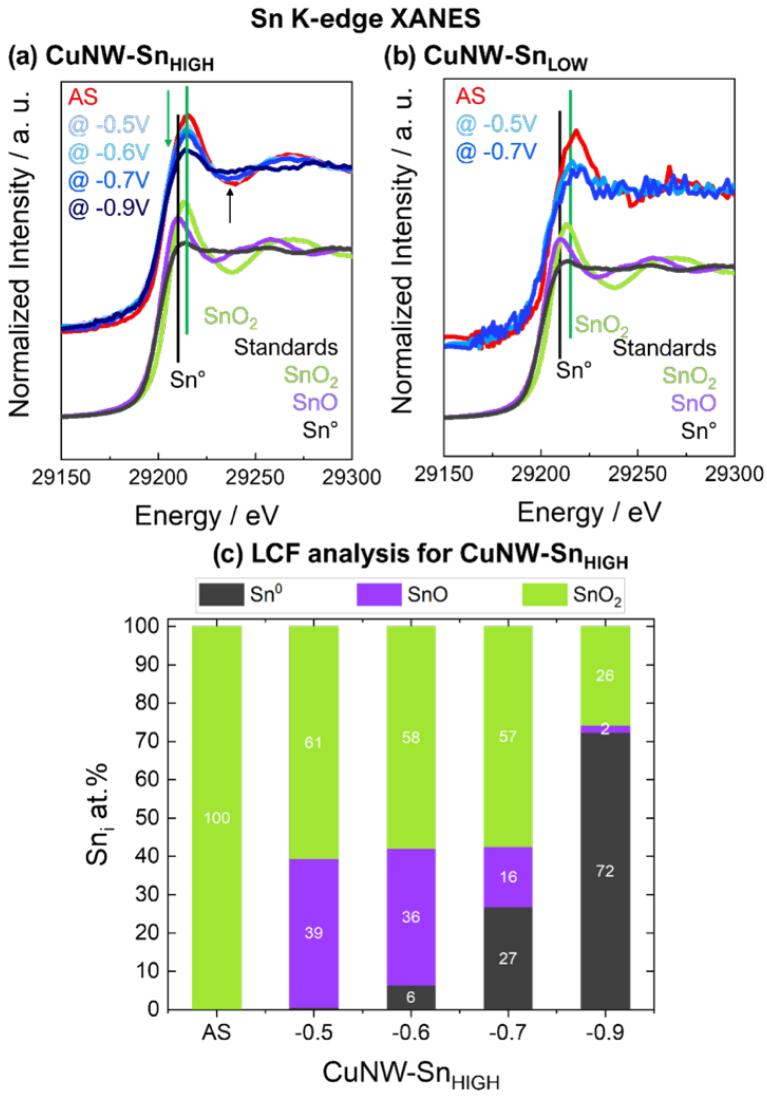

Figure 3.6. Sn K edge XANES spectra of CuNW-Sn$_{LOW}$, CuNW-Sn$_{HIGH}$ and Sn reference materials, recorded *ex-situ* for the as-synthesized (AS) samples and reference materials and *in-situ* for the CuNW-Sn$_{LOW}$ **(a)** and CuNW-Sn$_{HIGH}$ **(b)** during CO_2 electrolysis in the range of applied potentials between –0.5 and –0.9 V. Linear combination (fitting) analysis (LCF or LCA) generated from the Sn K edge XANES spectra **(c)**.

Being aware of the limitations of both *ex-situ* soft and *in-situ* hard x-rays XAS, a compromise was found in utilizing the surface sensitive technique XPS under so called *quasi in-situ* conditions. In this case the CO_2 electrolysis was performed under inert conditions (in glovebox) like in the case of the sample preparation for the soft x-rays XAS, but the electrocatalyst samples were transferred from the glovebox into the XPS analyzer under vacuum without being exposed to air. Cu 2p, Cu LMM Auger and Sn 3d XPS spectra were recorded for the bare CuNW, CuNW-Sn$_{LOW}$ and CuNW-Sn$_{HIGH}$ materials under various conditions. The as-prepared bare CuNW resembles Cu^{2+} attributed to $Cu(OH)_2$, which agrees

with the previously discussed characterization results (from the XRD and XAS studies), being completely reduced into metallic Cu after applying potential, as low negative as –0.5 V, interpretated from the Cu 2p and Cu Auger spectra (data presented in **Chapter 4**). However, the most important samples are the CuNW-Sn_{LOW} and CuNW-Sn_{HIGH} materials, as selective electrocatalysts for CO_2 to CO and $HCOO^-$, respectively. Namely, the Cu and Sn surface species quantification results for the CuNW-Sn_{LOW} and CuNW-Sn_{HIGH} are presented in **Figure 3.7**. From these results, the as-prepared CuNW-Sn_{LOW} resemble fully oxidized Cu and Sn surface species, thus typically the CuO is dominating (**Figure 3.7a**) due to the low number of ALD cycles for this sample (15c). On the other hand, the surface of the as-prepared CuNW-Sn_{HIGH}, is completely covered with SnO_x thus no Cu species can be observed (**Figure 3.7b**), as expected when the nanowires are functionalized with 182 ALD cycles - corresponding to a thickness of around 20 nm. Hence, these results agree with the ones from the XAS studies for all probed edges. When negative bias is applied in the range between –0.5 and –0.9 V, Cu undergoes complete reduction to metallic, yet certain fraction of SnO_x remains persistent, while traces of metallic Sn can be observed in the case of the CO selective CuNW-Sn_{LOW} electrocatalyst (**Figure 3.7a**). The SnO_x surface species in the CuNW-Sn_{HIGH} (**Figure 3.7b**) do not undergo reduction at –0.5 V, yet significant fraction of metallic Sn can be observed at more negative potentials i.e., at –0.7 and –0.9 V. In contrast, the results from the Sn K edge spectra LCF for the CuNW-Sn_{HIGH} sample (**Figure 3.6c**), show that the metallic Sn fraction is rather dominant over the SnO_x, but most probably this is an effect coming from the bulk sensitivity of the hard x-rays XAS. Regarding the Cu speciation in the CuNW-Sn_{HIGH} (**Figure 3.7b**), traces of metallic Cu can be observed at –0.5 V and this fraction increases significantly at –0.7 and –0.9 V simultaneously with decrease of the Sn fraction as a consequence of the previously discussed Sn removal from the surface of the material and/or additionally possible migration of Sn to the bulk and Cu to the surface. Comparing the *quasi in-situ* XPS results with the previously discussed *ex-situ* soft and *in-situ* hard x-rays XAS for the CuNW-Sn_{LOW} electrocatalyst, it can be summarized that metallic Cu is dominant specie, thus the presence of Cu^+/Cu^{2+} species most probably is a consequence of air exposure during the sample transfer in the case of *ex-situ* soft x-ray XAS. Moreover, this is confirmed with XPS after exposing the sample in air, post-electrolysis. A decrease in the total Sn fraction for the above stated reasons, is also observable in the case of the CuNW-Sn_{LOW}. Regarding the Sn speciation for this electrocatalyst, the comparison of the results and additional XPS analysis of air exposed samples, post-electrolysis, suggest that even though the air-exposure indeed oxidizes the metallic Sn to SnO_x, these species co-persist with Sn^0 during the electrolysis at –0.7 V (**Figure 3.7a**) i.e., when the highest CO selectivity is observed (**Figure 3.3c**). Similar can be claimed in the case of the CuNW-Sn_{HIGH}, yet both metallic and SnO_x surface fractions are higher than in the case of CuNW-Sn_{LOW} sample. Moreover, the increase in the fraction of metallic Sn

surface species at –0.7 and –0.9 V in the CuNW-Sn_{HIGH} (**Figure 3.7b**) appear to be beneficial for enhancing the $HCOO^-$ selectivity (cf. CO_2ER activity results in **Figure 3.3d**).

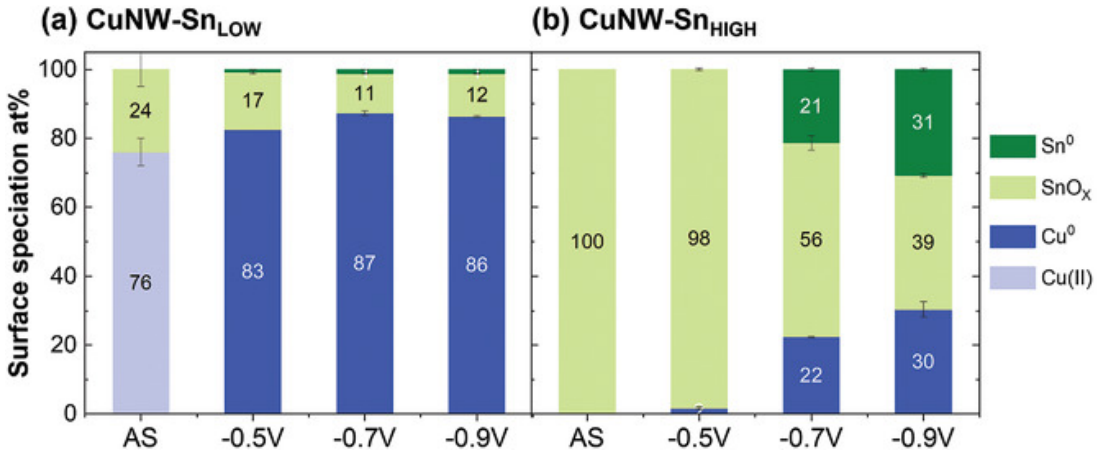

Figure 3.7. Results from the quasi *in-situ* XPS quantification of the surface species in the as-synthesized (AS), and post-electrolysis CuNW-Sn_{LOW} **(a)** and CuNW-Sn_{HIGH} **(b)** samples. The CO_2 electrolysis was conducted in the range of potentials between –0.5 and –0.9 V. The highest FE for CO is obtained at –0.7 V on the CuNW-Sn_{LOW} corresponding to total Sn fraction of ~13 at.%, while the highest FE for $HCOO^-$ at –0.9 V, on the CuNW-Sn_{HIGH} electrocatalyst (total Sn fraction of ~70 at.%).

Additional post-electrolysis studies with energy filtered transmission electron microscopy (EF-TEM) showed that nanowire's core and SnO_x shell are persistent during the electrocatalysis processes. GI-XRD, high resolution-transmission electron microscopy (HR-TEM) and selected area electron diffraction (SAED) indicate that in the case of the CuNW-Sn_{HIGH}, Cu_6Sn_5 phase is being formed at the boundary between the nanowire's core and SnO_x shell at potential of –0.9 V (results presented in **Chapter 4**). Moreover, the SAED analysis showed that at the same applied potential, when the selectivity for $HCOO^-$ is significantly peaking, the Cu nanowire core is fully reduced to metallic Cu, surrounded by inner shell of Cu_6Sn_5, second shell of metallic Sn and outer shell composed of SnO_x. In contrast, at potentials less negative than –0.7 V, the shell around the nanowire's core resembles SnO_x. It appears that the Cu nanowire's core does not contribute to the electrocatalysis processes. The enhancement in the $HCOO^-$ selectivity (**Figure 3.3d**) at more negative potentials on the CuNW-Sn_{HIGH} electrocatalyst comes from the increase in the metallic Sn species fraction, which is observable from the *in-situ* Sn K edge XAS (**Figure 3.6c**) and the *quasi in-situ* XPS (**Figure 3.7b**).

A summary of all experimental results discussed in this study in terms of the composition, Cu and Sn fractions and their speciation in the CO and $HCOO^-$ selective CuNW-Sn_{LOW} and CuNW-Sn_{HIGH} electrocatalysts, respectively, is presented in **Figure 3.8**.

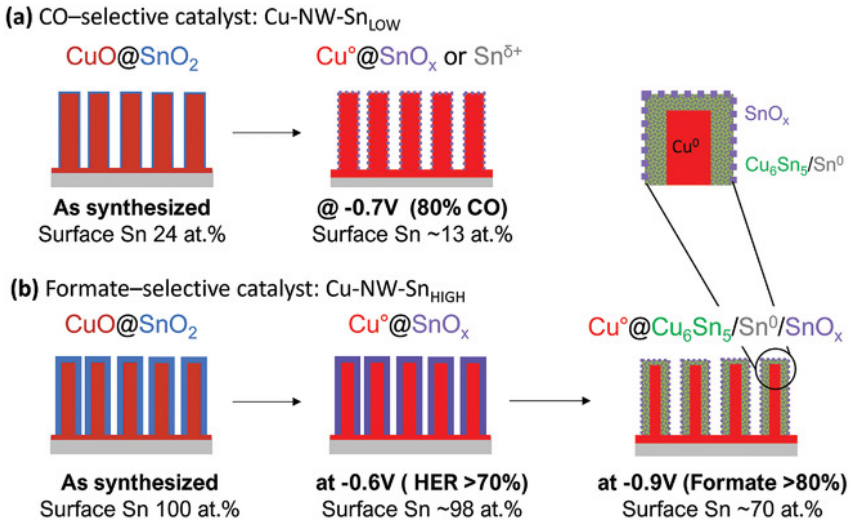

Figure 3.8. Schematic summary of the composition-speciation transformation results for the CO selective CuNW-Sn_{LOW} **(a)** and for the $HCOO^-$ selective CuNW-Sn_{HIGH} **(b)** electrocatalysts, at various potentials.

Besides the above discussed experimental study of this Cu-Sn system, DFT modeling was applied to further understand the effects of the various catalyst compositions and surface species on the intermediate binding modes (results presented in **Chapter 4**). As a reminder of the discussion in the previous section (3.1.), Cu rich Cu-Sn surfaces predominantly bind the *COOH, while the Sn rich ones tend to bind the *OCHO* intermediate, following the CO and $HCOO^-$ pathways, respectively (**Figure 3.1**). On Cu rich Cu-Sn surfaces, the *COOH is transformed into *CO intermediate in the second electron/proton step. Focusing on the *CO intermediate, the DFT modeling results showed that in the case of low surface Sn content (11 at.%), $Sn^{\delta+}$ species are being formed due to charge redistribution from Sn to Cu. Their presence destabilizes the binding of the *CO intermediate on Cu, leading to its desorption and evolution of CO as product. On the other hand, in the case of Sn intermediate and rich surfaces (Sn≥45 at.%), the *OCHO* intermediate binds the strongest on metallic Sn and Cu_6Sn_5, while the *H binding is weaker on these surfaces, leading to enhanced $HCOO^-$ production and HER suppression. Moreover, the Sn intermediate and rich Cu-Sn surfaces (Sn≥45 at.%) show pure Sn-like electrocatalytic activity behaviour, hence the electronic redistribution from Sn to Cu (**Figure 3.1c**) is negligible. Finally, the binding of all intermediates on SnO_x surface (as major fraction at applied potentials less negative than –0.7 V - **Figure 3.7**) is weaker compared to metallic Sn/Cu_6Sn_5, thus the HER is favorable compared to CO_2ER in the case of the former surface sites.

Even though the CuNW-Sn_{LOW} and CuNW-Sn_{HIGH} catalysts show very good selectivity for converting CO_2 into CO and $HCOO^-$, respectively, the synthesis procedure for these materials is rather long and requires sophisticated equipment. This would add to the overall cost if materials prepared with such approach are possibly utilized for future large scale CO_2 electrolysis. Therefore, the next study presents a simple and fast approach for recycling/repurposing waste bronze alloy to derive CO selective Cu-Sn foam electrocatalyst. These electrocatalysts show performance equivalent to other catalyst materials for this purpose that are prepared from high purity precursors and sometimes sophisticated and expensive approaches. That study serves as a proof-of-concept that efficient electrocatalysts can be synthesized from waste materials thus contributing towards building a future sustainable industry in which the extraction of minerals from Earth's crust will be majorly replaced with utilization of secondary raw materials. Regarding the CO_2ER into $HCOO^-$, as already showed in this study, CuNW-Sn_{HIGH} materials are quite efficient electrocatalysts for this purpose, yet even though both Cu and Sn are endangered elements with future risk for supply, Cu is more recycled and cheaper than Sn. Therefore, reasonable catalyst materials for CO_2ER into $HCOO^-$ should be the ones based on Cu-sulfide materials, considering that the supply of sulfur is not endangered. Hence, the third study that is discussed in this chapter, besides revealing the role of sulfur and its chemical nature during CO_2ER, presents a very simple synthesis approach for Cu_xS materials, that could be potentially adapted for future large-scale CO_2 conversion into $HCOO^-$.

3.3. Deriving CO selective Cu-Sn electrocatalyst from waste bronze alloy

As already mentioned at the end of the previous section (3.2.), the purpose of this study, is to present a successful proof-of-concept for synthesizing CO_2ER to CO selective Cu-Sn electrocatalysts from industrial waste bronze alloy. As already mentioned, recycling or repurposing waste material for selective electrochemical reduction of CO_2 is a promising strategy to tackle environmentally relevant issues that cause the climate change and moreover that endanger the future supply of natural resources due to their massive extraction from Earth's crust for various requirements of the human society.

The electrocatalyst's synthesis procedure involves a single step electrochemical oxidation and dissolution of Cu and Sn from waste bronze with nominal Cu_xSn (x=14-16) composition in acidic medium. The dissolved Cu and Sn undergo simultaneous electrodeposition as Cu-Sn foam with surface composition of $Cu_{10}Sn$, as schematically presented in **Figure 3.9**. In order to achieve synthesis of materials with porous morphology

and high active surface area, the dynamic hydrogen bubble template (DHBT) technique was utilized during the electrodeposition where HER generated H_2 bubbles in acidic medium serve as templates around which the Cu-Sn foam is being formed. The synthesis method and the Cu-Sn foam were carefully optimized in order to obtain high selectivity for CO_2ER into CO and simultaneously suppress the HER. Yet, before discussing the electrocatalytic activity, the results from characterization of the waste bronze and the bronze-derived Cu-Sn electrocatalyst will be briefly discussed in the following paragraph.

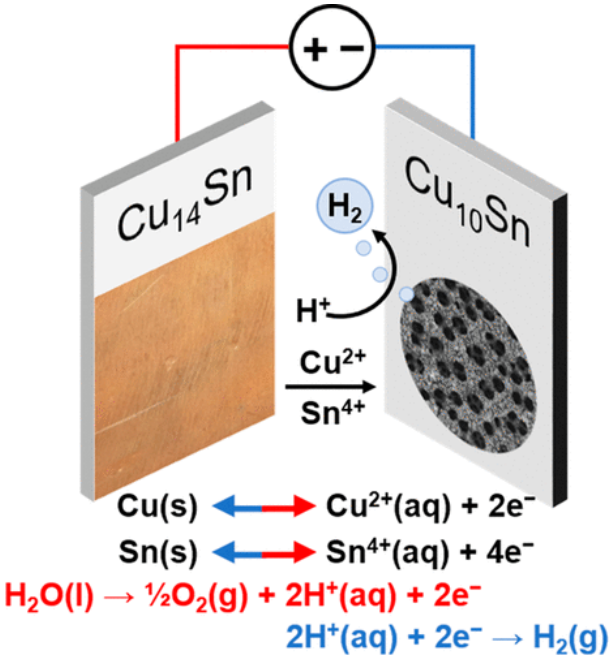

Figure 3.9. Schematic illustration of the electrochemical approach for deriving Cu-Sn foam catalyst from waste bronze alloy. The anodic processes resemble Cu and Sn oxidation into Cu^{2+} and Sn^{4+} and their dissolving in H_2SO_4(aq) as medium. The dissolved Cu and Sn are simultaneously electrodeposited on the cathode using HER generated H_2 bubbles as templates around which Cu-Sn foam microstructures are formed. Both anode and cathode (substrate) are made from the waste bronze. The surface compositions of the waste bronze ($Cu_{14}Sn$) and Cu-Sn foam ($Cu_{10}Sn$) are estimated from XPS.

The waste bronze XRD characterization results presented in **Figure 3.10a**, show typical broadening and shift in the diffraction patterns towards smaller 2theta angles compared to pure polycrystalline Cu, which is attributed to an increase in the lattice parameters of bronze's crystal structure (alloying effect). Similar broadening and shift of XRD patterns can be observed for the bronze-derived Cu-Sn foam when compared to the diffractogram of pure Cu foam that is synthesized under identical conditions as the Cu-Sn foam but using Cu foil as anode instead of the waste bronze. The SEM images in **Figures 3.10b-e** reveal the foam like morphology that consists of dendrite microstructures. Even though both foams were prepared

under identical conditions, the dendrite microstructures in Cu-Sn resemble blunted edges (**Figure 3.10c**) compared to the pure Cu foam (**Figure 3.10e**). Moreover, the pure Cu foam was found to be much thicker and with slightly larger pore sizes.

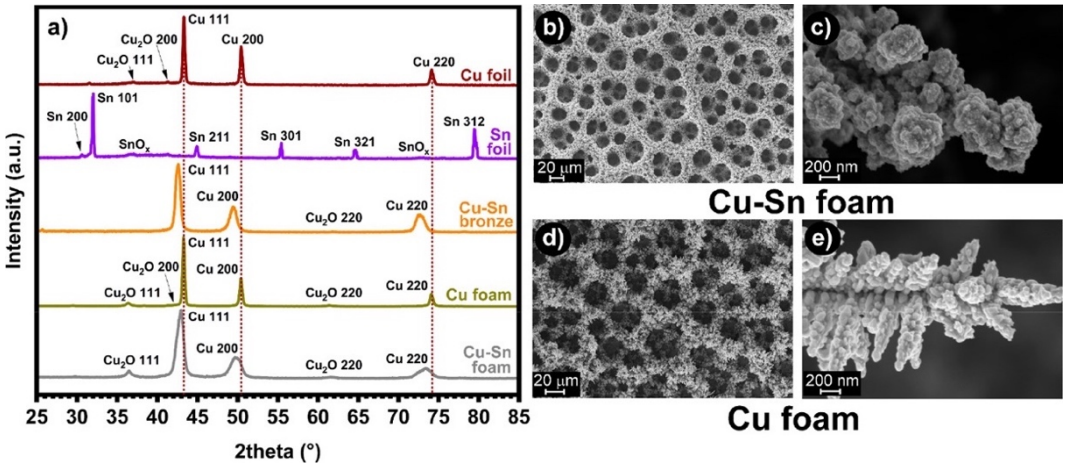

Figure 3.10. GI-XRD patterns of Cu foil, Sn foil, waste bronze, Cu foam and Cu-Sn foam **(a)**. SEM images revealing the foam-like morphology that is composed of dendrite microstructures for Cu-Sn foam derived from bronze **(b, c)** and pure Cu foam derived from Cu foil **(d, e)**.

The question that may rise is, what is the reason for deriving Cu-Sn foam in the first place, instead of simply utilizing the waste bronze itself as a catalyst for CO_2ER into CO, having in mind that the estimated composition resembles Cu-rich Cu-Sn material? According to the electrocatalytic activity results presented in **Figure 3.11**, bronze favors HER instead of CO_2ER into CO in the range of applied potentials between –0.5 and –0.7 V, then both processes show similar FE at –0.8 V and eventually the CO_2ER surpasses the HER at –0.9 and –1.0 V, but rather not selective towards a single CO_2ER product (the FE for CO and $HCOO^-$ are almost identical). The reason for such electrocatalytic behavior can be attributed to two important effects. The first effect is the actual surface composition of the waste bronze having a total Sn fraction of ~6.7 at.% (or $Cu_{14}Sn$ ratio, estimated from XPS), while for the electrocatalyst achieving the highest CO selectivity at –0.7 V discussed in the previous study (section 2.2.) i.e., the CuNW-Sn_{LOW}, the total Sn fraction is ~13 at.%. Besides the lower surface Sn content, it cannot be omitted that the waste bronze material does not resemble roughened morphology (planar electrode), thus double layer (local) CO_2 depletion effect is very possible to occur. On the other hand, the bronze derived Cu-Sn foam has a porous morphology and much higher relative surface roughness that prevents the local depletion of CO_2. Moreover, the surface Sn fraction in the Cu-Sn foam is higher (~9 at.%) than the in the case of the bronze leading to an enhancement in the CO selectivity and suppression of H_2 and $HCOO^-$ production at similar applied potentials as in the case of the CuNW-Sn_{LOW} electrocatalyst.

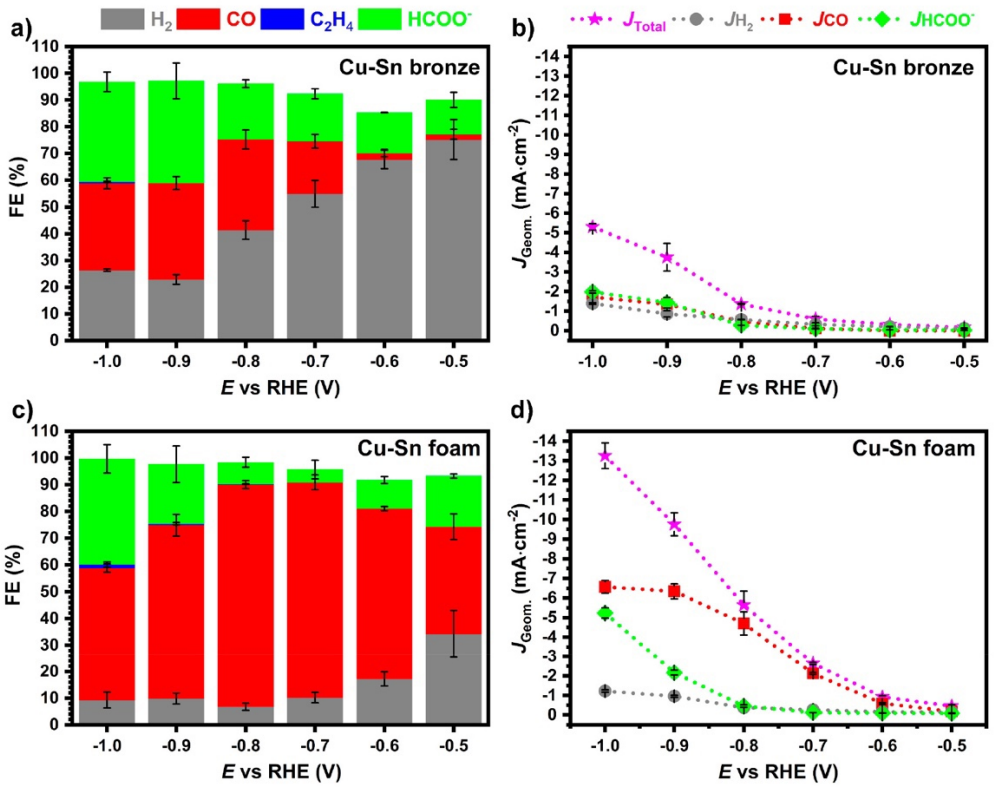

Figure 3.11. Faradaic efficiency (FE) and partial and total current density distribution for CO, H_2, $HCOO^-$ and C_2H_4 on waste bronze alloy **(a, b)** and Cu-Sn foam electrocatalyst **(c, d)** in the range of potentials between –0.5 and –1.0 V. The electrocatalytic activity for both materials, is studied in CO_2 saturated 0.1 mol·dm^{-3} $KHCO_3$(aq) as electrolyte.

A comparation of the CO_2ER catalytic activities on the bronze and on foils made of Cu and Sn, as constituent elements of the bronze itself, at –0.7 V, is presented in **Figure 3.12a**. The Cu foil mainly favors the HER at this potential due to the previously stated reason of local CO_2 depletion on planar electrodes, while the Sn foil predominantly converts CO_2 into $HCOO^-$, thus displaying the intrinsic properties of this metal, yet significant fraction of the FE belongs to the HER, again due to local CO_2 depletion. As already discussed, the CO_2 depletion effect is also very prominent in the case of the bronze, but the synergy between Cu and a small amount of Sn is very obvious. This is observable as a change of the selectivity towards CO as major CO_2ER product, when compared with the previously mentioned selectivity on pristine Cu and Sn electrocatalysts (**Figure 3.12a**). On the other hand, the Cu foam has higher relative surface roughness compared to the planar Cu, yet the HER dominates the CO_2ER at this potential as is the case for the planar Cu foil, however small FE fraction of C_2H_4 can be observed. Finally, it can be summarized that the Cu-Sn foam shows both intrinsic synergy between Cu and optimal amount of surface Sn which together with the porous morphonology prevents the local CO_2 depletion and the competitive HER. Hence, the reaction mechanism

follows the *COOH intermediate pathway (**Figure 3.1b**) towards enhanced CO production, as in the case of CuNW-Sn_{LOW} electrocatalyst discussed in the previous study (section 3.2).

The stability of the waste bronze derived Cu-Sn foam electrocatalysts was examined for 15 h of continuous electrolysis, and the results show that the selectivity for CO (FE of ~86%), total current density and morphology (**Figures 3.12c-g**) did not undergo significant changes over time.

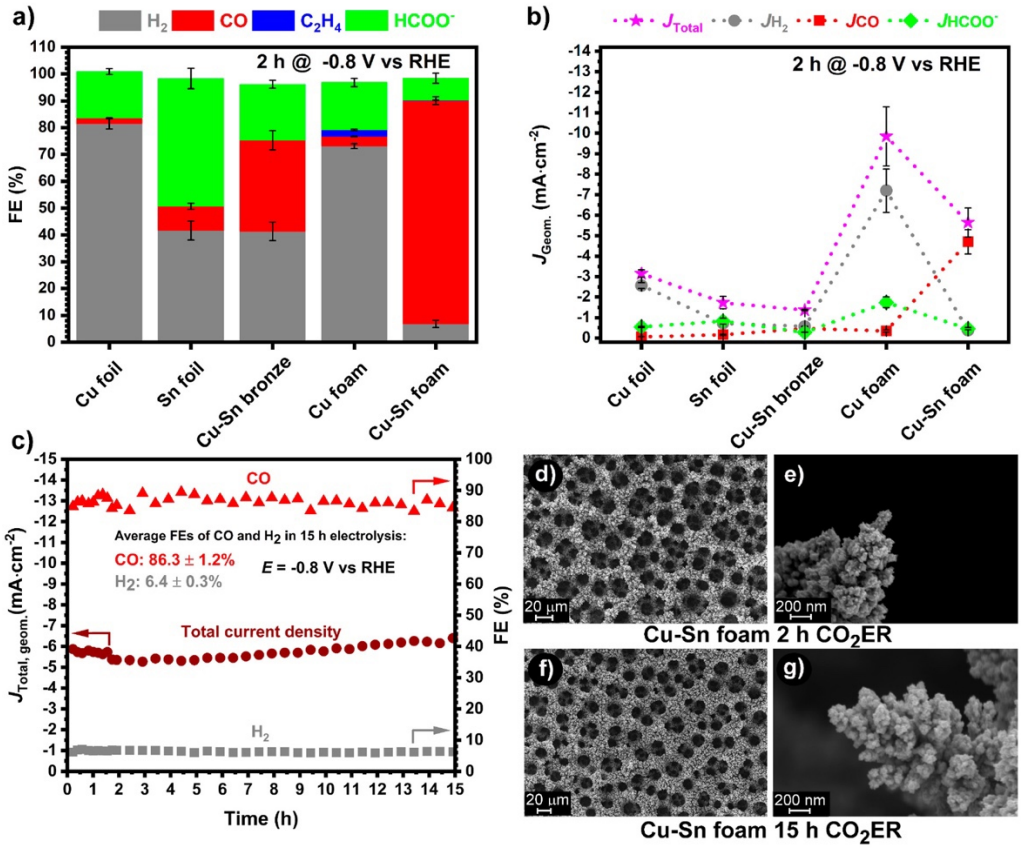

Figure 3.12. Comparison of the faradaic efficiency (FE), partial and total current density distribution for CO, H_2, $HCOO^-$ and C_2H_4 on Cu and Sn foils, waste bronze alloy, pure Cu foam and Cu-Sn foam **(a, b)**, FE for CO and H_2 and total current density during 15 h continuous electrolysis at –0.8 V on the waste bronze derived Cu-Sn foam electrocatalyst **(c)**, SEM images of the Cu-Sn foam after 2 **(d, e)** and 15 h electrolysis **(f, g)**. The electrocatalytic activity is studied in CO_2 saturated 0.1 mol·dm^{-3} $KHCO_3$(aq) as electrolyte.

Besides the as discussed approach for recycling/repurposing waste bronze for deriving CO selective Cu-Sn foam electrocatalyst, other possibility involving chemical roughening of the surface of the bronze with simultaneous leaching of Cu and Sn and their subsequent electrodeposition on the same sample from which they were extracted, was tested.

Unfortunately, due to reproducibility challenges in this approach the FE for CO did not exceed 50% in most cases.

Regarding simple synthesis and cost-wise suitable catalyst for CO_2ER into $HCOO^-$, as already discussed in the previous sections, the CuNW-Sn_{HIGH} can reach significantly high FE, yet the synthesis procedure is rather long and possibly too sophisticated for application in practice, and moreover both Cu and Sn are endangered for future supply. A possible option is to develop similar methods or further optimize the one described in this study for recycling/repurposing waste bronze, but for synthesis of material with higher surface Sn fraction. Alternatively, Cu-S (Cu_xS) based electrocatalysts can be used for CO_2ER into $HCOO^-$ instead of Sn rich Cu-Sn or Sn/SnO_2 based materials as the supply of sulfur is not endangered and Cu can be obtained as secondary raw material via its recycling. Nevertheless, most of the Cu_xS synthesis methods include utilization of toxic and sometimes expensive precursors and solvents, long synthesis times, elevated temperatures etc. Most of these methods are highly sophisticated when Cu_xS with specific composition, structure, particle sizes and/or morphology are required regarding the intended application. However, this is not always necessary, and as already mentioned, in the next (third) study a very simple, fast and reproducible method for synthesis of CO_2ER into $HCOO^-$ selective Cu_xS electrocatalyst via direct reaction between Cu and S is discussed. Besides the synthesis method, central focus on that study is placed on attempting to understand the catalyst's composition, morphology, surface Cu and S speciation, their chemical nature and electrochemical activation effects on the CO_2ER selectivity without which future practical application of such materials is hardy imaginable.

3.4. Composition-structure-activity relations in Cu-S electrocatalysts prepared via facile synthesis method

The electrochemical reduction of CO_2 into $HCOO^-$ on Cu-S based materials has been studied to some extent and many reports suggested that the presence of persistent sulfur residues under moderate electrochemical biases is stabilizing the $Cu^{\delta+}$ specie on the surface of the catalysts. This specie is oxophilic and, as already discussed in section 2.1. of this chapter, is favorably binding the *OCHO* intermediate that transforms into $HCOO^-$ in a second electron step (**Figure 3.1d**). This can be defined as a synergy between both elements that is affecting the intrinsic properties of pure Cu electrocatalyst, that typically is capable of reducing CO_2 into various product including multi electron/proton steps. However, there is lack of evidence for presence of partially positive or oxidized Cu species on the surface of the electrocatalysts under operating or near operating electrolysis. Therefore, one of the main

goals in this study is to probe the surface of Cu_xS catalyst and examine the oxidation states and chemical nature of both Cu and S using the *quasi in-situ* XPS approach. As already discussed in section 3.2 of this chapter, this approach was found beneficial for probing the oxidation states of surface Cu and Sn in Cu-Sn electrocatalysts and relating the obtained results with the CO_2ER activity. Nevertheless, in the scope of the Cu-S based materials study, various other effects that are possibly related to the selectivity for CO_2ER into $HCOO^-$, such as electrochemical activation of the Cu_xS catalysts at more negative applied potentials and presence of sulfur species in the electrolyte, were also investigated.

As already mentioned at the end of section 3.3., most of the reported methods for synthesis of Cu_xS involve utilization of toxic precursors such as H_2S, sulfide salts, thio-compounds, long synthesis procedures, elevated temperatures etc. Hence, a simple, fast and reliable method for synthesis of Cu_xS with porous morphology based on reaction between elemental Cu and sulfur was developed in this study. This method consists of electrodeposition of Cu foam that is subsequently sulfidated with sulfur dissolved in toluene. The electrodeposition step utilizes the DHBT phenomenon, already discussed in the previous section (3.3), for deriving CO selective Cu-Sn foam electrocatalyst from waste bronze alloy. Yet, in this case Cu mesh is used as cathode (substrate) and Cu foil as anode, as illustrated in **Figure 3.13**. Namely, the Cu from the foil undergoes oxidation into Cu^{2+} ions which simultaneously reduce and deposit on the Cu mesh cathode as porous foam. The Cu foam formation is templated by the H_2 bubbles evolved on the cathode in acidic medium.

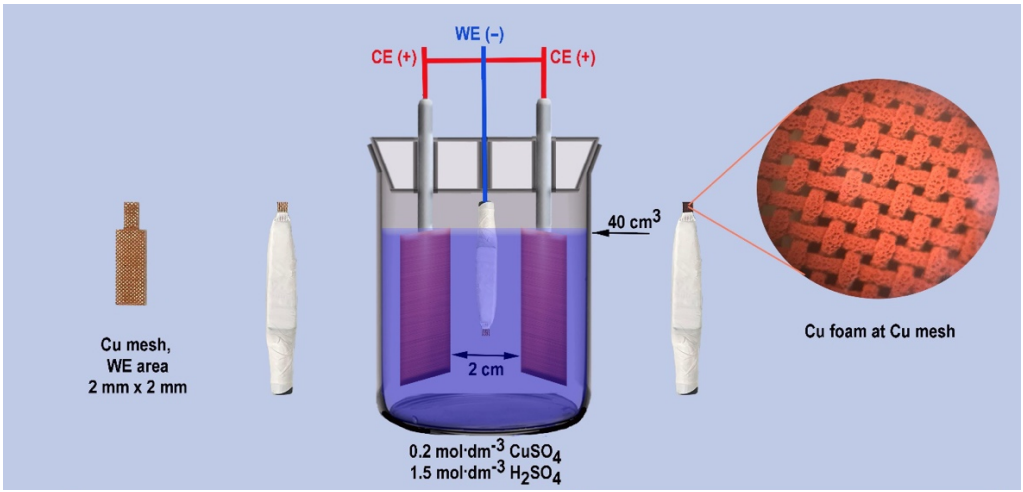

Figure 3.13. Schematic representation of dynamic hydrogen bubble template (DHBT) electrodeposition of Cu foam on Cu mesh as a substrate in a two-electrode setup. Cathode - Cu mesh, anode - Cu foil, duration of electrodeposition 9.5 s under geometric current density of 5 $mA \cdot cm^{-2}$.

In the next step the as-prepared Cu foam was subjected to the sequential procedure, presented in **Figure 3.14**, that includes etching of Cu's surface, washing in water, *i*-propanol and toluene, sulfidation with saturated solution of sulfur in toluene and termination of the reaction via second immersion in toluene, followed by thorough washing in *i*-propanol. The sulfur in toluene solution can be reused numerous times, as long as the concentration of sulfur is kept at saturation level hence, avoiding organic waste generation.

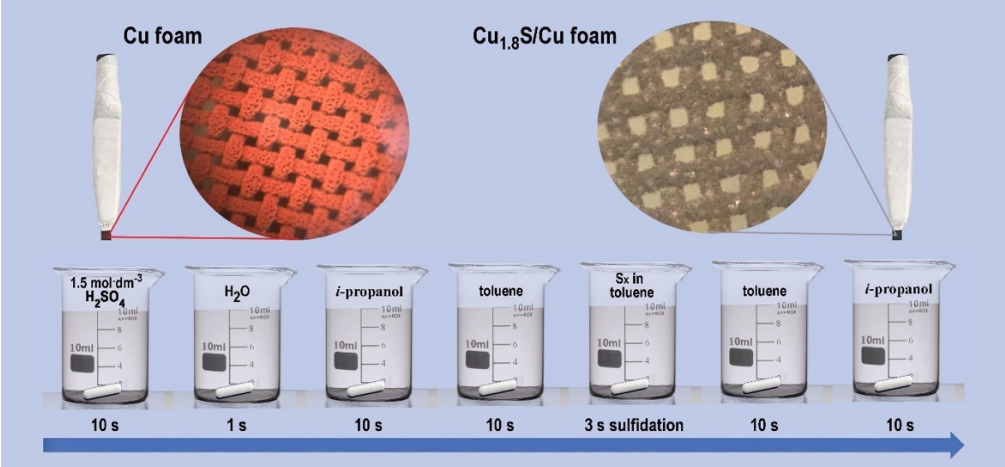

Figure 3.14. Schematic representation of the procedure for sulfidation of Cu foam. The Cu foam was subsequently immersed in each of the beakers under constant stirring and at room temperature, for amount of time presented in the scheme. The sulfidation is observable by instantaneous color change of the Cu foam from metallic Cu-like into bluish.

The SEM images of the Cu foam, before and after sulfidation are presented in **Figures 3.15a** and **b**, respectively. The typical foam morphology composed of dendrite-like microstructures was preserved during the sulfidation process, yet slight blunting of their edges can be observed, as in the case of the Cu-Sn foam discussed in the previous section (3.3.). The results from the GI-XRD characterization presented in **Figure 3.15c** showed that the Cu foam undergoes transformation into Cu_xS with digenite/roxbyite mixed phase composition and average stoichiometry of $Cu_{1.8}S$. Sulfidation of metallic Cu can also be achieved using CS_2 as a sulfur solvent instead of toluene and identical phase digenite/roxbyite composition with slight difference in their ratio can be obtained, yet this approach was abandoned due to the toxicity of CS_2.

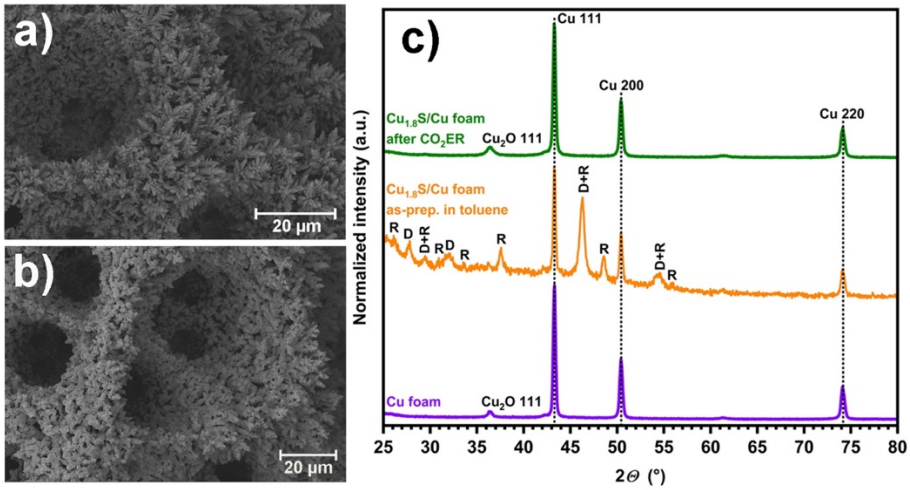

Figure 3.15. SEM images of pristine **(a)** and sulfidated Cu foam **(b)**. XRD patterns of pristine Cu foam, and sulfidated Cu foam, examined as-prepared and post-electrolysis **(c)**. D and R stand for Digenite ($Cu_{1.765}S$) and Roxbyite (Cu_7S_4) phases, respectively. The digenite is a major phase with fraction of ~70 wt.%.

In the next step, the CO_2ER catalytic activity of the sulfidated Cu foam (abbreviated as $Cu_{1.8}S$/Cu foam in the following text) and pristine Cu foam were examined under identical conditions for comparison, and the results are presented in **Figure 3.16**. The electrocatalysts were pre-reduced with linear sweep voltammetry (LSV) until reaching the potential under which the electrocatalytic activity was measured in chronoamperometry (CA) mode. The initial comparison of the electrocatalytic activity results on $Cu_{1.8}S$/Cu foam vs. pristine Cu foam show the typical shift of selectivity from several CO_2ER products on pristine Cu foam (**Figures 3.16d, e**) into $HCOO^-$ on the $Cu_{1.8}S$/Cu foam (**Figures 3.16a, b**) as practically exclusive product. However, there are differences in the CO_2ER catalytic performance on the $Cu_{1.8}S$/Cu foam that are dependent on the direction of altering the applied potential i.e., ramping in less negative (RLN) and ramping in more negative (RMN) direction via keeping each potential constant for 1 h. Namely, in both cases of altering the applied potential the FE for $HCOO^-$ is peaking at –0.7 V, but in the case of the RLN direction the FE for $HCOO^-$ is reaching ~65% (**Figure 3.16a**) while in RMN ~50% (**Figure 3.16b**), even though there is no significant difference in the total current densities in both directions except at –0.9 V (**Figures 3.16c, f**). Hence, it can be presumed that some sort of electrochemical activation of the $Cu_{1.8}S$/Cu foam occurs at –0.9 V that is enhancing the $HCOO^-$ selectivity at –0.7 V. Therefore, a control experiment was made in which the $Cu_{1.8}S$/Cu foam was directly subjected to –0.7 V (results presented in **Chapter 6**), thus the FE for $HCOO^-$ was not significantly different than in case of studying the material via

altering the potential in RMN direction i.e., starting at –0.5 V until –0.7 V was reached. This is suggesting that indeed the $Cu_{1.8}S$/Cu foam electrocatalysts undergoes activation at –0.9 V.

The question that is expected to follow is, how this electrochemical activation affects the catalysts material causing $HCOO^-$ selectivity differences, especially at –0.7 V, under which the highest FE for $HCOO^-$ is observed?

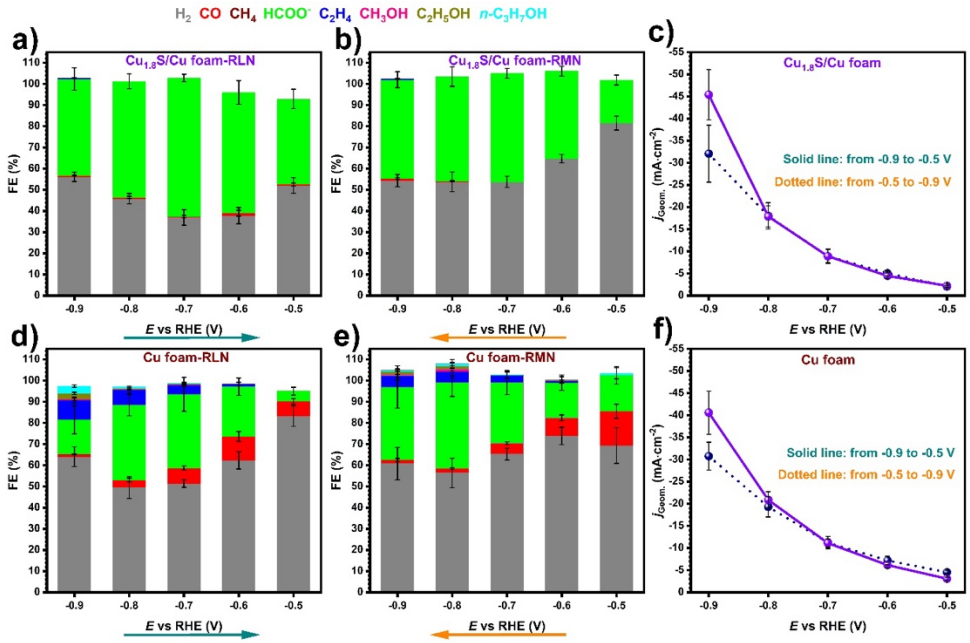

Figure 3.16. Faradaic efficiency (FE) and total current density distribution for various products on $Cu_{1.8}S$/Cu foam **(a-c)** and pristine Cu foam **(d-f)**. The arrows show the direction of ramping the applied potential i.e., ramping in less negative direction (RLN) from –0.9 to –0.5 V vs. RHE **(a, d)** and ramping in more negative direction (RMN) from –0.5 to –0.9 V vs. RHE **(b, e)**. During altering in both directions, each applied potential was kept constant for 1 h. The solid line on **(c, f)** represent the total current density when altering the potential in RLN, while the dotted line - in RMN direction. The electrocatalytic activity is studied in CO_2 saturated 0.1 mol·dm^{-3} $KHCO_3$(aq) as electrolyte.

Thermodynamically, it is expected that under all examined potentials (**Figure 3.16**) and near neutral bulk pH of the electrolyte (6.8 for CO_2 saturated 0.1 mol·dm^{-3} $KHCO_3$), cuprous sulfides should be subjected to reduction accompanied with evolution of H_2S in aqueous medium. Furthermore, these materials should be theoretically completely reduced to metallic Cu at applied potentials that are more negative than –0.7 V. However, the latter statement does not apply in practice, as evident from the different catalytic behavior for CO_2ER on $Cu_{1.8}S$/Cu foam and pristine Cu foam (**Figure 3.16**), even at potentials as negative as –0.9 V. Namely, these results are supporting various literature reports claiming persistent sulfur residues in the structure of materials that are electrochemically derived from Cu_xS. Yet, the amount of residual

sulfur in the electrocatalysts might be different when the $Cu_{1.8}S$/Cu foam is activated at –0.9 V compared to the case when the reduction starts either at –0.5 V (RMN direction) or directly at –0.7 V (control experiment mentioned before). Additional reasons could be difference in the electrolyte concentration of sulfur species that are in equilibrium (S^{2-}/HS^-/H_2S) and difference in the residual sulfur surface speciation (oxidation states) caused by the same catalyst activation effect hence, related to the $HCOO^-$ selectivity enhancement.

These effects were studied using *in-situ* mass spectrometry coupled with electrolysis (EC-MS) to track the H_2S evolution in both RLN and RMN directions of altering the applied potential, ICP-OES to quantify the post-electrolysis concentration of sulfur in the electrolyte and *quasi in-situ* XPS to reveal the Cu and S surface speciation under various conditions. Besides that, additional experiments were conducted that eventually led to even higher enhancement of the $HCOO^-$ selectivity, as discussed later in this section.

The results from the *in-situ* EC-MS studies intended to track the evolution of H_2S from the $Cu_{1.8}S$/Cu foam during the LSV pre-reduction and altering the applied potential in RLN and RMN direction are presented in **Figures 3.17** and **3.18**, respectively (*m*/*z* signals of 33 and 34, attributed to HS and H_2S). Prior to applying potential in chronoamperometry (CA) mode that is altered every 30 minutes, the material was pre-reduced with three linear sweep voltammetry (LSV) scans from 0 V vs. RHE to the start potential in CA mode, that is –0.9 V in RLN and –0.5 V in RMN direction. The onset for H_2S evolution (*m*/*z* signals of 33 and 34) can be observed at –0.47 V during the first LSV scan in both **Figures 3.17** and **3.18**. However, when the LSV is scanned to –0.9 V and then the same potential is applied in CA mode in order to proceed with altering the potential in RLN, the duration of the H_2S evolution extends up to ~17 min under –0.9 V in CA mode. That is around ~33 min in total since the electrochemical bias is applied (**Figure 3.17**). Under these conditions, the H_2S evolution is peaking when –0.9 V are reached in the first LSV scan (**Figure 3.17b**). On the other hand, when the three LSV repetitions were scanned to –0.5 V and proceeded at the same potential in CA mode, the H_2S evolves step-wise under each LSV scan, thus peaking ~3 min after –0.5 V are applied in CA mode (**Figure 3.18b**). The total duration of the H_2S evolution extends in the region of the next applied potential (–0.6 V), approaching ~1 h since the bias is applied. The twice longer duration of the H_2S evolution in the RMN direction comes from the sluggish reduction kinetics of $Cu_{1.8}S$/Cu foam at insufficiently high overpotentials (–0.5 and –0.6 V). Moreover, in the RLN direction i.e., starting the reduction at more negative potentials, the effect of enhanced local electrode double-layer H^+ consumption leading to local pH increase that affects the S^{2-}/HS^-/H_2S equilibrium can suppress the H_2S evolution due to decrease of the fraction of this specie. However, in both cases of altering the potential in RLN and RMN direction, the H_2S evolution is no longer observable at –0.7 V, under which the highest FE for $HCOO^-$ is achieved in the RLN direction i.e., after the electrocatalyst is activated at –0.9 V (**Figure 3.17b** vs. **Figure**

3.18b). Additionally, the bulk sulfur content in the $Cu_{1.8}S$/Cu foam was estimated post-electrolysis with EDX after each ramping sequence in both directions and in all cases, except at –0.5 and –0.6 V, an average sulfur fraction of ~1 at.% was found (presented in **Chapter 6**). At both –0.5 and –0.6 V in the RMN direction, bulk sulfur fraction of ~1.5 at.% was estimated, which is expected from the sluggish $Cu_{1.8}S$/Cu foam reduction kinetics at these applied potentials.

From these results can be summarized that even though the highest FE for $HCOO^-$ is achieved at –0.7 V after activation of the electrocatalyst at –0.9 V i.e., in the RLN direction, there is neither observable H_2S evolution, nor difference in the electrocatalyst's bulk sulfur fraction at –0.7 V, regardless of the potential ramping direction until –0.7 V are reached.

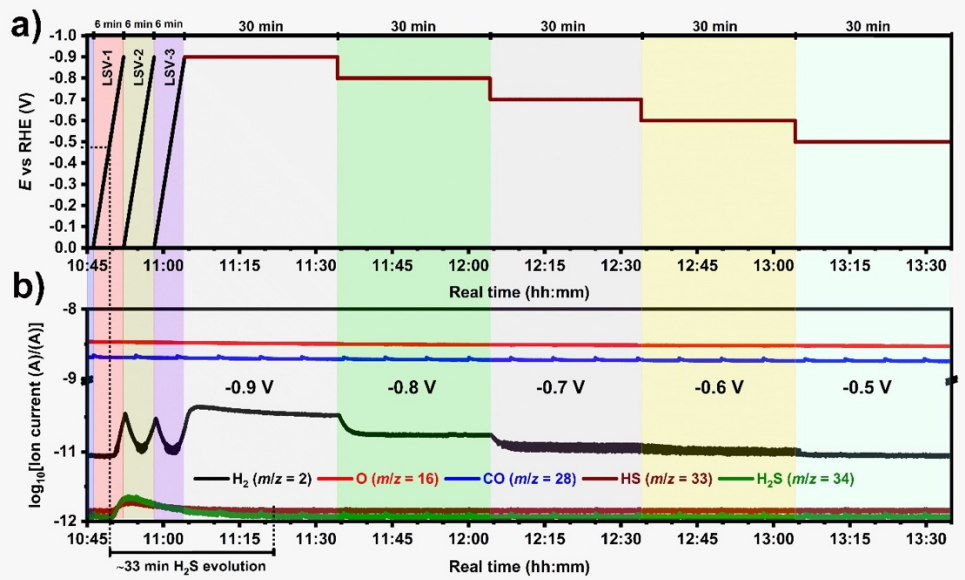

Figure 3.17. *In-situ* EC-MS tracking of the H_2S evolution from $Cu_{1.8}S$/Cu foam electrocatalysts via altering the applied potential in RLN direction (–0.9 to –0.5 V). Potential (*E*) in linear sweep voltammetry (LSV) and chronoamperometry (CA) modes **(a)** and mass vs. charge signal (*m*/z) of various species **(b)** plotted vs. time. Each applied potential was kept constant for 30 min. The tracking of the H_2S evolution is studied in CO_2 saturated 0.1 mol·dm^{-3} $KHCO_3$(aq) as electrolyte.

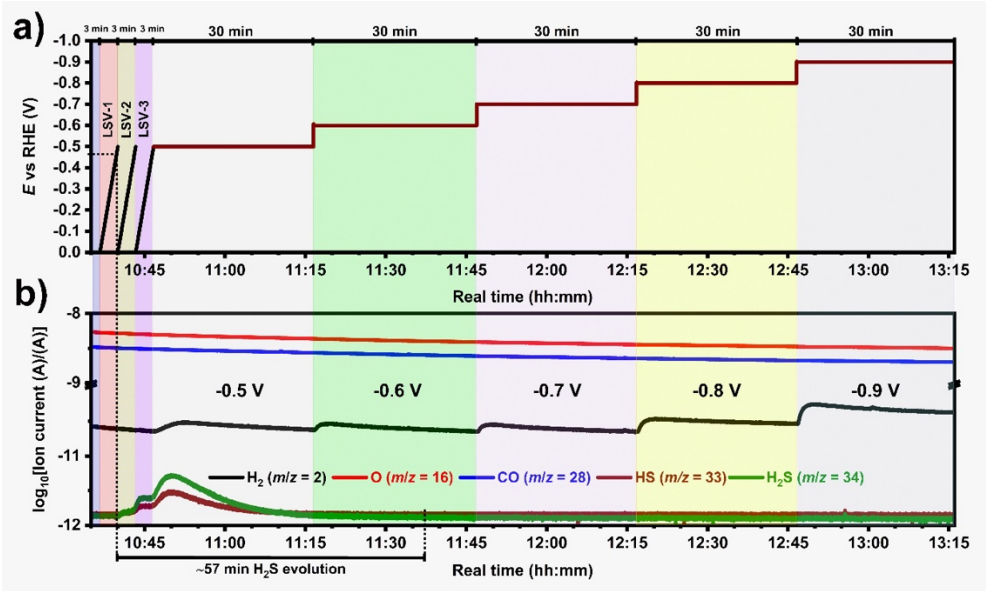

Figure 3.18. *In-situ* EC-MS tracking of the H_2S evolution on $Cu_{1.8}S$/Cu foam electrocatalysts via altering the applied potential in RMN direction (–0.5 to –0.5 9). Potential (*E*) in linear sweep voltammetry (LSV) and chronoamperometry (CA) modes **(a)** and mass signal vs. charge (*m*/*z*) of various species **(b)** plotted vs. time. Each applied potential was kept constant for 30 min. The tracking of the H_2S evolution is studied in CO_2 saturated 0.1 mol·dm^{-3} $KHCO_3$(aq) as electrolyte.

However, considering that there might be certain local pH effects that are dependent on the applied potential thus affecting the $S^{2-}/HS^{-}/H_2S$ equilibrium and concentration of these species in the electrolyte, various control experiments were conducted. In the first set of experiments, pristine Cu foams were immersed in electrolytes in which previously $Cu_{1.8}S$/Cu foam samples were reduced with one LSV scan until –0.9, –0.7 or –0.5 V thus achieving sulfidation with the $S^{2-}/HS^{-}/H_2S$ species present in the bulk electrolyte. The CO_2ER catalytic activity results for these `electrolyte sulfidated` Cu foams are presented in **Figure 3.19**, abbreviated as Cu foam-S-0.9, Cu foam-S-0.7 and Cu foam-S-0.5. Both Cu foam-S-0.9 and Cu foam-S-0.7 materials showed FE for $HCOO^{-}$ (70-75%) when compared to the $Cu_{1.8}S$/Cu foam (~45%), when examined at –0.9 V (**Figure 3.19a**). On the other hand, the Cu foam-S-0.5 shows significantly lower FE for $HCOO^{-}$, at the same applied potential (**Figure 3.19a**). The $HCOO^{-}$ selectivity on the Cu foam-S-0.9 and Cu foam-S-0.7 materials at –0.9 V does not change significantly when the Cu foam sample the electrolyte is purged with CO_2 for 20 min or 1 h after the LSV reduction of the $Cu_{1.8}S$/Cu foam i.e., prior immersing the pristine Cu foam, or when the electrolyte was replaced with fresh one and the electrocatalyst was re-examined at –0.9 V (samples: Cu foam-S-NP, -P1h, -P-1h-NE), presented in **Figure 3.19a**.

The second set of control experiments includes re-examination of the CO_2ER catalytic activity on the $Cu_{1.8}S$/Cu foam-RLN materials (or just previously activated at –0.9 V) after air

exposure and once or twice replacement of the electrolyte with fresh one (samples: $Cu_{1.8}S$/Cu foam-air, -NE, -NE2). Besides this, an electrolysis of previously activated $Cu_{1.8}S$/Cu foam was performed at –0.9 V in fresh electrolyte under inert conditions in a glovebox ($Cu_{1.8}S$/Cu foam-inert) in order to investigate whether possible surface re-oxidation might be a reason for the $HCOO^-$ selectivity enhancement. Again, at applied potential of –0.9 V, these electrocatalysts show significantly higher FE for $HCOO^-$ reaching 68-70% compared to the $Cu_{1.8}S$/Cu foam at the same potential that is examined immediately after activation and without electrolyte replacement (presented as $Cu_{1.8}S$/Cu foam-RLN in **Figure 3.19a**). Thus, it can be assumed that the surface re-oxidation due to air exposure does not affect the selectivity.

In the next step, the electrocatalyst materials from the first and second set of control experiments were examined at –0.7 V. All electrocatalysts show slight enhancement in the FE for CO compared to the $Cu_{1.8}S$/Cu foam-RLN, however, no significant difference can be observed in the FE for $HCOO^-$ (58-65%), with some discrepancies for the Cu foam-S-0.9 and Cu foam-S-0.5 (**Figure 3.19c**). Additional control experiment was conducted where $Cu_{1.8}S$/Cu foam was directly examined at –0.7 V (without activation at –0.9 V i.e., altering the potential in RLN direction) and re-examined again after replacing the electrolyte (see **Chapter 6**), yet no significant increase in the FE for $HCOO^-$ was observed i.e., it is similar as in the case of $Cu_{1.8}S$/Cu foam-RLN (50-55%) presented in **Figure 3.19c**.

Thus, it can be concluded that in order to achieve higher FE for $HCOO^-$ (up to 65%) at –0.7 V (**Figure 3.19c**), all samples in this study must be subjected to previous activation at –0.9 V. On the other hand, the enhancement in the $HCOO^-$ selectivity (from ~45% up to 70%) in the case of `electrolyte sulfidated` (Cu foam-S samples) and re-examined $Cu_{1.8}S$/Cu foam electrocatalysts after air exposure, electrolyte replacement etc., compared to only activated $Cu_{1.8}S$/Cu foam is observable at –0.9 V (**Figure 3.19a**). Both effects are probably somehow related to the concentration of sulfur in the electrolyte and/or the electrocatalysts' surface composition and speciation.

The concentration of sulfur in the electrolyte and the electrocatalysts' surface composition and speciation (Cu and S oxidation states) are studied with ICP-OES and *quasi in-situ* XPS, respectively, and the results are discussed in the following text.

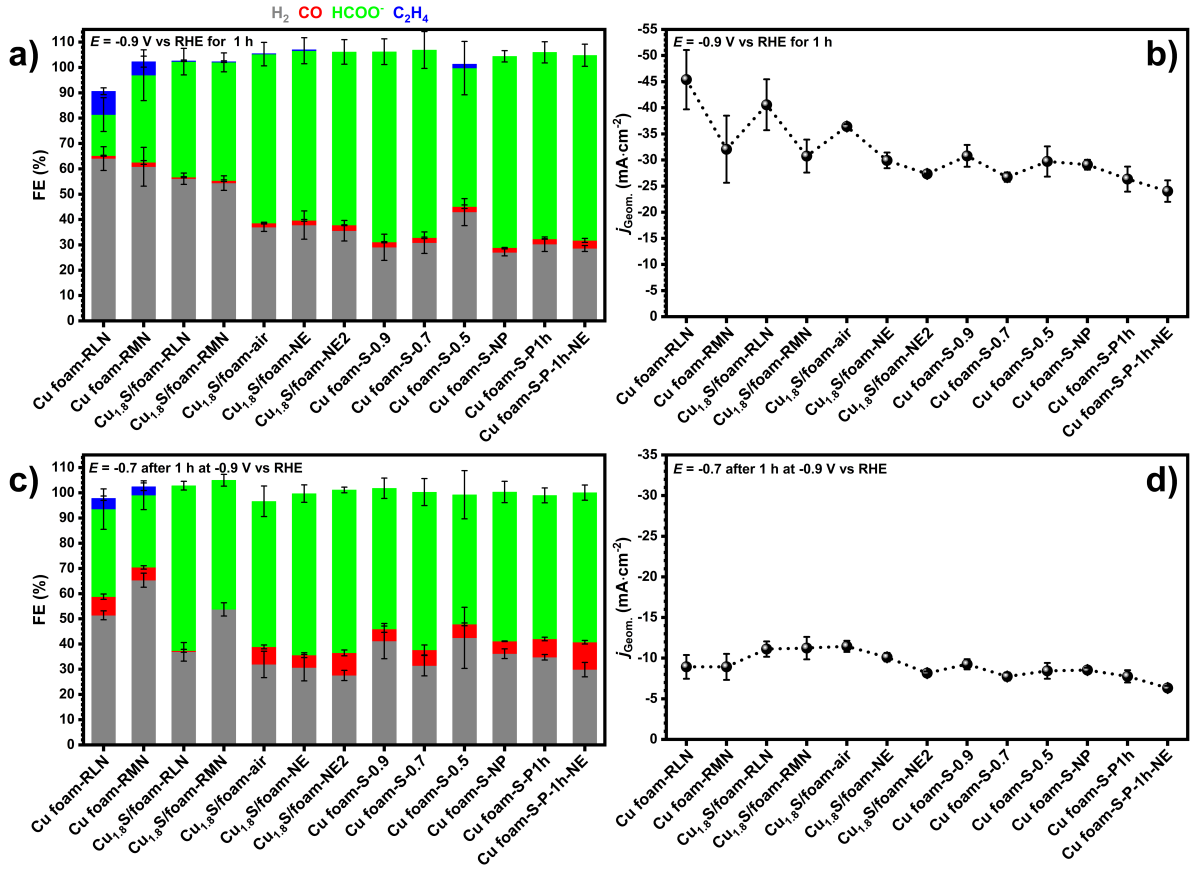

Figure 3.19. Comparison of the electrocatalytic activity for all examined catalyst materials: FE distribution of various products and total current density at –0.9 V **(a, b)** and at –0.7 V **(c, d)**. The electrocatalytic activity is studied in CO_2 saturated 0.1 mol·dm^{-3} $KHCO_3$(aq) as electrolyte.

The results from the analysis of the post-electrolysis sulfur concentration in the electrolyte under various conditions with ICP-OES are presented in **Figure 3.20**. It is obvious that the concentration of sulfur is the highest when the $Cu_{1.8}S$/Cu foam is reduced with one LSV scan from 0 to –0.9 V thus decreases when the LSV is scanned to –0.7 and –0.5 V. Yet, three LSV scans to –0.9 V generate the same sulfur concentration as one scan to –0.5 V. Moreover, three LSV scans to –0.5 V show higher sulfur concentration than three LSV scans to –0.9 V and this is supporting the observed prolonged H_2S evolution in the *in-situ* EC-MS data when altering the potential in RMN compared to RLN direction i.e., ~57 (**Figure 3.17**) vs. ~27 min (**Figure 3.18**), respectively. However, no difference in the sulfur concentration can be observed at –0.7 V for $Cu_{1.8}S$/Cu foam regardless of whether this potential was reached via altering in RLN, RMN direction, or the sample was subjected directly at –0.7 V. This means that the bulk sulfur post-electrolysis concentration cannot explain the $HCOO^-$ selectivity enhancement at –0.7 V caused by the activation at –0.9 V. Moreover, the analysis of the sulfur concentration after electrolysis using the `electrolyte sulfidated` Cu foams (Cu foam-S) and the

activated $Cu_{1.8}S$/Cu foams after replacement of the electrolyte ($Cu_{1.8}S$/Cu foam-0.9(7)-NE), that are selectivity-wise equivalent in the CO_2ER to $HCOO^-$ performance at –0.9 V, show differences in the bulk sulfur concentration. These observations are suggesting that the bulk sulfur concentration in the electrolyte cannot explain the $HCOO^-$ selectivity enhancement at –0.9 V either. Hence, more insights regarding this matter will be provided from the *quasi in-situ* XPS results that are discussed in the upcoming text.

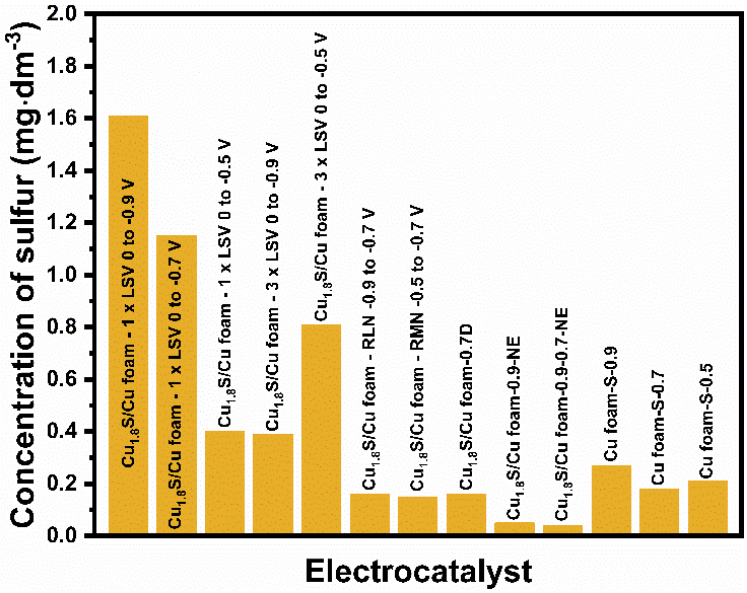

Figure 3.20. Post-electrolysis results from the inductively coupled plasma – optical emission spectrometry (ICP-OES) analysis of the concentration of sulfur in the electrolyte under various conditions.

The results from the electrocatalyst materials surface composition and speciation (Cu and S oxidation states and chemical nature) examined with *quasi in-situ* XPS, are presented in **Figure 3.21**. The full XPS data is presented in **Chapter 6**. Before, continuing with the discussion of the activation and other effects that enhance the $HCOO^-$ selectivity, it is important to discuss the surface speciation of the sulfidated vs. pristine Cu foam. Namely, **Figure 3.21a** shows that the pristine Cu foam undergoes complete reduction to metallic Cu at all applied potentials, while all sulfidated materials, besides metallic, show presence of Cu^+ species even at potentials, as negative as –0.9 V. Therefore, it can be concluded that indeed the Cu^+ specie is persistent on the surface of the Cu-S based electrocatalyst materials, stabilized by the presence of residual sulfur hence, supporting the claim that most probably the CO_2 conversion into $HCOO^-$ mechanism occurs via the $Cu^{\delta+}$ or Cu^+ bound *OCHO* intermediate, as presented in (**Figure 3.1d**). It is important to note, that the Cu^+ species on the surface of the sulfidated materials are not generated post-electrolysis and the evidence for that is the absence of such

species on the surface of the pristine Cu foam that is completely reduced to metallic, suggesting that the *quasi in-situ* XPS approach is indeed very useful for this purpose, as in the case of the Cu-Sn study discussed in section 3.2 and fully presented in **Chapter 4**.

Focusing again on the discussion regarding the $HCOO^-$ selectivity differences caused by the electrocatalyst materials activation and other effects, from **Figure 3.21** can be observed that even though Cu resembles +1 oxidation state species, the surface sulfur speciation is not exclusively attributed to S^{2-}, but also SO_4^{2-} can be observed (**Figure 3.21b**).

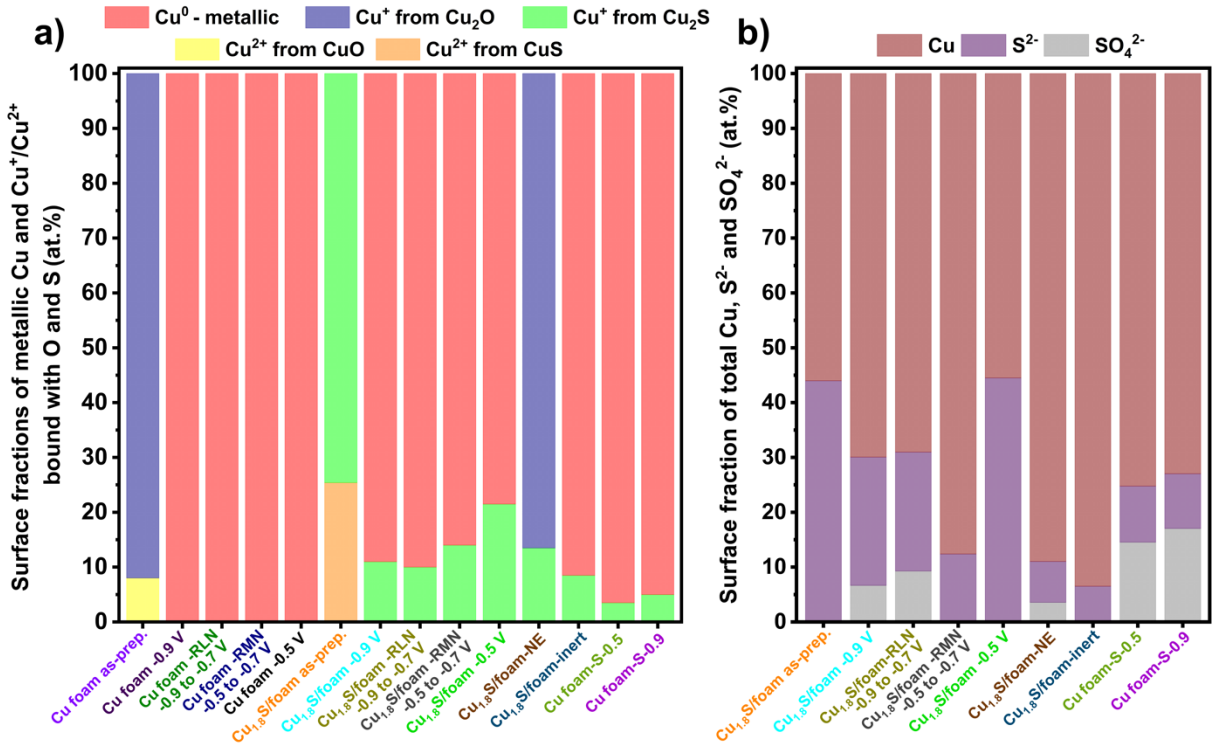

Figure 3.21. *Quasi in-situ* XPS quantification results: Surface fractions of various Cu species obtained from the Cu $L_3M_{4,5}M_{4,5}$ Auger spectra **(a)** and of total Cu and S^{2-}/SO_4^{2-} surface species obtained from Cu 2p and S 2p core levels spectra, respectively **(b)**. In the case of the $Cu_{1.8}S$/Cu foam-inert sample, it was not possible to quantify the fraction of the SO_4^{2-} surface due to high noisiness in the S 2p spectra (data showed in **Chapter 6**).

Interestingly, the SO_4^{2-} specie is observed in all cases when the sulfidated materials were subjected to applied potential of –0.9 V and moreover the total surface sulfur fraction for the $Cu_{1.8}S$/Cu foam-RLN (–0.9 to –0.7 V) and the $Cu_{1.8}S$/Cu foam sample that is only examined at –0.9 V are almost identical, while significantly smaller in the case of $Cu_{1.8}S$/Cu foam-RMN (–0.5 to –0.7 V). These observations are the first obvious evidence that there are differences in both total surface sulfur fraction and moreover in the speciation that can be related to the $HCOO^-$ selectivity difference on $Cu_{1.8}S$/Cu foam at –0.7 V that is reached via RLN vs. RMN

direction of altering the applied potential (cf. **Figure 3.16**). Regarding the $HCOO^-$ selectivity enhancement at –0.9 V, observed via re-examination of $Cu_{1.8}S$/Cu foam after electrolyte replacement, air exposure etc., there are various discrepancies for both S^{2-} and SO_4^{2-} fractions among samples that are practically showing equivalent electrocatalytic performance. It could be the case, that the surface sulfur, especially the SO_4^{2-} specie as readily soluble in water undergoes dynamic distribution between the electrode's surface and the electrolyte and it is uncertain whether it is incorporated in the structure of the electrocatalyst or just deposited on its surface. But yet, how the SO_4^{2-} is being formed in the first place, since the sulfur in this specie resembles the highest oxidation state of +6 and why this is only observable in all samples subjected to –0.9 V? Possible explanation is that oxidation of S^{2-} specie occurs in the double layer when the electrochemical bias is terminated thus sudden change in the electrode's polarity could be a cause of such reaction. Moreover, the S^{2-} oxidation process is favorable under strong alkaline environment that can be caused by local pH increase under more negative potentials that may be the answer why SO_4^{2-} specie is observed only after subjecting the electrocatalysts at –0.9 V. Furthermore, the presence of the Cu^+ specie is most probably not related with oxidation caused by possible electrode polarity switch, since only metallic Cu was observed in the case when pristine Cu foam was examined with *quasi in-situ* XPS under identical conditions.

It can be summarized that the observed differences in the CO_2ER to $HCOO^-$ selectivity on the Cu-Sn electrocatalysts examined in this study under various conditions are most probably related to processes that are occurring in the electrode double layer and the surface of the electrode. These processes are of rather complex and dynamic nature, and in which most probably the local pH change plays a key role. However, not everything can be revealed and understood in one study, yet it gives motivation for further research involving methods with which various species and processes can be probed on the catalyst's surface and in the electrode double layer during CO_2 electrolysis, such as the *in-situ* infrared and Raman spectroscopies.

Having in mind the complexity and broadness of this research in terms of the number of different samples, conditions, experiments, other details etc., a schematic illustration is presented in **Figure 3.22** that recapitulates the most important findings in this study, intended for the reader to grasp the very essential information. All other information in the scope of this study and the other two studies that are focused on the Cu-Sn system based electrocatalysts can be found in **Chapters 4**-**6**

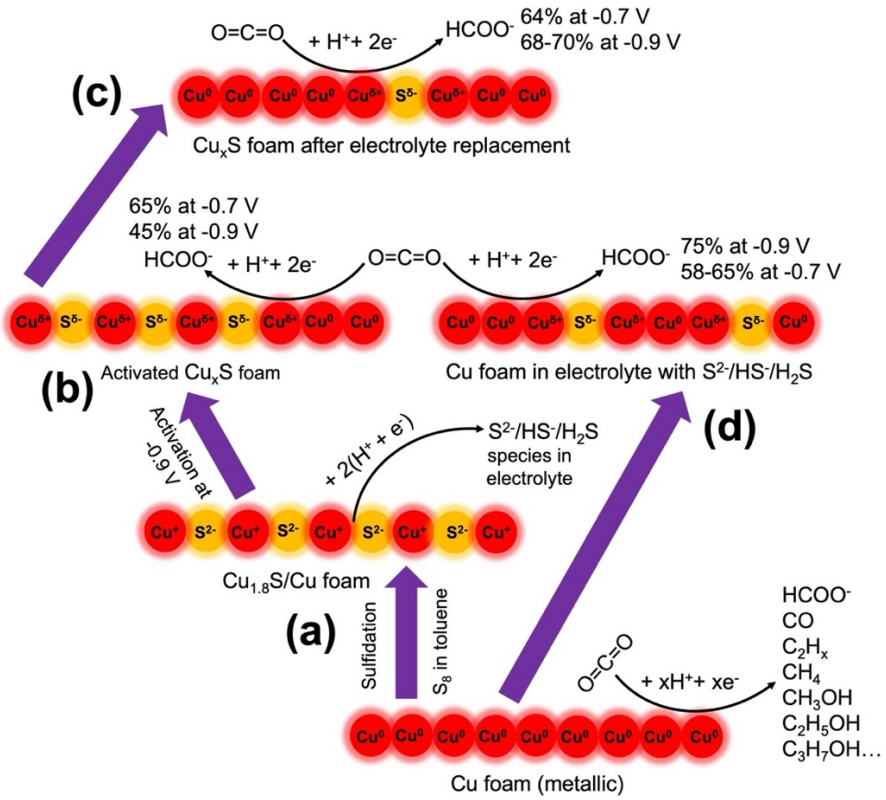

Figure 3.22. Summary of the composition-structure-activity relations in the Cu-S electrocatalyst materials and conclusion of the research and findings in this study.

The metallic Cu foam is sulfidated with sulfur dissolved in toluene producing $Cu_{1.8}S$/Cu foam, encompassing facile synthesis method applied for this purpose **(a)**. When the $Cu_{1.8}S$/Cu foam is activated at applied potential of –0.9 V, the FE for $HCOO^-$ reaches ~45% at –0.9 V and ~65% at –0.7 V **(b)** in comparison with 50-55% when the sample is directly examined at –0.7 V, or the potential is ramped from –0.5 to –0.7 V. When the activated $Cu_{1.8}S$/Cu foam is re-examined in fresh electrolyte, the FE for $HCOO^-$ increases to 68-70% at –0.9 V, while it is not significantly affected at –0.7 V **(c)**. If a pristine Cu foam is placed in electrolyte in which $Cu_{1.8}S$/Cu foam was previously reduced with one LSV scan to –0.7 or –0.9 V **(d)**, the as-sulfidated Cu foam, with the sulfur species present in the electrolyte, can reach up to 75% FE for $HCOO^-$, while at –0.7 V the selectivity is similar as the in the case of the results for the electrocatalyst materials presented with **(b)** and **(c)** under the same applied potential. The *quasi in-situ* XPS results revealed that under electrochemical bias, the surface of pristine Cu foam is completely reduced to metallic Cu, while in the case of the sulfidated materials, Cu^+ specie is present. The Cu^+ is stabilized by the residual sulfur species and preferably binds the *OCHO* intermediate that transforms into $HCOO^-$ in a second electron step. Finally, the unexpected presence of SO_4^{2-} specie in the case of the activated electrocatalysts on which the highest $HCOO^-$ selectivity is reached, is believed to be associated with various electrode-electrolyte interface effects, requiring further *in-situ* based studies to be fully understood.

Even though facile methods are developed for synthesis of CO- Cu-Sn and $HCOO^-$ selective Cu-S electrocatalysts via recycling/repurposing of waste bronze alloy and direct reaction between Cu and S, respectively, their CO_2ER activities are examined in laboratory scale electrochemical setups. Under such experimental conditions, the obtained current densities are around order of magnitude lower compared to what is considered as industrially relevant current density (≥100 $mA \cdot cm^{-2}$) i.e., relevant CO_2 conversion rates for application in practice. Therefore, the future research challenges include adapting and further optimization of the Cu-Sn and Cu-S synthesis methods described in this study, for preparation of electrocatalyst loaded gas-diffusion electrodes (GDE) and study of their CO_2ER activity in GDE configuration electrolyzers, in which such CO_2 to CO or $HCOO^-$ conversion rates could be achieved.

CHAPTER 4. Determining structure-activity relationships in oxide derived Cu–Sn catalysts during CO_2 electroreduction using x-ray spectroscopy

Published in:

Advanced Energy Materials 12, **2022**, 2103328.

DOI: https://doi.org/10.1002/aenm.202103328

Authors:

L.C. Pardo Pérez, A. Arndt, **S. Stojkovikj**, I.Y. Ahmet, J.T. Arens, F. Dattila, R. Wendt, A. Guilherme Buzanich, M. Radtke, V. Davies, K. Höflich, E. Köhnen, F. Tockhorn, R. Golnak, J. Xiao, G. Schuck, M. Wollgarten, N. López, M.T. Mayer.

Individual contribution:

- L.C. Pardo Pérez: Project planning, samples preparation, data collection, discussion of results, all data final processing, manuscript writing.
- A. Arndt: Project planning, samples preparation, data collection, Cu K edge XAS data processing and analysis, discussion of results.
- **S. Stojkovikj**: Project planning, samples preparation, data collection, responsible for all soft x-ray XAS data processing and analysis, discussion of results, manuscript review.
- I.Y. Ahmet: XPS data collection, data processing and analysis.
- J.T. Arens: DFT calculations.
- F. Dattila: DFT calculations.
- R. Wendt: TEM.
- A. Guilherme Buzanich: Sn K edge XAS.
- M. Radtke: Sn K edge XAS, beamtime supervision.
- V. Davies: Samples preparation, pre-treatment, Cu anodization.
- K. Höflich: FIB-SEM measurements.
- E. Köhnen: Samples preparation (ALD on Cu nanowires).
- F. Tockhorn: Samples preparation (ALD on Cu nanowires).
- R. Golnak: XAS discussions, beamtime supervision
- J. Xiao: XAS discussions for data processing.
- G. Schuck: Cu K edge XAS beamtime supervision.

- M. Wollgarten: TEM supervision.
- N. López: DFT calculations supervision.
- M.T. Mayer: Project supervision, data discussion, manuscript review.

Various figures and the whole paper are republished in the thesis in **Chapters 3** and **4**, respectively.

RESEARCH ARTICLE

ADVANCED ENERGY MATERIALS

www.advenergymat.de

Determining Structure-Activity Relationships in Oxide Derived Cu—Sn Catalysts During CO_2 Electroreduction Using X-Ray Spectroscopy

Laura C. Pardo Pérez, Alexander Arndt, Sasho Stojkovikj, Ibbi Y. Ahmet, Joshua T. Arens, Federico Dattila, Robert Wendt, Ana Guilherme Buzanich, Martin Radtke, Veronica Davies, Katja Höflich, Eike Köhnen, Philipp Tockhorn, Ronny Golnak, Jie Xiao, Götz Schuck, Markus Wollgarten, Núria López, and Matthew T. Mayer**

The development of earth-abundant catalysts for selective electrochemical CO_2 conversion is a central challenge. Cu—Sn bimetallic catalysts can yield selective CO_2 reduction toward either CO or formate. This study presents oxide-derived Cu—Sn catalysts tunable for either product and seeks to understand the synergetic effects between Cu and Sn causing these selectivity trends. The materials undergo significant transformations under CO_2 reduction conditions, and their dynamic bulk and surface structures are revealed by correlating observations from multiple methods—X-ray absorption spectroscopy for in situ study, and quasi in situ X-ray photoelectron spectroscopy for surface sensitivity. For both types of catalysts, Cu transforms to metallic Cu^0 under reaction conditions. However, the Sn speciation and content differ significantly between the catalyst types: the CO-selective catalysts exhibit a surface Sn content of 13 at. % predominantly present as oxidized Sn, while the formate-selective catalysts display an Sn content of ≈70 at. % consisting of both metallic Sn^0 and Sn oxide species. Density functional theory simulations suggest that $Sn^{\delta+}$ sites weaken CO adsorption, thereby enhancing CO selectivity, while Sn^0 sites hinder H adsorption and promote formate production. This study reveals the complex dependence of catalyst structure, composition, and speciation with electrochemical bias in bimetallic Cu catalysts.

1. Introduction

Copper-based electrocatalysts have been widely studied for CO_2 electrochemical reduction (CO_2ER) due to their unique capability to produce valuable products such as CO, hydrocarbons, and alcohol. As many as 16 products have been observed during CO_2ER on polycrystalline Cu.[1] The typical major products are formate, CO, ethylene, and methane, minor ones include alcohols and other oxygenates, and the hydrogen evolution reaction (HER) is an (often significant) parasitic reaction. Directing selectivity among this wide variety of products remains a pressing challenge in the field.[2] Diverse catalyst engineering approaches to improve the selectivity of Cu have been advanced in the field including the use of nanostructured[3–6] as well as oxide-derived Cu catalysts,[7–12] as discussed in the comprehensive review by Nitopi et al.[13] Another possible approach to modulate

L. C. Pardo Pérez, A. Arndt, S. Stojkovikj, V. Davies, M. T. Mayer
Young Investigator Group Electrochemical Conversion of CO2
Helmholtz-Zentrum Berlin für Materialien und Energie GmbH
Hahn-Meitner-Platz 1, 14109 Berlin, Germany
E-mail: lcpardop@gmail.com; m.mayer@helmholtz-berlin.de

A. Arndt, S. Stojkovikj, V. Davies
Institut für Chemie & Biochemie
Freie Universität Berlin
Arnimallee 22, 14195 Berlin, Germany

The ORCID identification number(s) for the author(s) of this article can be found under https://doi.org/10.1002/aenm.202103328.

[+]Present address: Ferdi d-Braun-Institut gGmbH, Leibniz-Institut für Höchstfrequenztechnik, 12489 Berlin, Germany

DOI: 10.1002/aenm.202103328

I. Y. Ahmet, R. Wendt, K. Höflich,[+] M. Wollgarten
Institute for Solar Fuels
Helmholtz-Zentrum Berlin für Materialien und Energie GmbH
Hahn-Meitner-Platz 1, 14109 Berlin, Germany

J. T. Arens, F. Dattila, N. López
Institute of Chemical Research of Catalonia (ICIQ)
The Barcelona Institute of Science and Technology (BIST)
Av. Països Catalans 16, Tarragona 43007, Spain

A. Guilherme Buzanich, M. Radtke
Division 6.3 Structure Analysis
Bundesanstalt für Materialforschung und -prüfung (BAM)
Richard-Willstätter-Straße 11, 12489 Berlin, Germany

E. Köhnen, P. Tockhorn
Young Investigator Group Perovskite Tandem Solar Cells
Helmholtz-Zentrum Berlin für Materialien und Energie GmbH
Kekuléstraße 5, 12489 Berlin, Germany

R. Golnak, J. Xiao
Department Highly Sensitive X-ray Spectroscopy
Helmholtz-Zentrum Berlin für Materialien und Energie GmbH
Albert-Einstein-Straße 15, 12489 Berlin, Germany

Cu selectivity is to functionalize the Cu surfaces with a second metal to form Cu−M bimetallic catalysts.[14,15] In particular, several studies on the CO_2ER activity of Cu−Sn catalysts have demonstrated remarkably high selectivity towards CO[16,17] or formate.[18,19] Although a number of empirical trends correlating composition and structure with observed selectivity have been reported, an understanding of the precise mechanistic effects directing selectivity remains elusive.

Comparison of several studies employing various Cu−Sn stoichiometries with similar morphologies[20–22] indicates generally that Cu−Sn catalysts with low Sn content are typically selective towards CO production, while those with high Sn content favors formate ($HCOO^-$). However, specific optimal compositions leading to high activity towards CO or formate vary significantly among reports. Furthermore, improved activity and selectivity are reported in catalysts with high surface area. Highly CO-selective catalysts have been achieved by the functionalization of high surface area Cu nanostructures with low amounts of Sn by electrodeposition,[23–25] electroless deposition,[26] or atomic layer deposition (ALD) of SnO_2.[16] Interestingly, high surface area Cu nanostructures functionalized with Sn overlayers have also been reported as highly selective catalysts towards formate.[19,22,27] Presumably, significant differences in Cu−Sn surface structure and composition exist among these high surface area catalysts selective toward different products, but unfortunately the detailed analysis of surface composition is rarely reported. Therefore, an investigation of composition and speciation in Sn-functionalized Cu nanostructures tuned to yield radically different selectivity (namely CO or formate) is of high interest to help unravel the factors which direct this selectivity.

Various explanations of the synergetic effects that yield these high selectivities of Cu−Sn bimetallic catalysts have been proposed. According to density functional theory (DFT) investigations, increased HER overpotentials are predicted on Cu−Sn surfaces compared to pure Cu,[17] leading to an increased relative selectivity for CO_2ER over HER on Cu−Sn materials. As for the possible effects of Cu−Sn composition directing selectivity among CO or formate pathways, Vasileff[28] reported a Bader charge analysis indicating a partial electron transfer (ET) from Sn to Cu in CuSn alloys, leading to the formation of partially oxidized $Sn^{\delta+}$ sites and partially reduced $Cu^{\delta-}$ sites. This partial ET is proposed to gradually weaken the adsorption of *COOH (leading to CO) with increasing Sn content and enhance *OCHO adsorption (leading to $HCOO^-$). Meanwhile, the persistence of oxidized Sn as an active site during CO_2ER experiments has been invoked by Li et al. based on DFT studies,[22] who proposed that Cu-doped uniaxially-compressed SnO_2 is the active site for selective reduction of CO_2 to CO in Cu@SnO_2 (core@shell) nanoparticle catalysts.

These DFT studies on Cu−Sn bimetallic CO_2ER catalysts indicate that charge distribution among metal sites and their oxidation states play a crucial role in the binding strength of the key intermediates directing selectivity between H_2, CO, and formate. At the center of the debate is the possible persistence of oxidized metal sites under CO_2ER reduction conditions and the precise nature of the active site. While these DFT models are typically based on compositions observed either before or after electrocatalyst testing, it is well known that electrocatalyst materials can transform significantly under CO_2 reduction conditions, presenting challenges in identifying their actual active forms. In this context, the complementary techniques of X-ray absorption (XAS) and X-ray photoelectron (XPS) spectroscopy are powerful techniques to probe the chemical environment and oxidation state of Cu and Sn and gather relevant information on the active form of the catalysts.

Herein, we present an X-ray spectroscopy study of a Cu−Sn bimetallic system with tunable Sn content capable of achieving high selectivity to either CO or formate. Complementary information on the composition and chemical environment of metals in the electrocatalysts' bulk and surface was revealed by correlating observations from multiple X-ray spectroscopy methods (in situ hard-XAS, ex situ soft-XAS, and quasi in situ XPS). Finally, DFT simulations unveil the role of Sn speciation in driving CO and $HCOO^-$ selectivity. Our study reveals a complex correlation between catalyst structure, composition, and speciation with applied electrochemical bias in Sn-functionalized Cu catalysts.

2. Results & Discussion

2.1. Material Synthesis & Characterization

The preparation of nanostructured Cu−Sn electrocatalysts was adapted from the method reported by Schreier et al.[16] Complete experimental details are provided in Section S1, Supporting Information. In a first step, electrodes based on arrays of $Cu(OH)_2$ nanowires, denoted hereafter CuNW, were synthesized by anodization of Cu films (1 μm) sputter deposited on glass substrates. The anodization was carried out at a constant current of 8 mA cm^{-2} to reach a total charge of 1.35 C cm^{-2} and the samples were subsequently annealed in air at 150 °C for 1 h (**Figure 1**a). This procedure yields reproducible bundled nanowire arrays with lengths of several μm (≈8–10 μm) and diameters of hundreds of nm (200–400 nm), which are attached to a continuous Cu base layer, as seen in Figure 1b–d.

The so-obtained $Cu(OH)_2$ nanowires were then modified by ultrathin SnO_2 layers generated by ALD with varied number of deposition cycles, denoted hereafter CuNW-SnXc (Xc = X number of ALD cycles). The ALD method allows uniform and conformal coating of the high surface area nanostructures with SnO_2, and variation of the deposition cycles enables us to precisely modulate the surface Sn content, while avoiding significant changes in morphology (Figure 1 and Figure S1, Supporting Information). The number of deposition cycles was varied across the range 1–182, which correspond to expected nominal thicknesses of approximately 0.1–20 nm based on calibrated deposition rates. The X-ray diffraction (XRD) patterns of the samples modified with 15 and 182 ALD cycles of SnO_2 display the typical pattern for CuO (Figure 1e), indicating that the $Cu(OH)_2$ nanowires are dehydrated under the ALD conditions (120 °C under vacuum). Note that the observed Cu^0 metallic diffraction peaks arise from the underlying residual sputtered Cu, as can be seen in the cross-section scanning electron microscopy (SEM) micrograph (Figure 1d). This continuous Cu layer—a result of only partially anodizing the original film—is

G. Schuck
Department Structure and Dynamics of Energy Materials
Helmholtz-Zentrum Berlin für Materialien und Energie GmbH
Hahn-Meitner-Platz 1, 14109 Berlin, Germany

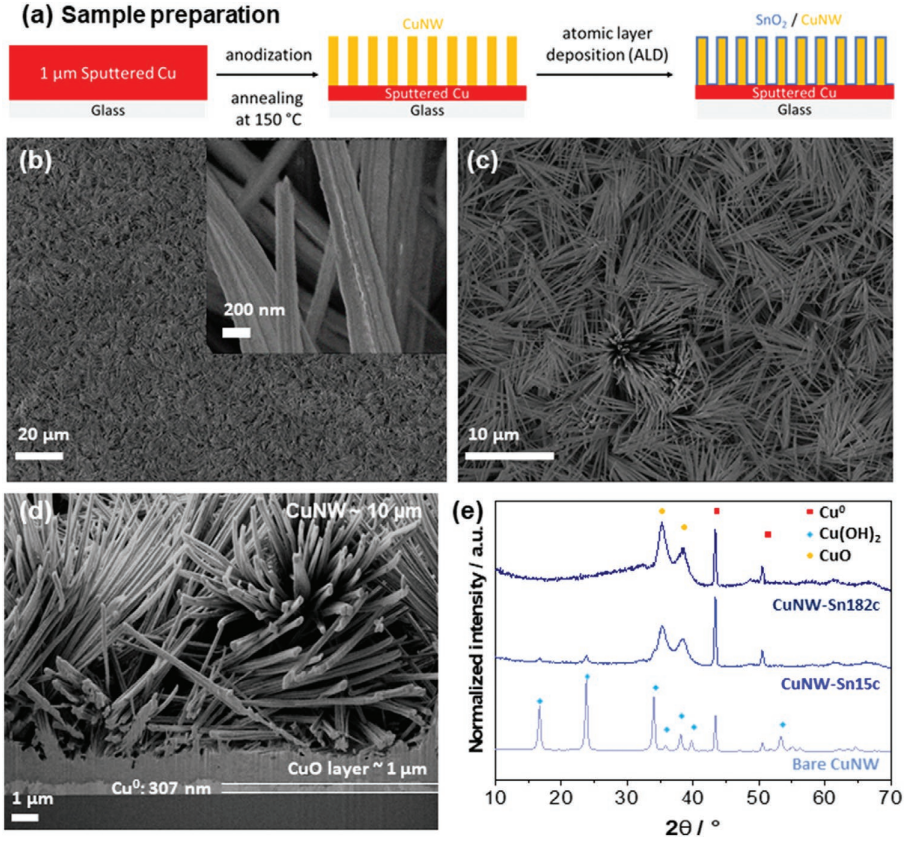

Figure 1. a) Schematic of synthesis procedure. b,c) SEM micrographs of the AS CuNW modified with 15 cycles of ALD SnO_2. d) Cross-section SEM micrograph of CuNW-Sn-15c at the site of a Focused Ion Beam cut. e) Grazing incidence XRD patterns of AS CuNW bare and modified with 15 or 182 cycles of SnO_2 ALD.

important for maintaining the integrity and conductivity of the NW arrays as a functioning electrode. As seen in Figure 1d, a compact CuO layer above it likely prevents the metallic underlayer from contributing to the electrocatalysis.

The samples were tested for CO_2 electroreduction in CO_2 saturated 0.1 M $KHCO_3$ in a custom-made three-electrode two-compartment cell separated by a Nafion 115 membrane, under a constant flow of CO_2. Since the CuNW-SnXc was originally composed of $Cu(OH)_2$ (bare CuNW) or CuO (SnO_2 ALD modified samples) and variable amounts of SnO_2, the oxide composites were pre-reduced by chronopotentiometry (CP) at a constant current of –2 mA cm^{-2} to reach a potential of –0.5 V versus RHE (reversible hydrogen electrode; all potentials reported hereafter are referred to RHE unless otherwise specified). Directly after the pre-reduction step, the samples were set at the desired CO_2 electrolysis potential, typically –0.7 V where the maximum efficiency for CO has been reported for this system.[16] Representative pre-reduction CP and chronoamperometry data are presented in Figure S2, Supporting Information. The CO_2ER activity at –0.7 V for samples modified with various numbers of SnO_2 ALD cycles (between 1–182) is displayed as faradaic efficiency and partial current densities in **Figure 2**a,b. The results show that modifying the CuNW with a single cycle of SnO_2 induces a significant shift in selectivity, namely the near-complete suppression of formate and a large increase in CO selectivity. Increasing the SnO_2 to 15 cycles further improves CO selectivity over H_2 and ethylene, reaching an optimal faradaic efficiency together with the highest CO partial current density (Figure 2b). Further increasing SnO_2 to 20, 25, and 182 cycles (≈20 nm) induces a decrease in CO selectivity and production rate, as well as total current density. Such volcano-type behavior was previously reported by Schreier et al.[16] albeit with different optimal numbers of SnO_2 ALD cycles, presumably due to the use of different ALD system conditions. As noted above, the $Cu(OH)_2$ dehydrates to CuO during the ALD process. We performed a series of control experiments, pre-dehydrating $Cu(OH)_2$ to CuO before ALD (Figure S3, Supporting Information). The results indicate that the dehydration of $Cu(OH)_2$ to CuO itself induces only minor changes in CO_2ER selectivity, whereas after the addition of 15 ALD cycles of SnO_2 to each, the Sn-functionalized $Cu(OH)_2$ and CuO nanowire samples both obtained high CO faradaic efficiency (79% and 83% respectively).

The CuNW modified with 15 ALD cycles, hereafter denoted CuNW-Sn_{LOW}, displays the optimal composition for CO production with the highest faradaic selectivity (79%) and CO partial current density of ≈–2.5 mA cm^{-2}. Its CO_2ER performance was further investigated in the potential range from –0.5 to –0.9 V (Figure 2c). This composite displays high CO selectivity across the moderate overpotential range –0.6 to –0.8 V, decreasing at lower and higher potentials in favor of increased hydrogen

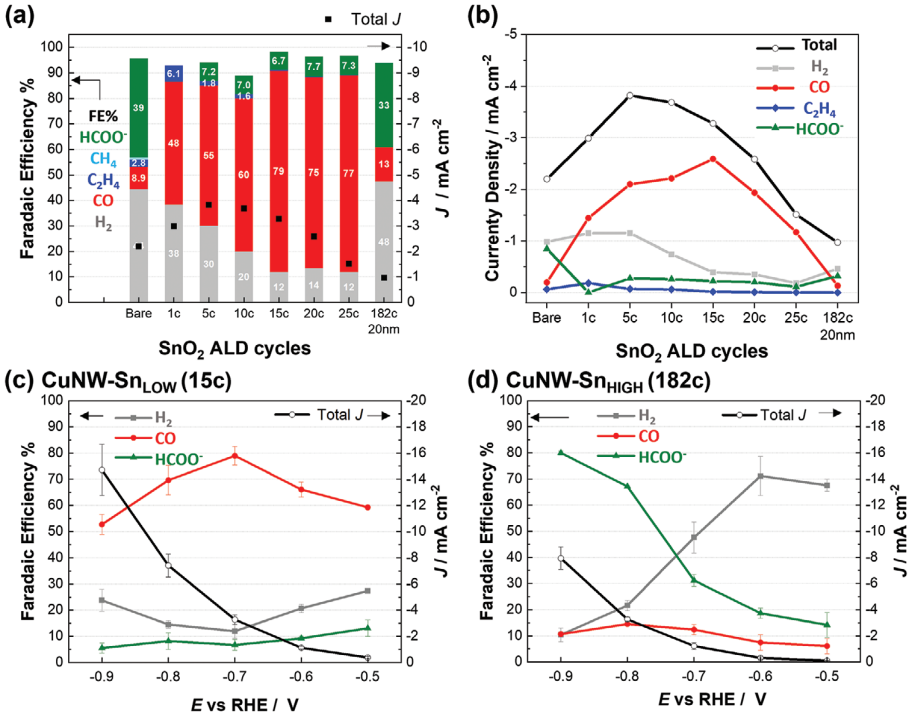

Figure 2. CO_2ER activity for different CuNW samples modified with various numbers of SnO_2 ALD cycles, each tested at –0.7 V versus RHE in 0.1 M $KHCO_3$. a) Faradaic efficiencies and b) partial current densities. CO_2ER as a function of applied potential for c) CuNW-Sn15c and d) CuNW-Sn182c. Error bars correspond to standard deviation of at least three independent samples tested at each potential.

evolution. Low formate selectivity is observed across the examined range. Therefore, this addition of an ultrathin ALD layer of SnO_2 (15 cycles correspond to a nominal thickness ≈1.6 nm) results in a significant alteration of product selectivity toward CO, as compared to the mixture of several products observed on bare CuNW (CO_2ER activity shown in Figure S4, Supporting Information). The observation that this intermediate loading of SnO_2 produced the best selectivity and rate for CO formation suggests that there is an important synergy between Cu and Sn which is responsible for this optimized activity.

The CuNW modified with a high SnO_2 content (182 ALD cycles, corresponding to a nominal film thickness of approx. 20 nm), hereafter denoted CuNW-Sn_{HIGH}, was also investigated across the same potential range (Figure 2d). Although at –0.7 V this catalyst produced a mix of products dominated by H_2, at more negative potentials the selectivity to hydrogen greatly decreases while formate increases significantly to become the primary product (FE 80% at –0.9 V). Meanwhile, the CO selectivity for this composite remains low at all tested potentials. Thus, at sufficiently high loading of Sn, the composite samples exhibit high formate selectivity comparable to what has been reported for pure Sn catalysts.[29–31]

Scanning electron microscopy (SEM) characterization of the catalysts after CO_2 electrolysis is presented in Figure S5, Supporting Information. The materials display mostly preserved nanowire structures with roughened surfaces. Energy-dispersive X-ray spectroscopy (EDX) quantification of bulk composition (**Table 1**, Figures S6 and S7, Supporting Information) shows that a decreased Sn content is observed after electrolysis experiments; in CuNW-Sn_{LOW} the bulk Sn fraction (referred to total metal Sn+Cu) decreases from 2.2 ± 0.3 at. % in the as-synthesized (AS) catalyst to 1.9 ± 0.2 at. % after electrolysis at –0.9 V. In the case of CuNW-Sn_{HIGH} the Sn content decreases from 23 ± 1.1 at. % in the AS catalyst to 16 ± 1.3 at. % after electrolysis at –0.9 V. Partial dissolution of Sn was further confirmed by inductively coupled plasma-optical emission spectrometry (ICP-OES) analysis of electrolyte (Table S1, Supporting Information). Together these results demonstrate that the SnO_2 ALD modification of CuNW electrodes enables the modulation of the Cu—Sn bimetallic composition to reach high selectivity toward either CO in CuNW-Sn_{LOW} or formate in CuNW-Sn_{HIGH} with minor changes to the nanoscale morphology of the electrodes (Figure S1 and Section S5, Supporting Information).

These two composites were selected as CO- and formate-selective Cu—Sn catalysts for further investigation of synergetic effects between metals through correlation of observations gathered by different X-ray spectroscopy methods (in situ hard-XAS, ex situ soft-XAS, and quasi in situ XPS). Complimentary information on oxidation states and chemical environment of Cu and Sn in CuNW-Sn electrocatalysts' bulk and surface following progressive electroreduction stages has been assessed to gather relevant information on the active form of the catalysts. The X-ray spectroscopy observations and their correlation with CO_2ER activity trends are discussed in the following sections.

2.2. In Situ Investigation of Cu and Sn K-Edges during CO_2ER via Hard X-Ray Absorption Spectroscopy

The Cu K-edge XAS measurements were conducted at the KMC-2 beamline at the BESSY II synchrotron.[32] The

Table 1. Summary of bulk and surface characterization XRD, EDX, and XPS for CuNW modified with low and high Sn content by ALD overlayers AS and following CO_2 reduction at different applied potentials.

Sample description		CO_2ER Main product (FE)	Bulk structure XRD/Hard XAS	Sn at. %[a),b)]		Surface speciation
				Bulk (SEM-EDX)	Surface (XPS)	
CuNW-Sn_{LOW}	as-synthesized		CuO	2.2 ± 0.3	24 ± 4.9	CuO/ SnO_x
	–0.5 V	CO (60%)	Cu^0		19 ± 1.9	Cu^0/SnO_x
	–0.7 V	CO (79%)	Cu^0	1.5 ± 0.1	13 ± 0.7 (14 ± 0.8)[c)]	Cu^0/SnO_x
	–0.9 V	CO (53%)	Cu^0	1.9 ± 0.2	14 ± 0.3 (14 ± 3.8)[c)]	Cu^0/SnO_x
CuNW-Sn_{HIGH}	as-synthesized		CuO	23 ± 1.1	100 ± 0	CuO/SnO_x
	–0.5 V	H_2 (67%)	Cu^0		98 ± 0.4	Cu^0/SnO_x
	–0.6 V	H_2 (71%)	Cu^0		93 ± 1.5	Cu^0/SnO_x
	–0.7 V	Formate (67%)	Cu^0/Cu_6Sn_5	17 ± 2.6	78 ± 0.2 (82± 1.4)[c)]	$Cu^0/Sn^0/SnO_x$
	–0.9 V	Formate (80%)	Cu^0/Cu_6Sn_5	16 ± 1.3	70 ± 2.3 (77± 2.1)[c)]	$Cu^0/Sn^0/SnO_x$

[a)]Sn at. % relative to total metal (Cu+Sn); [b)]Sn at. % data presented as the average value ± standard deviation at 3 different sample locations; [c)]Sn at. % after intentional exposure of samples to air for 20 min

penetration length of X-ray photons through matter is a function of their energy and the phases through which they pass, with higher energy photons capable of traveling further through condensed matter without complete attenuation. This enables the use of high-energy "hard" X-rays for in situ studies of electrode materials in operating electrochemical cells. Photons with energy corresponding to the Cu K-edge (located at 8979 eV) have an approximate probing depth of ≈4 µm in Cu and ≈1.4 mm in water.[33,34] A custom electrochemical cell with a polymer window and a thin electrolyte layer of ≈500 µm (CO_2 sat. 0.1 M $KHCO_3$) was fabricated to enable hard X-ray absorption measurements of the electrode in fluorescence detection mode, under electrochemical CO_2ER conditions. The cell and spectroscopy setup employed for these measurements are shown in Figure S9, Supporting Information. Considering that the CuNW arrays atop the glass substrate exhibit a porous structure with thickness in the µm range (see Figure 1 b–d), it is expected that the incoming radiation probes the bulk of CuNW and the underlying sputtered Cu as well, as will be discussed later. According to FIB cross-section images the samples have an underlying sputtered Cu^0 layer of 300–400 nm thickness (Figure 1d and Figure S1, Supporting Information).

The CuNW samples modified with different amounts of SnO_2 were investigated in their AS state as well as in situ during both the CP pre-reduction step and CO_2 electrolysis. The Cu K-edge X-ray Absorption Near-Edge Structure (XANES) spectra and Fourier Transform Extended X-ray Absorption Fine Structure (FT-EXAFS) analyses are shown in **Figure 3**. In the AS state the bare CuNW electrode displays a XANES spectrum typical of $Cu(OH)_2$ (Figure 3c). In samples CuNW-Sn_{LOW} and CuNW-Sn_{HIGH} the spectra resemble the standard CuO spectrum as indicated by the shoulder ≈8982 eV, presumably due to dehydration of $Cu(OH)_2$ to CuO under ALD conditions (120 °C under vacuum, see experimental details in the Supp. Info.) in agreement with the diffraction patterns (Figure 1e). Additionally, all AS samples exhibit an early shoulder at ≈8977 eV attributable to the sputtered metallic Cu^0 layer below the CuNW (Figure 1d). The k2-weighted FT-EXAFS analysis of AS samples Cu K-edge spectra are displayed in Figure 3d. The peak 1.6 Å corresponds to the Cu—O distance in both CuO and $Cu(OH)_2$, while the peak at 2.3 Å corresponds to the Cu—Cu distance in the underlying sputtered metallic Cu layer, in agreement with previous reports.[35,36]

With the aim of investigating possible effects of Sn content on the progressive reduction of Cu, several Cu K-edge XANES spectra (each acquired for ≈20 min) were collected during chronopotentiometric (CP) pre-reduction of bare CuNW as well as samples CuNW-Sn_{LOW} and CuNW-Sn_{HIGH}. Although under standard conditions this pre-reduction step was typically carried out at –2 mA cm^{-2}, taking on average 8–10 min (see Figure S2, Supporting Information), here the activation was carried out at a lower current density of –0.2 mA cm^{-2} in order to allow sufficient time to collect a series of XANES spectra at different stages during the activation step. These spectra are shown in Figure 3a, color-coded to match the CP time frame in which they were collected (Figure 3b). For all types of samples, with or without Sn deposited, the experiments show the progressive transition from Cu^{2+} to Cu^0 that completes after about 70 min of CP pre-reduction. The results indicate that roughly the same amount of charge has been passed on all samples at the point where defined XANES Cu° features are observed; this signifies that about the same amount of Cu^{2+} has been reduced in each case, although more reductive potentials are required for reduction of samples containing Sn (Figure 3b and Figure S2, Supporting Information).

After CP pre-reduction until reaching a potential of –0.4 V, the samples were held at this potential for 30 min for collection of additional XANES spectra (see Figure S10, Supporting Information). However, at this stage the samples transition from self-reduction to electrocatalytic CO_2ER and HER, and bubble formation due to the formation of gaseous products commences, causing disruptions to the measurement of a stable signal. To perform EXAFS data collection, a longer collection time in the post edge region is necessary, requiring a very stable signal over a duration of ca. 2.5 h per spectrum. Thus, to allow EXAFS collection, the reduction bias was decreased to –0.1 V, a potential sufficiently reducing to observe a sustained

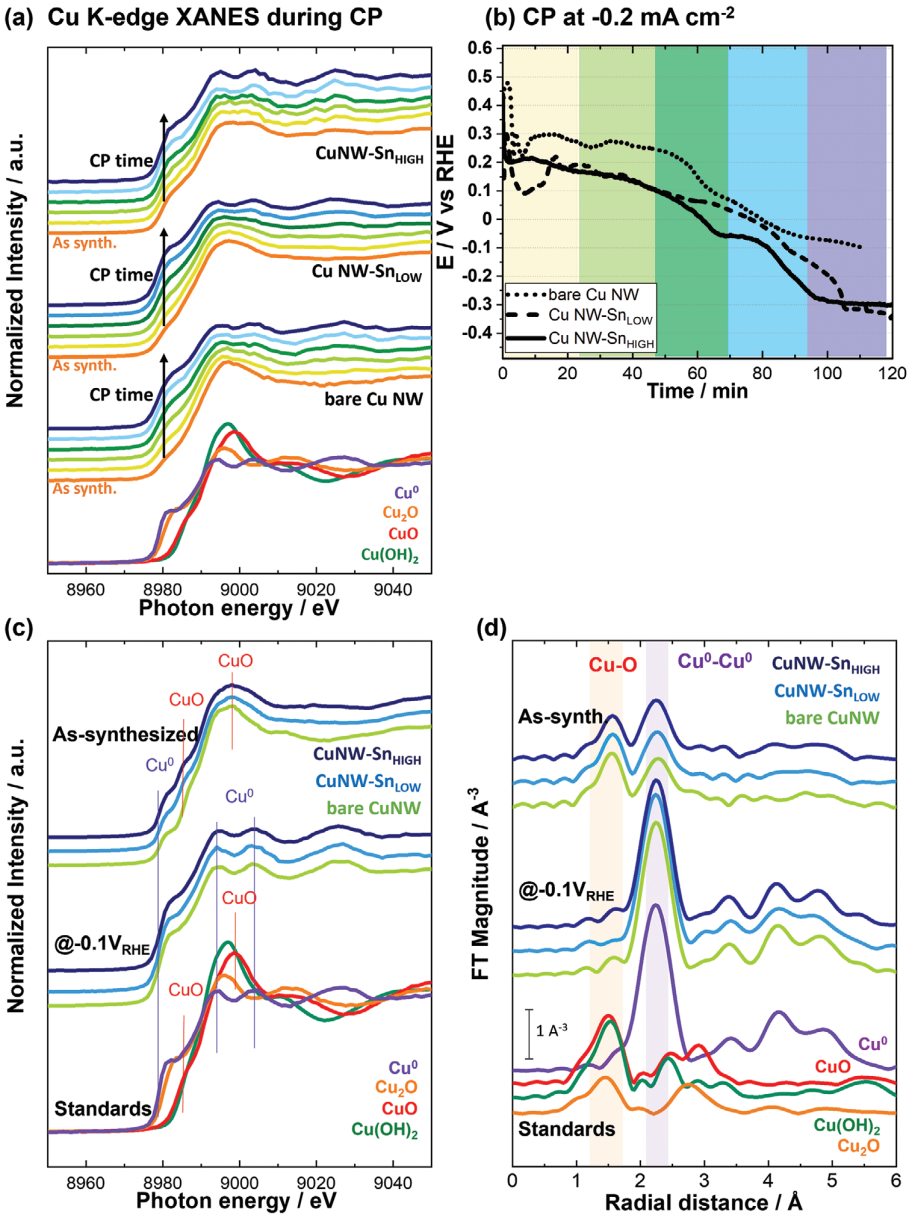

Figure 3. In situ Cu K-edge XAS investigation of CuNW electrodes modified with variable number of SnO_2 ALD cycles. a) XANES spectra collected during CP activation, b) CP activation at –0.2 mA cm^{-2}. The spectra in (a) are color-coded to match the CP time frame (b) in which they were collected. Cu K-edge spectra, c) Cu K-edge XANES spectra collected in the AS state and during CO_2ER at –0.1 V, and d) corresponding k2-weighted FT-EXAFS in the k range between 3–12 (note displayed FT-EXAFS is not phase corrected). Reference spectra collected from standards of metallic Cu^0, CuO, $Cu(OH)_2$, and Cu_2O are presented for comparison.

catalytic reduction current (≈–150–200 μA cm^{-2}) without observable bubble-induced noise. The resulting Cu K-edge XANES spectra at –0.1 V are shown in Figure 3c; all the samples exhibit the typical features of metallic Cu° characterized by an early shoulder ≈8977 eV, and all show a dominant EXAFS peak at 2.3 Å (Figure 3d) attributable to the Cu—Cu distance in metallic Cu^0 during CO_2ER turnover. No significant differences were observed between the XANES spectra collected at –0.4 or –0.1 V versus RHE—for both conditions, all samples have spectra closely matching that of metallic Cu^0, as shown in Figure S10, Supporting Information.

These results are in good agreement with ex situ GI-XRD characterization (Figure S8, Supporting Information): after electrolysis CuNW-Sn_{LOW} displays the diffraction pattern of metallic Cu^0, while CuNW-Sn_{HIGH} shows a mix of Cu^0 and Cu_6Sn_5 alloy. These observations indicate that the bulk of the CuNW samples is reduced under CO_2ER catalytic conditions and the use of hard X-rays enabled the observation of the

dynamic transformation of reduction of Cu. Note that Cu−Sn and Cu−Cu distances in Cu_6Sn_5 and metallic Cu are very close (≈2.3 Å without phase correction)[18,36] and are not distinguishable from each other in EXAFS analysis. However, as will be discussed below, the transmission electron microscopy (TEM) investigation of CuNW-Sn_{HIGH} (Figure 6 and Figure S15, Supporting Information) provided further evidence of the formation of Cu_6Sn_5 during CO_2 electrolysis.

The Sn speciation during CO_2ER was investigated by in situ XANES at the Sn K-edge (with hard X-ray energies ca. 29.2 keV), conducted at the BAMline at BESSY II.[37] The experimental details can be found in Section S3.2, Supporting Information. Both sample types in the AS condition showed the typical features of SnO_2. CuNW-Sn_{HIGH} was further investigated during CO_2ER at increasingly negative bias between –0.5 and –0.9 V, which led to a progressive decrease in the relative amplitude of the white line peak prominent in the oxides SnO_2 and SnO, indicating the growth of a metallic Sn component (Figure S12a, Supporting Information). Linear combination fitting analysis of the XANES spectra (Figure S12c, Supporting Information) indicates that at –0.5 and –0.6 V the SnO_2 oxide is partially reduced to SnO and a minor amount of Sn^0 (< 6 % at –0.6 V), at –0.7 V and –0.9 V the Sn° component grows with increasingly reductive bias (to 72% at –0.9 V), and SnO_2 is observed to persist at all tested potentials.

In the case of CuNW-Sn_{LOW}, XANES spectra collected at –0.5 and –0.7 V also display a partial flattening of the SnO_2 white line feature, indicative of partial reduction of SnO_2 (Figure S12b, Supporting Information). However, the low Sn content leads to a low signal-to-noise ratio, hindering further quantitative analysis of the data. Nevertheless, the persistence of the white line feature in the spectra collected during CO_2ER at –0.5 and –0.7 V indicates that Sn is (at least partially) present in an oxidized state.

Overall, the in situ XAS investigation of Cu and Sn K-edges revealed dynamic potential-dependent transformations of both elements in the CuNW-Sn electrocatalysts under CO_2 electroreduction conditions. For Cu, the bulk reduction of CuO NW to Cu^0 in all CuNW-Sn samples (regardless of Sn content) is verified during CP activation at potentials as mild as –0.4 V versus RHE. In contrast, CuNW-Sn_{HIGH} and CuNW-Sn_{LOW} samples both displayed partial reduction of the SnO_2 layer into metallic Sn^0 while retaining features of persistent oxidized Sn at potentials as reductive as –0.7 and –0.9 V.

Given the bulk sensitivity of the XAS measurements conducted using hard X-rays, the possibility of persistent surface or subsurface copper oxide (as reported in some previous studies on pure Cu catalysts)[38,39] could not be adequately investigated by this method. To more selectively probe the catalysts' surfaces, complimentary investigations by soft X-ray XAS and XPS were conducted, as discussed in the following sections.

2.3. Investigation of Surface Composition via Ex Situ Soft XAS and Quasi In Situ XPS

The electrode surface composition was initially investigated by ex situ XAS, using the LiXEdrom experimental station at the UE56/2 PGM-2 beamline at BESSY II.[40] The Cu L- and Sn M-edge spectra were investigated in the soft X-ray range using total electron yield (TEY) detection mode, whereby the probing depth is less than 10 nm, limited by the mean free path of generated photoelectrons.[41,42] While this method offers good surface sensitivity, the attenuation of soft X-rays and photoelectrons in water prevents this method from being applied in situ during electrocatalysis. To achieve surface-sensitive analysis of samples resembling their catalytically-active form, we compromised by first conducting the electrochemical experiments (CP pre-reduction until –0.5 V, and electrolysis a constant potential of –0.7 V) inside an O_2-free glovebox and then transferring them directly into the high-vacuum chamber for soft XAS analysis, thus mitigating electrode re-oxidation in air, although a brief period of air exposure (≈15–20 min) was unavoidable during the transfer step. CuNW samples and a series of relevant standards (Cu and Sn metals and oxides) were measured. The results are presented in Section S3.3 and Figure S13, Supporting Information).

The soft X-ray absorption investigation provides insight on the surface structure and composition changes taking place in the CuNW-Sn samples during CO_2 electroreduction. In all samples, surface Cu appears readily reduced from Cu^{2+} to Cu^0/Cu^+ after the pre-reduction step to –0.5 V (Figure S13a, Supporting Information). On the other hand, Sn persists as a SnO_x enriched surface overlayer after the pre-reduction step (Figure S13b, Supporting Information). However, after electrolysis at –0.7 V, the Sn M-edge signal decreases for both samples CuNW-Sn_{LOW} and CuNW-Sn_{HIGH} in comparison to the AS state, indicating a significant decrease in Sn content at the near-surface depth (<10 nm) probed by soft XAS, presumably due to migration from surface to bulk or dissolution. Additionally, the results indicate residual surface content of oxidized Cu as Cu^+ and Cu^{2+}, as well as SnO. Due to the surface-sensitive nature of this ex situ method and the unavoidable air exposure which likely induced some degree of surface oxidation, we cannot be certain whether the observed Cu^+, Cu^{2+}, and SnO surface species persisted under CO_2ER conditions or if they were formed spontaneously by oxidation in air. Nevertheless, a reproducible trend of Cu^{2+} signal in CuNW-Sn_{LOW} sample in the different conditions tested suggests that the presence of low amounts of Sn may render near-surface Cu atoms more prone to oxidation, in contrast to the Sn-free bare CuNW sample which is free of Cu^{2+} signal after CO_2ER. Similar trends were observed in ex situ surface-sensitive XPS investigations of CuSn alloys.[20,21]

In order to investigate if the copper and tin oxidized species observed by ex situ soft XAS (Figure S13a,b, Supporting Information) are the product of fast reoxidation during brief air exposure and quantify the observed decrease of surface Sn during catalytic turnover, a quasi in situ investigation by XPS was conducted.[43] XPS spectra for CuNW samples with different SnO_x content (bare CuNW, CuNW-Sn_{LOW}, and CuNW-Sn_{HIGH}) were collected in AS condition as well progressive reductive conditions after CP pre-reduction to –0.5 V, after 2 h catalysis at –0.7 V, and after 2 h catalysis at –0.9 V. The electrochemical testing was conducted under inert atmosphere in a glovebox, then the samples were dried, and promptly transferred to the XPS chamber using a gastight transfer module. By this method, the exclusion of atmospheric oxygen exposure is ensured, preventing oxidation and making the resulting electrode surfaces more representative of their active forms, while also taking advantage of the surface sensitivity of XPS.

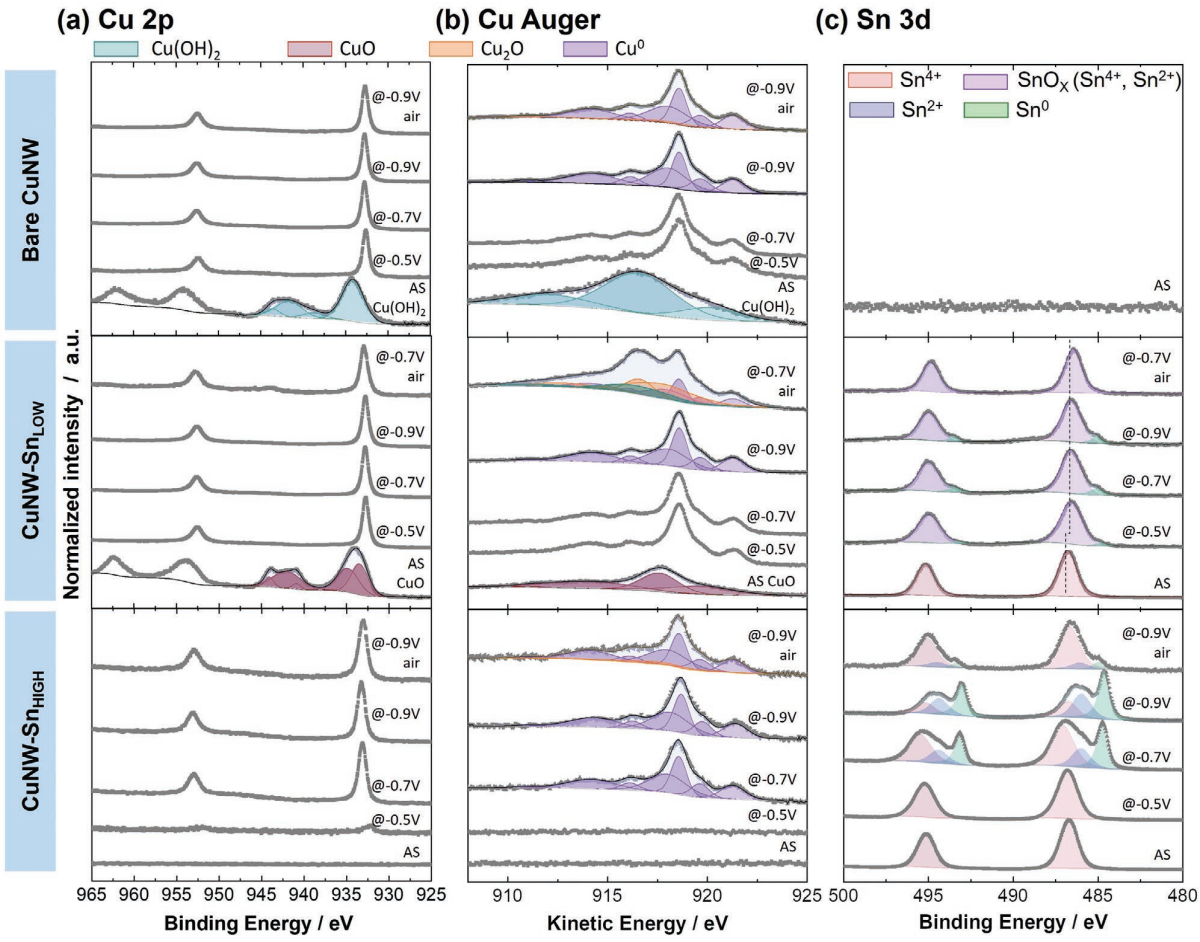

Figure 4. XPS spectra for a) Cu 2p, b) Cu Auger, and c) Sn 3d core levels for CuNW samples modified with different SnO_2 content (bare CuNW (top), CuNW-Sn_{LOW} (middle), and CuNW-Sn_{HIGH} (bottom)) in their AS state and after different electrochemical tests: after CP activation at –2 mA cm^{-2} up to –0.5 V, after 2 h CO_2ER at –0.7 and –0.9 V, and after exposure to air. Spectra are presented with a vertical offset to facilitate comparison. Electrochemical tests were conducted in an inert gas glovebox at the specified potential for 2 h followed by removal from the electrolyte and transfer to the XPS chamber without air exposure.

The AS samples display the expected spectral features (**Figure 4**). In agreement with the XRD characterization bare CuNW displays a Cu 2p spectrum (main peak at binding energy (BE) of 933.9 eV and shake-up satellite structure) and Cu LMM Auger spectrum typical for $Cu(OH)_2$. The sample modified with a low content of Sn, CuNW-Sn_{LOW}, exhibits Cu 2p (main peak at BE 934.1 eV and shake-up satellite structure) and Cu LMM spectral features of CuO. For both samples, Cu 2p and Cu LMM Auger spectra can be accurately fitted with the peak model described by Biesinger et al.[44] for $Cu(OH)_2$ and CuO (see details on peak model in Section S4.1, Table S3, Supporting Information).

The study of progressive reduction on the bare CuNW sample indicates that the catalysts' surfaces are fully reduced to metallic Cu^0 after CP activation up to –0.5 V (Figure 4a,b) as indicated by the sharp Cu 2p doublet with the main peak at BE 932.7 eV, as well as the metallic Cu° Cu LMM Auger fingerprint characterized by a multiplet centered at a sharp main peak at a kinetic energy (KE) of 918.6 eV. The Cu LMM spectra can be evaluated by the peak model described by Biesinger et al. for freshly sputtered metallic Cu surface and validated by an additional internal reference measurement of an Ar sputtered Cu foil (see details on peak model in Section S4.1, Table S2, Supporting Information). Similar Cu 2p and Cu LMM spectra are observed for samples after CO_2 electrolysis at –0.7 and –0.9 V, indicating that Cu is fully reduced at the surface to metallic Cu after pre-reduction up to –0.5 V and stays reduced during electrolysis at higher bias. No evidence of residual Cu oxides on the electrode surface is detected by XPS when transferred to the analysis chamber under inert atmosphere, contrasting the above observations from ex situ soft XAS following brief air exposure, and validating the usefulness of the air-free transfer methodology.

A similar behavior was observed for Cu in CuNW-Sn_{LOW}—it appears to be fully reduced to metallic Cu^0 after CP activation up to –0.5 V and remains reduced after CO_2 electrolysis at –0.7 and –0.9 V (Figure 4 a,b). As observed in the soft-XAS measurements, the sample CuNW-Sn_{HIGH} does not show any Cu-related signals in the AS state, indicating that the SnO_2

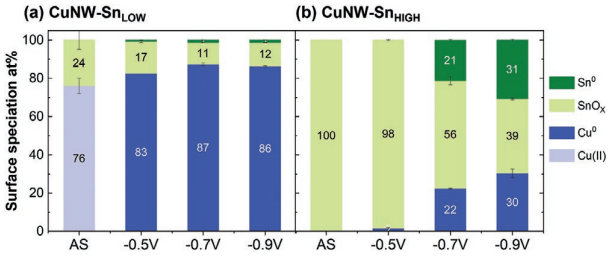

Figure 5. Surface metal speciation derived from XPS analysis, expressed as at. % of each species relative to total metal (Cu+Sn) for a) CuNW-Sn_{LOW} and b) CuNW-Sn_{HIGH}, following CO_2 electrolysis at the indicated potential and air-free transfer to the XPS analysis chamber.

ALD layer (≈20 nm) covers all the CuNW surface (Figure 4a,b). After CP pre-reduction up to –0.5 V an incipient Cu 2p signal appears at the position expected for metallic Cu^0 indicating that a SnO_2 ALD layer remains enriched at the catalyst surface after the CP pre-reduction step, as previously observed by soft XAS (Figure S13b, Supporting Information). After CO_2 electrolysis at –0.7 V and –0.9 V, typical Cu 2p and Cu LMM spectral features assigned to metallic Cu^0 are dominant, indicating a full reduction of Cu and its migration from core to surface during CO_2 electrolysis (Figure 4a,b).

The investigation of the progressive reduction of the SnO_2 layer by XPS (Figure 4c) indicates different Sn speciation in CO-selective (CuNW-Sn_{LOW}) and formate-selective (CuNW-Sn_{HIGH}) catalysts. In the AS state, both display a doublet with the main peak for the Sn $3d_{5/2}$ component at BE 486.7 eV in agreement with the reported value for SnO_2.[29,30] CuNW-Sn_{LOW} exhibits a slight shift towards lower BE 486.5 eV after CP activation to –0.5 V, indicating a partial reduction to SnO (i.e., Sn^{2+}), as well as peak broadening which may indicate a mixed contribution of both Sn^{2+} and Sn^{4+} oxidation states. Due to this convolution, we denote this composition as SnO_x. After CO_2 electrolysis at –0.7 and –0.9 V, a peak at 486.5 eV assigned to SnO_x and a small shoulder at 485 eV assigned to metallic Sn^0 are observed (Figure 4c). The results indicate that following operation under all tested CO_2ER conditions (–0.5, –0.7, and –0.9 V), CuNW-Sn_{LOW} surface is composed of fully reduced metallic Cu^0 and Sn predominantly in an oxidized state (Figure 4c, **Figure 5**a). These results are in good agreement with the persistence of SnO_x species observed for CuNW-Sn_{LOW} by in situ Sn K-edge XANES (Figure S12b, Supporting Information) and provide experimental support for previous DFT studies which identify persistent oxidized Sn as a crucial selectivity director in Cu–Sn CO-selective catalysts.[22,28]

The surface composition and speciation results are summarized in Table 1 and Figure 5. The CuNW-Sn_{LOW} catalyst surface displays an Sn fraction (relative to total Cu + Sn content) of 24 at. % in the AS condition, which decreases to 19 at. % after CP activation and at ≈13 at. % after electrolysis at –0.7 and –0.9 V. This Sn content is in line with surface composition reported in previous studies on low surface area CO-selective Cu–Sn catalysts[21,22,28] and Sn functionalized Cu foams.[23] The observed surface Sn content decrease after CO_2ER is in agreement with the redistribution of Sn from the surface to the core reported by Schreier et al.[16] which is observed by STEM-EDX elemental mapping.

For the formate-selective catalyst, CuNW-Sn_{HIGH}, the Sn 3d signal broadens but remains at the same position after CP pre-reduction, indicating that the SnO_x ALD layer persists mostly unchanged, as observed by soft XAS (Figure S13, Supporting Information). Examination of electrodes after CO_2 electrolysis at –0.7 and –0.9 V, the Sn 3d spectra develop new peaks assigned to Sn^{2+} (486.4 eV) and metallic Sn^0 (484.9 eV) (Figure 4c). Thus, after CO_2 electrolysis at –0.7 and –0.9 V the CuNW-Sn_{HIGH} catalyst surface is composed of metallic Cu and a mixture of metallic Sn and SnO_x (Figures 4c and 5b). The observation of persistent SnO_x species following CO_2ER in Cu–Sn formate-selective catalysts is in good agreement with Sn K-edge XANES experiments (Figure S12, Supporting Information) and a previous report on in situ Sn K-edge EXAFS.[18]

2.4. Microstructure Analysis by Electron Microscopy and Elemental Mapping

The structural transformation of CuNW-Sn_{HIGH} during CO_2ER was further investigated by TEM in the AS state and following CO_2ER experiments at different applied biases. To minimize the impact of air exposure on post-electrolysis samples, every sample preparation, electrochemical testing, and TEM sample preparation were conducted inside a glovebox (as for quasi in situ XPS experiments). The post-electrolysis samples were then transferred under inert atmosphere into the TEM instrument. A brief exposure to air (<10 s) was unavoidable during sample loading.

The TEM characterization for CuNW-Sn_{HIGH} is displayed in **Figure 6**. The AS sample shows CuO nanowires of approx. 100–200 nm diameter coated with an amorphous layer (Figure 6b). SAED analysis (Figure 6a) indicates that the wires are composed of CuO (*C2/c*) in agreement with GI-XRD (Figure S8, Supporting Information). Additionally, a broad diffuse ring ascribed to the SnO_2 amorphous layer is observed at d spacings between 2.7–3.3 Å where SnO_2 (*P42/mnm*) diffraction signals are expected. Detailed lattice spacing assignment information is provided in Table S4, Supporting Information. Energy-filtered transmission electron microscopy (EFTEM)[45,46] mapping (Figure 6c) provides further evidence of a conformal coating (15–25 nm) of SnO_2 along the CuNW structures, as expected from the ALD synthesis method and in agreement with the XPS results displaying exclusively SnO_2 at the catalyst surface (Figure 4a).

Following CO_2 electrolysis at –0.6 V for 2 h, the SAED analysis (Figure 6d) indicates that the CuO nanowire core of the sample has been fully reduced to Cu^0 while the outer SnO_2 layer remains in a rather amorphous state as observed in TEM micrographs (Figure 6e) and indicated by the persistence of the diffuse broad diffraction ring ascribed to the SnO_x amorphous layer. The EFTEM mapping further confirms the persistence of an Sn-enriched shell after electrolysis. HR-TEM analysis of the core-shell interface (Figure S14, Supporting Information) indicates that the outer shell is amorphous while at the interface small crystallites (<5 nm) are observed, with lattice spacings d = 2.8–3.0 Å ascribed to Cu_6Sn_5 alloy or Sn^0 and d = 1.6 and 1.9 Å ascribed to SnO. The results suggest that at –0.6 V the SnO_2 layer persists as a SnO_x amorphous layer with only

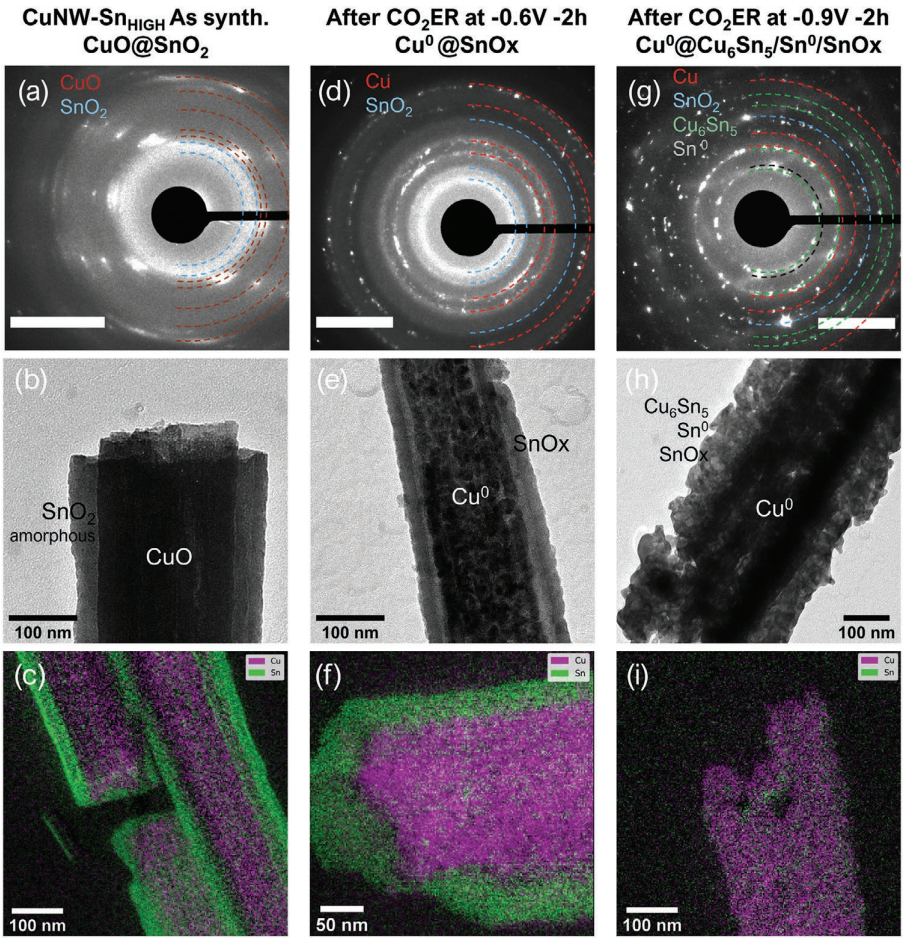

Figure 6. TEM characterization of a–c) CuNW-Sn$_{HIGH}$ AS, and after electrolysis at d–f) –0.6 and g–i) –0.9 V. Top images correspond to SAED analysis (scale bar 5 nm^{-1}), middle images correspond to TEM micrographs and bottom images correspond to EFTEM mappings of Cu (L-edge: purple) and Sn (M-edge: green).

partial reduction to Cu_6Sn_5 alloy, Sn^0, and SnO at the interface with the Cu^0 nanowire core. These findings agree with previous observations of the persistence of an enriched SnO_x layer at this potential by in situ Sn K-edge XAS (Figure S12, Supporting Information) and quasi in situ XPS (Figure 4).

As the reductive electrolysis bias is increased to –0.9 V, further structural changes were verified by TEM (Figure 6g–i). The TEM micrograph in Figure 6h shows that the outer layer appears crystalline in contrast with the same sample in AS condition and after CO_2ER at –0.6 V. SAED analysis reveals that the diffuse rings assigned to the SnO_x layer have disappeared after CO_2 electrolysis at –0.9 V (Figure 6g) while diffraction signals at d = 2.9, 2.8, and 2.1 Å ascribed to Cu_6Sn_5 or Sn^0 are observed, indicating the reduction of the SnO_x layer. Nevertheless, a diffraction signal or ring at 1.7 Å that could be ascribed to SnO_2 and SnO was also observed. The observation of lattice fringes in HR-TEM images of the shell (Figure S15, Supporting Information), as well as bright areas in dark-field images, confirm the presence of small crystallites (<5 nm) with lattice spacings concordant with Cu_6Sn_5 or Sn^0 (d = 2.8–3.0 Å) and SnO/SnO_2 (d = 1.6–1.9 Å). Additionally, EFTEM mapping displays the content of both Sn and Cu in the nanowire shell (Figure 6i) in contrast with the enriched SnO_x shell observed after electrolysis at –0.6 V (Figure 6f). The results indicate that at this potential the electrolysis process leads to the reduction of the amorphous SnO_x layer to Cu_6Sn_5 and Sn^0, mostly to Cu_6Sn_5 as indicated by the predominance of the Cu_6Sn_5 pattern over Sn^0 in GI-XRD pattern (Figure S8, Supporting Information) as well as the occurrence of both Cu and Sn in the catalyst shell. Indeed, the surface composition determined by XPS (Figure 5 and Table 1) demonstrates that CuNW-Sn$_{HIGH}$ catalyst surface is initially composed of SnO_2 exclusively (≈20 nm), which remains largely unaffected after CP pre-reduction (98 at. % Sn). However, after CO_2 electrolysis at –0.7 and –0.9 V the SnO_x layer is reduced to Cu_6Sn_5 alloy according to TEM-SAED (Figure 6g) and GI-XRD (Figure S8, Supporting Information) while Cu migrates from the CuNW core to the surface region, as confirmed by the EFTEM mapping (Figure 6i and Figure S16, Supporting Information), corresponding with a decrease in surface Sn content to 78 and 70 at. %, respectively (Figure 5). These results are in good agreement with the bulk composition of $CuSn_3$ reported for nanostructured formate-selective catalysts.[18]

Overall, the TEM investigation of structural changes in CuNW-Sn_{HIGH} reveals the selective reduction of Cu and the persistence of the outer SnO_x layer to yield a Cu^0@SnO_x core@shell structure at a low reductive bias (> −0.6 V), while high reductive bias < −0.7 V triggers a partial reduction of the outer SnO_x layer predominantly to Cu_6Sn_5 with the persistence of SnO_x domains, in good agreement with the Sn speciation results investigated by quasi in situ XPS (Figure 4) and in situ Sn K-edge XANES (Figure S12, Supporting Information).

It is worth noting that the potentials where metallic Sn emerges at the surface (–0.7 V) correspond with the potentials at which formate selectivity increases to reach high selectivity of 80% at –0.9 V. In contrast, at less reductive potentials (>−0.6 V) where a Cu^0@SnO_x core@shell structure is observed (see XPS Figure 4, XRD Figure S8, Supporting Information, and TEM Figure 6d–f), H_2 is the dominant product (Figure 2d). While the persistence of surface SnO_x moieties has been demonstrated as beneficial for formate selectivity in pure Sn catalysts,[29–31,47] our results indicate that only when reduced metallic Sn^0 is formed at the catalyst surface, high formate selectivity is observed, indicating that metallic Sn^0 sites play a crucial role in formate production pathway.

Another interesting effect in CuNW-Sn catalysts is the decrease in surface Sn content observed by XPS after CO_2ER testing for both samples, CuNW-Sn_{LOW} and CuNW-Sn_{HIGH}. (Figure 5 and Table 1). This Sn decrease is presumably due to a combined effect of Cu migration from the CuNW core to the surface during electrolysis (as previously reported by Schreier et al.[16] and further confirmed in this study by EFTEM mapping and XPS) and a partial Sn loss, as evidenced by the decrease of bulk Sn content observed by SEM-EDX and further confirmed by ICP-OES analysis of electrolyte samples (Table S1, Supporting Information). In view of this dynamic surface composition, the CO_2ER activity and surface composition in CuNW-Sn_{LOW} and CuNW-Sn_{HIGH} were investigated for extended electrolysis duration (Figure S17, Supporting Information). The product selectivity and surface composition exhibit negligible changes over this extended time, indicating that the redistribution of Cu−Sn at the surface occurs early during CO_2 electrolysis and stabilizes over time. Taken together, our observations (electrochemical and spectroscopic) all indicate that the major transformations happen early during an "activation" period and then stabilize into a structure that persists afterwards, maintaining the structure and activity which dictates the catalytic selectivity.

Overall, the "quasi in situ XPS" experiments demonstrate that in all CuNW samples the Cu is readily reduced to Cu^0 during CP pre- reduction at mild reductive bias and remains reduced after CO_2 electrolysis at –0.7 and –0.9 V. The observation of surface Cu present exclusively as metallic Cu (Figure 5) indicates that at least within the XPS detection limit no oxidation of surface Cu occurs due to the removal of reductive bias removal during sample handling under inert atmosphere. The results correlate with bulk Cu reduction observed in situ by hard X-ray spectroscopy (Figure 3) and demonstrate the efficacy of the quasi in situ approach to protect surface Cu from oxidation in air. The oxidation state in pure Cu catalysts during CO_2ER has been widely investigated and remains a topic of debate.[48] Some studies have found evidence of persistence of surface or subsurface oxide[38,39,49,50] while our observation of full reduction to Cu^0 under CO_2ER conditions is in agreement with recent investigations performed by in situ XAS[35,51,52] and quasi in situ XPS[53] for pure Cu catalysts. In the context of a bimetallic Cu−Sn structure, it is interesting to note that the functionalization of the $Cu(OH)_2$ nanowires with SnO_2 does not affect their full reduction to Cu^0.

Regarding the Sn speciation investigated by "quasi in situ XPS", SnO_x surface moieties have been observed after CO_2ER tests at potentials as reductive as –0.9 V. While we cannot exclude that the observed SnO_x species are at least partially created upon bias removal even under complete O_2-free handling, the in situ Sn K-edge XANES study further confirmed that SnO_x moieties are indeed present during CO_2ER at reductive bias as high as –0.9 V (Figure S12, Supporting Information). As stated above for Cu, the good correlation of observations on Sn speciation by in situ XAS and quasi in situ XPS demonstrate the persistence of SnO_x species during CO_2ER and validate the observations gathered by the quasi in situ approach and the efficacy of handling the post-electrolysis samples under inert atmosphere to minimize the impact of air oxidation in surface composition analysis. It is worth noting that the surface speciation assessed by XPS reveals a larger contribution of SnO_x (Figures 4 and 5) in contrast with the larger Sn^0 contribution observed Sn K-edge XANES spectra (Figure S12, Supporting Information). This variation likely arises due to the different probing depths of the techniques. XPS is more surface sensitive, providing information on the outermost shell (< 3nm) of the material in direct contact with electrolyte which is more likely to persist oxidized. In contrast, Sn-Kedge XANES probes the entire cross-section of the material and provides more bulk-sensitive information dominated by the reduced Cu_6Sn_5 and Sn^0 grains formed during electrolysis at high bias as observed by the TEM study (Figure 6 and Figure S15, Supporting Information).

2.5. Effects of Air Exposure

To investigate the impact of air exposure in the surface composition of Cu−Sn bimetallic catalysts, some "post-electrolysis" samples were remeasured by XPS after intentional exposure to air for a duration of 20 min (labeled "air" in Figure 4). Minor changes are observed on the Cu 2p and Cu LMM spectra for bare CuNW and CuNW-Sn_{HIGH} indicating the presence of small amounts of Cu_2O. However, the CuNW-Sn_{LOW} sample displays growth of Cu^{2+} shake-up structure in the Cu 2p spectrum, and the Cu LMM Auger spectrum was found to be composed of a mix of Cu^0, Cu_2O, and $Cu(OH)_2$ (Figure 4a,b). These results are in good agreement with the observation of persistent Cu^{2+} signal in ex situ soft XAS Cu L-edge spectra (Figure S13a, Supporting Information). The quasi in situ XPS experiments demonstrate, however, that the oxidized Cu^+/Cu^{2+} signals observed in the ex situ XAS study are generated during the brief period of exposure to air, which suggests that the modification of CuNW structures with low Sn content may facilitate the oxidation of Cu^0 in air.

Furthermore, and most significantly, the metallic Sn^0 formed after CO_2 electrolysis at –0.7 and –0.9 V is quickly re-oxidized

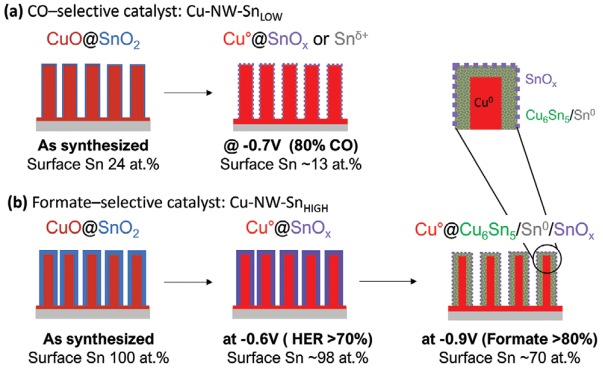

Scheme 1. Structural transformation during CO_2ER at different applied bias for a) CO–selective catalyst: Cu-NW-Sn$_{LOW}$ and b) Formate–selective catalyst: Cu-NW-Sn$_{HIGH}$.

in air, displaying spectra mostly composed by SnO_x (Figure 4c bottom). Further details on the effect of air exposure are discussed in Section S7 and Figure S18, Supporting Information.

Interestingly, air exposure can also influence the Cu/Sn surface quantification. As an example, after CO_2ER at –0.9 V the total Sn surface content determined by XPS on the CuNW-Sn$_{HIGH}$ sample increases from 70 to 77 at. % after air exposure (Table 1), while for CuNW-Sn$_{LOW}$ under similar conditions there is no significant change in Sn content. These observations confirm that ex situ characterization of catalysts conducted "post-mortem" after electrochemical testing and with air exposure can be susceptible to significant changes in surface speciation and quantification due to fast oxidation of metal surfaces in air, and migration of oxophilic metals such as Sn towards the surface upon air exposure.

The quasi in situ XPS results demonstrate that conducting electrochemical testing in an O_2-free environment and transferring the samples under an inert atmosphere to the XPS analysis chamber can successfully prevent surface re-oxidation and allows one to analyze the catalyst surface as close as possible to in situ conditions in the absence of more sophisticated and challenging approaches such as near ambient pressure (NAP) XPS.[54–56]

2.6. Structure-Activity Correlations Using DFT

The detailed investigation of the structural transformation in oxide-derived CuNW-Sn catalysts during CO_2ER testing presented in previous sections identified the structures of the CO-selective and formate-selective CuNW-Sn catalysts in their active and most selective form. The CO-selective catalyst, CuNW-Sn$_{LOW}$ is transformed from an original CuO@SnO$_2$ core@shell to a Cu^0-SnO$_x$ structure during CO_2ER as depicted in **Scheme 1**a. The optimal CO selectivity is observed at a medium bias of –0.7 V with an Sn surface content of ≈13 at %. The formate-selective catalyst CuNW-Sn$_{HIGH}$ is also transformed from an original CuO@SnO$_2$ core@shell to a Cu^0@SnO$_x$ structure at mild reductive bias (E > –0.6 V) where H_2 is observed as a major product, while more reductive potentials (E < –0.7 V) trigger the partial reduction of the outer SnO_x layer to Cu_6Sn_5 and Sn^0 with evidence of persistent SnO_x domains to yield a Cu^0@Cu$_6$Sn$_5$/Sn^0/SnO$_x$ structure, which produces formate with high selectivity. These observations are summarized in Scheme 1b. Considering that the metallic Cu core in the wires is buried under the Cu$_6$Sn$_5$/Sn^0/SnO$_x$ layer, its participation in the catalysis towards formate production is unlikely. The correlation of the outer layer composition and speciation suggests that the metallic Sn sites in Cu_6Sn_5 and Sn^0 phases that emerge at high reductive bias (E < –0.7 V) are essential to the formate production pathway and therefore these phases were investigated as models in the DFT mechanistic study detailed below.

To understand the influence of Cu—Sn surface structure on CO_2ER selectivity, we employed DFT on selected models with the PBE functional (Section S8, Supporting Information, **Figure 7**a).[58] Different systems were considered depending on the experimentally-observed correlations between surface speciation and product selectivity (Scheme 1). To model the CO-evolving catalysts characterized by overall Sn content around 13 at. %, we built Cu(111) (3 × 3) and Cu(100) (3 × 3) supercells and substituted three surface Cu atoms with Sn (Figure 7a), thus equating to an Sn content of 11 at. %. The Bader charge analysis of Cu(111) (3 × 3) 11 at. % Sn model indicates a positive polarization of the Sn sites of around +0.6 |e$^-$| (Table S5, Supporting Information), in agreement with the presence of SnO_x or Sn$^{\delta+}$ observed for CuNW-Sn$_{LOW}$ by in situ XAS and quasi in situ XPS. Cu(111) (3 × 3) and Cu(100) (3 × 3) related models with 1 surface Sn substituent (4 Sn at. %) were investigated for comparison. As for the HCOO$^-$-selective catalysts, we chose two models, Sn(100) (1 × 1) and Cu_6Sn_5 (102) (1 × 1),[59,60] since formate selectivity in CuNW-Sn$_{HIGH}$ increased upon formation of Sn^0 in metallic Sn and Cu_6Sn_5 phases (Figure 4c and Table 1). The chosen Cu, Sn, and Cu_6Sn_5 facets present the lowest surface energies (Table S6, Supporting Information), and are thus expected to be the most abundant orientations on nanoparticles according to the Wulff theorem under equilibrium.[61] To further assess the reactivity of residual SnO_x species and undercoordinated Sn sites, we built two epitaxial supercells, SnO$_2$(110) (4 × 3)/Sn(100) (2 × 3) and SnO(001) (3 × 5)/Sn(100) (2 × 3), see Figure S19, Supporting Information. SnO$_2$(110) and SnO(001) were chosen since they are the most stable crystalline facets for these oxides.[62] After depletion of surface oxygens to achieve an overall Sn content of 84 and 73 at. % for SnO$_2$/Sn and SnO/Sn respectively, we optimized both systems through ab initio molecular dynamics to allow surface reconstruction (Section S8, Supporting Information).

On transition metals, the pathway for CO_2ER to CO and HCOO$^-$ is assumed to bifurcate at an early stage (Figure 7b).[57] Carbon monoxide is formed upon adsorption of CO_2 in a $\eta^2_{C,O}$ or η^1_C configuration via an ET, followed by a proton transfer (PT) which leads to a *COOH intermediate (Figure 7b, red path). The OH group is then protonated via a proton-coupled electron transfer (PCET) and H_2O desorbs, leaving a *CO species on the surface. Finally, *CO desorbs through a chemical step. Alternatively, formate production occurs via adsorption of CO_2 through its terminal oxygens ($\eta^2_{O,O}$) favored by an ET, followed by a PT to the carbon atom and desorption of *HCOO as HCOO$^-$ (Figure 7b, green path). CO_2 adsorption and protonation can as well occur as PCET steps, as considered by previous theoretical studies on copper-tin alloys.[28,63] In this study, we will

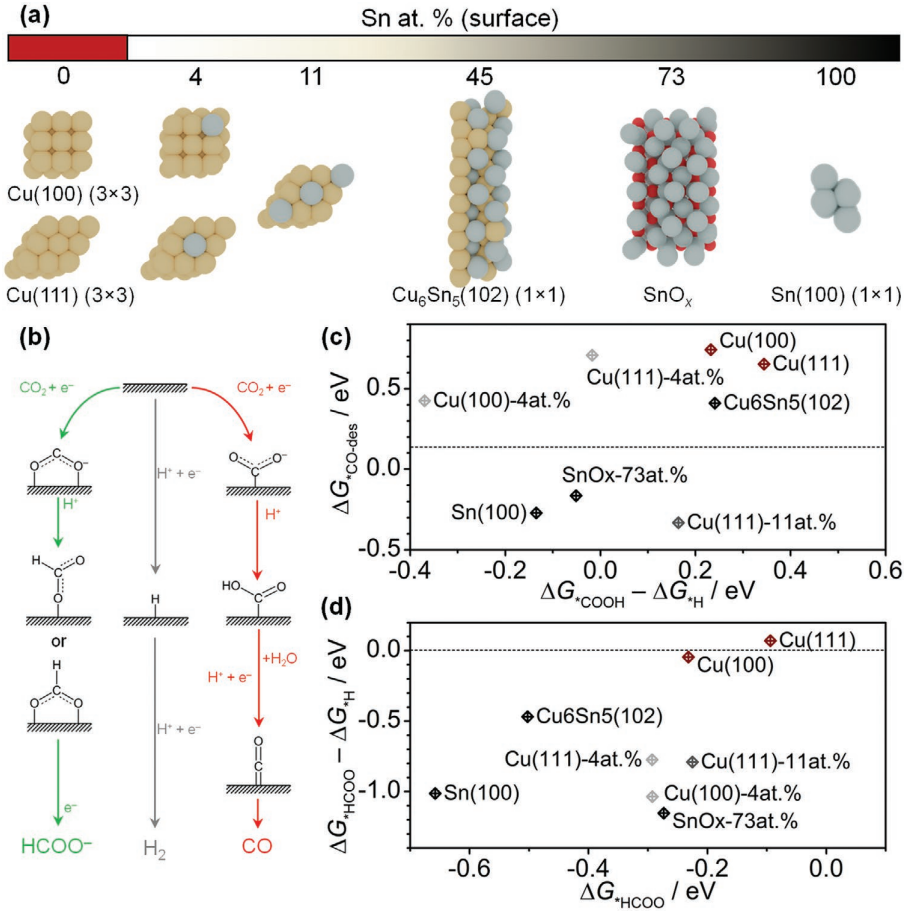

Figure 7. a) Models for DFT simulations at different Sn atomic ratio: Cu(100) (3 × 3) and Cu(111) (3 × 3) (0 Sn at. %); three Cu—Sn solid solutions with 1 to 3 Sn surface substituents in the Cu supercell (overall Sn content of 4–11 at. %); Cu_6Sn_5(102) (1 × 1) (45 at. % Sn); SnO_x model (73 at. % Sn, see Figure S19, Supporting Information) and Sn(100) (1 × 1) (100 Sn.%). Light brown and grey balls represent Cu and Sn, respectively. b) Pathways for CO_2ER to $HCOO^-$ and CO and HER, respectively defined in green, grey, and red, as defined from the state-of-the-art.[57] c) $\Delta G_{*CO\text{-}des}$ (*y*-axis) and $\Delta G_{*COOH} - \Delta G_{*H}$ (*x*-axis) as descriptors for CO selectivity: Cu(111)-11at. %Sn and SnO_x-73at. % bind COOH and H isoenergetically, yet allowing a exergonic desorption of CO ($\Delta G_{*CO\text{-}des} \leq 0$). d) $\Delta G_{*HCOO} - \Delta G_{*H}$ (*y*-axis) and ΔG_{*HCOO} (x-axis) as effective descriptors for CO selectivity: increasing Sn content leads to stronger *HCOO binding and weaker H binding, thus enabling CO_2ER to $HCOO^-$ in detriment of HER.

apply the latter reaction scheme for consistency. The HER competes with CO_2ER under cathodic bias. State-of-the-art modeling usually assumes HER to proceed via reduction of an adsorbed proton and its successive coupling with a second proton either adsorbed or from solution (Figure 7b, grey path).[57]

Bagger et al. proposed a thermoneutral CO binding energy as a key property of catalysts evolving CO, while they attributed a high performance toward formic acid to a highly endergonic *H adsorption.[64] Pure copper displays low CO selectivity (Figure 2a), as CO desorption is endergonic by 0.5 eV (Figure 7c, Figure S20, Supporting Information),[64] while faradaic efficiencies toward hydrogen and formate on Cu are both ≈40% at –0.7 V versus RHE (Figure 2a) since H and $HCOO^-$ binding energies are nearly equivalent (Figure 7d, Figure S21, Supporting Information).

In contrast, the Cu(111)-11at. Sn% model presents the weakest CO binding energy among the considered systems (Figure 7c), yet shows nearly equivalent energetics for *COOH and *H adsorptions. Thus, the reduction pathway toward CO is open at –0.7 V versus RHE (Figure S20, Supporting Information), in excellent agreement with experimental results for the CuNW-Sn_{LOW} catalysts with 13 at. % Sn content (Figure 2c). In the Sn enriched models, pure Sn and Cu_6Sn_5 have the strongest $HCOO^-$ binding energies and $HCOO^-$ adsorbs more favorably than H by at least 0.5 eV (Figure 7d). Hence, the pathway toward formate is increasingly more favorable than HER for higher content of Sn, leading to the >80% FE toward formate at –0.9 V versus RHE for the CuNW-Sn_{HIGH} sample (Figure 2d, Figure S21, Supporting Information). In general, the SnO_x model exhibits weaker *HCOO, *COOH, and *H binding energies than Sn(100) (Figure 2d, Table S7, Supporting Information), thus motivating the poor CO_2R reduction performance of the Cu^0@SnO_x system at –0.6 V (Scheme 1b).

The modulation of CO_2ER selectivity observed with increasing Sn content, making Cu—Sn first selective toward CO and then to $HCOO^-$, is caused by changes in the electronic

state of Sn. As proposed by Vasileff et al.,[28] for low Sn content, the copper matrix withdraws electronic density from Sn sites, as predicted by Bader charge analysis (Table S5, Supporting Information). The $Sn^{\delta+}$ sites destabilize CO adsorption on Cu sites, thus enabling the subsequent release of CO which is hindered on the pure copper system. In the Sn enriched models (Sn ≥ 45 at. %)—Cu_6Sn_5 and pure Sn—this localized effect is absent, since Sn sites are mainly metallic for both systems (according to Bader charge analysis, Table S5, Supporting Information). These Sn^0 sites are responsible for a weaker H binding and stronger $HCOO^-$ adsorption, thus making CO_2ER formate more favorable than HER.[64] Furthermore, at high Sn content, the relatively close proximity of Sn sites to one another leads to ensemble effects that strengthen adsorption of CO_2 through its terminal oxygens ($\eta^2_{O,O}$), which opens the formate pathway.

3. Conclusions

$Cu(OH)_2$ nanowire array electrodes modified by SnO_2 ALD overlayers were optimized to reach high selectivity towards either CO or formate depending on the number of ALD cycles (15 or 182 cycles, respectively) with negligible differences in electrode morphology. These Cu−Sn mixed oxide composites were studied via a comprehensive investigation of metal oxidation states and chemical environments following progressive reduction of the materials during CO_2ER by bulk sensitive hard XAS, and surface-sensitive soft X-ray absorption and XPS, in order to reach a better understanding of Cu−Sn synergetic effects.

Our results indicate that Cu−Sn-based CO-selective catalysts display optimal selectivity at a medium bias of –0.7 V, where their surface is composed of metallic Cu and SnO_x with an Sn surface content of ≈13 at %. On the other hand, formate-selective catalysts display optimal selectivity at a higher bias of –0.9 V, under these conditions their surface is composed of metallic Cu and a mixture of metallic Sn and SnO_x, with an Sn surface content of ≈70 at. %. The correlation of Sn surface speciation with CO_2ER selectivity in the formate-selective catalyst indicates that metallic Sn sites enable high formate selectivity. DFT simulations indicate two regimes on Cu−Sn catalysts. At low Sn content, localized electronic effects lead to the formation of $Sn^{\delta+}$, which weaken CO adsorption on Cu and thus enable CO formation. For Sn content ≥ 45 the overall system shows similar reactivity as pure Sn, hindering H adsorption while promoting formate production. Further improvement of Cu−Sn catalysts performance by increasing the catalytic current density may be achieved by targeting the above-mentioned surface compositions through functionalization of high surface area Cu nanostructures with Sn overlayers integrated into gas diffusion electrode configurations.[65] Such approaches can potentially enable selective and energy-efficient CO or formate production at practical conversion rates using earth-abundant catalyst materials.

Overall, the complementary information gathered by bulk and surface sensitive characterization techniques has allowed us to unravel the complex and dynamic nature of structural and compositional changes observed in Cu−Sn bimetallic electrocatalysts under CO_2ER turnover. Our findings highlight the importance of conducting thorough structural characterization by in situ or quasi in situ approaches with consideration to bulk versus surface sensitivity, and, when possible, avoiding ambient conditions (such as air exposure) which can drastically affect observed composition and speciation. In situ studies by hard XAS can reveal structural information under true operating conditions, but this typically requires a synchrotron and furthermore gives predominantly bulk-sensitive information. Methods which are mostly surface-sensitive (such as soft XAS and XPS) are more challenging to accomplish in situ, so a good compromise is to conduct electrocatalyst testing and then transfer the samples to the analysis chamber under inert atmosphere, in order to study the electrode material as close as possible to relevant catalytic conditions.

4. Experimental Section

Complete details regarding materials and methods are provided in the Supporting Information file.

Supporting Information

Supporting Information is available from the Wiley Online Library or from the author.

Acknowledgements

This work was supported by the Helmholtz Association's Initiative and Networking Fund (Helmholtz Young Investigator Group VH-NG-1225) and the Helmholtz Climate Initiative (Net-Zero-2050). The research utilized instrumentation within the Helmholtz Energy Materials Foundry (HEMF), the HySPRINT Helmholtz Innovation Lab, the HZB X-ray core lab, the HZB corelab Correlative Microscopy and Spectroscopy, and the HZB Institute for Solar Fuels. The authors thank HZB for the allocation of beamtime at the BESSY II synchrotron where X-ray absorption measurements were conducted at beamlines KMC-2, UE56-2_PGM-2 and BAMline. J.T.A., F.D., and N.L. acknowledge the financial support from the European Union (project FlowPhotoChem 862453-FLOWPHOTOCHEM), from the Spanish Ministry of Science and Innovation ("Severo Ochoa Center", MCIN/AEI/10.13039/501100011033 CEX2019-000925-S), as well as the Barcelona Supercomputing Center (BSC-RES) for providing generous computational resources. The authors thank the following colleagues for experimental and technical support: Lifei Xi, Álvaro Diaz Duque, Christian Höhn, Karsten Harbauer, Ursula Michalczik, Kirill Yusenko, René Gunder, and Michael Tovar.

Open access funding enabled and organized by Projekt DEAL.

Conflict of Interest

The authors declare no conflict of interest.

Data Availability Statement

The data that support the findings of this study are available from the corresponding author upon reasonable request. The density functional theory data sets generated during the current study are available in the ioChem-BD database[66] at DOI: https://doi.org/10.19061/iochem-bd-1-211.

Keywords

CO_2 conversion, electrocatalysis, non-noble catalysts, X-ray spectroscopy

Received: October 25, 2021
Revised: December 6, 2021
Published online: December 24, 2021

[1] K. P. Kuhl, E. R. Cave, D. N. Abram, T. F. Jaramillo, *Energy Environ. Sci.* **2012**, *5*, 7050.
[2] J. B. Greenblatt, D. J. Miller, J. W. Ager, F. A. Houle, I. D. Sharp, *Joule* **2018**, *2*, 381.
[3] S. Sen, D. Liu, G. T. R. Palmore, *ACS Catal.* **2014**, *9*, 3091.
[4] A. Dutta, M. Rahaman, M. Mohos, A. Zanetti, P. Broekmann, *ACS Catal.* **2017**, *7*, 5431.
[5] K. D. Yang, W. R. Ko, J. H. Lee, S. J. Kim, H. Lee, M. H. Lee, K. T. Nam, *Angew. Chem., Int. Ed.* **2017**, *56*, 796.
[6] K. Klingan, T. Kottakkat, Z. P. Jovanov, S. Jiang, C. Pasquini, F. Scholten, P. Kubella, A. Bergmann, B. Roldan Cuenya, C. Roth, H. Dau, *ChemSusChem* **2018**, *11*, 3449.
[7] F. S. Roberts, K. P. Kuhl, A. Nilsson, *Angew. Chem., Int. Ed.* **2015**, *54*, 5179.
[8] C. W. Li, J. Ciston, M. W. Kanan, *Nature* **2014**, *508*, 504.
[9] M. Ma, K. Djanashvili, W. A. Smith, *Phys. Chem. Chem. Phys.* **2015**, *17*, 20861.
[10] Y. Lum, B. Yue, P. Lobaccaro, A. T. Bell, J. W. Ager, *J. Phys. Chem. C* **2017**, *121*, 14191.
[11] H. Mistry, A. S. Varela, C. S. Bonifacio, I. Zegkinoglou, I. Sinev, Y. W. Choi, K. Kisslinger, E. A. Stach, J. C. Yang, P. Strasser, B. R. Cuenya, *Nat. Commun.* **2016**, *7*, 12123.
[12] D. Ren, Y. Deng, A. D. Handoko, C. S. Chen, S. Malkhandi, B. S. Yeo, *ACS Catal.* **2015**, *5*, 2814.
[13] S. Nitopi, E. Bertheussen, S. B. Scott, X. Liu, A. K. Engstfeld, S. Horch, B. Seger, I. E. L. Stephens, K. Chan, C. Hahn, J. K. Nørskov, T. F. Jaramillo, I. Chorkendorff, *Chem. Rev.* **2019**, *119*, 7610.
[14] A. Vasileff, C. Xu, Y. Jiao, Y. Zheng, S. Z. Qiao, *Chem* **2018**, *4*, 1809.
[15] M. K. Birhanu, M.-C. Tsai, A. W. Kahsay, C.-T. Chen, T. S. Zeleke, K. B. Ibrahim, C.-J. Huang, W.-N. Su, B.-J. Hwang, *Adv. Mater. Interfaces* **2018**, *5*, 1800919.
[16] M. Schreier, F. Héroguel, L. Steier, S. Ahmad, J. S. Luterbacher, M. T. Mayer, J. Luo, M. Grätzel, *Nat. Energy* **2017**, *2*, 17087.
[17] S. Sarfraz, A. T. Garcia-Esparza, A. Jedidi, L. Cavallo, K. Takanabe, *ACS Catal.* **2016**, *6*, 2842.
[18] K. Ye, Z. Zhou, J. Shao, L. Lin, D. Gao, N. Ta, R. Si, G. Wang, X. Bao, *Angew. Chem., Int. Ed.* **2020**, *59*, 4814.
[19] X. Hou, Y. Cai, D. Zhang, L. Li, X. Zhang, Z. Zhu, L. Peng, Y. Liu, J. Qiao, *J. Mater. Chem. A* **2019**, *7*, 3197.
[20] A. Vasileff, C. Xu, L. Ge, Y. Zheng, S. Z. Qiao, *Chem. Commun.* **2018**, *54*, 13965.
[21] M. Morimoto, Y. Takatsuji, R. Yamasaki, H. Hashimoto, I. Nakata, T. Sakakura, T. Haruyama, *Electrocatalysis* **2018**, *9*, 323.
[22] Q. Li, J. Fu, W. Zhu, Z. Chen, B. Shen, L. Wu, Z. Xi, T. Wang, G. Lu, J. J. Zhu, S. Sun, *J. Am. Chem. Soc.* **2017**, *139*, 4290.
[23] J. Zeng, K. Bejtka, W. Ju, M. Castellino, A. Chiodoni, A. Sacco, M. A. Farkhondehfal, S. Hernández, D. Rentsch, C. Battaglia, C. F. Pirri, *Appl. Catal., B* **2018**, *236*, 475.
[24] W. Ju, J. Zeng, K. Bejtka, H. Ma, D. Rentsch, M. Castellino, A. Sacco, C. F. Pirri, C. Battaglia, *ACS Appl. Energy Mater.* **2019**, *2*, 867.
[25] S. Stojkovikj, G. A. El-Nagar, F. Firschke, L. C. Pardo Pérez, L. Choubrac, M. Najdoski, M. T. Mayer, *ACS Appl. Mater. Interfaces* **2021**, *13*, 38161.
[26] Y. Zhao, C. Wang, G. G. Wallace, *J. Mater. Chem. A* **2016**, *4*, 10710.
[27] C. Chen, Y. Pang, F. Zhang, J. Zhong, B. Zhang, Z. Cheng, *J. Mater. Chem. A* **2018**, *6*, 19621.
[28] A. Vasileff, X. Zhi, C. Xu, L. Ge, Y. Jiao, Y. Zheng, S. Z. Qiao, *ACS Catal.* **2019**, *9*, 9411.
[29] Y. Chen, M. W. Kanan, *J. Am. Chem. Soc.* **2012**, *134*, 1986.
[30] S. Zhang, P. Kang, T. J. Meyer, *J. Am. Chem. Soc.* **2014**, *136*, 1734.
[31] D. H. Won, C. H. Choi, J. Chung, M. W. Chung, E. H. Kim, S. I. Woo, *ChemSusChem* **2015**, *8*, 3092.
[32] Helmholtz-Zentrum Berlin für Materialien und Energie, *J. large-scale Res. Facil.* **2016**, *2*, A49.
[33] B. L. Henke, E. M. Gullikson, J. C. Davis, *At. Data Nucl. Data Tables* **1993**, *54*, 181.
[34] G. S. Henderson, F. M. F. de Groot, B. J. A. Moulton, *Rev. Mineral. Geochem.* **2014**, *78*, 75.
[35] S. H. Lee, J. C. Lin, M. Farmand, A. T. Landers, J. T. Feaster, J. E. Avilés Acosta, J. W. Beeman, Y. Ye, J. Yano, A. Mehta, R. C. Davis, T. F. Jaramillo, C. Hahn, W. S. Drisdell, *J. Am. Chem. Soc.* **2021**, *143*, 588.
[36] M. Farmand, A. T. Landers, J. C. Lin, J. T. Feaster, J. W. Beeman, Y. Ye, E. L. Clark, D. Higgins, J. Yano, R. C. Davis, A. Mehta, T. F. Jaramillo, C. Hahn, W. S. Drisdell, *Phys. Chem. Chem. Phys.* **2019**, *21*, 5402.
[37] H. Riesemeier, K. Ecker, W. Görner, B. R. Müller, M. Radtke, M. Krumrey, *X-Ray Spectrom.* **2005**, *34*, 160.
[38] F. Cavalca, R. Ferragut, S. Aghion, A. Eilert, O. Diaz-Morales, C. Liu, A. L. Koh, T. W. Hansen, L. G. M. Pettersson, A. Nilsson, *J. Phys. Chem. C* **2017**, *121*, 25003.
[39] A. Eilert, F. Cavalca, F. S. Roberts, J. Osterwalder, C. Liu, M. Favaro, E. J. Crumlin, H. Ogasawara, D. Friebel, L. G. M. Pettersson, A. Nilsson, *J. Phys. Chem. Lett.* **2017**, *8*, 285.
[40] Helmholtz-Zentrum Berlin für Materialien und Energie, *J. large-scale Res. Facil.* **2016**, *2*, A80.
[41] M. Abbate, J. B. Goedkoop, F. M. F. de Groot, M. Grioni, J. C. Fuggle, S. Hofmann, H. Petersen, M. Sacchi, *Surf. Interface Anal.* **1992**, *18*, 65.
[42] R. Qiao, I. T. Lucas, A. Karim, J. Syzdek, X. Liu, W. Chen, K. Persson, R. Kostecki, W. Yang, *Adv. Mater. Interfaces* **2014**, *1*, 1300115.
[43] J. Timoshenko, B. R. Cuenya, *Chem. Rev.* **2021**, *121*, 882.
[44] M. C. Biesinger, *Surf. Interface Anal.* **2017**, *49*, 1325.
[45] T. Heil, B. Gralla, M. Epping, H. Kohl, *Ultramicroscopy* **2012**, *118*, 11.
[46] B. Schaffer, G. Kothleitner, W. Grogger, *Ultramicroscopy* **2006**, *106*, 1129.
[47] M. F. Baruch, J. E. Pander, J. L. White, A. B. Bocarsly, *ACS Catal.* **2015**, *5*, 3148.
[48] Z.-Z. Wu, F.-Y. Gao, M.-R. Gao, *Energy Environ. Sci.* **2021**, *14*, 1121.
[49] M. Favaro, H. Xiao, T. Cheng, W. A. Goddard, J. Yano, E. J. Crumlin, *Proc. Natl. Acad. Sci. U. S. A.* **2017**, *114*, 6706.
[50] Y. Zhao, X. Chang, A. S. Malkani, X. Yang, L. Thompson, F. Jiao, B. Xu, *J. Am. Chem. Soc.* **2020**, *142*, 9735.
[51] N. J. Firet, T. Burdyny, N. T. Nesbitt, S. Chandrashekar, A. Longo, W. A. Smith, *Catal. Sci. Technol.* **2020**, *10*, 5870.
[52] J. J. Velasco-Velez, J. J. Velasco-Velez, R. V. Mom, L. E. Sandoval-Diaz, L. J. Falling, C. H. Chuang, D. Gao, D. Gao, T. E. Jones, Q. Zhu, Q. Zhu, R. Arrigo, B. Roldan Cuenya, A. Knop-Gericke, A. Knop-Gericke, T. Lunkenbein, R. Schlögl, R. Schlögl, *ACS Energy Lett.* **2020**, *5*, 2106.
[53] R. M. Arán-Ais, F. Scholten, S. Kunze, R. Rizo, B. R. Cuenya, *Nat. Energy* **2020**, *5*, 317.
[54] A. Knop-Gericke, V. Pfeifer, J. J. Velasco-Velez, T. Jones, R. Arrigo, M. Hävecker, R. Schlögl, *J. Electron Spectrosc. Relat. Phenom.* **2017**, *221*, 10.
[55] M. Salmeron, *Top. Catal.* **2018**, *61*, 2044.
[56] M. Favaro, F. Abdi, E. Crumlin, Z. Liu, R. van de Krol, D. Starr, *Surfaces* **2019**, *2*, 78.
[57] R. Kortlever, J. Shen, K. J. P. Schouten, F. Calle-Vallejo, M. T. M. Koper, *J. Phys. Chem. Lett.* **2015**, *6*, 4073.

[58] J. P. Perdew, K. Burke, M. Ernzerhof, *Phys. Rev. Lett.* **1996**, *77*, 3865.
[59] N. Saunders, A. P. Miodownik, *Bull. Alloy Phase Diagrams* **1990**, *11*, 278.
[60] S. Fürtauer, D. Li, D. Cupid, H. Flandorfer, *Intermetallics* **2013**, *34*, 142.
[61] G. Wulff, *Z. Kristallogr. – Cryst. Mater.* **1901**, *34*, 449.
[62] Y. Duan, *Phys. Rev. B: Condens. Matter Mater. Phys.* **2008**, *77*, 045332.
[63] W. Ren, X. Tan, J. Qu, S. Li, J. Li, X. Liu, S. P. Ringer, J. M. Cairney, K. Wang, S. C. Smith, C. Zhao, *Nat. Commun.* **2021**, *12*, 1449.
[64] A. Bagger, W. Ju, A. S. Varela, P. Strasser, J. Rossmeisl, *ChemPhysChem* **2017**, *18*, 3266.
[65] B. H. Frazer, B. Gilbert, B. R. Sonderegger, G. De Stasio, *Surf. Sci.* **2003**, *537*, 161.
[66] M. Álvarez-Moreno, C. de Graaf, N. López, F. Maseras, J. M. Poblet, C. Bo, *J. Chem. Inf. Model.* **2015**, *55*, 95.

ADVANCED ENERGY MATERIALS

Supporting Information

for *Adv. Energy Mater.*, DOI: 10.1002/aenm.202103328

Determining Structure-Activity Relationships in Oxide Derived Cu—Sn Catalysts During CO2 Electroreduction Using X-Ray Spectroscopy

Laura C. Pardo Pérez, Alexander Arndt, Sasho Stojkovikj, Ibbi Y. Ahmet, Joshua T. Arens, Federico Dattila, Robert Wendt, Ana Guilherme Buzanich, Martin Radtke, Veronica Davies, Katja Höflich, Eike Köhnen, Philipp Tockhorn, Ronny Golnak, Jie Xiao, Götz Schuck, Markus Wollgarten, Núria López, and Matthew T. Mayer**

Supporting Information

Determining structure-activity relationships in oxide derived Cu-Sn catalysts during CO_2 electroreduction using X-ray spectroscopy

Laura C. Pardo Pérez, Alexander Arndt, Sasho Stojkovikj, Ibbi Y. Ahmet, Joshua T. Arens, Federico Dattila, Robert Wendt, Ana Guilherme Buzanich, Martin Radtke, Veronica Davies, Katja Höflich, Eike Köhnen, Philipp Tockhorn, Ronny Golnak, Jie Xiao, Götz Schuck, Markus Wollgarten, Núria López and Matthew T. Mayer**

*Corresponding authors. E-mail: lcpardop@gmail.com, m.mayer@helmholtz-berlin.de

Sections overview

S.1 Experimental details
S.2 Additional characterization data
S.3 X-ray absorption methods
S.4 Quasi in situ XPS measurements
S.5 Structural characterization by TEM
S.6 Surface composition stability
S.7 Effect of air exposure on observed surface composition
S.8 Computational details
S.9 CO_2ER Activity of planar Cu-Sn catalysts
References

S.1 Experimental details

S.1.1 Catalyst synthesis

Synthesis of CuO_x Nanowires: A Cu layer of 1 μm is sputtered atop glass substrate. The glass substrates are pretreated prior Cu sputtering by sonication in 8 M KOH for 5 days, and subsequently cleaned by 30 min sonication in water, 1 M HCl to remove excess base, water and then dried with a N_2 gun. $Cu(OH)_2$ nanowires, denoted CuNW, are synthesized by anodization of the sputtered Cu in 3 M KOH at constant current of 8 mA cm^{-2} to reach a charge of 1.35 C cm^{-2}. The anodization is conducted in an Autolab potentiostat PGSTAT204, using a 3-electrode configuration, with Ag/AgCl in 3M KCl and carbon felt as reference and counter electrodes, respectively. The $Cu(OH)_2$ nanowires are then annealed at 150 °C for 1h in air.

SnO_2 ALD deposition: The CuNW were functionalized with SnO_2 overlayers by variable number of cycles of ALD, denoted CuNW-SnXc where X is the number of SnO_2 ALD cycles. The ALD deposition was conducted in an Arradiance GEMStar system, SnO_2 was deposited at 120 °C, tetrakis(dimethylamino)-tin(IV) (TDMASn, 99% (99.99%-Sn)) was used as precursor kept at 60 °C, water as oxidizer and N_2 as carrier gas. The ALD sequence was programmed as follows: (1) TDMASn 1 s (N_2 30 sccm), (2) Purge 1 10s (N_2 90 sccm), (3) H_2O 0.2 s (N_2 90 sccm) and (4) Purge 2 15 s (N_2 90 sccm). The growth per cycle is 1.1 Å. (182 cycles yield a SnO_2 layer of 20 nm on a flat Si surface). For ultrathin depositions (< 30 cycles) the purge time in steps (2) and (4) was increased to 20 s and 25 s respectively, to ensure full reaction of the precursors.

S.1.2 CO_2 electroreduction testing

Electrolysis tests were carried out using a BioLogic SP-200 potentiostat in a custom two compartment cell separated by a Nafion 115 membrane, in CO_2 saturated 0.1 M $KHCO_3$ (pH 6.8) under constant CO_2 flow of 20 mL min^{-1}. Ag/AgCl in 3 M KCl and Pt mesh were used as reference and counter electrodes, respectively. All potentials presented through the manuscript are referred to the reversible hydrogen electrode (RHE). The CuNW-Sn samples are activated by chronopotentiometry (CP) at constant cathodic current of –2 mA cm^{-2} to reach a potential –

0.5 V. After this pre-reduction step, CO_2 electrolysis test is performed by chronoamperometry at constant potential of choice, typically –0.7 V for 1-2 h.

The gas products are quantified by in-line gas chromatography with a Thermo TRACE 1310 gas chromatograph using He as a carrier gas. The Gas Chromatographer is equipped with two columns: HayeSepS column (1 mm ID, Restek) and molecular sieve MS5a column (1 mm ID, Restek); as well as two detectors: Pulse Discharge Detector (PDD) and Flame Ionization Detector (FID). The outlet flow of the cathode compartment headspace of the H -cell was fed into GC through a transfer line (heated at 60 °C). The product concentration was measured every 15 minutes for the duration of the CO_2ER catalytic test, typically 1-2h. The Faradaic efficiency (FE) was calculated according to Equation 1, where ***[X]*** is the concentration measure for gas ***X*** determined by gas chromatography, ***flowrate*** corresponds to the constant inlet rate of CO_2 into the cell (20 ml min^{-1}), ***z*** the number of mols of electrons required to produce 1 mol of gas ***X***, and ***i*** is the recorded experimental current and F is the Faraday constant.

$$Faradaic\ Efficency\ \%\ \ Gas\ X = \frac{[X]*Flowrate*z*F}{i} * 100 \qquad \text{(Eq. 1)}$$

Liquid products are analyzed post electrolysis by HPLC, using a Thermo Scientific Dionex UltiMate 3000 UHPLC instrument equipped with UV (UltiMate 3000, Dionex) and RI (RefractoMax 520, ERC) detectors and an autosampler unit. The separation is achieved with a HyperREZ XP H+ column using 5 mM H_2SO_4(aq) as eluent. The electrolyte was sampled at the end of each electrolysis test by taking a 1 mL aliquot. Formate faradaic efficiency was determined based on the experimentally determined formate concentration $[HCOO^-]$, the total amount of charge passed (**q**) and the total volume of electrolyte ($\boldsymbol{V_{electrolyte}}$), as shown in Equation 2.

$$Faradaic\ Efficency\ \%\ HCOO^- = \frac{[HCOO^-]*Velectrolyte*2*F}{q} \qquad \text{(Eq. 2)}$$

S.1.3 Materials characterization

Grazing incidence x-ray diffraction (GIXRD) was performed on a PANalytical X'Pert Pro MPD diffractometer for thin film analysis, using a Cu Kα radiation (λ = 1.5418 Å), and a Xenon scintillation counter detector with parallel plate collimator. The diffractograms were collected at an incidence angle of 0.5°, with a step size of 0.06 and collection time of 10 s. Top view ***SEM images and EDX spectra*** were collected on a Zeiss LEO 1530 Gemini SEM system with a ThermoFisher UltraDry EDX detector. The SEM images were acquired at 3 kV using the in lens secondary electron detector and EDX spectra were collected at an acceleration voltage of 15 kV. ***Cross sections*** were cut by focused Ga ion beam milling in a Zeiss Crossbeam 340 KMAT dual beam instrument. Due to the extreme aspect ratio of the CuNW, no protection layer was deposited. Instead, the patterning was directly carried out at the unmodified sample surface using an acceleration voltage of 30 kV and three different currents. For the actual cross section 7 nA were used, followed by a first rough polishing step at 1.5 nA and a final polishing step at 50 pA. ***Inductively Coupled Plasma – Optical Emission Spectrometry (ICP-OES) measurements*** were conducted in an iCAP 7400 Duo MFC ICP-OES Analyzer system (Thermo Scientific) in axial Ar (5.0 purity, Air Liquide) plasma mode.

S.2 Additional characterization data

SEM characterization of as-synthesized catalysts

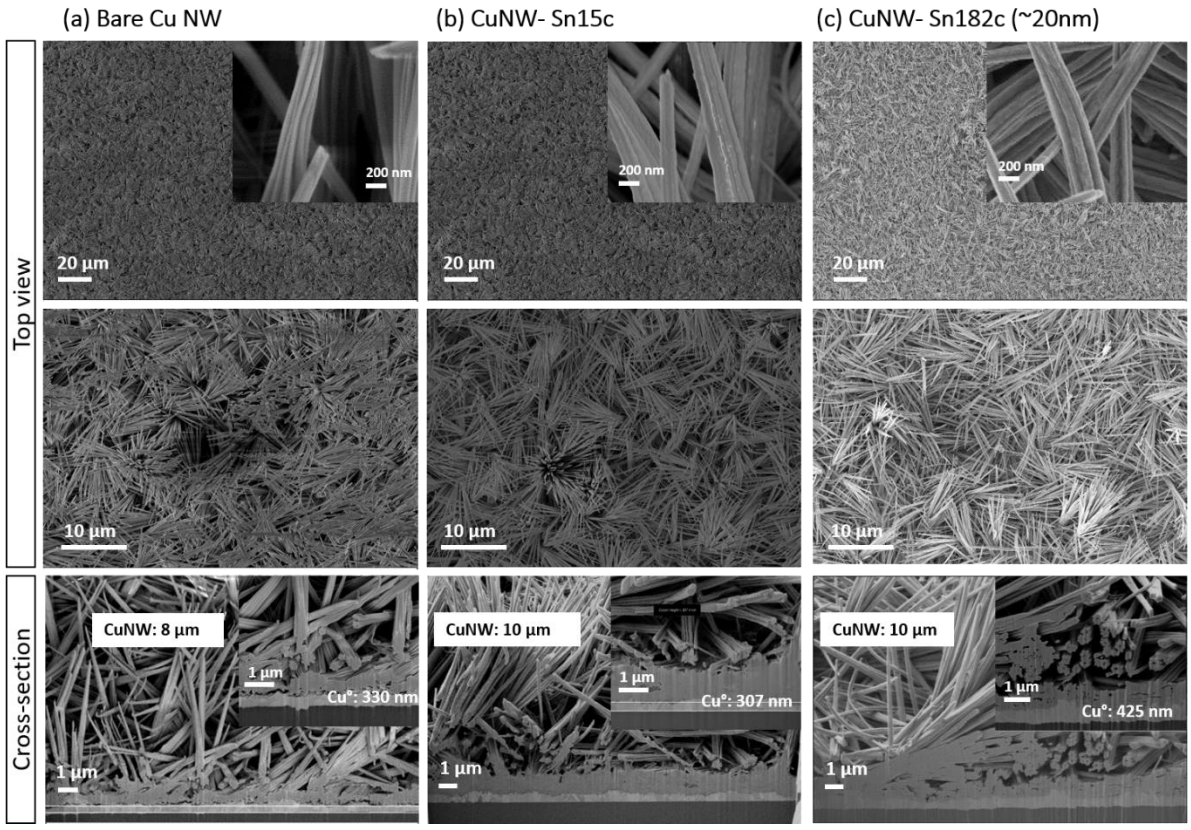

Figure S1. Top view and cross section SEM micrographs of the as synthesized CuNW with different SnO_2 content. Bare CuNW (left), CuNW modified with 15 cycles (center) and 182 cycles (right).

CO_2ER testing

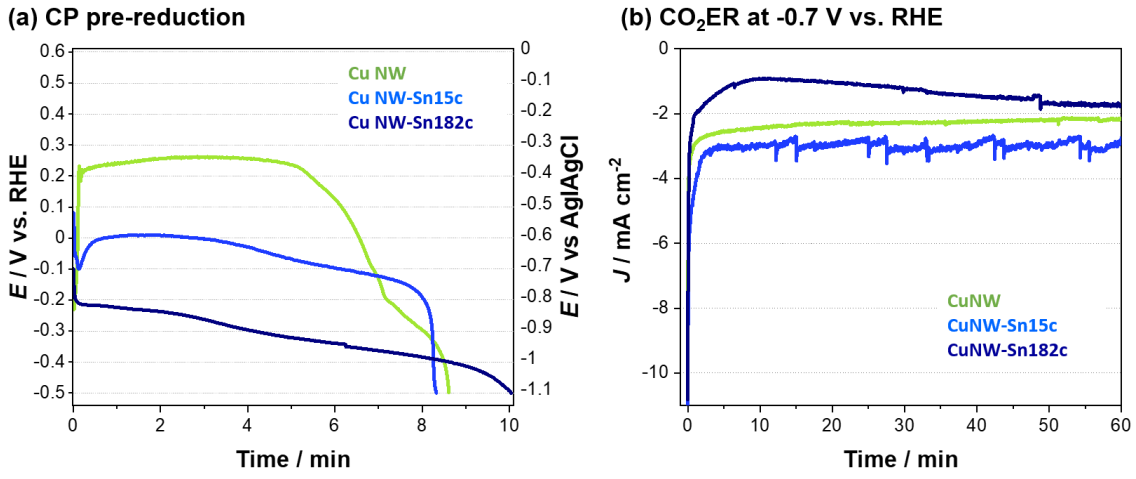

Figure S2. Representative (a) CP pre-reduction at 2 mA cm^{-2} and (b) CO_2 electrolysis at –0.7 V for CuNW bare and modified with low or high Sn content.

Effect of $Cu(OH)_2$ NW dehydration in observed CO_2ER selectivity

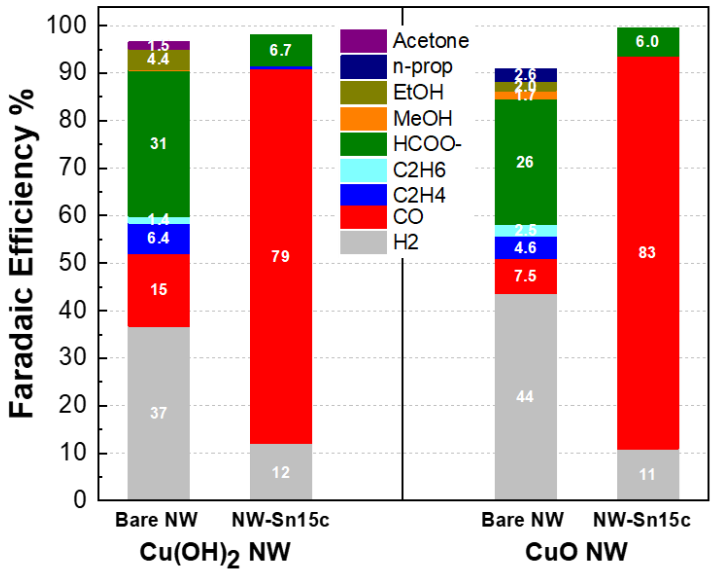

Figure S3. CO_2ER activity of $Cu(OH)_2$ (left) or CuO NW (right) bare and modified with 15 cycles of SnO_2 ALD. Electrolysis at –0.7 V vs RHE in CO_2 sat. 0.1 M $KHCO_3$.

CO_2ER electrolysis on bare CuNW

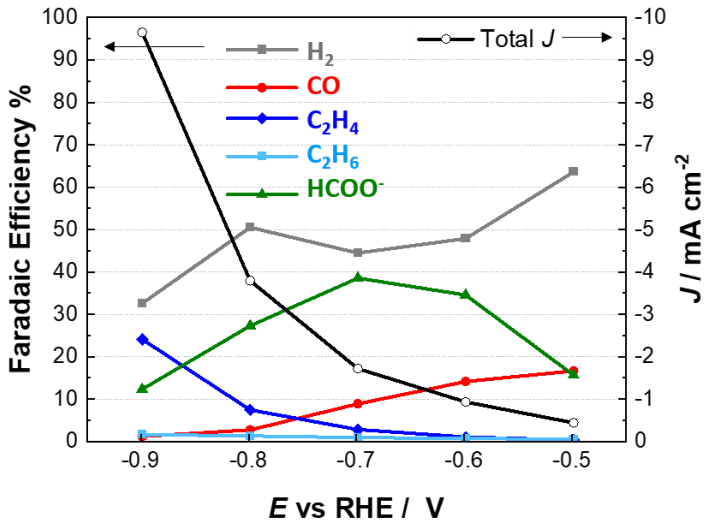

Figure S4. CO_2ER as a function of applied potential for the bare CuNW.

SEM characterization of the CuNW – Sn catalysts after CO_2ER electrolysis

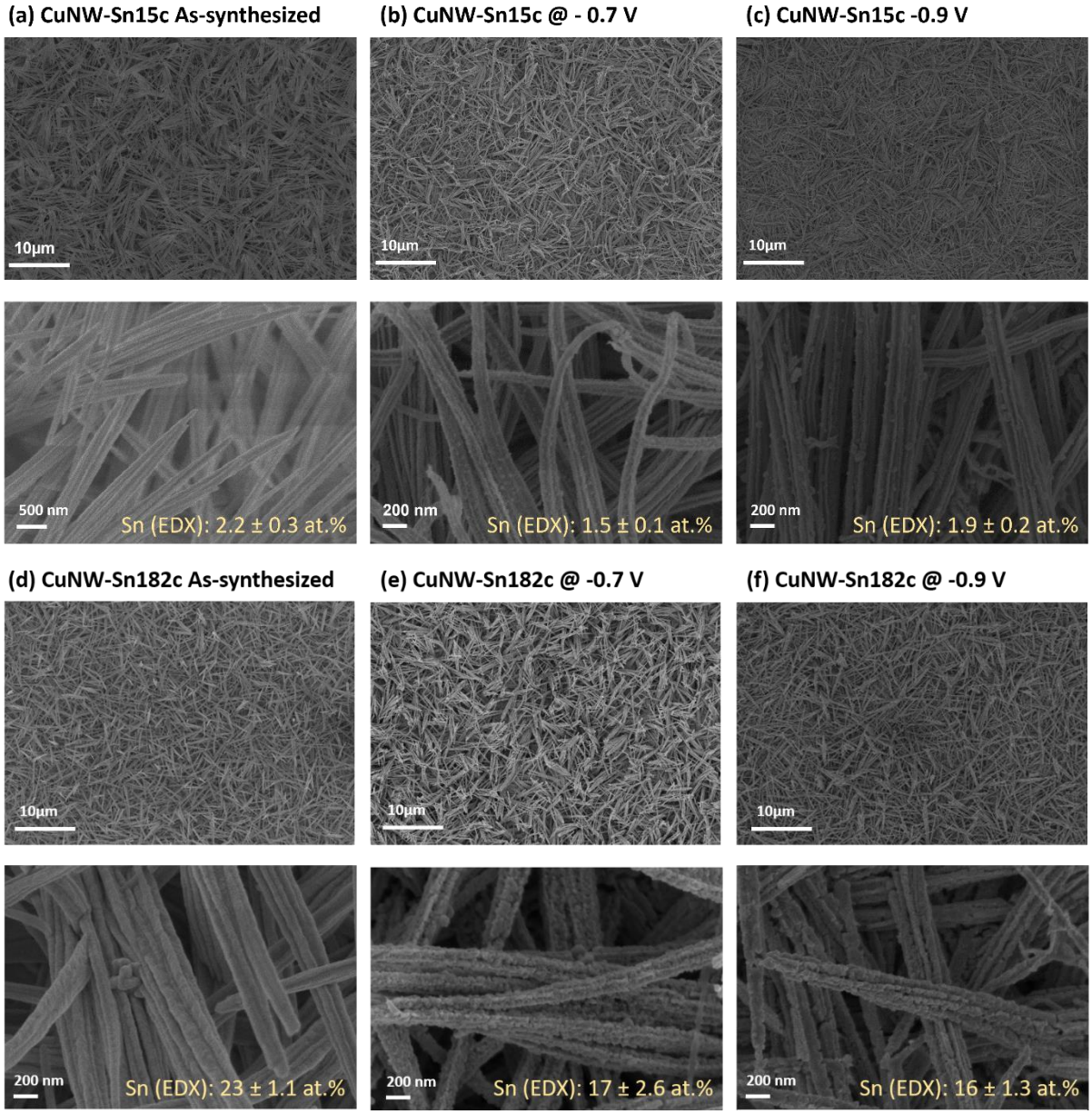

Figure S5. SEM micrographs of CuNW with different SnO_2 content after CO_2ER testing in CO_2 sat. 0.1 M $KHCO_3$. CuNW modified with 15 cycles as synthesized (a), after electrolysis at –0.7 V for 2h (b) and -0.9 V for 2h (c). CuNW modified with 182 cycles as synthesized (d), after electrolysis at –0.7 V for 2h (e) and –0.9 V for 2h (f). The Sn content referred total metal (Sn+Cu) as determined by EDX is displayed on the images.

EDX characterization of the CuNW – Sn catalysts

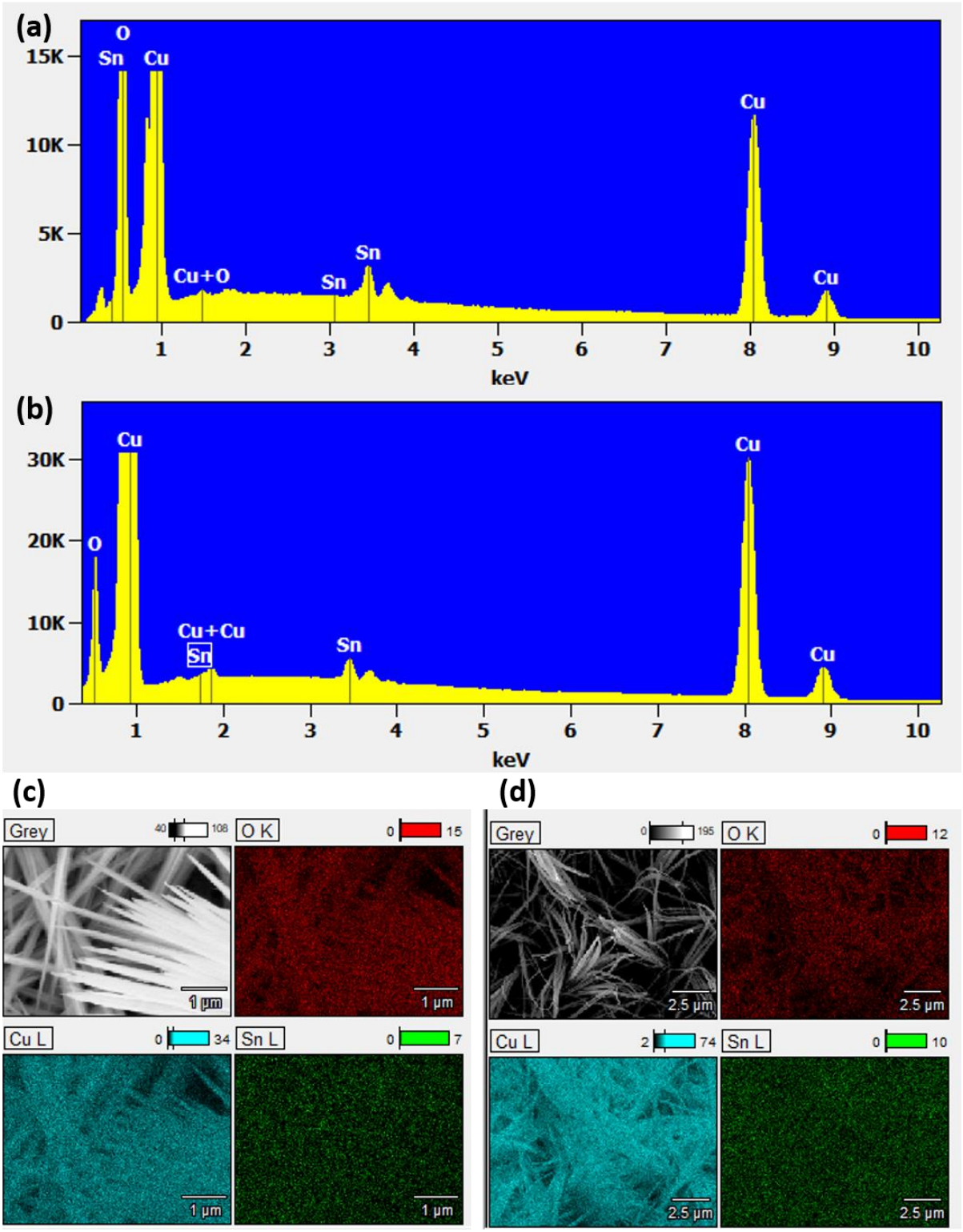

Figure S6. EDX characterization of CuNW-Sn_{LOW}. Spectra collected at 15keV for CuNW-Sn15c (a) as-synthesized and (b) after CO_2ER at -0.7V. Corresponding mapping images (c) and (d) using Cu Lα (0.93 kV), Sn Lα (3.44 kV) and O Kα (0.525 kV)- lines. Note that quantification results presented in main text (Table 1) are calculated based on Cu Kα (8.04 kV) and Sn L lines. The signals observed between 1.5-2keV correspond to sum Cu+Cu or Cu+O peaks and Sn scape peaks.

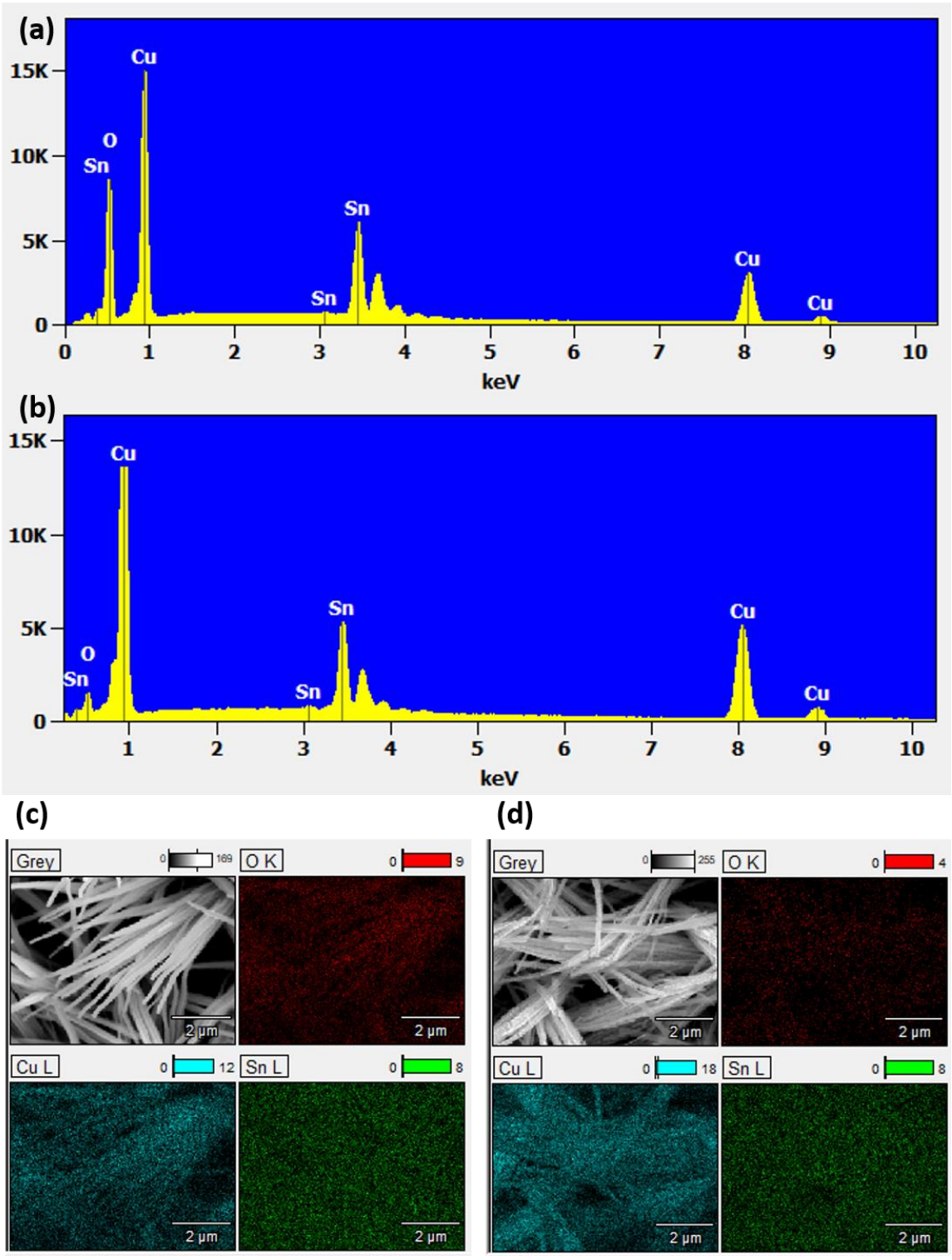

Figure S7. EDX characterization of CuNW-Sn_{HIGH}. Spectra collected at 15keV for CuNW-Sn_{HIGH} (a) as-synthesized and (b) after CO_2ER at -0.9V. Corresponding mapping images (c) and (d) using Cu Lα (0.93 kV), Sn Lα (3.44 kV) and O Kα (0.525 kV) lines. Note that quantification results presented in main text (Table 1) are calculated based on Cu Kα (8.04 kV) and Sn L lines.

ICP-OES analysis of electrolyte

Electrolyte samples collected after 1 h of CO_2 electrolysis were analyzed using ICP-OES to detect possible Cu and Sn dissolution during catalysis. The electrolyte samples were acidified by addition of HCl 5% prior ICP-OES analysis. The observed concentrations of Cu and Sn were converted to area-normalized mass loss values by accounting for the total electrolyte volume and the electrode surface area. The results are summarized in Table S1.

Table S1. Cu and Sn mass loss as determined by ICP-OES

Sample	[Cu][(a)]	[Sn][(a)]	Mass loss[(b)]	
	µg L^{-1}	µg L^{-1}	Cu (µg cm^{-2})	Sn (µg cm^{-2})
CuNW-Sn_{LOW} @ –0.7 V	77.5	49.3	2.3	1.5
@ –0.9 V	106.1	98.6	3.2	3.0
CuNW-Sn_{HIGH} @ –0.7 V	29.5	218.5	0.9	6.6
@ –0.9 V	41.9	322.0	1.3	9.7

[(a)] Metal concentration in electrolyte as determined by ICP-OES (normalized per electrode area)
[(b)] Mass loss normalized per electrode area

The results show a minor dissolution of Cu and Sn in CuNW-Sn_{LOW} after electrolysis at –0.7 V and –0.9 V. CuNW-Sn_{HIGH} displays higher mass loss of Sn and lower mass loss of Cu in comparison with CuNW-Sn_{LOW}.

GI-XRD characterization of CuNW – Sn catalysts after CO_2ER electrolysis

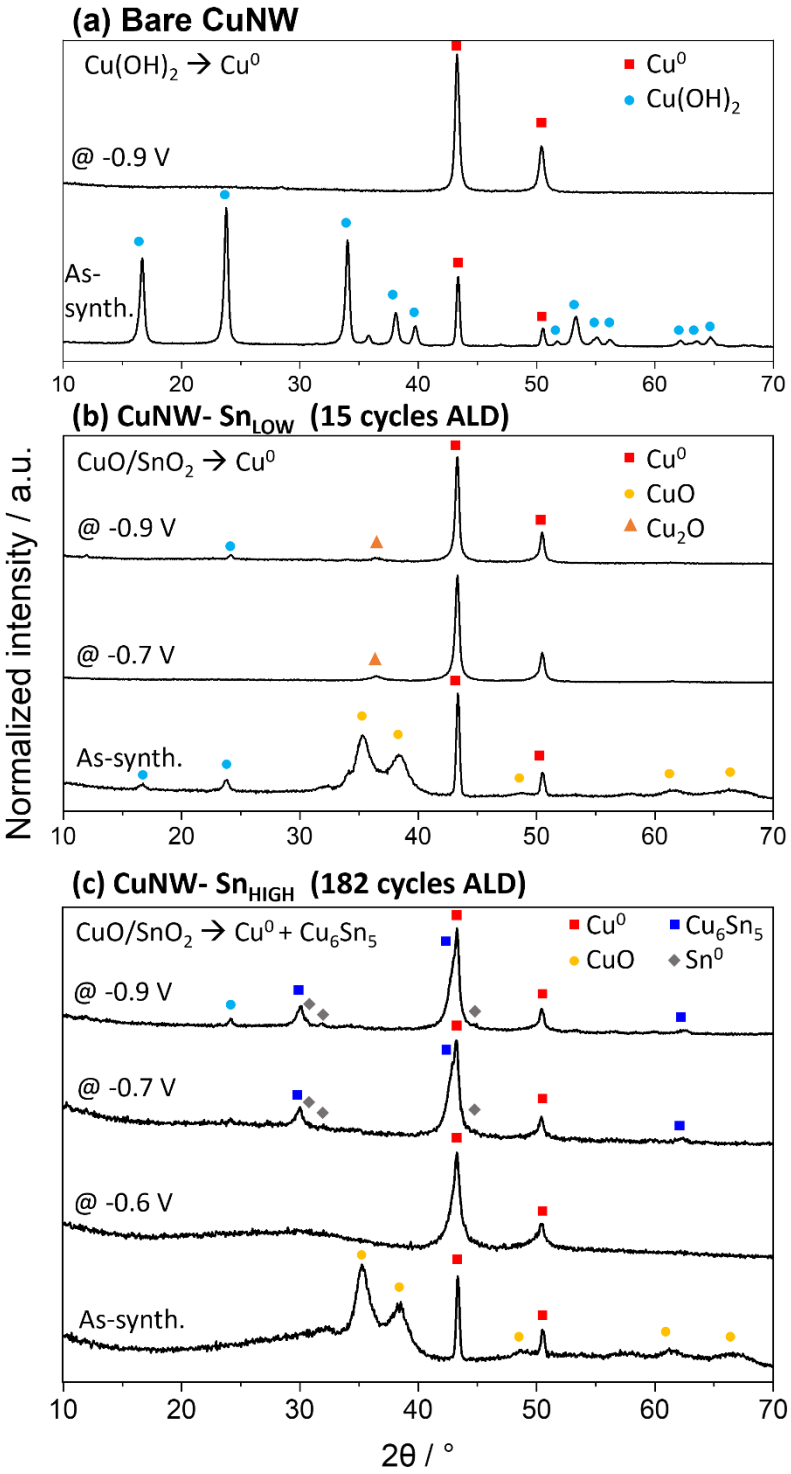

Figure S8. Grazing incidence XRD of (a) CuNW bare and modified with (b) 15 or (c) 182 cycles of SnO_2 ALD in as-synthesized condition and after CO_2ER electrolysis at different applied potentials. The displayed reference patterns correspond to of $Cu(OH)_2$ (PDF 00-013-0420), CuO (PDF 04-007-1375), Cu_2O (PDF 04-007-9767), Cu^0 (PDF 00-004-0836),Cu_6Sn_5 (PDF 00-045-1488) and Sn^0 (PDF 04-004-7747).

Grazing incidence XRD was collected on as-synthesized samples and post electrochemical samples ex-situ. The as-synthesized bare CuNW (Figure S8a) displays the diffraction pattern

of $Cu(OH)_2$ (COD 9011547). After CO_2ER electrolysis the main peaks correspond to metallic Cu° pattern (PDF 00-004-0836) and a small peak assigned to Cu_2O (PDF 04-007-9767) presumably due to Cu surface oxidation in air prior analysis. The as-synthesized CuNW samples modified with 15 or 182 cycles (Figure S8b, c) display the typical pattern of CuO (PDF 04-007-1375). After CO_2ER electrolysis, the sample modified with 15 SnO_2 ALD cycles, displays a similar pattern to bare CuNW sample; the main peaks correspond to metallic Cu^0 pattern (PDF 00-004-0836) and a small peak assigned to Cu_2O (PDF 04-007-9767). No peak shift indicative of alloying is observed. In the sample modified with 182 cycles (Figure S8c) after electrolysis at –0.6 V the sample displays only metallic Cu^0 peaks while no indication of a crystalline Sn containing phase is observed. After electrolysis at higher reductive bias –0.7 V or –0.9 V, in addition to metallic Cu^0, the formation of a Cu_6Sn_5 alloy (PDF 00-045-1488) is observed, along with small features corresponding to metallic Sn^0 (PDF 04-004-7747). These results indicate that a reductive bias of –0.7 V or higher is required to form Sn^0 crystalline phase in the sample modified with 182 cycles; the quasi in situ XPS study (Figure 5 main text) also indicated that surface Sn^0 is observed only after reduction at –0.7 V or higher reductive bias.

S.3 X-ray absorption methods

(Hard and soft) X-ray absorption measurements were conducted at an average nominal ring current of 300 mA in top-up and multi-bunch mode at the BESSY II synchrotron operated by Helmholtz-Zentrum Berlin.

S.3.1 In situ Hard- Cu K-edge XAS experimental details

The Cu K-edge XAS measurements were conducted at the KMC-2 beamline at BESSY II.[1] The spectra were collected in fluorescence mode using an energy-dispersive detector (Bruker X-Flash 6|60). The Cu K-edge is located at 8979 eV, this photon energy has an associated penetration depth of ~4 µm in Cu and ~1.5 mm in water.[2,3] These conditions allow to conduct XAS experiments in situ during electrochemical testing using front illumination with the incoming radiation penetrating through a LDPE window and a thin ~500 µm aqueous electrolyte (0.1 M $KHCO_3$) layer to probe the CuNW-Sn sample. The electrochemical cell and set up employed for these measurements are shown in Figure S9. The electrochemical measurements were conducted on a potentiostat BioLogic SP-200, Pt mesh and Ag/AgCl (3 M KCl) were used as counter and reference electrodes respectively and the electrolyte was constantly purged with 20 mL min^{-1} of CO_2 during measurements. Cu K-edge reference spectra for metallic Cu, Cu_2O and CuO were collected in fluorescence detection mode on thin film samples. Sputtered Cu (1 µm) on glass was used as metallic Cu reference, the Cu layer was leached in HCl 15% for 3 mins prior measurement to remove native oxide layer. A Cu_2O thin film (~300 nm) deposited on quartz by PLD and annealed at 600 °C in Ar was used as standard for Cu_2O. A Cu_2O thin film annealed in air for 5 h to complete oxidation to CuO (as verified by XRD, data not shown) was used as standard for CuO. $Cu(OH)_2$ reference spectra was collected in transmission on a pellet of $Cu(OH)_2$ powder diluted in cellulose matrix. All spectra were processed Athena software from the Demeter 0.9.26 software suite[4] using metallic Cu spectrum as a reference for energy calibration. XANES and EXAFS spectra were collected between 8779 eV and 9729 eV (k=14). XANES spectra were collected within ~25 mins (step size 0.07 eV-4s), while EXAFS spectra required 2.5 h (collection per EXAFS step increases

from 8 s to 40s during scan) and at least 2 repetitions per sample. FT-EXAFS analysis was conducted by k2-weighted fourier transform in the K range 3-12.

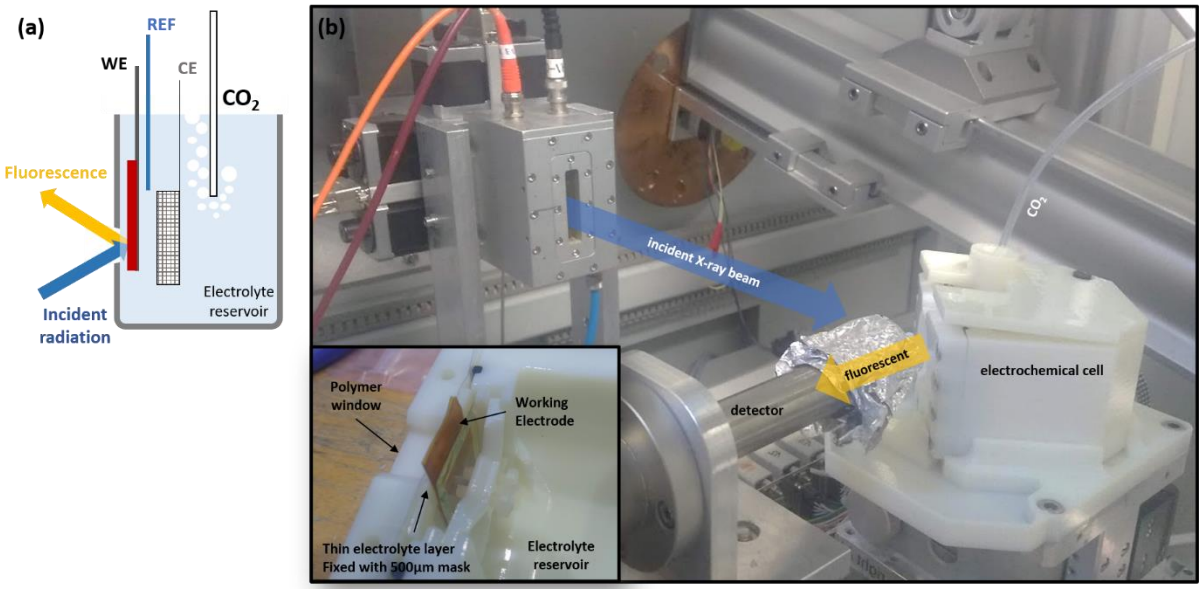

Figure S9. *In situ* Cu K-edge hard XAS set up scheme (a) and photographs(b)

The CuNW samples with or without SnOx ALD overlayers were tested in the as-synthesized state in the dry cell. The samples were then immersed in CO_2 saturated electrolyte inside the cell and activated by CP pre-reduction at –0.2 mA cm^{-2} (10 times slower than typical rate) in order to have sufficient time to collect a set of XANES spectra following the progressive reduction of Cu in the samples until a potential of –0.4 V was reached. At this potential all samples displayed the typical spectral features of metallic Cu°. (See main text Figure 3a-b). The samples were then held at –0.4 V potential for 30 min, sufficient time to collect a XANES spectra at this potential (See Figure S10). Periodical product bubble formation was observed at –0.4 V thus the potential was lowered to –0.1 V to decrease the catalytic current (<200 µA) and avoid bubble noise during EXAFS data collection. The Cu K-edge XANES spectra collected at –0.4 V and –0.1 V are shown in Figure S10, where it can be seen that in both conditions all samples display the typical spectrum of metallic Cu^0. This indicates that the (low) sustained catalytic cathodic current is sufficient to maintain Cu in its reduced state.

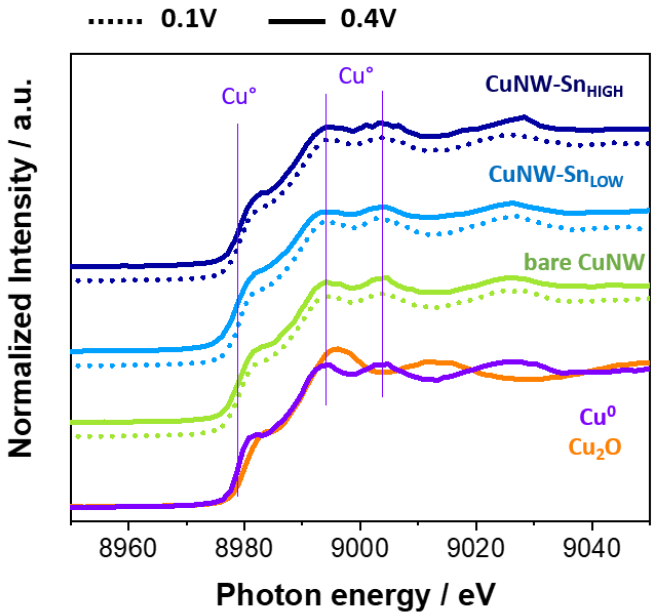

Figure S10. In situ Cu K-edge XANES spectra collected during CO_2ER electrolysis at –0.4 V and –0.1 V vs RHE. Reference spectra collected for metallic Cu° and Cu_2O are presented for comparison.

S.3.2 In situ Hard Sn K-edge XAS experimental details

The Sn K-edge XANES measurements were conducted at the BAMline beamline at BESSY II.[5] This edge is at 29.2 keV in the hard X-ray regime with a high penetration capacity through water/electrolyte (29 mm) and sample components such as Cu (98 µm) and substrate materials used for synthesis such as glass (4.8 mm).[2,3] The high probing depth capability in this energy range enables the measurement of *in situ* XANES during CO_2ER testing. The beam was monochromatized using a double-crystal monochromator (DCM) Si(111). The size of the beam spot was 4 mm × 1 mm. The excitation energy was varied in 0.5 eV step in the near-edge region. The Sn K-edge measurements were performed with fluorescence detection. The characteristic fluorescence radiation (Sn-Kα line) was measured with a custom made four-element SDD in backscatter geometry (LLA Instruments GmbH & Co. KG, Berlin, Germany). The single 30 mm2 detector modules were supplied by Ketek (Munich, Germany). The measurements were conducted in back illumination mode in a customized electrochemical cell with a Kapton tape window as depicted in Figure S11. The CuNW-Sn samples were fixed to the cell window with the sample facing the 0.1 M $KHCO_3$ electrolyte reservoir, which was continuously purged with CO_2 (20 mL min^{-1}) during measurements. In order to minimize (back)-scattering signal from the sample substrate (typically glass), the samples were prepared onto Kapton film (25 µm thick). Additionally, the electrolyte layer thickness in front of the sample in the radiation pathway was restricted to approx. 3 mm by insertion of a hollow tube fitted with a Kapton window as depicted in Figure S11. Sn foil (10µm) was used as metallic Sn reference. SnO_2 and SnO reference spectra were on pellets diluted in cellulose matrix. All spectra were processed Athena software from the Demeter 0.9.26 software suite[4] using metallic Cu spectrum as a reference for energy calibration.

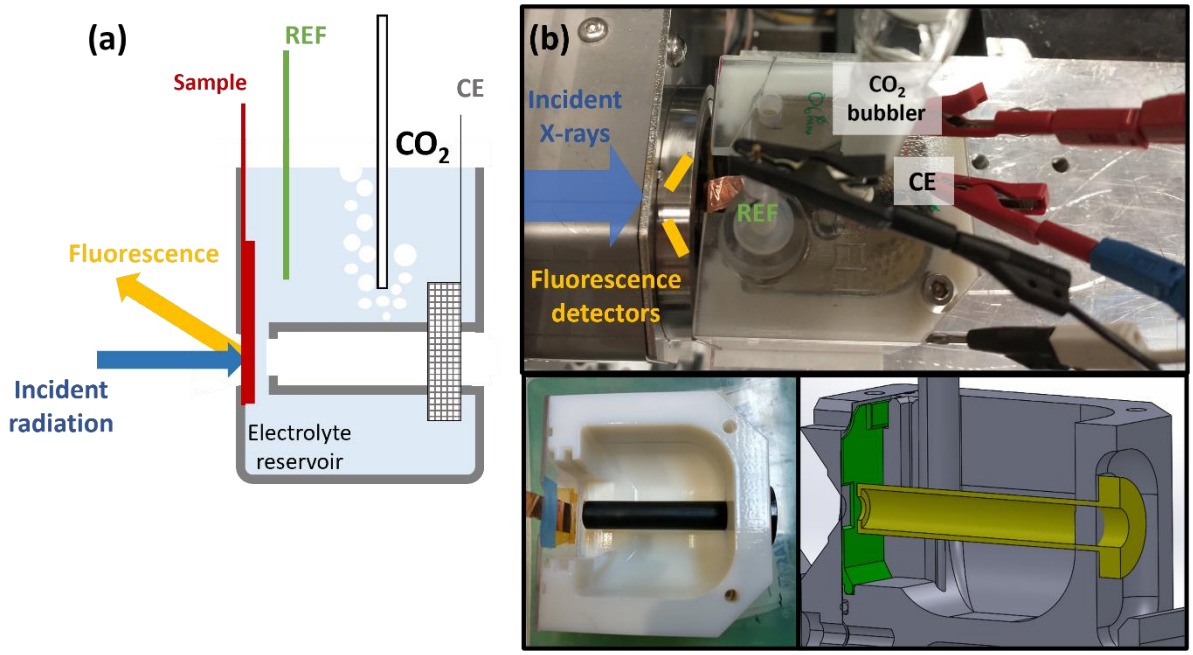

Figure S11. *In situ* Sn K-edge XAS measurement setup. (a) Schematic depiction of the electrochemical cell and. (b) Images of the electrochemical cell.

The Sn K-edge XANES spectra recorded for CuNW-Sn_{HIGH} and CuNW-Sn_{LOW} are displayed in Figure S12. The samples were investigated in the as-synthesized conditon as well as during CO_2ER electrolysis at increasing reductive potentials between –0.5 V and –0.9 V. CuNW-Sn_{HIGH} XANES spectra were quantified by linear combination fitting (LCF) analysis according to Equation 3, where X, Y and Z are the spectra of reference materials Sn^0, SnO and SnO_2, respectively; and x, *y* and *z* correspond to the atomic fraction for each component. The results are presented in Figure S12c.

$$\text{Sample spectrum} = x*\text{X} + y*\text{Y} + z*\text{Z} \qquad \text{(Eq. 3)}$$

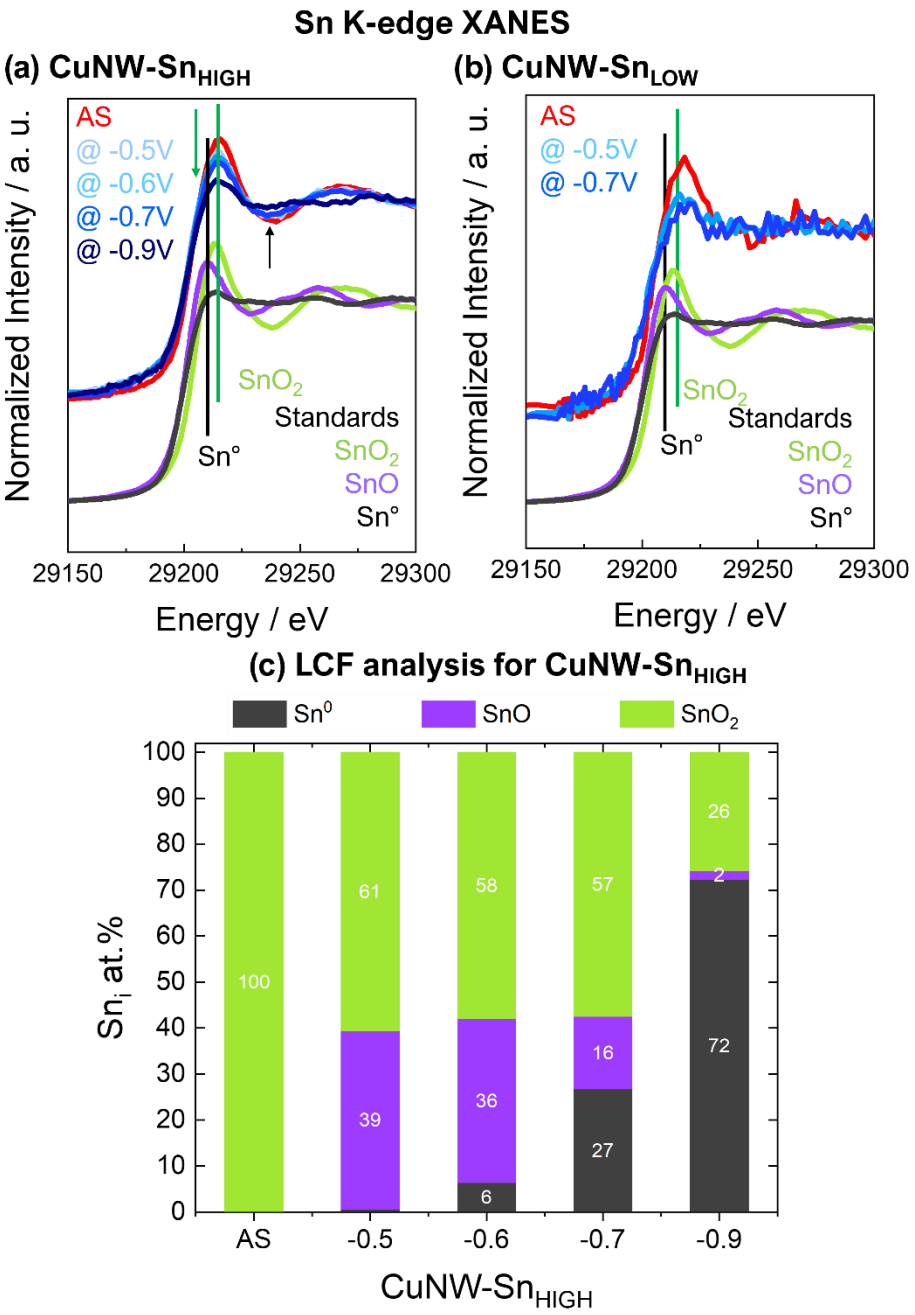

Figure S12. *In situ* Sn K-edge X-ray absorption spectroscopy investigation of CuNW electrodes modified with a variable number of SnO_2 ALD cycles. XANES spectra were collected in as-synthesized condition (red) and during CO_2R electrolysis at different applied potentials for (a) CuNW-Sn_{HIGH} and (b) CuNW-Sn_{LOW}. Reference spectra collected from standards of metallic Sn^0, SnO and SnO_2 are presented for comparison. (c) Sn speciation in CuNW-Sn_{HIGH} as a function of applied bias as investigated by LCF analysis of *in situ* XANES.

S.3.3 Ex situ investigation of Cu L- and Sn M-Edges via soft X-ray absorption spectroscopy

The Cu L- and Sn M-edge XAS experiments were conducted at the LiXEdrom experimental station at the UE56/2 PGM-2 beamline at BESSY II.[6] Cu L- and Sn M-edge spectra for CuNW-Sn samples were measured at room temperature and in Total Electron Yield (TEY) detection mode and with horizontally linear polarization of the beam (Figure S13a-b). The TEY measurements were carried out by collecting the drain current from the sample. The sample

holder was connected to an ammeter (Keithley 6514). In order to avoid radiation damage, the incoming photon flux was adjusted to get a TEY current from the sample of around 10 pA. XAS spectra for each sample were collected at a few locations to ensure reproducibility of the data and to further minimize radiation damage as well as local heating. The probing depth is restricted to the mean free path of generated photoelectrons (<10 nm[7,8]) providing significant surface sensitivity in comparison with fluorescence or transmission detection. The CO_2ER electrolysis tests were performed inside a O_2-free glovebox (O_2 <30 ppm) using the typical H cell and experimental conditions described in CO_2ER testing details (***Section S.1.2***). The samples were dried and stored under N_2 atmosphere inside the glovebox prior XAS measurements. A brief period of exposure to air (~15-20 min) was necessary to transfer the samples from the glove box to the high vacuum chamber. A series of relevant standards (Cu and Sn metals and oxides) were also measured for reference (Figure S13c-d).

In the as-synthesized condition, the Cu L-edge spectra (Figure S13a) for the bare CuNW and CuNW-Sn_{LOW} exhibit white line L_3 and L_2 peaks typical of $Cu(OH)_2$ (931.1, 950.9 eV) and CuO (931.4, 951.4 eV) reference spectra.[9–11] For CuNW-Sn_{HIGH} (which are coated by approximately 20 nm ALD SnO_2) the Cu L-edge region is completely featureless due to blocking of Cu photoelectrons by the SnO_2 overlayer, providing evidence of both the surface sensitivity of the method and of the conformal nature of the ALD SnO_2 film. The Sn M-edge spectra (Figure S13b) of as-synthesized CuNW-Sn_{LOW} and CuNW-Sn_{HIGH} display signals in the expected positions for the main peaks in SnO (487.9 eV and 495.5 eV)[12,13] and SnO_2 (~492 eV and ~500 eV).[12,13] The spectra best resemble the SnO reference; however, the SnO reference spectrum is likely to display a mixture of SnO and SnO_2 features due to surface oxidation during handling in air (Figure S13d). On the other hand, CuNW-Sn samples composed of SnO_2 ALD layers, as confirmed by Sn 3d XPS spectra (*vide infra*), can display SnO features due radiation induced (partial) reduction of SnO_2 layer. These convoluted features of Sn^{2+} and Sn^{4+} are hereafter denoted SnO_x.

After pre-reduction to −0.5 V, the bare CuNW and CuNW-Sn_{LOW} display Cu L_3, L_2 peaks at 933.9 and 953.8 eV respectively, which can be assigned to a mix of reduced Cu in Cu^0 or Cu^+ oxidation states.[9,10] Similar features are observed after electrolysis at −0.7 V. Interestingly, at both reduction stages (−0.5 V and −0.7 V) CuNW-Sn_{LOW} displays Cu^{2+} features (931.1, 950.9 eV) which decrease at higher reductive bias. After the CuNW-Sn_{HIGH} undergoes pre-reduction, it still shows no peaks in the Cu-L edge region, indicating the persistence of a Sn enriched surface, at least as thick as the probing depth (~10 nm). However, after electrolysis at −0.7 V, CuNW-Sn_{HIGH} displays incipient Cu-L edge features at the positions expected for the main features of metallic Cu, but without any evidence of Cu^{2+}. The emergence of Cu signal in this sample coincides with the decrease in surface Sn signal observed in Sn M-edge spectra.

The Sn M-edge spectra (Figure S13b) reveal that the SnO_x overlayer persists unchanged after the CP pre-reduction up to −0.5 V. However, after CO_2 electrolysis at −0.7 V a decrease in Sn signal is observed for both CuNW-Sn_{LOW} and CuNW-Sn_{HIGH}, suggesting that the surface Sn content decreases under CO_2ER conditions (possibly due to migration from surface to bulk or dissolution) to yield a surface composition differing from the as-synthesized state. This is consistent with the observations of Schreier et al.,[14] and are discussed in more detail in the XPS section in main text. In the sample with high Sn content (CuNW-Sn_{HIGH}) the weakened signal (Figure S13b) displays a shoulder at ~485 eV characteristic of metallic Sn^0,[8] in agreement with

GI-XRD characterization displaying formation of Cu_6Sn_5 alloy (ESI Figure S8), as well as the typical features of SnO.[8,12] In comparison, the sample with little Sn ($CuNW\text{-}Sn_{LOW}$) shows a significant attenuation of its SnO_x signal after just 10 min of electrolysis at −0.7 V, and after 2 h at −0.7 V no signal from Sn is observable.

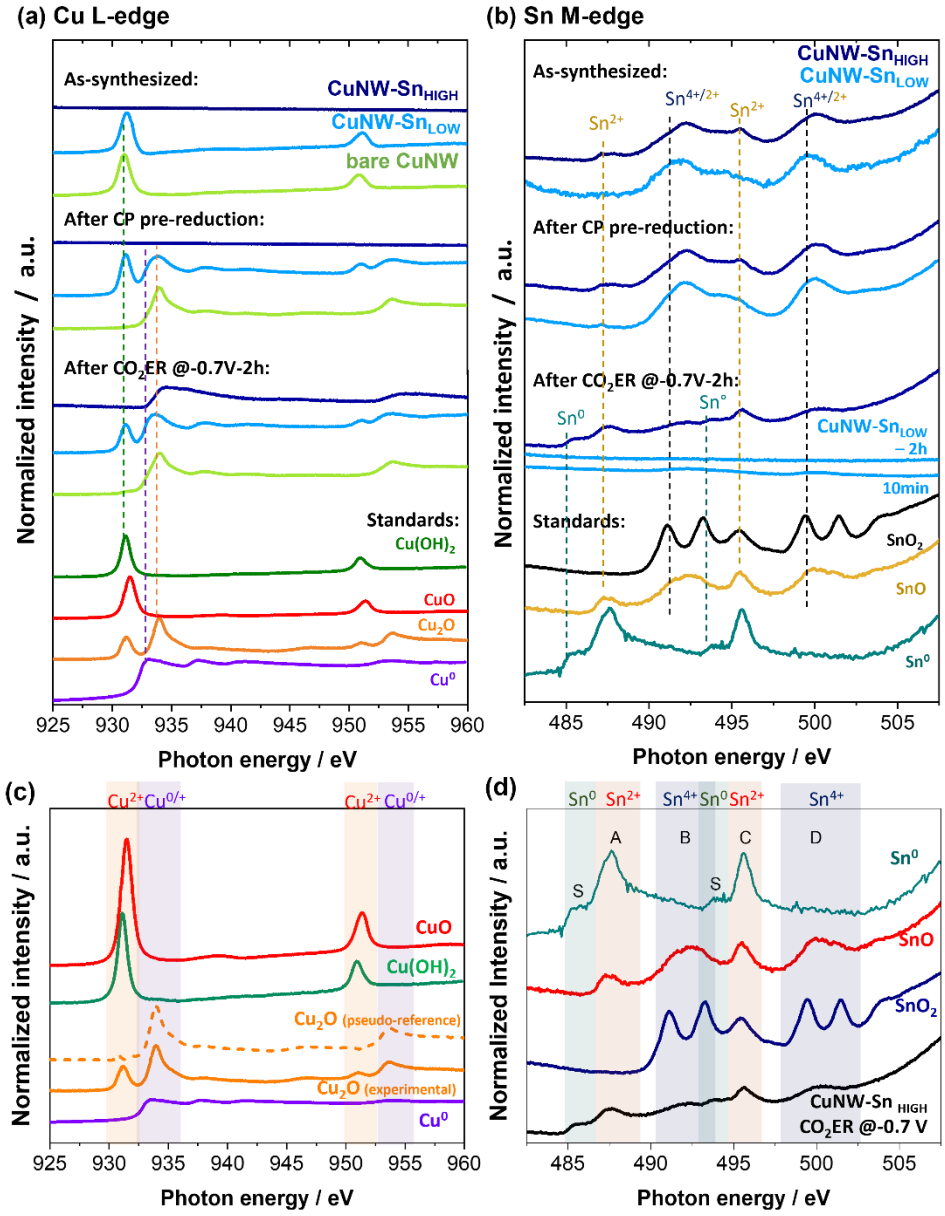

Figure S13. Ex-situ soft XAS investigation of CuNW sample modified with low or high SnO_2 content. (a) Cu L-edge and (b) Sn M-edge spectra in the as-synthesized state (top), after CP pre-reduction at –2 mA cm^{-2} to –0.5 V (middle) and after CO_2ER at –0.7 V for 2 h unless otherwise specified (bottom). Reference spectra collected from standards of metallic Cu and Sn as well are their oxides are presented, and all spectra are offset vertically to facilitate their comparison. Soft XAS reference spectra for (c) Cu L-edge and (d) Sn M-edge collected for metallic Cu and Sn as well are their oxides. Note that the Cu_2O reference spectrum displays a Cu^{2+} contribution (931 and 951 eV) due to partial oxidation in air, this Cu^{2+} contribution was subtracted to yield a clean pseudo-reference Cu_2O spectrum, presented as a dotted orange line in (a).

The soft X-ray absorption investigation indicates that in all samples, surface Cu appears readily reduced from Cu^{2+} to Cu^0/Cu^+ after the pre-reduction step to −0.5 V. On the other hand, Sn persists as a SnO_x enriched surface overlayer after the pre-reduction step. However, after

electrolysis at −0.7 V, the Sn M-edge signal decreases for both samples CuNW-Sn_{LOW} and CuNW-Sn_{HIGH} in comparison to the as-synthesized state, indicating a significant decrease in Sn content at the near surface depth (<10 nm) probed by soft XAS, presumably due to migration from surface to bulk or dissolution. Additionally, the results indicate residual surface content of oxidized Cu as Cu^{+} and Cu^{2+}, as well as SnO. Due to the brief exposure to air of the sample prior to insertion into the vacuum chamber, it is not possible to know if the observed Cu^{+}, Cu^{2+}, SnO surface species persist at the applied reductive bias or if they are quickly and spontaneously formed after removing the bias during sample handling. For this reason, a quasi insitu XPS study was conducted (main text Figure 4). Nevertheless, the reproducible trend of Cu^{2+} signal in CuNW-Sn_{LOW} sample in the different conditions tested suggests that the inclusion of low amounts of Sn may render near-surface Cu atoms more prone to oxidation. Similar trends were observed in *ex situ* surface-sensitive XPS investigations of CuSn alloys.[15,16]

Reference spectra for metallic Cu were collected on a metal foil in total fluorescence yield (TFY) detection mode to minimize contribution from the native surface oxide layer. The Cu foil was leached in HCl 15% prior measurement. The photon intensity was detected using a GaAsP diode (Hamamatsu, model G-1127-04). Sn foil was leached in a mixture of 4 mL HCl 20% and 0.5g of Zn for 10 min prior measurement and the spectrum collected in TEY mode. Cu_2O, CuO, $Cu(OH)_2$, SnO and SnO_2 powders were used as reference materials and their spectra were measured as finely dispersed powders attached to Carbon tape and collected in TEY mode. Cu_2O was stored and handled under N_2 atmosphere but was briefly exposed to air during sample transfer to vacuum chamber leading to a detected $Cu(OH)_2$ surface contamination, see peaks at 931.4 and 951.4 eV (Figure S13c). The $Cu(OH)_2$ component was subtracted to yield a clean Cu_2O "pseudo-reference" spectrum. (See Fig. S13c).

The collected Sn M-edge reference spectra for metallic Sn foil, and powder SnO and SnO_2 are displayed in Figures S13b. The SnO_2 powder reference spectrum displays the typical features reported in literature in the regions labeled B, D assigned to Sn^{4+}.[12,13] The SnO powder was stored and handled inside the glovebox under N_2 atmosphere but was briefly exposed to air prior sample insertion to vacuum chamber. The SnO spectrum displays the typical features reported in literature for SnO in the regions labeled A, C assigned Sn^{2+} and broad signals are observed in the areas labeled B, D.[12,13] The latter are probably associated to the presence of SnO_2 at the powder surface due to oxidation in air. The metallic Sn reference spectrum was collected on a Sn foil leached in a mix of 4mL HCl 20% and 0.5g Zn during 10 min prior testing. The Sn° spectrum displays the typical shoulders at 485 eV and 293 eV (labeled S in the figure) as well as strong signals in the regions A, C,[8] which are most likely due to the presence of surface SnO. The surface oxidation in SnO and Sn° as well as the rise in background at high energy range due to the signal of O K-edge, impose limitations on the quantitative analysis of the Sn M-edge spectra.

S.4 Quasi in situ XPS measurements

X-ray photoelectron spectroscopy measurements were carried out in a SPECS PHOIBOS 100 analyzer using Monochromatic Al Kα radiation (hν = 1486.74 eV, SPECS FOCUS 500 monochromator). The pass energy was set to 10 eV with step size of 0.05 eV. The spectra were fitted in CasaXPS software using a Shirley background subtraction. The as-synthesized samples were calibrated with respect to the adventitious carbon C 1s peak at 285 eV. The CO_2ER electrolysis tests were performed inside a O_2-free glovebox (O_2 < 1 ppm) using the typical H cell and experimental conditions described in CO_2ER testing details (***Section S.1.2***). The post-electrolysis samples were dried and stored under N_2 atmosphere inside the glovebox prior XPS measurements. In order to avoid any exposure to air the samples were transferred from the glovebox to the XPS vacuum chamber under inert atmosphere using a transfer arm.

S.4.1 Peak model details for Cu 2p and Cu LMM Auger spectra

The raw spectra collected on post-electrolysis samples display very good alignment for expected Cu 2p and Cu LMM auger components of metallic Cu according to the values reported by Biesinger[17] and a metallic Cu standard measured in our XPS instrument, see Table S2. The metallic Cu reference was cleaned by Ar sputtering inside the vacuum chamber to remove surface oxide.

Table S2. XPS peak model details for metallic Cu

		Parameters reported by Biesinger				Sputtered Cu°				CuNW		
		KE (eV)	Area %	FWHM	A/A1	KE (eV)	Area %	FWHM	A/A1	No Sn -0.7V	low Sn -0.7V	high Sn -0.7V
	Comp.									KE (eV)	KE (eV)	KE (eV)
Cu LMM[(a)]	1	921.35	13	1.28		921.27	12.8	1.4		921.32	921.29	920.98
	2	919.7	10	1.11	0.77	919.62	9.4	1.11	0.73	919.67	919.64	919.33
	3	918.64	23	0.84	1.77	918.56	21.3	0.86	1.67	918.61	918.58	918.27
	4	918.09	29	2.32	2.23	918.01	30.6	2.37	2.40	918.06	918.03	917.72
	5	916.2	6	1.1	0.46	916.12	5.7	1.13	0.44	916.17	916.14	915.83
	6	914.26	18	2.78	1.38	914.18	18.7	2.80	1.46	914.23	914.20	913.89
	7	910.94	1	1.42	0.08	910.86	1.5	1.50	0.12	910.91	910.88	910.57
Cu 2p[(b)]	3/2	932.63	100	0.83		932.71		0.86		932.74	932.78	933.1
	1/2					952.46		1.47		952.49	952.53	952.87

[(a)] Cu LMM model built with GL(30) line-shape. [(b)]Cu 2p spectra modeled with GL(90) line-shape for metallic Cu°.

The CuO, $Cu(OH)_2$ and Cu_2O peak models used for analysis of Cu 2p and Cu LMM spectra of as synthesized samples: Bare CuNW ($Cu(OH)_2$), CuNW-Sn_{LOW} (CuO) and post electrolysis samples as summarized in Table S3. The peak models are based in previous report by Biesinger[17] presented in the table for comparison.

Table S3. XPS peak model details for oxidized copper species

		Parameters reported by Biesinger					CuNW-Sn$_{LOW}$ (As-synth.)		
		Comp	**KE (eV)**	**Area%**	**FWHM**	**A/A1**	**KE (eV)**	**Area%**	**FWHM**
CuO	**Cu LMM[a]**	Comp. 1	919.9	26.0	3.7		919.7	23.5	3.5
		Comp. 2	917.9	40.0	2.0	10.9	917.6	38.1	2.1
		Comp. 3	914.2	31.0	4.7	8.4	914.0	33.6	4.7
		Comp. 3	911.4	3.0	2.2	0.8	911.1	2.8	2.1
	Cu 2p[b]	Comp. 1	933.11	31	2.07		933.5	30.0	2.2
		Comp. 2	934.48	33	3.05	1.37	934.9	33.0	3.2
		Comp. 3	940.52	3	1.03	6.04	940.9	3.0	1.19
		Comp. 4	941.66	28	3.55	1.13	942.0	29.0	3.7
		Comp. 5	944.12	7	1.17	2.05	944.1	5.5	1.2
							Bare CuNW (As-synth.)		
Cu(OH)$_2$	**Cu LMM[a]**	**Comp**	**KE (eV)**	**Area%**	**FWHM**	**A/A1**	**KE (eV)**	**Area%**	**FWHM**
		Comp. 1	920.1	10.0	3.3		920.2	16.3	3.5
		Comp. 2	916.5	69.0	4.1	20.8	917.6	63.8	4.10
		Comp. 3	911.9	21.0	4.5	6.3	912.0	20.0	4.6
	Cu 2p[b]	Comp. 1	934.7	60.0	2.9		934.3	59.6	3.0
		Comp. 2	939.3	6.0	2.8	0.2	938.9	7.9	3.0
		Comp. 3	942.2	28.0	3.7	0.9	941.8	27.2	3.7
		Comp. 4	944.1	7.0	1.8	0.2	943.8	6.3	2.0
							CuNW-Sn$_{LOW}$ (after CO_2ER at 0.7V and exposure to air 20mins)		
		Comp	**KE (eV)**	**Area%**	**FWHM**	**A/A1**	**KE (eV)**	**Area%**	**FWHM**
Cu$_2$O	**Cu LMM[a]**	Comp. 1	921.7	5	2.2		921.5	5.0	2.3
		Comp. 2	918.0	55	4.01	11.00	917.7	55.0	4.1
		Comp. 3	916.9	23	1.57	4.60	916.6	23.0	1.7
		Comp. 4	913.2	17	4.1	3.40	913.0	17.0	4.2
	Cu 2p[c]	Comp. 1	932.2	100	1				

[a] Cu LMM model built with GL(30) line-shape. [b] Cu 2p spectra modeled with GL(30) for CuO and CU(OH)$_2$.[c] Cu 2p spectra modeled with GL(80) line-shape for metallic Cu$_2$O.

S.5 Structural characterization by TEM

The structure of the CuNW-Sn samples was investigated by transmission electron microscopy (TEM) in as-synthesized state and following CO_2ER experiments at different applied biases. To minimize the impact of air exposure on post-electrolysis samples, electrochemical testing and TEM sample preparation were conducted inside a glovebox. The post-electrolysis samples were deposited on carbon-coated Ni TEM grids, mounted on a TEM specimen holder and transferred under inert atmosphere into the TEM (Zeiss LIBRA 200FE). A brief exposure to air (<10 s) was unavoidable during sample loading to the TEM instrument.

Detailed information on lattice spacing assignments from SAED analysis is presented in Table S4.

Table S4. SAED assignment in CuNW-Sn samples

	SAED	Assignment			Assignment		
	d / Å	***Phase***	***Hkl***	***d / A***	***phase***	***hkl***	***d / Å***
CuNW-Sn_{HIGH} As-syynthesized	2.55	CuO *C2/c*	-111 ; 002	2.53			
	2.31	CuO *C2/c*	111 ; 200	2.31			
	1.87	CuO *C2/c*	-202	1.87			
	1.59	CuO *C2/c*	202	1.58			
	1.43	CuO *C2/c*	022	1.42			
CuNW-Sn_{HIGH} after CO_2ER at -0.6 V	3.34	SnO_2 *P42/mnm*	110	3.34			
	2.71	SnO_2 *P42/mnm*	101	2.64	SnO *P4/nmm*	-1-10	2.69
	2.10	Cu *Fm-3m*	111	2.08			
	1.83	Cu *Fm-3m*	200	1.80			
	1.73	SnO_2 *P42/mnm*	211	1.76	SnO *P4/nmm*	-1-1-2	1.80
	1.45	SnO *P4/nmm*	-10-3	1.48			
	1.29	Cu *Fm-3m*	220	1.28			
	1.10	Cu *Fm-3m*	311	1.09			
	1.05	Cu *Fm-3m*	222	1.04			
CuNW-Sn_{HIGH} after CO_2ER at -0.9 V	2.94	Cu_6Sn_5 *C12/c1*	-1-13	2.97	*Sn I41/amd*	-200	2.92
	2.77	SnO2 *P42/mnm*	101	2.64	*Sn I41/amd*	-10-1	2.80
	2.11	Cu_6Sn_5 *C12/c1*	-1-3-2	2.11	Cu *Fm-3m*	111	2.08
	1.74	SnO2 *P42/mnm*	211	1.76	Cu *Fm-3m*	200	1.80
	1.49	Cu_6Sn_5 *C12/c1*	-2-26	1.48	SnO *P4/nmm*	-10-3	1.48
	1.33	Cu *Fm-3m*	220	1.28			
	1.22	Cu_6Sn_5 *C12/c1*	-3-36	1.21			
	1.09	Cu Fm-3m	311	1.09			
CuNW-Sn_{LOW} As-syynthesized	2.54	CuO C2/c	-111 ; 002	2.53			
	2.37	CuO C2/c	111 ; 200	2.31			
	1.86	CuO C2/c	-202	1.87			
	1.61	CuO C2/c	202	1.58			
	1.40	CuO C2/c	22	1.42			

HR-TEM images and correponding FFT analysis for lattice spacing assignments for CuNW-Sn_{HIGH} after CO_2ER electrolysis at –0.6 V and –0.9 V are presented in Figure S14 and S15 .

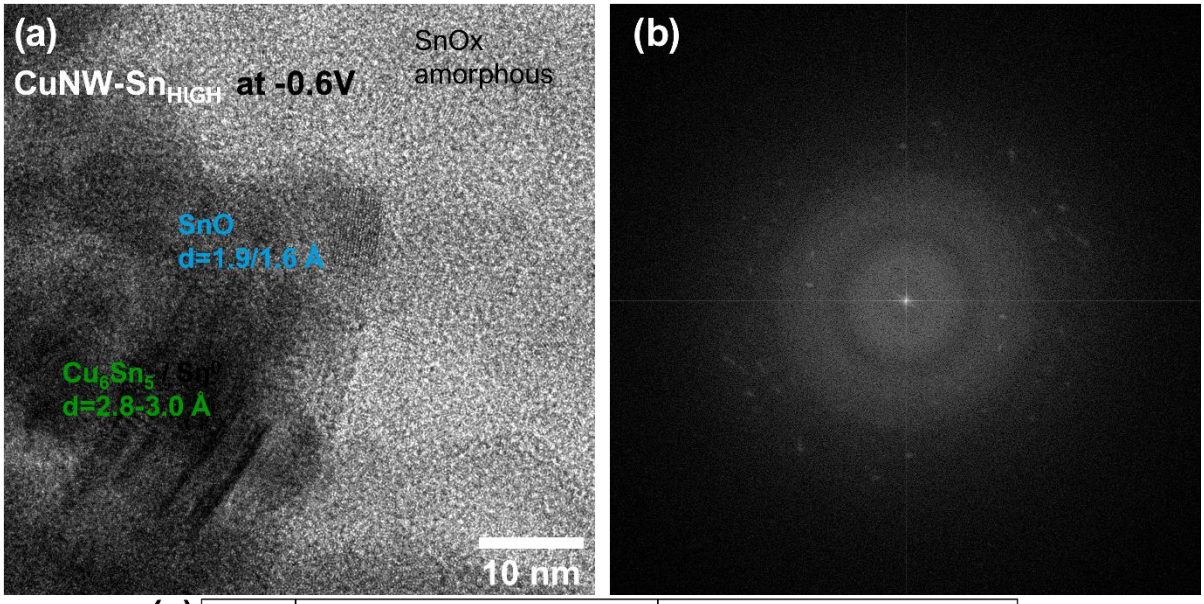

(c)

FFT	Assignment			Assignment		
d / A	*phase*	*hkl*	*d / A*	*phase*	*hkl*	*d / A*
3	SnO *P4/nmm*	-10-1	2.99			
2.9	Cu_6Sn_5 *C12/c1*	-1-13	2.97	*Sn I41/amd*	-200	2.92
2.8				*Sn I41/amd*	-10-1	2.80
1.9	SnO *P4/nmm*	-200	1.90			
1.7-1.6	SnO *P4/nmm*	-2-1-1	1.60	SnO2 *P42/mnm*	211	1.76

Figure S14. HR-TEM micrographs of CuNW-Sn_{HIGH} (20nm SnO_2 layer) after CO_2ER at -0.6 V (a) corresponding FFT analysis (b). (c) Table of assignment of lattice spacing identified by FFT.

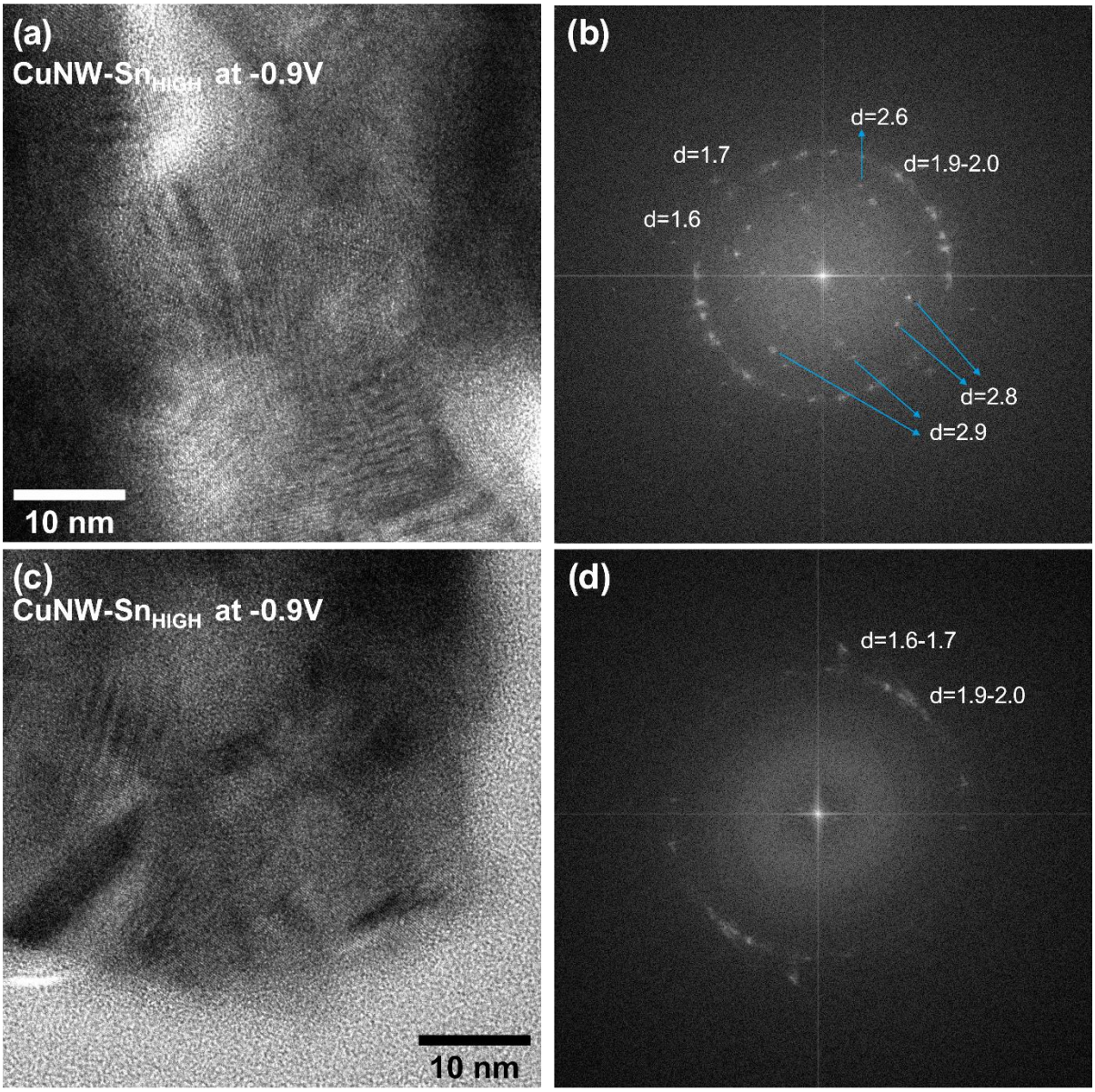

(e)

FFT	Assignment			Assignment		
d / A	*phase*	*hkl*	*d / A*	*phase*	*hkl*	*d / A*
2.9	Cu_6Sn_5 *C12/c1*	-1-13	2.97	*Sn I41/amd*	-200	2.92
2.8				*Sn I41/amd*	-10-1	2.80
2.0	Cu_6Sn_5 *C12/c1*	-1-3-2	2.11			
1.9	SnO *P4/nmm*	-200	1.90			
1.6	SnO *P4/nmm*	-2-1-1	1.60	SnO2 *P42/mnm*	211	1.76

Figure S15. HR-TEM micrographs of CuNW-Sn$_{HIGH}$ (20nm SnO_2 layer) after CO_2ER at -0.9 V (a,c) corresponding FFT analysis (b,d). (e) Table of assignment of lattice spacing identified by FFT.

Additional details on Cu-Sn EF-TEM mappings for CuNW-Sn$_{HIGH}$ as synthesized and after CO_2ER electrolysis at –0.6 V and –0.9 V are presented in Figure S16.

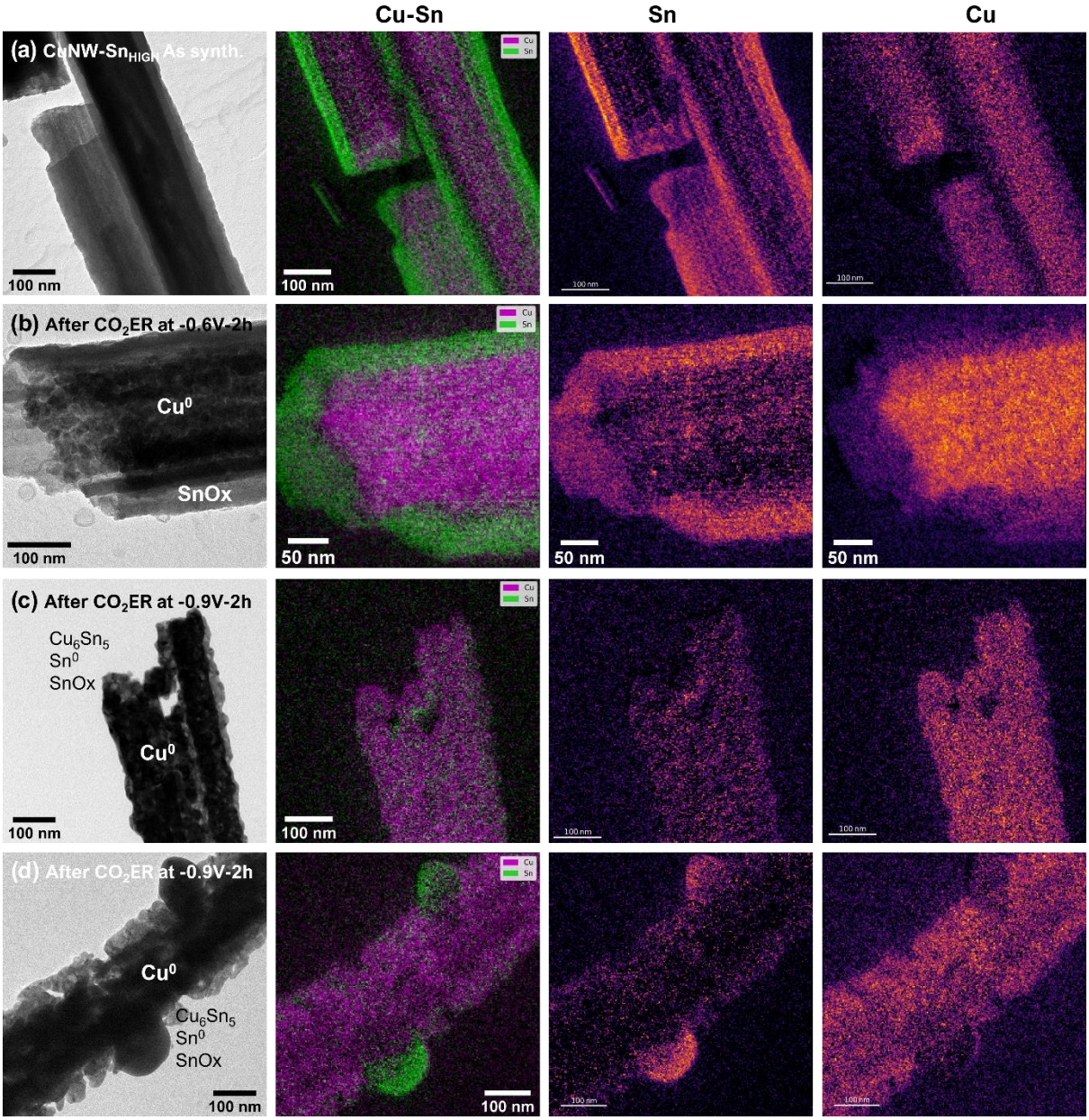

Figure S16. EF-TEM mappings of Cu (L-edge: purple) and Sn (M-edge: green) in CuNW-Sn$_{HIGH}$ as synthesized (a), and after electrolysis at (b) –0.6 V and (c-d) –0.9 V.

S.6 Surface composition after extended electrolysis

The Sn at.% surface composition was examined by quasi *in situ* XPS after extended electrolysis time of 4 h for CO- and formate-selective catalyst electrodes. The CO_2ER activity of CuNW-Sn_{LOW} and CuNW-Sn_{HIGH} display very good stability over the course of the 4 h test. Furthermore, the surface composition after 4h electrolysis test displays very minor changes as compared the one observed after 2h electrolysis (reported in main text Figure 4 and 5, and Table 1). The results indicated that although the CuNW-Sn samples have dynamic surface composition during initial stage of electrolysis, the surface composition estabilizes over time yielding stable activity.

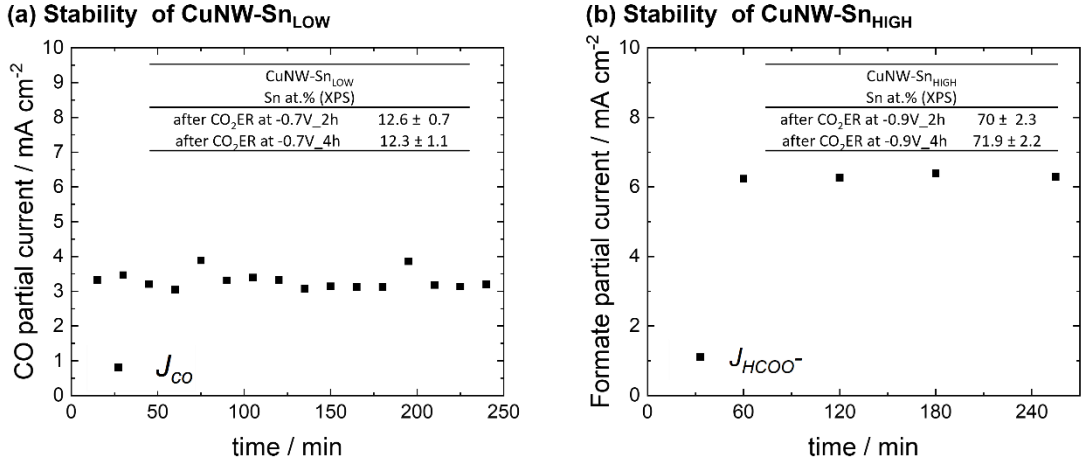

Figure S17. CO_2ER activity during 4h of electrolysis for (a) CuNW-Sn_{LOW} and (b) CuNW-Sn_{HIGH}. The Surface Sn composition after 2h and 4h of electrolysis for each sample type are displayed as a table inset. Differences in the periodicity of product measurements are due to the different analytical methods employed for CO and $HCOO^-$ quantification (in-line GC and post-run HPLC, respectively).

S.7 Effect of air exposure on observed surface composition

The surface composition of the samples after CO_2ER electrolysis at different potentials -0.7 V and –0.9 V was investigated by quasi in situ XPS (preventing any exposure to air) and after exposing the samples to air for 20 mins. The observed speciation for Sn and Cu is summarized in Fig. S18. The Sn speciation was calculated by deconvolution of the Sn 3d signal spectrum and Cu speciation was calculated by deconvolution of the Cu LMM spectra according to the peak model described in section S.4.1. The results show that for samples CuNW-Sn_{LOW} and CuNW-Sn_{HIGH} the metallic Sn component formed during CO_2 electrolysis at –0.7 V and –0.9 V is rapidly re-oxidized to SnO_x (combined Sn^{2+} and Sn^{4+} components) after a brief exposure to air (20 mins). In the case of Cu, the Quasi in situ XPS Cu LMM spectra of all post electrolysis samples display fully reduced Cu. After exposure to air for 20 mins, the XPS data indicates a minor oxidation (<16%) to Cu_2O in the bare CuNW and CuNW-Sn_{HIGH}; while CuNW-Sn_{LOW} displays major oxidation to both Cu_2O and $Cu(OH)_2$ in the same time frame indicating that this sample is more prone oxidation in air. A similar trend was observed in the quantitative analysis of the soft XAS Cu L-edge spectra of samples after CO_2 electrolysis at –0.7 V. These results

highlight the importance of conducting quasi in situ analysis of surface composition, since even brief exposure to air can yield strong effect of oxidation of metal components.

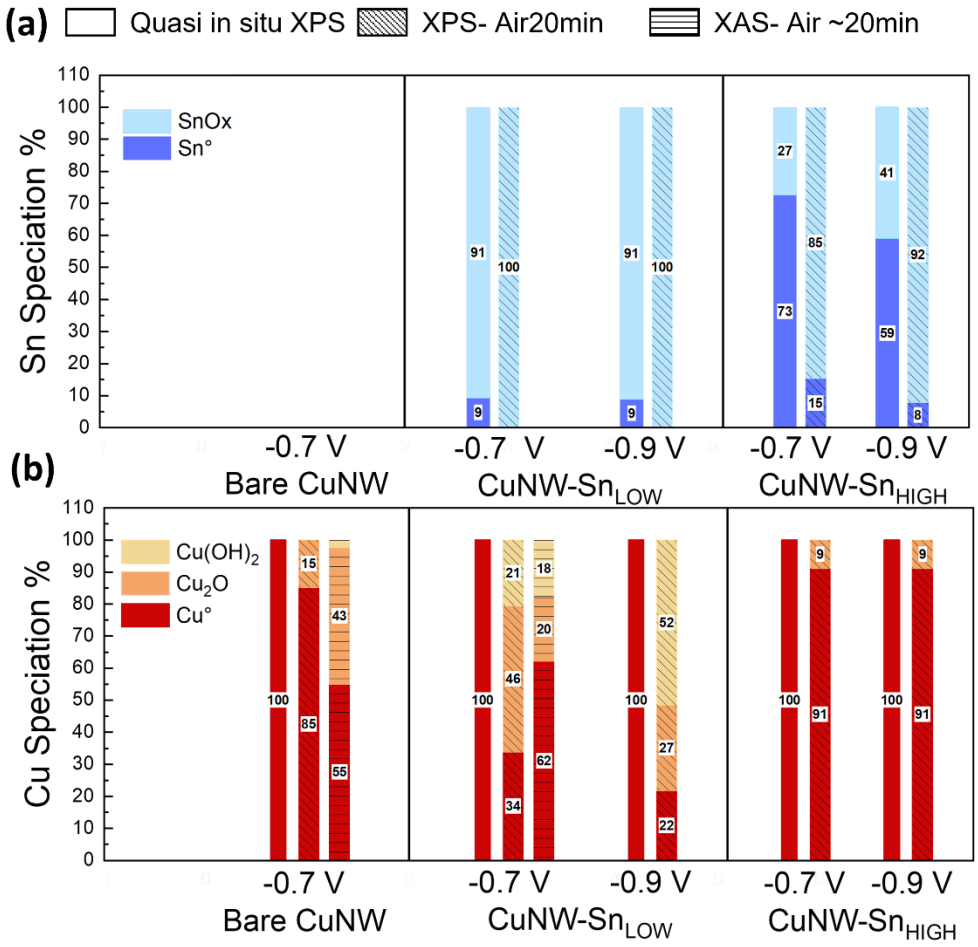

Figure S18. Effect of air exposure on surface speciation for (a) Sn and (b) Cu in CuNW samples after CO_2ER electrolysis at –0.7 V or –0.9 V investigated by quasi in situ XPS (no exposure to air), after 20mins of air exposure (XPS) and by ex situ XAS (~20-30 mins or air exposure). Each species M_X % is referred to total metal M, i.e. Cu° %= Cu°/(Cu°+Cu^++Cu^{2+})*100.

S.8 Computational details

Density functional theory (DFT) modeling was carried out through the Vienna Ab Initio Simulation Package (VASP).[18,19] We chose the PBE density functional[20] including dispersion through the DFT-D2 method,[21,22] with reparametrization of C_6 coefficients for metals performed by one of our group.[23] We accounted for implicit solvation via the VASP-MGCM framework.[24,25] Inner electrons were represented by PAW pseudopotentials[26,27] and the monoelectronic states for the valence electrons expanded as plane waves with a kinetic energy cutoff of 450 eV.

We modeled the Sn-rich catalyst, selective to $HCOO^-$ as Cu_6Sn_5(102). We also designed three impurity models to reproduce the CO-selective $Cu_{10}Sn$ solid solution. For the three impurity models, we replaced 1, 1, and 3 surface atoms on Cu(100) (3×3), (111) (3×3), and (111) (3×3) matrices with Sn substituents, thus accounting for an overall Sn content of 4, 4, and 11 Sn at. %, respectively.

Since both metallic and oxidic Sn species were observed under electrochemical CO_2 reduction conditions (Figure S12), we built two epitaxial supercells from the most stable facets of SnO_2 and SnO.[28] 4 layers of SnO_2(110) (4×3) were deposited on 4 layers of Sn(100) (2×3), while the second system consisted of a 3L SnO(001) (3×5)/3L Sn(100) expitaxy, see Figure S19. The three outermost SnO_2 layers and the SnO surface layer were depleted of atomic oxygen to achieve a Sn content of 84 at.% and 73 at.% as in the CuNW-Sn_{HIGH} catalyst. Following the framework developed to assess surface reconstruction on oxide-derived copper,[29] we employed *ab initio* molecular dynamics[30] on both system for 1.0 + 5.0 ps (SnO_2/Sn) and 1.0 + 5.0 ps (SnO/Sn) at T = 700 K (3.0 fs time step, canonical ensemble, NVT, Nosé-Hoover thermostat)[31]. The resulting systems exhibited multiple surface sites including residual SnO_x species and undercoordinates domains, whose reactivity for HER and CO_2R was then assessed (Table S7).

All the models contained at least six layers, where the three uppermost were fully relaxed to mimic the surface layer and the rest fixed to the bulk distances. The vacuum between the slabs was at least 12 Å. We sampled the Brillouin zone by a Γ-centered k-points mesh from the Monkhorst-Pack method,[32] with a reciprocal grid size smaller than 0.03 $Å^{-1}$. For calculating adsorption energies, we placed the adsorbates only on one side of the slab, thus we introduced an artificial dipole correction to remove spurious contributions arising from the asymmetric slab model.[33] Adsorption energies are reported using the following as references: CO_2(g), H_2(g), and the Cu, Cu-Sn, and Sn surfaces. When proton-coupled electron transfers were considered, the relative energy between the H^+ and the H_2(g) at U = 0 V was calculated applying the Computational Hydrogen Electrode (CHE) formalism.[34,35] Conversely, the Gibbs free energy of $HCOO^-$ was obtained from its corresponding conjugated acid from Equation 4.[36]

$$G_{B^-} = G_{HB} - k_B \cdot T \cdot \ln(10) \cdot (pH - pK_a) \qquad \text{(Eq. 4)}$$

Table S5. Bader charges (in elementary charge, $|e^-|$) for surface Sn and Cu on the selected Cu-Sn models

Model	q_{Sn} / $\|e^-\|$	q_{Cu} / $\|e^-\|$
Cu(100)-4at.%	0.29	–0.07
Cu(111)-4at.%	0.69	–0.02
Cu(111)-11at.%	0.63	–0.11
Cu_6Sn_5(102)	0.25	–0.16
Sn(100)	0.02	

Table S6. Surface energies γ (J m^{-2}) for selected facets of Cu_6Sn_5 and Sn. Lowest energy configurations are highlighted in grey.

Facet	γ / J m^{-2}
Cu_6Sn_5(100)	1.07
Cu_6Sn_5(102)	0.71
Cu_6Sn_5(110)	0.92
Sn(010)	0.35
Sn(100)	0.35
Sn(110)	0.51

Table S7. Gibbs free energy of adsorption for *H, *COOH, *CO, and *HCOO on different active sites on Sn(100) and SnO_x derived catalysts versus average Sn-Sn coordination number $\overline{N}_{Sn\text{-}Sn}$ and average Sn Bader charge $\overline{q}_{Sn}$. Highlighted values indicate residual SnO_x sites. Coordination numbers have been calculated according to Sn-Sn distances in the bulk (3.11 Å first neighbor, 3.82 Å second neighbor).

Adsorbate	*Adsorption site*	$\overline{N}_{Sn\text{-}Sn}$	$\overline{q}_{Sn}$ / $\lvert e^- \rvert$	ΔG / eV
**H*	Sn(100)	8.00	+0.02	+0.36
	SnO_2(110)/Sn(100)	7.97	+0.06	+0.54
		8.00	+0.01	+0.75
		7.95	+0.00	+0.78
	SnO(001)/Sn(100)	7.97	–0.03	+0.47
		6.50	+0.15	+0.91
		6.44	+0.13	+0.85
**COOH*	Sn(100)	8.00	+0.02	+0.22
	SnO_2(110)/Sn(100)	7.95	+0.05	+0.58
		8.00	+0.01	+0.76
		9.94	+0.03	+0.87
	SnO(001)/Sn(100)	6.00	+0.02	+0.67
		7.00	+0.17	+0.81
		6.87	+0.13	+0.84
**CO*	Sn(100)	8.00	+0.02	+0.57
	SnO_2(110)/Sn(100)	7.95	+0.05	+0.46
		8.50	+0.00	+0.47
		7.43	+0.05	+0.38
	SnO(001)/Sn(100)	6.50	–0.06	+0.48
		5.00	+0.17	+0.46
		7.00	+0.13	+0.46
**HCOO*	Sn(100)	8.00	+0.02	–0.66
	SnO_2(110)/Sn(100)	6.47	+0.05	–0.21
		7.96	+0.10	–0.16
		6.47	+0.05	–0.21
	SnO(001)/Sn(100)	6.00	+0.02	–0.02
		6.94	+0.15	–0.31
		6.87	+0.14	–0.24

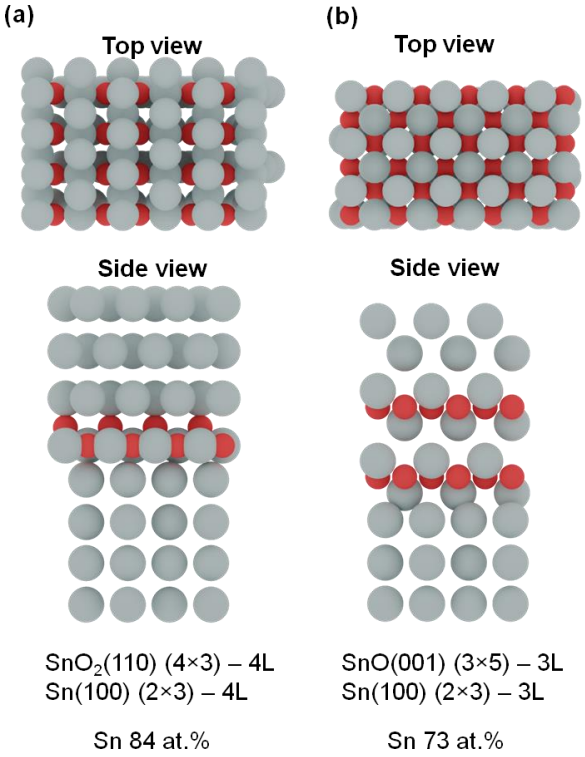

Figure S19. (a) Top and side view for SnO_2(110) (4×3)/Sn(100) (2×3) precursor. Atomic oxygens in the three outermost SnO_2 layers have been removed to mimic reduction conditions. (b) Top and side view for SnO(001) (3×5)/Sn(100) (2×3). Atomic oxygens in the outermost SnO layer have been removed to mimic reduction conditions.

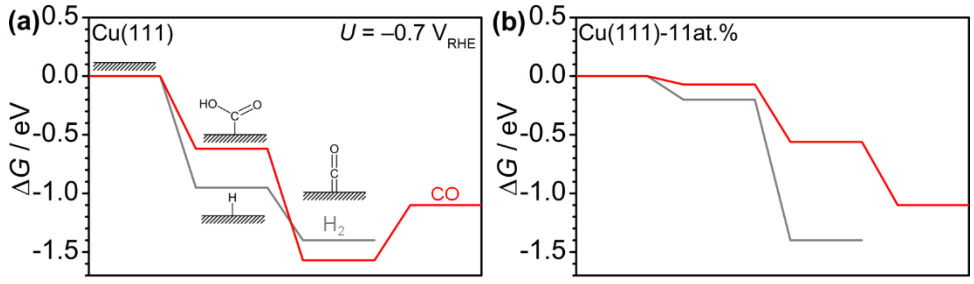

Figure S20. Gibbs free energy diagrams of selected DFT models toward CO (red) and H_2 (grey) at –0.7 V vs RHE: (a), Cu(111) (b), Cu(111)-11at.Sn%.

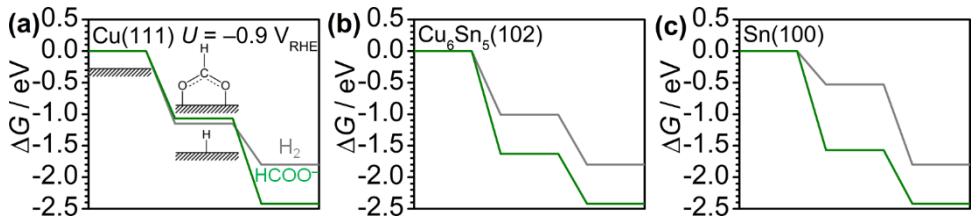

Figure S21. Gibbs free energy diagrams of selected DFT models toward $HCOO^-$ (green) and H_2 (grey) at –0.9 V vs RHE: (a), Cu(111) (b), Cu_6Sn_5(102) (c), Sn(100).

S.9 CO_2ER Activity of planar Cu-Sn catalysts

Flat CuSn catalysts were prepared by deposition of SnO_2 atop flat Cu surfaces. Sputtered Cu (1 µm) samples were modified with SnO_2 by ALD with low (15 cycles) and high (182 cycles) SnO_2 content, denoted sCu-LowSn and sCu-High Sn respectively. The CO_2ER activity results obtained at -0.7 V and -0.9 V are displayed in Figure S22. sCu-LowSn displays improved CO selectivity as compared to a bare Sputtered Cu surface at both potentials, however the maximum CO selectivity observed (66% at -0.9V) is lower than that observed for CuNW-Sn_{LOW} (80% at -0.7 V). Similar trends are observed for sCu-HighSn, at -0.9 V the formate selectivity is 60% significantly lower than that observed for CuNW-Sn_{HIGH} at the same potential (80%). The results indicate that flat Cu-Sn catalysts display similar CO_2ER selectivity trends as high surface area CuNW-Sn catayst. However, lower faradaic efficiencies can be attained with flat catalysts as compared to nanostructured CuNW-Sn indicating that high selectivity towards CO or formate is also favored by HER suppression in nanostructured catalysts.

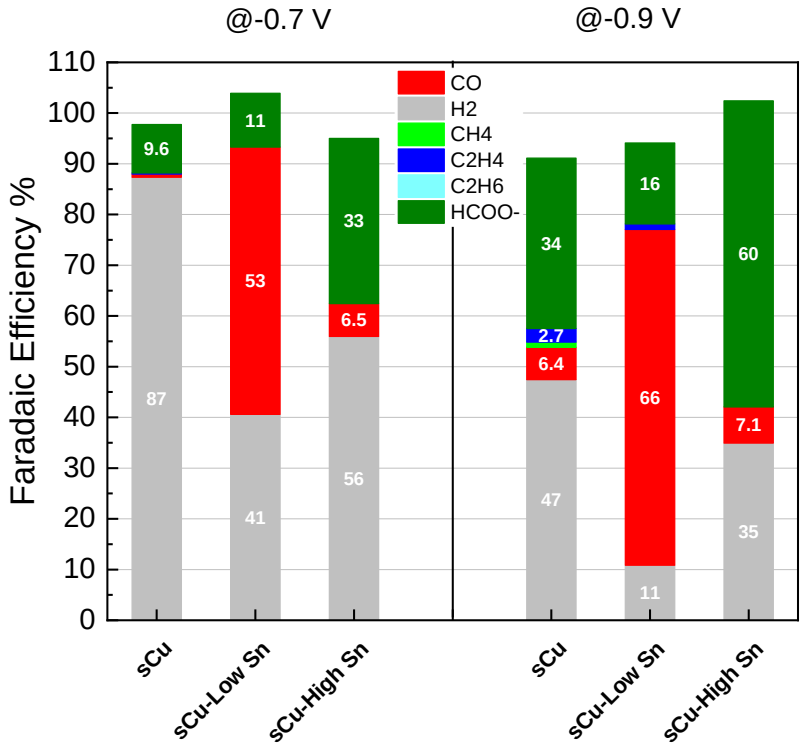

Figure S22. CO_2ER activity of planar Cu-Sn catalysts in CO_2 sat. 0.1M $KHCO_3$ at -0.7V (left) and -0.9V (right).

References

(1) Energie", "Helmholtz-Zentrum Berlin für Materialien und. KMC-2: An X-Ray Beamline with Dedicated Diffraction and XAS Endstations at BESSY II. *J. large-scale Res. Facil. JLSRF* **2016**, *2* (A49), A49. https://doi.org/10.17815/jlsrf-2-65.

(2) Henke, B. L.; Gullikson, E. M.; Davis, J. C. X-Ray Interactions: Photoabsorption, Scattering, Transmission, and Reflection at E = 50-30, 000 EV, Z = 1-92. *Atomic Data and Nuclear Data Tables*. 1993, pp 181–342. https://doi.org/10.1006/adnd.1993.1013.

(3) Henderson, G. S.; de Groot, F. M. F.; Moulton, B. J. A. X-Ray Absorption Near-Edge Structure (XANES) Spectroscopy. *Rev. Mineral. Geochemistry* **2014**, *78* (1), 75–138. https://doi.org/10.2138/rmg.2014.78.3.

(4) Ravel, B.; Newville, M. ATHENA, ARTEMIS, HEPHAESTUS: Data Analysis for X-Ray Absorption Spectroscopy Using IFEFFIT. *J. Synchrotron Radiat.* **2005**, *12* (Pt 4), 537–541. https://doi.org/10.1107/S0909049505012719.

(5) Riesemeier, H.; Ecker, K.; Görner, W.; Müller, B. R.; Radtke, M.; Krumrey, M. Layout and First XRF Applications of the BAMline at BESSY II. *X-Ray Spectrom.* **2005**, *34* (2), 160–163. https://doi.org/10.1002/xrs.750.

(6) Energie", "Helmholtz-Zentrum Berlin für Materialien und. LiXEdrom: High Energy Resolution RIXS Station Dedicated to Liquid Investigation at BESSY II. *J. large-scale Res. Facil. JLSRF* **2016**, *2*, A80. https://doi.org/10.17815/jlsrf-2-85.

(7) Abbate, M.; Goedkoop, J. B.; de Groot, F. M. F.; Grioni, M.; Fuggle, J. C.; Hofmann, S.; Petersen, H.; Sacchi, M. Probing Depth of Soft X-ray Absorption Spectroscopy Measured in Total-electron-yield Mode. *Surf. Interface Anal.* **1992**, *18* (1), 65–69. https://doi.org/10.1002/sia.740180111.

(8) Qiao, R.; Lucas, I. T.; Karim, A.; Syzdek, J.; Liu, X.; Chen, W.; Persson, K.; Kostecki, R.; Yang, W. Distinct Solid-Electrolyte-Interphases on Sn (100) and (001) Electrodes Studied by Soft X-Ray Spectroscopy. *Adv. Mater. Interfaces* **2014**, *1* (3), 1–6. https://doi.org/10.1002/admi.201300115.

(9) Hollmark, H. M.; Keech, P. G.; Vegelius, J. R.; Werme, L.; Duda, L. C. X-Ray Absorption Spectroscopy of Electrochemically Oxidized Cu Exposed to Na2S. *Corros. Sci.* **2012**, *54* (1), 85–89. https://doi.org/10.1016/j.corsci.2011.09.001.

(10) Jiang, P.; Prendergast, D.; Borondics, F.; Porsgaard, S.; Giovanetti, L.; Pach, E.; Newberg, J.; Bluhm, H.; Besenbacher, F.; Salmeron, M. Experimental and Theoretical Investigation of the Electronic Structure of Cu2O and CuO Thin Films on Cu(110) Using x-Ray Photoelectron and Absorption Spectroscopy. *J. Chem. Phys.* **2013**, *138* (2). https://doi.org/10.1063/1.4773583.

(11) Shimizu, K. I.; Maeshima, H.; Yoshida, H.; Satsuma, A.; Hattori, T. Ligand Field Effect on the Chemical Shift in XANES Spectra of Cu(II) Compounds. *Phys. Chem. Chem. Phys.* **2001**, *3* (5), 862–866. https://doi.org/10.1039/b007276l.

(12) Sharma, V.; Vyas, R.; Bazylewski, P.; Chang, G. S.; Asokan, K.; Sachdev, K. Probing the Highly Transparent and Conducting SnOx/Au/SnOx Structure for Futuristic TCO Applications†. *RSC Adv.* **2016**, *6* (35), 29135–29141. https://doi.org/10.1039/c5ra24422f.

(13) Shaposhnik, A. V.; Shaposhnik, D. A.; Turishchev, S. Y.; Chuvenkova, O. A.;

Ryabtsev, S. V.; Vasiliev, A. A.; Vilanova, X.; Hernandez-Ramirez, F.; Morante, J. R. Gas Sensing Properties of Individual SnO2 Nanowires and SnO2 Sol-Gel Nanocomposites. *Beilstein J. Nanotechnol.* **2019**, *10*, 1380–1390. https://doi.org/10.3762/bjnano.10.136.

(14) Schreier, M.; Héroguel, F.; Steier, L.; Ahmad, S.; Luterbacher, J. S.; Mayer, M. T.; Luo, J.; Grätzel, M. Solar Conversion of CO2 to CO Using Earth-Abundant Electrocatalysts Prepared by Atomic Layer Modification of CuO. *Nat. Energy* **2017**, *2* (7), 17087. https://doi.org/10.1038/nenergy.2017.87.

(15) Morimoto, M.; Takatsuji, Y.; Yamasaki, R.; Hashimoto, H.; Nakata, I.; Sakakura, T.; Haruyama, T. Electrodeposited Cu-Sn Alloy for Electrochemical CO 2 Reduction to CO / HCOO −. *Electrocatalysis* **2018**, *9*, 323–332.

(16) Vasileff, A.; Xu, C.; Ge, L.; Zheng, Y.; Qiao, S. Z. Bronze Alloys with Tin Surface Sites for Selective Electrochemical Reduction of CO2. *Chem. Commun.* **2018**, *54* (99), 13965–13968. https://doi.org/10.1039/c8cc08066f.

(17) Biesinger, M. C. Advanced Analysis of Copper X-Ray Photoelectron Spectra. *Surf. Interface Anal.* **2017**, *49* (13), 1325–1334. https://doi.org/10.1002/sia.6239.

(18) Kresse, G.; Furthmüller, J. Efficiency of Ab-Initio Total Energy Calculations for Metals and Semiconductors Using a Plane-Wave Basis Set. *Comput. Mater. Sci.* **1996**, *6*, 15–50. https://doi.org/10.1016/0927-0256(96)00008-0.

(19) Kresse, G.; Furthmüller, J. Efficient Iterative Schemes for Ab Initio Total-Energy Calculations Using a Plane-Wave Basis Set. *Phys. Rev. B* **1996**, *54*, 11169–11186. https://doi.org/10.1103/PhysRevB.54.11169.

(20) Perdew, J. P.; Burke, K.; Ernzerhof, M. Generalized Gradient Approximation Made Simple. *Phys. Rev. Lett.* **1996**, *77* (18), 3865–3868. https://doi.org/10.1103/PhysRevLett.77.3865.

(21) Grimme, S. Semiempirical GGA-Type Density Functional Constructed with a Long-Range Dispersion Correction. *J. Comput. Chem.* **2006**, *27*, 1787–1799. https://doi.org/10.1002/jcc.

(22) Bucko, T.; Hafner, J.; Lebègue, S.; Ángyán, J. G.; Bučko, T.; Hafner, J.; Lebegue, S.; Angyán, J. G. Improved Description of the Structure of Molecular and Layered Crystals: Ab Initio DFT Calculations with van Der Waals Corrections. *J. Phys. Chem. A* **2010**, *114*, 11814–11824. https://doi.org/10.1021/jp106469x.

(23) Almora-Barrios, N.; Carchini, G.; Błoński, P.; López, N. Costless Derivation of Dispersion Coefficients for Metal Surfaces. *J. Chem. Theory Comput.* **2014**, *10*, 5002–5009. https://doi.org/10.1021/ct5006467.

(24) Garcia-Ratés, M.; López, N. Multigrid-Based Methodology for Implicit Solvation Models in Periodic DFT. *J. Chem. Theory Comput.* **2016**, *12*, 1331–1341. https://doi.org/10.1021/acs.jctc.5b00949.

(25) Garcia-Ratés, M.; García-Muelas, R.; López, N. Solvation Effects on Methanol Decomposition on Pd(111), Pt(111), and Ru(0001). *J. Phys. Chem. C* **2017**, *121*, 13803–13809. https://doi.org/10.1021/acs.jpcc.7b05545.

(26) Blöchl, P. E. Projector Augmented-Wave Method. *Phys. Rev. B* **1994**, *50*, 17953–17979. https://doi.org/10.1103/PhysRevB.50.17953.

(27) Kresse, G.; Joubert, D. From Ultrasoft Pseudopotentials to the Projector Augmented-Wave Method. *Phys. Rev. B* **1999**, *59*, 1758–1775. https://doi.org/10.1103/PhysRevB.59.1758.

(28) Duan, Y. Electronic Properties and Stabilities of Bulk and Low-Index Surfaces of SnO in Comparison with Sn O2: A First-Principles Density Functional Approach with an Empirical Correction of van Der Waals Interactions. *Phys. Rev. B - Condens. Matter Mater. Phys.* **2008**, *77* (4), 1–22. https://doi.org/10.1103/PhysRevB.77.045332.

(29) Dattila, F.; Garclá-Muelas, R.; López, N. Active and Selective Ensembles in Oxide-Derived Copper Catalysts for CO2Reduction. *ACS Energy Lett.* **2020**, *5* (10), 3176–3184. https://doi.org/10.1021/acsenergylett.0c01777.

(30) Marx, D.; Hutter, J. *Ab Initio Molecular Dynamics: Basic Theory and Advanced Methods*; Cambridge University Press: Cambridge, 2009. https://doi.org/DOI: 10.1017/CBO9780511609633.

(31) Nosé, S. A Unified Formulation of the Constant Temperature Molecular Dynamics Methods. *J. Chem. Phys.* **1984**, *81* (1), 511–519. https://doi.org/10.1063/1.447334.

(32) Monkhorst, H. J.; Pack, J. D. Special Points for Brillouin-Zone Integrations. *Phys. Rev. B* **1976**, *13*, 5188–5192. https://doi.org/10.1103/PhysRevB.16.1748.

(33) Makov, G.; Payne, M. C. Periodic Boundary Conditions in Ab Initio Calculations. *Phys. Rev. B* **1995**, *51*, 4014–4022. https://doi.org/10.1103/PhysRevB.51.4014.

(34) Peterson, A. a.; Abild-Pedersen, F.; Studt, F.; Rossmeisl, J.; Nørskov, J. K. How Copper Catalyzes the Electroreduction of Carbon Dioxide into Hydrocarbon Fuels. *Energy Environ. Sci.* **2010**, *3* (9), 1311. https://doi.org/10.1039/c0ee00071j.

(35) Nørskov, J. K.; Rossmeisl, J.; Logadottir, A.; Lindqvist, L.; Kitchin, J. R.; Bligaard, T.; Jónsson, H. Origin of the Overpotential for Oxygen Reduction at a Fuel-Cell Cathode. *J. Phys. Chem. B* **2004**, *108*, 17886–17892. https://doi.org/10.1021/jp047349j.

(36) García-Muelas, R.; Dattila, F.; Shinagawa, T.; Martín, A. J.; Pérez-Ramírez, J.; López, N. Origin of the Selective Electroreduction of Carbon Dioxide to Formate by Chalcogen Modified Copper. *J. Phys. Chem. Lett.* **2018**, *9*, 7153–7159. https://doi.org/10.1021/acs.jpclett.8b03212.

CHAPTER 5. Electrocatalyst derived from waste Cu-Sn bronze for CO_2 conversion into CO

Published in:

ACS Applied Materials and Interfaces, 13(32), **2021**, 38161–38169.

DOI: https://doi.org/10.1021/acsami.1c05015

Authors:

S. Stojkovikj, G.A. El-Nagar**,** F. Firschke, L.C. Pardo Pérez, L. Choubrac, M. Najdoski, M.T. Mayer.

Individual contributions:

- **S. Stojkovikj**: Project introduction and experiments planning, DHBT synthesis method application, development and optimization for the purpose of this study, electrodes pretreatments and samples synthesis, CO_2ER activity measurements, XRD measurements, SEM measurements, ICP-OES measurements, data analysis, data discussion, all data final processing, manuscript writing.
- G.A. El-Nagar: Introducing the DHBT method, XPS data collection/fitting, manuscript review.
- F. Firschke: Bronze electrodes pre-treatments, CO_2ER activity measurements.
- L.C. Pardo Pérez: Data discussion, manuscript review.
- L. Choubrac: XRF measurements data processing and discussion.
- M. Najdoski: Initial trials to synthesize bronze alloy from Cu and Sn, XRD measurements, design of some schemes, data discussion.
- M.T. Mayer: Project supervision, data discussion, final manuscript review and editing.

Various figures and the whole paper are republished in the thesis in **Chapters 3** and **4**, respectively.

ACS APPLIED MATERIALS & INTERFACES

www.acsami.org

Research Article

Electrocatalyst Derived from Waste Cu−Sn Bronze for CO_2 Conversion into CO

Sasho Stojkovikj, Gumaa A. El-Nagar,* Frederik Firschke, Laura C. Pardo Pérez, Léo Choubrac, Metodija Najdoski, and Matthew T. Mayer*

Cite This: *ACS Appl. Mater. Interfaces* 2021, 13, 38161−38169

Read Online

ACCESS | Metrics & More | Article Recommendations | Supporting Information

ABSTRACT: To sustainably exist within planetary boundaries, we must greatly curtail our extraction of fuels and materials from the Earth. This requires new technologies based on reuse and repurposing of material already available. Electrochemical conversion of CO_2 into valuable chemicals and fuels is a promising alternative to deriving them from fossil fuels. But most metals used for electrocatalysis are either endangered or at serious risk of limitation to their future supply. Here, we demonstrate a combined strategy for repurposing of a waste industrial Cu−Sn bronze as a catalyst material precursor and its application toward CO_2 reuse. By a simple electrochemical transfer method, waste bronzes with composition $Cu_{14}Sn$ were anodically dissolved and cathodically redeposited under dynamic hydrogen bubble template conditions to yield mesoporous foams with $Cu_{10}Sn$ surface composition. The bimetal foam electrodes exhibited high CO_2 electroreduction selectivity toward CO, achieving greater than 85% faradaic efficiency accompanied by a considerable suppression of the competing H_2 evolution reaction. The Cu−Sn foam electrodes showed good durability over several hours of continuous electrolysis without any significant change in the composition, morphology, and selectivity for CO as a target product.

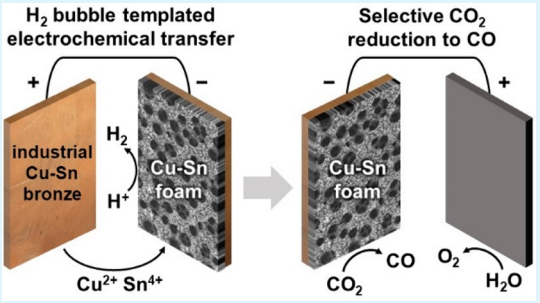

KEYWORDS: *electrochemical CO_2 conversion, Cu−Sn bronze, Cu−Sn foam, waste repurposing, carbon monoxide synthesis, electrodeposition, electrocatalysis*

INTRODUCTION

To develop a sustainable global society, it is crucial that we adapt our material consumption habits to fall within planetary boundaries. This will require limiting the extraction of materials from the Earth and developing alternative strategies based on repurposing and recycling the materials already available. Central to this effort is to slow the use of fossil-based sources of carbon to avoid unbalanced CO_2 emissions, which are contributing to climate change.[1] A sustainable alternative is to utilize CO_2 itself as a carbon feedstock, thereby transforming a waste product into a resource. Electrochemical reduction is an attractive method for CO_2 valorization under mild conditions driven simply by electricity.[2] While there are numerous possible products of CO_2 electrochemical reduction (CO_2ER),[3] carbon monoxide (CO) is currently one of the most techno-economically viable.[4] It is an important industrial feedstock that can be further converted into other valuable compounds using well-established technologies (e.g., the Fischer−Tropsch process).[5] Implementing CO_2ER (using renewable electricity and captured CO_2) to displace conventional routes of CO production could have a significant impact on decreasing CO_2 emissions.

We must keep in mind that a massive global transition to clean energy technologies will require massive quantities of raw materials, namely, metals, for building the new energy systems.[6] Because scalability is a prerequisite for these technologies, we will need to largely avoid materials of low abundance or availability. For CO_2ER this presents particular challenges for catalyst design. Although the best-known catalysts for electrochemical CO production are the precious metals Ag and Au,[7−9] recent studies have discovered a number of new catalysts for this reaction that are based on more abundant elements.[10] For instance, bimetallic combinations of Cu and Sn have demonstrated high activity and selectivity for CO_2 reduction to CO.[11−23] Although Cu and Sn are certainly more abundant than Ag and Au, both Cu and Sn are considered potentially endangered elements with increasingly limited availability and risk to their future supply.[6,24,25] With the goal of sustainable development, it is important that we look to existing raw or recycled materials, rather than new extractions, to supply new green technologies that must be implemented on a massive scale. Considering sources of Cu and Sn, a major application of both is their use in Cu−Sn

Received: March 17, 2021
Accepted: June 21, 2021
Published: August 9, 2021

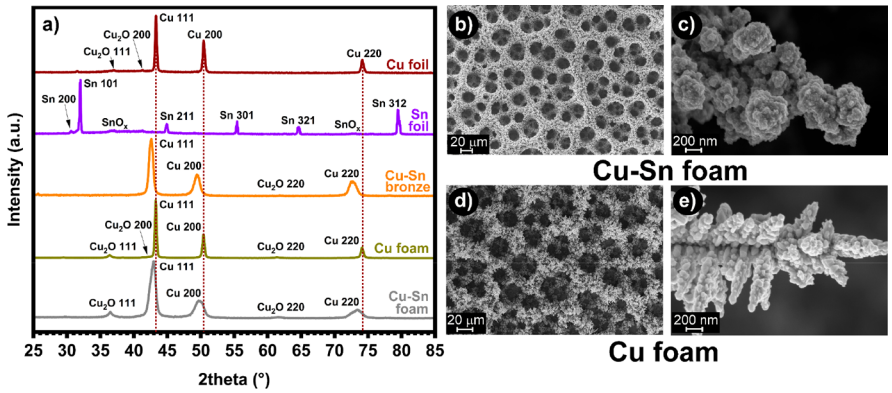

Figure 1. (a) Measured GI-XRD patterns of Cu foil (corresponds to JCPDS No. 04-0836), Sn foil (corresponds to JCPDS No. 01-086-2264), Cu–Sn bronze (corresponds to JCPDS No. 44-1477), Cu foam, and as-prepared Cu–Sn foam. SEM images of porous foams composed of dendrite-like microstructures: (b, c) Cu–Sn foam and (d, e) pure Cu foam.

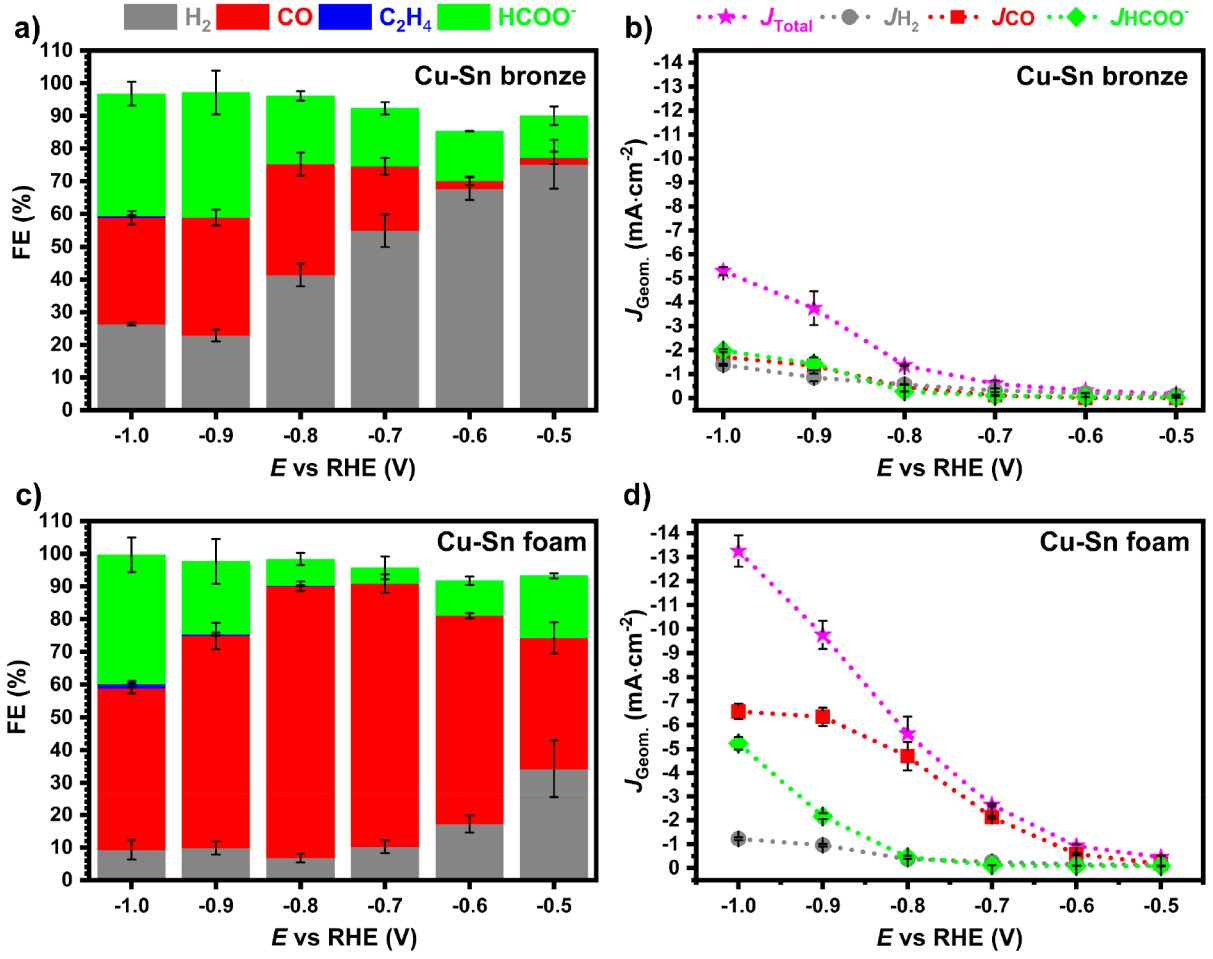

Figure 2. Electrocatalytic activity results; distribution of FEs and partial current densities for detected products at various potentials: (a) FEs and (b) total and partial current densities for products obtained on pristine Cu–Sn bronze; (c) FEs and (d) total and partial current densities obtained on Cu–Sn foam. All results are expressed as average values ± average mean absolute errors from replicate samples.

bronzes, attractive for their physical properties and use across a wide range of applications. Although the term "bronze" can refer to a wide range of alloys based on combining copper with other metals or metalloids in a variety of combinations and amounts, herein we refer to bronze only based on Sn as the major secondary element, a modern composition that is widely used in monuments, streetlamps, chandeliers, cutlery, and mechanical components including screws, nuts, washers, bearings, and gears.[26] These machine elements have a limited lifetime and need to be replaced, thus generating waste. Noting that one of the most common Cu–Sn bronzes has a Sn content (9–13 wt %) comparable to some recently reported Cu–Sn CO_2ER electrocatalysts,[17,19,20] we hypothesized that waste Cu–Sn bronzes could be repurposed for this application,

https://doi.org/10.1021/acsami.1c05015
ACS Appl. Mater. Interfaces 2021, 13, 38161–38169

either directly or with some modifications. An example is the utilization of leaded bronze, commonly used for production of bearings, for CO_2 to $HCOO^-$ conversion.[27]

This study introduces a simple, controllable, and potentially inexpensive strategy to repurpose industrial waste Cu−Sn bronze by employing it as a starting material for fabrication of electrocatalyst materials with a good selectivity for electroreduction of CO_2 into CO. By our method, industrial waste Cu−Sn bronze is converted into CO-selective electrocatalyst materials via a simple electrochemical transfer strategy, where Cu−Sn foams with high electrochemically active surface areas and controlled Cu−Sn composition were created from the planar waste Cu−Sn bronze.

RESULTS AND DISCUSSION

Samples of Cu−Sn bronze were obtained from the smelting facility RŽ Institut AD, Skopje, where they were prepared from molten Cu−Sn bronze wastes and cast into ingots (Figure S1, Supporting Information). These were cut into smaller rectangular platelike samples and mechanically polished prior to the characterization to eliminate any effect from surface inhomogeneities and to attain a near-planar surface (Figure S2). The detailed description of the applied pretreatments on the obtained waste Cu−Sn bronze is described in section S1.2. of the Supporting Information (SI).

The in-depth bulk, spatial, and surface characterization of the waste Cu−Sn bronze is of great importance for this research because it is utilized as a precursor for CO_2ER electrocatalyst preparation. Thus, the bulk and surface compositions of the waste Cu−Sn bronze were first investigated by ICP-OES, XRF, and EDX, as described in section S1.3 of the SI. This material showed a nominal bulk chemical composition of $Cu_{14}Sn$ (Table S1) on the basis of its ICP-OES analysis. The obtained XRF (Figure S3 and Table S2) and EDX (Figure S4) results show the distribution of both Cu and Sn with a nominal chemical composition of Cu_xSn with x = 14−16, which is in a good agreement with the ICP-OES results (Tables S1 and S2 and Figures S3 and S4). The GI-XRD characterization of the Cu−Sn bronze (Figure 1a) shows the typical diffraction peaks of Cu-rich α-bronze, in agreement with the reported results for similar materials with comparable Cu−Sn compositions.[17,20] The reflection peaks of the Cu−Sn bronze are broader and shift to smaller angles in comparison with the polycrystalline Cu foil ones. This can be attributed to the slightly larger lattice parameters in the crystal structure,[17] suggesting different structural identity in comparison to pristine Cu and Sn. That is, the presence of Sn in the alloy's crystal structure is affecting the position and width of the Cu diffraction peaks, but Sn itself does not show any noticeable signal. The surface composition of the Cu−Sn bronze was further investigated by XPS, which shows peaks only for elements Cu, Sn, and O (Figure S5). The surface Cu/Sn ratio of the Cu−Sn bronze is estimated from XPS to resemble $Cu_{14}Sn$ stoichiometry (in Table S3), which is in a good agreement with its bulk composition as estimated from XRF, ICP-OES, and EDX.

As the waste Cu−Sn bronze composition resembles that of some CO_2 reduction catalysts known for achieving good selectivity for CO production,[17,19,20] we first studied a bare Cu−Sn bronze directly as a CO_2 electrocatalyst to examine its intrinsic activity. The sample was connected to a wire and masked in PTFE tape to define a fixed active area and was tested in a three-electrode configuration in aqueous 0.1 mol·dm^{-3} $KHCO_3$ with bubbled CO_2 saturating the solution (Scheme S2). The electrodes were tested under potentiostatic control at several potentials, and generated gas and liquid products were analyzed by chromatography. See section S1.5 for a detailed explanation of the electrocatalysis activity testing. As shown in Figure 2a, the Cu−Sn bronze could reduce CO_2 to both $HCOO^-$ and CO at comparable faradaic efficiencies, while simultaneously producing significant amounts of H_2 at most applied potentials. For practical applications, a mixture of multiple products is usually undesirable, and chemical separation processes are challenging and expensive,[28] and thus designing CO_2ER catalysts that are selective for a single desired product is a central challenge in the field. This Cu−Sn bronze is therefore an inadequate CO_2ER electrocatalyst in its current form, so we next sought to use it as a precursor for synthesis of more complex nanostructured and selective electrocatalyst materials with a controlled Cu/Sn surface ratio and higher roughness and active site density.

Our goal was to take advantage of the near-ideal Cu−Sn composition of the Cu−Sn bronze and use it as starting material to create electrodes with tunable nanostructure morphologies because it has previously been shown that the electrode morphology can play a significant role in influencing product selectivity.[29,30] We explored a variety of different chemical and electrochemical methods for tuning the morphology and composition of the waste Cu−Sn bronze by dissolution and redeposition (see section S3 for a discussion of the strategies). We devised a simple strategy to electrochemically transfer the material from one substrate to another, via anodic dissolution, transport through the solution, and cathodic redeposition. As summarized in Scheme 1, the synthesis was conducted by arranging two cleaned Cu−Sn bronze samples as the anode and cathode in a solution of 1.5 mol·dm^{-3} H_2SO_4(aq) and applying a constant potential of −2.9 V vs Ag/AgCl to the cathode working electrode for a fixed duration. See section S1.4 and Figure S7 for a detailed

Scheme 1. Potentiostatically Controlled Dynamic H_2 Bubbling Templated (DHBT) Co-electrodeposition of Cu−Sn Porous Foam with a Surface Composition of $Cu_{10}Sn$ via Utilization of Cu−Sn Bronze as the Anode with a Surface Composition of $Cu_{14}Sn$[a]

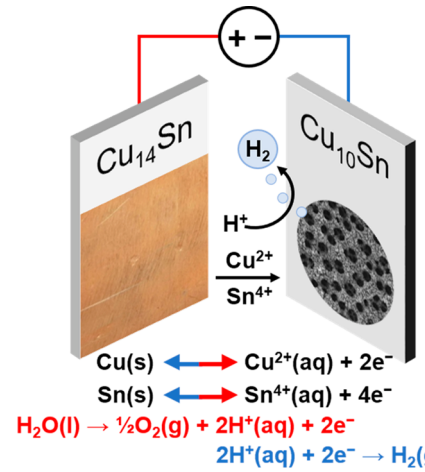

[a]Anode and cathode processes are shown in red and blue, respectively. A cathode potential of −2.9 V vs Ag/AgCl is applied (reference electrode not depicted).

https://doi.org/10.1021/acsami.1c05015
ACS Appl. Mater. Interfaces 2021, 13, 38161−38169

description of the method. Under these conditions, oxidation and reduction of the metals of the Cu−Sn bronze occur at the anode and cathode, respectively. At the cathode, the simultaneous reductive deposition of metals and H_2 evolution (from H^+ reduction) is used as a strategy to influence the nano- and mesoscale morphology of the deposited material via the so-called dynamic H_2 bubbling template (DHBT) phenomenon.[31]

The electrochemical transfer of Cu and Sn under DHBT conditions resulted in porous foamlike microstructures, as shown in Figure 1b,c and Figure S8. The in situ generated H_2 bubbles resulted in a deposited porous material with an interconnected structure around pores with an average pore diameter of 24 μm. At higher magnification (Figure 1c), it is seen that the pore walls form a nanoscale morphology of textured particles with a dendrite-like structure. Pure Cu foam was prepared using the same strategy for the purpose of comparison and to help in distinguishing the influences of roughness and composition on the Cu−Sn foams selectivity. Although both the pure Cu (Figure 1d,e) and Cu−Sn foams showed highly porous dendrite microstructures, their respective pore size, thickness, and nanoscale dendrites are quite different, as seen in Figure 1c,e, Figures S8−S10, and Table S4. The pure Cu foam is thicker (~82 μm) with slightly larger average pore sizes (~32 μm) and dendrites resembling a fern plantlike structure with sharp edges, whereas the Cu−Sn foam is thinner (~38 μm) with a smaller pore size (~24 μm) composed of blunted edge dendrites building from aggregated Cu−Sn bimetallic particles. To assess the electrochemically active surface area, we measured and used the double-layer capacitance (C_{DL}) of the samples to estimate the relative roughness factor of the foams versus their planar counterparts (see section S1.5). The Cu−Sn foam showed a significant increase of about 16-fold compared to the bare bronze, as well as a 2-fold higher roughness than that of the reference Cu foam prepared by the same technique, despite the fact that its total thickness was about half that of the Cu foam counterpart (Figure S12 and Table S6). The higher roughness of the Cu−Sn foam can be attributed to the differences in dendrite morphology and arrangement, together with its smaller average pore size compared to the reference pure Cu foam (Table S5).

The as-prepared Cu−Sn foam from the waste Cu−Sn bronze exhibited diffraction peaks of Cu(111), Cu(200), and Cu(220) planes like that of the pristine waste bronze, as shown in Figure 1a. These peaks are broader and slightly shifted toward lower angles compared to those of Cu foil and the pure Cu foam prepared via the same DHBT synthesis method (see section S1.4). This could be attributed to its smaller crystallites and/or the strain effect due to the chemical composition changes. Moreover, both Cu−Sn and Cu foams showed additional reflection peaks (Figure 1a) attributed to Cu_2O oxide coming from surface oxidation under air exposure, which are more noticeable than in the case of the near-planar Cu foil and Cu−Sn bronze. This is expected because the higher surface area of the pure Cu and Cu−Sn foams makes them prone to oxidation.

After establishing this method for synthesizing porous and rough Cu−Sn foams from the planar waste Cu−Sn bronze, we examined their bulk and surface compositions to evaluate whether they retained the composition of the starting material. The elemental mapping EDX analysis of the Cu−Sn foam suggests a homogeneous distribution of Cu and Sn over the entire Cu−Sn foam, as shown in Figure S11. Precise surface composition of the foams was determined by XPS (Figures S5 and S6 and Table S3). The Cu−Sn foam created from the waste bronze showed a surface composition of $Cu_{10}Sn$, which differed somewhat from the original composition of the pristine bronze Cu_xSn, x = 14−16 (as discussed in more detail below). In contrast, the EDX results show that the Sn bulk abundance is much lower than that in the pristine Cu−Sn bronze (Table S3).

The electrocatalytic activity results for the pristine Cu−Sn bronze are presented in Figure 2a,b and Figure S16. As discussed above, the CO_2 electroreduction performance of the pristine Cu−Sn bronze is poor in terms of selectivity, dominated by the thermodynamically favorable HER instead of CO_2ER at potentials more positive than −0.8 V vs RHE (all potentials hereafter are relative to RHE unless otherwise stated). Negative of −0.8 V, it generates CO and $HCOO^-$ with a comparable selectivity (~35−40%) while HER diminishes. The poor CO_2ER selectivity of the pristine bronze could be mainly attributed to its low electrochemically active surface area.[32,33]

The Cu−Sn foam showed quite different CO_2 electrocatalytic behavior in comparison with the pristine Cu−Sn bronze (Figure 2a,c and Figure S13a,b), most notable in its strong suppression of the HER at all applied potentials and emergence of CO as a dominant product. The bare Cu−Sn bronze and Cu−Sn foam showed comparable Tafel slopes, suggesting similar kinetics for the rate-determining step, as shown in Figure S14. The estimated Tafel slope values for the synthesized materials are in good agreement with the reported Tafel slopes for similar materials including Cu−Sn foam[19] and 3D hierarchical Cu−Sn structures and Cu−Sn rods.[23] The Cu−Sn foam exhibits FE of ~90% for C1 products (CO + $HCOO^-$) in the range between −0.7 and −1.0 V (Figure 2c and Figure S13b). Similarly, as in the case of the pristine Cu−Sn bronze, the FE for H_2 decreases when applying more negative potentials, although not changing much in the potential window from −0.8 to −1.0 V. Surprisingly, both the pristine bronze and Cu−Sn foam exhibited comparable Tafel slopes for HER with almost the same kinetics, as shown in Figure S14. Contrary to that of the HER, the FE for CO increases at more negative potentials, reaching a maximum of >85% at −0.8 V. This corresponds with a climbing CO partial current density toward a plateau at around −6 $mA{\cdot}cm^{-2}$ (Figure 2d). Whereas the CO generation appears limited to this rate at higher potentials, the rate of the $HCOO^-$ formation steeply increases at −0.9 V and beyond. Indeed, the enhanced CO production on Cu−Sn foam is believed to originate from the significantly slower $HCOO^-$ production kinetics, as demonstrated by the higher Tafel slope of $HCOO^-$ production on Cu−Sn foam compared to that of the pristine bronze.

The simultaneous discussion of both faradaic efficiency and partial current density is necessary to see the full picture toward understanding the electrocatalytic behavior of the prepared Cu−Sn foam because observing only the FE can be misleading. For instance, whereas the FE for CO decreases with a further increase of the cathodic potential beyond −0.8 V, its production rate does not decrease, as revealed from its steady-state partial current density. This suggests that CO_2ER into CO may be mass-transport-limited at higher negative potentials. The Cu−Sn foam showed ~2.5-fold higher FE for CO at −0.8 V with a 10-fold higher CO partial current density than the pristine Cu−Sn bronze at the same potential (Figure 2b,d). The observed enhanced CO_2ER on Cu−Sn foam could

https://doi.org/10.1021/acsami.1c05015
ACS Appl. Mater. Interfaces 2021, 13, 38161−38169

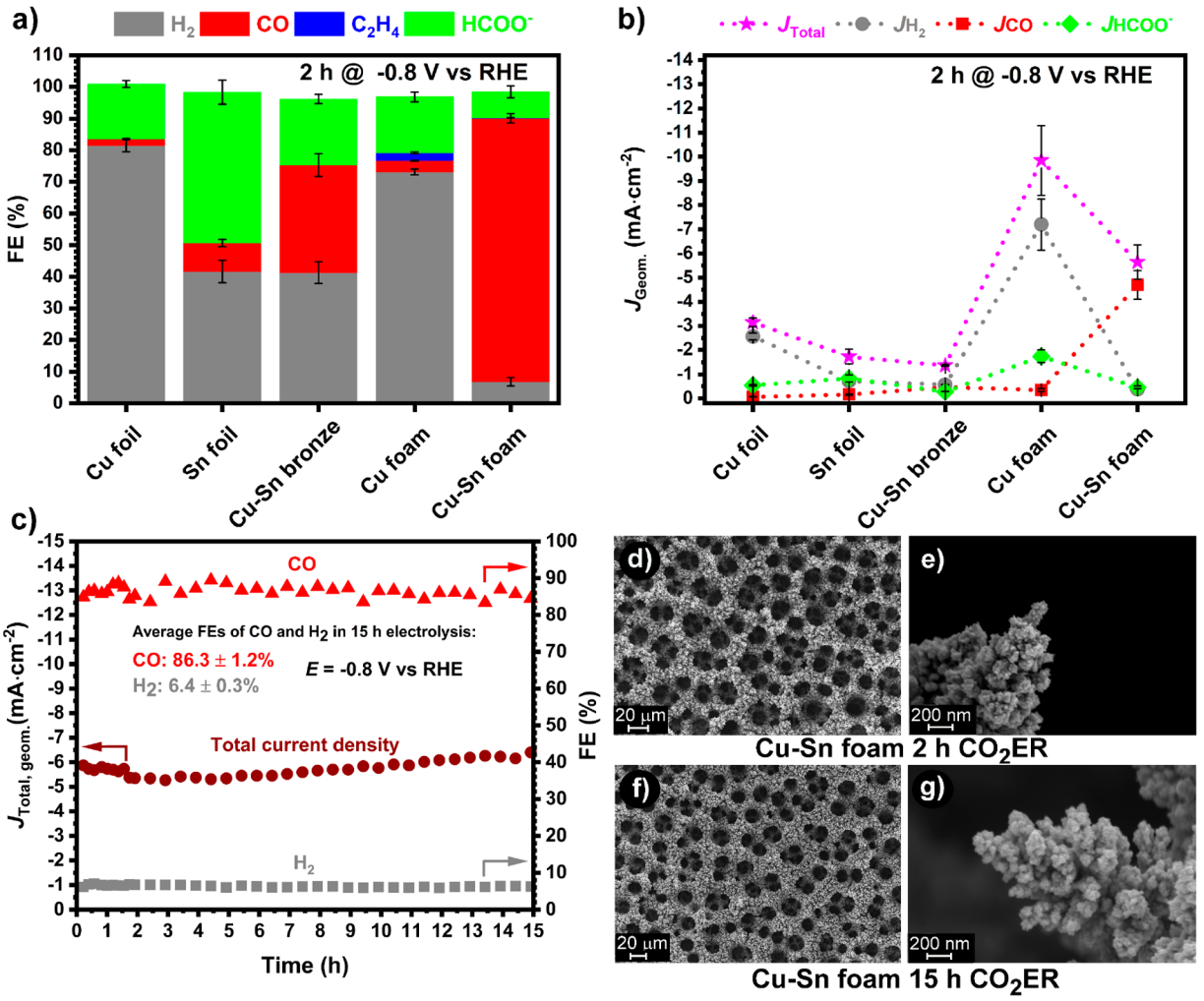

Figure 3. Selectivity and activity comparison at −0.8 V vs RHE: (a) distribution of FEs and (b) partial current densities. (c) Cu−Sn foam 15 h electrocatalytic durability test at −0.8 V vs RHE. SEM images of (d, e) Cu−Sn foam after 2 h and (f, g) after 15 h electrolysis. The FE and *J* results are expressed as average values ± average mean absolute error.

be attributed to its higher electrochemically active surface area together with its appropriate Cu−Sn surface composition (discussed below) compared to the bare Cu−Sn bronze (Figure S12 and Table S6). The best obtained electrocatalytic activity results for the Cu−Sn foam in terms of the FE and the partial current density for CO are quite comparable to the results reported for Sn-decorated Cu foams at identical applied potentials.[16,19]

On the other hand, the enhanced CO_2ER selectivity of the Cu−Sn foam toward CO compared to that of pure Cu foam cannot solely be attributed to the high electrochemically active surface area for both foams, even though the pure Cu foam has about half the surface roughness and gives ∼75% H_2 FE and only ∼5% CO at −0.8 V (Figure 3a). It is interesting to note that pure Cu foam with pore diameters between 50 and 100 μm was reported to convert CO_2 to C_2 products with 55% FE at the same applied potential in 0.5 mol·dm^{-3} $NaHCO_3$(aq) as a supporting electrolyte.[34] When that result is compared with those of the pure Cu foam demonstrated here (see Figure 3a and Table S5), it is obvious that the differences in the surface microstructure strongly affect the selectivity. However, in the case of the Cu−Sn foam, the presence of Sn surface sites plays an essential role in the CO_2 to CO selectivity enhancement accompanied by a significant decrease of the undesired HER. As mentioned above, the XPS analysis showed a slight variation between the surface compositions of the bare Cu−Sn bronze ($Cu_{14}Sn$) and the Cu−Sn foam ($Cu_{10}Sn$) (see Table S3), revealing that the electrodeposited foam has a higher Sn surface content than the starting material, for possible reasons discussed in section S1.4. Moreover, the Cu $2p_{3/2}$ peak position associated with Cu^0/Cu^+ oxidation states of the Cu−Sn foam is ∼1.0 eV negatively shifted (Figure S6a) compared to that observed on the Cu foil, pure Cu foam, and Cu−Sn bronze. Concurrently, the position of the Sn $3d_{5/2}$ peak associated with Sn^{2+} of the Cu−Sn foam is slightly shifted toward higher (0.2−0.3 eV) binding energy values (Figure S6c), in comparison with the peak positions in the Cu−Sn bronze and Sn foil spectra. This might suggest a difference in the charge redistribution between Cu and Sn in the Cu−Sn foam versus the Cu−Sn bronze arising from the changing of the Cu/Sn surface ratio.[20] This could be another contributor to the observed enhanced CO_2ER on the Cu−Sn foam.

The deconvolution of the surface roughness from the composition effect is aided by comparing the electrocatalytic activity of the Cu−Sn bronze with the activity to foils of Cu and Sn because all materials exhibit a near-planar surface

https://doi.org/10.1021/acsami.1c05015
ACS Appl. Mater. Interfaces 2021, 13, 38161−38169

(Figure 3a,b). The Cu−Sn bronze supports ∼7- and 3-fold higher J_{CO} compared to that of the Cu and Sn foils, respectively. Besides, it shows ∼4.5-fold lower J for H_2 than the Cu foil, whereas Sn foil gives ∼3- and 1.5-fold higher J for $HCOO^-$ compared to that of the Cu−Sn bronze and Cu foil, respectively (Figure 3b). Therefore, as expected, the activity variations on the Cu−Sn bronze when compared to that of its constituent elements can be attributed to intrinsic electrocatalytic activity properties of the bimetallic Cu−Sn system compared to those of pure Cu and Sn, which are further discussed below.

Nevertheless, as mentioned above, comparing the surface roughness effect on the activity of the Cu−Sn foam versus the pure Cu foam is not straightforward because the pure Cu foam showed about half the electrochemically active surface area (see Table S6) of the Cu−Sn foam but gave about 2 times the total current density and 10 times less J_{CO} together with far lower FE for CO than the Cu−Sn foam, as seen in Figure 3a,b. Thus, the significantly enhanced CO selectivity on Cu−Sn foam cannot simply be attributed to its higher electrochemically active surface area—rather the Cu−Sn surface composition is believed to be the key parameter. This claim is supported by the electrocatalytic activity results obtained on two control Cu−Sn foam samples with higher surface Sn content. The first control sample was prepared from a Sn-saturated electrodeposition solution, which refers to the electrodeposition solution that was repeatedly used to achieve the optimal CO_2 to CO performance of the Cu−Sn foam electrocatalyst (more details can be found in section S1.4). The Cu−Sn foam that was prepared from this electrodeposition solution has a Cu/Sn surface ratio of 1.4, a much higher Sn surface amount than $Cu_{10}Sn$ foam prepared from the optimal electrodeposition solution (Tables S3 and S4). A second control sample was prepared as a Sn-rich foam with $Cu_{0.6}Sn$ surface composition (see Figure S15). These foams with surface compositions of $Cu_{1.4}Sn$ and $Cu_{0.6}Sn$ showed ∼1.3 and 2 times lower J_{CO}, respectively, with an increase of the FEs for the HER and $HCOO^-$ at −0.8 V within a decrease of the Cu/Sn surface ratio (see Figure S15), despite their comparable electrochemically active surface area. Indeed, the selectivity of Cu−Sn foam shifts from CO to $HCOO^-$ with the increase of the Sn surface sites. This is an intrinsic property of the Cu−Sn CO_2ER electrocatalysts, where their selectivity can be tuned toward either CO or $HCOO^-$ via tuning the Cu/Sn surface ratio. This switching of the selectivity is generally attributed to the mutual perturbation of Cu and Sn electronic structures, which alters the preferential adsorption modes of the key intermediates.[20,35−37] Cu-rich Cu−Sn materials are found to drive the selectivity toward CO through stabilizing the C-bound adsorption mode of the *COOH key intermediate, whereas the O-bound *OCHO* pathway dominates on Sn-rich surfaces and thus favors the CO_2ER to $HCOO^-$,[20,36] as presented in Scheme S1. Besides affecting the absorption modes of the CO_2-derived intermediates, Sn weakens the adsorption of the *H intermediate, thus suppressing the HER.[11,35−37]

The durability of the Cu−Sn foam ($Cu_{10}Sn$ surface composition, Table S3) was examined at −0.8 V for 15 h. It maintained high activity for CO production with a FE > 85% and a partial current density of over −5 mA·cm^{-2} for (cf. Figure 3c and Figure 2c,d) retaining the dendrite morphology (Figure 3d−g and Figures S16 and S18) and the Cu/Sn = 10 surface composition (Table S3) during continuous electrolysis, indicating its stability. Indeed, the robustness and high CO selectivity of the Cu−Sn foam with dendrite microstructures prepared via one-pot, scalable, and fast DHBT is signifying that the utilization of the waste Cu−Sn bronze using this approach is a viable approach. Furthermore, according to previous reports, electrocatalysts with interconnected channels[38] and dendrite microstructures can promote CO_2 mass transport and thus prevent local CO_2 depletion near the electrode surface.[16,19,29]

Similarly, as in the case of the as-prepared Cu−Sn foam, the EDX mapping results after 2 and 15 h of CO_2 continuous electrolysis, data displayed in Figures S17 and S19, show good distribution of Cu and Sn over the entire foam, and again the EDX quantification showed much lower bulk abundance of the Sn in comparison with that of the pristine Cu−Sn bronze (Table S3). This suggests that the DHBT coelectrodeposition mechanism favors faster deposition of Cu over Sn in the bulk of the material, thus distributing the Sn on the surface of the dendrite microstructures as observed from the XPS results (Table S3). This is expected because Cu has a much lower exchange current and thus requires a lower overpotential for the formation of hydrogen templated foam morphology in comparison with Sn, which shows rather poor HER activity,[31,39] and pure Sn foam cannot be electrodeposited under the DHBT conditions we used in this study (see section S1.4).

When novel electrocatalyst materials are being studied, the avoidance of impurities such as trace metals is certainly important for obtaining a precise understanding of the intrinsic activity.[40−42] But production of high-purity materials is costly and resource-intensive, presenting challenges to upscaling. As mentioned above, the transition to sustainable energy systems will require massive amounts of raw materials with limited supply, so the utilization of recycled or repurposed materials is favored over increasing the rates of extraction from the Earth.[6] With this study, we showed that industrial-grade waste material that contains detectable impurities (see Table S1) can be used as raw material for fabrication of efficient and selective electrocatalysts. In fact, when comparing to the best published Cu−Sn-based catalysts optimized for CO selectivity and produced under careful synthetic conditions,[11−13,16,19] we find that our catalyst exhibited comparable or better CO selectivity, CO partial current density, and stability (compared at −0.8 V, for materials tested in CO_2-saturated aqueous solutions Table S7). This result shows promise that efficient catalysts can be produced from impure common materials such as industrial wastes. Although a proper techno-economic analysis would be needed to directly compare the repurposing of waste Cu−Sn bronze for electrocatalyst preparation against the conventional recycling methods (based on remelting), it is already apparent that repurposing a bulk material into a high surface area heterogeneous catalyst can be accomplished with efficient and minimized utilization of the starting material and without requiring high-temperature processes, as compared to bulk processing methods. Furthermore, the catalyst synthesis approach yields a product with a more specialized technological value and can contribute to the urgent goals of mitigating fossil carbon extraction and greenhouse gas emissions, as compared to the energy- and resource-intensive bulk recycling processes.

https://doi.org/10.1021/acsami.1c05015
ACS Appl. Mater. Interfaces 2021, 13, 38161−38169

CONCLUSIONS

In conclusion, we demonstrate a method for preparation of a CO-selective CO_2 conversion electrocatalyst via utilization of waste industrial Cu−Sn bronze. The approach identifies a straightforward and attractive route for repurposing waste material composed of Cu and Sn, metals which are on the list of elements with future endangered supply. The method is simple, fast, and controllable and requires no high-purity or expensive precursors, high temperatures, or sophisticated equipment. By a simple one-step DHBT coelectrodeposition method, Cu and Sn are transferred from a Cu−Sn bronze anode onto a surface of a cathode as a composite with a foam morphology that consists of dendrite microstructures and $Cu_{10}Sn$ surface stoichiometry. The as-prepared Cu−Sn foam has a slightly different Cu/Sn surface ratio and much higher surface roughness compared to the pristine Cu−Sn bronze, which results in a significant increase of the selectivity toward CO (FE > 85%) simultaneously with a great suppression of the thermodynamically favored H_2 evolution reaction (FE ∼ 5%) at a moderate applied potential of −0.8 V versus RHE in an aqueous electrolyte. The total C1-CO_2ER products' FE can reach values that are higher than 95%. The dendrite microstructures showed remarkable stability during 15 h of continuous electrolysis, thus preserving the electrocatalytic activity and Cu−Sn surface composition. Finally, the DHBT method serves as a proof-of-concept that such waste materials can be repurposed for electrocatalytic applications, with potential to be further developed and optimized for preparation of electrocatalysts on alternative substrates, such as gas diffusion electrodes, which can be implemented in larger scale CO_2 electrolyzers.[18]

ASSOCIATED CONTENT

Supporting Information

The Supporting Information is available free of charge at https://pubs.acs.org/doi/10.1021/acsami.1c05015.

Specifications of the utilized chemicals, materials, and techniques; synthesis procedures for creating Cu−Sn foams using the dynamic hydrogen bubble templated electrodeposition technique; data and methods for determination of electrochemically active surface area, Tafel slopes, and faradaic efficiencies of products; additional figures for characterization of the synthesized materials' morphology and composition including SEM images, elemental mapping, XPS, and XRD; cross-sectional SEM analysis of the synthesized Cu and Cu−Sn foams; additional electrochemical characterization data; table comparing the performance reported herein with other published results on similar materials (PDF)

AUTHOR INFORMATION

Corresponding Authors

Matthew T. Mayer − *Helmholtz Young Investigator Group: Electrochemical Conversion of CO_2, Helmholtz-Zentrum Berlin für Materialen und Energie GmbH, Berlin D-14109, Germany;* orcid.org/0000-0001-5379-2775; Email: m.mayer@helmholtz-berlin.de

Gumaa A. El-Nagar − *Helmholtz Young Investigator Group: Electrochemical Conversion of CO_2, Helmholtz-Zentrum Berlin für Materialen und Energie GmbH, Berlin D-14109, Germany;* orcid.org/0000-0001-8209-4597; Email: gumaa.el-nagar@helmholtz-berlin.de

Authors

Sasho Stojkovikj − *Helmholtz Young Investigator Group: Electrochemical Conversion of CO_2, Helmholtz-Zentrum Berlin für Materialen und Energie GmbH, Berlin D-14109, Germany; Institut für Chemie und Biochemie, Freie Universität Berlin, Berlin D-14195, Germany;* orcid.org/0000-0002-3346-2143

Frederik Firschke − *Helmholtz Young Investigator Group: Electrochemical Conversion of CO_2, Helmholtz-Zentrum Berlin für Materialen und Energie GmbH, Berlin D-14109, Germany; Institut für Chemie und Biochemie, Freie Universität Berlin, Berlin D-14195, Germany*

Laura C. Pardo Pérez − *Helmholtz Young Investigator Group: Electrochemical Conversion of CO_2, Helmholtz-Zentrum Berlin für Materialen und Energie GmbH, Berlin D-14109, Germany*

Léo Choubrac − *Department Structure and Dynamics of Energy Materials, Helmholtz-Zentrum Berlin für Materialen und Energie GmbH, Berlin D-14109, Germany;* orcid.org/0000-0003-3236-6376

Metodija Najdoski − *Institute of Chemistry, Faculty of Natural Sciences and Mathematics, Ss. Cyril and Methodius University Skopje, Skopje 1000, Republic of North Macedonia*

Complete contact information is available at: https://pubs.acs.org/10.1021/acsami.1c05015

Notes

The authors declare no competing financial interest.

ACKNOWLEDGMENTS

We thank the industrial smelting facility RŽ Institut AD Skopje, N. Macedonia, for donating the Cu−Sn bronze ingots that were used in this research. The authors acknowledge Veronica Davies, Alexander Arndt, Ursula Michalczik, Christian Höhn, Holger Kropf, and Siddharth Gupta for experimental support. This work was funded by the Helmholtz Association's Initiative and Networking Fund via the Helmholtz Young Investigators Group award (VH-NG-1225) and the Helmholtz-Climate-Initiative (HI-CAM). Instrumentation provided by the Helmholtz Energy Materials Foundry (HEMF) laboratories was used in this study.

ABBREVIATIONS USED

CO_2ER, electrochemical reduction of CO_2
DHBT, dynamic hydrogen bubbling template
EDX, energy dispersive X-ray spectrometry
FE, faradaic efficiency
GI-XRD, grazing-incidence X-ray diffraction
HER, hydrogen evolution reaction
ICP-OES, inductively coupled plasma-optical emission spectrometry
PTFE, polytetrafluoroethylene
SEM, scanning electron microscopy
XPS, X-ray photoelectron spectroscopy
XRF, X-ray fluorescence spectrometry

REFERENCES

(1) Chen, W.-Y.; Suzuki, T.; Lackner, M. *Handbook of Climate Change Mitigation and Adaptation*; Springer International Publishing: 2017. DOI: 10.1007/978-3-319-14409-2.

(2) De Luna, P.; Hahn, C.; Higgins, D.; Jaffer, S. A.; Jaramillo, T. F.; Sargent, E. H. What Would it Take for Renewably Powered

Electrosynthesis to Displace Petrochemical Processes? *Science* **2019**, *364* (6438), eaav3506.
(3) Kortlever, R.; Shen, J.; Schouten, K. J. P.; Calle-Vallejo, F.; Koper, M. T. M. Catalysts and Reaction Pathways for the Electrochemical Reduction of Carbon Dioxide. *J. Phys. Chem. Lett.* **2015**, *6* (20), 4073−4082.
(4) Jouny, M.; Luc, W.; Jiao, F. General Techno-Economic Analysis of CO_2 Electrolysis Systems. *Ind. Eng. Chem. Res.* **2018**, *57* (6), 2165−2177.
(5) de Klerk, A. Fischer−Tropsch Process. *Kirk-Othmer Encyclopedia of Chemical Technology* **2013**, 1−20.
(6) Sovacool, B. K.; Ali, S. H.; Bazilian, M.; Radley, B.; Nemery, B.; Okatz, J.; Mulvaney, D. Sustainable Minerals and Metals for a Low-Carbon Future. *Science* **2020**, *367* (6473), 30−33.
(7) Haas, T.; Krause, R.; Weber, R.; Demler, M.; Schmid, G. Technical Photosynthesis Involving CO_2 Electrolysis and Fermentation. *Nat. Catal.* **2018**, *1* (1), 32−39.
(8) Wu, J.; Huang, Y.; Ye, W.; Li, Y. CO_2 Reduction: From the Electrochemical to Photochemical Approach. *Adv. Sci.* **2017**, *4* (11), 1700194.
(9) Lee, S.; Choi, M.; Lee, J. Looking Back and Looking Ahead in Electrochemical Reduction of CO_2. *Chem. Rec.* **2020**, *20* (2), 89−101.
(10) Burkart, M. D.; Hazari, N.; Tway, C. L.; Zeitler, E. L. Opportunities and Challenges for Catalysis in Carbon Dioxide Utilization. *ACS Catal.* **2019**, *9* (9), 7937−7956.
(11) Sarfraz, S.; Garcia-Esparza, A. T.; Jedidi, A.; Cavallo, L.; Takanabe, K. Cu−Sn Bimetallic Catalyst for Selective Aqueous Electroreduction of CO_2 to CO. *ACS Catal.* **2016**, *6* (5), 2842−2851.
(12) Zhao, Y.; Wang, C.; Wallace, G. G. Tin Nanoparticles Decorated Copper Oxide Nanowires for Selective Electrochemical Reduction of Aqueous CO_2 to CO. *J. Mater. Chem. A* **2016**, *4* (27), 10710−10718.
(13) Li, Q.; Fu, J.; Zhu, W.; Chen, Z.; Shen, B.; Wu, L.; Xi, Z.; Wang, T.; Lu, G.; Zhu, J.-j.; Sun, S. Tuning Sn-Catalysis for Electrochemical Reduction of CO_2 to CO via the Core/Shell Cu/SnO_2 Structure. *J. Am. Chem. Soc.* **2017**, *139* (12), 4290−4293.
(14) Schreier, M.; Héroguel, F.; Steier, L.; Ahmad, S.; Luterbacher, J. S.; Mayer, M. T.; Luo, J.; Grätzel, M. Solar Conversion of CO_2 to CO using Earth-Abundant Electrocatalysts Prepared by Atomic Layer Modification of CuO. *Nat. Energy* **2017**, *2* (7), 17087.
(15) Hu, H.; Wang, Y.; Du, N.; Sun, Y.; Tang, Y.; Hu, Q.; Wan, P.; Dai, L.; Fisher, A. C.; Yang, X. J. Thermal-Treatment-Induced Cu−Sn Core/Shell Nanowire Array Catalysts for Highly Efficient CO_2 Electroreduction. *ChemElectroChem* **2018**, *5* (24), 3854−3858.
(16) Zeng, J.; Bejtka, K.; Ju, W.; Castellino, M.; Chiodoni, A.; Sacco, A.; Farkhondehfal, M. A.; Hernández, S.; Rentsch, D.; Battaglia, C.; Pirri, C. F. Advanced Cu-Sn Foam for Selectively Converting CO_2 to CO in Aqueous Solution. *Appl. Catal., B* **2018**, *236*, 475−482.
(17) Vasileff, A.; Xu, C.; Ge, L.; Zheng, Y.; Qiao, S.-Z. Bronze Alloys with Tin Surface Sites for Selective Electrochemical Reduction of CO_2. *Chem. Commun.* **2018**, *54* (99), 13965−13968.
(18) Ju, W.; Jiang, F.; Ma, H.; Pan, Z.; Zhao, Y.-B.; Pagani, F.; Rentsch, D.; Wang, J.; Battaglia, C. Electrocatalytic Reduction of Gaseous CO_2 to CO on Sn/Cu-Nanofiber-Based Gas Diffusion Electrodes. *Adv. Energy Mater.* **2019**, *9* (32), 1901514.
(19) Ju, W.; Zeng, J.; Bejtka, K.; Ma, H.; Rentsch, D.; Castellino, M.; Sacco, A.; Pirri, C. F.; Battaglia, C. Sn-Decorated Cu for Selective Electrochemical CO_2 to CO Conversion: Precision Architecture beyond Composition Design. *ACS Appl. Energy Mater.* **2019**, *2* (1), 867−872.
(20) Vasileff, A.; Zhi, X.; Xu, C.; Ge, L.; Jiao, Y.; Zheng, Y.; Qiao, S.-Z. Selectivity Control for Electrochemical CO_2 Reduction by Charge Redistribution on the Surface of Copper Alloys. *ACS Catal.* **2019**, *9* (10), 9411−9417.
(21) Zhang, S.-N.; Li, M.; Hua, B.; Duan, N.; Ding, S.; Bergens, S.; Shankar, K.; Luo, J.-L. A Rational Design of Cu_2O−SnO_2 Core-Shell Catalyst for Highly Selective CO_2-to-CO Conversion. *ChemCatChem* **2019**, *11* (16), 4147−4153.
(22) Zhao, S.; Li, S.; Guo, T.; Zhang, S.; Wang, J.; Wu, Y.; Chen, Y. Advances in Sn-Based Catalysts for Electrochemical CO_2 Reduction. *Nano-Micro Lett.* **2019**, *11* (1), 62.
(23) Yoo, C. J.; Dong, W. J.; Park, J. Y.; Lim, J. W.; Kim, S.; Choi, K. S.; Odongo Ngome, F. O.; Choi, S.-Y.; Lee, J.-L. Compositional and Geometrical Effects of Bimetallic Cu−Sn Catalysts on Selective Electrochemical CO_2 Reduction to CO. *ACS Appl. Energy Mater.* **2020**, *3* (5), 4466−4473.
(24) Poliakoff, M.; Licence, P.; George, M. W. UN Sustainable Development Goals: How Can Sustainable/Green Chemistry Contribute? By Doing Things Differently. *Curr. Opin. Green Sustain. Chem.* **2018**, *13*, 146−149.
(25) Endangered Elements. https://www.acs.org/content/acs/en/greenchemistry/research-innovation/endangered-elements.html (accessed 2021-05-12).
(26) Radu, S.; Demian, M.; Demian, G.; Ciobanu, M. Studies on the Possibility of Recycling Waste Bronze. *Adv. Mater. Res.* **2015**, *1128*, 303−311.
(27) Gálvez-Vázquez, M. d. J.; Moreno-García, P.; Guo, H.; Hou, Y.; Dutta, A.; Waldvogel, S. R.; Broekmann, P. Leaded Bronze Alloy as a Catalyst for the Electroreduction of CO_2. *ChemElectroChem* **2019**, *6* (8), 2324−2330.
(28) Greenblatt, J. B.; Miller, D. J.; Ager, J. W.; Houle, F. A.; Sharp, I. D. The Technical and Energetic Challenges of Separating (Photo)Electrochemical Carbon Dioxide Reduction Products. *Joule* **2018**, *2* (3), 381−420.
(29) Burdyny, T.; Graham, P. J.; Pang, Y.; Dinh, C.-T.; Liu, M.; Sargent, E. H.; Sinton, D. Nanomorphology-Enhanced Gas-Evolution Intensifies CO_2 Reduction Electrochemistry. *ACS Sustainable Chem. Eng.* **2017**, *5* (5), 4031−4040.
(30) Hui, S.; Shaigan, N.; Neburchilov, V.; Zhang, L.; Malek, K.; Eikerling, M.; Luna, P. D. Three-Dimensional Cathodes for Electrochemical Reduction of CO_2: From Macro- to Nano-Engineering. *Nanomaterials* **2020**, *10* (9), 1884.
(31) Vesztergom, S.; Dutta, A.; Rahaman, M.; Kiran, K.; Zelocualtecatl Montiel, I.; Broekmann, P. Hydrogen Bubble Templated Metal Foams as Efficient Catalysts of CO_2 Electroreduction. *ChemCatChem* **2021**, *13* (4), 1039−1058.
(32) Hall, A. S.; Yoon, Y.; Wuttig, A.; Surendranath, Y. Mesostructure-Induced Selectivity in CO_2 Reduction Catalysis. *J. Am. Chem. Soc.* **2015**, *137* (47), 14834−14837.
(33) Yoon, Y.; Hall, A. S.; Surendranath, Y. Tuning of Silver Catalyst Mesostructure Promotes Selective Carbon Dioxide Conversion into Fuels. *Angew. Chem., Int. Ed.* **2016**, *55* (49), 15282−15286.
(34) Dutta, A.; Rahaman, M.; Luedi, N. C.; Mohos, M.; Broekmann, P. Morphology Matters: Tuning the Product Distribution of CO_2 Electroreduction on Oxide-Derived Cu Foam Catalysts. *ACS Catal.* **2016**, *6* (6), 3804−3814.
(35) He, J.; Dettelbach, K. E.; Huang, A.; Berlinguette, C. P. Brass and Bronze as Effective CO_2 Reduction Electrocatalysts. *Angew. Chem., Int. Ed.* **2017**, *56* (52), 16579−16582.
(36) Vasileff, A.; Xu, C.; Jiao, Y.; Zheng, Y.; Qiao, S.-Z. Surface and Interface Engineering in Copper-Based Bimetallic Materials for Selective CO_2 Electroreduction. *Chem.* **2018**, *4* (8), 1809−1831.
(37) Wu, Y.; Iwase, K.; Harada, T.; Nakanishi, S.; Kamiya, K. Sn Atoms on Cu Nanoparticles for Suppressing Competitive H_2 Evolution in CO_2 Electrolysis. *ACS Appl. Nano Mater.* **2021**, *4*, 4994.
(38) Hyun, G.; Song, J. T.; Ahn, C.; Ham, Y.; Cho, D.; Oh, J.; Jeon, S. Hierarchically Porous Au Nanostructures with Interconnected Channels for Efficient Mass Transport in Electrocatalytic CO_2 Reduction. *Proc. Natl. Acad. Sci. U. S. A.* **2020**, *117* (11), 5680−5685.
(39) Nikolić, N. D. Influence of the Exchange Current Density and Overpotential for Hydrogen Evolution Reaction on the Shape of Electrolytically Produced Disperse Forms. *J. Electrochem. Sci. Eng.* **2020**, *10* (2), 111−126.
(40) Lum, Y.; Kwon, Y.; Lobaccaro, P.; Chen, L.; Clark, E. L.; Bell, A. T.; Ager, J. W. Trace Levels of Copper in Carbon Materials Show Significant Electrochemical CO_2 Reduction Activity. *ACS Catal.* **2016**, *6* (1), 202−209.

https://doi.org/10.1021/acsami.1c05015
ACS Appl. Mater. Interfaces 2021, 13, 38161−38169

(41) Wuttig, A.; Surendranath, Y. Impurity Ion Complexation Enhances Carbon Dioxide Reduction Catalysis. *ACS Catal.* **2015**, *5* (7), 4479−4484.
(42) Pander, J. E., III; Ren, D.; Yeo, B. S. Practices for the Collection and Reporting of Electrocatalytic Performance and Mechanistic Information for the CO_2 Reduction Reaction. *Catal. Sci. Technol.* **2017**, *7* (24), 5820−5832.

https://doi.org/10.1021/acsami.1c05015
ACS Appl. Mater. Interfaces 2021, 13, 38161−38169

Supporting Information

Electrocatalyst Derived from Waste Cu-Sn Bronze for CO_2 Conversion Into CO

Sasho Stojkovikj,[a,b] Gumaa A. El-Nagar,*[a] Frederik Firschke,[a,b] Laura C. Pardo Pérez,[a] Léo Choubrac,[c] Metodija Najdoski,[d] and Matthew T. Mayer*[a]

[a]Helmholtz Young Investigator Group: Electrochemical Conversion of CO_2, Helmholtz-Zentrum Berlin für Materialen und Energie GmbH, Hahn-Meitner-Platz 1, D-14109, Berlin, Germany.
[b]Institut für Chemie und Biochemie, Freie Universität Berlin, Arnimallee 22, D-14195 Berlin, Germany.
[c]Department Structure and Dynamics of Energy Materials, Helmholtz-Zentrum Berlin für Materialen und Energie GmbH, Hahn-Meitner-Platz 1, D-14109, Berlin, Germany.
[d]Institute of Chemistry, Faculty of Natural Sciences and Mathematics, Ss. Cyril and Methodius University Skopje, Arhimedova 5, 1000 Skopje, Republic of North Macedonia.

*Corresponding authors: Dr. Matthew T. Mayer (m.mayer@helmholtz-berlin.de) and Dr. Gumaa A. El-Nagar (gumaa.el-nagar@helmholtz-berlin.de)

Table of contents

Scheme S1 4
S1. Experimental section 5
S1.1. Materials and chemicals 5
S1.2. Pre-treatment of the industrial waste Cu-Sn bronze samples 5
S1.3. Material characterization methods 6
S1.4. Preparation of Cu-Sn foam electrocatalyst 9
S1.5. Electrochemical measurements 12
S2. Experimental results 15
Figure S1. 15
Figure S2. 16
Table S1. 17
Figure S3. 18
Table S2. 19
Figure S4. 20
Figure S5. 21
Figure S6. 22
Table S3. 23
Scheme S2 24
Figure S7. 25
Table S4 26
Figure S8. 27
Figure S9. 28
Figure S10. 29
Table S5 30
Figure S11. 31
Figure S12. 32
Table S6. 33
Figure S13. 34
Figure S14. 35
Figure S15. 36
Figure S16. 37
Figure S17. 38
Figure S18. 39
Figure S19. 40
Figure S20. 41
Figure S21. 42
Table S7. 43

S3. Another approach for conversion of the waste Cu-Sn bronze into CO-selective electrocatalyst 44

S3.1. Chemical bath method for growing nanostructures on the Cu-Sn bronze surface 44

S3.2. Decoration of the $CuO \cdot xH_2O$ nanostructures via electrodeposition of the leached Cu and Sn 45

Figure S22. 45

S3.3. Electrocatalytic activity results for the Cu_xO/SnO_x decorated $CuO \cdot xH_2O$ nanosheets .. 46

Figure S23. 46

REFERENCES 47

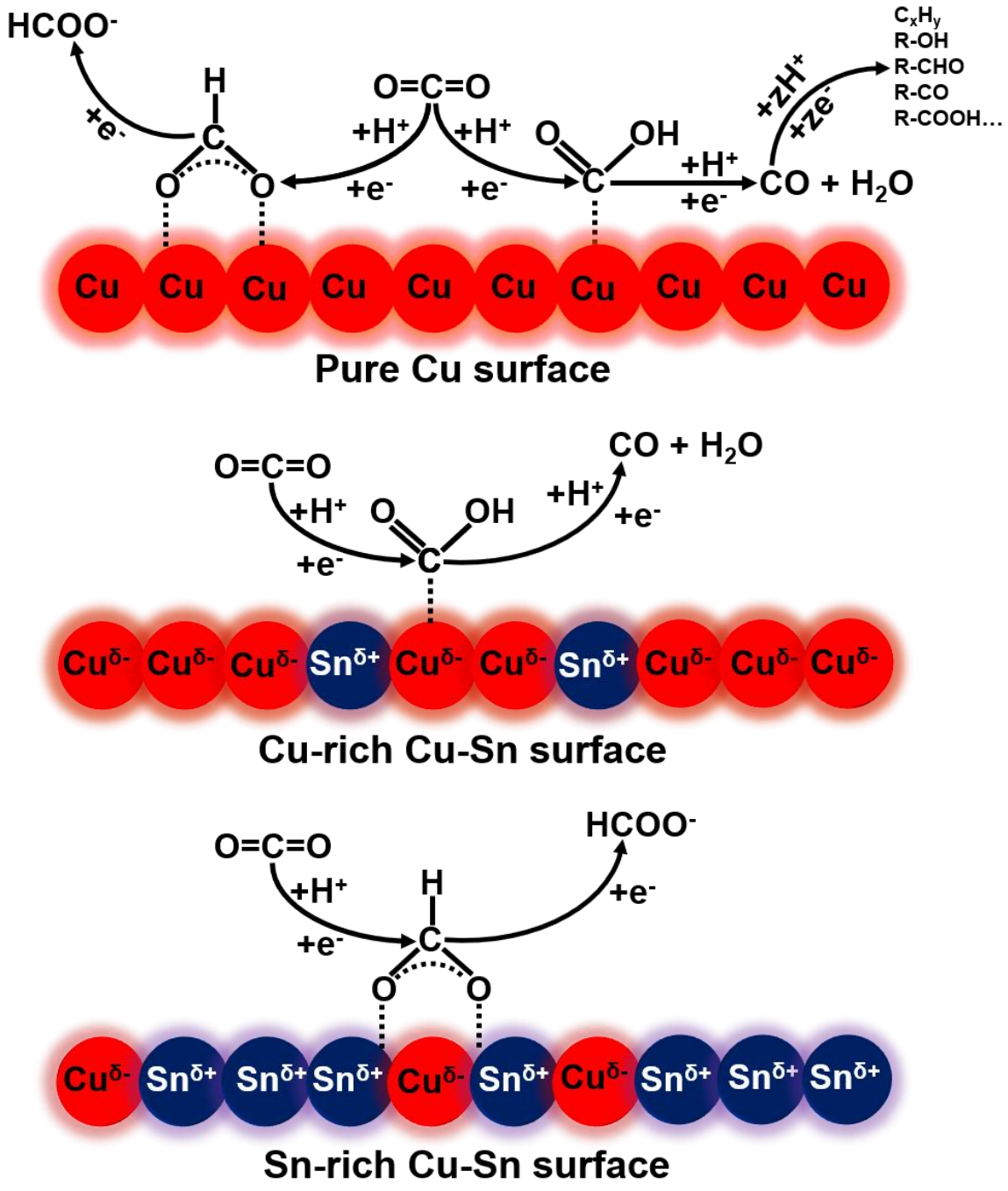

Scheme S1. Simple mechanistic overview of the electrochemical reduction of CO_2 on surfaces of pure Cu, Cu-rich and Sn-rich Cu-Sn electrodes. Switching the selectivity from multielectron/proton (ze^-) towards $2e^-$ products CO and HCOOH on Cu- and Sn-rich Cu-Sn electrocatalysts, respectively.
The addition and altering of the amount of Sn as a second element in the structure of Cu causes charge redistribution that affects the binding mode of *COOH/*OCHO* intermediate thus shifting the selectivity between CO and $HCOO^-$, according to the findings reported by Vasileff et al.[1-2]

S1. Experimental section

S1.1. Materials and chemicals

Industrial waste Cu-Sn Cu-Sn bronze that contains 9-13 wt.% Sn (produced according to the Standard MKC EN 1982:2019 in the Smelting Facility RŽ Institut AD Skopje); Alumina based abrasive polishing paper (Coated Abrasive Sheets, 3M Hookit, P400); Alumina-based polishing suspensions (MicroPolish^{TM}, Al_2O_3 particle sizes of 0.3 and 0.05 μm, Buehler); Nylon polishing pads (PSA Backing); Ultrapure water (18.20 MΩ·cm, purified using the Thermo Scientific Barnstead GenPurexCAD Plus system); 2-Propanol (≥99.8 wt.% ACS grade purity, Merck); HNO_3 (70 wt.%, redistilled, ≥99.999 wt.% trace metals purity, Sigma-Aldrich); HCl (37 wt.%, ACS, EMSURE® purity, Merck); H_2SO_4 (≥98 wt.% EMSURE® purity, Merck); $KHCO_3$ (99.7-100.5 wt.% ACS, EMSURE® purity, Merck); 0.5 mm Cu foil (99.98 wt.% trace metals purity, Sigma-Aldrich); 0.25 mm Sn foil (99.998 wt.% trace metals purity, Alfa Aesar); Single-side sticky Cu tape (12 mm x 0.1 mm, Plano); Double-side sticky carbon tape (8 mm x 0.15 mm, Plano); Cu and Sn reference materials for XRF (Bruker); PTFE tape (12 mm x 0.1 mm, Würth); CO_2 (4.8 grade purity, Linde Gas); 1000 mg·dm^{-3} in 6.5 wt.% HNO_3, ICP-OES multielement standard solution (Certipur-Certified Reference Material); 1000 mg·dm^{-3} Sn in 10 wt.% HCl, ICP-OES standard solution (Roti®Star, Carl Roth); $(NH_4)_2S_2O_8$ (≥98 wt.% ACS grade purity, Sigma-Aldrich); NaOH (pellets with 98% purity, Alfa Aesar). All chemicals were used as received, without further purification.

S1.2. Pre-treatment of the industrial waste Cu-Sn bronze samples

The as-received Cu-Sn bronze ingots (Fig. S1a) with dimensions of ~12 x 7 x 1 cm were cut into smaller plate-like samples with dimensions of ~1 x 2 x 0.25 cm (suitable for all experiments, except the ICP-OES analysis) using a cutting wheel tool and roughly polished using an abrasive wheel tool to remove any furrows coming from the cutting procedure. After this procedure, each sample was ultra-sonicated (Ultrasonicator: Emmi-H30 EMAG Technologies) for 15 min in 2-propanol to remove possible oily residues coming from the cutting tools. In the next step, the Cu-Sn bronze samples were subjected to procedures for fine surface polishing. Namely, each sample was manually polished from each side using Al_2O_3 particles based abrasive polishing paper. Each side of the samples was polished for 2 minutes with 8-like shapes hand movements, thus achieving bare-eye notable difference between the unpolished and the polished Cu-Sn bronze surfaces. Then all samples were ultra-sonicated 2 times for 15 min in 2-propanol and blow-dried with N_2. The next polishing procedure using alumina polishing suspension was adopted from Elgrishi et al.[3] It was conducted using Nylon polishing pad and alumina suspension with two different sizes of the Al_2O_3 particles. Each side of each sample's surface was polished for 2 minutes with 8-like shapes hand movements using the suspension with particle size of 0.3 μm. The polishing pad was wetted with ultrapure water, prior to the polishing procedure. Then the samples were sonicated in 2-propanol for 15 minutes and the polishing pad was thoroughly washed with ultrapure water. In the next step, the polishing procedure was repeated by the same manner as in the previous one, but this time by using finer suspension (particle size: 0.05 μm). At the end, the samples were sonicated in 2 times in 2-propanol for 15 min and blow-dried with N_2. The surface polishing outcome is prominent if we compare the SEM images of unpolished and fine polished surface of the Cu-Sn bronze samples, as showed on Fig. S2.

S1.3. Material characterization methods

The chemical composition, elemental distribution, surface morphology, crystalline- and electronic structures (oxidation state of the elements) of the Cu-Sn bronze and the electrocatalysts prepared from it, were characterized using variety of methods: Inductively Coupled Plasma - Optical Emission Spectroscopy (ICP-OES), X-Ray Fluorescence Spectroscopy (XRF), Scanning Electron Microscopy (SEM), Energy Dispersive X-Ray (EDX) Spectroscopy, Transmission Electron Microscopy (TEM), Focused Ion Beam (FIB) milling/Cross section SEM, Grazing Incidence X-Ray Diffraction (GI-XRD), and X-Ray Photoelectron Spectroscopy (XPS).

Scanning Electron Microscopy (SEM)/Energy Dispersive X-Ray (EDX) Spectrometry and Focused Ion Beam (FIB) milling for cross-section thickness determination. LEO GEMINI 1530 Field Emission Scanning Electron Microscope (FE-SEM) with acceleration voltage –4 kV, standard aperture size - 30 µm and Immersion Lens (InLens) Secondary Electron (SE) detection mode, was used for surface morphology imaging. The SEM surface morphology characterization was performed on the bare Cu-Sn bronze, and Cu-Sn and pure Cu foams. Average pore sizes were calculated from the corresponding mages of the foam samples using the open-source ImageJ software.[4] The EXD elemental mapping was conducted with same instrument using acceleration voltage of 15 kV, maximal aperture Size - 120 µm and EDX detector (Thermo Fischer). The mapping and quantification of Cu, Sn, C and O were conducted using the Cu L_{α}, and Sn $L_{\alpha, \beta}$, C K_{α} and O K_{α} emission spectral lines. Since the Cu and Sn from the Cu-Sn bronze can interfere with the Cu and Sn EDX signals in the case when the Cu-Sn foam alloy electrocatalyst samples are measured, a double-sided carbon tape was used to transfer the material on the carbon surface. This procedure was successfully performed by gently sticking one side of the carbon tape on the Cu-Sn composite surface, then pealing it off and performing EDX the elemental mapping and quantification. The thicknesses of the Cu-Sn and pure Cu foams were determined from cross-section SEM imaging after the samples were milled (ablated) using Focused Ion Beam (FIB). Zeiss Crossbeam 340 - GEMINI 1 SEM Column system with gallium ion source was used for this purpose. The operating parameters were set to: ion beam current - 80 nA, acceleration voltage - 15 kV, tilt angle - 36 ° and Secondary Electron (SE) detection mode for the imaging.

Inductively Coupled Plasma – Optical Emission Spectrometry (ICP-OES). The quantitative chemical composition of the Cu-Sn bronze and the electrolytes used during the electrocatalyst preparation were analyzed using Inductively Coupled Plasma - Optical Emission Spectroscopy (ICP-OES). The analysis was conducted utilizing the system iCAP 7400 Duo MFC ICP-OES Analyzer (Thermo Scientific) in axial Ar plasma mode. The instrument was purged with Ar (5.0 purity, Air Liquide) at least 2 hours prior to igniting the plasma. All glassware used for this purpose was thoroughly cleaned with ´´aqua regia´´ (freshly prepared from concentrated HNO_3 (70 wt.%) and (37 wt.%) in 1:3 volume ratio) and rinsed with large amount of ultrapure water. The volumetric flasks used were of A-class precision and the dilutions were conducted using high precision micropipettes. For the analysis of the Cu-Sn bronze, three individual replicate Cu-Sn bronze samples with dimensions of ~0.5 x 0.25 x 0.25 cm were mechanically cut (using cutting wheel tool) from three different ~1 x 2 x 0.25 cm ones and, carefully measured using analytical balance. The samples were placed in three 15 cm^3 test tubes and 1 cm^3 of concentrated HNO_3 (70 wt.%) and 3 cm^3 concentrated HCl (37 wt.%) were added to each test tube. The Cu-Sn bronze was left to react with the acids for 2-3 hours

at room temperature, after which 2 cm^3 of 10 wt.% HCl (freshly prepared from concentrated HCl, 37 wt.% and ultrapure water) were added. The test tubes were placed in an ultrasonicator (Emmi-H30 EMAG Technologies) and sonicated at 50 °C for 3 hours. After this procedure, the samples were fully dissolved and the content from each test tube was quantitatively transferred into 50 cm^3 volumetric flasks and diluted to the mark with 10 wt.% HCl(aq). A blank solution was prepared in a separate volumetric flask using the same amount of reagents that were used for dissolving the samples. For the determination of Cu, Sn and Zn, the solutions were 1000 and 5000-fold diluted with 10 wt.% HCl(aq), prior to the sampling for analysis. Identical dilution procedure was performed for the blank solutions. For the determination of the expected trace elements (Ag, Al, Ca, Cd, Co, Cr, Fe, Mg, Mn, Ni and Pb), the sampling was conducted directly from the 50 cm^3 flasks. A volume of 10 cm^3 was sampled from each solution (including the blanks) and these were used for the ICP-OES elemental analysis. Prior to the measurement, the autosampler was set to withdraw 3 replicates from each sample. The adequate emission spectral lines (recommended by the instrument producer) were chosen for each element and the instrument was calibrated with standard solutions in two sequences. The first sequence of standard solutions with concentrations in the range of 0.09-1.5 $mg \cdot dm^{-3}$ containing Ag, Al, Ca, Cd, Co, Cr, Cu, Fe, Mg, Mn, Ni and Pb, was prepared by diluting multielement standard solution (concentration of 1000 $mg \cdot dm^{-3}$ for each element) in 3 wt.% HNO_3(aq). The second sequence was used only for calibrating the instrument for Sn in the range of 0.05-2 $mg \cdot dm^{-3}$ and was prepared by diluting Sn-single element standard solution (also with concentration of 1000 $mg \cdot dm^{-3}$) in 10 wt.% HCl(aq). The ICP-OES quantification results are expressed as average wt. and at. % ± average mean absolute error calculated from multiple sample measurements and presented in Table S1. Additional ICP-OES analysis were conducted on the electrodeposition solutions used during the electrocatalyst preparation for the purpose of optimization of the Cu and Sn concentrations that lead to synthesis of Cu-Sn composite which maintains the best CO_2ER activity. The electrolytes were diluted 300 and 500-fold prior to the measurements that were conducted using the same manner as for the Cu-Sn bronze analysis.

X-Ray Fluorescence Spectrometry (XRF). The Cu-Sn bronze was studied using X-Ray Fluorescence Spectroscopy (XRF) to quantify the Cu and Sn bulk spatial distribution in a representative sample with dimensions (~1 x 2 x 0.25 cm) suitable to be used as a working electrode in the electrochemical experiments. The sample was analyzed in 425 points using Bruker M4 Tornado X-Ray Fluorescence Spectrometer with Rh tube having maximal excitation of 50 kV/30 W and SDD detector with energy resolution of 145 eV. The measurement was performed using the following instrument settings: sampling points - 424, spot size - 25 µm, anode current - 200 µA/50 kV, Acquisition time - 60 s, Pressure in the sample chamber -10 mbar and Recorded XRF spectra maximal range - 40 keV. The instrument was calibrated using certified metallic Cu and Sn calibration reference materials (Bruker), prior to the measurement. The elemental mapping and quantification were performed using the Cu $K_{\alpha,\beta}$ and Sn $L_{\alpha,\beta}$ spectral lines.

Grazing-Incidence X-Ray Diffraction (GI-XRD). The GI-XRD measurements were conducted using the PANalytical X'Pert Pro MPD (multi-purpose diffractometer) with Cu K_α X-Ray source and xenon scintillation counter detector with parallel plate collimator. The diffractograms were measured in the range from 15 to 100 2theta (°) using grazing incidence angle of 1°, divergence - 1/16°, mask - 2 mm, step size - 0.05° and collection time - 5 seconds.

X-Ray Photoelectron Spectroscopy (XPS). The X-Ray Photoelectron Spectroscopy (XPS) was performed using analyzer with a monochromatic Al K_α X-Ray source (Excitation Energy – EE of 1486.74 eV) type SPECS Phoibos HSA3500 100. The XPS survey spectra were measured on all Cu-Sn foam samples and on Cu and Sn foils and Cu foam as reference materials for comparison. These spectra were recorded as a single scan in the range 0-1400 eV, using dwell time 0.1, energy step - 0.5 eV, pass energy - 30 eV, bias voltage - 90 kV, detector voltage - 2200 kV and Work Function (WF) - 4.343 eV. The assignation of peaks in the survey spectra was performed via comparison of the measured peak-positions with the literature values for the identified core levels.[1, 5-7] The Cu 2p, Sn 3d core-levels spectra were recorded with high resolution in at least 3 spots per sample using energy step – 0.05 eV and pass energy – 10 eV, kV. All Cu 2p, Sn 3d and O 1s core-level peak positions were calibrated with respect to the adventitious carbon - C 1s peak at 284.8 eV that is attributed to C-C bond. The deconvolution and fitting of the Cu 2p, Sn 3d and O 1s spectra was performed using the XPS PeakFit software. The Cu Auger spectra was not fitted, and the Binding Energy (BE) was converted into Kinetic Energy using Eq. 1. All measurements were performed *ex situ*.

$$KE = EE - BE - WF \quad (1)$$

S1.4. Preparation of Cu-Sn foam electrocatalyst

The three-dimensional porous Cu-Sn foam electrocatalyst preparation was conducted using dynamic H_2 bubbling templated (DHBT) co-electrodeposition of Cu and Sn on a Cu-Sn bronze cathode, that are extracted from a Cu-Sn bronze anode in acidic medium. More information about the DHBT methods and their application for CO_2ER catalysts synthesis can be found elsewhere.[8] For preparation of Cu-Sn bronze cathodes, the pre-treated Cu-Sn bronze plate-like samples (pre-treatment explained in section S1.2.) were connected to Cu tape on one side and masked with PTFE tape thus leaving only the Cu tape protruding for providing electrical contact. Using a hole-puncher, a circle-like hole with diameter of 6 mm was carefully made in the PTFE on one of the flat sides of the samples thus fixing the geometric surface area of the exposed Cu-Sn bronze surface to 0.28 cm^2, as shown in Fig. S7. Regarding the Cu-Sn bronze anodes, the geometric surface area was fixed by masking the Cu-Sn bronze samples thus leaving exposed area with a rectangular shape. The geometric surface area of the anode was 2 cm^2. Both Cu-Sn bronze electrodes, together with a normal junction Ag/AgCl reference electrode (PalmSens) filled with 3 $mol \cdot dm^{-3}$ KCl(aq), were placed in a 50 cm^3 beaker in which 40 cm^3 of 1.5 $mol \cdot dm^{-3}$ H_2SO_4 (prepared from 98 wt.% H_2SO_4 and ultrapure water) were added (Fig. S7a). The distance between the cathode and the anode was kept fixed (5 mm). The co-electrodeposition was carried out in a potentiostatic mode thus applying cathodic potential of –2.9 V vs Ag/AgCl for 1 minute at room temperature and under constant stirring, using a Biologic SP-300 potentiostat with a voltage booster. The electrodeposition procedure was repeated 7 times, each time with a fresh bare Cu-Sn bronze cathode but without changing the electrolyte. In the first three depositions either no Cu-Sn foam was deposited on the Cu-Sn bronze cathode surface or its homogeneity and substrate surface coverage were poor. The 4th, 5th and 6th deposition produced a homogeneous foam (abbreviated as Cu-Sn foam in the main text and SI) and during the 7th deposition the solution became cloudy and white precipitate started to form.

The total geometric charge density per 1-minute electrodeposition time reached values of around –190 $C \cdot cm^{-2}$, as presented on Fig. S7b. The current density was quite noisy due to bubbles formation on the cathode, maintaining values between –3.3 and –3.8 $A \cdot cm^{-2}$ in the first ~20 seconds, after which a plateau was formed at around –3.1 $A \cdot cm^{-2}$ (Fig. S7c). The Cu-Sn bronze anode potential was simultaneously measured, and in the first 20 seconds its potential was in the range +0.8 to +1 V after which it jumped and formed a plateau at around +2.7 V vs Ag/AgCl, as presented in Fig. S7d. No bubbles were observed on the Cu-Sn bronze anode in the first 20 seconds. Namely, during this time interval the Cu and Sn from the Cu-Sn bronze anode are expected to completely oxidize into Cu^{2+} and Sn^{4+}, respectively, according to the Pourbaix diagrams for these elements[9-10] at such high overpotential and acidic environment (1.5 $mol \cdot dm^{-3}$ H_2SO_4, pH<0) - Eqs. 2 and 4. However, the partial oxidation to Sn^{2+} is not fully excluded (Eq. 3). The jump of the anodic potential (see Fig. S7d) is accompanied with vigorous bubbling, which suggests switching of the faradaic selectivity from Cu/Sn oxidation processes into O_2 evolution reaction that becomes a dominant process (Eq. 4).

Anodic reactions:

$Cu(s) \rightarrow Cu^{2+}(aq) + 2e^-$ (2)

$Sn(s) \rightarrow Sn^{2+}(aq) + 2e^-$ (3)

$Sn(s) \rightarrow Sn^{4+}(aq) + 4e^-$ (4)

$2H_2O(l) \rightarrow O_2(g) + 4H^+ + 4e^-$ (5)

On the other hand, the cathodic processes were accompanied with generation of H_2 (Eq. 6) bubbles during the whole 1-minute electrochemical experiment at fixed applied potential. However, similarly as in the case of the anodic potential change, the synchronous current density decrease (cf. Fig. S7c, d) could be attributed to switch from reduction of the Cu^{2+} and $Sn^{4+/2+}$ (Eqs. 7-9) into H_2 evolution reaction as a dominant process.

Cathodic reactions:

$2H^+(aq) + 2e^- \rightarrow H_2(g)$ (6)

$Cu^{2+}(aq) + 2e^- \rightarrow Cu(s)$ (7)

$Sn^{2+}(aq) + 2e^- \rightarrow Sn(s)$ (8)

$Sn^{4+}(aq) + 4e^- \rightarrow Sn(s)$ (9)

As mentioned above, during extensive use of the electrodeposition solution (7th time) a white precipitate starts to form. This could be attributed to hydrolysis of the Sn^{4+} (Eq. 10) most probably due to exceeding a saturated concentration. The Cu-Sn foam prepared from this Sn-saturated electrodeposition solution is abbreviated as $Cu_{1.4}Sn$ (Cu/Sn surface ratio of 1.4, as determined by XPS - Tab. S3) in the main text of the manuscript and in the SI. The foam that is prepared before such saturation occurs resembles Cu/Sn surface ratio - 10 and gives (Tab. S3) the best CO_2ER to CO selectivity (see Fig. S14 for selectivity comparison) and thus is abbreviated simply as Cu-Sn foam.

Hydrolysis of Sn^{4+} species:

$Sn^{4+}(aq) + 2H_2O(l) \rightarrow SnO_2(s) + 4H^+(aq)$ (10)

According to the ICP-OES results (Table S4) from the analysis of the electrodeposition solutions, the concentration of Sn in the saturated solution is indeed higher than the concentration of the same element in the solution from which the optimal Cu-Sn foam with Cu/Sn surface ratio 10 is co-electrodeposited. In correlation, the concentration of Cu is also higher in the Sn saturated electrodeposition solution. However, it is important to note that the Cu/Sn ratio in both solutions is 14-15, identical to the bulk composition of the Cu-Sn bronze. This behavior could be associated with the differences in the exchange current densities and overpotentials of both elements under the utilized DHBT conditions. Namely, Cu and Sn do not electrodeposit simultaneously i.e., the concentration of Cu^{2+} is much higher and this specie is more prone to be reduced faster due to its lower exchange current density and overpotential and thus takes deposition advantage over $Sn^{4+/2+}$.[8, 11] This leads to higher accumulation of Cu in the bulk of the foam than on the surface, as revealed from the EDX and XPS results on Table S3. On the other hand, the Sn^{4+} species are not able to electrodeposit with a foam morphology under the current density that is reached at applied potential of –2.9 V vs Ag/AgCl due to its poor H_2 evolution activity (as discussed below).[8, 11] Therefore, the electrodeposition of Sn is mostly concentrated on the surface of the Cu-Sn foam, rather than the bulk and this is even more obvious in the case of the foam prepared from the Sn saturated solution, where both elements resemble almost equal surface abundance (Table S3). The complete understanding of the mechanism and kinetics of the Cu-Sn bimetallic foam electrodeposition requires more extensive study and this worth to be investigated more thoroughly in the future.

For comparison, pure Cu foam was prepared using the same electrodeposition approach but utilizing Cu foil as an anode instead of Cu-Sn bronze (SEM images depicted on Figs. 1d, e and S9). Unfortunately, pure Sn foam could not be prepared via the DHBT method

under the same conditions as for preparation of the Cu-Sn and pure Cu foams since as aforementioned higher overpotential and exchange current are required due to its poor catalytic activity for HER.[8, 11] The constrain comes from the Biologic SP-300 potentiostat with a voltage amplifier and it cannot exceed –3 V vs Ag/AgCl under which such a current density cannot be achieved.

S1.5. Electrochemical measurements

Estimation of the Relative Surface Roughness Factor (RSRF). The relative surface roughness factor of the Cu-Sn foam electrocatalyst was estimated from the electrode double layer capacitance (C_{DL}) that was measured using cyclic voltammetry (CV) in a non-faradaic region of potentials at various scan rates (20-140 $mV \cdot s^{-1}$). The range of potentials was -0.15 to -0.05 V for the Cu-Sn bronze, and -0.12 to -0.08 V vs Ag/AgCl for the Cu-Sn foam. The C_{DL} was determined as a slope from the equation (Eq. 11) where the difference between the anodic (J_{Anodic}) and the cathodic ($J_{Cathodic}$) capacitive current density (measured capacitive current normalized to the geometric surface area) is linearly dependent from the scan rate (SR) at a fixed potential. All C_{DL} estimations were calculated at a potential of –0.1 V vs Ag/AgCl. Using Eq. 12, the RSRF was calculated as a ratio between the C_{DL} values of the Cu-Sn foam electrocatalyst and the bare Cu-Sn bronze (that has a near planar surface and was used as a starting material for the Cu-Sn foam electrocatalyst preparation). Additionally, the RSRF was estimated for a Cu foam (in the same applied potential range as for the Cu-Sn foam) that was prepared under the same electrodeposition conditions, as described in the previous Subsection. The electrochemical setup that was used for this purpose was identical as for the electrocatalytic activity measurements described in the text below. The results from these measurements are presented on Fig. S12 and the calculated RSRF values are presented in Table S6.

$$\Delta J_{Capacitive} = (J_{Anodic} - J_{Cathodic}) = C_{DL} \cdot SR + a_{Intercept} \quad (11)$$

$$RSRF = C_{DL,\ Cu\text{-}Sn\ foam} / C_{DL,\ Cu\text{-}Sn\ bronze} \quad (12)$$

Electrocatalytic activity measurements and product analysis. The CO_2 conversion electrochemical experiments were performed in H-type two-compartment gas-flow cell made of glass, where the cathodic and the anodic compartment are separated with a previously activated Nafion N-115 cation exchange membrane (Thickness - 0.125 mm, Alfa Aesar). Both compartments were filled with 30 cm^3 of 0.1 $mol \cdot dm^{-3}$ $KHCO_3$ (freshly prepared from $KHCO_3$ and ultrapure water) as a supporting electrolyte. The cathodic compartment was hermetically sealed except for a gas inlet port at the bottom and a headspace gas outlet at the top. The cell was continuously purged with CO_2, starting at least 30 min prior to the measurements (flow rate: 20 $cm^3 \cdot min^{-1}$, controlled by a mass-flow controller type Red-y GSC-A9TA-BB21, Vögtlin Instruments) through a porous glass frit to produce small CO_2 bubbles. Normal junction Ag/AgCl electrode filled with 3 $mol \cdot dm^{-3}$ KCl(aq) was used as a reference ($E°$ = +0.210 V vs SHE at 25 °C, PalmSens), Pt-mesh as a counter and Cu-Sn bronze, Cu-Sn foam, Cu foam, Cu foil and Sn foil were used as working electrodes. The geometric surface area of the working electrode was fixed to be 0.28 cm^2 using PTFE tape. The electrochemical cell is depicted in Scheme S2. Electrochemical bias was provided using Biologic SP-200 potentiostat. The electrochemical method that was used during the CO_2ER activity measurements consists of: Open Circuit Voltage (OCV) for 2 min, Resistance measurement (ZIR-1), Chronopotentiometry (CP) at –10 $mA \cdot cm^{-2}$ until –0.9 V vs RHE (threshold), Chronoamperometry (CA-1) for 2 h, at –0.9 V vs RHE for activation of the electrocatalyst, Chronoamperometry (CA-2) for electrolysis and Resistance measurement ZIR-2. The automatic correction of the IR drop was set to 85%. The CP and the CA-1 activation step drive an initial reduction of the surface oxides prior to applying the second constant potential method (CA-2) where all current is expected to be consumed for the electrolysis processes (CO_2ER and HER). All applied potentials for the study

of the electrocatalytic activity are converted to the Reversible Hydrogen Electrode (RHE) scale, according to Eq. 13, considering that the pH of the CO_2 saturated 0.1 mol·dm^{-3} $KHCO_3$(aq) is 6.8. The measured current was normalized to the geometric surface area of the working electrode.

$$E \text{ vs RHE (V)} = E \text{ vs Ag/AgCl (V)} + E°_{Ag/AgCl} \text{ (V)} + 0.059 \text{ pH} \quad (13)$$

All samples were examined in the potential range from –0.5 to –1.0 V vs RHE. The gaseous products were quantified using on-line Gas Chromatograph (GC) from Thermo Scientific, model Trace 1310, dual column system using He as carrier gas and equipped with Pulse Discharge Detector (PDD) for detection of the light components (H_2, CO, CH_4, O_2, N_2) and Flame Ionization Detector (FID) for detection of C_2-hydrocarbons. The temperature program of the method was set to be 80 °C for the pre-separation micro-packed HayeSepS column (1 mm ID, Restek), where the CO_2 and C_2-hydrocarbons are separated from the light components in a first step, and 100 °C for the micro-packed molecular sieve MS5a column (1 mm ID, Restek), where the light components are separated from each other in a second step. The GC was calibrated in the range 20-1000 ppm,v for each component by using a mixed gas standard (Linde Gas) diluted with CO_2 to different concentrations. The headspace of the electrochemical cell cathodic compartment was directly connected with the GC transfer line (heated at 60 °C). The product concentration in the CO_2 gas stream was measured every 10 or 15 minutes for at least 2 hours at each applied potential with exception for the long-term stability experiments, where the measurements were performed for 15 hours and the product quantification was performed every 30 minutes. The faradaic efficiency (FE) for the gaseous products at a fixed applied potential was calculated using Eq. 14, where z is the number of electrons (z = 2 for HER and CO_2ER to CO, and 12 for CO_2ER to C_2H_4), F is the Faraday constant (96485.33 C·mol^{-1}), x_i is molar fraction of the component i, Q_m is the molar flow of CO_2 (bulk gas) and I_{total} is the average total current in the time interval of 2 min prior to the GC injection point.

$$FE_{\text{Gaseous product}} (\%) = z \cdot F \cdot x_i \cdot Q_m \cdot 100\% / I_{total} \quad (14)$$

The quantification of the non-volatile liquid CO_2ER products ($HCOO^-$) was conducted using Ultra-High-Performance Liquid Chromatograph from Thermo Scientific (model UHPLC+ UltiMate 3000 Series, Dionex) with UV variable wavelength (UltiMate 3000, Dionex) and refraction index (RefractoMax 520, ERC) detectors. The instrument utilizes a single column type HyperREZ XP H+, 5 mM H_2SO_4(aq) as an eluent for isocratic elution and equipped with an auto sampling unit. The quantification of $HCOO^-$ was performed after completion of each CA - electrolysis sequence at a fixed applied potential via sampling 1 cm^3 of the electrolyte, transferring it into a vial and placing the vial into the instrument's auto sampling unit. The instrument was calibrated for the quantification of the mentioned compounds in the corresponding concentration range. The faradaic efficiency (FE) for $HCOO^-$ was calculated using Eq. 15, where z is the number of electrons (z = 2 for CO_2ER to $HCOO^-$), c_{HCOO^-} is the concentration of $HCOO^-$ in the catholyte, F is the Faraday constant (96485.33 C·mol^{-1}), $V_{Catholyte}$ is the volume of electrolyte in the cathodic compartment (30 cm^3), $I_{total} \cdot t$ is the integration of the measured total current over time of the potentiostatic (CA) electrolysis sequence.

$$FE_{HCOO^-} (\%) = (z \cdot c_{HCOO^-} \cdot F \cdot V_{Catholyte} \cdot 100\%) / (I_{Total} \cdot t) \quad (15)$$

All FE and current density results are expressed as average values calculated from measurement of at least three replicate samples ± average mean absolute (error bars).

Estimation of the Tafel slopes for H_2, CO and $HCOO^-$ on Cu-Sn bronze and Cu-Sn foam electrocatalysts. The estimation of Tafel slopes for the cathodic electrolysis products obtained on both Cu-Sn bronze ($Cu_{14}Sn$) and Cu-Sn foam ($Cu_{10}Sn$) was performed using the Tafel equation (Eq. 16) as a limiting case of the Butler–Volmer equation for a cathodic reaction (Eq. 17) when the overpotential - $\eta >> 0$. E is the potential, E^o is the thermodynamically determined reduction potential, A is the Tafel slope, α is the charge transfer coefficient, or symmetry factor, z is the number of exchanged electrons, F is the Faraday constant (96485.33 $C \cdot mol^{-1}$), R is the universal gas constant (8.314 $J \cdot mol^{-1} \cdot K^{-1}$), T is the absolute temperature, J_x is the partial and $J_{0,x}$ is the exchange geometric current density for product x.

$$\eta = E - E^o = -A \cdot \log_{10}(-J_x) + A \cdot \log_{10}(-J_{0,x}) \quad (16)$$

$$J_x = -J_{0,x} \cdot \exp(\alpha \cdot z \cdot F \cdot \eta / RT) \quad (17)$$

Eq. 16, as a linear equation can be rearranged to:

$$E = -A \cdot \log_{10}(-J_x) + E^o + A \cdot \log_{10}(-J_{0,x}) \quad (18)$$

And further simplified to:

$$E = Tafel\ slope \cdot \log_{10}(-J_x) + intercept \quad (19)$$

According to Eq. 19, the applied potentials (E) for each cathodic electrolysis product were plotted versus $\log_{10}(-J_x)$ in the range of potentials where linear dependence was observed. The results on Fig. S14 show that all Tafel slopes, especially for H_2 and $HCOO^-$, are higher than the electrochemical limiting value of 120 $mV \cdot dec^{-1}$ for a one-electron unimolecular reaction when α = 0.5 (from the Butler-Volmer equation - Eq. 17), thus indicating different reaction nature of the rate-determining steps which most probably does not involve electron transfer (chemical limitation). The Tafel slopes for both Cu-Sn bronze and foam electrocatalysts suggest that the lowest overpotential is required for production of CO among all products. The CO Tafel slope obtained for the Cu-Sn foam electrocatalyst is 19 $mV \cdot dec^{-1}$ higher than the value obtained for the Cu-Sn bronze. On the other hand, the Tafel slope for H_2 is 31 $mV \cdot dec^{-1}$ higher in the case of Cu-Sn bronze. However, the biggest difference is observed in the Tafel slopes for $HCOO^-$ production, where overpotential 204 $mV \cdot dec^{-1}$ is required for the Cu-Sn bronze electrocatalyst.

According to the literature,[1] the Tafel equation (Eq. 16) can be written in the form presented as Eq. 20 in order to show the dependence of the Tafel slope from the intermediate surface coverage (θ):

$$Tafel\ slope = 2.3 \cdot R \cdot T / [F \cdot (\alpha + \theta)] \quad (20)$$

Where a higher Tafel slope value means lower surface coverage and vice versa. This implies that in the case of $HCOO^-$ production, the much higher overpotential among all intermediates in the case on both Cu-Sn electrocatalyst is a consequence to the lower surface coverage of the *OCHO* intermediate, which is rather typical for a Cu-rich Cu-Sn electrocatalyst that favors the CO over the $HCOO^-$ pathway, as discussed in the Introduction section and presented on Scheme S1.

S2. Experimental results

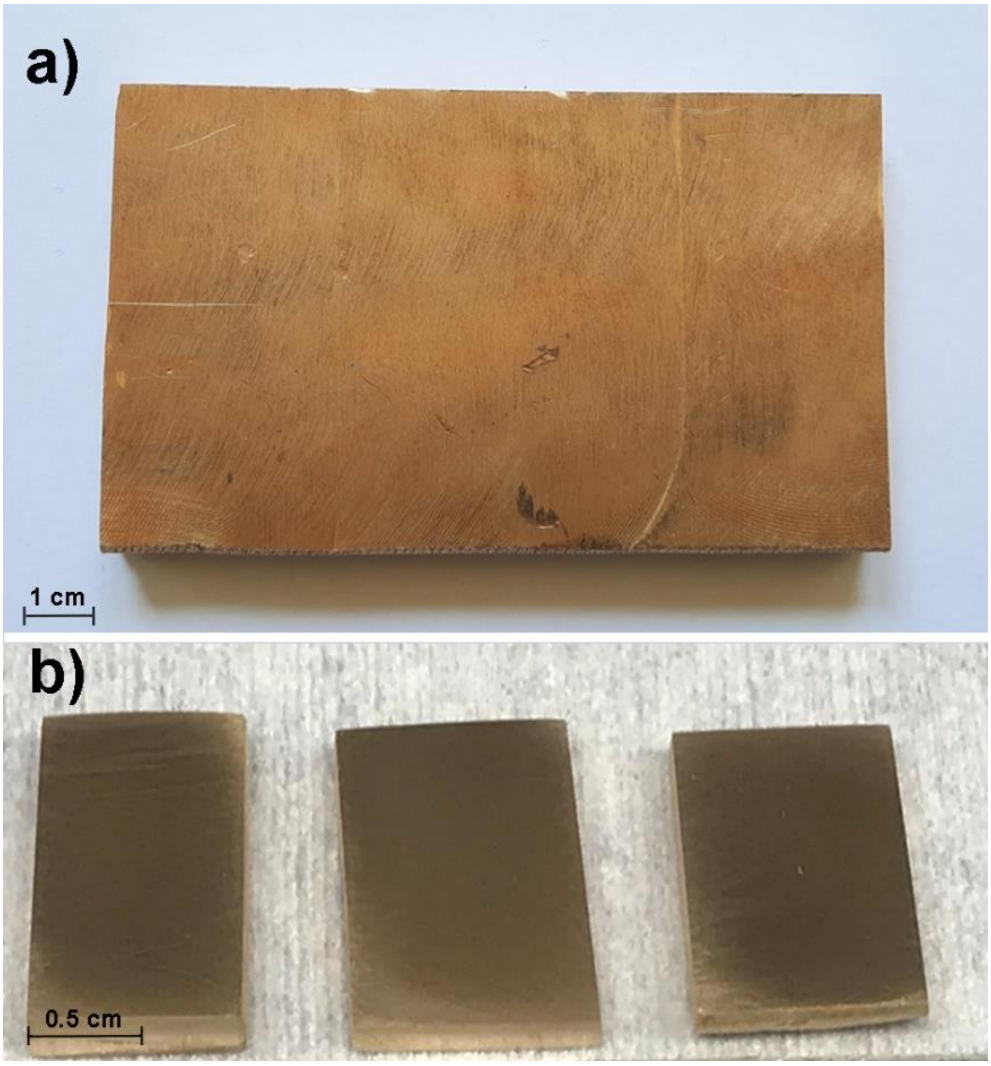

Figure S1. Waste industrial Cu-Sn bronze produced according to MKC EN 1982:2019: **(a)** casted ingot with dimensions of ~7 x 12 x 1 cm, as-received and **(b)** cut and mechanically polished plate-like samples, with dimensions of ~1 x 2 x 0.25 cm.

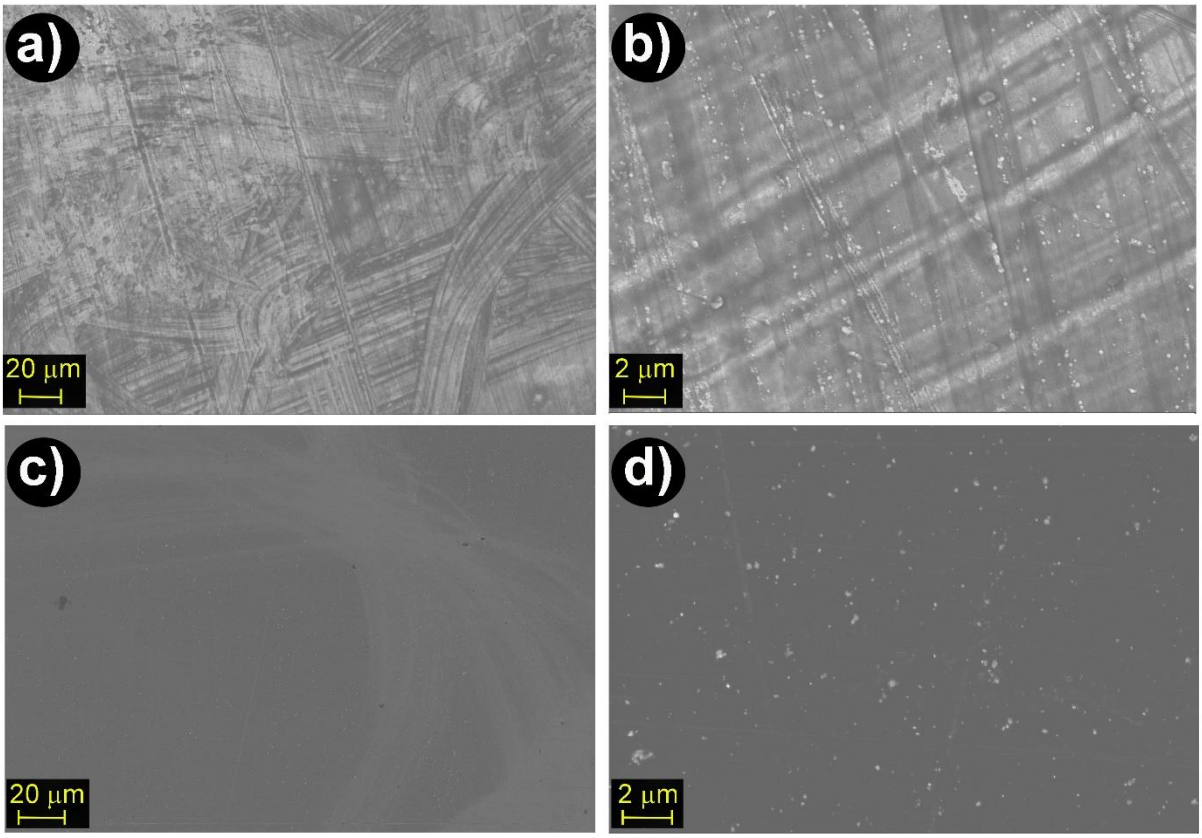

Figure S2. SEM images of the Cu-Sn bronze surface: comparison between **(a, b)** unpolished surface and **(c, d)** fine polished near-planar surface.

Table S1. Results from the ICP-OES bulk chemical composition analysis of the waste Cu-Sn bronze. The results are expressed as average values in wt. and at. % ± average mean absolute error. The Cu/Sn bulk ratio in the Cu-Sn bronze corresponds to nominal stoichiometry of $Cu_{14}Sn$.

Element	Fraction (wt. %)	Fraction (at. %)
Cu	87.784 ± 1.975	92.373 ± 2.078
Sn	11.744 ± 0.550	6.615 ± 0.310
Ag	0.021 ± 0	0.013 ± 0
Al	0.001 ± 0	0.002 ± 0.001
Ca	0.001 ± 0	0.001 ± 0.001
Cd	0.006 ± 0	0.004 ± 0
Co	N.D.	N.D.
Cr	N.D.	N.D.
Fe	0.001 ± 0	0.001 ± 0
Mg	N.D.	N.D.
Mn	N.D.	N.D.
Ni	0.088 ± 0.003	0.100 ± 0.030
Pb	0.131 ± 0.024	0.042 ± 0.008
Zn	0.829 ± 0.048	0.848 ± 0.049

N.D. – Not detected.

The small amounts seen here of Ni, Pb and Zn, with bulk fractions <1 wt.%, are not detectable on the surface of the Cu-Sn bronze by XPS analysis (see Fig. S5 and Table S3).

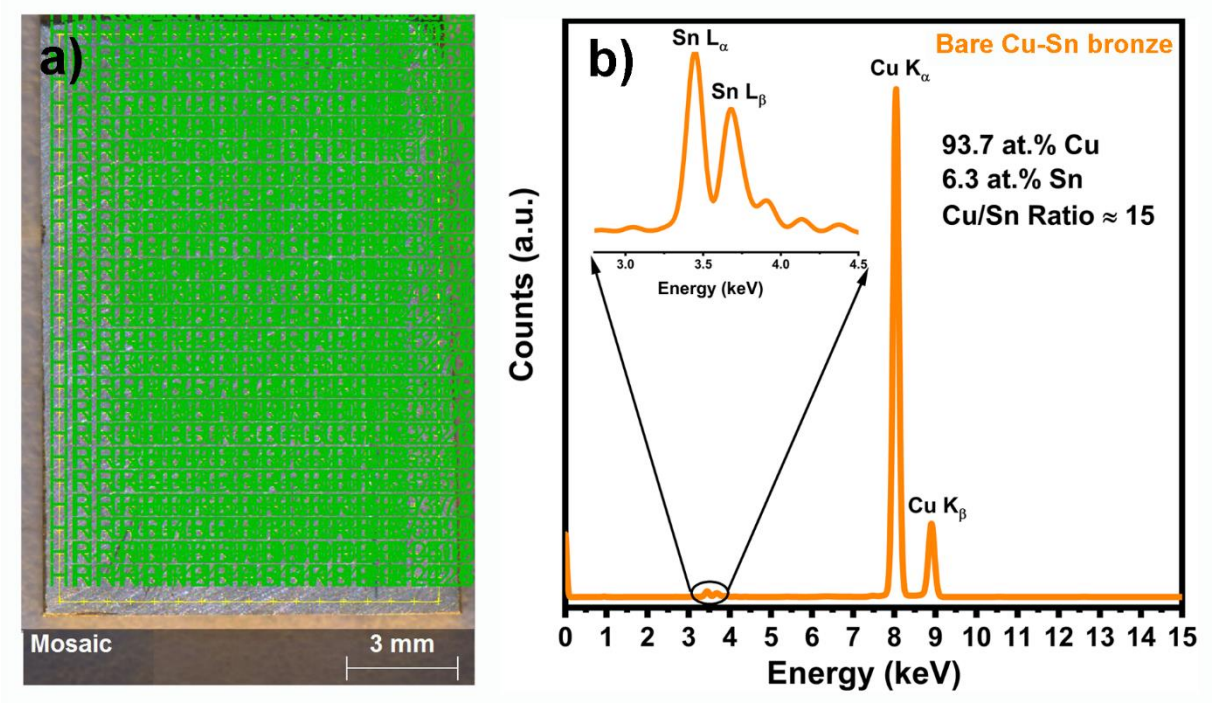

Figure S3. (a) Cu-Sn bronze sample (~1 x 2 x 0.25 cm) mapped in 425 points (green marks) in order to obtain representative XRF data in terms of the Cu and Sn bulk spatial distribution and quantification of the Cu-Sn stoichiometry. **(b)** representative XRF spectrum of the Cu-Sn bronze sample.

Table S2. XRF spatial distribution of the Cu/Sn atomic ratio in a bulk (~1 x 2 x 0.25 cm) Cu-Sn bronze sample expressed. The highest Cu/Sn ratio is labeled with dark green and lowest, with red color. The average (nominal) Cu/Sn ratio is 15.

15	11	13	14	17	15	18	20	15	16	8	20	14	13	18	16	17
16	15	12	21	17	13	15	11	14	14	16	18	18	13	16	16	14
14	20	18	12	20	18	11	17	11	19	8	20	20	12	20	20	12
10	14	14	13	20	13	17	15	14	23	18	11	9	23	11	20	19
17	14	20	12	24	12	18	17	13	16	14	15	14	13	20	14	12
15	18	15	16	14	19	21	13	13	12	24	15	18	14	16	14	16
16	13	16	16	12	19	14	11	17	17	14	18	18	15	17	20	16
15	15	13	19	19	13	21	16	19	18	20	15	11	13	14	18	18
12	13	15	15	10	17	14	15	16	13	12	21	15	18	11	17	17
13	12	16	16	13	11	9	16	14	10	13	15	13	14	19	18	12
15	13	18	16	12	13	21	14	18	12	16	21	17	17	16	16	21
16	16	18	16	16	23	12	9	15	16	15	15	20	17	12	10	17
17	12	12	18	14	14	13	12	14	15	16	13	17	21	19	16	14
17	11	16	13	18	12	11	16	11	14	14	12	15	15	15	19	20
14	18	14	12	12	9	18	14	14	19	14	13	13	14	15	15	18
18	20	13	16	13	17	14	19	14	22	19	14	18	15	10	15	17
12	16	15	14	16	14	14	14	19	13	18	14	17	14	16	18	14
17	16	23	11	20	12	16	14	18	12	13	9	17	16	14	10	14
22	14	18	14	13	15	16	15	16	10	13	15	17	22	15	20	16
17	10	14	17	17	16	16	20	14	11	16	11	20	16	13	16	19
15	15	9	19	15	14	19	17	12	15	15	21	18	20	11	18	15
17	14	12	18	10	10	15	19	16	21	9	15	16	15	18	21	12
21	11	19	19	16	14	19	15	10	20	19	12	12	15	16	18	18
17	18	15	18	15	15	19	15	12	11	17	19	16	12	11	20	23
17	15	18	14	12	15	17	14	12	16	13	15	14	16	13	11	18

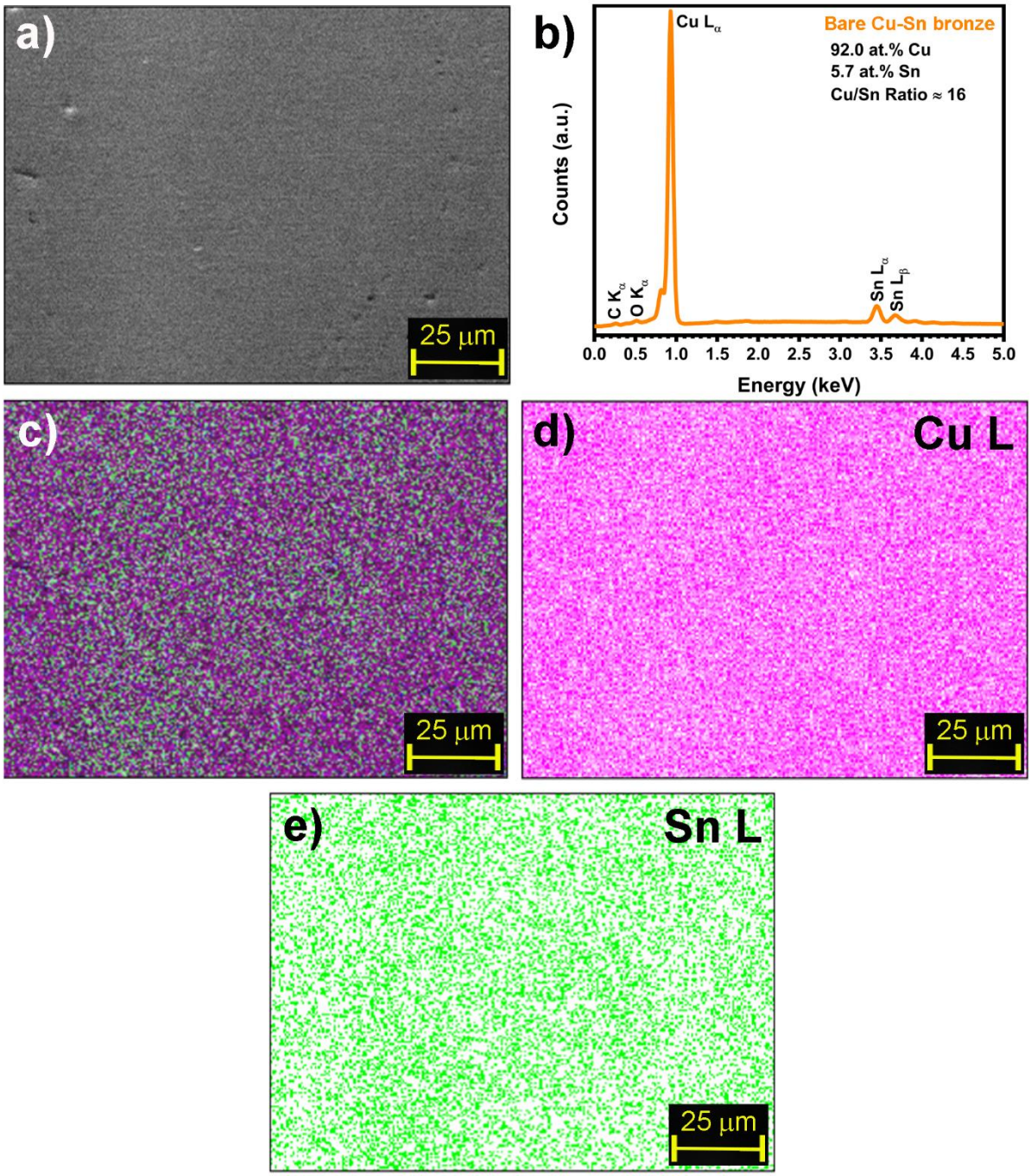

Figure S4. EDX mapping of pristine Cu-Sn bronze: **(a)** SEM image of the mapped area; **(b)** representative EDX spectrum; **(c)** distribution of all elements; **(d)** distribution of Cu and **(e)** Sn.

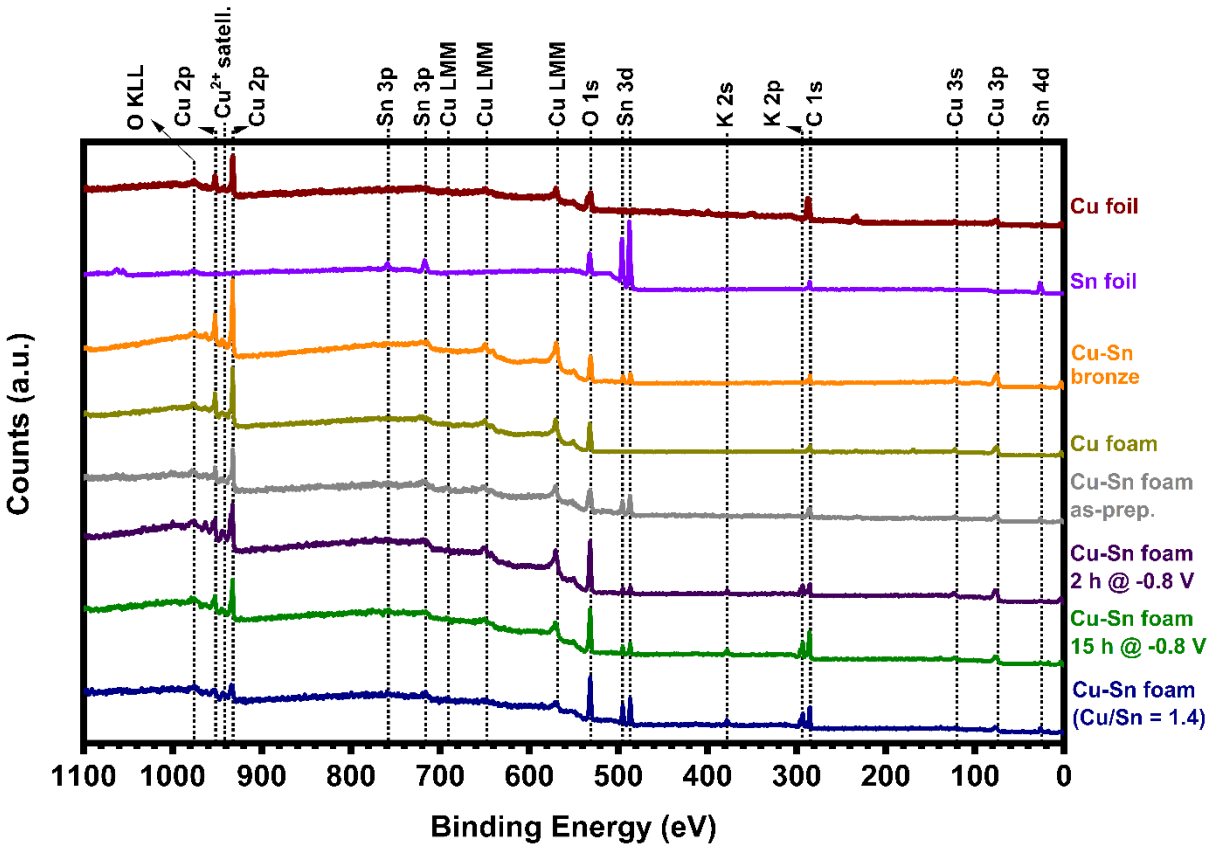

Figure S5. XPS survey spectra of samples under different conditions and peak assignments of the relevant core levels. Besides Cu, Sn, O, K and C, no other elements are detected on the surface of the samples that could potentially originate from the Cu-Sn bronze and are quantified with the ICP-OES (such as Ni, Zn, Pb with abundance <1 wt. %). K originates from the $KHCO_3$ electrolyte and appears on the Cu-Sn foams spectra that were subjected to 2 or 15 h electrolysis. Cu-Sn foam refers to the material with Cu/Sn surface ratio of 10 (which shows the best CO selectivity) and Cu-Sn foam with Cu/Sn ratio of 1.4 refers to the foam prepared from the Cu and Sn concentration-wise upper limit of re-used electrodeposition solution where the Sn extracted from the Cu-Sn bronze starts to precipitate (more explanation in section S1.4.).

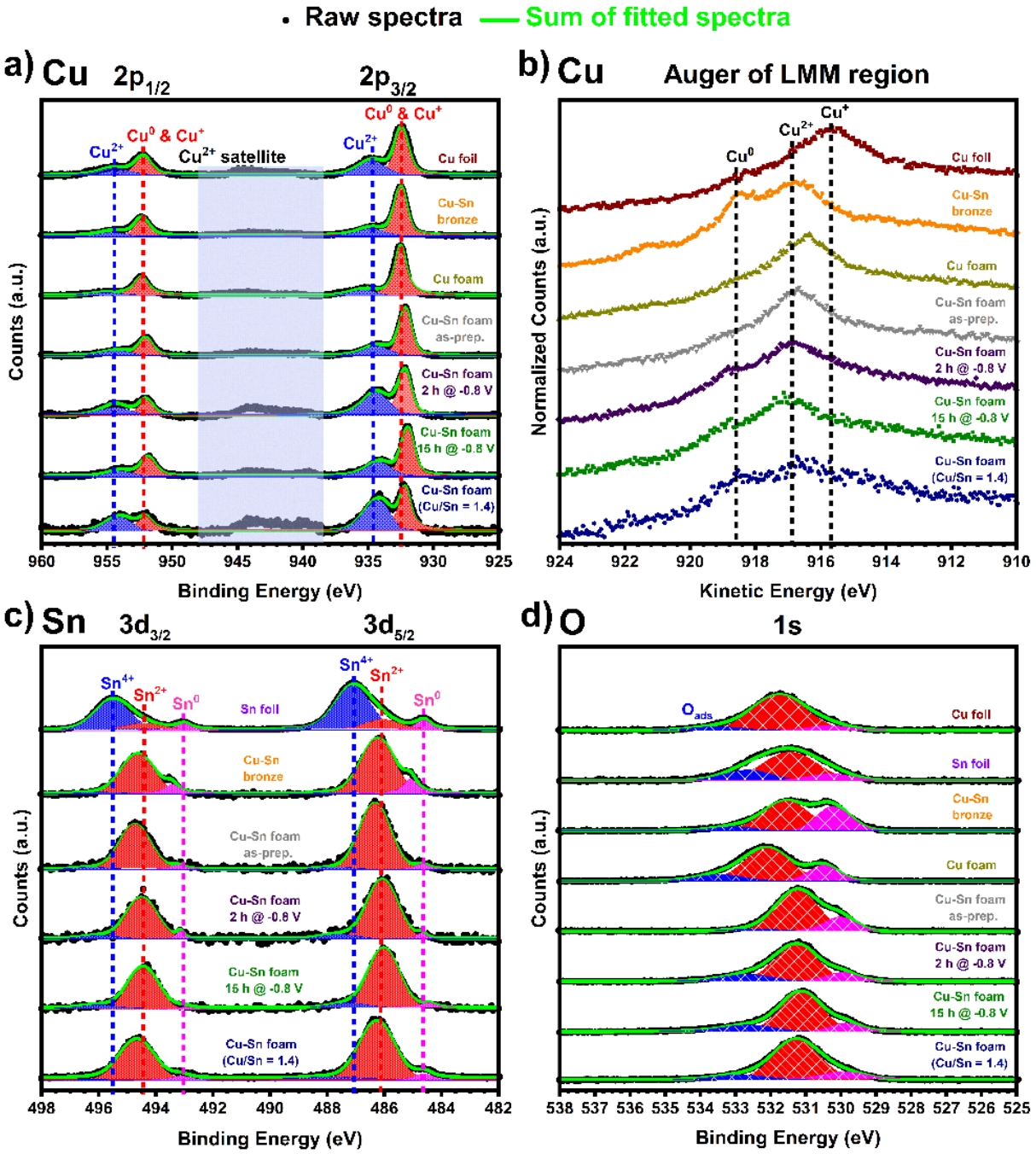

Figure S6. High resolution XPS spectra (Raw data, deconvoluted peaks assigned to different oxidation states and sum of fitted data)**: (a)** Cu 2p; **(b)** Cu Auger of LMM region; **(c)** Sn 3d and **(d)** O 1s. Cu-Sn foam refers to the material with Cu/Sn surface ratio of 10 - that shows the best CO selectivity and Cu-Sn foam with Cu/Sn ratio of 1.4 refers to the foam prepared from the Cu and Sn concentration-wise upper limit of re-used electrodeposition solution where the Sn extracted from the Cu-Sn bronze starts to precipitate (more explanation in section S1.4.).

The Cu 2p, Cu Auger, Sn 3d and O 1s XPS spectra on Fig. S6 show that the Cu-Sn foam and the Cu-Sn bronze are being oxidized during transfer to the XPS in air after the electrolysis which makes it difficult to identify which Cu and Sn valence species are involved in the CO_2ER mechanism. More advanced methods for *in situ* study of Cu-Sn catalysts under more relevant conditions are currently underway but beyond the scope of this work.

Table S3. Average values of the Cu/Sn surface and bulk ratios among different samples obtained from the high resolution XPS and EDX measurements, respectively. The Cu/Sn surface ratios are calculated from the Cu 2p and Sn 3d core levels peak-surface area of the high-resolution XPS spectra presented on Fig. S6.

Sample	Average Cu/Sn Surface Ratio	Average Cu/Sn Bulk Ratio
Bare Cu-Sn bronze	14	16
As-prepared Cu-Sn foam	10	113
Cu-Sn foam - after 2 h @ –0.8 V vs RHE	9.3	170
Cu-Sn foam - after 15 h @ –0.8 V vs RHE	10.2	101
*Cu-Sn foam - after 2 h @ –0.8 V vs RHE	1.4	Sn N.D.

*Cu-Sn foam with Cu/Sn ratio of 1.4 refers to the foam prepared from the Cu and Sn concentration-wise upper limit of re-used electrodeposition solution where the Sn extracted from the Cu-Sn bronze starts to precipitate (more explanation in section S1.4.)
N.D. – Not detected.

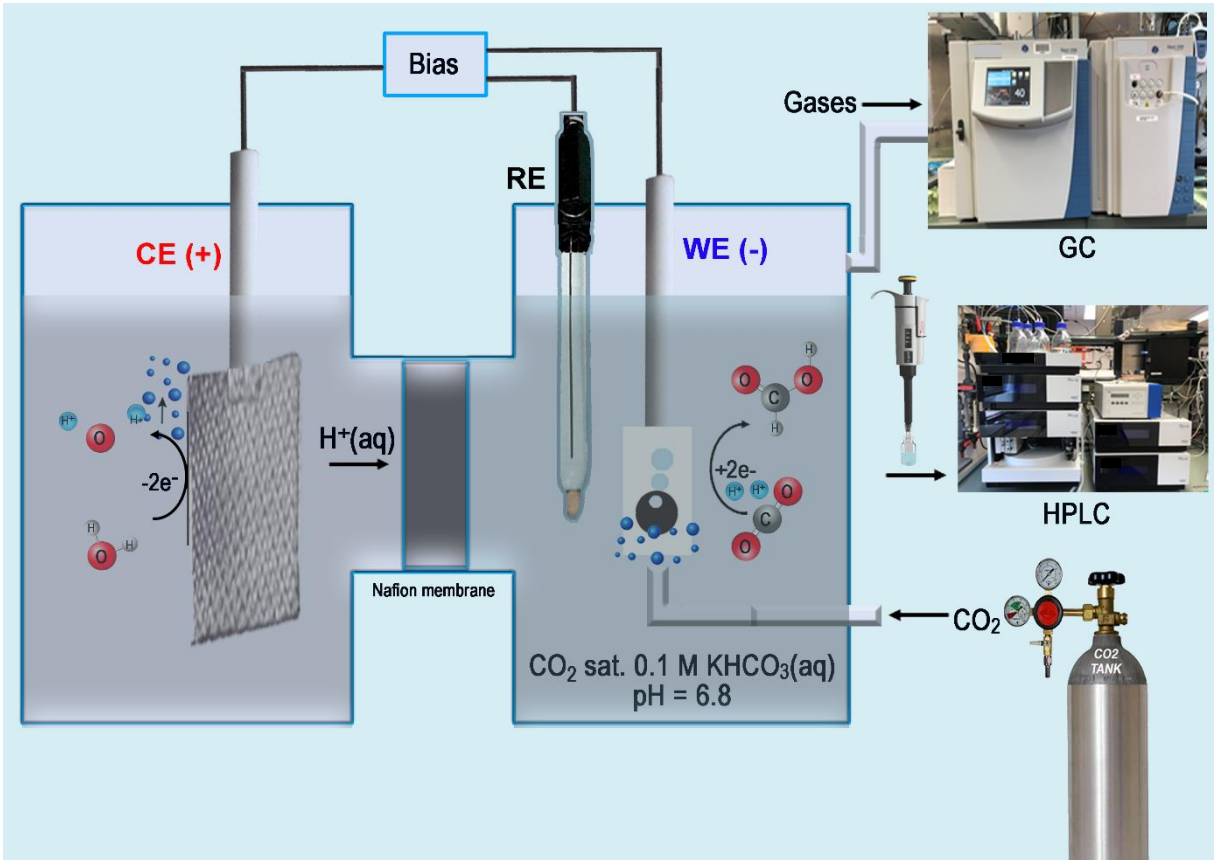

Scheme S2. H-type two-compartment electrochemical gas-flow cell, where the cathodic and the anodic compartment are separated with a Nafion membrane. Both compartments are filled with 0.1 mol·dm^{-3} $KHCO_3$(aq) as a supporting electrolyte, constantly purged with CO_2. The gaseous products are quantified using on-line Gas Chromatograph (GC), and the non-volatile liquid ones ($HCOO^-$) using Ultra-High-Performance Liquid Chromatograph from Thermo Scientific (UHPLC). The setup is described in section S1.5.)

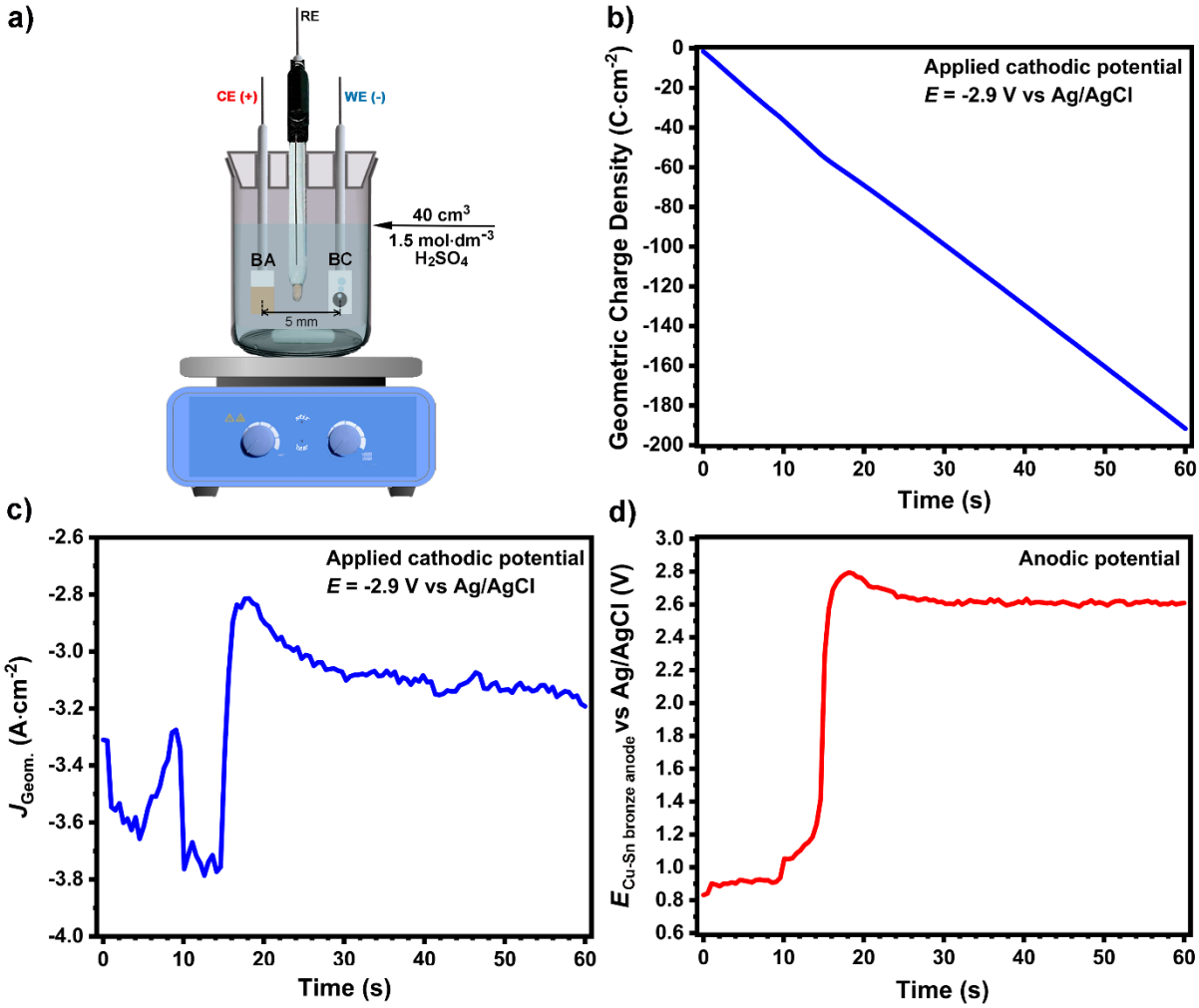

Figure S7. (a) Setup for preparation of porous Cu-Sn foam electrocatalysts via potentiostatic co-electrodeposition of Cu and Sn. BA refers to Cu-Sn bronze anode and BC to bronze cathode. Electrochemical conditions for preparation of Cu-Sn foam with Cu/Sn = 10 surface ratio: **(b)** total geometric charge and **(c)** current density that is passed in 1-minute time of electrodeposition at cathodic applied potential of –2.9 V vs Ag/AgCl (3 mol·dm^{-3} KCl). **(d)** Anodic potential versus time.

Table S4. Results from the ICP-OES analysis of the electrodeposition solution used for the DHBT co-electrodeposition of the Cu-Sn foams with Cu/Sn surface ratios of 10 and 1.4.

Element	Concentration of elements ($mmol \cdot dm^{-3}$) in the solution for preparation of Cu/Sn=10 foam (Optimal)	Concentration of elements ($mmol \cdot dm^{-3}$) in the solution for preparation of Cu/Sn=1.4 foam (Sn starts to precipitate)
Cu	29.38	39.42
Sn	2.09	2.51
Ag	N.D.	N.D.
Al	0.02	0.002
Ca	0.01	0.02
Cd	N.D.	N.D.
Co	N.D.	N.D.
Cr	N.D.	N.D.
Fe	N.D.	N.D.
Mg	N.D.	0.01
Mn	N.D.	N.D.
Ni	0.04	0.05
Pb	0.02	0.03
Zn	0.23	0.30

N.D. – Not detected.

Even though, the Cu/Sn ratio in both electrodeposition solutions is 14-15 as in the case of the bulk composition of the Cu-Sn bronze, the DHBT deposition mechanism is dependent from the concentrations of Cu and Sn, especially for altering the Cu/Sn surface ratio, as explained in section S1.4. and suggested from the XPS results (Table S3).

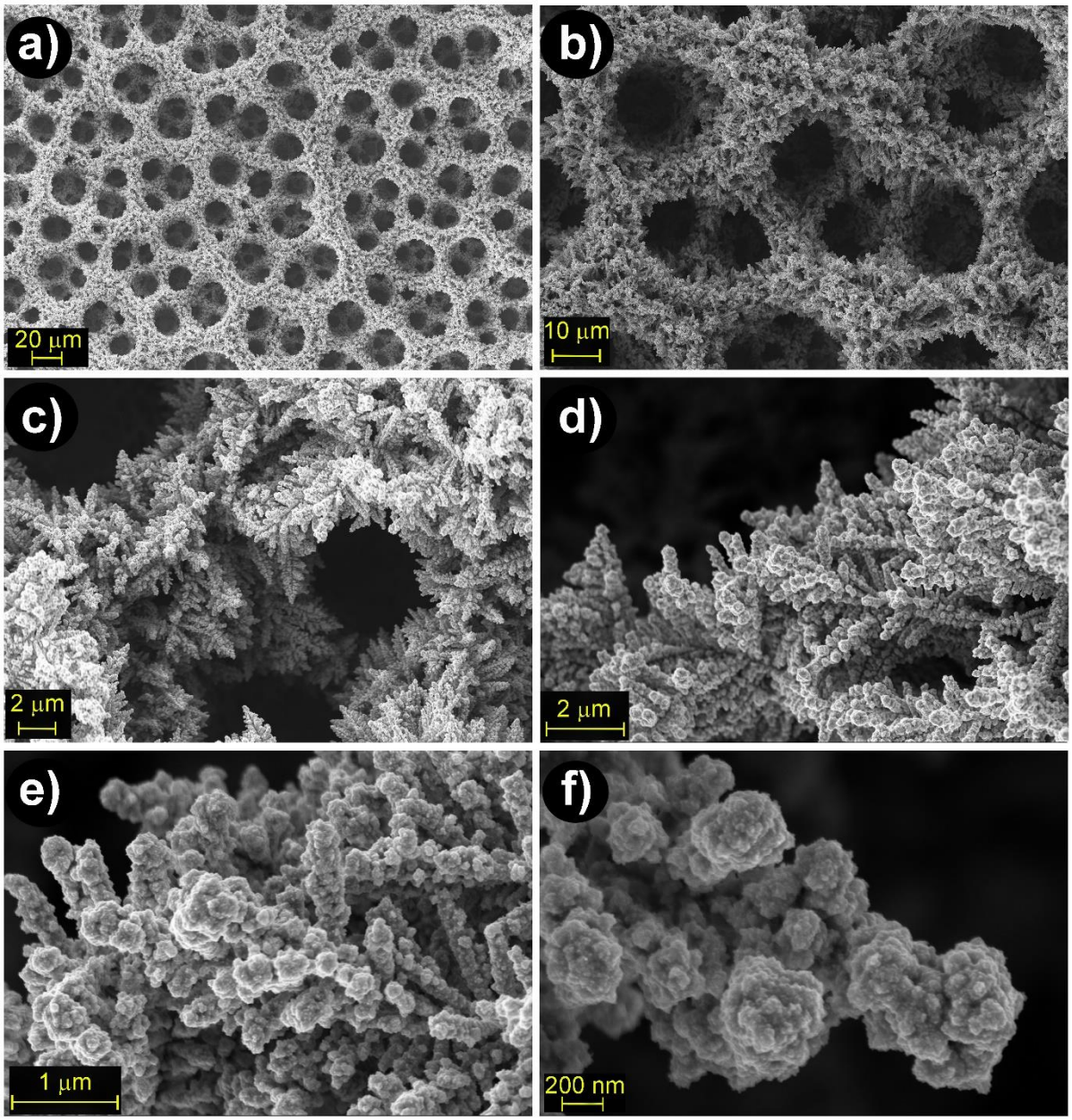

Figure S8. SEM images at various magnifications of as-prepared porous Cu-Sn foam consisting of dendrite microstructures. Figs. S8a, f appear as Figs. 1b, c in the main text, respectively.

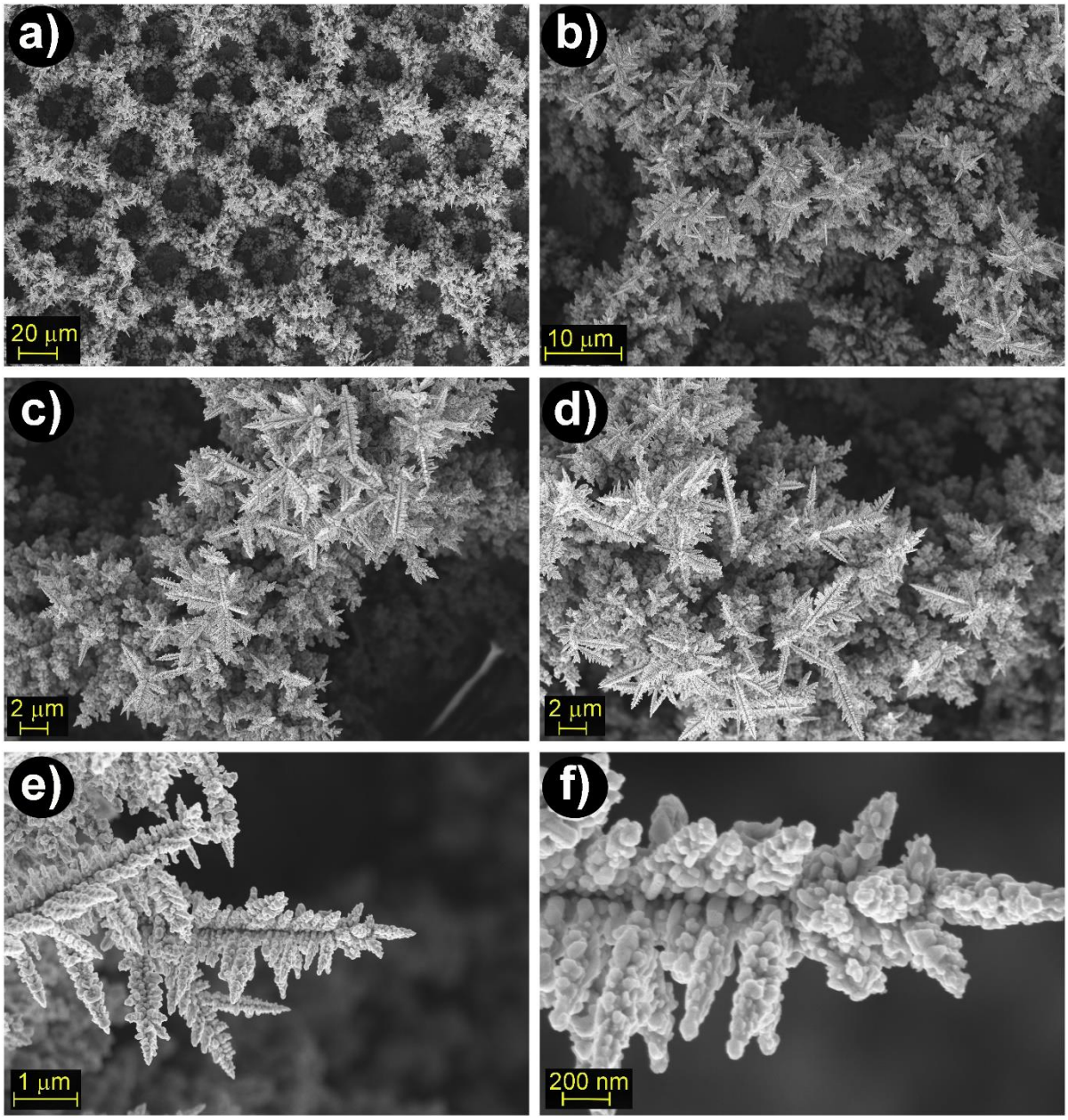

Figure S9. SEM images of pure Cu foam consisting of dendrite microstructures that remind of the leaves from fern plant species *Dicksonia antarctica.* Figs. S9a, f appear as Figs. 1d, e in the main text, respectively.

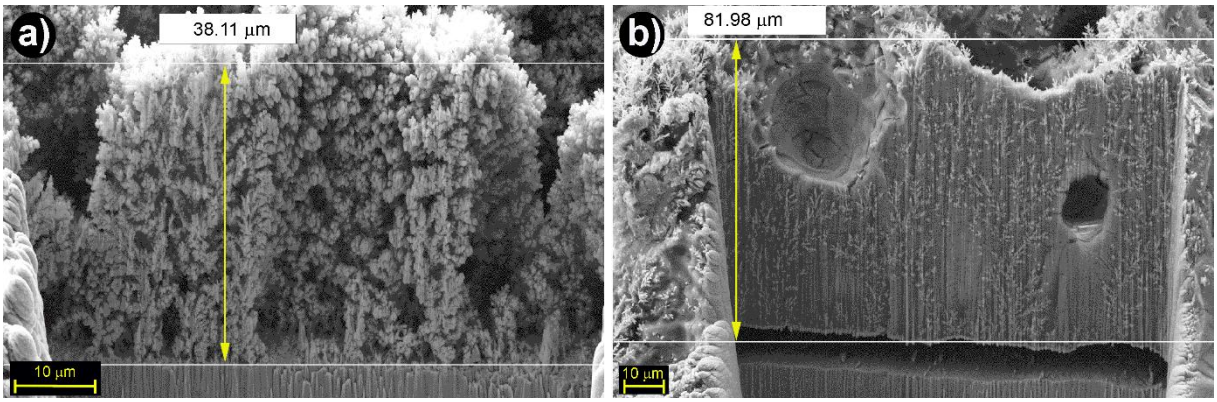

Figure S10. Cross-section SEM images of: **(a)** Cu-Sn and **(b)** pure Cu foam, after FIB ablation of the samples to form rectangular trenches. The thickness of the pure Cu (~82 µm) is around twice larger compared to the Cu-Sn foam (~38 µm).

Table S5. Average pore size (calculated from the SEM images on Figs. S8, 9) and cross-section thickness (FIB/SEM, from Fig. S10) of the Cu-Sn and pure Cu foams.

Sample	Average pore size (μm)	Average Foam thickness (μm)
Cu-Sn foam	24	38
Pure Cu foam	32	82

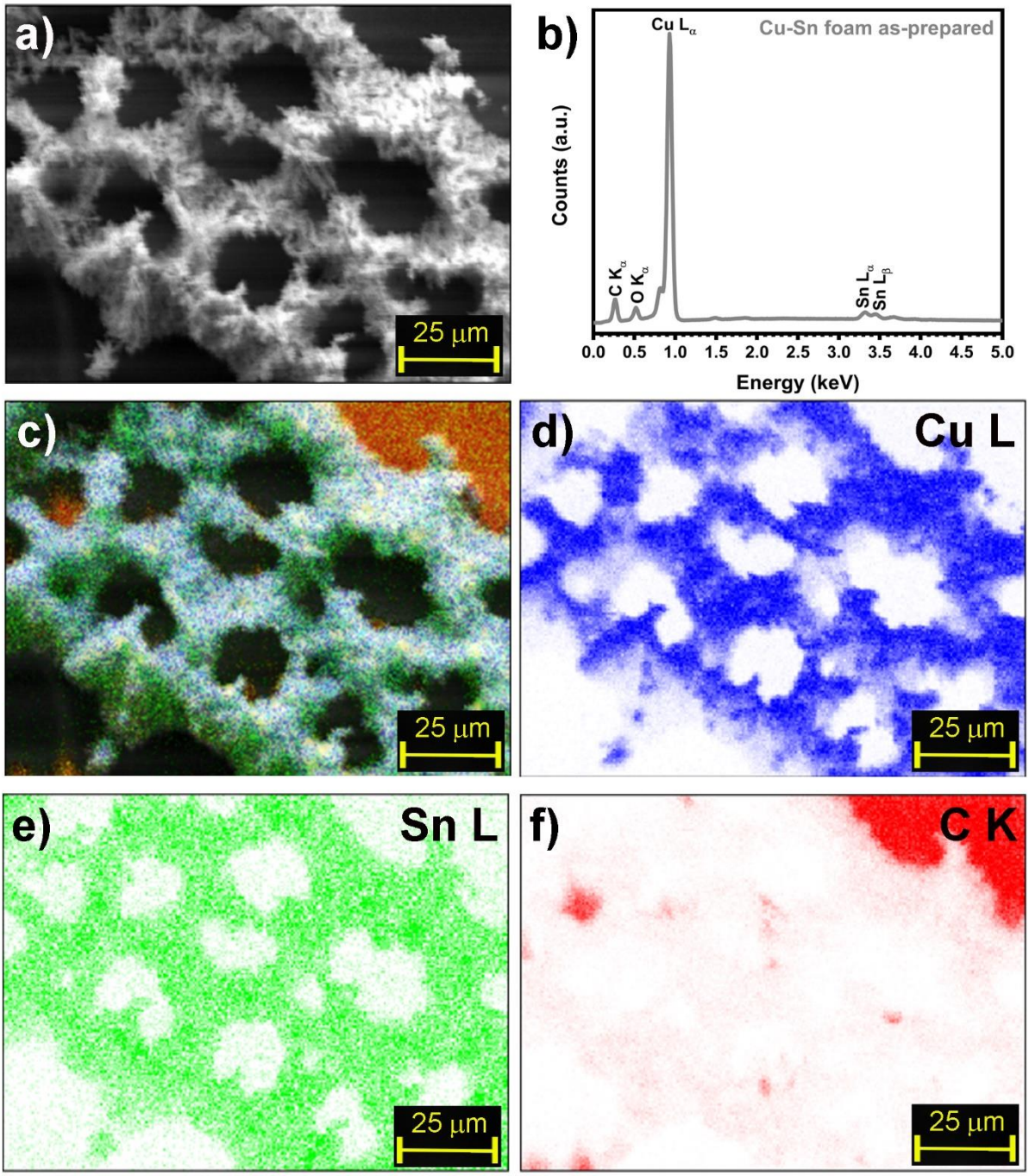

Figure S11. EDX mapping of as-prepared porous Cu-Sn foam: **(a)** SEM image of the mapped area; **(b)** representative EDX spectrum; **(c)** distribution of all elements; **(d)** distribution of Cu, **(e)** Sn, and **(f)** C from the background.

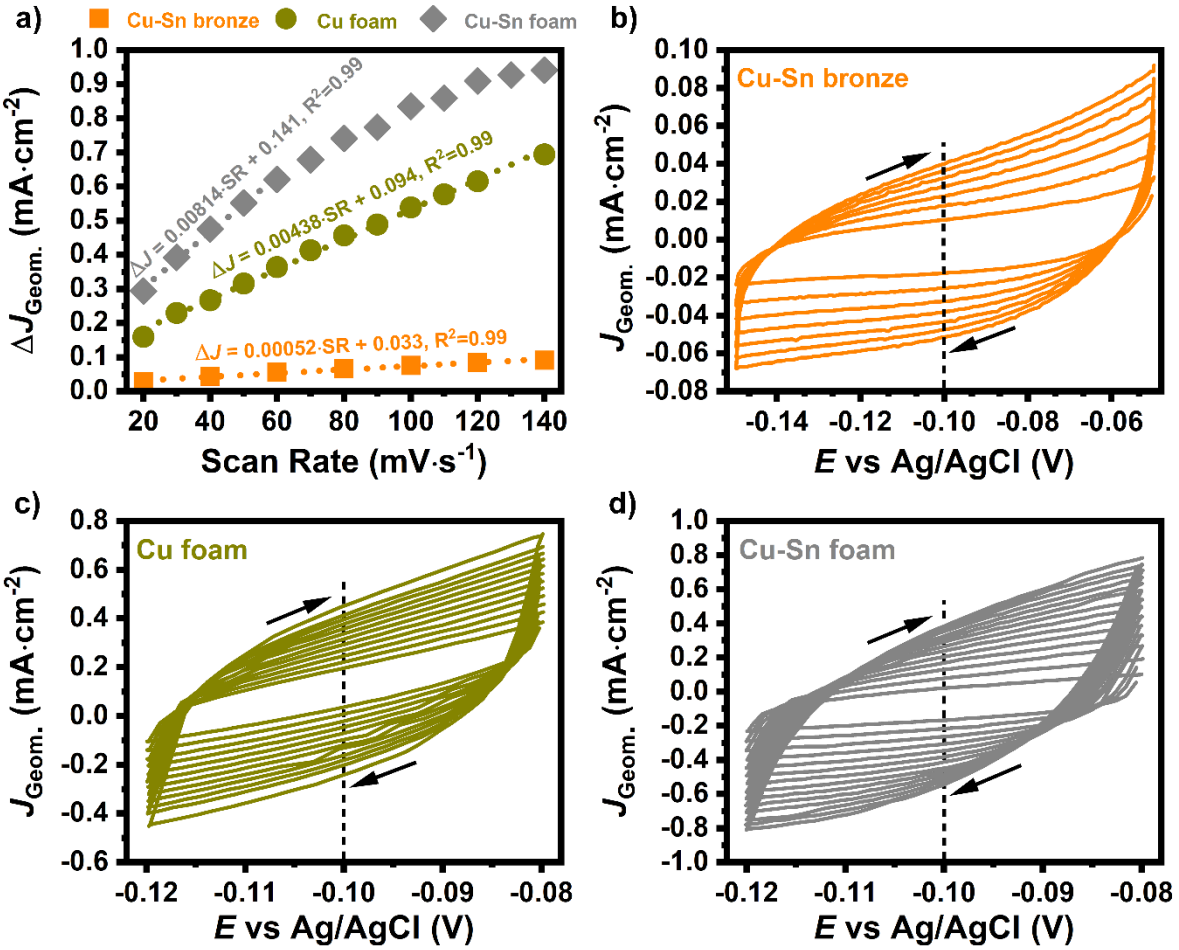

Figure S12. Estimation of the Relative Surface Roughness Factor (RSRF): **(a)** Linear plots – Capacitive Current Density (Δ*J*) vs. Scan Rate (SR), at a potential of –0.1 V vs Ag/AgCl. Cyclic voltammograms in a non-faradaic region of potentials at various scan rates for: **(b)** Cu-Sn bronze; **(c)** Cu foam and **(d)** Cu-Sn foam.

Table S6. Relative Surface Roughness Factors (RSRF) of bare Cu-Sn bronze, Cu foam and Cu-Sn foam.

Sample	RSRF
Bare Cu-Sn bronze	1
Cu foam	8.4
Cu-Sn foam	15.7

The linear plots - Capacitive Current (ΔJ) vs. Scan Rate on Fig. S12a shows that in the case of the Cu-Sn foam, an inflection of the linear behavior occurs at scan rates >60 $mV \cdot s^{-1}$, which is not observed in the case of the pure Cu foam and the Cu-Sn bronze, where the linearity is maintained up to 140 $mV \cdot s^{-1}$. This inflection in the linearity can be explained as a lack of diffusion i.e., sluggish capacitive charge/discharge at higher scan rates suggesting that the electroactive species need relatively more time to penetrate deeper in the Cu-Sn microstructure in comparison with the pure Cu foam. This can be explained by the larger average pore size of the pure Cu vs the Cu-Sn foam, even though the pure Cu foam is twice thicker than the Cu-Sn one, as presented in Table S5.

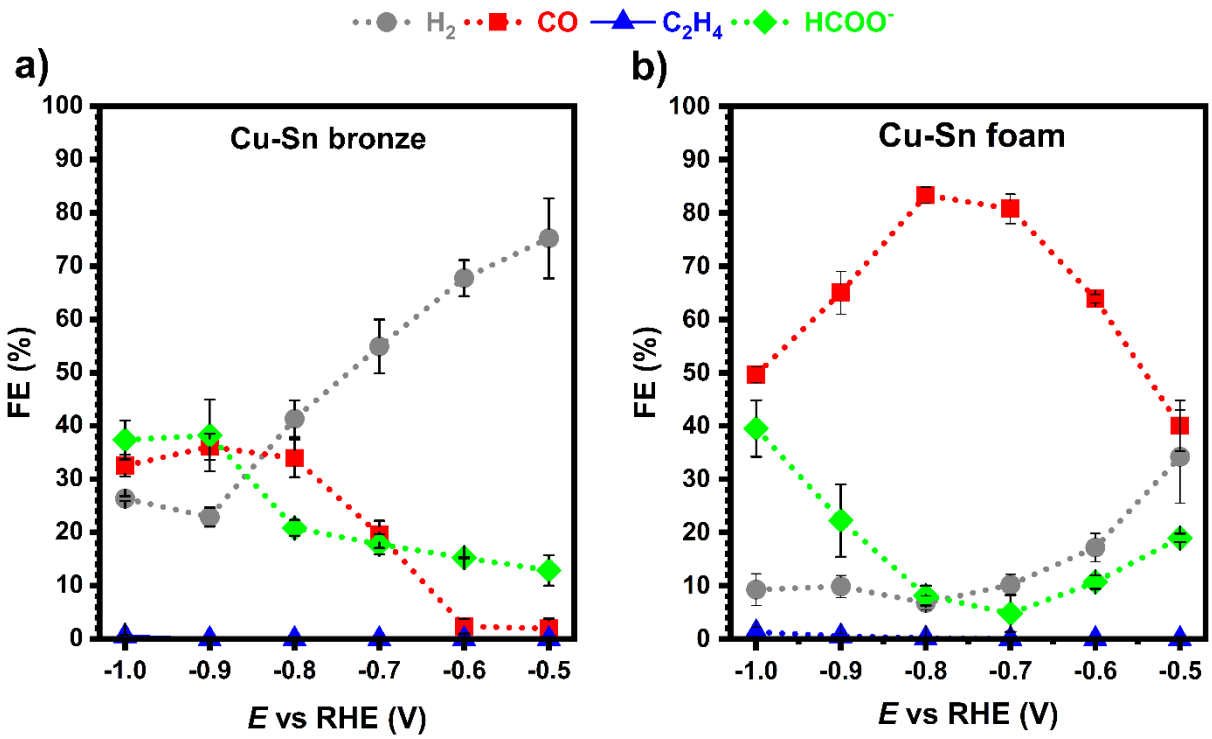

Figure S13. Replotted graphs from Fig. 2 (main text). Electrocatalytic activity results at various potentials: **(a)** distribution of FEs for products obtained on pristine Cu-Sn bronze and **(b)** on Cu-Sn foam. All results are expressed as average values ± average mean absolute error.

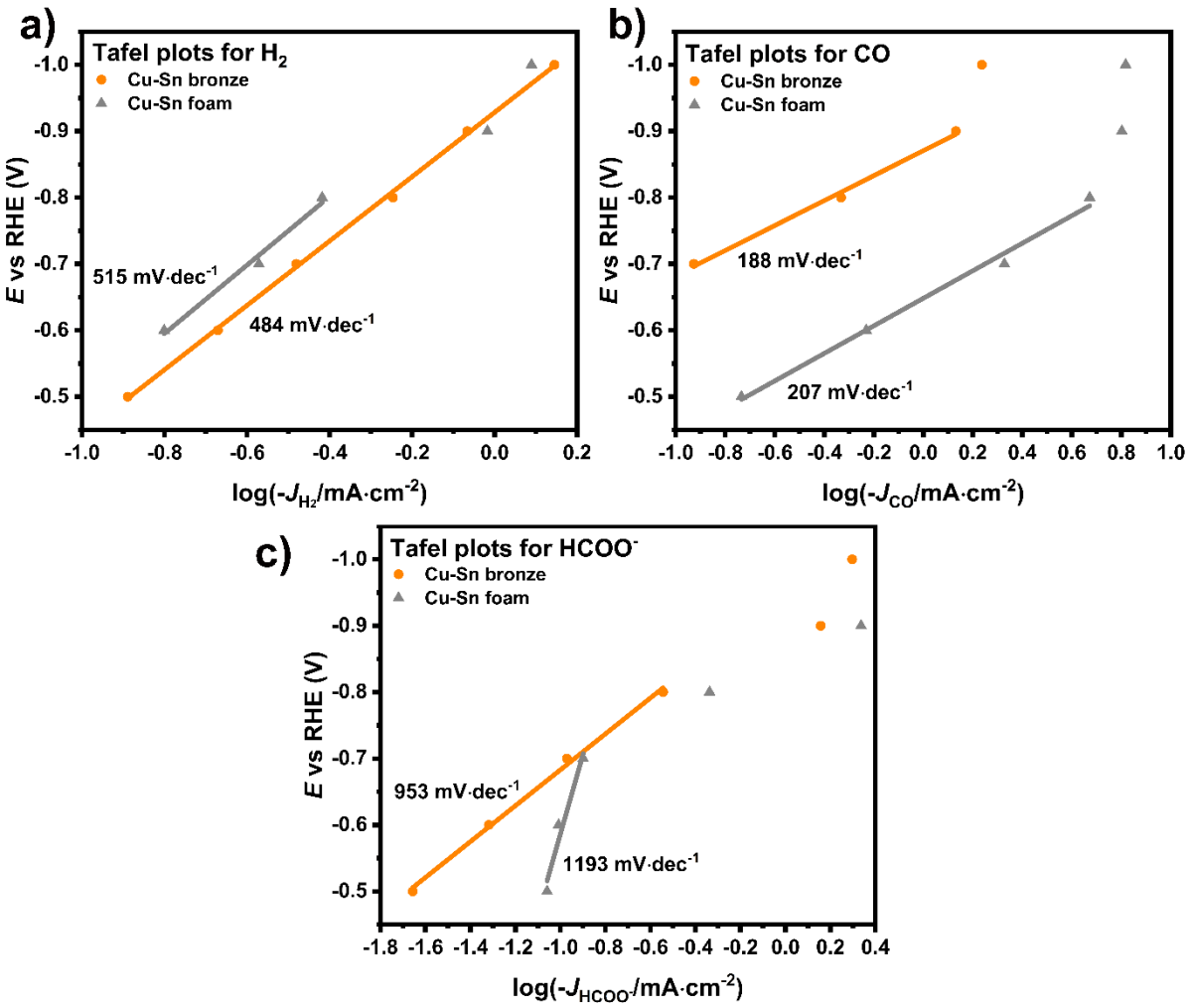

Figure S14. Tafel plots (E vs $\log_{10}(-J_x)$) for H_2, CO, and $HCOO^-$ obtained on Cu-Sn bronze and foam electrocatalysts, respectively.

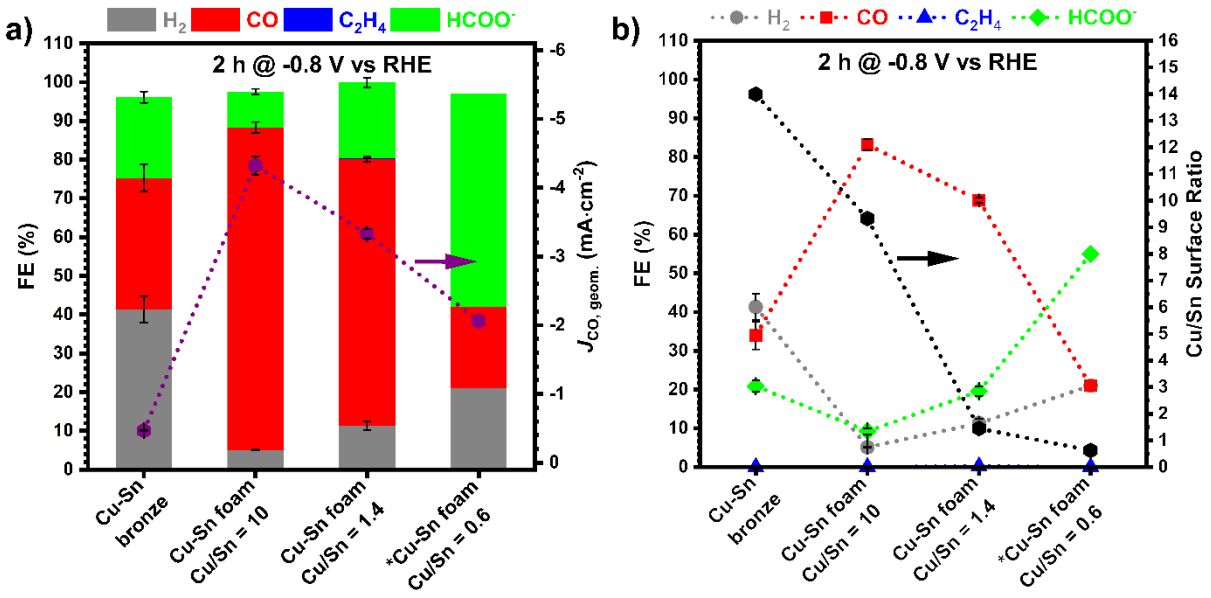

Figure S15. Selectivity vs Cu/Sn Surface Ratio for Cu-Sn bronze and Cu-Sn foam prepared from optimal (Cu/Sn = 10), from Sn saturated (Cu/Sn = 1.4) electrodeposition solution and *Sn-rich Cu-Sn foam, at –0.8 V vs RHE: **(a)** Distribution of FEs for H_2, CO, C_2H_4 and $HCOO^-$, and CO - Partial current density; **(b)** distribution of FEs for H_2, CO, C_2H_4 and $HCOO^-$ vs Cu/Sn Surface Ratio. The FE and current density results are expressed as average values ± average mean absolute error.
*Sn-rich Cu-Sn foam with Cu/Sn surface ratio of 0.6 was prepared from an electrolyte containing Cu^{2+} and Sn^{2+} with concentrations of 0.2 mol·dm^{-3} in 1.5 mol·dm^{-3} H_2SO_4 via galvanostatic DHBT electrodeposition method at 1 A. The CO_2ER activity of this catalysts was measured, and the results are presented in this figure in order to experimentally support the reaction mechanisms showed on Scheme S1 according to which the increase of the surface Sn in the Cu-Sn foam switches the selectivity from CO towards $HCOO^-$ production.

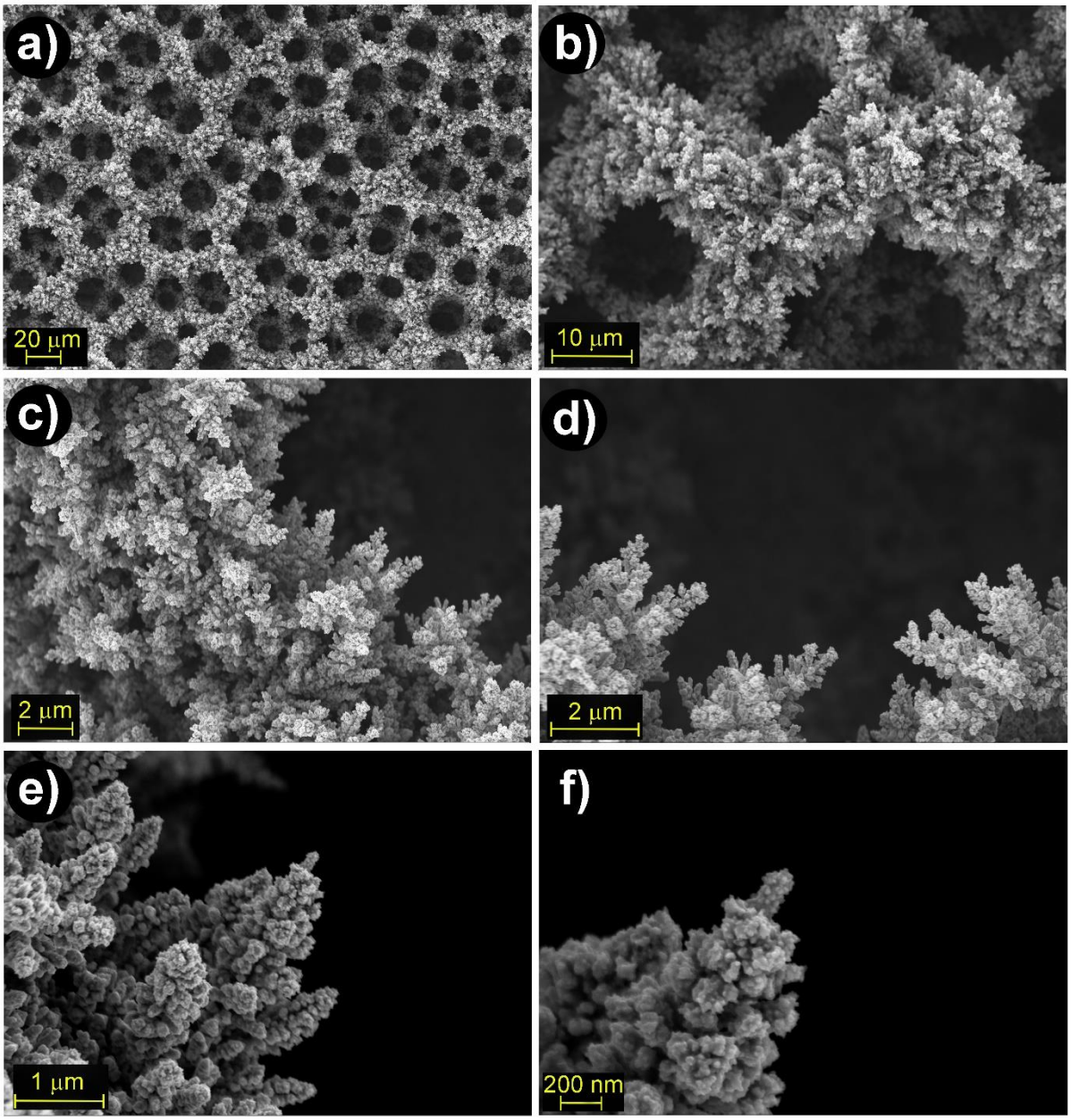

Figure S16. SEM images of Cu-Sn foam after 2 h electrolysis at –0.8 V vs RHE. Figs. S16a, f appear as Figs. 3d, e in the main text, respectively.

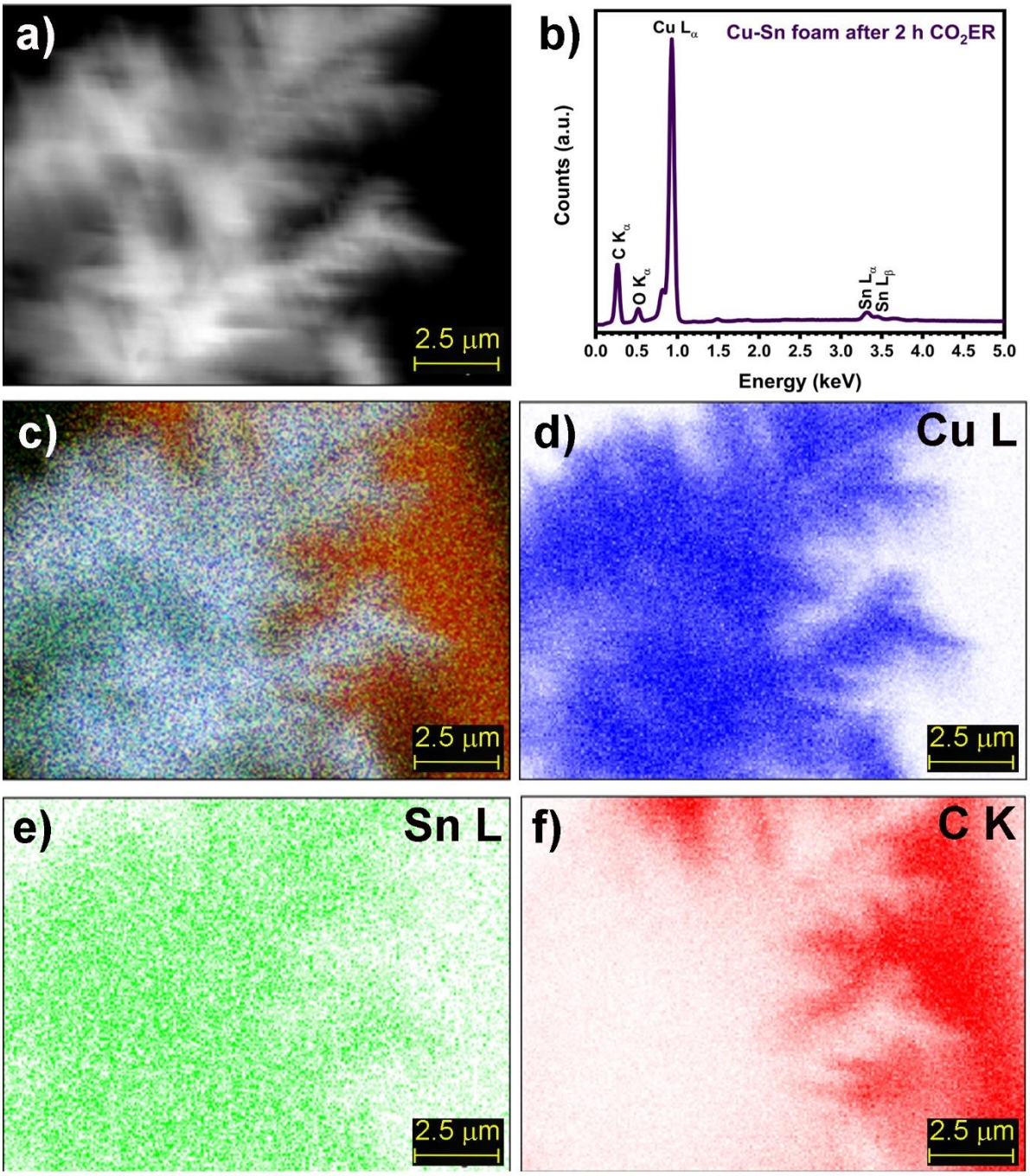

Figure S17. EDX mapping of dendrite microstructures in Cu-Sn foam after 2 h electrolysis at –0.8 V vs RHE: **(a)** SEM image of the mapped area; **(b)** representative EDX spectrum; **(c)** distribution of all elements; **(d)** distribution of Cu, **(e)** Sn, and **(f)** C from the background.

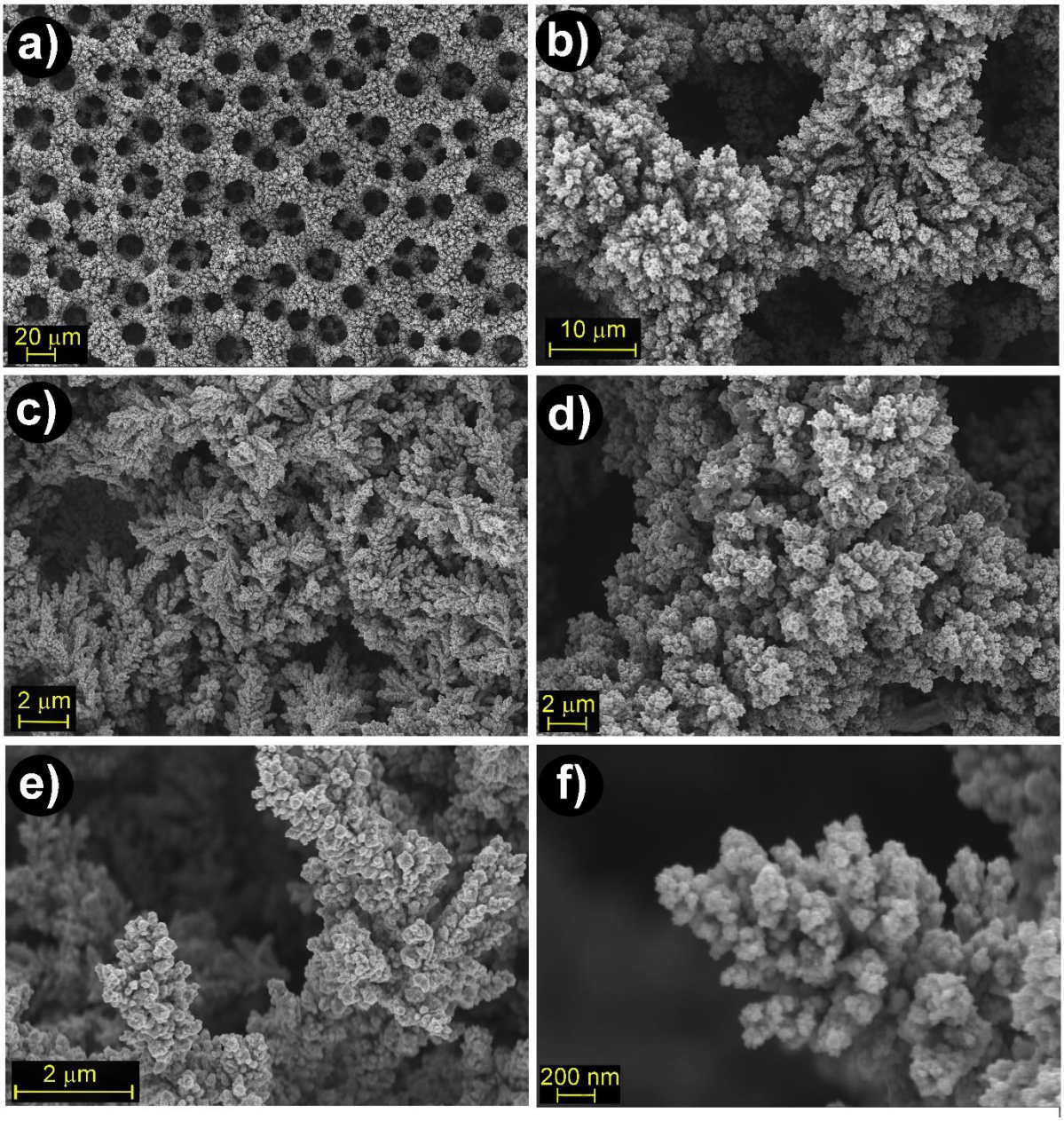

Figure S18. SEM images of Cu-Sn foam after 15 h electrolysis at –0.8 V vs RHE (stability/durability test). Figs. S18a, f appear as Figs. 3f, g in the main text, respectively.

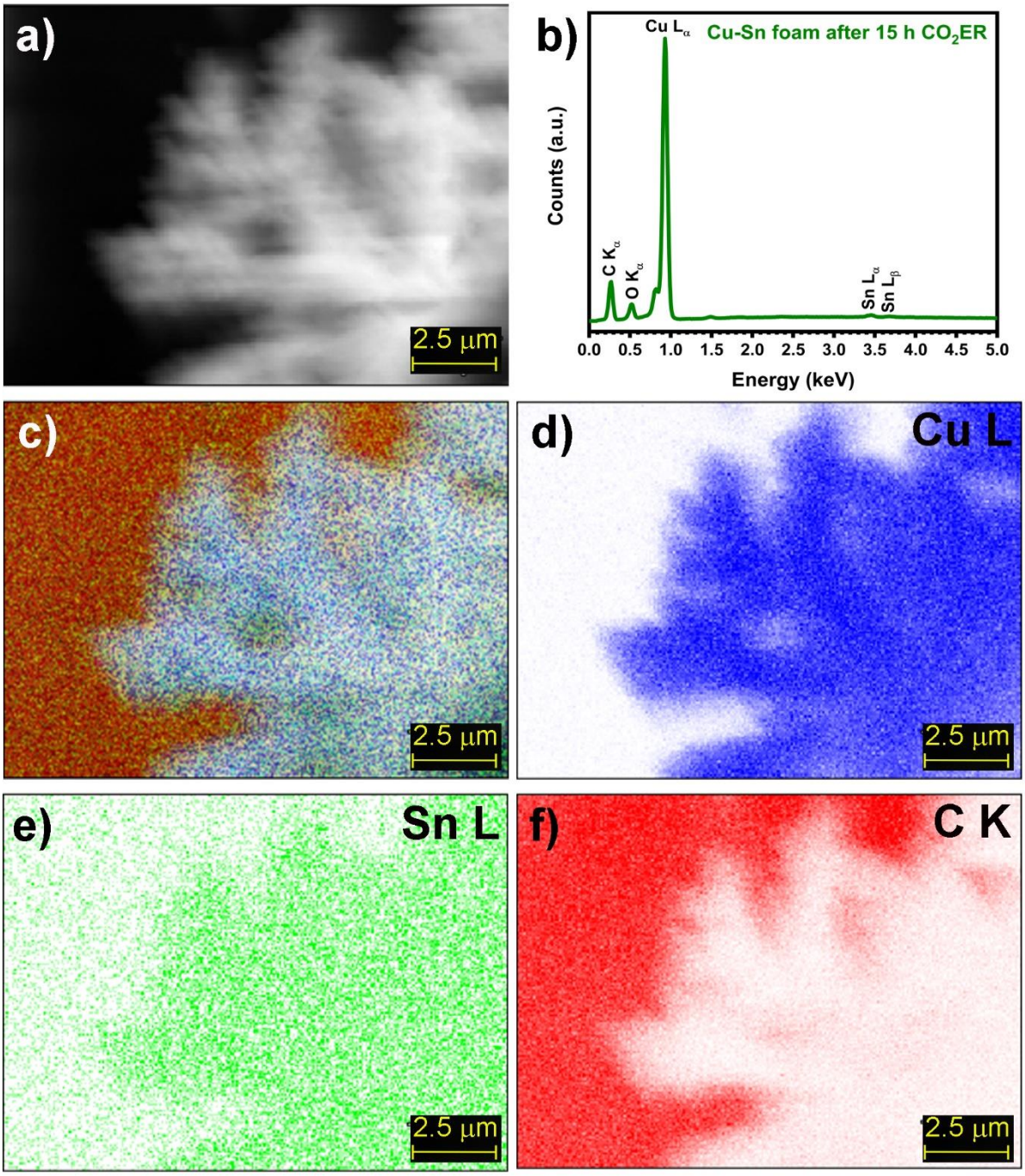

Figure S19. EDX mapping of dendrite microstructures in Cu-Sn foam after 15 h electrolysis at –0.8 V vs RHE: **(a)** SEM image of the mapped area; **(b)** representative EDX spectrum; **(c)** distribution of all elements; **(d)** distribution of Cu, **(e)** Sn, and **(f)** C from the background.

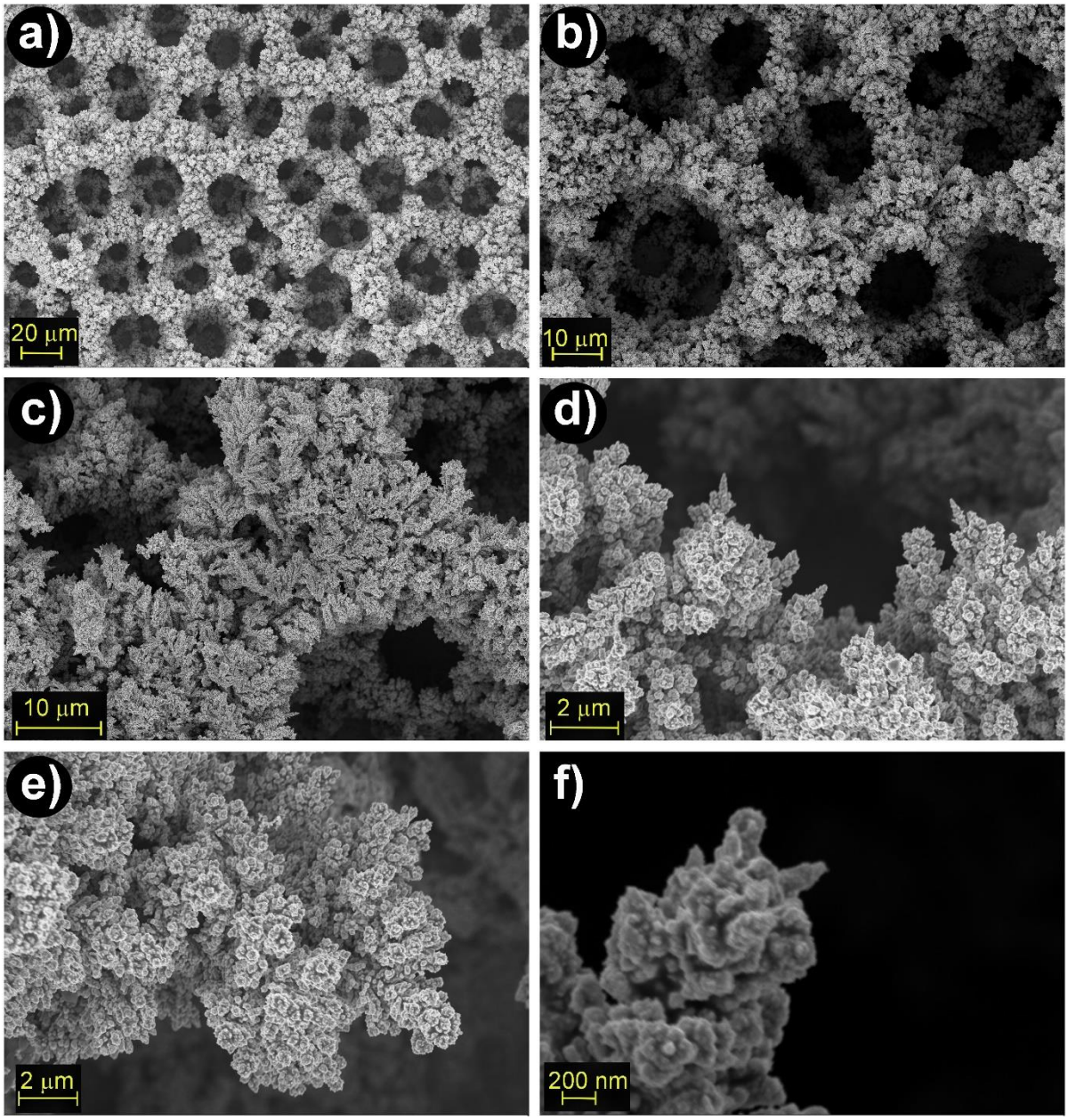

Figure S20. SEM images of Cu-Sn foam (Cu/Sn surface ratio = 1.4) prepared from Sn saturated electrodeposition solution after 2 h electrolysis at –0.8 V vs RHE.

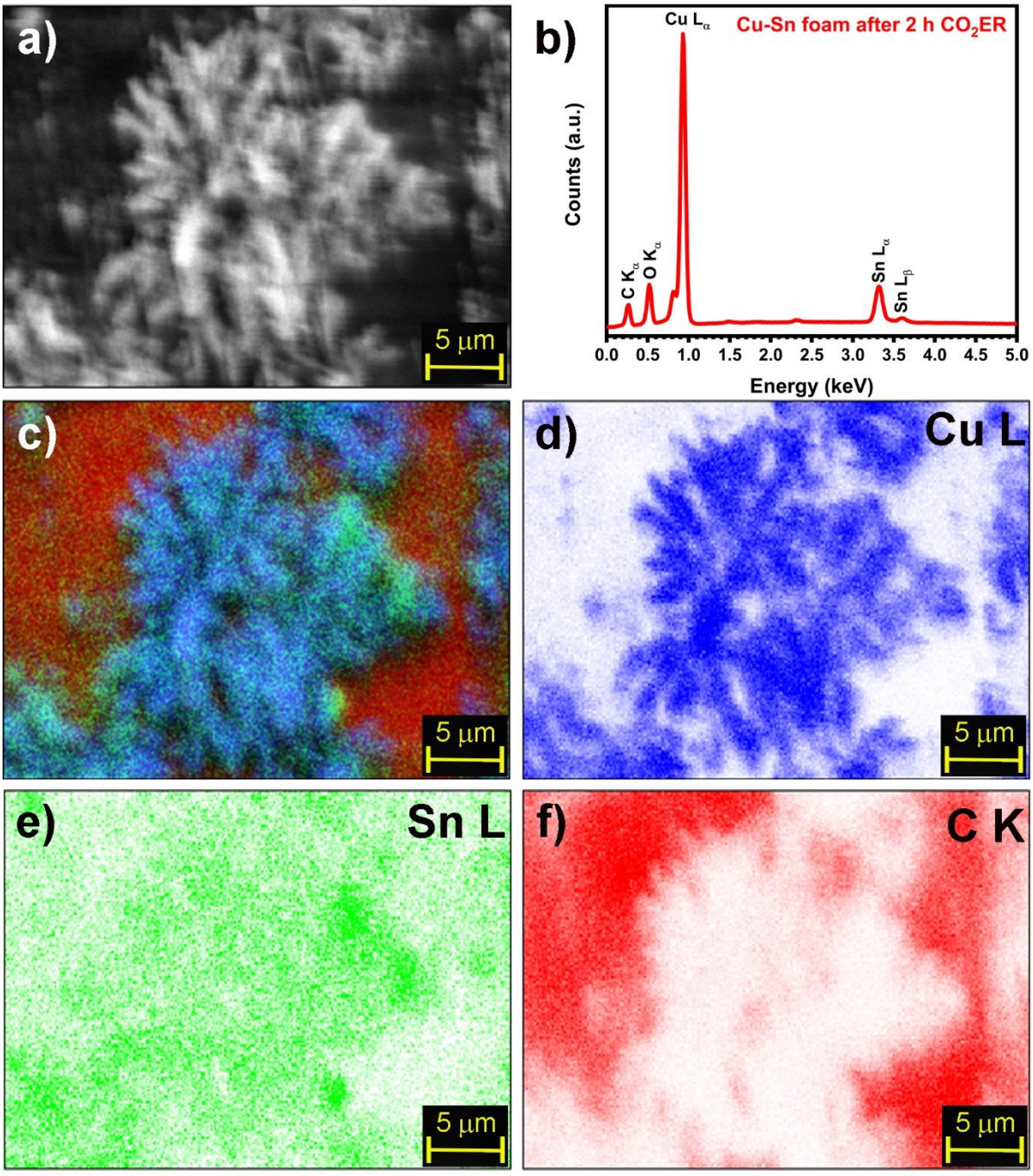

Figure S21. EDX mapping of dendrite microstructures in Cu-Sn foam (Cu/Sn surface ratio = 1.4) prepared from Sn saturated electrodeposition solution after 2 h electrolysis at –0.8 V vs RHE: **(a)** SEM image of the mapped area; **(b)** representative EDX spectrum; **(c)** distribution of all elements; **(d)** distribution of Cu, **(e)** Sn, and **(f)** C from the background.

Table S7. Comparison of the CO_2 to CO performance among several Cu-Sn electrocatalyst with foam (dendrites or particles), nanoparticles (NPs) and nanowires (NWs) morphology at moderate applied potential of –0.8 V vs RHE, examined in aqueous electrolytes using H-type gas-flow cell configuration. The Cu-Sn electrocatalysts with relatively low surface roughness and the ones examined under gas diffusion electrode configuration are omitted from this table.

Electrocatalyst	**Electrolyte**	**FE_{CO} (%)**	**J_{CO} ($mA \cdot cm^{-2}$)**	**J_{Total} ($mA \cdot cm^{-2}$)**	**Durability/FE_{CO} at the end of the test**	**References**
Cu-Sn foam (dendrites)	0.1 $mol \cdot dm^{-3}$ $KHCO_3$	>85	5	5.9	15 h/85%	This work
20 s - Sn NPs/ CuO_x NWs	0.1 $mol \cdot dm^{-3}$ $KHCO_3$	80 90*	2.5 4.5*	3 5*	12 h/78% /	Zhao et al.[12]
0.8 nm SnO_x / Cu NPs	0.5 $mol \cdot dm^{-3}$ $KHCO_3$	90	No data§	No data	10 h/No data	Li et al.[13]
SnO_x layer/ CuO_x NWs#	0.1 $mol \cdot dm^{-3}$ $NaHCO_3$	85	No data	1.4	6 h/80%	Schreier et al.[14]
Sn/Cu foam/ Cu foil	0.1 $mol \cdot dm^{-3}$ $KHCO_3$	93	4.7	No data	10 h/No data	Zeng et al.[15]
Sn/Cu foam (particles)/ Cu mesh	0.1 $mol \cdot dm^{-3}$ $KHCO_3$	82	6.1	7.5	No data	Ju et al.[7]
Sn/Cu foam (dendrites)/ Cu mesh	0.1 $mol \cdot dm^{-3}$ $KHCO_3$	89	6.5	7.2	10 h/No data	Ju et al.[7]
Cu_2O-SnO_2 nanocrystals	0.1 $mol \cdot dm^{-3}$ $KHCO_3$	90	3.3‡	No data	No data‡	Zhang et. al.[16]
3D-h Cu−Sn	0.1 $mol \cdot dm^{-3}$ $KHCO_3$	80Ƀ	9.3	No data	No dataƀ	Yoo et al.[17]

*For 5 s - Sn NPs/CuO_x NWs samples which are not tested for durability.

§J_{CO} = 4.6 $mA \cdot cm^{-2}$ at –0.7 V vs RHE.

#95% FE_{CO} for the 2 cycles SnO_x/CuO_x NWs samples at –0.6 V vs RHE.

‡Can reach J_{CO} of 11.4 $mA \cdot cm^{-2}$ in 0.5 $mol \cdot dm^{-3}$ $KHCO_3$. Was tested for 18 h in 0.5 $mol \cdot dm^{-3}$ $KHCO_3$ at –0.6 V vs RHE and reached ~85% FE_{CO}.

ƀReached FE_{CO} of 85% at –0.45 V vs RHE for 10 h in 0.1 $mol \cdot dm^{-3}$ $KHCO_3$. Max. reported FE_{CO} of 98.6% at –0.45 V vs RHE

S3. Another approach for conversion of the waste Cu-Sn bronze into CO-selective electrocatalyst

This strategy is based on three-step chemical bath/electrodeposition surface modification of the waste Cu-Sn bronze.

S3.1. Chemical bath method for growing nanostructures on the Cu-Sn bronze surface

The ~1 x 2 x 0.25 cm Cu-Sn bronze samples (Fig. S1b), after being polished according to the polishing procedure (described in section S1.2), were wrapped with PTFE tape, as described in section S1.4. Additionally, each sample was attached to 10-15 cm stripe of PTFE tape. After this preparation, the experiments were conducted according to the schematic presented on Fig. S22a. Namely, 15 cm^3 test tubes were filled with 2.5 cm^3 of 3 $mol \cdot dm^{-3}$ NaOH (freshly prepared from NaOH and ultrapure water) and placed in a water bath at 80 °C (large beaker filled with water and placed on a hot plate/electromagnetic stirrer). PTFE coated magnetic stirrers were placed in each test tube and loosely covered with caps to avoid water evaporation. When the NaOH(aq) reached temperature of 80 °C, the samples were etched in 10 wt.% HNO_3(aq) for 20 seconds, then washed with ultrapure water and immediately placed to hang (using the 10-15 cm PTFE stripes) in the test tubes. The samples were kept in the NaOH(aq) for 30 minutes at the same temperature. During this treatment, the surface of the Cu-Sn bronze loses its metallic-like shine and turns dark brown and according to the SEM images on Fig. S22b it resembles morphology typical for a deep-etched (corroded) surface. In the second step, i.e., immediately after the 30 minutes of alkaline treatment, 0.5 cm^3 of 0.75 $mol \cdot dm^{-3}$ $(NH_4)_2S_2O_8$ (freshly prepared from $(NH_4)_2S_2O_8$ and ultrapure water) were added in each test tube without removing the samples and then the test tubes were loosely capped again to avoid evaporation, but not too tight since NH_3 is being generated as a by-product. The temperature was kept constant at 80 °C throughout the whole procedure. The theoretical concentrations of $(NH_4)_2S_2O_8$ and NaOH at the beginning of the second step of the chemical bath treatment were 0.125 and ≤2.5 $mol \cdot dm^{-3}$, respectively. This process was terminated by removing the samples after 60 minutes, counting the time since the $(NH_4)_2S_2O_8$(aq) was added. During this treatment, the surface of the samples changed its color from dark brown into dark blue. Each removed sample was washed three times with 1 cm^3 of ultrapure water thus carefully collecting the liquid into the corresponding test tube in which it was chemically treated. After the washing procedure, the samples were left to dry under air at room temperature. The alkaline-persulfate method for growing variety of morphologies like nanowires, nanotubes and nanosheets on a surface of metallic Cu was already widely utilized.[18-20] The SEM images of the as-prepared $CuO \cdot xH_2O$ nanosheet-like structures are presented on Fig. S22c. The solution from the test tubes was quantitatively transferred into 50 cm^3 volumetric flasks to be used for the Cu and Sn electrodeposition procedure atop the chemically modified Cu-Sn bronze surfaces. According to the Pourbaix diagrams for Cu[9] and Sn[10] species, described in the literature, both elements should form hydroxo- complex compounds at pH>14, although, we do not have any empirical evidence about the chemical nature of the Cu and Sn – species in order to support this claim.

S3.2. Decoration of the $CuO \cdot xH_2O$ nanostructures via electrodeposition of the leached Cu and Sn

For the electrodeposition of the leached Cu and Sn atop the nanosheets that were grown via the two-step chemical bath treatment, the electrolyte was prepared via neutralization of the excess NaOH with 0.25 cm^3 concentrated HCl (37 wt.%) in the test tubes where the samples were treated. The liquid from the test tubes was quantitatively transferred into a 50 cm^3 beaker using 0.1 $mol \cdot dm^{-3}$ $KHCO_3$(aq) for washing. Finally, the beaker was filled with 0.1 $mol \cdot dm^{-3}$ $KHCO_3$(aq) up to a final volume of 30 cm^3. The electrolyte was purged with CO_2 under a moderate flow during the electrodeposition process, starting ~15 minutes before applying the bias. The electrodeposition was conducted potentiosatically at –1.5 V vs Ag/AgCl (3 $mol \cdot dm^{-3}$ KCl) for 10 minutes using Pt-mesh as a counter electrode. The samples were washed with ultrapure water and left to dry in air. The as-prepared samples resemble Cu_xO/SnO_x decorated $CuO \cdot xH_2O$ nanosheets, as presented on the SEM images on Fig. S22d.

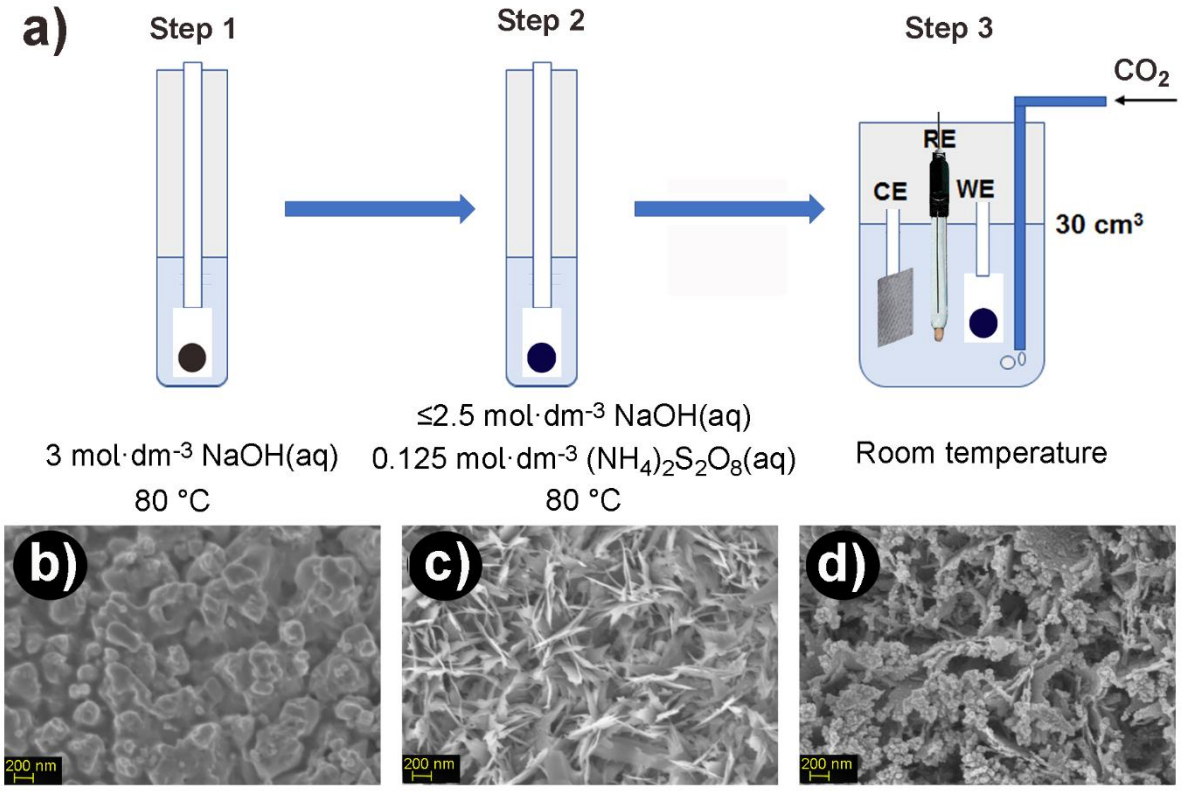

Figure S22. (a) Scheme of the chemical bath/electrodeposition method for surface modification of the waste Cu-Sn bronze. SEM images of: **(b)** surface of Cu-Sn bronze after treatment in NaOH(aq) at 80 °C; **(c)** surface of $CuO \cdot xH_2O$ nanosheets, after treatment in alkaline $(NH_4)_2S_2O_8$ at 80 °C; **(d)** surface of $CuO \cdot xH_2O$ nanosheets after electrodeposition of the leached Cu and Sn atop the $CuO \cdot xH_2O$ nanosheets.

S3.3. Electrocatalytic activity results for the Cu_xO/SnO_x decorated $CuO{\cdot}xH_2O$ nanosheets

The electrocatalytic activity measurements for the Cu_xO/SnO_x decorated $CuO{\cdot}xH_2O$ nanosheets were carried out using identical experimental setup, as described in section S1.5. The results from the FEs distribution of H_2, CO, C_2H_4 and $HCOO^-$ are presented on Fig. S23a, and the total current density and the partial current density for all products at applied potentials of –0.7, –0.8 and –0.9 V, on Fig. S23b. This electrocatalyst reached slightly lower FE_{CO} at –0.7 and -0.8 V and similar value at -0.9 V, but however the J_{CO} values are comparable, even 0.5-1 $mA{\cdot}cm^{-2}$ higher in comparison with the values obtained for the Cu-Sn foam (cf. Fig. S23 and Fig. 2c, d).

Even though this strategy was quite promising in the beginning, unfortunately, significant reproducibility issues were faced which were mainly caused by the difficulties to control the amount of leached surface Cu and Sn in the first step. Trying to overcome these issues we modified the first and second step of the method by altering the time of treatment, we even introduced HCl(aq) instead of NaOH(aq) for more selective leaching only the surface Sn instead both Cu and Sn in the first step, but in all cases up to date, we were not able to reach FEs for CO that are higher than 65% at -0.8 V. In most of the cases the FE for CO remained 40-50%.

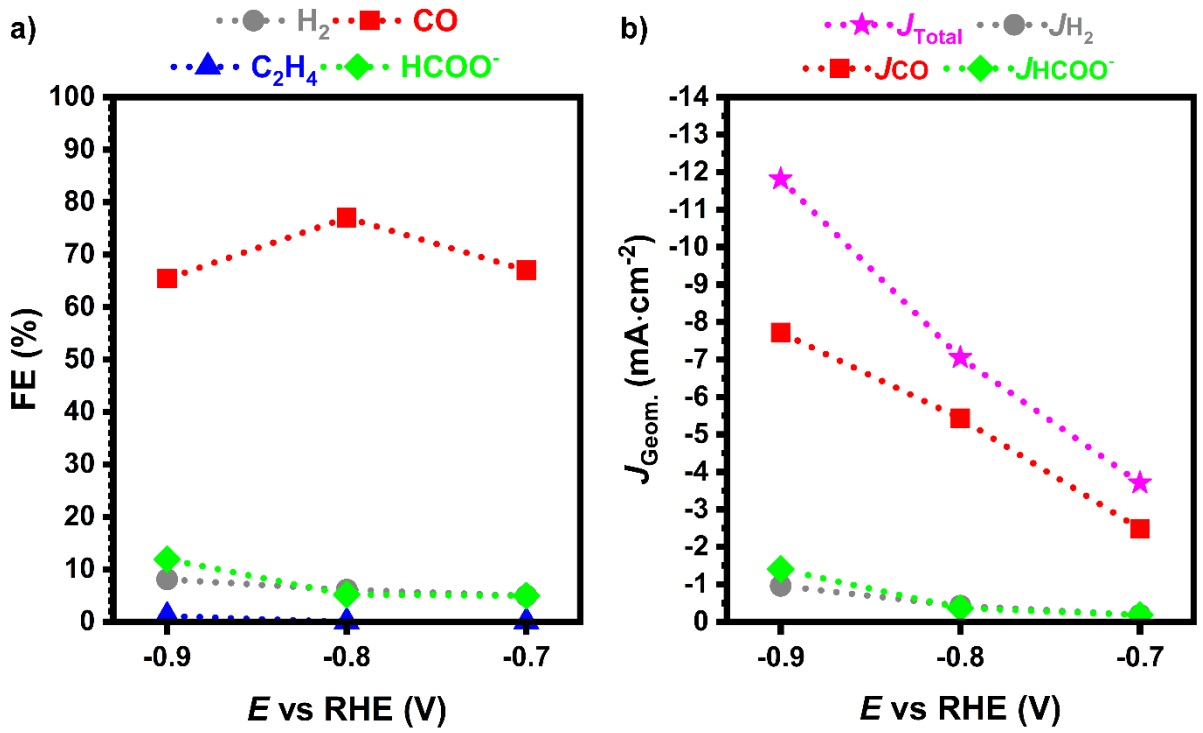

Figure S23. Electrocatalytic activity results for the Cu_xO/SnO_x decorated $CuO{\cdot}xH_2O$ nanosheets: **(a)** FEs distribution of H_2, CO, C_2H_4 and HCOOH and **(b)** total geometric and partial current density for CO at potentials of –0.7, –0.8 and –0.9 V vs RHE.

REFERENCES

1. Vasileff, A.; Xu, C.; Ge, L.; Zheng, Y.; Qiao, S.-Z., Bronze Alloys with Tin Surface Sites for Selective Electrochemical Reduction of CO_2. *Chem.Commun.* **2018,** *54* (99), 13965-13968. https://doi.org/10.1039/C8CC08066F
2. Vasileff, A.; Zhi, X.; Xu, C.; Ge, L.; Jiao, Y.; Zheng, Y.; Qiao, S.-Z., Selectivity Control for Electrochemical CO_2 Reduction by Charge Redistribution on the Surface of Copper Alloys. *ACS Catal.* **2019,** *9* (10), 9411-9417. https://doi.org/10.1021/acscatal.9b02312
3. Elgrishi, N.; Rountree, K. J.; McCarthy, B. D.; Rountree, E. S.; Eisenhart, T. T.; Dempsey, J. L., A Practical Beginner's Guide to Cyclic Voltammetry. *J. Chem. Educ.* **2018,** *95* (2), 197-206. https://doi.org/10.1021/acs.jchemed.7b00361
4. ImageJ. https://imagej.net/Welcome (accessed May 12, 2021).
5. XPS Simplified. https://xpssimplified.com/ (accessed May 12, 2021).
6. NIST X-ray Photoelectron Spectroscopy Database. https://srdata.nist.gov/xps/Default.aspx (accessed May 12, 2021).
7. Ju, W.; Zeng, J.; Bejtka, K.; Ma, H.; Rentsch, D.; Castellino, M.; Sacco, A.; Pirri, C. F.; Battaglia, C., Sn-Decorated Cu for Selective Electrochemical CO_2 to CO Conversion: Precision Architecture Beyond Composition Design. *ACS Appl. Energy Mater.* **2019,** *2* (1), 867-872. https://doi.org/10.1021/acsaem.8b01944
8. Vesztergom, S.; Dutta, A.; Rahaman, M.; Kiran, K.; Zelocualtecatl Montiel, I.; Broekmann, P., Hydrogen Bubble Templated Metal Foams as Efficient Catalysts of CO_2 Electroreduction. *ChemCatChem* **2020,** *13* (4), 1039-1058. https://doi.org/10.1002/cctc.202001145
9. Oh, Y.-J.; Park, G.-S.; Chung, C.-H., Planarization of Copper Layer for Damascene Interconnection by Electrochemical Polishing in Alkali-Based Solution. *J. Electrochem* **2006,** *153* (7), G617-G621. https://doi.org/10.1149/1.2200288
10. Al-Hinai, A. T.; Al-Hinai, M. H.; Dutta, J., Application of Eh-pH Diagram for Room Temperature Precipitation of Zinc Stannate Microcubes in an Aqueous Media. *Mater. Res. Bull.* **2014,** *49*, 645-650. https://doi.org/10.1016/j.materresbull.2013.10.011
11. Nikolić, N. D., Influence of the Exchange Current Density and Overpotential for Hydrogen Evolution Reaction on the Shape of Electrolytically Produced Disperse Forms. *J. Electrochem. Sci. Eng.* **2020,** *10* (2), 111-126. https://doi.org/10.5599/jese.707
12. Zhao, Y.; Wang, C.; Wallace, G. G., Tin Nanoparticles Decorated Copper Oxide Nanowires for Selective Electrochemical Reduction of Aqueous CO_2 to CO. *J. Mater. Chem. A* **2016,** *4* (27), 10710-10718. http://dx.doi.org/10.1039/C6TA04155H
13. Li, Q.; Fu, J.; Zhu, W.; Chen, Z.; Shen, B.; Wu, L.; Xi, Z.; Wang, T.; Lu, G.; Zhu, J.-j.; Sun, S., Tuning Sn-Catalysis for Electrochemical Reduction of CO_2 to CO via the Core/Shell Cu/SnO_2 Structure. *J. Am. Chem. Soc.* **2017,** *139* (12), 4290-4293. https://doi.org/10.1021/jacs.7b00261
14. Schreier, M.; Héroguel, F.; Steier, L.; Ahmad, S.; Luterbacher, J. S.; Mayer, M. T.; Luo, J.; Grätzel, M., Solar Conversion of CO_2 to CO using Earth-Abundant Electrocatalysts Prepared by Atomic Layer Modification of CuO. *Nat. Energy* **2017,** *2* (7), 17087. https://doi.org/10.1038/nenergy.2017.87
15. Zeng, J.; Bejtka, K.; Ju, W.; Castellino, M.; Chiodoni, A.; Sacco, A.; Farkhondehfal, M. A.; Hernández, S.; Rentsch, D.; Battaglia, C.; Pirri, C. F., Advanced Cu-Sn Foam for Selectively Converting CO_2 to CO in Aqueous Solution. *Appl. Catal. B* **2018,** *236*, 475-482. https://doi.org/10.1016/j.apcatb.2018.05.056
16. Zhang, S.-N.; Li, M.; Hua, B.; Duan, N.; Ding, S.; Bergens, S.; Shankar, K.; Luo, J.-L., A Rational Design of Cu_2O−SnO_2 Core-Shell Catalyst for Highly Selective CO_2-to-CO Conversion. *ChemCatChem* **2019,** *11* (16), 4147-4153. https://doi.org/10.1002/cctc.201900395
17. Yoo, C. J.; Dong, W. J.; Park, J. Y.; Lim, J. W.; Kim, S.; Choi, K. S.; Odongo Ngome, F. O.; Choi, S.-Y.; Lee, J.-L., Compositional and Geometrical Effects of Bimetallic Cu–Sn Catalysts on Selective Electrochemical CO_2 Reduction to CO. *ACS Appl. Energy Mater.* **2020,** *3* (5), 4466-4473. https://doi.org/10.1021/acsaem.0c00157
18. Mi, Y.; Shen, S.; Peng, X.; Bao, H.; Liu, X.; Luo, J., Selective Electroreduction of CO_2 to C_2 Products over Cu_3N-Derived Cu Nanowires. *ChemElectroChem* **2019,** *6* (9), 2393-2397. https://doi.org/10.1002/celc.201801826
19. Zhang, W.; Wen, X.; Yang, S.; Berta, Y.; Wang, Z. L., Single-Crystalline Scroll-Type Nanotube Arrays of Copper Hydroxide Synthesized at Room Temperature. *Adv. Mater.* **2003,** *15* (10), 822-825. https://doi.org/10.1002/adma.200304840
20. Tian, L.; Liu, B., Fabrication of CuO Nanosheets Modified Cu Electrode and its Excellent Electrocatalytic Performance Towards Glucose. *Appl. Surf. Sci.* **2013,** *283*, 947-953. https://doi.org/10.1016/j.apsusc.2013.07.048

CHAPTER 6. Facile method for synthesis of Cu_xS catalysts and study of various effects on the selectivity for electrochemical conversion of CO_2 into formate

Written manuscript – not submitted

Authors:

S. Stojkovikj, G. A. El-Nagar, S. Gupta, M. Najdoski, V. Koleva, T. Tzanoudakis, F. Firschke, P. Bogdanoff, M. T. Mayer.

Individual contributions:

- **S. Stojkovikj**: Project introduction and experiments planning, sulfidation method discovery and development, experimenting with sulfidation of various Cu substrates, DHBT synthesis method application, development and optimization for the purpose of this study, CO_2ER activity measurements, performing various composition-CO_2ER activity related control experiments, inert atmosphere electrolysis for *quasi in-situ* XPS, SEM-EDX characterization, ICP-OES measurements, data analysis, data discussion, all data final processing, manuscript writing.
- G. A. El-Nagar: Introducing the DHBT method, XPS data collection/fitting, cross section SEM measurements, data discussion, manuscript review.
- S. Gupta: Some of the SEM-EDX characterization, XPS data collection, manuscript review.
- M. Najdoski: Sulfidation method discovery and optimization, powder XRD measurements and Cu_xS composition revealing, design of schemes and data discussion.
- V. Koleva: Initial TGA-MS/DSC measurements, XRD data analysis, revealing Cu_xS phase composition, data discussion.
- T. Tzanoudakis: *In-situ* MS measurements for H_2S tracking during electrolysis, data discussion and suggestions.
- F. Firschke: Experimenting with sulfidation of various Cu substrates and CO_2ER activity measurements, data discussion and suggestions.
- P. Bogdanoff: *In-situ* MS data discussions, MS parameter settings.
- M. T. Mayer: Project supervision, data discussion and suggestions, manuscript review and editing.

Facile method for synthesis of Cu_xS catalysts and study of various effects on the selectivity for electrochemical conversion of CO_2 into formate

Sasho Stojkovikj,[a,b] Gumaa A. El-Nagar,[a] Siddharth Gupta,[a,b] Metodija Najdoski,[c] Violeta Koleva, [d] Theocharis Tzanoudakis,[a,b] Frederik Firschke,[a] Peter Bogdanoff, [e] and Matthew T. Mayer*[a]

[a]Helmholtz Young Investigator Group: Electrochemical Conversion, Helmholtz-Zentrum Berlin für Materialen und Energie GmbH, Hahn-Meitner-Platz 1, D-14109, Berlin, Germany.

[b]Institut für Chemie und Biochemie, Freie Universität Berlin, Arnimallee 22, D-14195 Berlin, Germany.

[c]Institute of Chemistry, Faculty of Natural Sciences and Mathematics, Ss. Cyril and Methodius University Skopje, Arhimedova 5, 1000 Skopje, Republic of North Macedonia.

[d]Institute of General and Inorganic Chemistry, Bulgarian Academy of Sciences, G. Bonchev Str. Bldg. 11, 1113 Sofia, Bulgaria.

[e]Institute of Solar Fuels, Helmholtz-Zentrum Berlin für Materialen und Energie GmbH, Hahn-Meitner-Platz 1, D-14109, Berlin, Germany.

*Corresponding author: Dr. Matthew T. Mayer (m.mayer@helmholtz-berlin.de)

Abstract: Electrochemical reduction of CO_2 (CO_2ER) to $HCOO^-$ using relatively cheap Cu-S system-based electrocatalysts is a feasible combination worth to be extensively studied. In this study, a simple and fast two-step method was developed for synthesis of $HCOO^-$ selective coper sulfide electrocatalyst. Cu foam was electrodeposited on Cu mesh substrate via DHBT method then subsequently sulfidated via immersion in sulfur saturated toluene solution. The synthesized material resembles mixed phase digenite/roxbyite composition with $Cu_{1.8}S$ stoichiometry. The sulfidated Cu foam was examined for its CO_2ER catalytic activity, leading to the observation that the $HCOO^-$ selectivity is highly dependent on the electrochemical test sequence, namely the direction of ramping the applied potential in the interval between –0.5 to –0.9 V *vs.* RHE. The best $HCOO^-$ selectivity is achieved at –0.7 V regardless of the direction of ramping, yet when the potential is ramped positively starting from –0.9 V, the peak faradaic efficiency (FE) reached is notably higher (~65%) than when starting at –0.5 V and ramping negatively (~50%). *In-situ* EC-MS tracking of the H_2S evolution from the electrocatalyst and post-electrolysis analysis of the bulk sulfur fraction in both directions of ramping the potential showed differences in the evolution duration but not a significant difference in the bulk sulfur content thus did not provide explanation regarding the differences in the electrocatalytic activity at –0.7 V. Various control experiments such as sample air or N_2 exposure, electrolyte replacement, sulfidation of Cu foam in electrolyte where $Cu_{1.8}S$/Cu foam was reduced, and analysis of the electrolyte sulfur concentration were conducted to investigate whether the electrolyte present sulfur has any effect on the activation of the electrocatalyst. The results showed that the $HCOO^-$ selectivity can be further enhanced reaching up to 75% FE at –0.9 V when the electrolyte is replaced or pristine Cu foam is `electrolyte sulfidated`, yet without significant change at –0.7 V. The post-electrolysis quantification of the electrolyte sulfur concentration showed discrepancies in electrocatalysts with similar performance at –0.9 V but no difference was observed for $Cu_{1.8}S$/Cu foam at –0.7 V regardless of the direction of ramping the potential. However, the results from *quasi in-situ* XPS did show differences in the surface sulfur fraction thus lower sulfur content is observed when the potential is ramped from –0.5 to –0.9 V compared when starting at –0.9 V. Moreover, besides S^{2-}, SO_4^{2-} surface species were found on the surfaces of the samples subjected to potential of –0.9 V suggesting that certain

processes in the electrolyte near the electrode surface could affect the local sulfur distribution thus influencing the $HCOO^-$ selectivity. Finally, the very important *quasi in-situ* XPS results show that the pristine Cu foam undergoes total reduction to metallic Cu while the in the case of the sulfidated Cu foam, besides metallic, Cu^+ species persist under all applied potentials in the range between –0.5 and –0.9 V. Thus, it appears that the presence of sulfur stabilizes the Cu^+ species thus supporting the *OCHO* pathway for CO_2 reduction into $HCOO^-$ suggested in the literature.

Keywords: CO_2 electrolysis, copper sulfides, formate, electrochemical activation, *in-situ* H_2S tracking, *quasi in-situ* XPS, stable Cu^+ surface species.

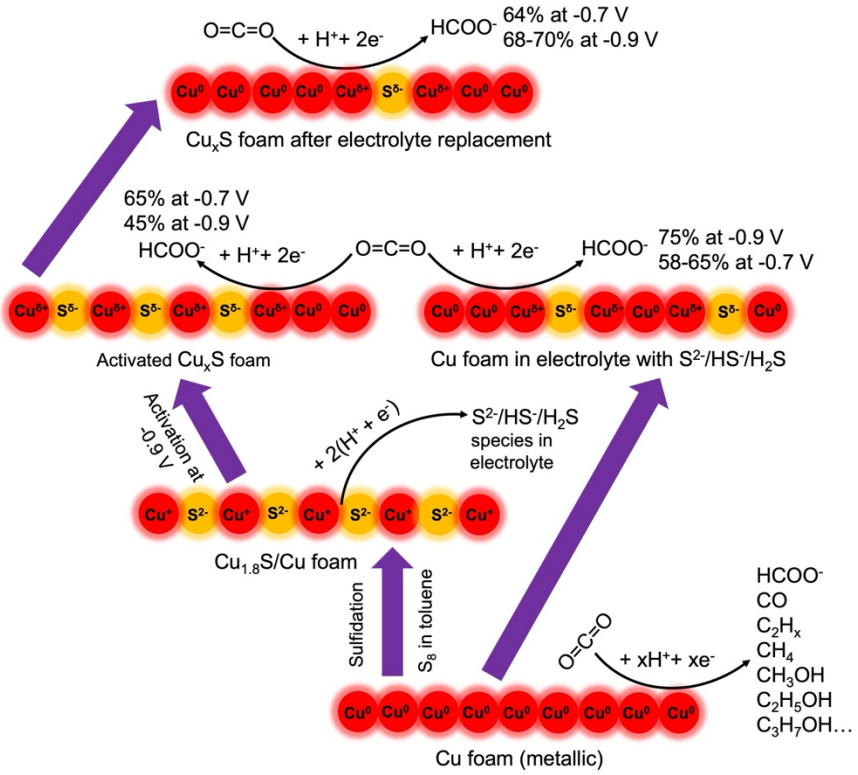

Graphical abstract

Introduction

The emission of the greenhouse gas CO_2 in the atmosphere is continuously increasing together with the energy demand that is still majorly produced from fossil fuels, caused by the development of the global society in all sectors since start of the industrial revolution.[1-2] Significant long-term measures are already taken in the past decades to mitigate the CO_2 emissions via decreasing the dependence from fossil fuels energy production,[3-4] however more immediate actions are necessary. Substantial parts of the scientific communities are focused on this topic with increasing interest over the years striving towards achieving efficient renewable energy driven CO_2 capture and its conversion into valuable products that can be utilized as fuels and chemicals in the existing industry.[3-4] The electrochemical reduction of CO_2 (CO_2ER) is a promising approach for CO_2 conversion to value-added products,[4] and among the wide range of possible products, to date the $2e^-$ CO_2ER products CO and formic acid/formate ($HCOOH/HCOO^-$) are closest to being techno-economically viable for a possible large-scale production.[3-5] Among metal catalysts explored for CO_2ER, only Cu is capable electrocatalyst for significantly reducing CO_2 beyond CO in multielectron steps thus producing hydrocarbons, alcohols, etc.[1, 3, 6-7] but unfortunately suffers from selectivity issues, hence requiring products separation leading to additional costs.[8] Therefore, studying and understanding the catalytic processes during CO_2ER into the most techno-economically viable products is of great importance for large scale production in the near future. The HCOOH and $HCOO^-$ salts are important feedstock chemicals used in broad industrial fields.[9] Moreover, there are significant research efforts to develop fuel cells that can efficiently run on formate which would provide advantages over H_2 in terms of safety, storage and transportation issues.[4, 10] Several elements (Cd, In, Sn, Hg, Tl, Pb, Bi)[7, 11] and their combinations (Sn-Pb, Cu-Sn, Cu-In, Cu-Pb, Cu-Pb-Sn, Cu-S etc.),[11-17] have been investigated as electrocatalyst materials for CO_2ER into $HCOO^-$. However, among them only Cu, Sn, In, Bi and S are not extremely toxic, and of these all but S are relatively rare on Earth's crust, and moreover are listed as elements with certain risk of future supply.[18-19] Therefore, the copper sulfides based electrocatalysts have emerged as attractive candidates for CO_2 conversion into $HCOO^-$.[17, 20-28]

Copper sulfides are binary compounds with general formula Cu_xS_y that exist in many complex variations in terms of Cu oxidation state, Cu:S stoichiometry, structure and morphology, thus defining their chemical and physical properties, hence their application in various fields.[17, 29-37] Cu_xS_y can be synthesized using numerous methods.[17, 29-37] In general these methods are based on reactions of copper or its compounds, and correspondingly, sulfur or its compounds, under variety of reaction conditions.[17, 36] Regarding the CO_2 to $HCOO^-$ conversion mechanism on Cu_xS_y based electrocatalysts, the presence of persistent residual sulfur in copper's structure most probably stabilizes the Cu^+ specie on the surface of the

catalyst and favors the binding of the *OCHO* intermediate (over *COOH) which transforms into $HCOO^-$ following a second electron transfer step.[20, 22, 25, 28] Moreover, it was found that the presence of sulfur suppresses the undesirable hydrogen evolution reaction (HER).[38] On the other hand, the *COOH intermediate pathway leads to CO_2ER into CO and further reduction to hydrocarbons, alcohols etc.[1, 3, 6-7] Even though it is already reported in the literature that under electrolysis the sulfur remains persistent in the structure of Cu,[20, 23, 27-28, 39] to the best of our knowledge there is no evidence whether under operating or near operating conditions the surface Cu maintains +1 oxidation state or is fully reduced to metallic. Therefore, in this study we sought to address this question via study of the chemical nature of surface Cu and S under near operating conditions. For this purpose, the electrocatalysts were examined with x-ray photoelectron spectroscopy (XPS) after conducting the electrolysis and transfer of the samples in the analyzer under inert atmosphere thus to prevent air caused re-oxidation when the electrochemical bias is removed (sometimes referred in the literature as *quasi in-situ* XPS[40-41]). Moreover, tracking the sulfur species evolved from the electrocatalyst under reductive bias and their transfer in the electrolyte thus possible effect on the selectivity is another goal we strive to tackle in this study. Even though most of the Cu_xS_y synthesis published methods are advanced in terms of preparation of materials with fine-tuned composition, morphology, structure etc., in dependence of their specific application,[17, 36] we decided that for our study we would like to utilize rather very fast, simple, cheap, and reproducible method under mild conditions to prepare a CO_2 to $HCOO^-$ conversion electrocatalyst with decent selectivity. Moreover, we sought to avoid usage of toxic or hazardous sulfur compounds like H_2S, S^{2-} salts, thiourea, thioacetamide or expensive ionic liquids as precursors. Therefore, a Cu foam was prepared via dynamic hydrogen bubble template (DHBT) electrodeposition,[42] which was subsequently sulfidated by immersing it into sulfur dissolved in toluene. All synthesized materials were examined with various characterization methods to reveal their chemical composition, structure, morphology, surface speciation and thermal properties. Examining the sulfidated Cu foam for its CO_2 conversion electrocatalytic activity, it was revealed that the $HCOO^-$ selectivity is dependent on the direction of ramping the initial applied potential. Whether this phenomenon is affected by the aforementioned surface speciation of the Cu and S in the catalyst and moreover the reductive evolution and presence of sulfur species in the electrolyte is thoroughly discussed based on the results from various *in-situ, quasi in-situ* and *ex-situ* experiments.

Experimental

All utilized reagents and materials for this study are listed and described in section S1.1. in the supporting information (SI). The synthesis of the sulfidated Cu foam (abbreviated as $Cu_{1.8}S$/Cu foam) electrocatalyst was performed in several simple and short-duration steps. In the first step, Cu foam was electrodeposited under dynamic H_2 bubble template (DHBT)[42] conditions on pre-cleaned Cu mesh cathode in an aqueous electrolyte containing 0.2 $mol \cdot dm^{-3}$ $CuSO_4$ and 1.5 $mol \cdot dm^{-3}$ H_2SO_4, by applying geometric current density of -5 $A \cdot cm^{-2}$ for duration of 9.5 seconds. A two-electrode setup with Cu foil as anode was used for this purpose. The schematic for the materials preparation, electrodeposition procedure and setup are depicted in Figure S1 and all information regarding the electrochemical processes during the DHBT deposition are presented and discussed in section S1.2. in the SI. In a following step, the as-prepared Cu foam was sulfidated by immersing the samples in sulfur saturated toluene solution for 3 seconds, at room temperature. The materials, chemicals and detailed experimental procedures are described in section S1.3. in the SI and schematically presented in Figure S2. The chemical and phase composition of the materials was characterized with x-ray diffraction (XRD), energy dispersive x-ray spectroscopy (EDX), thermogravimetric analysis coupled with mass spectrometry (*in-situ* TGA-MS) and differential scanning calorimetry (DSC). The oxidation states (speciation) of surface Cu, S and O were studied using x-ray photoelectron spectroscopy (XPS) in *ex-situ* and *quasi in-situ* approaches, where in the latter case the analyzer was coupled with transfer vessel in which samples can be loaded directly from a glovebox where electrochemical experiments were conducted under inert environment to avoid surface oxidation in air. The surface morphology and pore sizes were evaluated using scanning electron microscopy (SEM). The thickness of the foams was determined from cross-section SEM after vertical ablation of the samples using focused ion beam (FIB). All electrocatalytic activity measurements were conducted in H-type gas-flow cell filled with 0.1 $mol \cdot dm^{-3}$ $KHCO_3$(aq) as a supporting electrolyte, constantly purged with CO_2 in the cathodic compartment and providing bias in linear sweep voltammetry (LSV) and chronoamperometric (CA) modes. Simultaneously, the CO_2ER gaseous products and H_2 from HER were quantified using on-line gas chromatography (GC). The volatile (alcohols) and non-volatile CO_2ER liquid products ($HCOO^-$) were quantified post-electrolysis using headspace gas chromatography (GC-HS) and high-performance liquid chromatography (HPLC), respectively. The H_2S evolution during the electrolysis was followed via *in-situ* mass spectrometry (EC-MS) and the content of the sulfur species in the electrolyte was analyzed post-electrolysis with inductively coupled plasma-optical emission spectroscopy (ICP-OES). The materials characterization, electrochemical and product quantification methods are described in detail in sections S1.4. and S1.5. in the SI and additionally in our previous study.[43] The supporting

results are presented as schematics, graphs and tables in section S2. in the SI. All sample abbreviations and experimental conditions under which they were examined are described in Table S1.

Results and Discussion

Characterization of the synthesized material

Cu with foam-like morphology was electrodeposited on Cu mesh substrates via dynamic H_2 bubble template (DHBT) method,[42] as depicted in Figure S1 and described above in the experimental section and additionally in section S1.2. in the SI. The Cu foam consists of typical dendrite microstructures arranged as interconnected pores and channels (Figures 1a and S3) that were formed around the H_2 bubble templates during the electrodeposition,[42] with pore size of ~30 μm and thickness of ~40 μm (see Figure S4a and Table S2). The Cu foam was sulfidated via simple, fast, and reliable method based on a direct reaction between elemental Cu and sulfur dissolved in toluene and in CS_2, at room temperature. The sulfidation process only occurs when metallic Cu is exposed to the reactive sulfur species in the organic matrix, therefore an initial acidic etching step was used prior to sulfidation to remove native surface species (e.g., oxides, hydroxides and carbonates) which passivate the surface, as described at the end of section S1.3 in the SI. It is important to note that the material synthesized using CS_2 as solvent was only studies for its chemical composition, structure and thermal properties, but not subjected to additional examination due to the hazardous nature of this chemical, therefore all other studies were conducted using toluene as sulfur solvent. The sulfidation process did not significantly affect the bulk morphology thus the pore sizes and thickness are preserved (see Figures 1, S4, S5 and Table S2), yet blunting of the dendrite edges can be observed (cf. Figures 1a with Figure 1b, and Figure S3c with S5c respectively). The EDX mapping shows homogeneous distribution of Cu and S throughout the sulfidated foam with nominal sulfur fraction of ~30 at.% (Cu:S atomic ratio ~2), as presented in Figure S5(d-f). From the XRD analysis results (Figures 1c and S6) it was found that the Cu foam with polycrystalline Cu structure during the sulfidation procedure transforms into copper sulfide with mixed phase composition which corresponds to digenite $Cu_{1.765}S$ (ICDD PDF 2-023-0960) as a predominant phase, and roxbyite Cu_7S_4 (ICDD PDF 2-023-0958) as a secondary phase. The analysis of the phases was conducted from powder samples obtained via sulfidation of Cu foil and the results showed that roxbyite fractions of ~10 and ~30 wt.% were obtained when the sulfidation was conducted in CS_2 and toluene as sulfur solvents, respectively. Both phases resemble nominal $Cu_{1.8}S$ stoichiometry and therefore the sulfidation reaction can be described with Equation 1. To be best of our knowledge this is the first report where copper sulfide with digenite/roxbyite phase composition is utilized for electrochemical conversion of CO_2.

$$1.8xCu + S_x \rightarrow xCu_{1.8}S \text{ (digenite/roxbyite phase)} \quad (1)$$

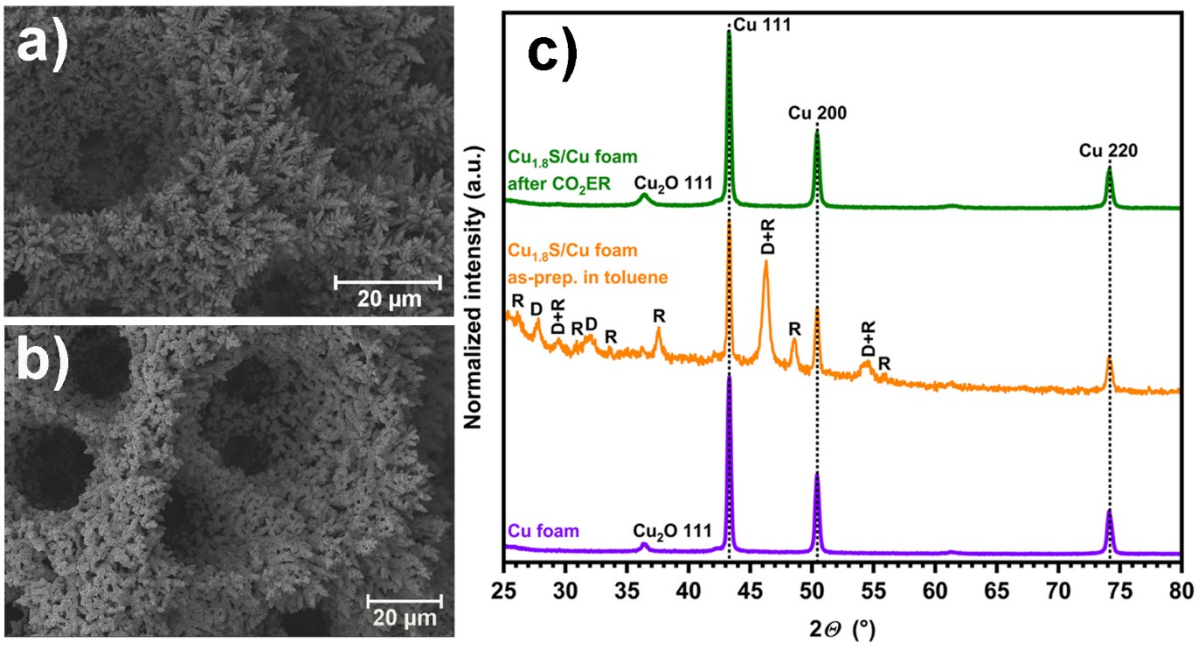

Figure 1. SEM images of Cu foam **(a)** and $Cu_{1.8}S$/Cu foam **(b)** composed of dendrite microstructures. GI-XRD patterns of Cu foam and sulfidized Cu foam, as-prepared and after CO_2 electrolysis from –0.9 to –0.7 V for 1 h at each potential. D stands for digenite and R for roxbyite phase, used to label peaks according to reflections in the corresponding database patterns.

The thermal properties of the $Cu_{1.8}S$ prepared in the two solvents (as powders via sulfidation of Cu foil) is studied with TGA-MS and DSC. Comparing the results from these analyses presented in Figure S7 it can be generally revealed that their behavior is similar as expected from their close chemical composition. The mass decrease process is developed in a very broad range from 100 to 1000 °C with close values for the overall mass loss: ~2.5 and ~3.3 wt.% for the samples sulfidated in CS_2 and toluene, respectively (Figures S7a, b). The TGA results are supported by the DSC curves, where a very broad complex exothermic peak is observed in the same temperature range thus the maximum is observed at 450-470 °C (Figures S7(e, f). Both TGA curves show two distinct mass loss regions: the first between 100 and 350-400 °C, and a second steeper one between 400 and 1000 °C. The corresponding mass losses are as follows: ~0.2 and ~2.3 wt.% for the sample in CS_2, and accordingly 0.7 and 2.6 wt.% for the sample in toluene. According to MS analysis (Figures S7c, d) the observed mass losses are due to S_2 volatilization (m/z = 64) which is caused by the thermal transformation of $Cu_{1.8}S$ into chalcocite phase Cu_2S.[44-46] Moreover, the S_2 volatilization takes place in two steps which is evident from the m/z = 64 signals for both samples: a very weak sharp signal around 260 and 230 °C for the samples sulfidated in CS_2 and toluene, respectively and other continuous signal extending from 400 to 1000 °C. Liu et al.[46] showed that the thermal transformation of nanocrystalline $Cu_{1.8}S$ takes place at 240 °C, which is a much lower temperature in comparison with that of bulk digenite mineral (above 500 °C).[44-45] It should be pointed out that there is inconsistency in the literature about the heat effect of the above

thermal transformation in inert atmosphere: endothermic effect,[46-47] or exothermic effect,[45] as observed in our case. Finally, based on the *in-situ* TGA-MS, and the data reported in the literature, we could suppose that a small part of our digenite samples (~10 wt.%) is in a form of nanosized material.

Following one of our main objectives in this study to utilize a simple method for synthesis of $HCOO^-$ selective CO_2ER catalysts, initially we started by sulfidation of Cu foil via immersing it in solution containing sulfur dissolved in toluene. It was found that the obtained sulfide material resembles similar phase composition as in the case of sulfidated Cu foam (Figure S6). However, the as-prepared $Cu_{1.8}S$ coating readily delaminated from the surface of the foil (Figure S8). Similar mechanical instability was observed when Cu mesh was used as a substrate (see Figure S9), even though Cu, or Cu alloy based meshes were previously reported to be successfully utilized substrates for preparation of copper sulfide based CO_2ER catalysts.[24-25, 48] In our case, to overcome this problem, microporous Cu foam was deposited on the mesh substrate and subsequently sulfidated, as described above. We note that direct reactions between elemental Cu and sulfur dissolved in organic solvents like CS_2, CCl_4, benzene, xylene and $CHCl_3$ are summarized in several publications,[49-51] but nevertheless all of them are more hazardous than the toluene used here. Regarding the sulfidation mechanism (Equation 1), we can propose two hypotheses based on the reported research in the literature. The first hypothesis is adopted from the literature,[51] and is based on a mechanism that involves disruption of the solvation shell around the S_8 molecules when dissolved in organic solvent. According to that claim, the actual reactive species are the solvated S_8 molecules. The second hypothesis is inspired by the research reported by Steudel and Holz.[52] It describes a procedure for quantitative analysis of different samples of commercial sulfur in powder with HPLC and using CS_2 as a solvent for preparing the analyte matrix. Namely, they found that all commercial sulfur samples, besides the main phase α-S_8, contain traces of S_7 (<1%) and also S_6, S_9, and poly-sulfur (S_n) species. These species are thermodynamically less stable than S_8 and therefore more reactive when dissolved in organic certain solvents (such as CS_2 and toluene), thus being able to oxidize metallic copper and therefore generate copper sulfides. The precise nature of the reaction mechanisms remains open question requiring further investigation which is outside the scope of the current study.

Electrocatalytic activity for CO_2 conversion

The $Cu_{1.8}S$/Cu foam CO_2ER catalytic activity results show typical behavior for the Cu-S materials when examined under similar conditions,[17, 20-26] hence the presence of sulfur in the Cu structure is driving the selectivity (expressed as faradaic efficiency - FE) towards $HCOO^-$

production as practically exclusive CO_2ER product in comparison with pristine Cu foam, in the examined potentials range between –0.5 to –0.9 V vs RHE, as presented in Figures 2 and S10. This means that the presence of sulfur is simultaneously suppressing the production of other CO_2ER products like CO, C_2H_4 and alcohols that are typically produced on Cu foam electrocatalyst.[40, 53] The production of these products is negligible, their total FE not exceeding 3% on the $Cu_{1.8}S$/Cu foam electrocatalyst, whereas some of them reached significant values in the case of pristine Cu foam (see Figure S11). The $HCOO^-$ production and undesirable hydrogen evolution reaction (HER) suppression on the $Cu_{1.8}S$/Cu foam *vs*. pristine Cu foam are significantly dependent from the direction of ramping the applied potential, that is, ramping in less negative (RLN: –0.9 to –0.5 V) or in more negative (RMN: –0.5 to –0.9 V) direction (cf. Figures 2a, b with 2d, e). The reaction kinetics expressed as partial current density (j_i) follows the behavior of the selectivity and the presence of sulfur in the $Cu_{1.8}S$/Cu foam electrocatalyst is enhancing the j_{HCOO^-} - while suppressing the j_{H_2}, but again in dependence of the direction of ramping the applied potential (cf. Figures 2c and 2f). Namely, it was found that ramping the potential in a less negative direction (RLN) in the case of $Cu_{1.8}S$/Cu foam is enhancing the $HCOO^-$ selectivity and reaction rate thus suppressing the HER, compared to the pristine Cu foam (regardless of the potential ramping direction for this material). Contrary to this, when the $Cu_{1.8}S$/Cu foam is examined via ramping the potential in a RMN direction, the enhancement of the $HCOO^-$ selectivity versus pristine Cu foam is less significant than in the previous case, moreover the suppression of H_2 selectivity is practically negligible and additionally the reaction rate is almost unaffected at the potentials of interest. Consequently, besides the differences in the selectivity and reaction rates of $HCOO^-$ and H_2 comparing the $Cu_{1.8}S$/Cu foam and pristine Cu foam, the ramping direction of the applied potential affects the $HCOO^-$ and H_2 selectivity in the case of $Cu_{1.8}S$/Cu foam electrocatalyst itself. Namely, when the applied potential is altered in RLN direction, the $Cu_{1.8}S$/Cu foam electrocatalyst exhibits higher FE_{HCOO^-} values peaking at –0.7 V (~65%) in the range from –0.6 to –0.8 V and with significant suppression of the HER at –0.6 and –0.7 V, in comparison when the electrocatalyst is studied in the RMN direction. In the RMN direction, the FE_{HCOO^-} reaches the highest value at –0.7 V, as in the case during the RLN direction, but the actual value is significantly smaller (~50%) and practically equal to the FE_{H_2}. At potentials of –0.8 and –0.9 V in the RMN direction, the differences between FE_{HCOO^-} and FE_{H_2} are small, but in favor of the HER which becomes dominant at –0.5 and –0.6 V. Yet, at –0.9 V no difference is observed between the FEs_{HCOO^-} (~45%) obtained under both RLN and RMN conditions and accordingly the same applies for the FEs_{H_2} (~55%). Furthermore, the j_{HCOO^-} show higher values in the case of RLN in comparison with the RMN direction (Figures 2c). This difference increases at more negative applied potentials (–0.7 to –0.9 V), while practically becomes negligible at –0.5 to –0.6 V, regardless the direction of the applied potential ramping. Comparing the j_{HCOO^-} with j_{H_2} in the RLN direction, it is obvious that the difference is

most significant at –0.7 V in favor of j_{HCOO^-}, the $HCOO^-$ production rate exceeding that of H_2 by a factor of ~2. These observations are in analogy with the results for the FE_{HCOO^-} that is peaking and FE_{H_2} which is most suppressed at applied potential of –0.7 V in the RLN direction while this difference between j_{HCOO^-} and j_{H_2} under all other applied potentials is lower. In the case of the RMN direction the j_{H_2} is either higher (at –0.5, –0.6 and –0.9 V) or practically equal (–0.7 and –0.8 V) to the j_{HCOO^-}. As in the case of the $Cu_{1.8}S$/Cu foam electrocatalyst, the FEs_{HCOO^-} and FEs_{H_2} on the pristine Cu foam presented in Figures 2d, e also show dependence on the direction of applied potential ramping, yet overall, less prompted than the $Cu_{1.8}S$/Cu foam. This ramping direction dependent FEs differences are most significant at –0.5 and –0.9 V, smaller at –0.6 and –0.7 V and almost negligible at –0.8 V. However, in both directions of ramping of the applied potential, the FEs_{H_2} and j_{H_2} are significantly higher than the FEs_{HCOO^-} and j_{HCOO^-}, respectively. Regarding the j_{HCOO^-} and j_{H_2} (see Figures 2c and 2f), the difference in the $HCOO^-$ and H_2 production rates from the potential ramping direction is negligible in the interval between –0.5 and –0.8 V. However, at –0.9 V there is a very significant enhancement it the H_2, hence suppression of the $HCOO^-$ production rate in the RLN direction, while this difference is rather smaller in the case of the RMN direction.

Up to now it is clear that the presence of sulfur typically enhances the $HCOO^-$ production and suppresses the HER and other CO_2ER products, even though the first two observations are only significant in the RLN direction. Additionally, from analysis of surface capacitance estimation of relative surface roughness (Table S3), the nearly identical roughness of pristine and sulfidated Cu foams suggests the $HCOO^-$ enhancement does not arise from roughness differences. Nevertheless, the dendrite microstructures composing the $Cu_{1.8}S$/Cu foam are being drastically transformed into sponge-like morphology, regardless of the direction of ramping of the applied potential (see Figures S13a-c to S22a-c), while the pristine Cu foam maintains the dendrite microstructures as in the pre-electrolysis samples (Figure S23a-c). This transformation of the dendrite microstructures in the case of $Cu_{1.8}S$/Cu foam was found to occur only when negative electrochemical bias is applied but not under open circuit conditions when the sample is immersed in the electrolyte (Figure S24a-c).

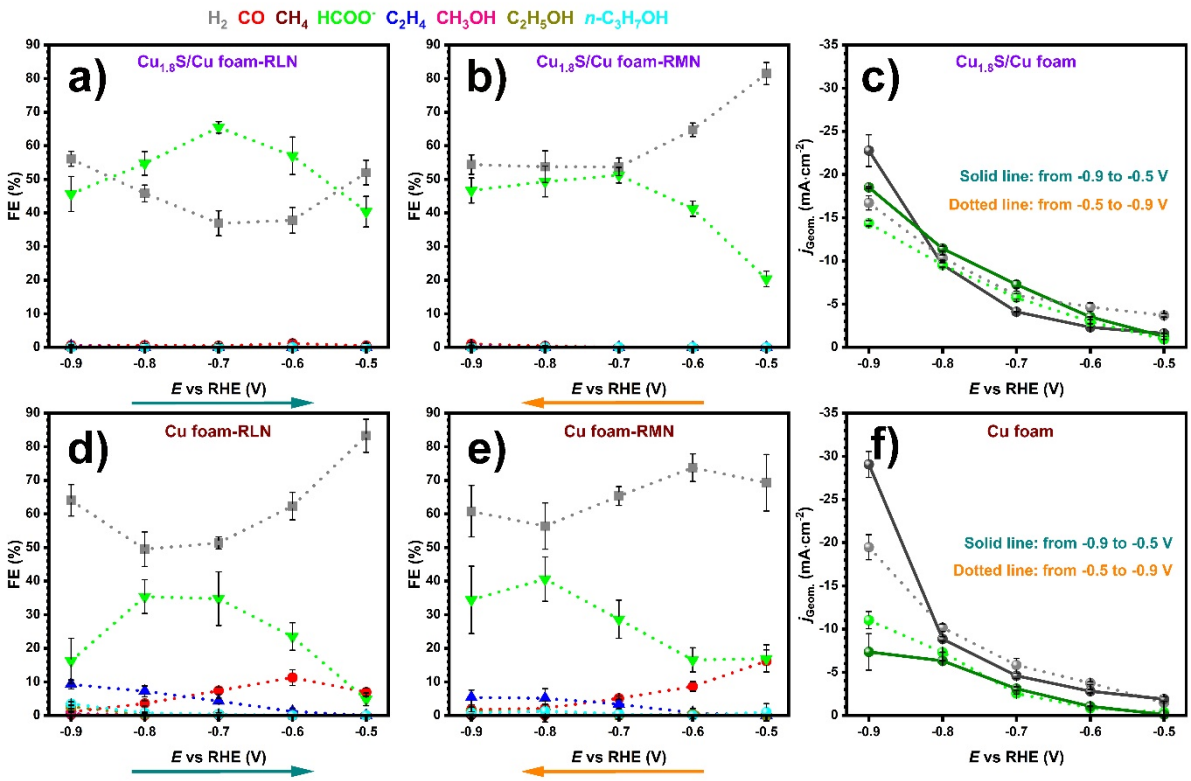

Figure 2. Distribution of FEs for H_2 and various CO_2ER products and partial current densities for H_2 and $HCOO^-$ obtained on $Cu_{1.8}S$/Cu foam and pristine Cu foam electrocatalysts during 1 h electrolysis at each potential: FEs distribution obtained with ramping the potential in less negative direction – RLN for $Cu_{1.8}S$/Cu foam **(a)** and pristine Cu foam **(d)**; FEs distribution examined with ramping the potential in more negative direction – RMN for $Cu_{1.8}S$/Cu foam **(b)** and pristine Cu foam **(e)**; Partial current densities for H_2 (dark and light grey lines) and $HCOO^-$ (dark and light green lines) obtained in RLN (solid line) and RMN (dotted line) direction for $Cu_{1.8}S$/Cu foam **(c)** and pristine Cu foam **(f)**. The arrows point the direction of ramping of the applied potential.

Having in mind all previous statements, naturally a question follows: Why ramping of the applied potential in less negative direction (RLN) shows higher FE_{HCOO^-} and j_{HCOO^-} than in the case when it is ramped in a more negative direction (RMN) thus achieving highest values of the FE_{HCOO^-} and accordingly lowest FE_{H_2} at –0.7 V? It appears that when the $Cu_{1.8}S$/Cu foam electrocatalyst is subjected to applied potential of –0.9 V prior to measuring the activity at –0.7 V, some sort of electrochemical activation occurs. Trying to explain this phenomenon, a series of electrochemical control experiments and further material characterizations were conducted. First, we started with testing the possible electrochemical activation effect via directly examining the $Cu_{1.8}S$/Cu foam electrocatalyst at applied potential of –0.7 V under different conditions, as presented in Figure S25 (additionally see Table S1 for sample abbreviations). Examining the electrocatalyst directly at –0.7 V showed very small difference in favor of enhancing the FE_{HCOO^-} and suppressing the FE_{H_2} in comparison when the activity is measured at the same potential in the RMN direction. On the other hand, total current density is somewhat higher than in the case when the material is studied under RMN and slightly higher

than in the case of RLN direction, probably due to still ongoing reduction process. Replacing the electrolyte with fresh one leads to drop of these partial current density values on the level of RMN while the FEs for both products are not affected. This behavior opens another question, but since it significantly affects the partial current densities for both products and the total current density in an increasing direction, it can be explained with possible still ongoing reduction of the material or presence of species near the electrode surface that lead to increase of the local electrolyte conductivity which is diminished via washing the sample and exchange of the electrolyte. Activating the electrocatalysts only with 1, 2 or 3 LSV scans from 0 to –0.9 V, then measuring the activity at fixed potential of –0.7 V shows gradual increase for both FE_{HCOO^-} and j_{HCOO^-} accompanied with decrease of FE_{H_2} and j_{H_2} until almost identical values as in the RLN direction are reached for the $Cu_{1.8}S$/Cu foam activated with 3 LSV scans. From these control experiments it can be generally concluded that the reason for enhancement in the $HCOO^-$ and accordingly suppression of the HER selectivity is indeed caused by the aforementioned electrochemical activation at –0.9 V. But what is really happening? Is this selectivity dependence from the direction of the applied potential somehow connected with the amount of sulfur present in the electrocatalyst when examined under both RLN and RMN conditions? In order to tackle this matter, the electrochemical evolution of sulfur was studied with *in-situ* mass spectrometry coupled with electrolysis (EC-MS), and the residual sulfur content in the electrocatalyst materials and electrolytes was examined with EDX/quasi *in-situ* XPS and ICP-OES, accordingly, as described in the following sections.

In-situ EC-MS tracking of the H_2S evolution, post-electrolysis examination of the residual sulfur content in the electrocatalysts and additional CO_2ER control experiments

The electrochemical setup was coupled with a MS capable of measuring H_2S produced by the $Cu_{1.8}S$/Cu foam cathode during electrolysis. H_2S starts to evolve (*m*/*z* signals of 33 and 34) at applied potential around –0.47 V during the first LSV scan (Figures 3a, 4a). Thus, this applied potential can be practically considered as an onset for evolution of H_2S via reduction of the $Cu_{1.8}S$. The reduction of the $Cu_{1.8}S$ generates S^{2-} species (Equation 2) in equilibrium with HS^-/H_2S[54-55] (Equation 3 and 4) under near neutral pH value of the CO_2 saturated $KHCO_3$(aq) electrolyte.

$$Cu_{1.8}S(s) + e^- \rightarrow 1.8Cu^0(s) + S^{2-}(aq) \quad E_{Onset} = -0.47\ V\ vs.\ RHE \tag{2}$$

$$S^{2-}(aq) + H^+(aq) \rightleftharpoons HS^-(aq) \tag{3}$$

$$HS^-(aq) + H^+(aq) \rightleftharpoons H_2S(aq) \rightleftharpoons H_2S(g) \tag{4}$$

Having a closer look at the *in-situ* EC-MS data of Figures 3 and 4, the duration of the H_2S evolution is dependent on the direction of ramping of the applied potential which is ~30 and ~60 minutes when the $Cu_{1.8}S$/Cu foam electrocatalyst is examined under RLN and RMN direction of potential altering conditions, respectively. Namely, when the electrocatalyst is examined in RLN direction (Figure 3), the H_2S evolution rate reaches a maximum at –0.9 V during the first *E vs*. time - LSV scan, followed by decreasing rates of evolution during the second and third scan. The H_2S associated *m*/*z* signals flatten ~17 minutes after constant potential of –0.9 V is applied in potentiostatic mode and remains flat during the whole duration of the electrolysis in RLN direction. For comparison, no *m*/*z* signals of 33 and 34 are observed from pristine Cu foam examined in the same manner, supporting that the signals originate from evolving S species on the $Cu_{1.8}S$/Cu foam electrocatalyst (Figure S27). Examining the *j*–*E* behaviors during repeated LSV scans (Figure S26a), the initial scan shows two distinctive reduction features, the first one a sharp peak at around –0.27 V and the second a broad and more complex feature starting at –0.55 V continuing to –0.75 V. The sharp peak resembles reduction of native Cu_xO on the surface of the pristine Cu foam, mainly Cu_2O (as observed from the XRD - Figure 1c), even though this reduction peak is broader thus stretching from to 0 and –0.36 V (cf. Figure S26a with S26c), most probably because the pristine Cu foam is more prone to oxidation than the sulfidated one. That is, besides Cu_2O, possible surface presence of CuO could contribute to the reduction processes. Yet, the reduction peak associated to Cu_2O in both pristine and sulfidated Cu foam (Figure S26a-c) show either ~200 mV more negative potential than that thermodynamically expected according to common Pourbaix diagrams for the Cu-H_2O system reported in the literature,[56] or is in agreement with existence of a monolayer oxide phase that can be reduced around –0.2 V under neutral pH.[57] The broad reduction feature after –0.55 V we attribute to reduction of the $Cu_{1.8}S$ in accordance with reports in the literature,[23, 28, 39, 55] and its complex peak shape likely arises from the $Cu_{1.8}S$ consisting of mixed phase of non-stoichiometric compounds.[58] The second and third LSV scans for the $Cu_{1.8}S$/Cu foam do not show any peaks suggesting that a thorough reduction of the $Cu_{1.8}S$ already occurred during the first scan. Additionally, the current density at –0.9 V achieved during the first LSV is ~15 $mA \cdot cm^{-2}$ higher than in the case of the second and third scan. Yet, the prolonged decay in the evolution of gaseous H_2S which stretches up to ~17 minutes since the CA is started at –0.9 V in the RLN direction (see Figure 3b) could be explained by an enhanced proton consumption near the electrode surface at more negative potentials that is leading to increase in the local pH,[59] thus affecting the $S^{2-}/HS^{-}/H_2S$ equilibrium (Equations 2-4) in favor of retaining the S^{2-}/HS^{-} species in the electrolyte.

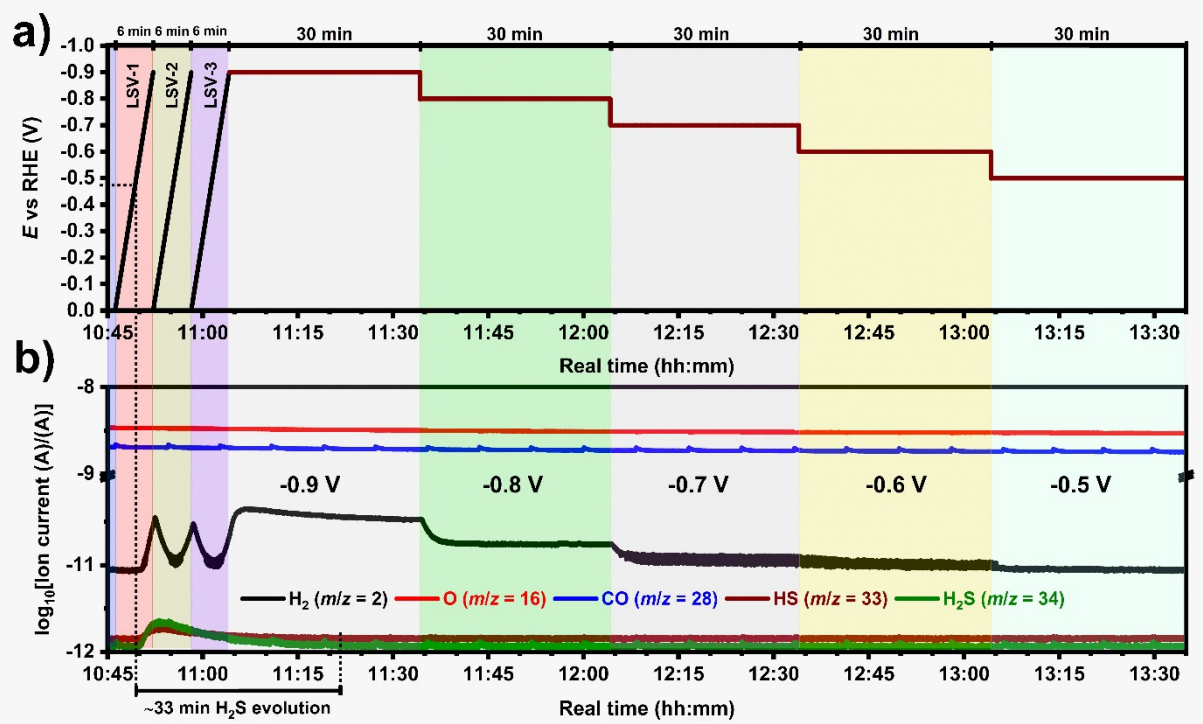

Figure 3. Tracking of the H_2S evolution with *in-situ* mass spectrometry coupled with electrolysis (EC-MS) when the $Cu_{1.8}S$/Cu foam electrocatalyst is examined in the RLN direction of altering the applied potential (–0.9 to –0.5 V): Applied potential in linear sweep voltammetry - LSV/chronoamperometry - CA modes **(a)** and mass signals/charge - *m*/*z* attributed to H_2, CO, O_2 and H_2S **(b)** plotted vs time of electrolysis.

Figure 4 shows the tracking of the H_2S evolution when the $Cu_{1.8}S$/Cu foam electrocatalyst is examined in the RMN direction of altering the applied potential (–0.5 to –0.9 V). In this case, as mentioned above in this section, the H_2S evolution duration is longer (~60 minutes) and the *m*/*z* signals associated with this species drop completely ~20 minutes after the potential is ramped from –0.5 to –0.6 V. Besides the evolution duration, another difference compared to the case when the potential is altered in the RLN direction is the step-wise increase of the H_2S - *m*/*z* signals within altering of the potential from 0 to –0.5 V during the first, second and third LSV scan thus peaking ~3 minutes after constant potential of –0.5 V is applied. This prolonged H_2S evolution behavior is to be expected because this potential is slightly more negative than the onset potential for the H_2S evolution and almost matching the broad reduction peak-potential (–0.55 V) for $Cu_{1.8}S$ to Cu when the LSV is scanned from 0 to –0.9 V prior to altering the potential in the RLN direction (cf. *j*–*E* scans in Figure 26a, b). With other words, at applied potential of –0.5 V, the reduction of $Cu_{1.8}S$ is ~2 times longer in the RMN *vs.* the RLN direction, thus prolonged H_2S evolution is observed, which finally terminates in the next ramping step at –0.6 V (RMN direction). Additionally, the HER onset appears at around –0.5 V which is slightly more negative than the onset potential for H_2S evolution (around –0.47 V) in both direction of ramping the applied potential (Figures 3, 4). Likewise, in the case of the pristine Cu foam, the HER onset is observed at identical potential. Moreover, the H_2 *m*/*z* signal follows the trend of

altering the applied potential (LSV+CA) in the RLN direction for both $Cu_{1.8}S$/Cu foam and pristine Cu foam in comparison with the H_2S evolution for the $Cu_{1.8}S$/Cu foam-RLN, where this is not the case (cf. Figures 3, 4 and S27). On the other hand, the HER does not start until potential of –0.5 V is applied that is, as expected no HER is observed during the three LSV scans from 0 to –0.5 V prior to altering the applied potential in RMN direction for the $Cu_{1.8}S$/Cu foam electrocatalyst (Figure 4).

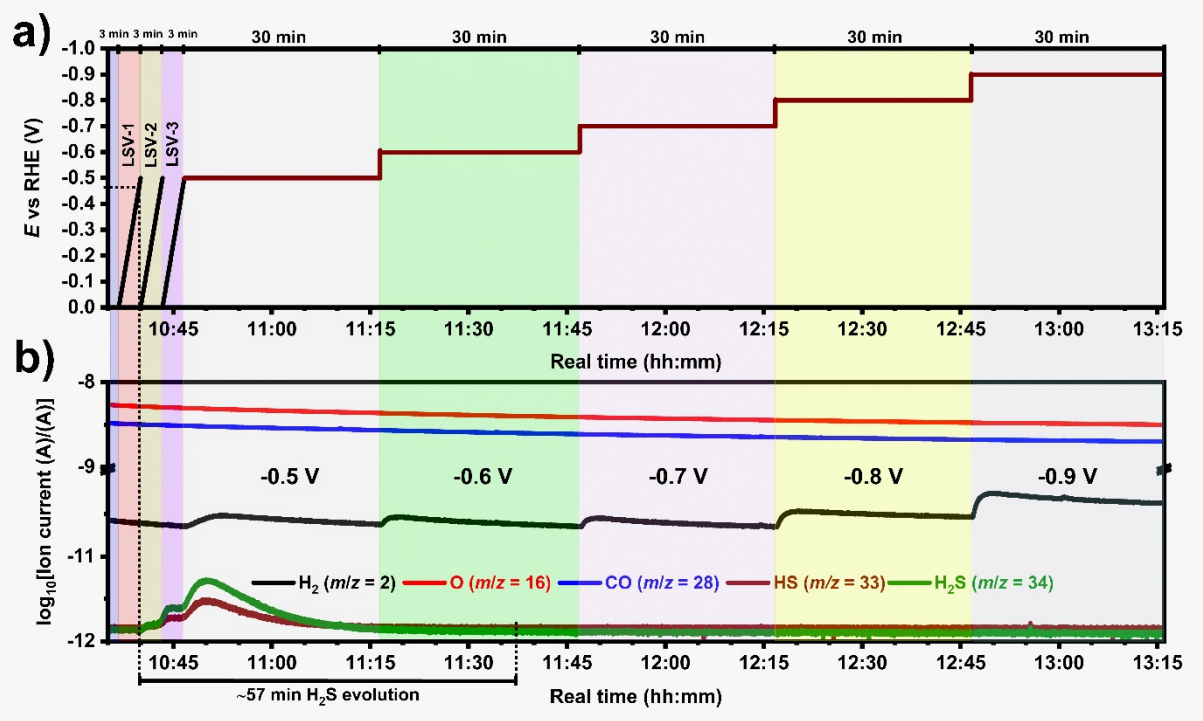

Figure 4. Tracking of the H_2S evolution with *in-situ* mass spectrometry coupled with electrolysis (EC-MS) when the $Cu_{1.8}S$/Cu foam electrocatalyst is examined in the RMN direction of altering the applied potential (–0.5 to –0.9 V): Applied potential in linear sweep voltammetry - LSV/chronoamperometry - CA modes **(a)** and mass/charge signals - *m*/*z* attributed to H_2, CO, O_2 and H_2S **(b)** plotted vs time of electrolysis.

However, in both direction of ramping the applied potential, there is no more observable H_2S evolution at –0.7 V where the highest $HCOO^-$ selectivity is observed (Figure 2a, b), thus only from the *in-situ* EC-MS experiments it is not yet clear why the activation of the $Cu_{1.8}S$/Cu foam electrocatalyst in the RLN *vs*. the RMN direction enhances the $HCOO^-$ selectivity at –0.7 V. From a thermodynamic point of view, the $Cu_{1.8}S$ should be completely reduced to metallic Cu at all potentials more negative than –0.7 V under near neutral pH.[21, 23, 28, 39, 55] Yet, according to various reports in the literature, this reduction is kinetically sluggish thus sulfur residues may persist during and after the electrolysis.[20, 23, 27-28, 39] Therefore, we sought to examine whether there is any significant difference in the sulfur fraction in the electrocatalyst itself at –0.7 V that could affect the $HCOO^-$ selectivity enhancement it the RLN *vs.* RLN direction of altering the applied potential. Composition analysis of the $Cu_{1.8}S$/Cu foam with EDX shows that the bulk

sulfur fraction resembles ~30 at.% for the as-prepared material and drops to ~1 at.% following electrolysis at all applied potentials except at –0.5 and –0.6 V in the RMN direction (Figure S28). In the exceptional cases slightly higher value of ~1.5 at.% are observed, which support the longer duration of the H_2S evolution at these potentials in the RMN direction (Figure 4). Similar low sulfur content was reported in the literature for the best producing $HCOO^-$ electrocatalysts derived from Cu_xS.[28, 38, 55] Hence, there is not yet explanation how the activation of the $Cu_{1.8}S$/Cu foam electrocatalyst at –0.9 V enhances the $HCOO^-$ selectivity since no H_2S evolution from the *in-situ* EC-MS (Figure 3 and 4) and ~1 at.% bulk sulfur fraction is observed from the EDX data (Figure S28) at –0.7 V, regardless of the direction of ramping the applied potential. However, it can be presumed that certain amount of $S^{2-}/HS^-/H_2S$ species in equilibrium should remain in the electrolyte for certain amount of time possibly with different concentration dependent on the direction of ramping the applied potential. Namely, as already mentioned, the direction of ramping the potential can affect the local pH, consequently the $S^{2-}/HS^-/H_2S$ equilibrium thus relating it with the origin of the activation and enhancement in the $HCOO^-$ selectivity. To test this hypothesis pristine Cu foam samples were sulfidated via immersing them in electrolytes in which previously $Cu_{1.8}S$/Cu foam was electrochemically reduced using one LSV scan from 0 to –0.9, –0.5 or –0.7 V (`electrolyte sulfidated`) and then their CO_2ER activity was examined at –0.9 and –0.7 V. Indeed, some literature reports have shown that purging the electrolyte with CO_2 containing small amount of H_2S or SO_2 as reactive sulfur species can result in $HCOO^-$ selective Cu_xS electrocatalysts formed by reaction with Cu electrodes.[20-21, 26] After performing such control experiments, the results in Figure 5 and S29 show that indeed the pristine Cu foam can be sulfidated with this approach. Variety of samples and experimental conditions were tested for this purpose and their description and abbreviations are presented in Table S1. When the $Cu_{1.8}S$/Cu foam is reduced with one LSV scan from 0 to –0.9 V, then removed and replaced with a pristine Cu foam to be tested in the same residual electrolyte (sample: Cu foam-S-0.9), and examined for its CO_2ER activity, the FE_{HCOO^-} can reach 70-75% and 58-65% at –0.9 and –0.7 V, respectively. Comparing these results with the ones for pristine Cu foam and $Cu_{1.8}S$/Cu foam, ramped in both directions, it is obvious that at –0.9 V, the FE_{HCOO^-} (Figure 5a) is ~5 times higher than the case of Cu foam-RLN, 2-2.5 times than Cu foam-RMN and ~1.5 times higher than both $Cu_{1.8}S$/Cu foam-RLN and $Cu_{1.8}S$/Cu foam-RMN. Regarding the j_{HCOO^-} (Figure 5b), the corresponding difference factors maintain similar trend in favor of enhanced $HCOO^-$ production rate with values of around 3, 2, 1.3 and 1.6 times higher than the case of Cu foam-RLN, Cu foam-RMN, $Cu_{1.8}S$/Cu foam-RLN and $Cu_{1.8}S$/Cu foam-RMN, respectively. The $HCOO^-$ selectivity at this potential is not affected when the Cu foam is immediately immersed, when the electrolyte is either purged with CO_2 for 1 h prior to immersing the Cu foam (Cu foam-S-P1h) or when the electrolyte is replaced with fresh one, and the sample is examined once more (Cu foam-S-P-1h-NE). On the

other hand, when the Cu foam is immersed in electrolyte in which the $Cu_{1.8}S$/Cu foam was reduced to –0.5 V (sample: Cu foam-S-0.5), the FE_{HCOO^-} and j_{HCOO^-} are significantly lower, compared to the samples prepared with reducing the $Cu_{1.8}S$/Cu foam to –0.9 V. Comparing this Cu foam-S-0.5 sample with the $Cu_{1.8}S$/Cu foam-RLN, it can be observed that the FE_{HCOO^-} is slightly higher while the j_{HCOO^-} is almost identical. Repeating the same experiment via examination of `electrolyte sulfidated` Cu foam prepared via immersing it in electrolyte in which $Cu_{1.8}S$/Cu foam was reduced with one LSV from 0 to –0.7 V (Cu foam-S-0.7), no significant difference in the FE_{HCOO^-} was observed while the j_{HCOO^-} shows some scattering in the values, when compared to all samples prepared via LSV reduction from 0 to –0.9 V, regardless of CO_2 purging prior to applying bias or electrolyte replacement. Under CO_2ER at –0.7 V (Figure 5c), no significant differences in the FE_{HCOO^-} are observed between the Cu foam immersed in electrolyte in which the $Cu_{1.8}S$/Cu foam was reduced to –0.7 (Cu foam-S-0.7) or –0.9 V (under various conditions) and the $Cu_{1.8}S$/Cu foam-RLN, except when the Cu foam sample is immediately immersed into the electrolyte after reduction to –0.9 V, or the LSV reduction is performed to –0.5 V (Cu foam-S-0.5) thus showing lower values for the later ones. The j_{HCOO^-} (Figure 5c), shows slightly higher value for $Cu_{1.8}S$/Cu foam-RLN compared to all other cases when the Cu foam is immersed in electrolytes after LSV reduction of $Cu_{1.8}S$/Cu foam samples under various conditions. The j_{HCOO^-} values obtained for all `electrolyte sulfidated` Cu foam (Cu foam-S) samples are either similar or slightly lower than the case of $Cu_{1.8}S$/Cu foam-RMN. Regarding the surface morphology, the `electrolyte sulfidated` Cu foam samples, examined post-electrolysis do not transform into sponge-like but instead preserve the dendrite microstructures as exhibited by the pristine Cu foam (Figures S30 and S31). From this it can be summarized that similar or somewhat different $HCOO^-$ selectivity can be obtained between Cu foam-S-0.9/Cu foam-S-0.7 and $Cu_{1.8}S$/Cu foam when the CO_2ER activity was examined at –0.7 V, while very significant enhancement of the $HCOO^-$ selectivity occurs in favor of the Cu foam-S-0.9/Cu foam-S-0.7 samples comparing the electrocatalytic activity at –0.9 V. The lower $HCOO^-$ selectivity at both –0.9 and –0.7 V in the case of Cu foam-S-0.5 sample suggests that maybe the amount of sulfur species in the electrolyte obtained with one LSV reduction of the $Cu_{1.8}S$/Cu foam is not sufficient for selectivity-wise satisfactory sulfidation since the potential of –0.5 V is near the onset potential for $Cu_{1.8}S$ reduction (Equation 2) thus weak *m*/*z* signals for H_2S evolution (Figure 4, first LSV scan). Additionally, several other control experiments were conducted in which already electrocatalytically examined $Cu_{1.8}S$/Cu foam-RLN was re-examined at the same potentials after being exposed to air, inert atmosphere and/or the electrolyte was replaced once or two times ($Cu_{1.8}S$/Cu foam-air, $Cu_{1.8}S$/Cu foam-inert, $Cu_{1.8}S$/Cu foam-NE and $Cu_{1.8}S$/Cu foam-NE2, respectively). The results in Figures 5 and S29 show $HCOO^-$ selectivity enhancement which in the case when the sample is either only exposed to air and re-examined in the same electrolyte ($Cu_{1.8}S$/Cu foam-air) or the electrolyte

is replaced with fresh one, once or twice ($Cu_{1.8}S$/Cu foam-NE and $Cu_{1.8}S$/Cu foam-NE2) are almost reaching the FE_{HCOO^-} with some discrepancies in the j_{HCOO^-} values as for the Cu foam-S-0.9/Cu foam-S-0.7 samples at both potentials (–0.9 and –0.7 V). Regarding the sample that was examined at –0.9 V then exposed to inert atmosphere (N_2) and re-examined under the same conditions, it was found that the FE_{HCOO^-} achieved ~68% which is almost identical as for the $Cu_{1.8}S$/Cu foam-NE and $Cu_{1.8}S$/Cu foam-NE2 samples. This suggests that the surface oxides, that is Cu_xO species do not have any influence on the electrocatalytic activity. These $Cu_{1.8}S$/Cu foam samples are being morphologically transformed during the electrolysis, resembling sponge-like features (Figure S32a-c and S33a-c) as in the case when the same samples were examined via ramping the applied potential in both directions. Contrary to the EDX results for the $Cu_{1.8}S$/Cu foam in Figure S28 where not much difference was observed in the bulk sulfur fraction (~1 at. %) examined in both directions of ramping the applied potential (–0.9 to –0.7 and –0.5 to –0.7 V), in the case of the $Cu_{1.8}S$/Cu foam that was re-examined after either air or inert atmosphere exposure and electrolyte replacement shows lower sulfur content (<0.5 at. %, Figure S32d-f and S33d-f). Moreover, in the case of the Cu foam-S-0.9 samples, the bulk sulfur content cannot be detected with EDX (Figures S30 and S31) and as a reminder the selectivity is very significantly enhanced compared to the $Cu_{1.8}S$/Cu foam-RLN at –0.9 V, while not much affected at –0.7 V. It seems that when the bulk sulfur fraction is either <0.5 at.% for the $Cu_{1.8}S$/Cu foam-air/NE/NE2, or not detectable in the Cu foam-S-0.9/-0.7, it is somewhat optimal Cu-S composition that leads to higher $HCOO^-$ selectivity compared to $Cu_{1.8}S$/Cu foam at –0.9 V where the sulfur fraction is ~1 at.% (Figure S28). Yet, the $HCOO^-$ selectivity is not much affected at –0.7 V where the activation of the $Cu_{1.8}S$/Cu foam at –0.9 V in the RLN takes effect compared to the RMN direction of altering the applied potential. On the other hand, the Cu foam-S-0.5 sample seems to be not sufficiently sulfidated thus the sulfur fraction is below the optimal thus leading to lower $HCOO^-$ selectivity at both –0.9 and –0.7 V compared to all previous samples. These findings could be associated with the aforementioned hypothesis thus the origin for the bulk sulfur fraction *vs.* selectivity may be affected by the concentration of sulfur species in the electrolyte. Therefore, for further clarification of this claim, the total sulfur concentration under various experimental conditions was quantified using ICP-OES.

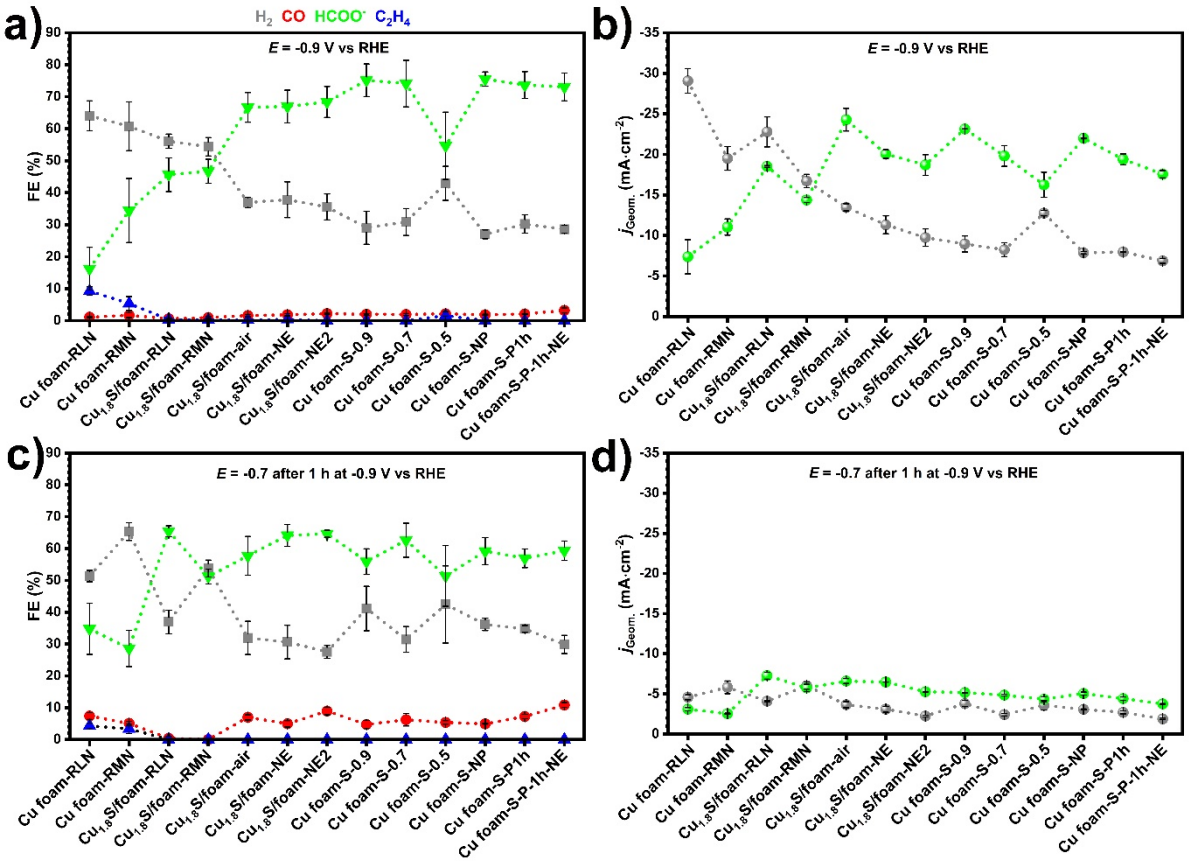

Figure 5. Distribution of FEs for H_2 and CO_2ER products and partial current densities for H_2 and $HCOO^-$ obtained on $Cu_{1.8}S$/Cu foam and `electrolyte sulfidated` Cu foam under 1 h electrolysis at various conditions: FEs distribution **(a)** and partial current densities for H_2 and $HCOO^-$ at –0.9 V **(b)**, and FEs distribution **(c)** and partial current densities for H_2 and $HCOO^-$ at –0.7 V vs RHE **(d)**. The sample abbreviations and experimental conditions are presented in Table S1.

The ICP-OES results are presented in Figure 6 and Table S4. According to them, the highest sulfur concentration is achieved when the $Cu_{1.8}S$/Cu foam is reduced with one LSV scan from 0 to –0.9 V and as expected from the *in-situ* EC-MS data (Figures 3 and 4) the concentration is lower in descending order in the case of reduction to –0.7 and –0.5 V. When three LSV scans are applied from 0 to –0.9 V and 0 to –0.5 V, the situation becomes different and the concentration of sulfur in the case of three LSV scans from 0 to –0.9 V becomes two times lower than in the case of 0 to –0.5 V. This finding is supported by the electrochemical (Figure S26a ,b) and *in-situ* EC-MS data in Figures 3 and 4, since as stated before the potential of –0.5 V is near the onset potential for reduction of the $Cu_{1.8}S$ material thus prolonged H_2S evolution is observed. The effect of prolonged $Cu_{1.8}S$ reduction in the case of altering the potential in RLN direction is rather caused by increase of the local pH,[59] as mentioned before. However, the concentration of sulfur drops and therefore equalizes when the applied potential is ramped in RLN starting from –0.9 to –0.7 V or in RMN from –0.9 to –0.7 V. Furthermore, almost identical concentration of sulfur in the electrolyte is achieved when the activity is studied directly at –0.7 V without ramping the potential ($Cu_{1.8}S$/Cu foam-0.7D). This means that the

activation of the electrocatalyst at –0.9 V thus achieving the best $HCOO^-$ selectivity at –0.7 V in the RLN *vs.* RMN direction (Figure 2) is probably not related with the bulk concentration of sulfur present in electrolyte during the CO_2ER and as a reminder from the EDX results in Figure S28, the activation is probably not related with the bulk sulfur fraction either. On the other hand, the $Cu_{1.8}S$/Cu foam samples that were re-examined first only at –0.9 and then at –0.9 at –0.7 V after air exposure and electrolyte replacement show identical concentration of sulfur after the electrolysis, which is much lower than in all other cases. Rather unexpected are the results found post-electrolysis for the `electrolyte sulfidated` Cu foam (Cu foam-S-0.9/-0.7/-0.5 samples) where the sulfur concentration is much higher than in the case for the $Cu_{1.8}S$/Cu foam samples that were re-examined after air exposure and electrolyte replacement even though they all showed similar $HCOO^-$ selectivity at both –0.9 at –0.7 V (Figure 5) and either not detected or below 0.5 at.% bulk sulfur fraction (Figures S30-33). Eventually, the concentration of sulfur in the case of all Cu foam-S samples is also higher than in the case of $Cu_{1.8}S$/Cu foam-RLN and RMN samples. As expected from the LSV reduction of the $Cu_{1.8}S$/Cu foam to –0.9 V, the highest sulfur concentration is observed in the case of Cu foam-S-0.9 sample. On the other hand, and rather not expected the sulfur concentration in the case of the Cu foam-S-0.5 showed slightly higher value than Cu foam-S-0.7 sample and from the activity results in Figure 5 the Cu foam-S-0.5 maintained the lowest $HCOO^-$ selectivity among all Cu foam-S samples, while between Cu foam-S-0.9 and Cu foam-S-0.7 is almost identical.

From the ICP-OES results it can be summarized that the sulfur concentration in the electrolyte is not affected by the potential ramping direction to –0.7 V in the case of $Cu_{1.8}S$/Cu foam and moreover almost identical concentration is achieved when –0.7 V are directly applied without ramping. This is suggesting that these results cannot explain the activation of the electrocatalyst at –0.9 V since no significant sulfur concentration differences are observed. Besides that, the lower sulfur concentration is maybe $HCOO^-$ selectivity-wise optimal for the air/inert exposure/electrolyte replacement when compared to $Cu_{1.8}S$/Cu foam in RLN/RMN direction of altering the applied potential under electrolysis at –0.9 and not affected at –0.7 while not equally optimal for the `electrolyte sulfidated` Cu foam (Cu foam-S), as hypothesized before. The $Cu_{1.8}S$/Cu foam and Cu foam-S samples are indeed morphologically different, that is sponge *vs.* dendrite composed foam (cf. Figures S13-22, 32 and 33 with S30-31), yet the relative surface roughness factors are in the same order of magnitude (Table S3).

Having in mind that the quantification of the sulfur species in the electrolyte cannot give all answers associated to the $HCOO^-$ selectivity and moreover the bulk sensitivity of the EDX that shows similar sulfur fractions in all cases except at –0.5 V, the samples were subjected to examination with XPS as rather surface sensitive technique that should provide more insights regarding the Cu and S composition and chemical nature, as discussed in the following section.

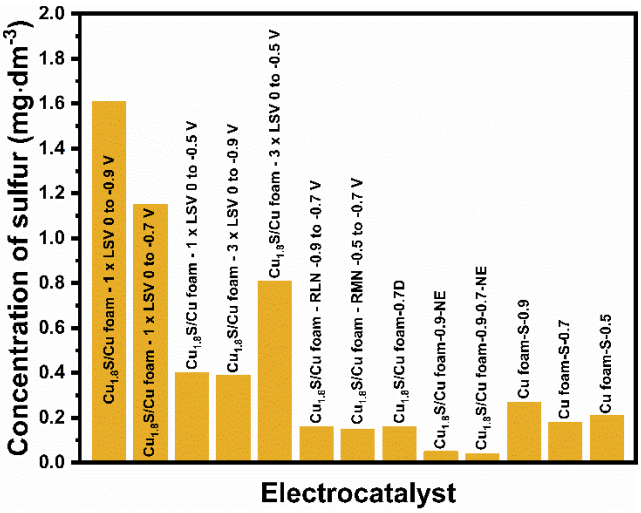

Figure 6. ICP-OES analysis of the concentration of sulfur in the electrolyte examined post-electrolysis under various conditions. More information regarding the experimental conditions can be found in Table S4.

Quasi in-situ XPS - Examination of the Cu and S surface fractions and speciation

Even though it is already known from the literature[20, 23, 27-28, 39] and supported in this study from the EDX analysis that sulfur species do persist during the CO_2 electrolysis in the structure of the catalysts, to the best of our knowledge the chemical nature related to speciation and oxidation state of Cu and S under operating or near-operating conditions are not yet resolved. Therefore, a *quasi in-situ* XPS approach was utilized in this study, with experimental details provided in section S1.5. of the SI. The XPS survey spectra for all examined samples is presented in Figure S34 and the high-resolution Cu 2p, O 1s, Cu LMM Auger and S 2p spectra are presented in Figures S35-38. The Cu 2p core level XPS spectra in Figure S35 show that the surface Cu species resemble either metallic (Cu^0) or Cu^+ oxidation state from the Cu $2p_{3/2}$ peak positions at ~932.5 eV in the case of all examined materials, except the pristine and sulfidated Cu where additional peaks at ~934 eV corresponding to presence of Cu^{2+} can be observed.[60] This is expected since the surface of the as-prepared Cu foam is prone to oxidation in air and regarding the sulfidated foam, $Cu_{1.8}S$ resembles mixed Cu^+/Cu^{2+} stoichiometry in the digenite/roxbyite phases. Regarding the O 1s core level XPS spectra, an evidence for lattice oxygen species at ~530.5 eV[60] in the catalysts' surface structure can be observed in the case of as-prepared Cu foam and the sample that was exposed to air after the electrolysis (Figure S36). In the case of all other examined samples, the O 1s peak positions are above 531 eV thus these peaks can be assigned to adsorbed oxygen species coming from OH^-, CO_3^{2-}, HCO_3^-, O vacancies etc.[60-61] Comparing the O 1s of the air exposed $Cu_{1.8}S$/Cu foam and the one used as a catalyst for electrolysis under inert conditions ($Cu_{1.8}S$/Cu foam-inert) where no lattice oxygen species are observed is good evidence that the electrolysis in

inert atmosphere approach indeed provides preservation of the Cu oxidation states after terminating the electrochemical bias. Moreover, the best surface oxidation states speciation was achieved from the Cu LMM Auger spectra using fitting parameters reported in the literature.[60] The Cu Auger spectra are presented in Figure S37 and the extracted results regarding the speciation and quantification of the electrocatalysts' surface in Table S5 and Figure 7. The results in Figure 7a show that the as-prepared Cu foam resembles 92 at.% Cu^+ and 8 at.% Cu^{2+} originating from Cu_2O and CuO, respectively. The presence of oxidized Cu species on the surface of this material supports the above mentioned Cu^{2+} assigned peaks in the Cu 2p spectra and the lattice oxygen species signal in the O 1s XPS spectra. The presence of Cu_2O as main surface phase is in agreement with the XRD data for this material (Figures 1c and S6), while the presence of CuO explains the aforementioned broadening of the reduction peak during the first LSV scan in Figure S26c. Regarding the sulfidated Cu foam ($Cu_{1.8}S$/Cu foam), the surface is composed of ~75 at.% Cu^+ and ~25 at.% Cu^{2+} originating from Cu_2S and CuS, respectively, which is expected having in mind the mixed stoichiometry of the phase composition. When negative electrochemical bias is applied under CO_2 electrolysis conditions, the pristine Cu foam undergoes complete surface reduction to metallic Cu in the case of all examined samples regardless of the potential and direction in which it is applied in the range between –0.5 and –0.9 V. On the other hand, the Cu Auger spectra results show that during the reduction process, the $Cu_{1.8}S$/Cu foam undergoes significant but incomplete reduction to metallic copper, with 10-15 at.% Cu^+ associated to Cu_2S observed at applied potential of –0.9 V and also when the potential is altered in RLN (–0.9 to –0.7 V) and RMN (–0.5 to –0.7 V) direction. However, at –0.5 V for 1 h, the fraction of Cu^+ associated with Cu_2S is higher (~22 at.%) which as stated in the previous sections is expected, considering that the reduction of the material is sluggish at this potential since it is near the onset potential for this process (Figure S26), thus prolonged H_2S evolution (*in-situ* EC-MS - Figure 4) and higher bulk sulfur amount in the catalyst is observed (~1.5 at.% from EDX - Figure S28). It seems that the activation of the $Cu_{1.8}S$/Cu foam electrocatalyst cannot be really explained from the Cu^+ fractions which are not significantly different regardless of the direction of ramping the applied potential in analogy to the previous characterization methods (EDX and ICP-OES) where identical trend was observed. Regarding the $Cu_{1.8}S$/Cu foam that was exposed to air after electrolysis and re-examined in a fresh electrolyte at –0.9 V and –0.7 V thus analyzed *ex-situ*, showed fully oxidized surface without any presence of metallic Cu (Figure 7a). This material contains ~13 at.% Cu^+ associated to Cu_2S, similar as in the case of $Cu_{1.8}S$/Cu foam examined via altering the applied potential in RLN (–0.9 and –0.7 V) and RMN (–0.5 and –0.7 V) direction, while rather different since the rest is ~87 at.% Cu^+ associated to Cu_2O. Contrary to this, when $Cu_{1.8}S$/Cu foam is examined via the same manner but under inert (N_2 filled glovebox) conditions, no evidence of Cu^+ originating from Cu_2O is observable thus the surface consists

of metallic Cu and ~8 at.% Cu^+ from Cu_2S, that is not much different than the air exposed one, and as a reminder both materials showed similar $HCOO^-$ selectivity (Figure 5). This is another evidence that, as mentioned before, the inert atmosphere electrolysis approach preserves the Cu oxidation states. The electrocatalysts prepared via `electrolyte sulfidation` of Cu foam in electrolyte in which $Cu_{1.8}S$/Cu foam was reduced with one LSV scan to –0.5 and –0.9 V (Cu foam-S-0.5 and Cu foam-S-0.9), besides metallic Cu as main surface fraction they contain ~3 and 5 at.% Cu^+ species from Cu_2S for the Cu foam-S-0.5 and for Cu foam-S-0.9, respectively. This is not expected since both materials have similar Cu^+ fraction, but at –0.9 V much higher $HCOO^-$ selectivity is observed in the case of Cu foam-S-0.9 at (Figure 5). Figure 7b shows the quantification results of the total surface Cu from the Cu 2p (Figure S35) and the sulfur species (assigned to S^{2-} at ~162 eV and SO_4^{2-} at ~170 eV[20, 61]) from the S 2p (Figure S38) core levels XPS spectra normalized peak areas. The as-prepared $Cu_{1.8}S$/Cu foam resembles much higher surface sulfur fraction in all cases compared to the EDX analysis (Figure S28) thus suggesting that the sulfur is distributed on the surface rather than the bulk of the material. Moreover, in the case of the as-prepared $Cu_{1.8}S$/Cu foam the surface sulfur resembles S^{2-} specie and its fraction shows higher values than expected, most probably originating from the lower signal to noise ratio in the case of the S 2p compared to Cu 2p XPS spectra. However, it is obvious that the as-prepared $Cu_{1.8}S$/Cu foam undergoes sulfur loss during electrolysis in all cases except at –0.5 V when the total sulfur fraction is similar as in the case of the as-prepared material which is for expectance according to the aforementioned sluggish reduction of the material under near onset potential for this process (Figure S26). Contrary to what was observed from the EDX and ICP-OES results (Figure S28 and 6, respectively) where the bulk sulfur fraction and the concentration of sulfur in the electrolyte and moreover the Cu^+ fractions (Figure 7a) at –0.7 V are not much different regardless of the applied potential ramping direction, the total sulfur surface fraction is significantly lower in the RMN direction (–0.5 to –0.7 V). This is the first evidence showing differences dependent from the potential ramping direction. Yet, besides S^{2-}, the existence of SO_4^{2-} species post-electrolysis is unusual considering that SO_4^{2-} contains sulfur in its highest oxidation state (+6) and it appears on the surface of a cathode material. According to Figures 7b and S38, the presence of SO_4^{2-} specie is observed in all $Cu_{1.8}S$/Cu foam samples when the electrolysis is conducted at –0.9 V or the potential is ramped from –0.9 to –0.7 V (RLN), but not when the electrolysis is conducted at –0.5 V or the potential is ramped from –0.5 to –0.7 V (RMN). In the latter case, the sulfur exclusively resembles S^{2-} species which again is another evidence regarding differences dependent from the potential ramping direction. Additionally, the actual fractions of the S^{2-} and SO_4^{2-} species are similar for $Cu_{1.8}S$/Cu foam-RLN (–0.9 to –0.7 V) compared to the same sample after electrolysis at fixed potential of –0.9 V. The presence of the SO_4^{2-} specie is most evident on the surface of the `electrolyte sulfidated` Cu foam (Cu foam-S-0.5/-0.9) where the fractions of this specie are

even higher than the fractions of S^{2-}, thus in these cases the electrolysis was also conducted at –0.9 V. Regarding the actual fractions of the species, they both resemble similar values thus the higher $HCOO^-$ selectivity in this case cannot be only explained from the S^{2-} fractions but having in mind that the SO_4^{2-} are more soluble than S^{2-} in the presence of Cu ions it could be possible that the sulfur distribution between electrocatalyst and electrolyte is dynamic. Similarly, the SO_4^{2-} specie can be observed in the case of air exposed $Cu_{1.8}S$/Cu foam sample that was subjected to second electrolysis in fresh electrolyte at –0.9 and –0.7 V, while in the case of the sample exposed to inert atmosphere SO_4^{2-} cannot be quantified due to the noisiness of the spectra but still cannot be fully excluded. Again, the possible dynamic distribution of SO_4^{2-} can affect the final surface quantification of this specie and moreover it is uncertain whether this specie is incorporated into the structure of the electrocatalyst material, or it is only a surface deposit. The formation of the SO_4^{2-} must occur via oxidation of the S^{2-} specie since there is no other sulfur source but it is rather not evident why this is observable only after electrolysis at –0.9 V is applied. The presence of surface SO_4^{2-} detected from *ex-situ* XPS, was already reported in the literature for Cu nanoparticles that were *in-situ* sulfidated with SO_2 after galvanostatic electrolysis reaching potentials similar or more negative compared to our case when these species are observed (–0.9 V).[20] Moreover, in the same study, SO_4^{2-} were also observed in the case of Ag and Sn nanoparticles examined under the same electrochemical conditions. Possible explanation is that the SO_4^{2-} specie does not exist during the electrolysis process, and it is formed via disturbance of the near electrode surface equilibrium possibly leading to sudden switch of the electrodes polarity when the electrochemical bias is terminated thus causing oxidation of the S^{2-}. Such a reaction is favored in strong alkaline environment[62] thus the aforementioned local pH increase[59] at more negative potentials could be a possible reason why the SO_4^{2-} specie is observed only when the electrolysis was performed at the most negative potential of –0.9 V, but not at –0.5 or –0.7 V. Moreover, as stated in the discussion of the *in-situ* EC-MS results (Figure 3), the local pH increase disturbs the $H_2S/HS^-/S^{2-}$ equilibrium thus favoring concentrating of the S^{2-} species near the electrode surface and causing prolonged decay in the evolution of H_2S which stretches up to ~17 minutes since the CA is started at –0.9 V in RLN direction. Therefore, it is expected that the oxidation of S^{2-} into SO_4^{2-} occurs locally in the electrolyte near the electrode surface thus these species are observed on the surface of the electrocatalyst. Naturally, the follow-up question will be whether oxidation happens to the Cu on the surface of the electrocatalyst thus the origin of the observed Cu^+ species from the *quasi in-situ* XPS results (Figure S37)? If this is possible, then such oxidation should occur on the surface of pristine Cu foam, which is rather not the case since only metallic Cu is observed for all examined samples after the electrolysis, regardless of the applied potential.

Therefore, characterization of the electrocatalyst under *in-situ* conditions with near ambient XPS without stopping the electrolysis as in the case of *quasi in-situ* XPS is worth considering for a follow-up study. Moreover, estimation of the local pH change with *in-situ* Raman or IR spectroscopy and possible measurements of the local sulfur concentration should provide more evidence for better understanding of how the potential driven activation of the electrocatalyst enhances the $HCOO^-$ selectivity and moreover help understand why electrocatalysts with similar CO_2ER activity (`electrolyte sulfidated` Cu foam *vs.* $Cu_{1.8}S$/Cu foam after electrolyte replacement) at –0.9 V, show different surface sulfur fractions and concentrations of the sulfur species in the electrolyte.

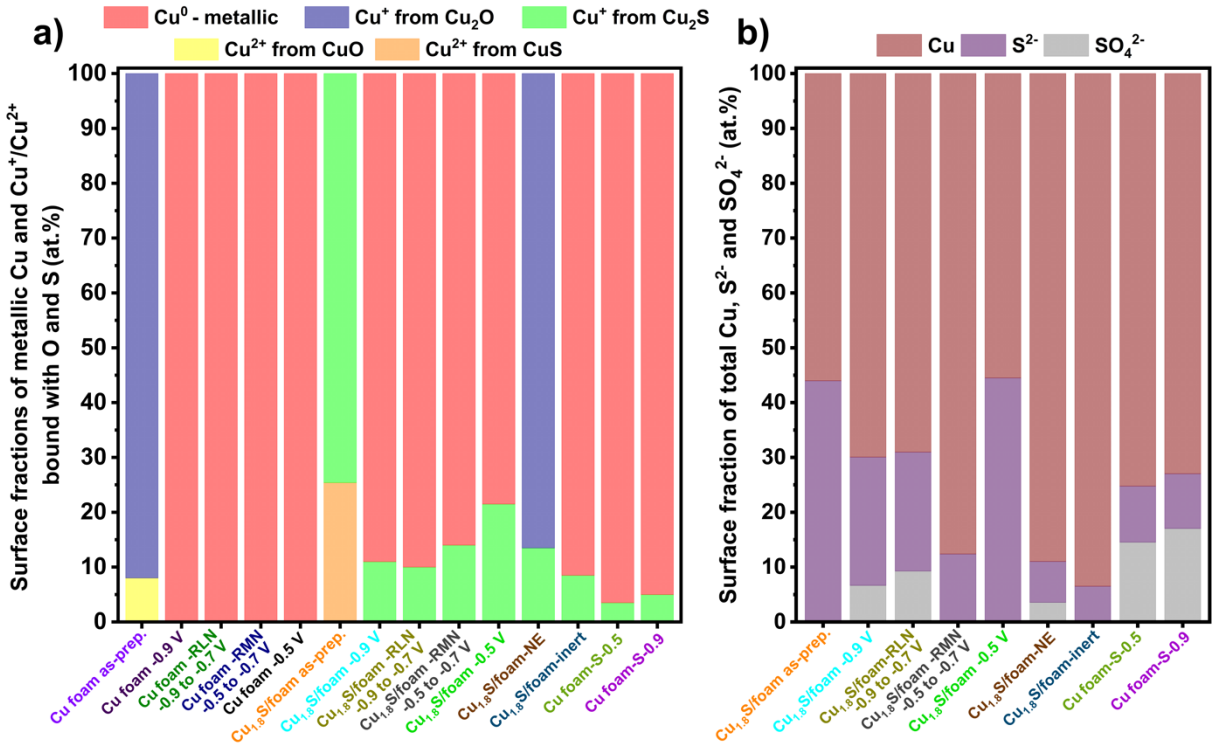

Figure 7. Quantification of Cu surface species **(a)** and total Cu, and S^{2-}/ SO_4^{2-} surface species **(b)** with XPS under *ex-situ* and quasi *in-situ* conditions. The quantification of the Cu surface species (oxidation states) was conducted from the Cu $L_3M_{4.5}M_{4.5}$ Auger (Figure S37), while the total surface Cu and S^{2-}/SO_4^{2-} as sulfur species were quantified from the Cu 2p and S 2p core levels spectra (Figures S35 and S38, respectively). The names of the samples are color coded to match the corresponding names in the XPS spectra in SI for better distinction and all quantification values are presented in Table S5.

CONCLUSIONS

In this study, a facile, cheap, and fast method combining DHBT electrochemical deposition of Cu foam and its subsequent chemical sulfidation using elemental sulfur saturated toluene solution was developed for preparation electrocatalyst for CO_2 conversion into $HCOO^-$. It was found that the as-prepared material resembles mixed phase composition from digenite and roxbyite with nominal stoichiometry of $Cu_{1.8}S$ and foam morphology consisting of dendrite microstructures. The thermal properties of the material were studied with *in-situ* TGA-MS and DSC. From environmental point of view, the sulfur/toluene solution can be reused for the synthesis purpose after adjusting the sulfur concentration to maintain saturation level which contributes to minimizing the amount of required solvent. The results from the electrocatalytic activity typically showed that on sulfidated Cu foam the CO_2 converts almost exclusively to $HCOO^-$ and simultaneously the HER is suppressed in comparison to the pristine Cu foam where various CO_2ER products and higher H_2 faradaic efficiency can be observed. However, it was found that the $HCOO^-$ *vs*. H_2 selectivity on the sulfidated Cu foam ($Cu_{1.8}S$/Cu foam) is dependent on the ramping direction of the applied potential. Thus, higher $HCOO^-$ and accordingly lower H_2 selectivity is observed at –0.7 V when the potential is ramped from –0.9 to –0.7 V (RLN) compared to the ramping from –0.5 to –0.9 V (RMN). It appears that at –0.9 V the material undergoes activation which affects the electrocatalytic activity at –0.7 V. Seeking for answers why such a phenomenon is observed, the evolution of H_2S was studied *in-situ* during the electrolysis, while the Cu-S composition/chemical nature and sulfur concentration were examined post-electrolysis. Under negative electrochemical bias, the $Cu_{1.8}S$ undergoes reduction thus morphological transformation from dendrite composed into sponge like foam and H_2S evolution are observed from SEM and *in-situ* EC-MS, respectively. The H_2S evolution duration is dependent from the direction of ramping the applied potential. Namely, when the potential is ramped from –0.9 to –0.7 V the H_2S evolution is shorter in comparison when the ramping is conducted from –0.5 to –0.9 V. In the first case, even though the $Cu_{1.8}S$ reduction onset potential is estimated at around –0.47 V, a prolonged H_2S evolution duration occurs most probably caused by local pH increase that disturbs the $H_2S/HS^-/S^{2-}$ equilibrium favoring increase of the S^{2-} species under alkaline local electrolyte environment near the electrode surface. On the other hand, when the potential is ramped from –0.5 to –0.9 V, H_2S evolves ~2 times longer extending to the next ramping step at –0.6 V most probably because both potentials of –0.5 and –0.6 V are not much higher than the onset potential for reduction of the material. Regardless of the potential ramping direction no H_2S evolution occurs and moreover the bulk sulfur fraction in the material from EDX resemble very similar sulfur content at –0.7 V where the aforementioned difference in $HCOO^-$ and H_2 selectivity is observed. Various control experiments such as sample air or inert atmosphere exposure, electrolyte replacement, *in-situ*

sulfidation of Cu foam in electrolyte where $Cu_{1.8}S$/Cu foam was reduced, and analysis of the electrolyte sulfur concentration with ICP-OES were conducted to investigate whether the electrolyte present sulfur has any effect on the activation of the electrocatalyst. The results showed that the $HCOO^-$ selectivity can be further enhanced reaching up to 75% FE at –0.9 V when the electrolyte is replaced and Cu foam is `electrolyte sulfidated`, yet without significant change at –0.7 V. The post-electrolysis quantification of the electrolyte sulfur concentration showed discrepancies in electrocatalysts with similar performance at –0.9 V ($Cu_{1.8}S$/Cu foam after air/inert exposure, electrolyte replacement and `electrolyte sulfidated` Cu foam) but no difference in the sulfur concentration was observed for $Cu_{1.8}S$/Cu foam at –0.7 V regardless of the direction of ramping the potential. On the other hand, electrolytes with similar sulfur concentrations post-electrolysis showed significantly different $HCOO^-$ selectivity at –0.9 ($Cu_{1.8}S$/Cu foam without electrolyte replacement or air/inert exposure *vs.* `electrolyte sulfidated` Cu foam). However, the *quasi in-situ* XPS results, showed that the pristine Cu foam undergoes total reduction to metallic Cu while in the presence of sulfur, besides metallic, Cu^+ species are observed in all cases regardless of the applied potential or experimental conditions such as exposure to air/inert atmosphere after the electrolysis or electrolyte replacement. This implies that the sulfur species are stabilizing the Cu^+ sites on the electrocatalyst surface thus supporting the *OCHO* mechanism proposed in the literature. Observing significantly smaller surface sulfur fraction in the case of the $Cu_{1.8}S$/Cu foam when the potential is altered in RMN (–0.5 to –0.7 V) compared to RLN (–0.9 to –0.7 V) direction suggest that there are indeed surface composition-based differences driven from the activation of the electrocatalyst at –0.9 V. Therefore, higher $HCOO^-$ selectivity and accordingly suppression of the HER are observed. Nevertheless, the sulfur species besides the expected S^{2-}, additionally resemble SO_4^{2-} . They are generated in the cases when potential of –0.9 V is applied thus higher current density is achieved which could indicate that near the electrode surface the environment such as local pH thus the concentration of sulfur species might be different than in the bulk electrolyte, unfortunately not observable from the ICP-OES. Moreover, the electrolyte replacement/air/inert exposure driven enhancement of $HCOO^-$ the selectivity on $Cu_{1.8}S$/Cu foam at –0.9 V and thus achieving similar selectivity for the `electrolyte sulfidated` Cu foam (in which previously $Cu_{1.8}S$/Cu foam was reduced) even though both surface fraction and electrolyte concentration of sulfur are significantly different could be another insight into the near electrode surface local environment effects on the electrocatalytic performance. Thus, further study of the local near electrode surface under *in-situ* conditions is worth considering for better understanding of the effects.

Acknowledgements

The authors acknowledge Max Rieckert, René Gunder, Christian Höhn, Claudia Leistner, Mahboubeh Maleki and Ursula Michalczik for experimental support. This work was funded by the Helmholtz Association's Initiative and Networking Fund via the Helmholtz Young Investigators Group award (VH-NG-1225). Instrumentation provided by the Helmholtz Energy Materials Foundry (HEMF) laboratories was used in this study. Additional financial support came from the European Union project FlowPhotoChem Grant Agreement No. 862453).

Conflicts of interest statement. The authors declare that they have no conflict of interest.

REFERENCES

1. Wu, J.; Huang, Y.; Ye, W.; Li, Y., CO_2 Reduction: From the Electrochemical to Photochemical Approach. *Advanced Science* **2017,** *4* (11), 1700194. https://doi.org/10.1002/advs.201700194
2. Ritchie, H.; Roser, M., Energy: Fossil Fuels. *Our World in Data* **2020**. https://ourworldindata.org/fossil-fuels#citation
3. Nitopi, S.; Bertheussen, E.; Scott, S. B.; Liu, X.; Engstfeld, A. K.; Horch, S.; Seger, B.; Stephens, I. E. L.; Chan, K.; Hahn, C.; Nørskov, J. K.; Jaramillo, T. F.; Chorkendorff, I., Progress and Perspectives of Electrochemical CO_2 Reduction on Copper in Aqueous Electrolyte. *Chemical Reviews* **2019,** *119* (12), 7610-7672. https://doi.org/10.1021/acs.chemrev.8b00705
4. De Luna, P.; Hahn, C.; Higgins, D.; Jaffer, S. A.; Jaramillo, T. F.; Sargent, E. H., What Would it Take for Renewably Powered Electrosynthesis to Displace Petrochemical Processes? *Science* **2019,** *364* (6438), eaav3506. http://science.sciencemag.org/content/364/6438/eaav3506.abstract
5. Jouny, M.; Luc, W.; Jiao, F., General Techno-Economic Analysis of CO_2 Electrolysis Systems. *Ind. Eng. Chem. Res.* **2018,** *57* (6), 2165-2177. https://doi.org/10.1021/acs.iecr.7b03514
6. Kortlever, R.; Shen, J.; Schouten, K. J. P.; Calle-Vallejo, F.; Koper, M. T. M., Catalysts and Reaction Pathways for the Electrochemical Reduction of Carbon Dioxide. *J. Phys. Chem. Lett.* **2015,** *6* (20), 4073-4082. https://doi.org/10.1021/acs.jpclett.5b01559
7. Bagger, A.; Ju, W.; Varela, A. S.; Strasser, P.; Rossmeisl, J., Electrochemical CO_2 Reduction: A Classification Problem. *ChemPhysChem* **2017,** *18* (22), 3266-3273. https://doi.org/10.1002/cphc.201700736
8. Greenblatt, J. B.; Miller, D. J.; Ager, J. W.; Houle, F. A.; Sharp, I. D., The Technical and Energetic Challenges of Separating (Photo)Electrochemical Carbon Dioxide Reduction Products. *Joule* **2018,** *2* (3), 381-420. https://doi.org/10.1016/j.joule.2018.01.014
9. Hietala, J.; Vuori, A.; Johnsson, P.; Pollari, I.; Reutemann, W.; Kieczka, H., Formic Acid. In *Ullmann's Encyclopedia of Industrial Chemistry*, Wiley-VCH Verlag GmbH & Co. KGaA: 2016; pp 1-22. https://doi.org/10.1002/14356007.a12_013.pub3
10. Lan, L.; Yang, W.; Li, J.; Zhang, L.; Fu, Q.; Liao, Q., Membrane-less Direct Formate Fuel Cell Using an Fe–N-Doped Bamboo Internode as the Binder-Free and Monolithic Air-Breathing Cathode. *ACS Applied Materials & Interfaces* **2020,** *12* (24), 27095-27103. https://doi.org/10.1021/acsami.0c04277
11. Yang, Z.; Oropeza, F. E.; Zhang, K. H. L., P-block metal-based (Sn, In, Bi, Pb) electrocatalysts for selective reduction of CO_2 to formate. *APL Materials* **2020,** *8* (6), 060901. https://doi.org/10.1063/5.0004194
12. Moore, C. E.; Gyenge, E. L., Tuning the Composition of Electrodeposited Bimetallic Tin–Lead Catalysts for Enhanced Activity and Durability in Carbon Dioxide Electroreduction to Formate. *ChemSusChem* **2017,** *10* (17), 3512-3519. https://doi.org/10.1002/cssc.201700761
13. Rahaman, M.; Kiran, K.; Zelocualtecatl Montiel, I.; Dutta, A.; Broekmann, P., Suppression of the Hydrogen Evolution Reaction Is the Key: Selective Electrosynthesis of Formate from CO_2 over Porous $In_{55}Cu_{45}$ Catalysts. *ACS Applied Materials & Interfaces* **2021,** *13* (30), 35677-35688. https://doi.org/10.1021/acsami.1c07829
14. Gálvez-Vázquez, M. d. J.; Moreno-García, P.; Guo, H.; Hou, Y.; Dutta, A.; Waldvogel, S. R.; Broekmann, P., Leaded Bronze Alloy as a Catalyst for the Electroreduction of CO_2. *ChemElectroChem* **2019,** *6* (8), 2324-2330. https://doi.org/10.1002/celc.201900537
15. Ren, M.; Zheng, H.; Lei, J.; Zhang, J.; Wang, X.; Yakobson, B. I.; Yao, Y.; Tour, J. M., CO_2 to Formic Acid Using Cu–Sn on Laser-Induced Graphene. *ACS Applied Materials & Interfaces* **2020,** *12* (37), 41223-41229. https://doi.org/10.1021/acsami.0c08964
16. Chen, C.; Pang, Y.; Zhang, F.; Zhong, J.; Zhang, B.; Cheng, Z., Sharp Cu@Sn nanocones on Cu foam for highly selective and efficient electrochemical reduction of CO_2 to formate. *Journal of Materials Chemistry A* **2018,** *6* (40), 19621-19630. http://dx.doi.org/10.1039/C8TA06826G

17. Chen, Y.; Chen, K.; Fu, J.; Yamaguchi, A.; Li, H.; Pan, H.; Hu, J.; Miyauchi, M.; Liu, M., Recent Advances in the Utilization of Copper Sulfide Compounds for Electrochemical CO_2 Reduction. *Nano Materials Science* **2020,** *2* (3), 235-247. https://doi.org/10.1016/j.nanoms.2019.10.006
18. Hori, Y. i., Electrochemical CO_2 Reduction on Metal Electrodes. In *Modern Aspects of Electrochemistry*, Springer: 2008; pp 89-189.
19. Poliakoff, M.; Licence, P.; George, M. W., UN Sustainable Development Goals: How Can Sustainable/Green Chemistry Contribute? By Doing Things Differently. *Curr. Opin. Green Sustain. Chem.* **2018,** *13*, 146-149. https://doi.org/10.1016/j.cogsc.2018.04.011
20. Luc, W.; Ko, B. H.; Kattel, S.; Li, S.; Su, D.; Chen, J. G.; Jiao, F., SO_2-Induced Selectivity Change in CO_2 Electroreduction. *Journal of the American Chemical Society* **2019,** *141* (25), 9902-9909. https://doi.org/10.1021/jacs.9b03215
21. Lim, J. W.; Dong, W. J.; Park, J. Y.; Hong, D. M.; Lee, J.-L., Spontaneously Formed CuS_x Catalysts for Selective and Stable Electrochemical Reduction of Industrial CO_2 Gas to Formate. *ACS Applied Materials & Interfaces* **2020,** *12* (20), 22891-22900. https://doi.org/10.1021/acsami.0c03606
22. Pan, Z.; Wang, K.; Ye, K.; Wang, Y.; Su, H.-Y.; Hu, B.; Xiao, J.; Yu, T.; Wang, Y.; Song, S., Intermediate Adsorption States Switch to Selectively Catalyze Electrochemical CO_2 Reduction. *ACS Catalysis* **2020,** *10* (6), 3871-3880. https://doi.org/10.1021/acscatal.9b05115
23. Liu, D.; Liu, Y.; Li, M., Understanding How Atomic Sulfur Controls the Selectivity of the Electroreduction of CO_2 to Formic Acid on Metallic Cu Surfaces. *The Journal of Physical Chemistry C* **2020,** *124* (11), 6145-6153. https://doi.org/10.1021/acs.jpcc.9b11830
24. Wang, S.; Kou, T.; Varley, J. B.; Akhade, S. A.; Weitzner, S. E.; Baker, S. E.; Duoss, E. B.; Li, Y., Cu_2O/CuS Nanocomposites Show Excellent Selectivity and Stability for Formate Generation via Electrochemical Reduction of Carbon Dioxide. *ACS Materials Letters* **2021,** *3* (1), 100-109. https://doi.org/10.1021/acsmaterialslett.0c00520
25. Dou, T.; Qin, Y.; Zhang, F.; Lei, X., CuS Nanosheet Arrays for Electrochemical CO_2 Reduction with Surface Reconstruction and the Effect on Selective Formation of Formate. *ACS Applied Energy Materials* **2021,** *4* (5), 4376-4384. https://doi.org/10.1021/acsaem.0c03190
26. Dong, W. J.; Navid, I. A.; Xiao, Y.; Lim, J. W.; Lee, J.-L.; Mi, Z., CuS-Decorated GaN Nanowires on Silicon Photocathodes for Converting CO_2 Mixture Gas to HCOOH. *Journal of the American Chemical Society* **2021,** *143* (27), 10099-10107. https://doi.org/10.1021/jacs.1c02139
27. Phillips, K. R.; Katayama, Y.; Hwang, J.; Shao-Horn, Y., Sulfide-Derived Copper for Electrochemical Conversion of CO_2 to Formic Acid. *The Journal of Physical Chemistry Letters* **2018,** *9* (15), 4407-4412. https://doi.org/10.1021/acs.jpclett.8b01601
28. Deng, Y.; Huang, Y.; Ren, D.; Handoko, A. D.; Seh, Z. W.; Hirunsit, P.; Yeo, B. S., On the Role of Sulfur for the Selective Electrochemical Reduction of CO_2 to Formate on CuS_x Catalysts. *ACS Applied Materials & Interfaces* **2018,** *10* (34), 28572-28581. https://doi.org/10.1021/acsami.8b08428
29. Coughlan, C.; Ibáñez, M.; Dobrozhan, O.; Singh, A.; Cabot, A.; Ryan, K. M., Compound Copper Chalcogenide Nanocrystals. *Chemical Reviews* **2017,** *117* (9), 5865-6109. https://doi.org/10.1021/acs.chemrev.6b00376
30. Zhou, X.; Soldat, A. C.; Lind, C., Phase selective synthesis of copper sulfides by non-hydrolytic sol–gel methods. *RSC Advances* **2014,** *4* (2), 717-726. http://dx.doi.org/10.1039/C3RA45053H
31. Quintana-Ramirez, P. V.; Arenas-Arrocena, M. C.; Santos-Cruz, J.; Vega-González, M.; Martínez-Alvarez, O.; Castaño-Meneses, V. M.; Acosta-Torres, L. S.; de la Fuente-Hernández, J., Growth Evolution and Phase Transition from Chalcocite to Digenite in Nanocrystalline Copper Sulfide: Morphological, Optical and Electrical properties. *Beilstein Journal of Nanotechnology* **2014,** *5*, 1542-1552. https://doi.org/10.3762/bjnano.5.166
32. Abouserie, A.; El-Nagar, G. A.; Heyne, B.; Günter, C.; Schilde, U.; Mayer, M. T.; Stojkovikj, S.; Roth, C.; Taubert, A., Facile Synthesis of Hierarchical CuS and CuCo2S4 Structures from an Ionic Liquid Precursor for Electrocatalysis Applications. *ACS Applied Materials & Interfaces* **2020,** *12* (47), 52560-52570. https://doi.org/10.1021/acsami.0c13927
33. Roy, P.; Srivastava, S. K., Nanostructured Copper Sulfides: Synthesis, Properties and Applications. *CrystEngComm* **2015,** *17* (41), 7801-7815. http://dx.doi.org/10.1039/C5CE01304F

34. Shamraiz, U.; Hussain, R. A.; Badshah, A., Fabrication and Applications of Copper Sulfide (CuS) Nanostructures. *Journal of Solid State Chemistry* **2016,** *238*, 25-40. https://doi.org/10.1016/j.jssc.2016.02.046
35. Balischewski, C.; Choi, H.-S.; Behrens, K.; Beqiraj, A.; Körzdörfer, T.; Geßner, A.; Wedel, A.; Taubert, A., Metal Sulfide Nanoparticle Synthesis with Ionic Liquids – State of the Art and Future Perspectives. *ChemistryOpen* **2021,** *10* (2), 272-295. https://doi.org/10.1002/open.202000357
36. Sun, S.; Li, P.; Liang, S.; Yang, Z., Diversified Copper Sulfide ($Cu_{2-x}S$) Micro-/Nanostructures: A Comprehensive Review on Synthesis, Modifications and Applications. *Nanoscale* **2017,** *9* (32), 11357-11404. http://dx.doi.org/10.1039/C7NR03828C
37. Najdoski, M.; Oklevski, S.; Demiri, S.; Stojkovikj, S., Cuprous Sulfide Deposition Method for Visualization of Latent Fingermarks on Unfired Cartridge Cases. *Journal of the Chinese Chemical Society* **2020,** *67* (8), 1415-1422. https://doi.org/10.1002/jccs.202000034
38. Huang, Y.; Deng, Y.; Handoko, A. D.; Goh, G. K. L.; Yeo, B. S., Rational Design of Sulfur-Doped Copper Catalysts for the Selective Electroreduction of Carbon Dioxide to Formate. *ChemSusChem* **2018,** *11* (1), 320-326. https://doi.org/10.1002/cssc.201701314
39. van Oversteeg, C. H. M.; Tapia Rosales, M.; Helfferich, K. H.; Ghiasi, M.; Meeldijk, J. D.; Firet, N. J.; Ngene, P.; de Mello Donegá, C.; de Jongh, P. E., Copper Sulfide Derived Nanoparticles Supported on Carbon for the Electrochemical Reduction of Carbon Dioxide. *Catalysis Today* **2021,** *377*, 157-165. https://doi.org/10.1016/j.cattod.2020.09.020
40. Scholten, F.; Sinev, I.; Bernal, M.; Roldan Cuenya, B., Plasma-Modified Dendritic Cu Catalyst for CO_2 Electroreduction. *ACS Catalysis* **2019,** *9* (6), 5496-5502. https://doi.org/10.1021/acscatal.9b00483
41. Pardo Pérez, L. C.; Arndt, A.; Stojkovikj, S.; Ahmet, I. Y.; Arens, J. T.; Dattila, F.; Wendt, R.; Guilherme Buzanich, A.; Radtke, M.; Davies, V.; Höflich, K.; Köhnen, E.; Tockhorn, P.; Golnak, R.; Xiao, J.; Schuck, G.; Wollgarten, M.; López, N.; Mayer, M. T., Determining Structure-Activity Relationships in Oxide Derived Cu-Sn Catalysts During CO_2 Electroreduction Using X-Ray Spectroscopy. *Advanced Energy Materials* **2021,** *12* (5), 2103328. https://doi.org/10.1002/aenm.202103328
42. Vesztergom, S.; Dutta, A.; Rahaman, M.; Kiran, K.; Zelocualtecatl Montiel, I.; Broekmann, P., Hydrogen Bubble Templated Metal Foams as Efficient Catalysts of CO_2 Electroreduction. *ChemCatChem* **2020,** *13* (4), 1039-1058. https://doi.org/10.1002/cctc.202001145
43. Stojkovikj, S.; El-Nagar, G. A.; Firschke, F.; Pardo Pérez, L. C.; Choubrac, L.; Najdoski, M.; Mayer, M. T., Electrocatalyst Derived from Waste Cu–Sn Bronze for CO_2 Conversion into CO. *ACS Appl. Mater. Interfaces* **2021,** *13* (32), 38161-38169. https://doi.org/10.1021/acsami.1c05015
44. Will, G.; Hinze, E.; Abdelrahman, A. R. M., Crystal Structure Analysis and Refinement of Digenite, $Cu_{1.8}S$, in the Temperature Range 20 to 500 °C Under Controlled Sulfur Partial Pressure. *European Journal of Mineralogy* **2002,** *14* (3), 591-598. https://doi.org/10.1127/0935-1221/2002/0014-0591
45. Ge, Z.-H.; Zhang, B.-P.; Chen, Y.-X.; Yu, Z.-X.; Liu, Y.; Li, J.-F., Synthesis and Transport Property of $Cu_{1.8}S$ as a Promising Thermoelectric Compound. *Chemical Communications* **2011,** *47* (47), 12697-12699. http://dx.doi.org/10.1039/C1CC16368J
46. Liu, L.; Zhou, B.; Deng, L.; Fu, W.; Zhang, J.; Wu, M.; Zhang, W.; Zou, B.; Zhong, H., Thermal Annealing Effects of Plasmonic $Cu_{1.8}S$ Nanocrystal Films and Their Photovoltaic Properties. *The Journal of Physical Chemistry C* **2014,** *118* (46), 26964-26972. https://doi.org/10.1021/jp506043n
47. Selivanov, E. N.; Gulyaeva, R. I.; Vershinin, A. D., Thermal Expansion and Phase Transformations of Copper Sulfides. *Inorganic Materials* **2007,** *43* (6), 573-578. https://doi.org/10.1134/S0020168507060027
48. Kahsay, A. W.; Ibrahim, K. B.; Tsai, M.-C.; Birhanu, M. K.; Chala, S. A.; Su, W.-N.; Hwang, B.-J., Selective and Low Overpotential Electrochemical CO_2 Reduction to Formate on CuS Decorated CuO Heterostructure. *Catalysis Letters* **2019,** *149* (3), 860-869. https://doi.org/10.1007/s10562-019-02657-2
49. Fiscebeck, K., Der Anlauf des Kupfers in Schwefeldampf. *Zeitschrift für anorganische und allgemeine Chemie* **1926,** *154* (1), 261-266. https://doi.org/10.1002/zaac.19261540125

50. Llopis, J.; Gamboa, J. M.; Arizmendi, L., Sulphuration of Copper and Silver with Benzene Solutions of Sulphur. *Electrochimica Acta* **1961,** *4* (2), 294-305. https://doi.org/10.1016/0013-4686(61)80024-8
51. Urbanová, M.; Kupčík, J.; Bezdička, P.; Šubrt, J.; Pola, J., Room-Temperature Sulfidation of Copper Nanoparticles with Sulfur Yielding Covellite Nanoparticles. *Comptes Rendus Chimie* **2012,** *15* (6), 511-516. https://doi.org/10.1016/j.crci.2012.03.014
52. Steudel, R.; Holz, B., Detection of Reactive Sulfur Molecules (S_6, S_7, S_9, S_∞) in Commercial Sulfur, in Sulfur Minerals, and in Sulfur Melts Slowly Cooled to 20 °C [1]. *Zeitschrift für Naturforschung B* **1988,** *43* (5), 581-589. https://doi.org/10.1515/znb-1988-0516
53. Dutta, A.; Rahaman, M.; Luedi, N. C.; Mohos, M.; Broekmann, P., Morphology Matters: Tuning the Product Distribution of CO_2 Electroreduction on Oxide-Derived Cu Foam Catalysts. *ACS Catalysis* **2016,** *6* (6), 3804-3814. https://doi.org/10.1021/acscatal.6b00770
54. Miloshova, M.; Baltes, D.; Bychkov, E., New Chalcogenide Glass Chemical Sensors for S^{2-} and Dissolved H_2S Monitoring. *Water Science and Technology* **2003,** *47* (2), 135-140. https://doi.org/10.2166/wst.2003.0104
55. Shinagawa, T.; Larrazábal, G. O.; Martín, A. J.; Krumeich, F.; Pérez-Ramírez, J., Sulfur-Modified Copper Catalysts for the Electrochemical Reduction of Carbon Dioxide to Formate. *ACS Catalysis* **2018,** *8* (2), 837-844. https://doi.org/10.1021/acscatal.7b03161
56. Celante, V. G.; Freitas, M. B. J. G., Electrodeposition of Copper from Spent Li-Ion Batteries by Electrochemical Quartz Crystal Microbalance and Impedance Spectroscopy Techniques. *Journal of Applied Electrochemistry* **2010,** *40* (2), 233-239. https://doi.org/10.1007/s10800-009-9996-x
57. Chu, Y. S.; Robinson, I. K.; Gewirth, A. A., Comparison of Aqueous and Native Oxide Formation on Cu(111). *The Journal of Chemical Physics* **1999,** *110* (12), 5952-5959. https://doi.org/10.1063/1.478495
58. Huang, H.-H., The Eh-pH Diagram and Its Advances. *Metals* **2016,** *6* (1), 23. https://doi.org/10.3390/met6010023
59. Yang, K.; Kas, R.; Smith, W. A., In Situ Infrared Spectroscopy Reveals Persistent Alkalinity near Electrode Surfaces during CO_2 Electroreduction. *Journal of the American Chemical Society* **2019,** *141* (40), 15891-15900. https://doi.org/10.1021/jacs.9b07000
60. Biesinger, M. C., Advanced Analysis of Copper X-ray Photoelectron Spectra. *Surface and Interface Analysis* **2017,** *49* (13), 1325-1334. https://doi.org/10.1002/sia.6239
61. NIST X-ray Photoelectron Spectroscopy Database. https://srdata.nist.gov/xps/Default.aspx (accessed 21.04.2022).
62. Awe, S. A.; Sundkvist, J.-E.; Sandström, Å., Formation of Sulphur Oxyanions and their Influence on Antimony Electrowinning from Sulphide Electrolytes. *Minerals Engineering* **2013,** *53*, 39-47. https://doi.org/10.1016/j.mineng.2013.07.001

Supporting information

Facile method for synthesis of Cu_xS catalysts and study of various effects on the selectivity for electrochemical conversion of CO_2 into formate

Sasho Stojkovikj,[a,b] Gumaa A. El-Nagar,[a] Siddharth Gupta,[a,b] Metodija Najdoski,[c] Violeta Koleva, [d] Theocharis Tzanoudakis,[a,b] Frederik Firschke,[a] Peter Bogdanoff, [e] and Matthew T. Mayer*[a]

[a]Helmholtz Young Investigator Group: Electrochemical Conversion, Helmholtz-Zentrum Berlin für Materialen und Energie GmbH, Hahn-Meitner-Platz 1, D-14109, Berlin, Germany.
[b]Institut für Chemie und Biochemie, Freie Universität Berlin, Arnimallee 22, D-14195 Berlin, Germany.
[c]Institute of Chemistry, Faculty of Natural Sciences and Mathematics, Ss. Cyril and Methodius University Skopje, Arhimedova 5, 1000 Skopje, Republic of North Macedonia.
[d]Institute of General and Inorganic Chemistry, Bulgarian Academy of Sciences, G. Bonchev Str. Bldg. 11, 1113 Sofia, Bulgaria.
[e]Institute of Solar Fuels, Helmholtz-Zentrum Berlin für Materialen und Energie GmbH, Hahn-Meitner-Platz 1, D-14109, Berlin, Germany.

*Corresponding author: Dr. Matthew T. Mayer (m.mayer@helmholtz-berlin.de)

Table of contents

S1. Experimental section 4
S1.1. Materials and chemicals 4
S1.2. Preparation of Cu foam on Cu mesh via DHBT electrodeposition 4
S1.3. Sulfidation of the Cu foam 5
S1.4. Material characterization methods 6
S1.5. Electrochemical measurements and post analysis 7
S2. Figures and schemes 14
References 56

List of figures

Figure S1 14
Figure S2 15
Figure S3 16
Figure S4 17
Figure S5 18
Figure S6 20
Figure S7 21
Figure S8 22
Figure S9 23
Figure S10 24
Figure S11 25
Figure 12 26
Figure S13 28
Figure S14 29
Figure S15 30
Figure S16 31
Figure S17 32
Figure S18 33
Figure S19 34
Figure S20 35
Figure S21 36
Figure S22 37
Figure S23 38
Figure S24 39
Figure S25 40
Figure S26 41
Figure S27 42
Figure S28 43
Figure S29 44
Figure S30 45
Figure S31 46
Figure S32 47
Figure S33 48
Figure S34 50
Figure S35 51
Figure S36 52
Figure S37 53
Figure S38 54

List of tables

Table S1.....9
Table S2.....19
Table S3.....27
Table S4.....49
Table S5.....55

S1. Experimental section

S1.1. Materials and chemicals

The following chemicals and materials were used for this study: Cu mesh (Cu gauze, 100 mesh woven, thickness: 0.11 mm, Alfa Aesar); Sulfur (S_8, powder, 99,98% trace metals purity, Sigma-Aldrich); Toluene ($C_6H_5CH_3$, for pesticide residue analysis purity acc. FDA, Honeywell, Riedel-de Haën); Carbon disulfide (CS_2, anal. grade purity, Merck); Ultrapure water (18.20 MΩ·cm, purified using the Thermo Scientific Barnstead GenPurexCAD Plus system, fed with de-ionized water); 2-Propanol ($CH_3CH(OH)CH_3$, ≥99.8 wt.% ACS grade purity, Merck); 1-Propanol ($CH_3CH_2CH_2OH$, ≥99.9 wt.% for HPLC, Sigma-Aldrich); Ethanol (C_2H_5OH, Reag. Ph. Eur. ≥99.8 wt.%, Sigma-Aldrich); Methanol (CH_3OH, Reag. Ph. Eur. For HPLC/UHPLC, VWR Chemicals); $CuSO_4 \cdot 5H_2O$ (99.995 wt.%, trace metals basis purity, Sigma-Aldrich); H_2O_2 - aqueous solution (30 wt.%, for analysis, EMSURE® purity, Merck); HCl (37 wt.%, ACS, EMSURE® purity, Merck); H_2SO_4 (≥98 wt.% EMSURE® purity, Merck); $KHCO_3$ (99.7-100.5 wt.% ACS, EMSURE® purity, Merck); KOH pellets 85 wt.% min (99.98 wt.% metals basis, Thermo Scientific); Cu foil (0.5 mm – thickness, 99.98 wt.% trace metals purity, Sigma-Aldrich); NaCl (>99.5 wt.% puriss, p.a., Sigma-Aldrich); ICP-OES sulfur standard (1000 mg·dm^{-3} S in water, Honeywell, Fluka™); Double-side sticky carbon tape (8 mm x 0.15 mm, Plano); PTFE tape (12 mm x 0.1 mm, Würth); Laboratory film (Parafilm® ``M``, Pechiney Plastic Packaging); CO_2 (4.8 grade purity, Linde Gas) and Mixed gas standard (containing H_2, CO, CH_4, C_2H_4 and C_2H_6 in bulk N_2, Linde). All chemicals were used as received, without further purification.

S1.2. Preparation of Cu foam on Cu mesh via DHBT electrodeposition

The preparation of the Cu foam on Cu mesh was conducted via dynamic H_2 bubbling templated (DHBT) electrodeposition method. More information about the DHBT methods and their application for CO_2ER metallic foams catalyst synthesis can be found elsewhere.[1-3] The cathode was prepared from Cu mesh (thickness: 0.11 mm) that was cut in polygonal shape samples as presented in Figure S1. The samples were cleaned via subsequent ultra-sonication (Ultrasonicator: Emmi-H30 EMAG Technologies) in 2-propanol, 2 mol·dm^{-3} HCl (prepared by diluting 37 wt.% HCl in ultrapure water), ultrapure water and again in 2-propanol for duration of 15 min for each step. Each sample was masked using PTFE tape thus fixing 2 mm x 2 mm (total 0.08 cm^2 – both sides included) geometric surface area and an electrical contact was provided using ``crocodile`` clamps (Figure S1). The anode was prepared from two pieces of 0.5 mm thick Cu foil that was pre-cut in dimensions of 2.2 x 5 cm. One half of each Cu foil piece was masked with PTFE tape on both sides thus fixing the total geometric surface area to 22 cm^2 (including both Cu foil pieces). The Cu foil pieces were connected together using ``crocodile`` clamps and electrical wire and mounted parallel to each other with a distance of 2 cm (see Figure S1). The cathode (Cu mesh) was placed between the parallel Cu foil pieces (anode) in order to maintain uniform electric field and homogeneous electrodeposition. The whole setup was placed in a 70 cm^3 beaker filled with 40 cm^3 of

electrodeposition solution that contains 0.2 mol·dm^{-3} $CuSO_4$ and 1.5 mol·dm^{-3} H_2SO_4 (prepared by dissolving $CuSO_4 \cdot 5H_2O$ and 98 wt.% H_2SO_4 in ultrapure water). The Cu foam DHBT electrodeposition was performed galvanostatically in a two-electrode mode via passing current of –400 mA (geometric current density of –5 A·cm^{-2}) for 9.5 seconds, and at room temperature. The open circuit voltage prior to applying the bias was between –5 and –10 mV for each sample. Each batch of electrodeposition solution was used for preparation of 10 Cu foam samples. The bias was applied using a Biologic SP-240 potentiostat with a voltage booster. The charge density and the voltage during the 9.5 seconds electrodeposition duration reached value of 50 C·cm^{-2}. (Figure S1). During the electrodeposition process, the Cu from the anode's surface is being oxidized into Cu^{2+}, according to Equation S1, and the oxygen evolution reaction in such conditions is negligible since no O_2 bubbles were visually observed.

Anodic reaction:

$$Cu(s) \rightarrow Cu^{2+}(aq) + 2e^- \quad (1)$$

Simultaneously, the cathodic processes involve generation of H_2 bubbles (Equation S2) which serve as a template for deposition of Cu with 3-dimensional porous foam morphology via reduction of the Cu^{2+} cations (Equation S3).[2, 3] The voltage in the two-electrode system starts at around –2.4, when the bias is applied and suddenly drops to –2.6 V in the first 0.5 s (Figure S1). This voltage behavior could be associated with the formation of Cu seeds on the surface of the mesh substrate, after which both Cu^{2+} reduction and H_2 evolution occur at comparable reaction rates.[2]

Cathodic reactions:

$$2H^+(aq) + 2e^- \rightarrow H_2(g) \quad (2)$$

$$Cu^{2+}(aq) + 2e^- \rightarrow Cu(s) \quad (3)$$

The as-prepared Cu foam was thoroughly washed with ultrapure water, 2-propanol and left to dry in air. Average pore size and foam thickness of ~30 and ~40 μm, respectively, were obtained under the aforementioned DHBT electrodeposition conditions (see Figures S3, S4a and Table S2), which is for expectation in comparison with the pore sizes of Cu foams deposited on Cu wafers and foils under similar DHBT conditions.[1, 3]

S1.3. Sulfidation of the Cu foam

The procedure for sulfidation of the Cu foam starts by preparation of saturated stock solution of elemental sulfur in toluene. 1.2 g S_8, 100 cm^3 toluene and a stirring bar were added in 100 cm^3 Erlenmeyer flask. The flask was sealed to avoid evaporation and left to stir on electromagnetic stirrer (IKA®RH-KT/C) for 1 h at room temperature. In the next step, 10 cm^3 of 1.5 mol·dm^{-3} H_2SO_4 (prepared via diluting 98 wt.% H_2SO_4 in ultrapure water); ultrapure water, 2-propanol; toluene; S_8 in toluene solution, were placed separately in 10 cm^3 beakers. Stirring bars were added in each beaker and they

were placed on electromagnetic stirrer, keeping all reagents at room temperature. Additionally, 10 cm^3 of toluene and 2-propanol were added separately in two more 10 cm^3 beakers, later used for terminating the sulfidation reaction and washing of the sulfidated samples, respectively. The as-prepared Cu foam samples were dipped one-by-one in the following sequence of reagents under constant stirring, as depicted in Figure S2:

- 10 s in 1.5 $mol \cdot dm^{-3}$ H_2SO_4 (for etching the Cu foam surface of oxide species);
- 1 s in ultrapure water (for washing the H_2SO_4 residuals);
- 10 s in propane-2-ol (for washing the water residuals);
- 10 s in toluene (for washing the propane-2-ol residuals);
- 3 s in the S_8/toluene solution (sulfidation reaction);
- 20 s in fresh toluene (for terminating the reaction and washing the sulfur residuals);
- 20 s in fresh propane-2-ol (for washing the toluene residuals).

The reagents were replaced with fresh ones for each batch of max. 10 samples. The as prepared sulfidated Cu foam samples (abbreviated as $Cu_{1.8}S$/Cu foam/Cu mesh or simply $Cu_{1.8}S$/Cu foam further in the text) were left to dry in air. The sulfidation of Cu foam is observable as instantaneous color change from typical copper brown reddish into petroleum dark bluish color (Figure S2). After the sulfidation procedure, the solution can be reused for the same purpose as soon as the concentration of sulfur in toluene is kept steady state at a saturation level (~1.5 wt.%)[4] at room temperature, i.e. more sulfur should be occasionally added until small amount of insoluble particles are still observable after 1 h of constant stirring. As a control experiment, the same synthesis procedures were repeated using non-etched Cu foam, and no reaction was observed upon immersing them in sulfur dissolved in both organic solvents. This behavior is attributable to the presence of oxide, hydroxide and/or carbonate layers on the metallic Cu surface that block its exposure to the reactive sulfur species in the organic matrix.

The synthesis of the $Cu_{1.8}S$ electrocatalysts was originally planned and performed via immersing Cu foil and/or Cu mesh substrates in sulfur dissolved either in toluene or in CS_2. However, due to mechanical instability i.e., delamination of the sulfide coating over the Cu foil and mesh (see SEM images in Figures S8 and S9), the synthesis was modified by electrodeposition of porous Cu foam on Cu mesh substrates which ware subsequently sulfidated in sulfur dissolved in toluene, as described above in this paragraph. Regarding the utilization of CS_2 as sulfur solvent, it was abandoned due to its toxicity.

S1.4. Material characterization methods

The chemical composition, elemental distribution, surface morphology, foam- thickness and foam pore sizes, crystal- and electronic structures (oxidation states of the elements) were characterized using scanning electron microscopy (SEM), energy dispersive x-ray (EDX) spectroscopy, focused ion beam (FIB) ablation/cross section SEM, grazing incidence x-ray diffraction (GI-XRD), x-ray photoelectron

spectroscopy (XPS) and inductively coupled plasma-optical emission spectroscopy (ICP-OES). The experimental details for these characterization methods regarding the instruments can be found in section S1.3. in the SI of our previous study.[3] In the case of the XPS and ICP-OES, there are some differences in the measurement setups and sample preparation compared to our previous study, thus additional details regarding the experimental procedures are provided in the next section (S1.5.) Additionally, XRD for powder samples, thermogravimetric analysis coupled with mass spectrometry (TGA-MS) and differential scanning calorimetry (DSC) were included in this study. Regarding the additional characterization methods, the x-ray powder diffraction (XRPD) analysis was conducted using Rigaku Ultima IV x-ray diffractometer with CuKα radiation. The diffractograms were measured from 5 to 90° (2Θ) with 5°·min^{-1} and step of 0.02°, for the copper sulfide samples that were scrapped-off as powder from sulfidated Cu foil with sulfur dissolved in toluene and CS_2. The XRPD raw data was processed using the PowderCell software for phase qualitative and quantitative characterization. The TGA-MS and DSC analysis were conducted on identical powder samples that were scrapped-off from sulfidated Cu foil (as for the powder XRD). The TGA analysis was performed with the system Netzsch TG209 F1 Iris with mass resolution 0.1 µg. The samples were placed in alumina crucible and heated from 30 to 1000 °C in N_2 atmosphere with heating rate of 10 K·min^{-1}. The thermal decomposition products were analyzed with Netzsch QMS 403C Aeolos mass spectrometer set to mass vs charge ratios (*m/z*) of 32, 64, 96, 160, 192, 224, 238, 256, 258 and 262, that correspond to various possible sulfur species. The DSC analysis was conducted with the Netzsch STA 449F5 system using identical samples, crucibles, heating range and rate as for the TGA-MS but in Ar atmosphere.

All measured data using the techniques described in this section and in the next one was converted into graphics and exported into high-resolution images using the OriginPro 2019b software or placed in tables.

S1.5. Electrochemical measurements and post analysis

***Activation of the Nafion cation exchange membrane*:** The Nafion N-115 cation exchange membrane (Thickness - 0.125 mm, Alfa Aesar) was cut into circular shapes with diameter of 3.5 cm. In the next step, the membranes were treated for 1 h at 80 °C in the following sequence of reagents: 3 wt.% H_2O_2 (freshly prepared via diluting 30 wt.% H_2O_2 in ultrapure water), ultrapure water, 2 mol·dm^{-3} H_2SO_4 (prepared via diluting 98 wt.% H_2SO_4 in ultrapure water), and ultrapure water again. Each reagent was placed in a separate beaker. After the activation process, the membranes were stored in ultrapure water at room temperature prior to usage. This method was adopted from Bagger et al.[5] and modified as described in this procedure.

***Electrocatalytic activity measurements and product analysis*:** The CO_2 conversion electrocatalytic activity measurements were performed in a two-compartment H-type gas-flow cell, custom made of glass, where the cathodic and the anodic compartment (both filled with 0.1 mol·dm^{-3} $KHCO_3$) are separated with a previously activated and thoroughly washed (with ultrapure water) Nafion N-115 cation

exchange membrane. The cathodic compartment was continuously purged with 20 $cm^3 \cdot min^{-1}$ CO_2 bubbled into the electrolyte via a fine glass frit. More information regarding the electrochemical setup and the gaseous and non-volatile products quantification methodology using gas and liquid chromatography are presented in section S1.5. and Scheme S2 in the SI of our previous publication.[3] $Cu_{1.8}S$/Cu foam and pristine Cu foam were used as working electrodes. The geometric surface area of the working electrode was masked first with Parafilm® then with PTFE tape, thus exposing 0.08 cm^2 geometric surface area. The electrochemical bias for the electrocatalytic activity measurements was provided using Biologic SP-200 potentiostat. A normal junction Ag/AgCl electrode filled with 3 $mol \cdot dm^{-3}$ KCl(aq) with potential of $E°$ = +0.210 V vs the standard hydrogen electrode at 25 °C (PalmSens), was used as a reference and a custom-made Pt (99.99 wt.%, metals basis purity, 0.1 mm thick, Alfa Aesar) mesh as a counter electrode. All applied potentials under which the electrocatalytic activities were measured are converted and presented with respect to the reversible hydrogen electrode (RHE), according to Equation S4, considering that the pH of the CO_2 saturated 0.1 $mol \cdot dm^{-3}$ $KHCO_3$(aq) is 6.8. The measured current at each applied potential was normalized to the geometric surface area of the working electrode and expressed as geometric current density (j). The automatic correction of the IR drop was set to 85% in the Biologic EC-Lab software.

$$E \text{ vs RHE (V)} = E \text{ vs Ag/AgCl (V)} + E°_{Ag/AgCl} \text{ (V)} + 0.059 \cdot pH \quad (4)$$

Each sample was pre-reduced with three linear sweep voltammetry scans (3 x LSV) from 0 V to the required potential under which the electrocatalytic activity was measured (scan rate: 150 $mV \cdot min^{-1}$). The open circuit potential prior to the LSV reduction was around between –125 and –130 mV. All samples were examined potentiostatically using chronoamperometry (CA) in the potential range from –0.9 to –0.5 V and from –0.5 to –0.9 vs RHE via ramping the potential from more negative to less negative direction (RLN) and vice versa (RMN). The ramping of the potential was conducted in one direction per sample and at least 3 sample replicates were used for each material and from different batches. For control experiments, the $Cu_{1.8}S$/Cu foam and pristine Cu foam electrocatalysts were subjected under various conditions like air and inert atmosphere exposure, electrolyte change and *in-situ* sulfidation of the Cu foam with the sulfur species generated from reduction of the $Cu_{1.8}S$/Cu foam. The examined electrocatalysts under various conditions are presented in the following list of samples with their abbreviations used in the graphs and tables:

Table S1. List of samples and their abbreviations that were studied under various electrochemical conditions.

- **$Cu_{1.8}S$/Cu foam-RLN:** $Cu_{1.8}S$/Cu foam measured via ramping the applied potential in a less negative direction (RLN from –0.9 to –0.5 V). The electrocatalyst was pre reduced with 3 x LSV scans from 0 to –0.9 V.
- **$Cu_{1.8}S$/Cu foam-RMN:** $Cu_{1.8}S$/Cu foam measured via ramping the applied potential in a more negative direction (RMN from –0.5 to –0.9 V). The electrocatalyst was pre reduced with 3 x LSV scans from 0 to –0.5 V.
- **Cu foam-RLN:** Cu foam measured via ramping the applied potential in a less negative direction (RLN from –0.9 to –0.5 V). The electrocatalyst was pre reduced with 3 x LSV scans from 0 to –0.9 V.
- **Cu foam-RMN:** Cu foam measured via ramping the applied potential in a more negative direction (RMN from –0.5 to –0.9 V). The electrocatalyst was pre reduced with 3 x LSV scans from 0 to –0.5 V.
- **$Cu_{1.8}S$/Cu foam-NE:** $Cu_{1.8}S$/Cu foam remeasured after changing the electrolyte. Previously measured via ramping the applied potential in a less negative direction (RLN from –0.9 to –0.5 V). The electrocatalyst was pre reduced with 3 x LSV scans from 0 to –0.9 V.
- **$Cu_{1.8}S$/Cu foam-NE2:** $Cu_{1.8}S$/Cu foam remeasured $Cu_{1.8}S$/Cu foam-NE after changing the electrolyte second time.
- **$Cu_{1.8}S$/Cu foam-air:** $Cu_{1.8}S$/Cu foam measured and exposed in air for 1 h, then remeasured in the same electrolyte.
- **$Cu_{1.8}S$/Cu foam-inert:** $Cu_{1.8}S$/Cu foam measured and exposed in inert N_2 atmosphere for 1 h, then remeasured in the same electrolyte.
- **Cu foam-S-0.9 or ``electrolyte sulfidated`` Cu foam:** Cu foam that was immediately placed and measured in electrolyte in which previously $Cu_{1.8}S$/Cu foam sample was subjected to one linear sweep voltammetry (1 x LSV) scan from 0 to –0.9 V.
- **Cu foam-S-0.7 or ``electrolyte sulfidated`` Cu foam:** Cu foam that was immediately placed and measured in electrolyte in which previously $Cu_{1.8}S$/Cu foam sample was subjected to one linear sweep voltammetry (1 x LSV) scan from 0 to –0.7 V.
- **Cu foam-S-0.5 or ``electrolyte sulfidated`` Cu foam:** Cu foam that was immediately placed and measured in electrolyte in which previously $Cu_{1.8}S$/Cu foam sample was subjected to one linear sweep voltammetry (1 x LSV) scan from 0 to –0.5 V.
- **Cu foam-S-NP:** Cu foam that was immediately placed, kept 1 h without CO_2 purge, after that the CO_2 was purged for 20 min and the sample was measured in electrolyte in which previously $Cu_{1.8}S$/Cu foam sample was subjected to one linear sweep voltammetry (1 x LSV) scan from 0 to –0.9 V.
- **Cu foam-S-P1h:** Cu foam that was immediately placed, kept 1 h under CO_2 purging and then measured in electrolyte in which previously $Cu_{1.8}S$/Cu foam sample was subjected to one linear sweep voltammetry (1 x LSV) scan from 0 to –0.9 V.
- **Cu foam-S-P1h-NE:** Cu foam that was immediately placed, kept 1 h under CO_2 purging and measured in electrolyte in which previously $Cu_{1.8}S$/Cu foam sample was subjected to one linear sweep voltammetry (1 x LSV) scan from 0 to –0.9 V and then remeasured after exchanging the electrolyte.
- **$Cu_{1.8}S$/Cu foam-0.7D:** $Cu_{1.8}S$/Cu foam measured at –0.7 V for 1 h after being subjected to 3 scans of LSV from 0 to –0.7 V.

- **$Cu_{1.8}S$/Cu foam-0.7NE:** $Cu_{1.8}S$/Cu foam remeasured after exchanging the electrolyte for $Cu_{1.8}S$/Cu foam-0.7D.
- **$Cu_{1.8}S$/Cu foam-LSVx1:** $Cu_{1.8}S$/Cu foam measured at –0.7 V for 1 h after being subjected to 1 scan of LSV from 0 to –0.9 V.
- **$Cu_{1.8}S$/Cu foam-LSVx2:** $Cu_{1.8}S$/Cu foam measured $Cu_{1.8}S$/Cu foam measured at –0.7 V for 1 h after being subjected to 2 scans of LSV from 0 to –0.9 V.
- **$Cu_{1.8}S$/Cu foam-LSVx3:** $Cu_{1.8}S$/Cu foam measured $Cu_{1.8}S$/Cu foam measured at –0.7 V for 1 h after being subjected to 3 scans of LSV from 0 to –0.9 V.

The CO_2ER/HER products were quantified using dual channel (on-line gas and headspace channels) gas chromatograph (GC) model Trace 1310 (Thermo Scientific), dual column system using He as carrier gas and equipped with helium pulse discharge detector (PDD, VICI Valco Instruments Co. Inc.) for detection of H_2, CO, CH_4, O_2, N_2 and flame ionization detector (FID, VICI Valco Instruments Co. Inc.) for detection of C_2-hydrocarbons (C_2H_2, C_2H_4 and C_2H_6). The gaseous products concentrations were measured every 10, 15, 30 or 60 minutes from 1 to 24 hours (stability measurements) at each applied potential. The faradaic efficiency (FE) for the gaseous products at each potential was calculated using Equation S5, where z_i is the number of electrons (z_i = 2e$^-$ for HER and CO_2ER to CO, and 8 and 12e$^-$ for CO_2ER to CH_4 and C_2H_4, respectively),[6] F is the Faraday constant (96485.33 C·mol^{-1}), x_i is molar fraction of the component i, Q_m is the molar flow of CO_2 (bulk gas) and I_{total} is the average total current in the time interval of 5 min prior to the GC injection point.

$$FE_{Gaseous\ product}(\%) = z_i \cdot F \cdot x_i \cdot Q_m \cdot 100\% / I_{total} \quad (5)$$

For detailed description of the GC gas-channel operating conditions and the procedure for quantification of the gaseous products, see section S1.5. and Scheme S2 in the SI of our previous publication.[3]

Regarding the quantification of volatile CO_2ER compounds such as alcohols, aldehydes, ketones etc., the gas chromatograph headspace channel (GC-HS) TriPlus RSH unit of the Trace 1310 instrument was used. 5 cm^3 aliquot of the catholyte was sampled after terminating each potentiostatic electrolysis sequence. The samples were placed in 20 cm^3 GC-HS vials (Thermo Scientific) in which 2.5 g of pre-dried NaCl (at least 48 h at 120 °C) were added. The vials were immediately sealed and placed on the sample holder. The GC-HS unit is equipped with robotic arm that was programed to transfer each vial into an incubator/agitator unit (pre-heated at 80 °C) where the samples were stirred for 10 mins. A volume of 1 cm^3 was withdrawn from the headspace vapor phase in each vial via the sampling syringe (pre-heated at 90 °C) controlled by the robotic arm and injected into the GC-HS inlet unit (pre-heated at 150 °C). The separation of the volatile CO_2ER products occurred in a 60 m long capillary column (ID 32 mm, Restek). The temperature of the column oven was kept at 35 °C until 6 min retention time, then ramped up to 120 °C reaching this temperature at 14.5 min thus kept constant until the end of the measurement (retention time of 21.5 min). The faradaic efficiency (FE) for the liquid products was calculated using Equation S6, where z is the number of electrons (z_i = 6e$^-$ for CO_2ER to CH_3OH, 12e$^-$ to C_2H_5OH and 18e$^-$ to C_3H_7OH),[6] c_i is the concentration of component i in the catholyte, F is the Faraday

constant (96485.33 $C \cdot mol^{-1}$), $V_{Catholyte}$ is the volume of electrolyte in the cathodic compartment (30 cm^3), $I_{total} \cdot t$ is the total charge consumed during the electrolysis.

$$FE_{HCOO^-}(\%) = (z_i \cdot c_i \cdot F \cdot V_{Catholyte} \cdot 100\%)/(I_{Total} \cdot t) \quad (6)$$

The quantification of the non-volatile liquid CO_2ER products ($HCOO^-$) was conducted using ultra-high-performance liquid chromatograph from Thermo Scientific (model UHPLC+ UltiMate 3000 Series, Dionex) with UV detector (UltiMate 3000, Dionex) set to wavelength of 210 nm. For description of the instrument operating parameters and sample preparation, please see section S1.5. and Scheme S2 in the SI of our previous publication.[3] The faradaic efficiency (FE) for $HCOO^-$ was also calculated using Equation S6, where $z_i = 2e^-$ for CO_2ER to $HCOO^-$.[6]

All FE and current density results are expressed as average values calculated from measurement of at least three replicate samples ± average mean absolute error from at least three replicate samples (error bars).

***In-situ mass spectrometry coupled with electrolysis (EC-MS) for tracking of H_2S evolution*:** The gaseous products (H_2S) evolved during the electrochemical reduction of the $Cu_{1.8}S$/Cu foam electrode under CO_2 electrolysis conditions was followed *in-situ* using Hi Cube mass spectrometer with PrismaPlus quadrupole detector (from Pfeiffer Vacuum). For this purpose, the gas-outlet of the cathodic compartment from the previously described electrochemical H-type cell filled with 30 cm^3 of 0.1 $mol \cdot dm^{-3}$ $KHCO_3$(aq) as a supporting electrolyte and constantly purged with CO_2, was connected with the mass spectrometer inlet. Identically as for the electrocatalytic activity measurements, the $Cu_{1.8}S$/Cu foam samples were examined potentiostatically using chronoamperometry in the potential range from –0.9 to –0.5 V and from –0.5 to –0.9 V, via ramping the applied potential from more negative to less negative direction (RLN) and vice versa (RMN). For the electrolysis product analysis, mass *vs.* charge ratios (*m/z*) of 2, 16, 28, 33 and 34 were chosen. All measurements were conducted in the secondary electron multiplier mode. The *m/z* ratio of 2 resembles H_2 that comes from the HER, *m/z* = 16 can be attributed to oxygen that is coming from residual air thus any increase of this signal over time is a good indicator for gas-leaks in the electrochemical cell. Moreover, the experiment was started when this signal dropped to continuous constant value. The *m/z* signal of 28 resembles CO which in this case comes from the bulk CO_2 that is constantly purged in the electrochemical cell since $Cu_{1.8}S$/Cu foam electrocatalyst is barely active towards CO_2 to CO conversion (see Figures 2 and S10). This signal becomes constants when the electrolyte is fully saturated with CO_2. The signals of 33 and 34 are believed to be attributed to single charged HS and H_2S species obtained via electrochemical reduction of the $Cu_{1.8}S$. To prove this, a control experiment was conducted using a bare Cu foam electrode under the same conditions via altering the applied potential in a RMN direction (–0.5 to –0.9 V), thus no change in the *m/z* signals of 32 and 64 can be observed in the mass spectra, which proves that these signals can be exclusively assigned to the evolution of H_2S.

***Inert atmosphere electrochemical experiments and transfer of the into the XPS analyzer (sometimes referred as quasi in-situ XPS)*:**[7] Besides, studying the as-synthesized Cu foam and $Cu_{1.8}S$/Cu foam in *ex-situ* mode, more knowledge about the electrocatalysts surface composition and Cu, and S oxidation states i.e., electronic structure as closely as possible related to the actual conditions (transformation of the catalysts during the CO_2 electrolysis) was gained when the electrochemical experiments were conducted in inert atmosphere to avoid reoxidation of the material due to air exposure. For this purpose, the H-type electrochemical cell (identical as for the other experiments described above) was placed in a glovebox purged with N_2 where the O_2 level (from the O_2 sensor) was constantly bellow 1 ppm,v. The measurements were conducted using $Cu_{1.8}S$/Cu foam and pristine Cu foam electrocatalysts via altering the potential in both RLN and RMN direction. The selected potentials were –0.9 and –0.7 V in the RLN and –0.5 and –0.7 V in the RMN direction, respectively. Additionally, for control experiments, the *quasi in-situ* XPS measurements were conducted on several important samples selected from the list above that were subjected under various conditions like air and inert atmosphere exposure, electrolyte replacement and *in-situ* sulfidation of the Cu foam with the sulfur species generated from reduction of the $Cu_{1.8}S$/Cu foam. After removing the electrochemical bias, the samples were washed with ultrapure water, dried, and placed in a stainless-steel transfer vessel (that was previously attached to the glovebox). The transfer vessel was evacuated, sealed, detached from the glovebox, and attached to the XPS analyzer without exposure to air. Additional information regarding the XPS instrument and measurement parameters can be found S1.3. in the SI of our previous study.[3] The Cu oxidation states corresponding to metallic Cu and O, and S bound Cu species (metallic Cu^0, Cu^+ from Cu_2O, Cu^+ from Cu_2S, Cu^{2+} from CuO, Cu^{2+} from CuS) on the electrocatalyst surface under various experimental conditions were estimated quantified from the Cu $L_3M_{4.5}M_{4.5}$ Auger spectra using the Fytik software and fitting parameters for these species reported by Biesinger.[8] For calculation of the surface sulfur species fractions, the peak areas for the Cu 2p and S 2p core levels were estimated with the Fytik software and subsequently normalized to the corresponding energy pass (10 for Cu 2p and 30 for S 2p, except for the as-prepared $Cu_{1.8}S$/Cu foam when energy pass 10 was used for recording the S 2p spectrum) according to Equation S7. Additionally, the normalized peak areas for both Cu 2p and S 2p were corrected with respect to the relative sensitivity factors (RSF, due to their different photoionization cross-section) for Cu 2p of 30.87 and S 2p of 1.65 defined by the instrument under Al x-ray source *vs.* analyzer angle of 54°, using Equation S8. Finally, the fractions for the S^{2-} and SO_4^{2-} species in at.% were calculated using Equation S9, respectively. Adventitious C 1s core level peak attributed to single C-C bond (284.8 eV) was used to correct the peak positions in all core levels spectra where it was necessary, after fitting these peaks with Lorentzian function.

$$\text{Peak area}_{\text{normalized } vs. \text{ energy pass}} = \text{Peak area/Energy pass} \quad (7)$$

$$\text{Peak area}_{\text{corrected } vs. \text{ RSF}} = \text{Peak area}_{\text{normalized } vs. \text{ energy pass}} / \text{RSF}_{\text{for specific core level}} \quad (8)$$

$$\text{Sulfur fraction}_{\text{specie}}\ (\text{at.}\%) = 100 \cdot (\text{S 2p Peak area}_{\text{corr. } vs. \text{ RSF}})_{\text{specie}} / \text{Total norm. corr. peak area for Cu 2p + S 2p for all sulfur species} \quad (9)$$

The XPS survey and Cu 2p, Cu Auger, S 2p and O 1s-core levels spectra for all examined samples are presented in Figures S35-38 and the surface species quantification results in Table S5 and Figure 7.

***Analysis of sulfur content in the electrolyte with ICP-OES*:** After the electrolysis experiments under various conditions in the H-type cell (described previously in this section), 15 cm^3 of the electrolyte, for certain electrocatalysts presented in Table S4, were immediately sampled, and placed in a 20 cm^3 volumetric flask in which 2 cm^3 of 3 $mol \cdot dm^{-3}$ KOH (freshly prepared via dissolving KOH pellets in ultrapure water) and 2 cm^3 of 30 wt.% H_2O_2(aq) were previously added. The volumetric flask was filled up to the mark with 0.1 $mol \cdot dm^{-3}$ $KHCO_3$(aq). The role of H_2O_2 is to oxidize the $S^{2-}/HS^-/H_2S$ into SO_4^{2-} species in strongly alkaline medium thus preventing evaporation of the sulfur species as H_2S(g) and causing analysis error. The series of ICP-OES sulfur standard solutions with concentrations of 200, 400, 600, 800 and 1000 $\mu g \cdot dm^{-3}$ were prepared via diluting the commercial 1000 $mg \cdot dm^{-3}$ sulfur standard solution with 0.1 $mol \cdot dm^{-3}$ $KHCO_3$(aq) in which identical concentrations of H_2O_2 and KOH are present as in the solutions with the samples. The blank solution was prepared via the same manner but without adding the commercial sulfur standard solution. The ICP-OES analysis was performed using the system iCAP 7400 Duo MFC ICP-OES Analyzer (Thermo Scientific) in axial Ar plasma mode,[3] set to characteristic sulfur wavelengths of 180.731 and 182.034 nm.

***Estimation of the relative surface roughness factor (RSRF)*:** The RSRF of Cu mesh, Cu foam, $Cu_{1.8}S$/Cu mesh and $Cu_{1.8}S$/Cu foam, pre- and post- CO_2 electrolysis, was estimated from the working electrode double layer capacitance (C_{DL}), as described in the SI of our previous publication.[3] Cyclic voltammetry (CV) scans were recorded at various scan rates - SR (5-225 $mV \cdot s^{-1}$) using the same electrochemical setup, as for the measurements of the CO_2 conversion electrocatalytic activity. The range of potentials for the CV measurements was selected from –0.13 to –0.09 V and the RSRF were calculated at –0.11 V vs Ag/AgCl (3 $mol \cdot dm^{-3}$ KCl). The results from these measurements are presented in Figure S12 and the calculated RSRF values are presented in Table S3.

S2. Figures and schemes

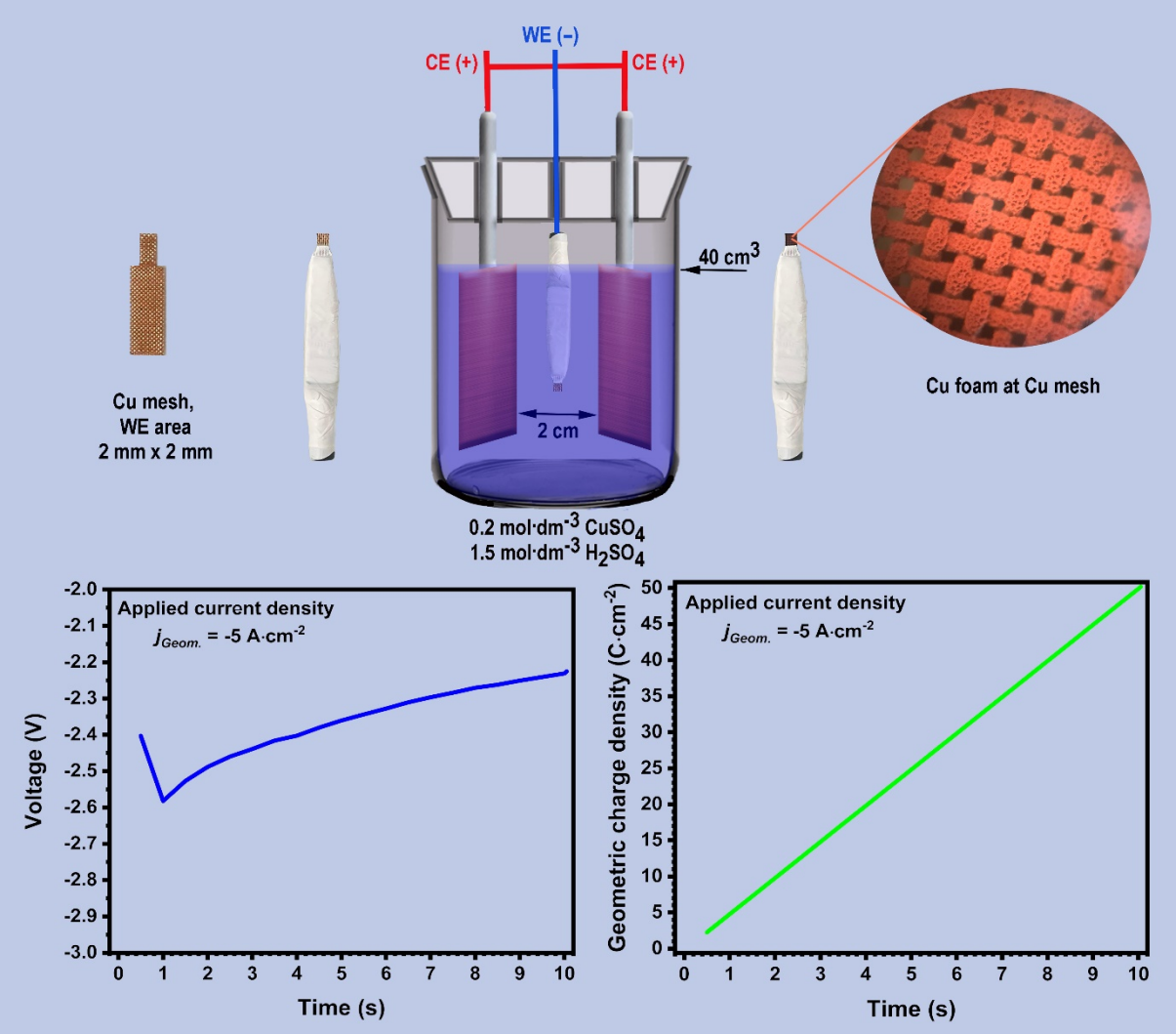

Figure S1. Schematic representation of the experimental steps for preparation of Cu foam via DHBT electrodeposition. The Cu mesh samples were first cut into rectangular shapes of 4 x 20 mm, then one side was additionally cut to resemble polygonal shape. The working electrode surface area was fixed via masking with PTFE tape thus exposing 2 x 2 mm. The DHBT electrodeposition was conducted in two-electrode setup with duration of 9.5 seconds at applied current density of –5 A·cm^{-2} under which uniform Cu foam was deposited on the mesh substrate, as showed in the optical microscopy image.

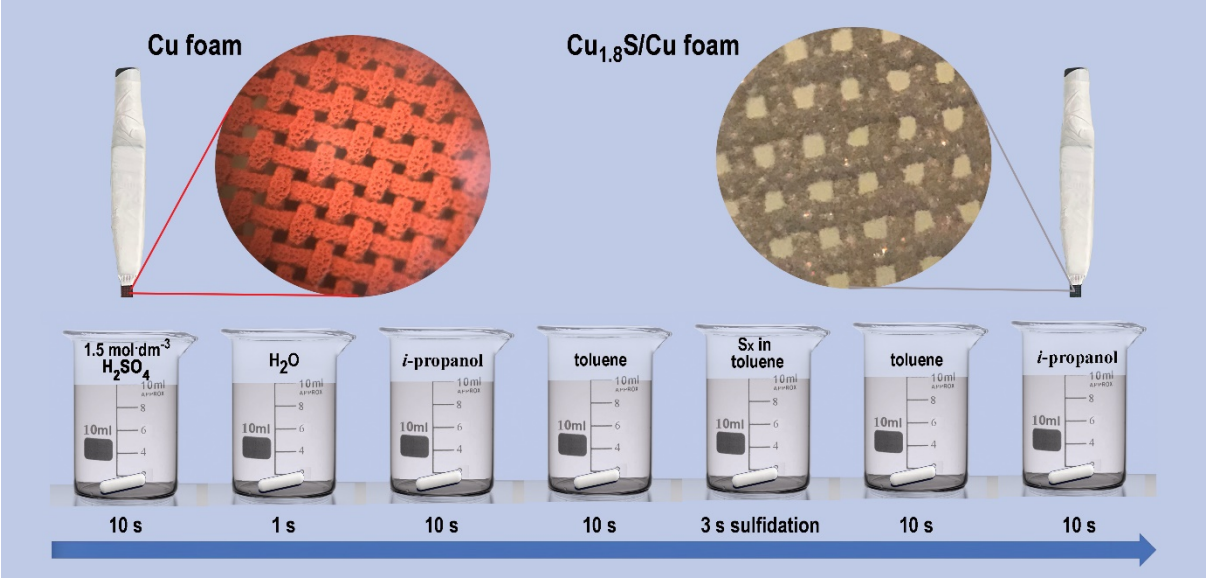

Figure S2. Schematic representation of the Cu foam sulfidation procedure. The blue arrow shows the sequence order of the subsequent treatments of the Cu foam in the corresponding reagents thus leading to uniform sulfidation (insets: optical microscopy image).

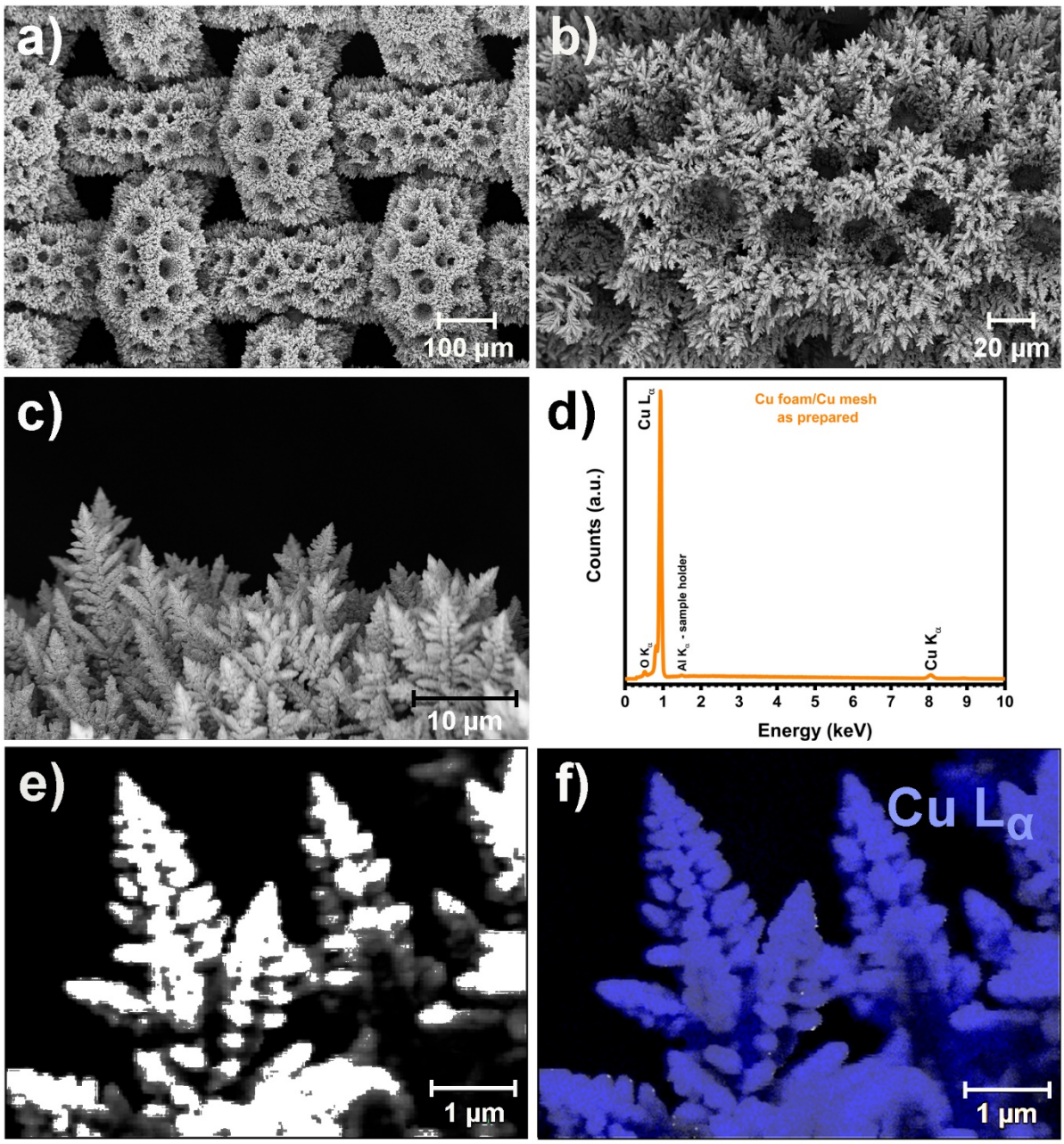

Figure S3. DHBT electrodeposited Cu foam composed of fern-plant like dendrite microstructures on Cu mesh substrate: SEM images **(a-c)**; EDX spectrum **(d)** and elemental mapping **(e, f)**.

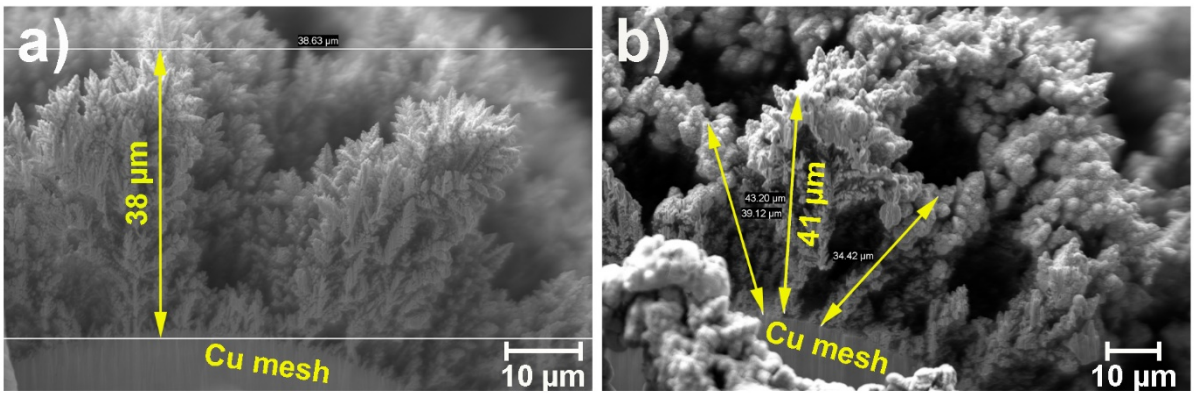

Figure S4. SEM cross-section images after FIB ablation: DHBT electrodeposited Cu foam, before **(a)** and after sulfidation – $Cu_{1.8}S$/Cu foam **(b)**. Average thickness of 38 and 41 µm for the pristine and sulfidated Cu foam, respectively.

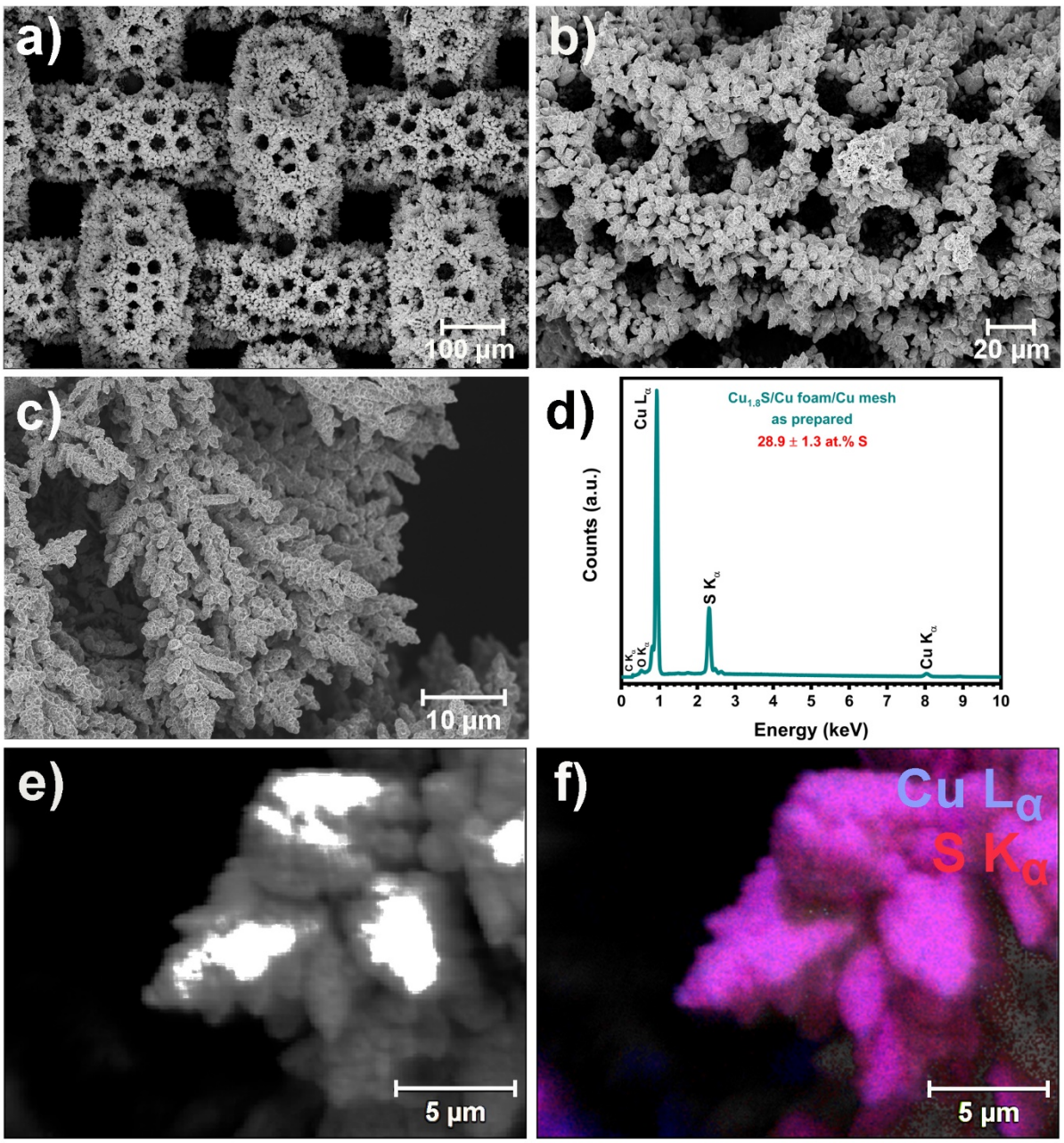

Figure S5. Sulfidated Cu foam ($Cu_{1.8}S$/Cu foam) composed of dendrite microstructures: SEM images **(a-c)**, EDX spectrum and bulk sulfur content **(d)**, and elemental mapping of Cu and S **(e, f)**.

Table S2. Average pore size (estimated from the SEM images in Figures S3 and S5) and cross-section thickness (FIB/SEM, from Figure S4) of as prepared Cu foam and sulfidated Cu foam ($Cu_{1.8}S$/Cu foam).

Sample	Average pore size (µm)	Average Foam thickness (µm)
Cu foam	30	38
$Cu_{1.8}S$/Cu foam	31	41

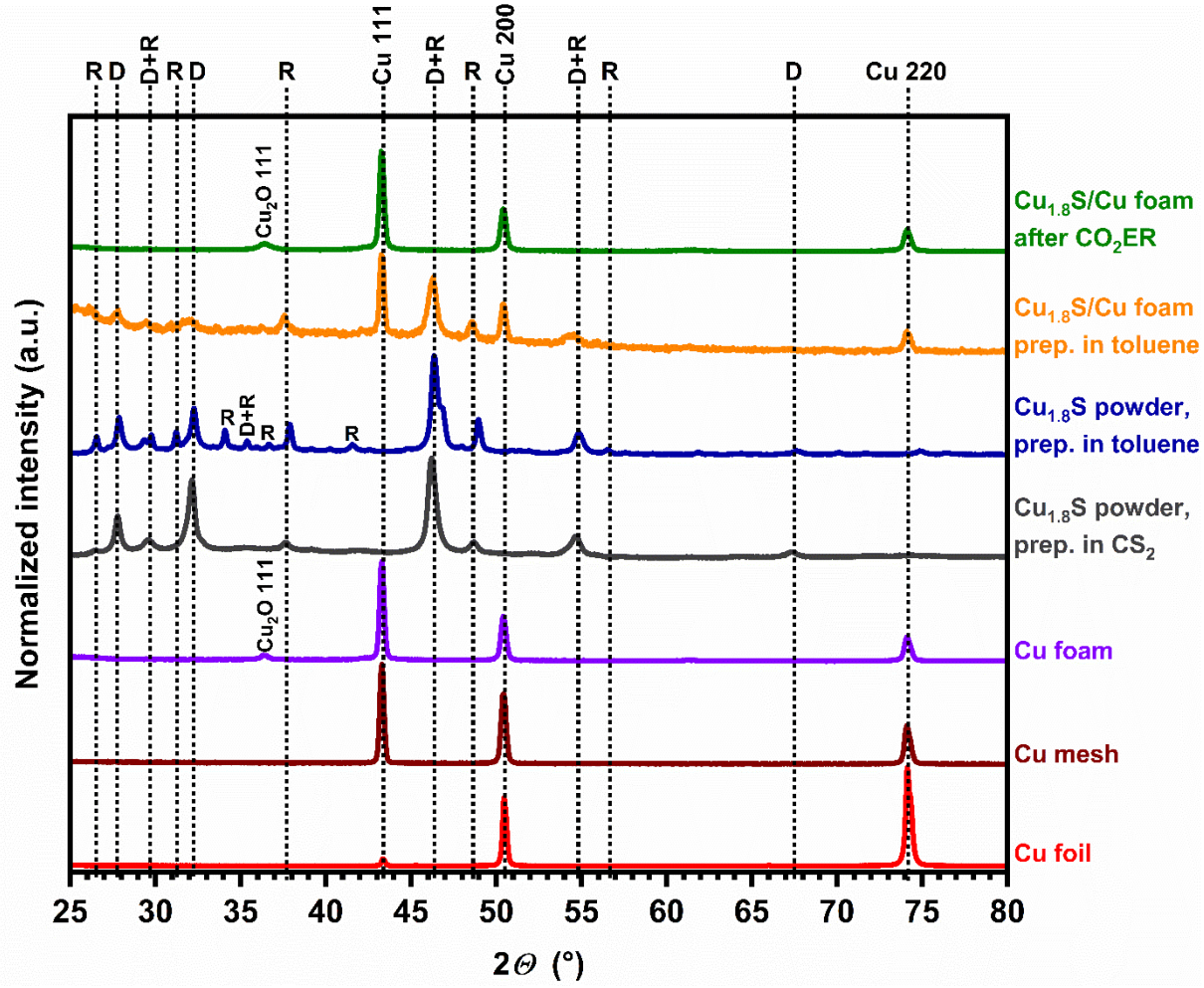

Figure S6. XRD patterns of: Cu foil, Cu mesh, Cu foam, $Cu_{1.8}S$ powder prepared via sulfidation of Cu foil in sulfur dissolved in CS_2, and toluene and $Cu_{1.8}S$/Cu foam prepared via sulfidation of Cu foam in sulfur dissolved in toluene, before and after CO_2 electrolysis (from –0.9 to –0.7 V for 1 h at each potential). D - digenite (ICDD PDF 2-023-0960) and R - roxbyite (ICDD PDF 2-023-0958) phases.

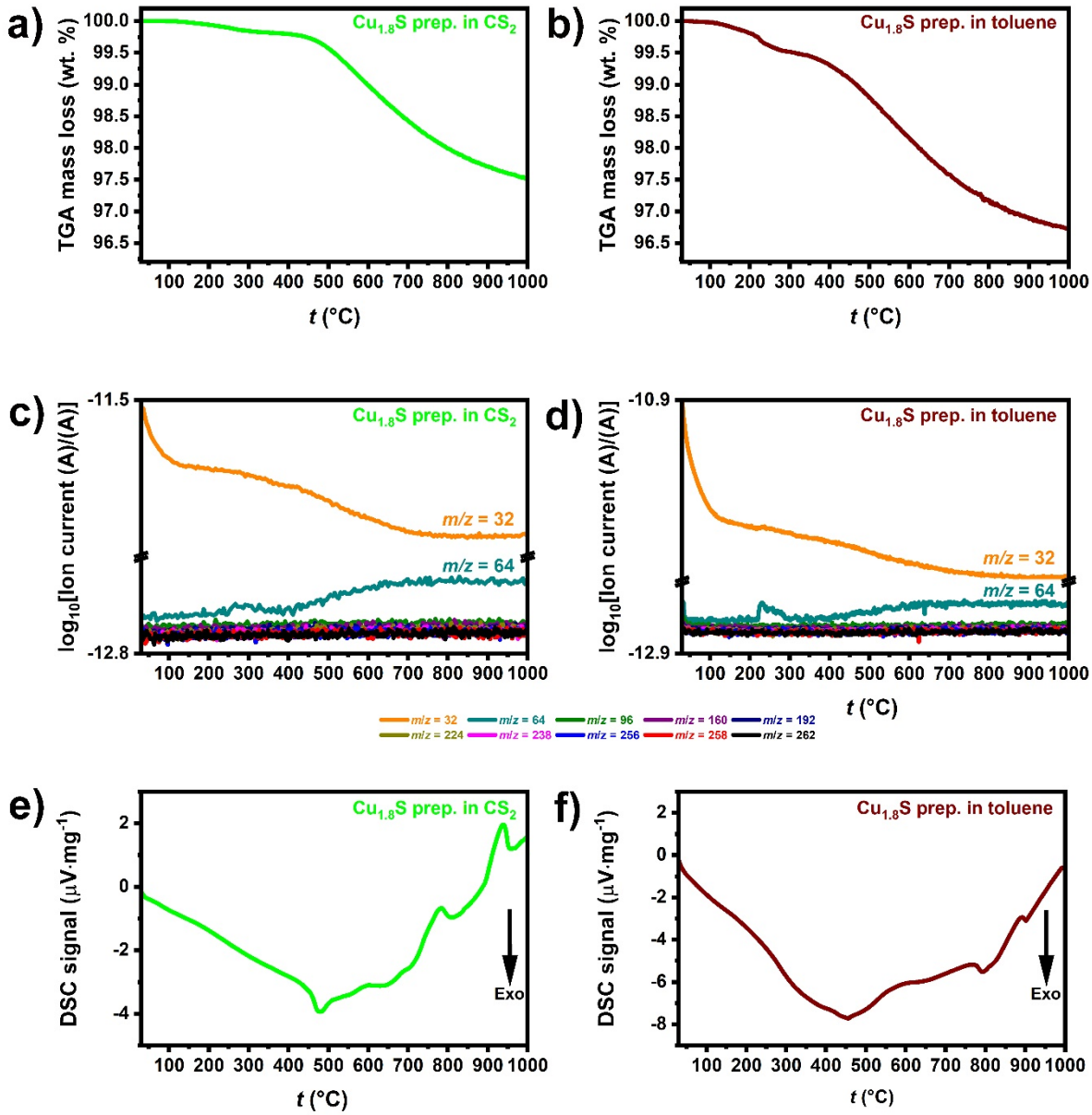

Figure S7. Thermal properties results: Thermogravimetric analysis - TGA **(a, b)** coupled with mass spectrometry – TGA-MS **(c, d)** and differential scanning calorimetry - DSC **(e, f)** plots for $Cu_{1.8}S$ powder prepared from Cu foil immersed in sulfur dissolved in CS_2 **(a, c, e)** and toluene **(b, d, f)**.

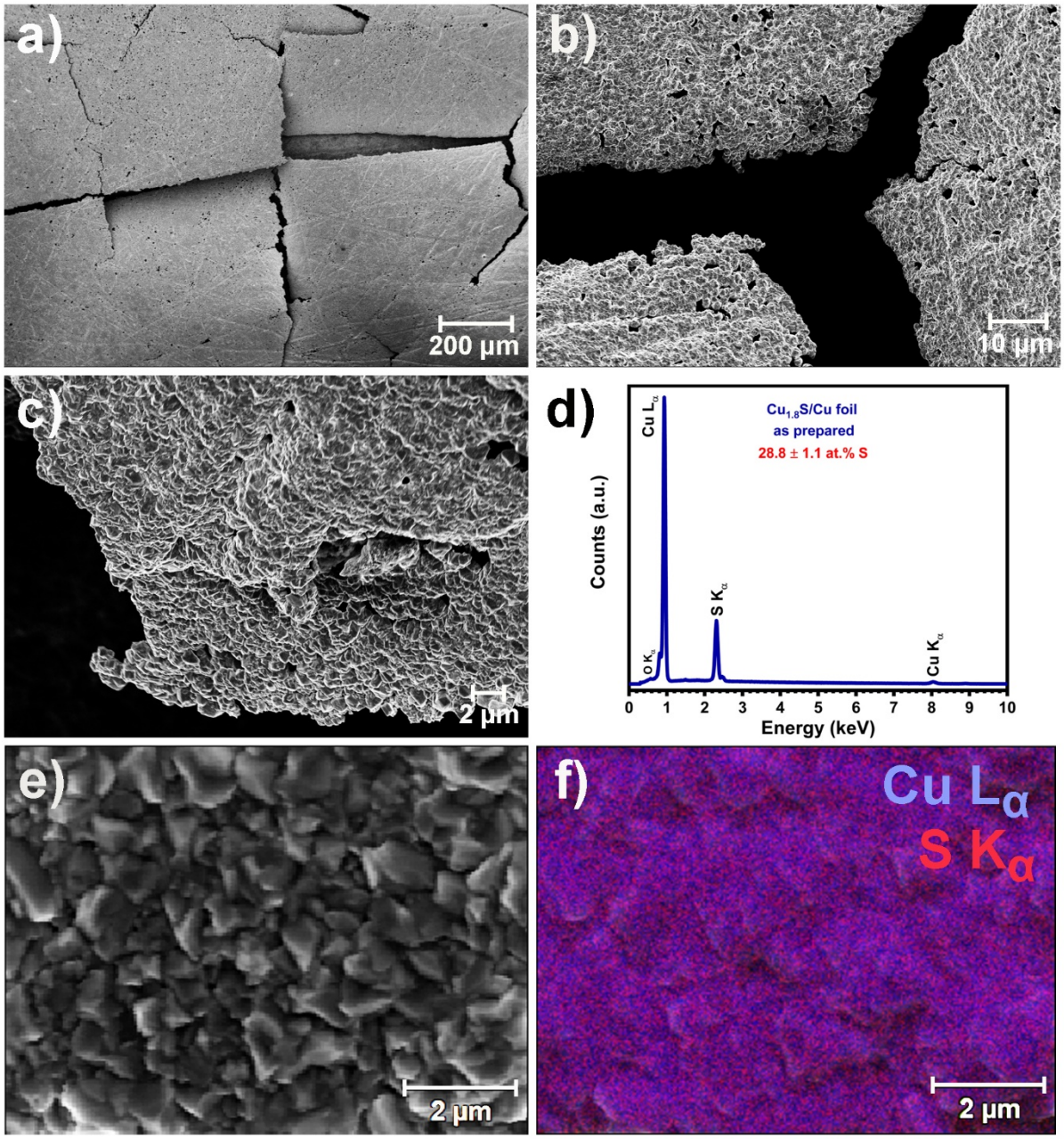

Figure S8. Sulfidated Cu foil ($Cu_{1.8}S$/Cu foil): SEM images **(a-c)**, EDX spectrum and bulk sulfur content **(d)**, and elemental mapping of Cu and S **(e, f)**. The $Cu_{1.8}S$ layer is pealing from the surface of the Cu foil.

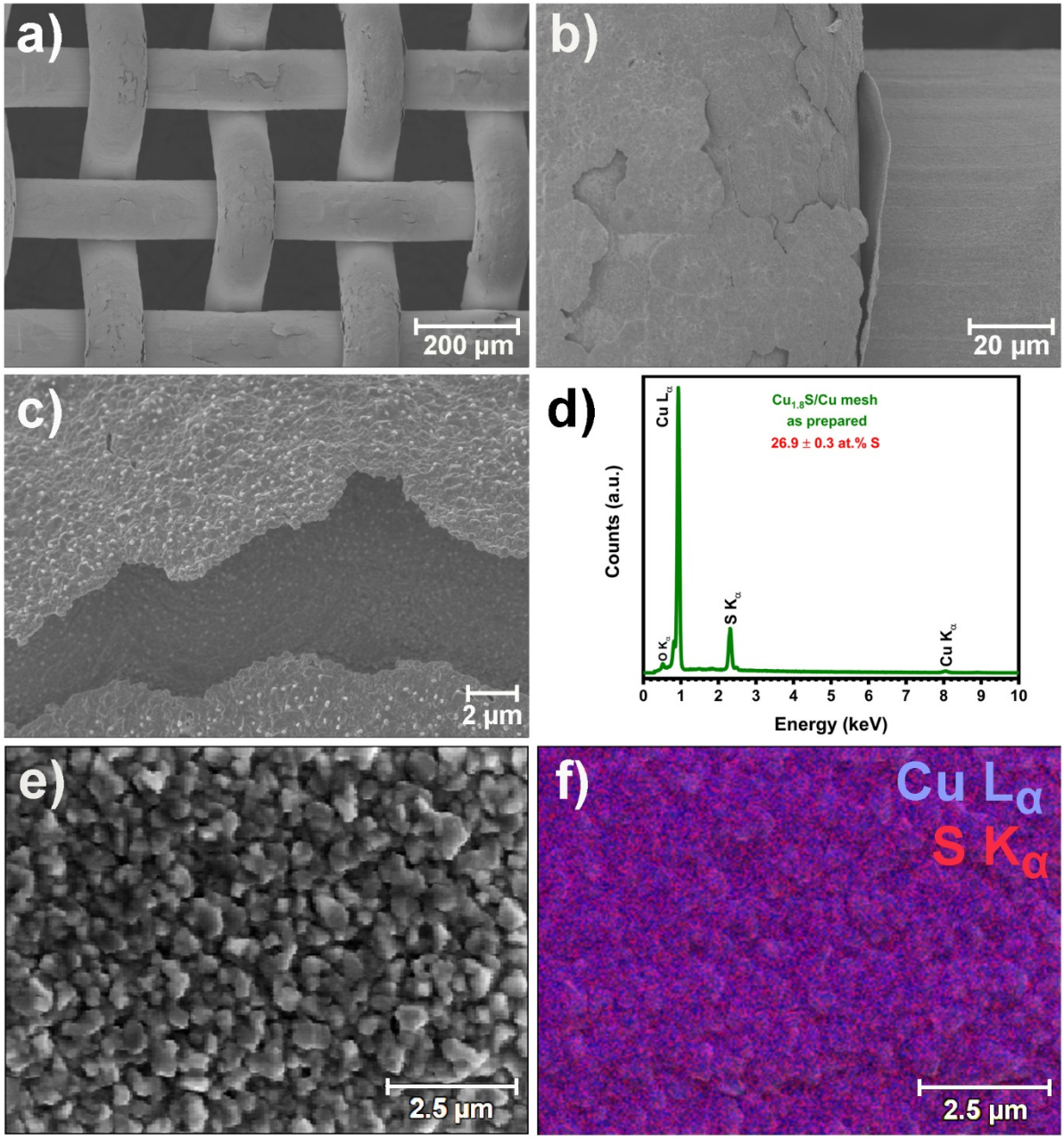

Figure S9. Sulfidated Cu mesh ($Cu_{1.8}S$/Cu mesh): SEM images **(a-c)**, EDX spectrum and bulk sulfur content **(d)**, and elemental mapping of Cu and S **(e, f)**. The $Cu_{1.8}S$ layer is pealing from the surface of the Cu mesh, similarly as in the case of the sulfidated Cu foil (Figure S8).

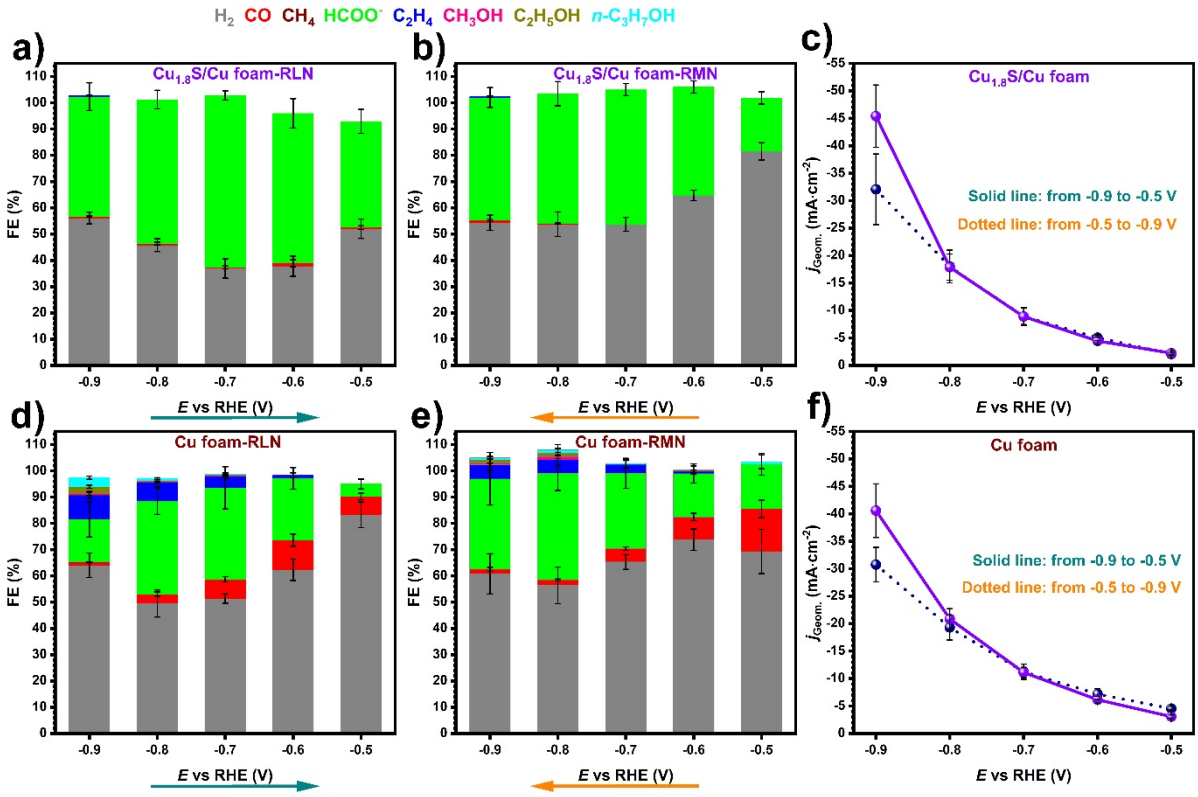

Figure S10. Replotted graphs from Figure 2 (main text), as stacked-column diagrams. Distribution of FEs for H_2 and various CO_2ER products and partial current densities for H_2 and $HCOO^-$ obtained on $Cu_{1.8}S$/Cu foam and pristine Cu foam electrocatalysts: FEs distribution obtained with ramping the potential in less negative direction - RLN for $Cu_{1.8}S$/Cu foam **(a)** and pristine Cu foam **(d)**; FEs distribution obtained with ramping the potential in more negative direction - RMN for $Cu_{1.8}S$/Cu foam **(b)** and pristine Cu foam **(e)**; Total current densities obtained in RLN (solid violet line) and RMN (dotted blue line) direction for $Cu_{1.8}S$/Cu foam **(c)** and pristine Cu foam **(f)**. The arrows point the direction of ramping of the applied potential.

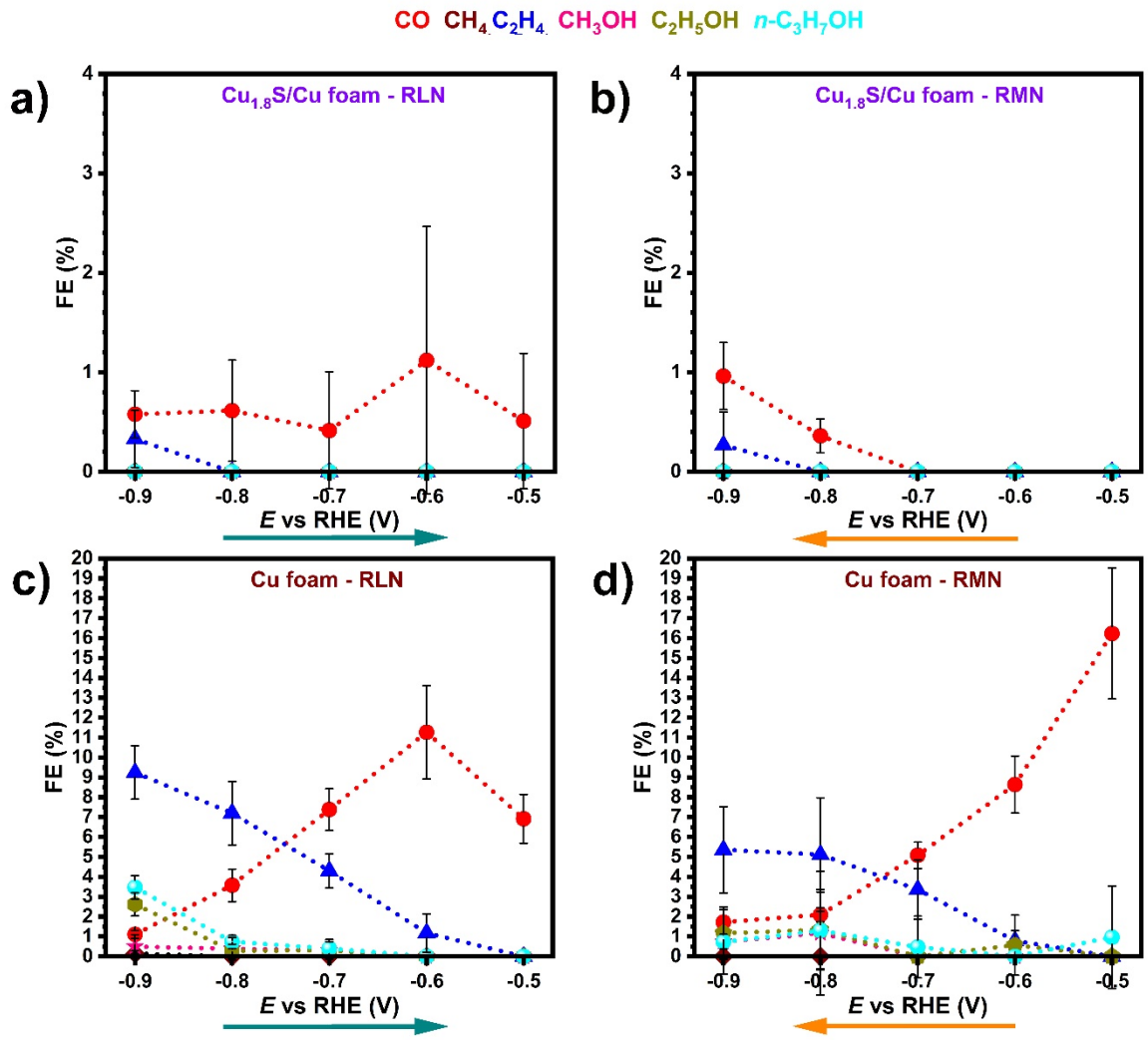

Figure S11. Replotted graphs from Figure 2 (main text). Distribution of FEs for small amounts of CO_2ER products CO, CH_4, C_2H_4, CH_3OH, C_2H_5OH and n-C_3H_7OH, obtained on $Cu_{1.8}S$/Cu foam and pristine Cu foam electrocatalysts: FEs distribution obtained with ramping the potential in less negative direction – RLN for $Cu_{1.8}S$/Cu foam **(a)** and pristine Cu foam **(c)**; FEs distribution obtained with ramping the potential in more negative direction – RMN for $Cu_{1.8}S$/Cu foam **(b)** and pristine Cu foam **(d)**. The arrows point the direction of ramping of the applied potential.

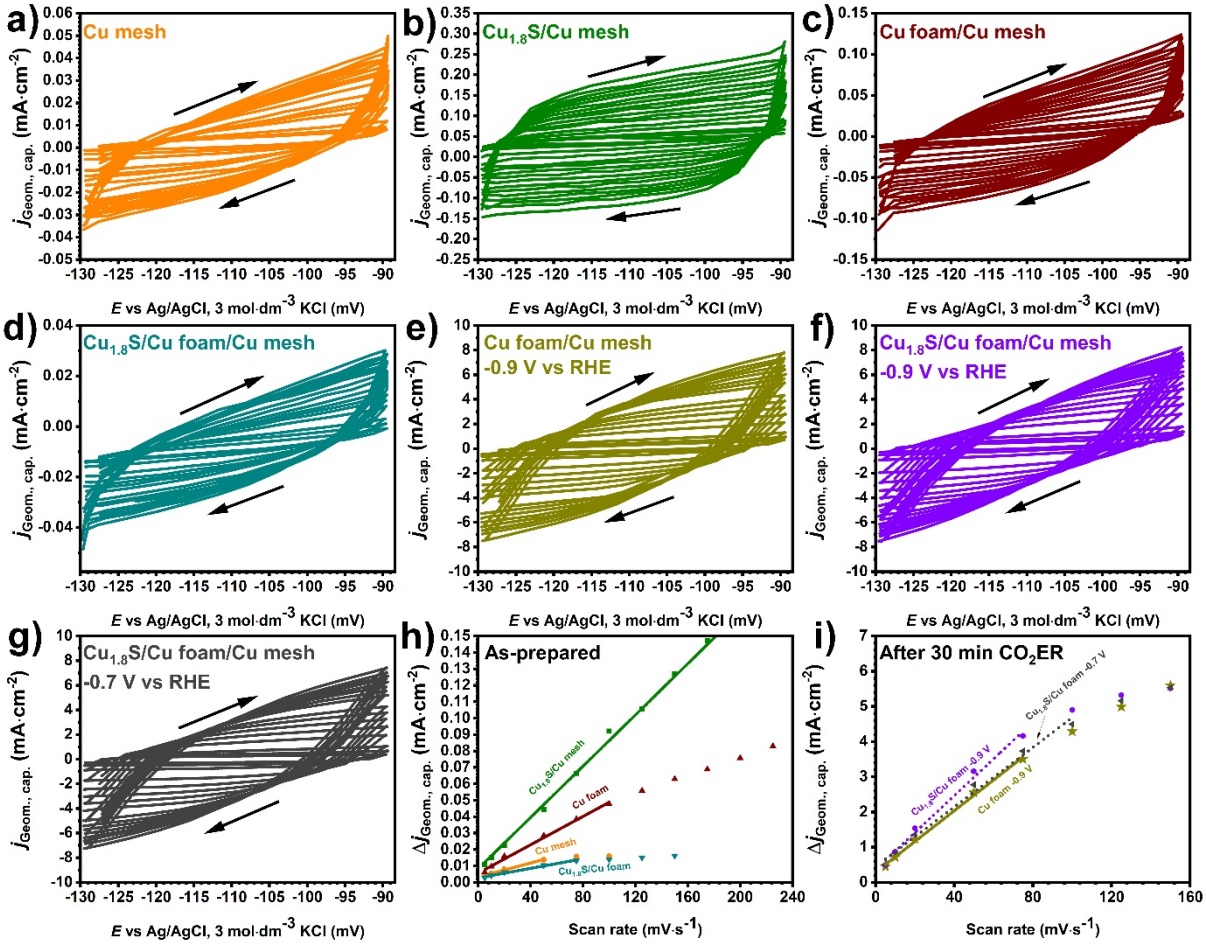

Figure 12. Estimation of the relative surface roughness factor (RSRF). Cyclic voltammograms in a non-faradaic region of potentials in the scan rates range between 5 and 225 mV·s^{-1} for: Cu mesh **(a)**, $Cu_{1.8}S$/Cu mesh **(b)**, Cu foam/Cu mesh **(c)**, $Cu_{1.8}S$/Cu foam/Cu mesh **(d)**, Cu foam/Cu mesh **(e)**, $Cu_{1.8}S$/Cu foam/Cu mesh after CO_2ER at –0.9 V **(f)**, $Cu_{1.8}S$/Cu foam/Cu mesh after CO_2ER at –0.9 V and via RLN direction at –0.7 V vs RHE for 30 min at each potential **(g)**. Linear plots – capacitive current density (Δj) vs. scan rate (SR), at a potential of –110 mV vs Ag/AgCl (3 mol·dm^{-3} KCl) for the electrocatalysts before **(h)**, and after 30 min CO_2 electrolysis at –0.9 and via RLN direction at –0.7 V vs RHE **(i)**.

Table S3. Capacitance normalized to the geometric surface area and relative surface roughness factors (RSRF) for various materials.

Sample	C_{DL} ($mF \cdot cm^{-2}$)	RSRF	Scan rate linear range with $R^2 = 0.99$ ($mV \cdot s^{-1}$)
Cu mesh	$2 \cdot 10^{-4}$	N/A	5-50
$Cu_{1.8}S$/Cu mesh, as-prepared	$8 \cdot 10^{-4}$	4[a]	5-175
Cu foam/Cu mesh, as-prepared	$4 \cdot 10^{-4}$	2[a]	5-100
$Cu_{1.8}S$/Cu foam/Cu mesh, as-prepared	$2 \cdot 10^{-4}$	½[b]/¼[c]/1[a]	5-50
Cu foam/Cu mesh after 1 h electrolysis at –0.9 V	$4 \cdot 10^{-2}$	100[b]	5-75
$Cu_{1.8}S$/Cu foam/Cu mesh after 1 h CO_2ER at –0.9 V	$5 \cdot 10^{-2}$	250[d]/125[b]	5-75
$Cu_{1.8}S$/Cu foam/Cu mesh after 1 h CO_2ER at –0.7 V	$4 \cdot 10^{-2}$	200[d]/100[b]	5-100

N/A: Not applicable.

[a] Relative to Cu mesh.

[b] Relative to Cu foam/Cu mesh, as-prepared.

[c] Relative to $Cu_{1.8}S$/Cu mesh, as-prepared.

[d] Relative to $Cu_{1.8}S$/Cu foam/Cu mesh, as-prepared.

Even though the RSRF does not undoubtedly correlate with the real electrochemical active surface area, it is still a good indicator to withdraw some conclusions about the surface roughness properties. Yet, the C_{DL} values should not be taken for granted when calculating the RSRF but rather the order of magnitude should be used for this estimation for reasons described in the following text. The C_{DL} of the as-prepared materials (Cu foam and sulfidated foam and mesh) are in the same order of magnitude as the bare Cu mesh. Yet, their actual values and thus the RSRF factors are the highest in the case of $Cu_{1.8}S$/mesh which also maintains linearity in the widest scan rates range. Even though, it is for expectation that the as-prepared and Cu foam and $Cu_{1.8}S$/Cu foam should have much higher RSRF comparing the phenomenologically much rougher dendrite composed foam versus the rather flatter particle composed layered morphology (cf. SEM images, Figure S5 with Figure S9), this is not the case most probably due to the difference in their chemical composition, electrical properties, thickness of the double layer and other factors. Contrary to this, the sulfidated Cu foam, shows RSRF factors of ¼, ½ and 1, when compared to the C_{DI} of pristine Cu foam, $Cu_{1.8}S$/Cu foam and Cu mesh, respectively. In this instance, the reason for such behavior might come from electrical contact disputes between the sulfide layer atop the Cu dendrites. However, as stated before, the order of magnitude of the C_{DL} should be a better descriptor for estimation of the RSRF. Thus, is it obvious from the values in Table S3, that the difference between the C_{DL} and RSRF between the materials under as-prepared and post-electrolysis conditions is 2 orders of magnitude. Thus, order of magnitude-wise comparing the RSRF of all post-electrolysis samples shows no significant difference among each other. The actual values do show factor of 2-higher RSFR for the $Cu_{1.8}S$/Cu foam when compared to the as-prepared $Cu_{1.8}S$/Cu mesh, but since there is not much sulfur left post-electrolysis (Figure S28), a better comparison is between the RSRF of the $Cu_{1.8}S$/Cu foam samples after CO_2ER and the as-prepared Cu foam. In this case, no significant difference in the post-electrolysis samples is observed and therefore the morphology can be excluded as a factor affecting the CO_2ER selectivity between the pristine and sulfidated Cu foam, regardless from the examined potentials under which the electrolysis was conducted.

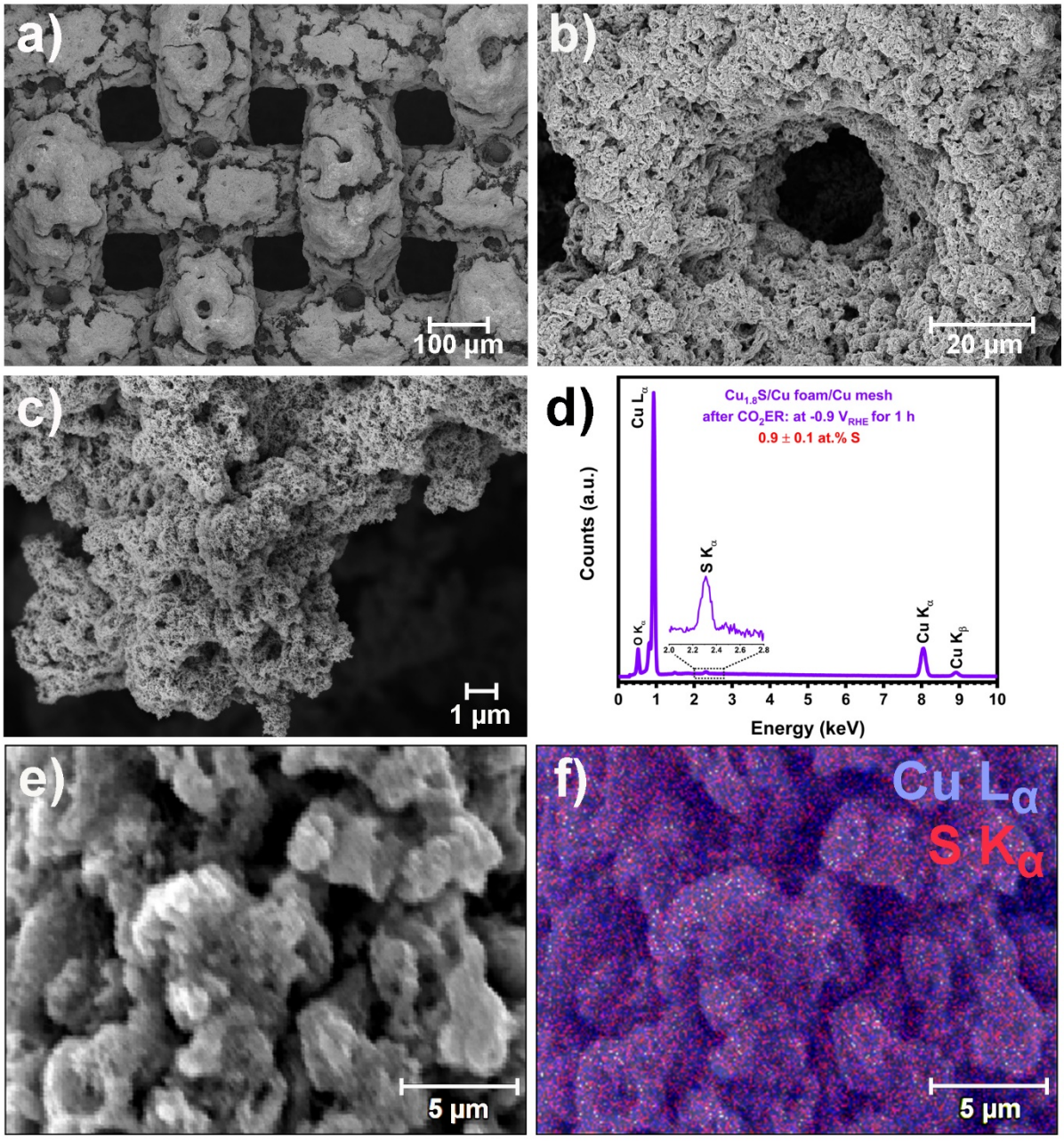

Figure S13. $Cu_{1.8}S$/Cu foam derived foam composed of sponge-like microstructures after electrolysis at –0.9 V for 1 h: SEM images **(a-c)**, EDX spectrum and bulk sulfur content **(d)**, and elemental mapping of Cu and S **(e, f)**.

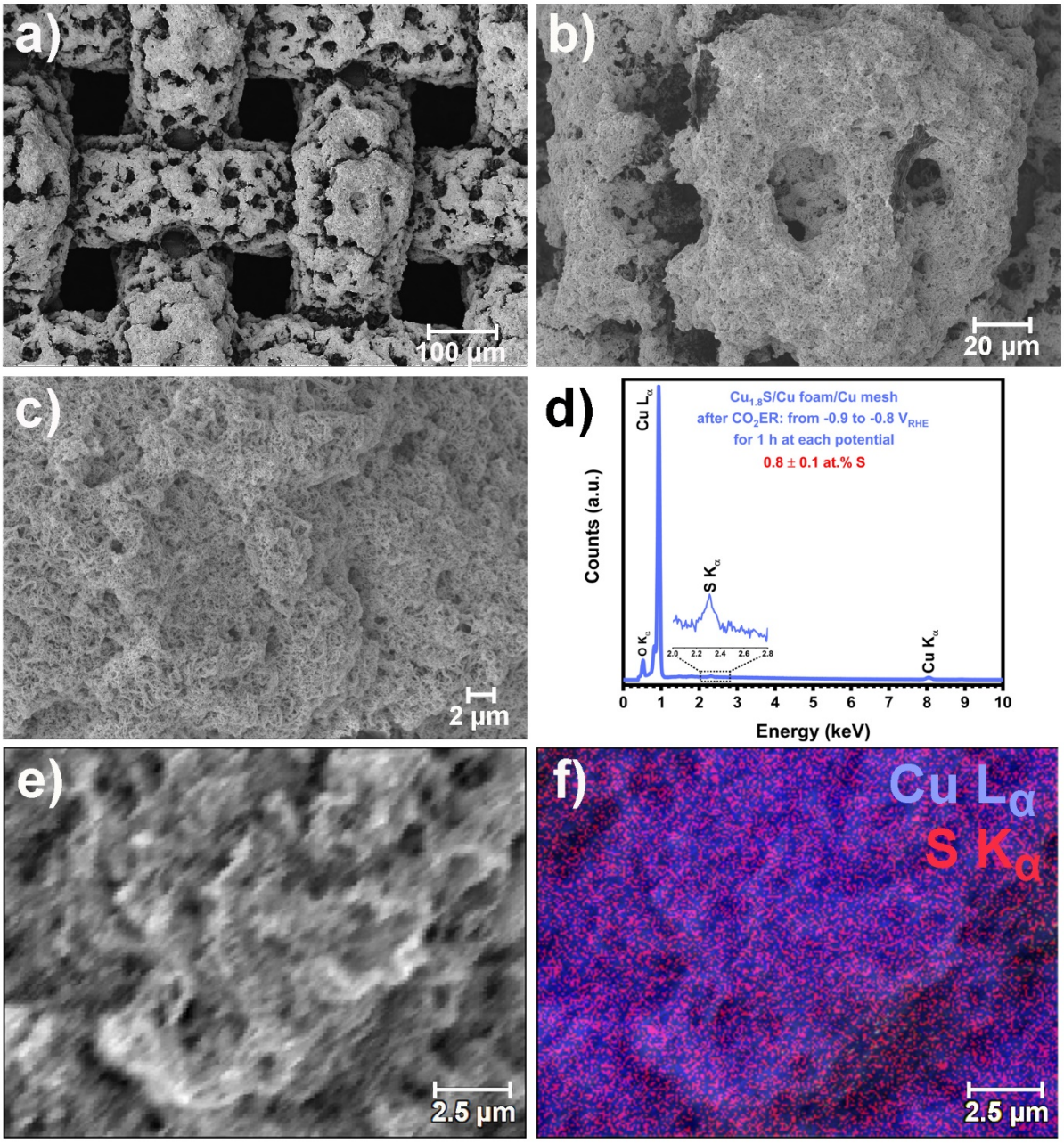

Figure S14. $Cu_{1.8}S$/Cu foam derived foam composed of sponge-like microstructures after electrolysis at –0.9 and –0.8 V in RLN direction, for 1 h at each potential: SEM images **(a-c)**, EDX spectrum and bulk sulfur content **(d)**, and elemental mapping of Cu and S **(e, f)**.

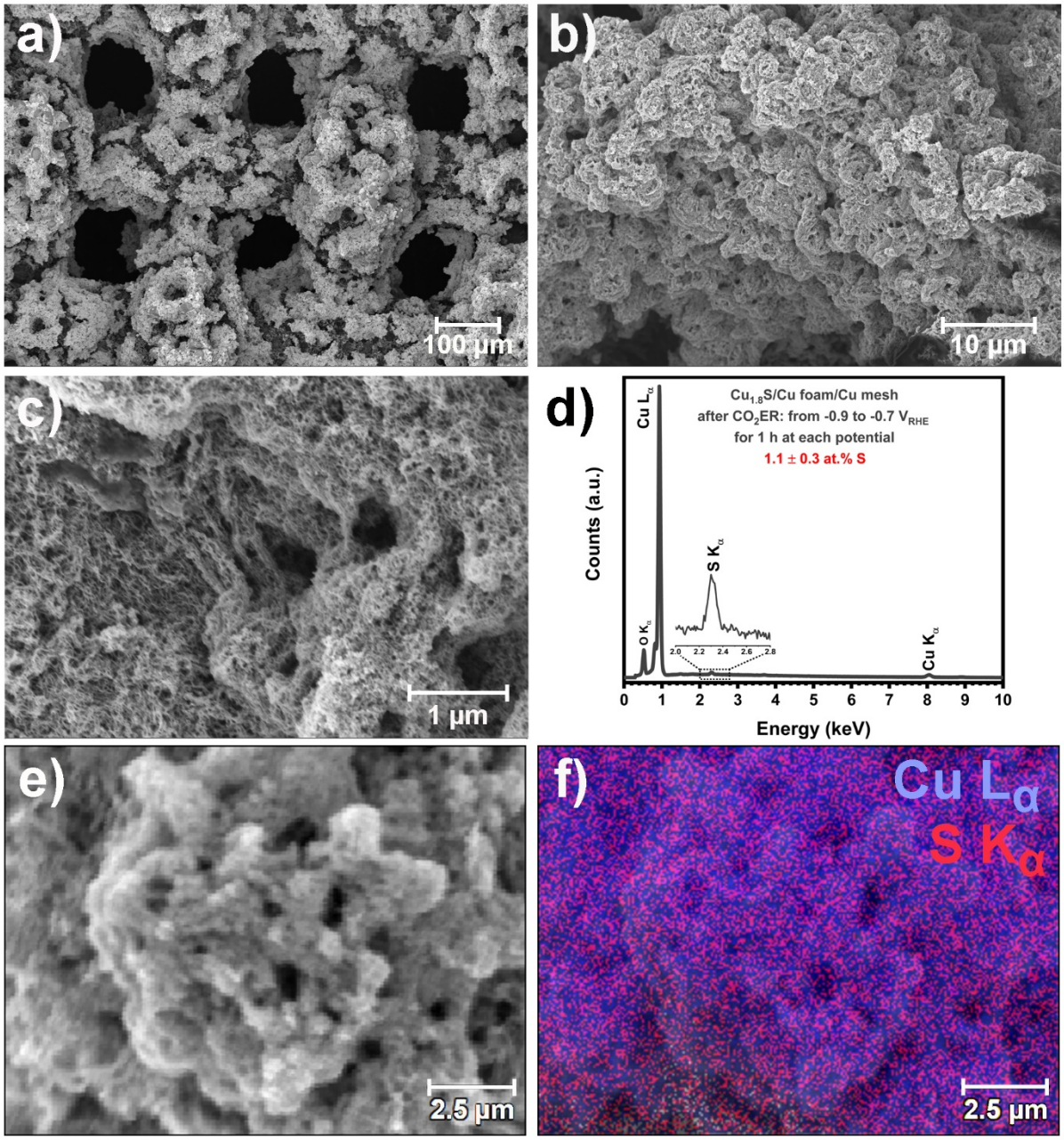

Figure S15. $Cu_{1.8}S$/Cu foam derived foam composed of sponge-like microstructures after electrolysis at –0.9 to –0.7 V in RLN direction, for 1 h at each potential: SEM images **(a-c)**, EDX spectrum and bulk sulfur content **(d)**, and elemental mapping of Cu and S **(e, f)**.

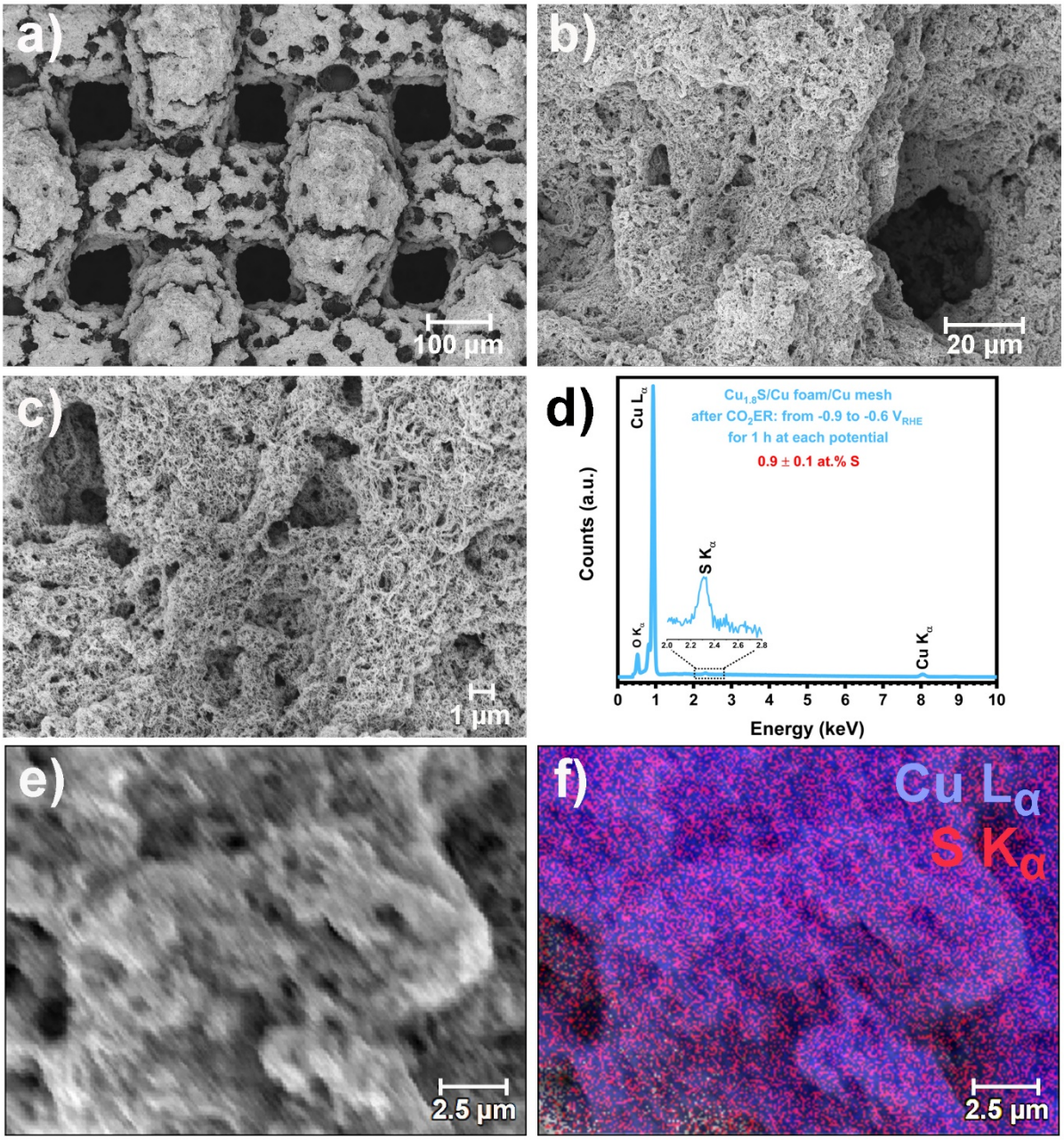

Figure S16. $Cu_{1.8}S$/Cu foam derived foam composed of sponge-like microstructures after electrolysis at –0.9 to –0.6 V in RLN direction, for 1 h at each potential: SEM images **(a-c)**, EDX spectrum and bulk sulfur content **(d)**, and elemental mapping of Cu and S **(e, f)**.

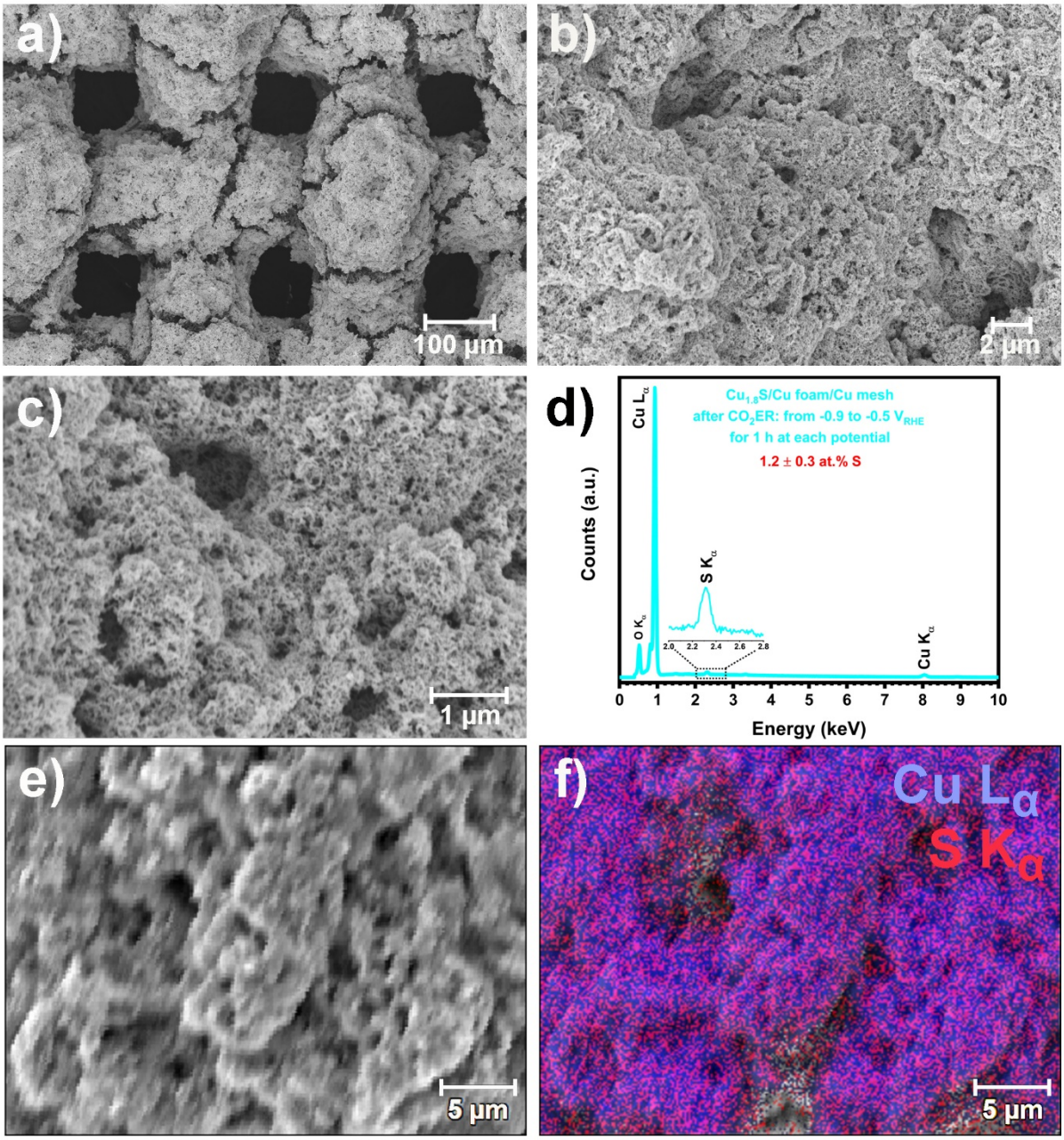

Figure S17. $Cu_{1.8}S$/Cu foam derived foam composed of sponge-like microstructures after electrolysis at –0.9 to –0.5 V in RLN direction, for 1 h at each potential: SEM images **(a-c)**, EDX spectrum and bulk sulfur content **(d)**, and elemental mapping of Cu and S **(e, f)**.

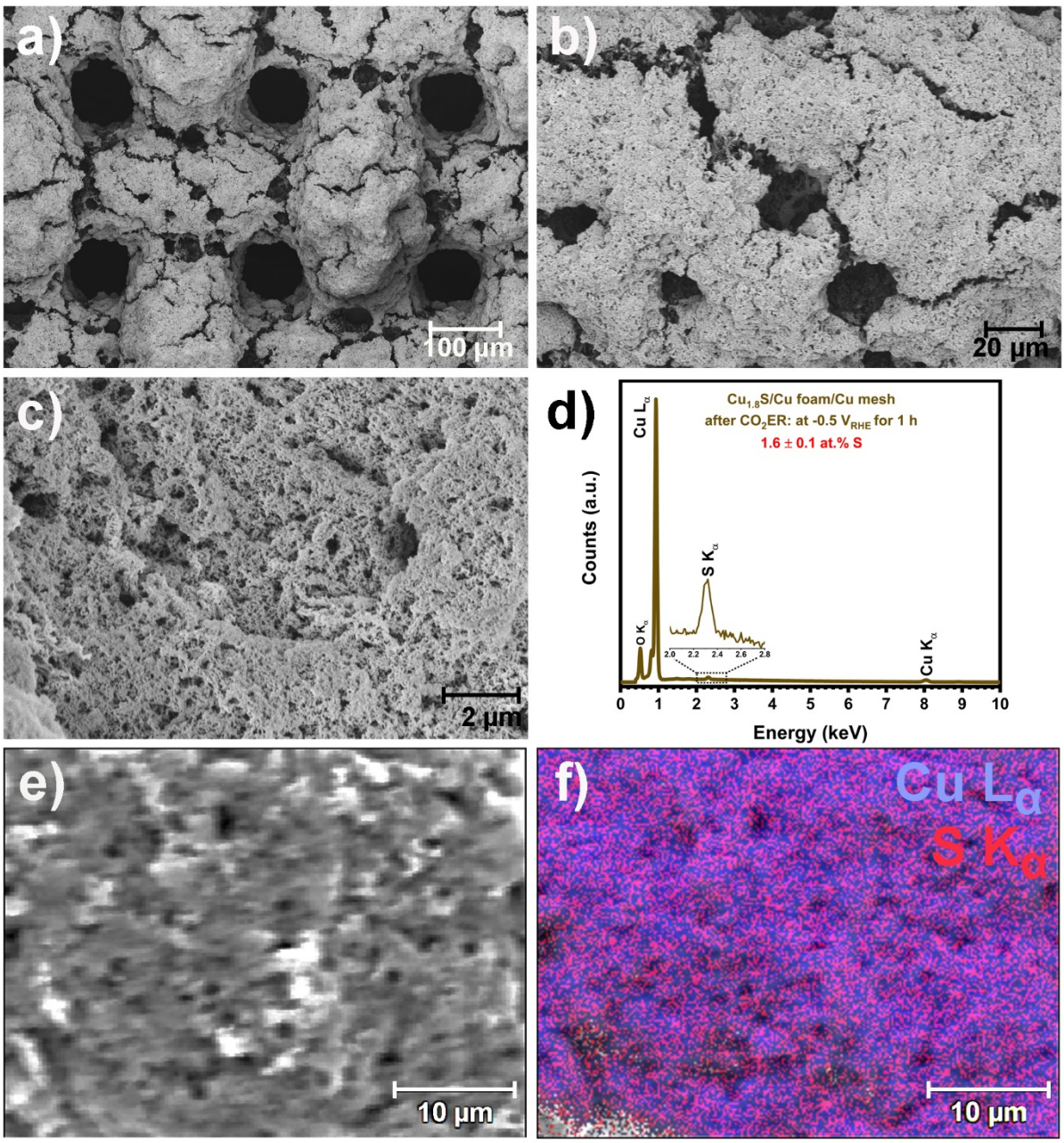

Figure S18. $Cu_{1.8}S$/Cu foam derived foam composed of sponge-like microstructures after electrolysis at –0.5 V for 1 h: SEM images **(a-c)**, EDX spectrum and bulk sulfur content **(d)**, and elemental mapping of Cu and S **(e, f)**.

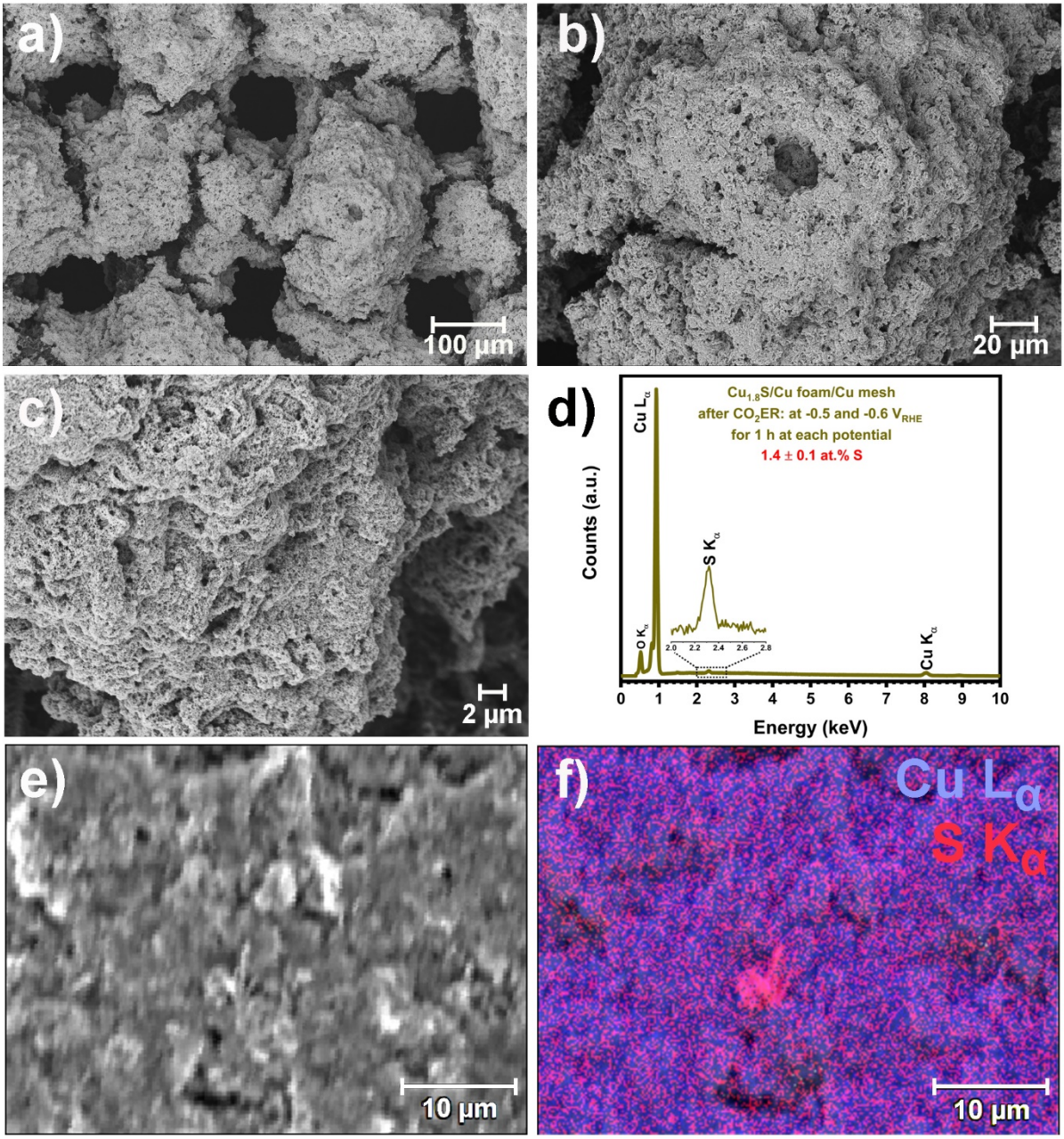

Figure S19. $Cu_{1.8}S$/Cu foam derived foam composed of sponge-like microstructures after electrolysis at –0.5 and –0.6 V in RMN direction, for 1 h at each potential: SEM images **(a-c)**, EDX spectrum and bulk sulfur content **(d)**, and elemental mapping of Cu and S **(e, f)**.

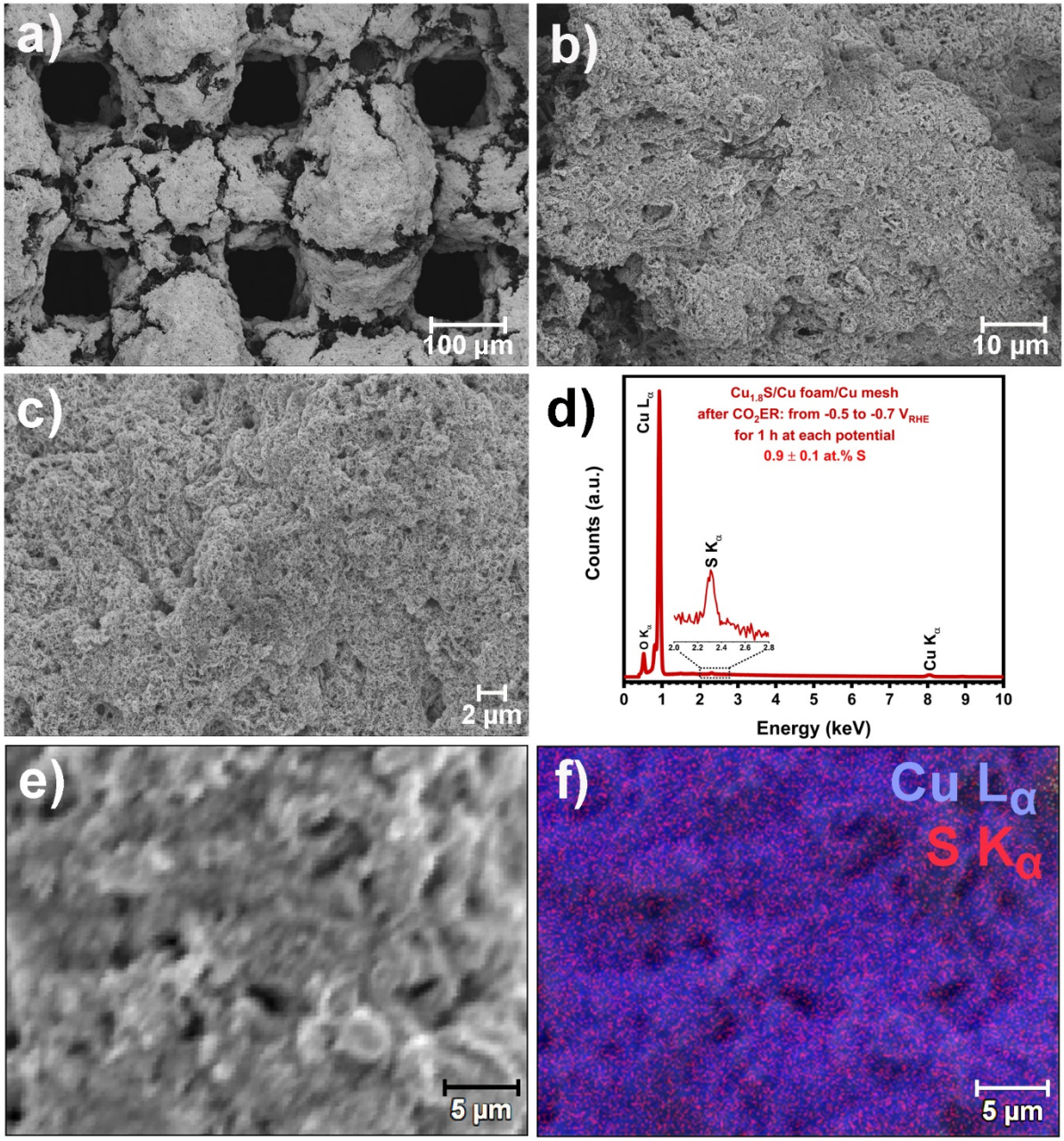

Figure S20. $Cu_{1.8}S$/Cu foam derived foam composed of sponge-like microstructures after electrolysis at –0.5 to –0.7 V in RMN direction, for 1 h at each potential: SEM images **(a-c)**, EDX spectrum and bulk sulfur content **(d)**, and elemental mapping of Cu and S **(e, f)**.

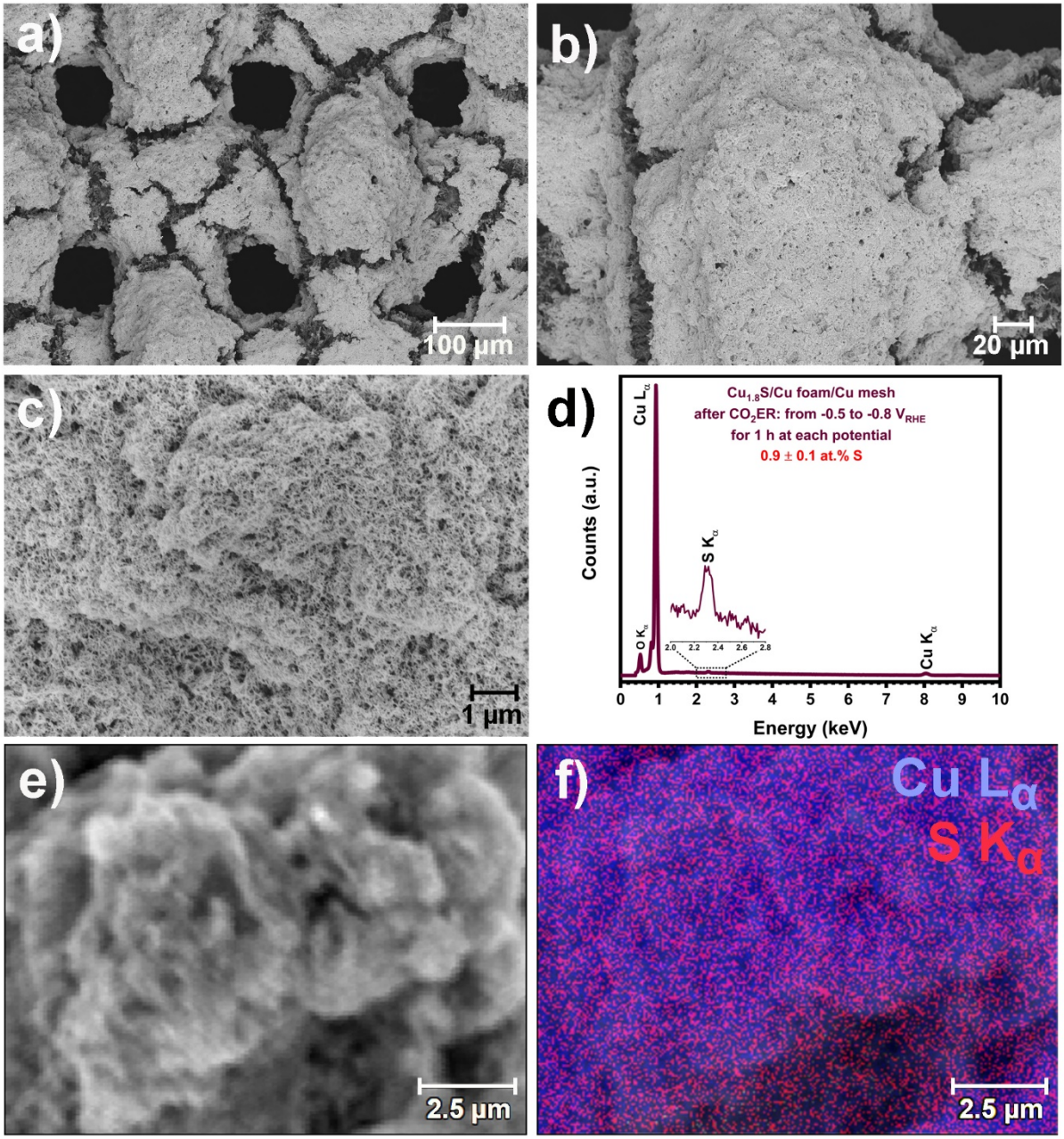

Figure S21. $Cu_{1.8}S$/Cu foam derived foam composed of sponge-like microstructures after electrolysis at –0.5 to –0.8 V in RMN direction, for 1 h at each potential: SEM images **(a-c)**, EDX spectrum and bulk sulfur content **(d)**, and elemental mapping of Cu and S **(e, f)**.

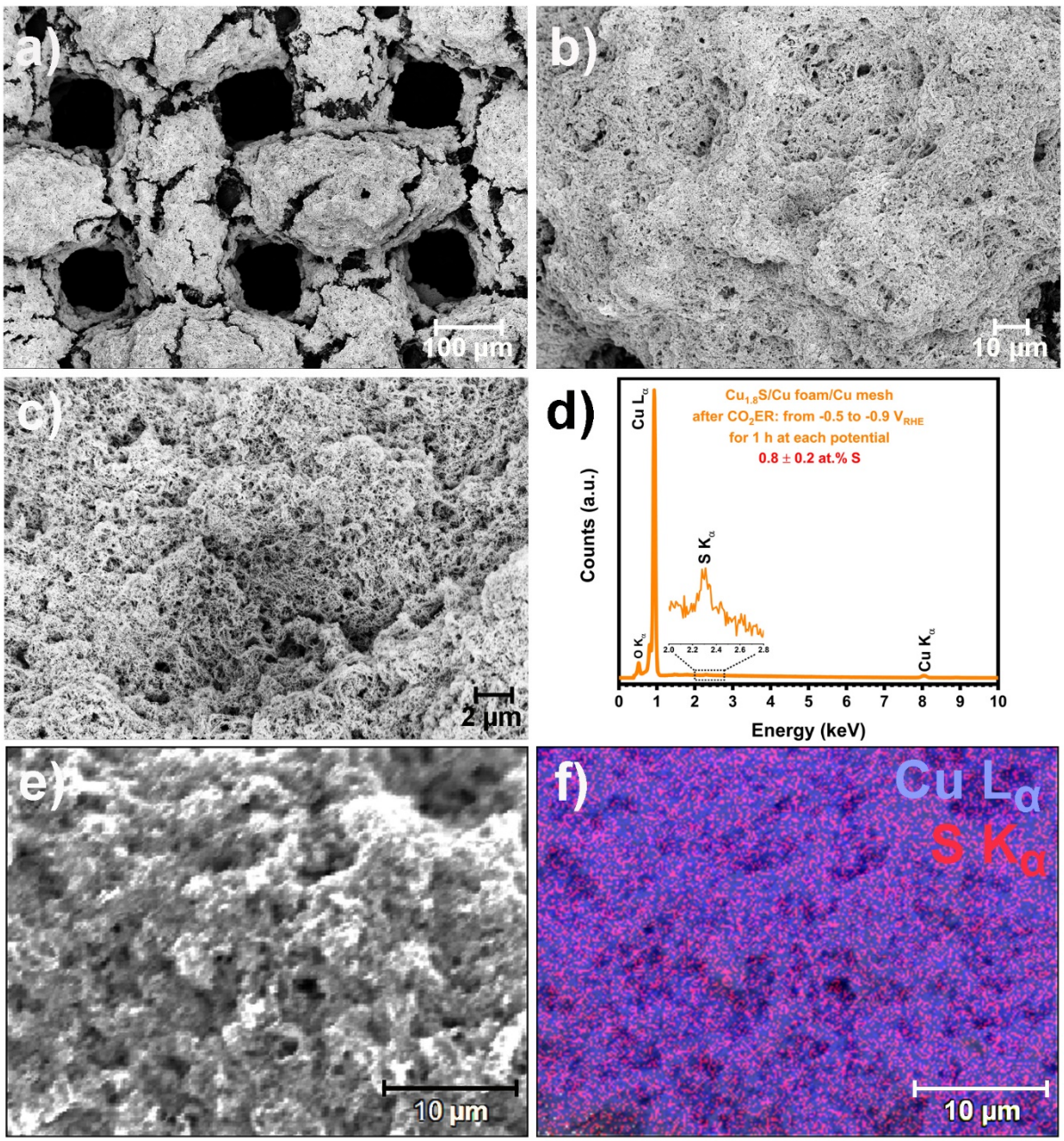

Figure S22. $Cu_{1.8}S$/Cu foam derived foam composed of sponge-like microstructures after electrolysis at –0.5 to –0.9 V in RMN direction, for 1 h at each potential: SEM images **(a-c)**, EDX spectrum and bulk sulfur content **(d)**, and elemental mapping of Cu and S **(e, f)**.

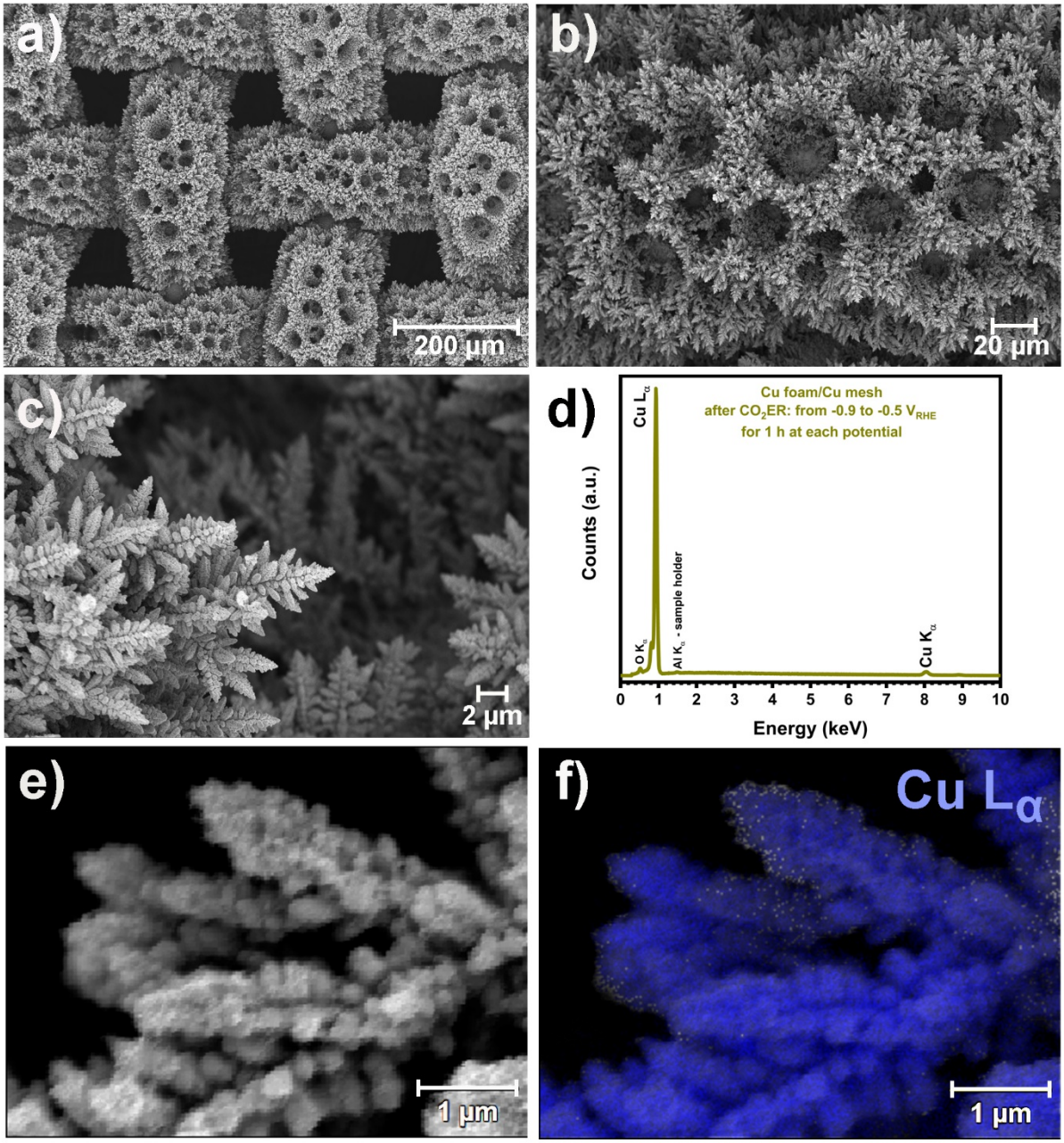

Figure S23. Cu foam composed of fern plant-like dendrite microstructures on Cu mesh substrate after electrolysis at –0.5 to –0.9 V in RLN direction, for 1 h at each potential: SEM images **(a-c)**; EDX spectrum **(d)** and elemental mapping **(e, f)**.

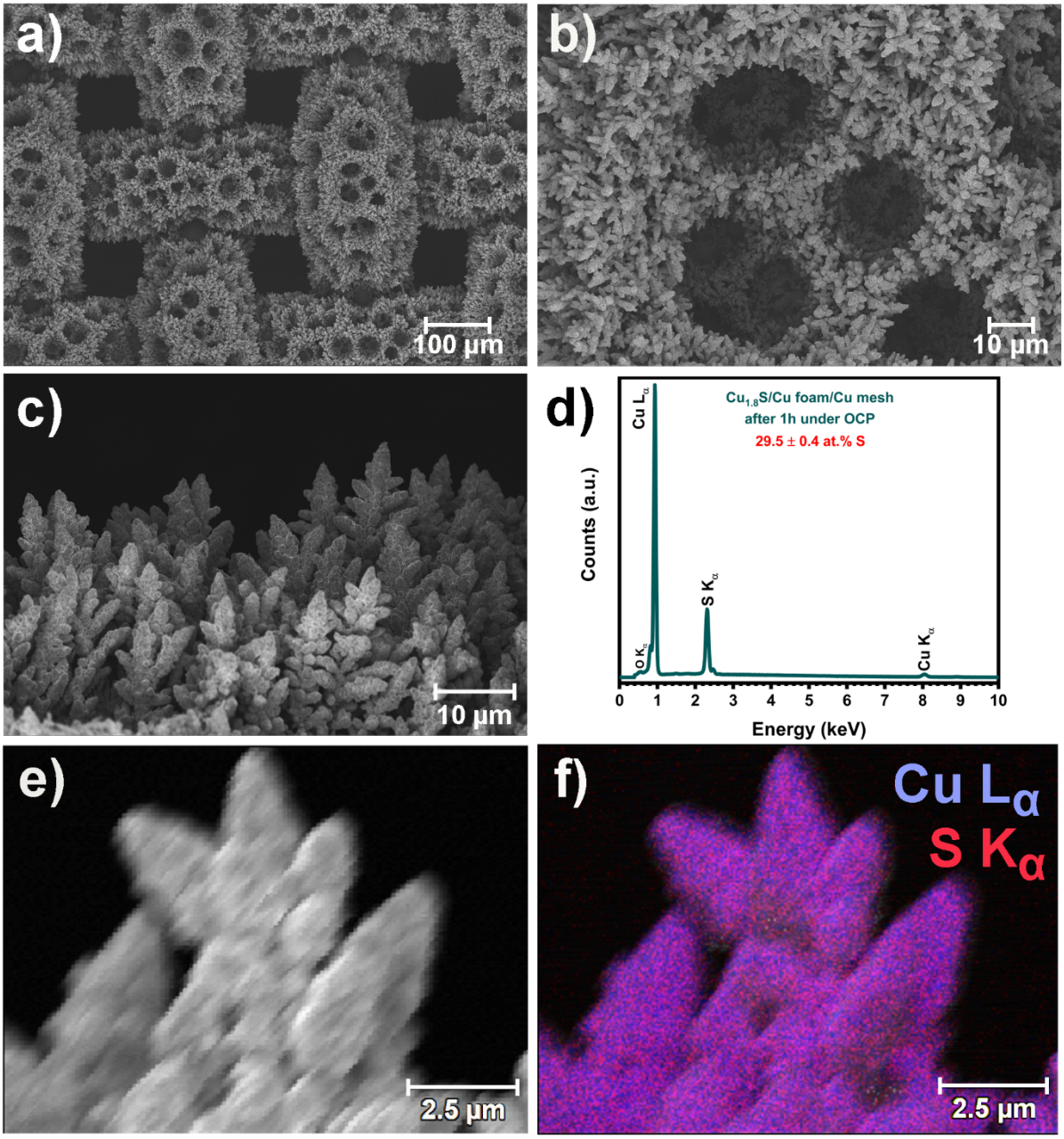

Figure S24. $Cu_{1.8}S$/Cu foam derived foam composed of dendrite-like microstructures after 1 h immersed in electrolyte solution under open circuit potential (OCP): SEM images **(a-c)**, EDX spectrum and bulk sulfur content **(d)**, and elemental mapping of Cu and S **(e, f)**.

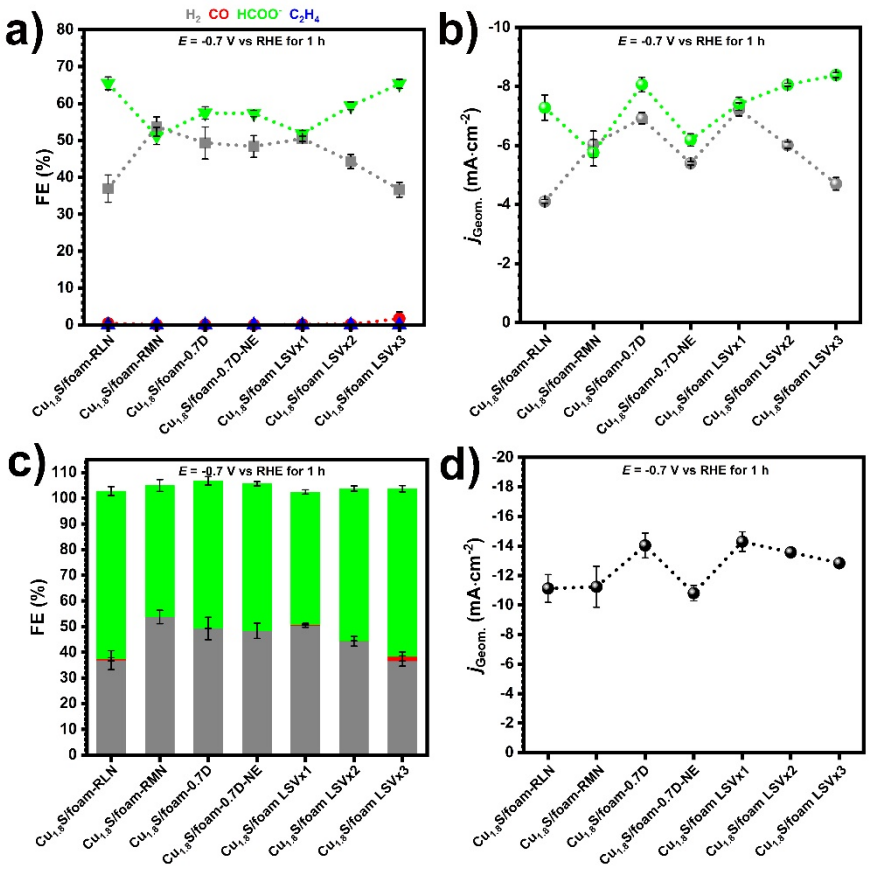

Figure S25. Distribution of FEs and partial current densities for H_2 and $HCOO^-$ and total current densities obtained on $Cu_{1.8}S$/Cu foam under various conditions at –0.7 V vs RHE: FEs **(a)** and partial current density distribution for H_2 and $HCOO^-$ **(b)**. Replotted FEs distribution from Figure S25a as stacked-column diagrams and **(c)** and total current density distribution **(d)**. The LSV scans for the $Cu_{1.8}S$/Cu foam-LSVx1, x2 and x 3 set of samples was performed from 0 to –0.9 V *vs.* RHE with 1, 2 and 3 repetitions.

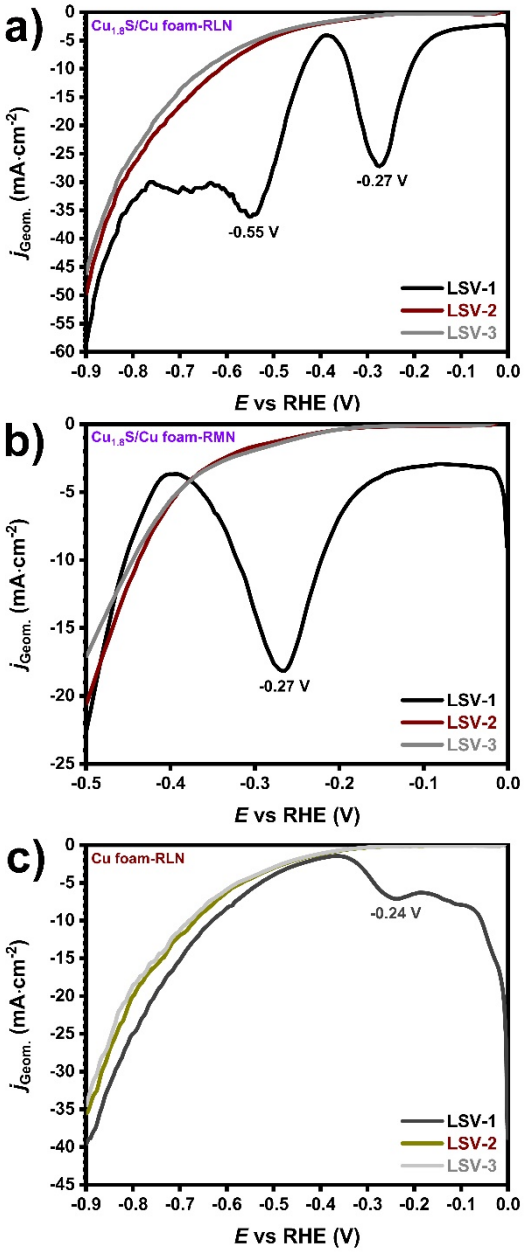

Figure S26. Linear sweep voltammetry (LSV) curves recorded with 150 mV·min^{-1}, re-plotted as j vs. E from Figures 3, 4 and S27: $Cu_{1.8}S$/Cu foam - 3 LSV scans from 0 to –0.9 V **(a)**, $Cu_{1.8}S$/Cu foam - 3 LSV scans from 0 to –0.5 V **(b)** and pristine Cu foam - 3 LSV scans from 0 to –0.9 V vs. RHE **(c)**. The onset potential when H_2S is first observed from the reduction of the $Cu_{1.8}S$ appears around –0.47 V vs. RHE.

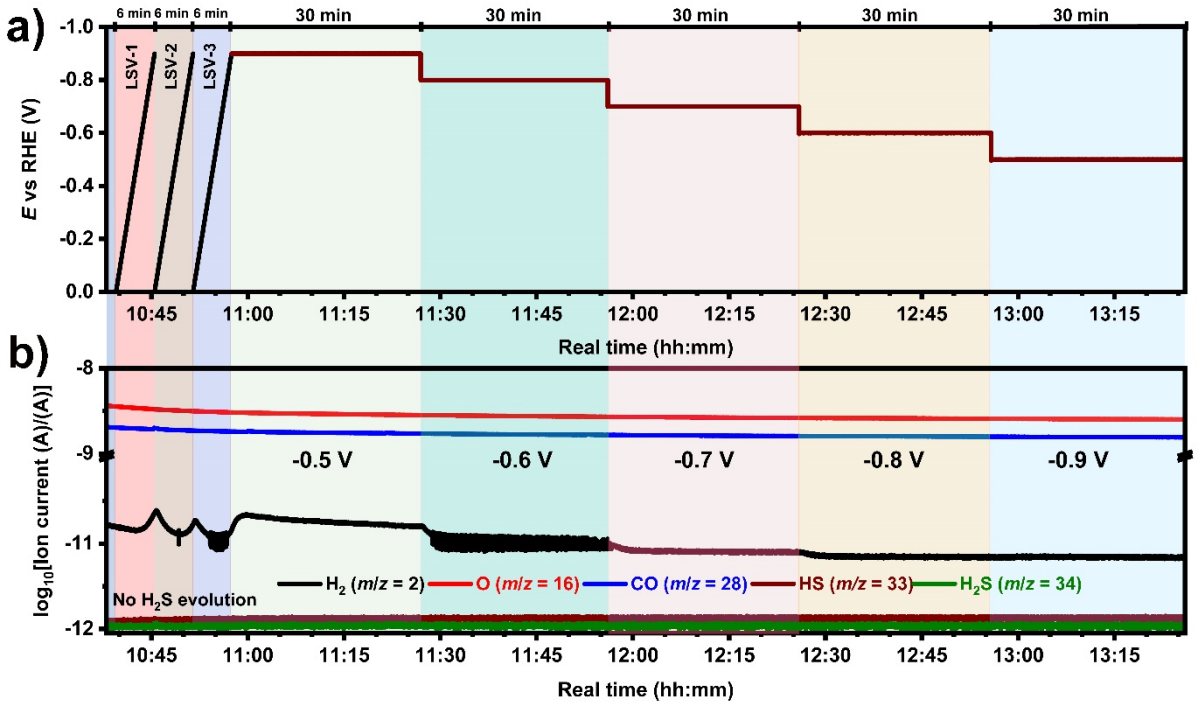

Figure S27. Tracking of product evolution with *in-situ* mass spectrometry coupled with electrolysis (EC-MS) when the pristine Cu foam electrocatalyst is examined in the RLN direction of altering the applied potential (–0.9 to –0.5 V *vs*. RHE): Applied potential in linear sweep voltammetry - LSV/chronoamperometry - CA modes **(a)** and mass/charge signals - *m/z* attributed to H_2, CO, O_2 and H_2S **(b)** plotted *vs*. time of electrolysis.

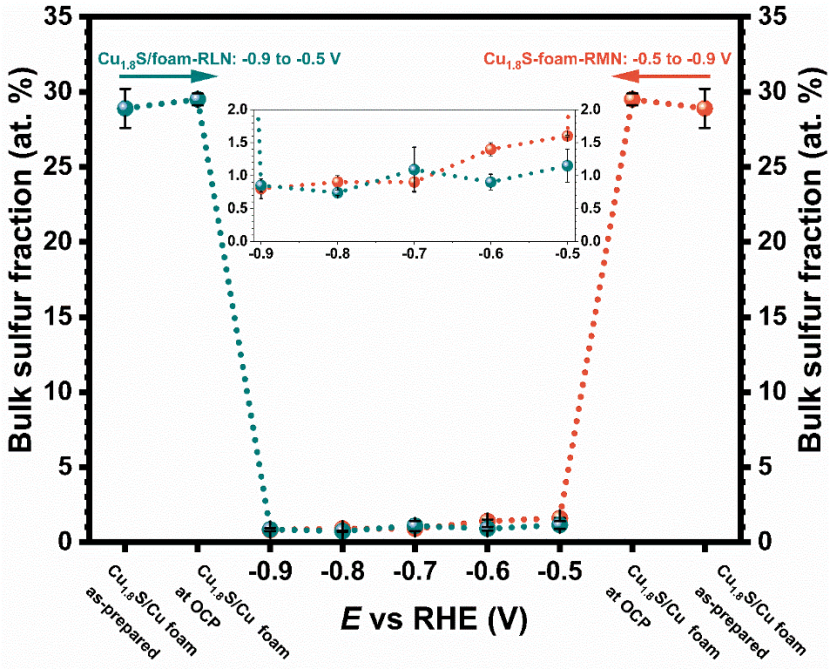

Figure S28. Distribution of the bulk sulfur fraction in pre- and post-electrolysis $Cu_{1.8}S$/Cu foam in the potential range between –0.5 and –0.9 V *vs.* RHE ramped in both less negative (RLN-olive green) and more negative (RMN-orange) direction. The values are plotted from the EDX results presented in Figures S5, S13-22d and S24d.

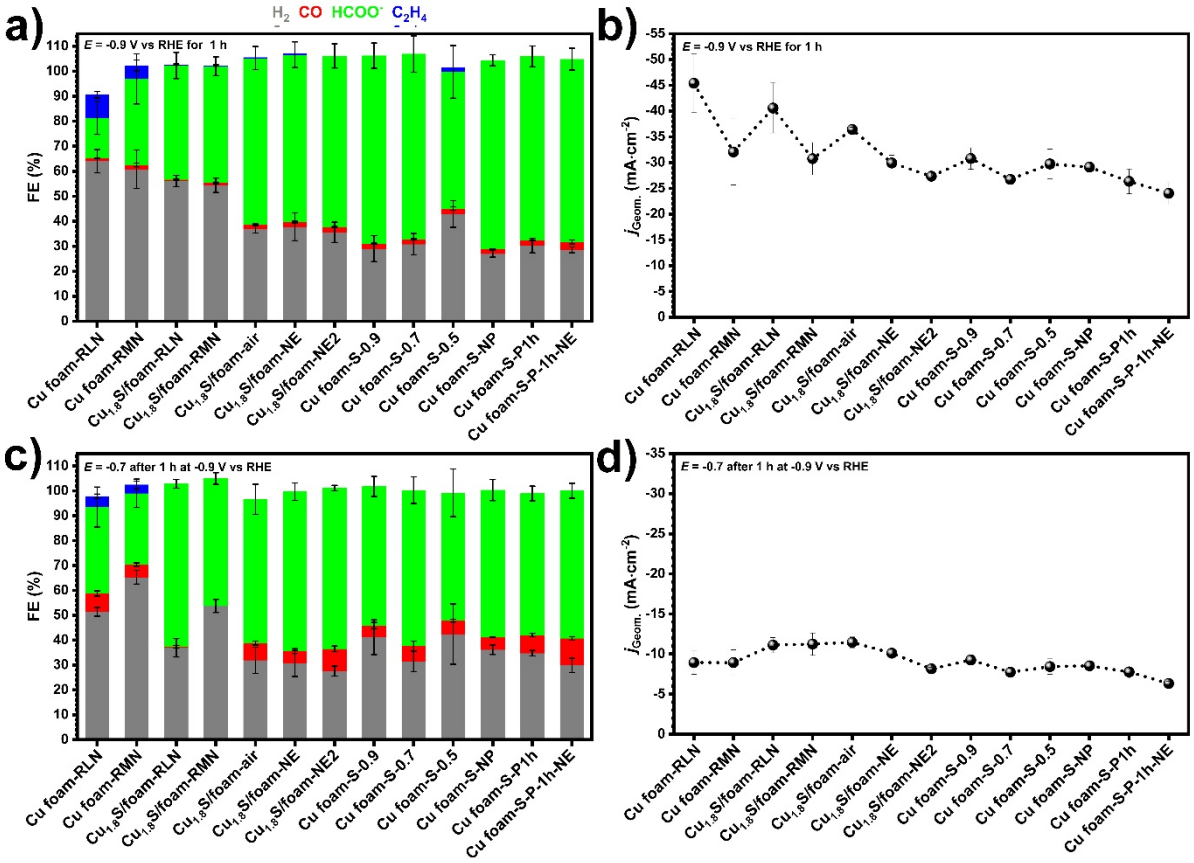

Figure S29. Electrocatalytic activity results from the control experiments replotted from Figure 5 as stacked column-diagrams. Distribution of FEs for H_2 and CO_2ER products and partial current densities for H_2 and $HCOO^-$ obtained on $Cu_{1.8}S$/Cu foam and electrolyte sulfidated Cu foam under various conditions: FEs distribution **(a)** and total current density at –0.9 V **(b)**, and FEs distribution **(c)** and total current density at –0.7 V vs RHE **(d)**. Sample abbreviations and experimental conditions are presented in Table S1.

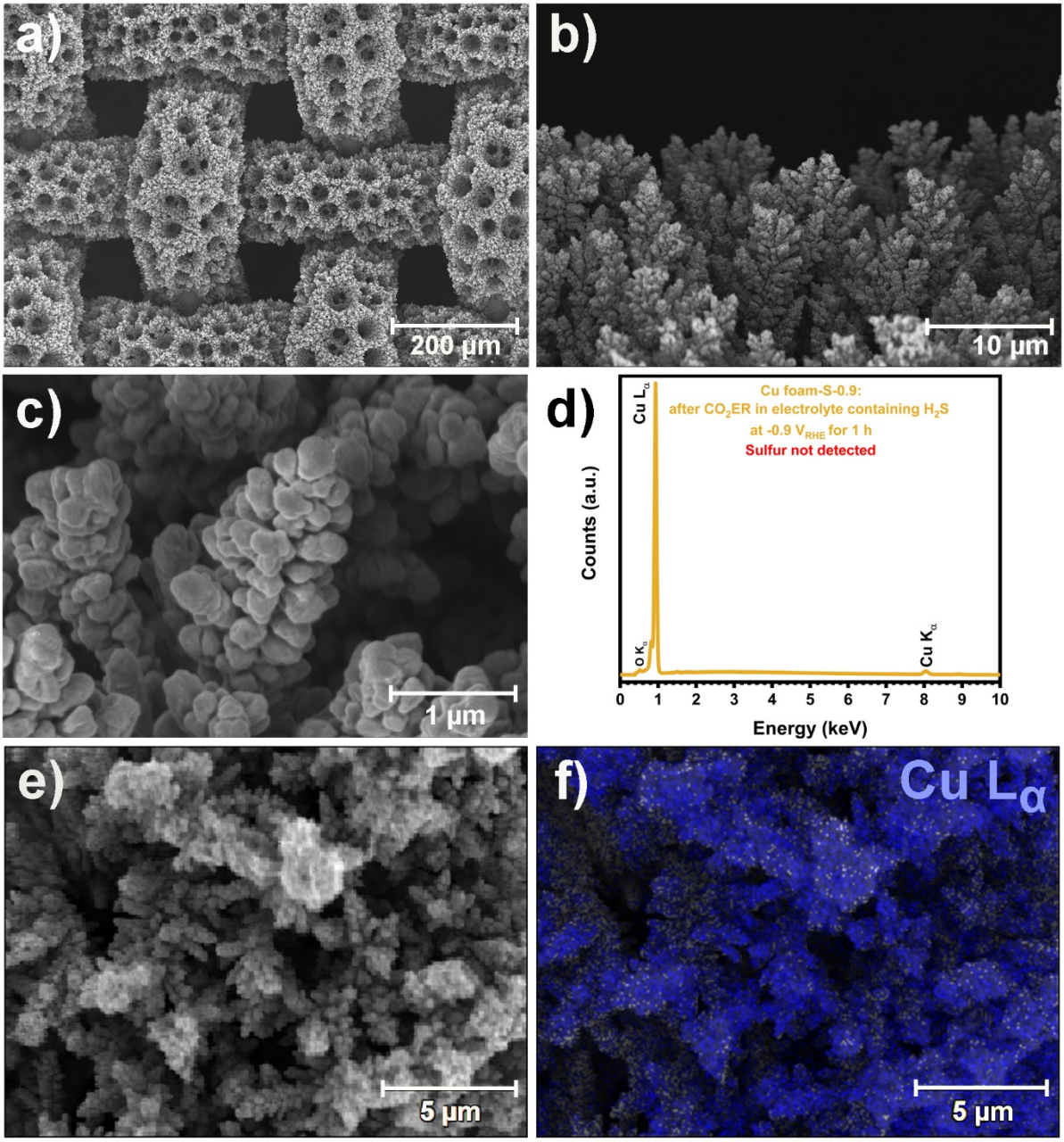

Figure S30. Cu foam composed of fern plant-like dendrite microstructures on Cu mesh substrate after electrolysis at –0.9 V for 1 h in an electrolyte in which previously $Cu_{1.8}S$/Cu foam was reduced with 1 x LSV from 0 to –0.9 V (sample: Cu foam-S-0.9, see Table S1): SEM images **(a-c)**; EDX spectrum **(d)** and elemental mapping **(e, f)**.

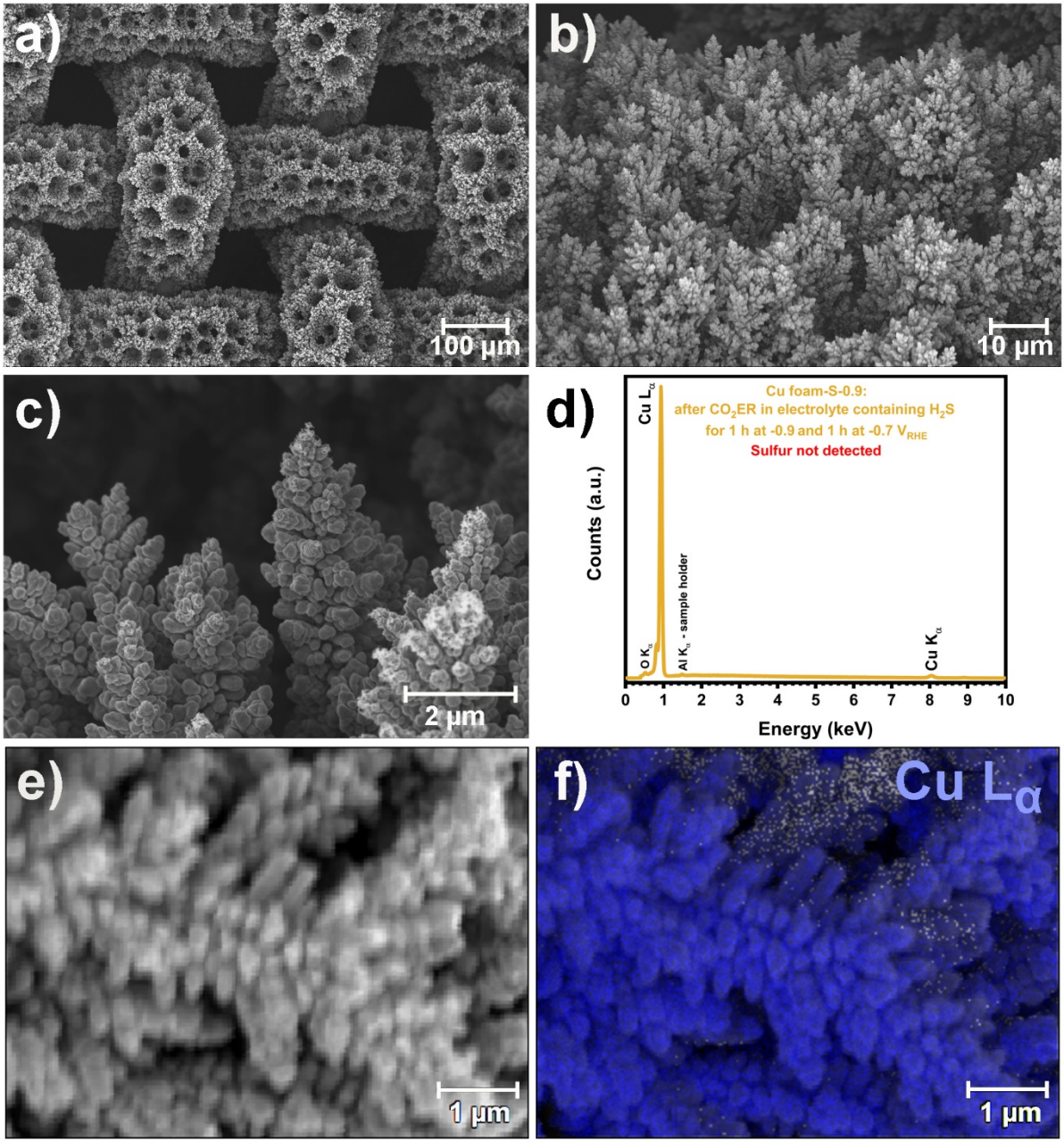

Figure S31. Cu foam composed of fern plant-like dendrite microstructures on Cu mesh substrate after electrolysis at –0.9 and –0.7 V for 1 h at each potential in an electrolyte in which previously $Cu_{1.8}S$/Cu foam was reduced with 1 x LSV from 0 to –0.9 V (sample: Cu foam-S-0.7, see Table S1): SEM images **(a-c)**; EDX spectrum **(d)** and elemental mapping **(e, f)**.

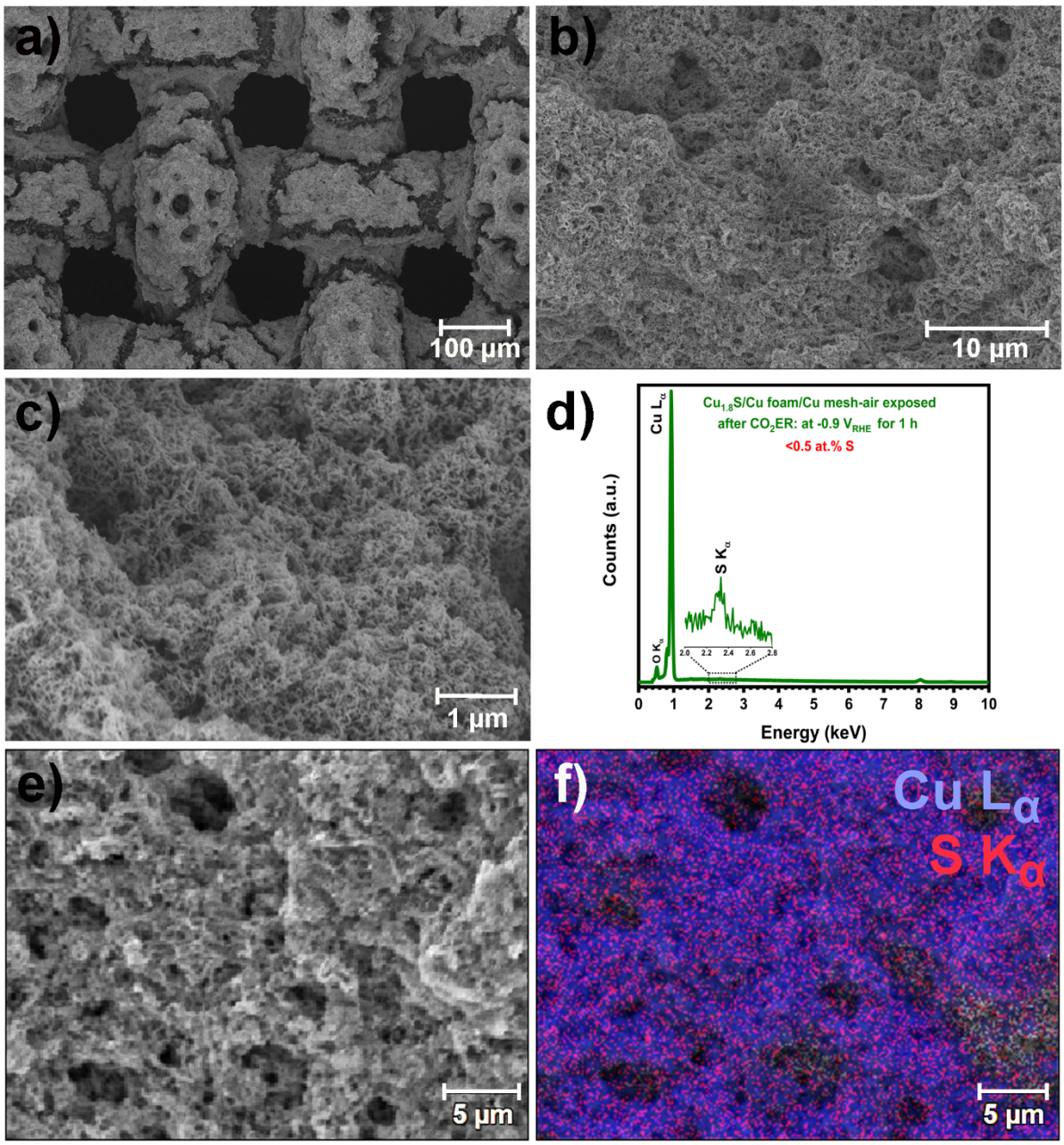

Figure S32. $Cu_{1.8}S$/Cu foam derived foam composed of sponge-like microstructures after electrolysis at –0.9 V for 1 h, then 1 h air exposure and repeating the electrolysis in fresh electrolyte at the same potential and duration: SEM images **(a-c)**, EDX spectrum and bulk sulfur content **(d)**, and elemental mapping of Cu and S **(e, f)**.

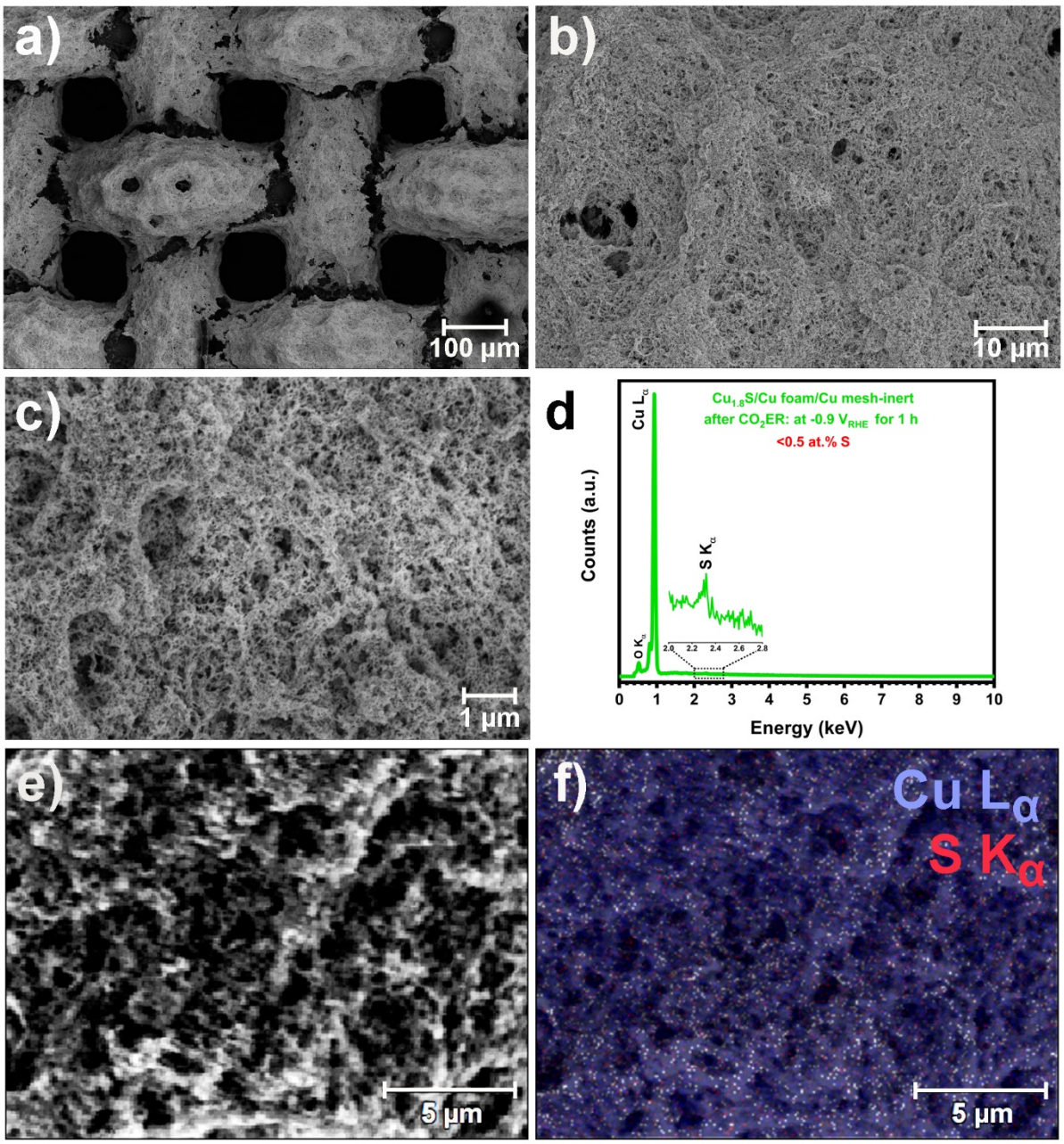

Figure S33. $Cu_{1.8}S$/Cu foam derived foam composed of sponge-like microstructures after electrolysis at –0.9 V for 1 h, then 1 h exposure in inert atmosphere (N_2) in a glovebox and repeating the electrolysis in fresh electrolyte at the same potential and duration: SEM images **(a-c)**, EDX spectrum and bulk sulfur content **(d)**, and elemental mapping of Cu and S **(e, f)**. Note: For this sample only the concentration of $HCOO^-$ was measured thus the FE for of ~68% was obtained at –0.9 V which is similar as in the case of the $Cu_{1.8}S$/Cu foam that was re-examined at –0.9 V after 1 h air exposure and electrolyte replacement.

Table S4. ICP-OES results from post-electrolysis sulfur quantification, generated from under various electrochemical conditions.

Sample and experimental conditions*	Nominal concentration of S ($mg \cdot dm^{-3}$)
• $Cu_{1.8}S$/Cu foam: 1 x LSV from 0 to –0.9 V	1.61
• $Cu_{1.8}S$/Cu foam: 1 x LSV from 0 to –0.7 V	1.15
• $Cu_{1.8}S$/Cu foam: 1 x LSV from 0 to –0.5 V	0.40
• $Cu_{1.8}S$/Cu foam: 3 x LSV from 0 to –0.9 V	0.39
• $Cu_{1.8}S$/Cu foam: 3 x LSV from 0 to –0.5 V	0.81
• $Cu_{1.8}S$/Cu foam: RLN - CA from –0.9 to –0.7 V, 1 h at each potential	0.16
• $Cu_{1.8}S$/Cu foam: RMN - CA from –0.5 to –0.7 V, 1 h at each potential	0.15
• $Cu_{1.8}S$/Cu foam: 3 x LSV from 0 to –0.7 V, then CA at –0.7 V for 1 h ($Cu_{1.8}S$/Cu foam-0.7D)	0.16
• $Cu_{1.8}S$/Cu foam: 3 x LSV from 0 to –0.7, then CA at –0.7 V for 1 h, electrolyte replacement, air exposure of the sample and remeasuring at –0.7 V for 1 h ($Cu_{1.8}S$/Cu foam-0.7-NE)	0.04
• $Cu_{1.8}S$/Cu foam: 3 x LSV 0 to –0.9 V, then CA at –0.9 V for 1 h, electrolyte replacement, air exposure of the sample and remeasuring at –0.9 and –0.7 V for 1 h, at each potential ($Cu_{1.8}S$/Cu foam-NE)	0.05
• $Cu_{1.8}S$/Cu foam: 1 x LSV from 0 to –0.9 V, then 3 x LSV 0 to –0.9 V, CA at –0.9 and –0.7 V, for 1 h at each potential using Cu foam as electrode in the same electrolyte (Cu foam-S-0.9)	0.27
• $Cu_{1.8}S$/Cu foam: 1 x LSV from 0 to –0.7 V, then 3 x LSV 0 to –0.9 V, CA at –0.9 and –0.7 V, for 1 h at each potential using Cu foam as electrode in the same electrolyte (Cu foam-S-0.7)	0.18
• $Cu_{1.8}S$/Cu foam: 1 x LSV from 0 to –0.5 V, then 3 x LSV 0 to –0.9 V, CA at –0.9 and –0.7 V, for 1 h at each potential using Cu foam as electrode in t same electrolyte (Cu foam-S-0.5)	0.21

* Addditional information regarding the electrochemical conditions are presented in Section S1.5. and Table S1.

LSV: Linear sweep voltammetry.

CA: Chronoamperometry.

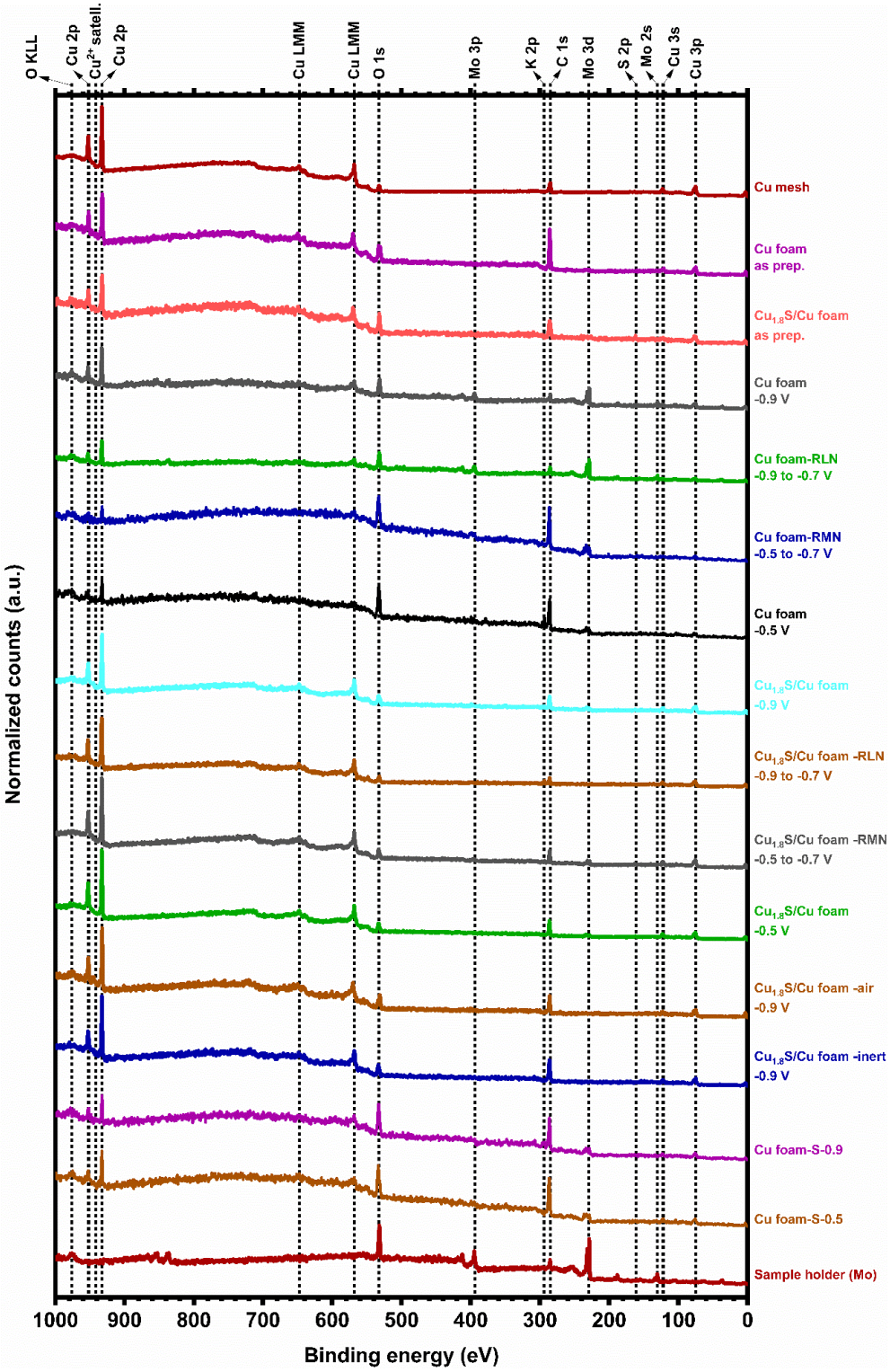

Figure S34. XPS survey spectra of all examined samples including the Mo sample holder which in some cases gave signals that appear in the samples' spectra.

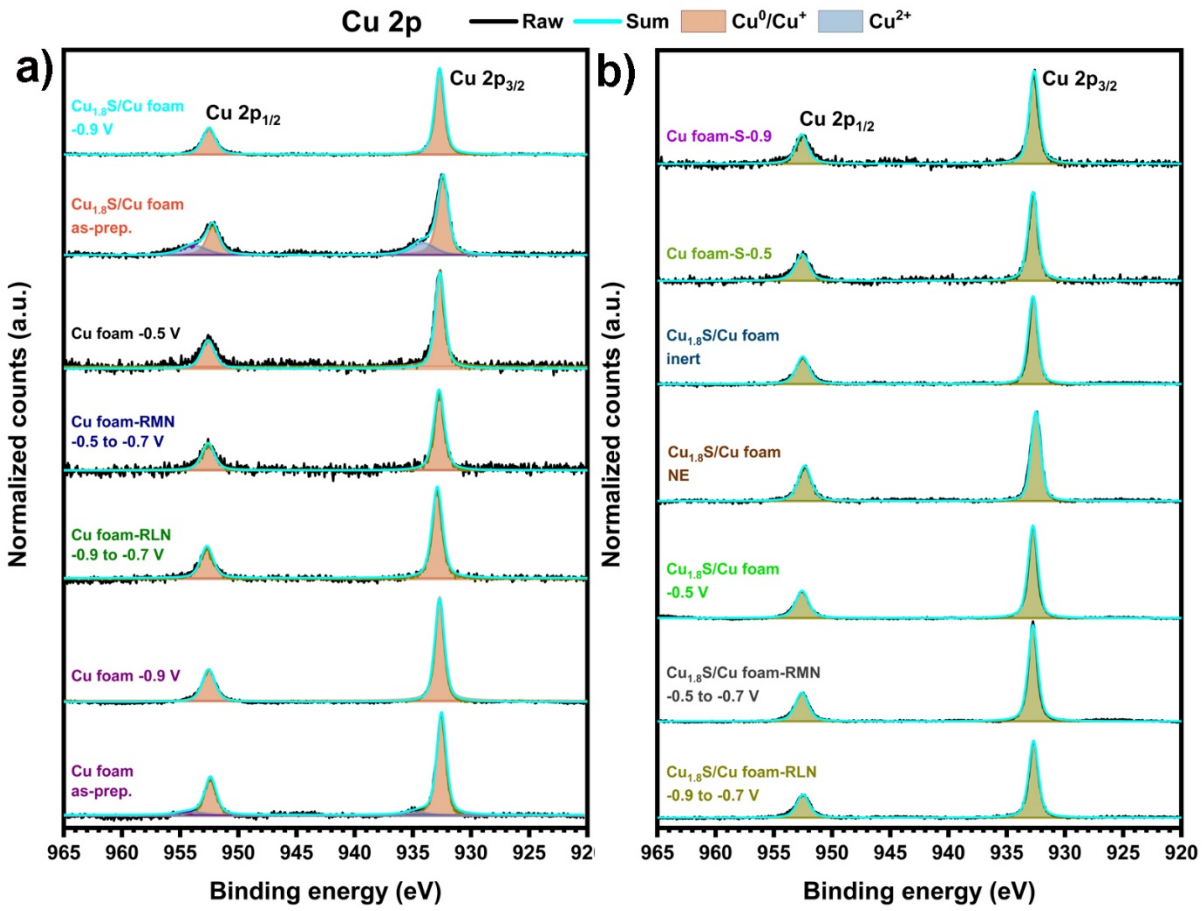

Figure S35. Cu 2p core level XPS spectra of all examined samples. The plots are divided in two graphs for better visualization.

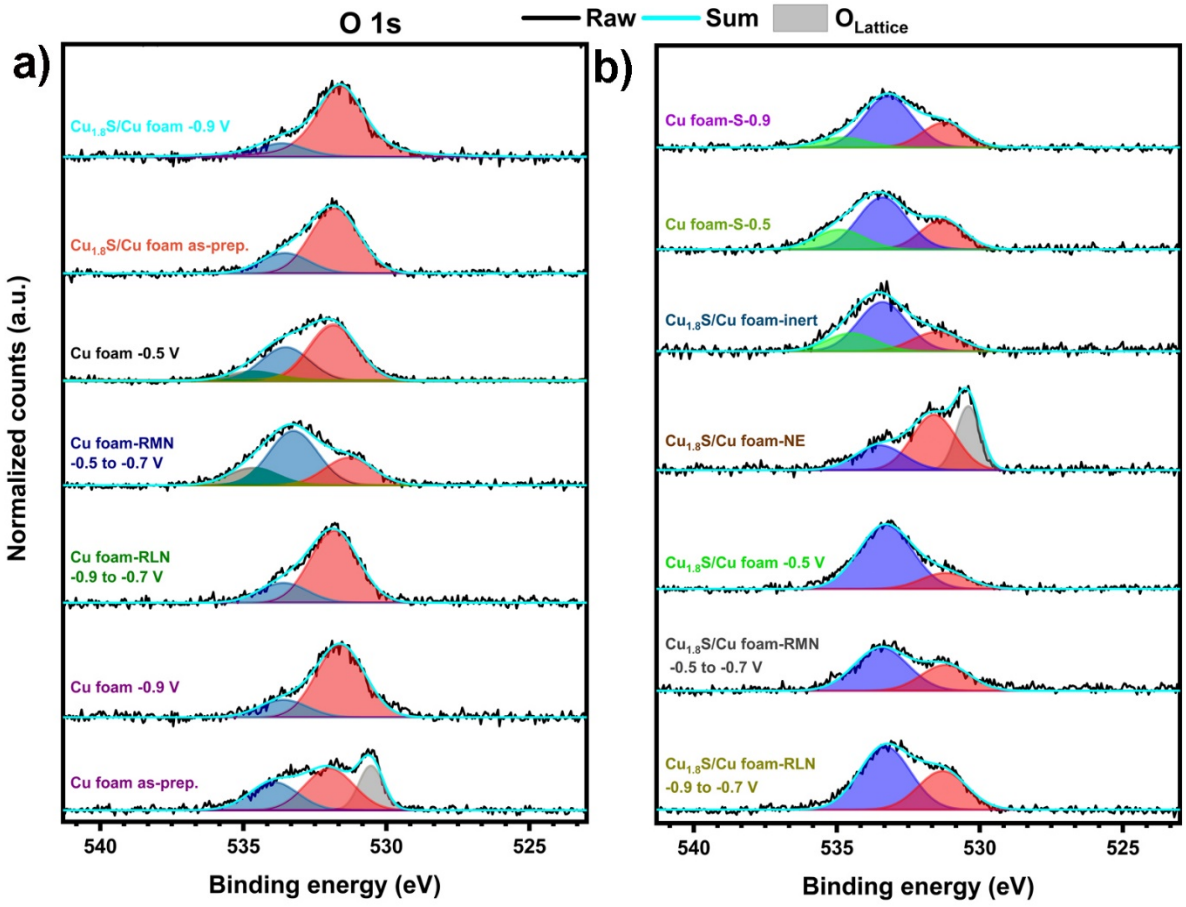

Figure S36. O 1s core level XPS spectra of all examined samples. The plots are divided in two graphs for better visualization.

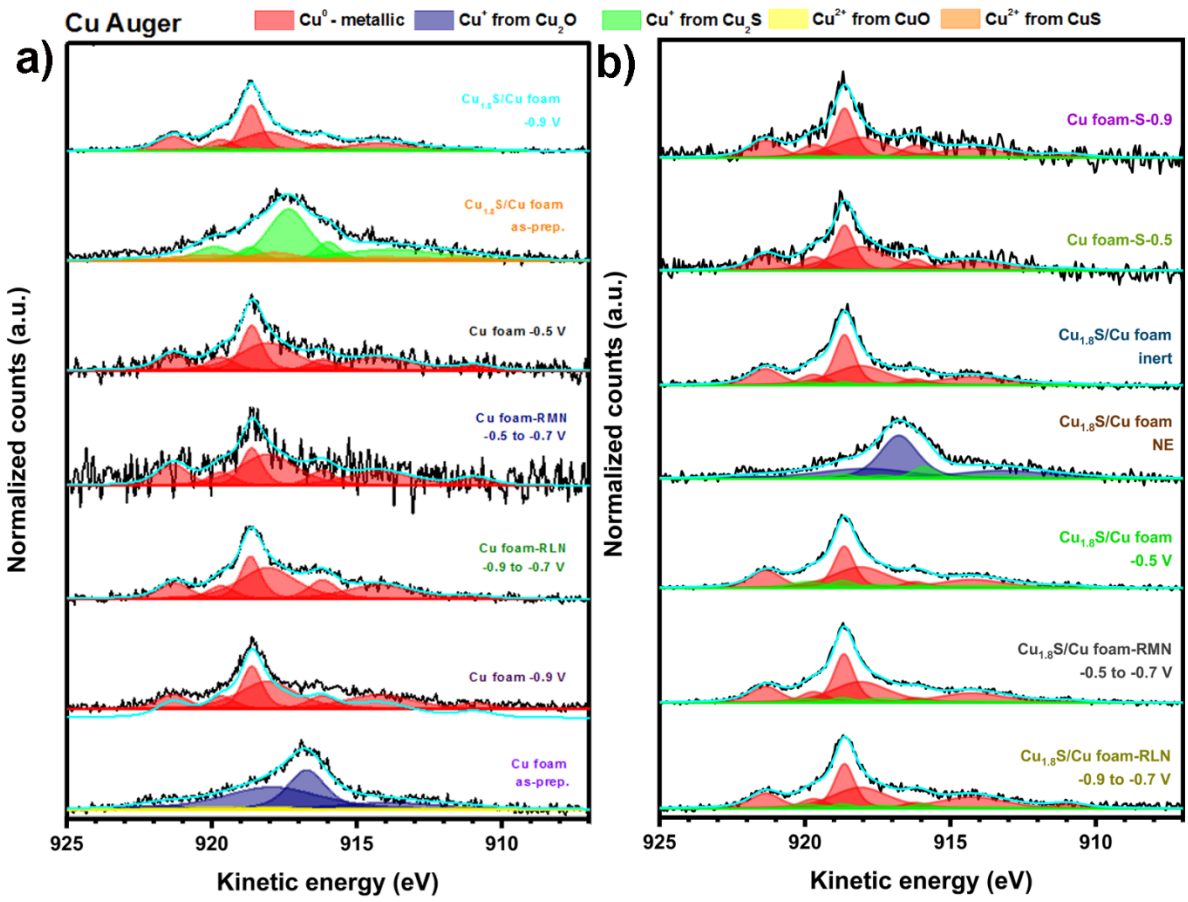

Figure S37. Cu $L_3M_{4.5}M_{4.5}$ Auger spectra of all examined samples. The plots are divided in two graphs for better visualization.

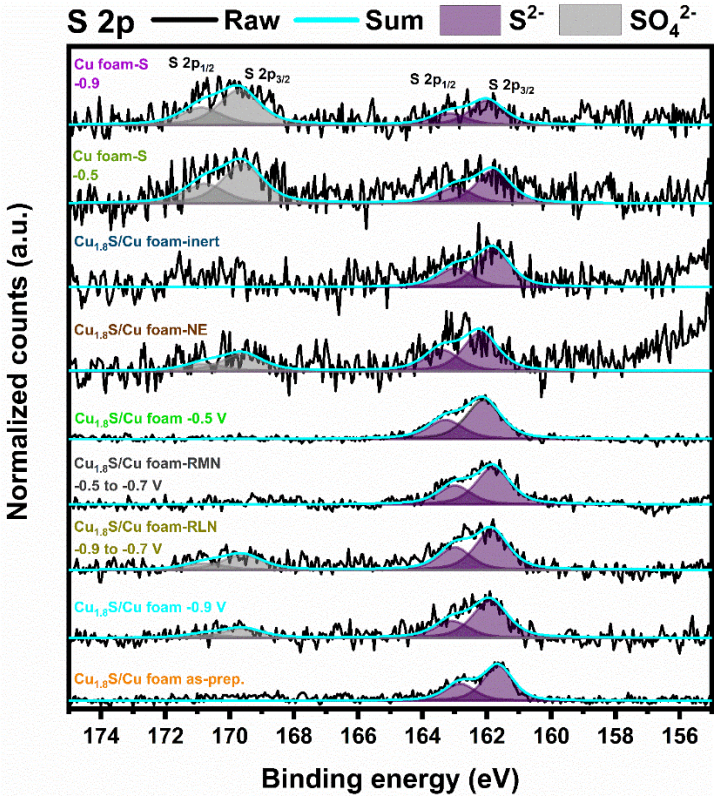

Figure S38. S 2p core level XPS spectra of the samples that contain sulfur.

Table S5. Quantification of surface species (Cu^0, Cu^+-O, Cu^+-S, Cu^{2+}-O and Cu^{2+}-S, S^{2-} and SO_4^{2-}) fractions with XPS under *ex-situ* and *quasi in-situ* conditions. The quantification of total surface Cu and sulfur species (S^{2-} and SO_4^{2-}) was conducted from the Cu 2p and S 2p core levels (Figures S35 and S38, respectively), while the quantification of the different Cu oxidation state fractions from the Cu $L_3M_{4.5}M_{4.5}$ Auger in Figure S37. The qualitative estimation of the lattice vs. adsorbed oxygen species was performed based on the O 1s core level peak position (Figure S36).

Sample	Cu^0 fraction (at.%)	Cu^+-O fraction (at.%)	Cu^+-S fraction (at.%)	Cu^{2+}-O fraction (at.%)	Cu^{2+}-S fraction (at.%)	Oxygen: lattice/ adsorbed species	S^{2-} fraction (at.%)	SO_4^{2-} fraction (at.%)
Cu foam as-prep.	N.D.	92	N.D.	8	N.A.	Lattice	N.A.	N.A.
$Cu_{1.8}S$/Cu foam as-prep.	N.D.	N.D.	75	N.D.	25	Ads.	44	N.D.
$Cu_{1.8}S$/Cu foam, 1h at –0.9 V	89	N.D.	11	N.D.	N.D.	Ads.	23.4	6.7
$Cu_{1.8}S$/Cu foam-RLN: from –0.9 to –0.7 V	90	N.D.	10	N.D.	N.D.	Ads.	21.7	9.3
$Cu_{1.8}S$/Cu foam, 1h at –0.5 V	78.5	N.D.	21.5	N.D.	N.D.	Ads.	44.5	N.D.
$Cu_{1.8}S$/Cu foam-RMN: from –0.5 to –0.7 V	86	N.D.	14	N.D.	N.D.	Ads.	12.4	N.D.
Cu foam, 1h at –0.9 V	100	N.D.	N.A.	N.D.	N.A.	Ads.	N.A.	N.A.
Cu foam-RLN: from –0.9 to –0.7 V	100	N.D.	N.A.	N.D.	N.A.	Ads.	N.A.	N.A.
Cu foam, 1h at –0.5 V	100	N.D.	N.A.	N.D.	N.A.	Ads.	N.A.	N.A.
Cu foam-RMN: from –0.5 to –0.7 V	100	N.D.	N.A.	N.D.	N.A.	Ads.	N.A.	N.A.
Cu foam-S-0.5	96.5	N.D.	3.5	N.D.	N.D.	Ads.	10.2	14.5
Cu foam-S-0.9	95	N.D.	5	N.D.	N.D.	Ads.	10.0	17.1
$Cu_{1.8}S$/Cu foam-NE –0.9 and –0.7 V, 1 h at each potential, after air exposure	N.D.	86.5	13.5	N.D.	N.D.	Lattice	7.5	3.6
$Cu_{1.8}S$/Cu foam-inert –0.9 and –0.7 V, 1 h at each potential	91.5	N.D.	8.5	N.D.	N.D.	Ads.	6.5	N.D.

N.A. - not applicable

N.D. - not detected

References

(1) Dutta, A.; Rahaman, M.; Luedi, N. C.; Mohos, M.; Broekmann, P. Morphology Matters: Tuning the Product Distribution of CO_2 Electroreduction on Oxide-Derived Cu Foam Catalysts. *ACS Catalysis* **2016**, *6* (6), 3804-3814. https://doi.org/10.1021/acscatal.6b00770.
(2) Vesztergom, S.; Dutta, A.; Rahaman, M.; Kiran, K.; Zelocualtecatl Montiel, I.; Broekmann, P. Hydrogen Bubble Templated Metal Foams as Efficient Catalysts of CO_2 Electroreduction. *ChemCatChem* **2021**, *13* (4), 1039-1058. https://doi.org/10.1002/cctc.202001145.
(3) Stojkovikj, S.; El-Nagar, G. A.; Firschke, F.; Pardo Pérez, L. C.; Choubrac, L.; Najdoski, M.; Mayer, M. T. Electrocatalyst Derived from Waste Cu–Sn Bronze for CO_2 Conversion into CO. *ACS Applied Materials & Interfaces* **2021**, *13* (32), 38161-38169. https://doi.org/10.1021/acsami.1c05015.
(4) Jay, S.; Cézac, P.; Serin, J.-P.; Contamine, F.; Martin, C.; Mercadier, J. Solubility of Elemental Sulfur in Toluene between (267.15 and 313.15) K under Atmospheric Pressure. *Journal of Chemical & Engineering Data* **2009**, *54* (12), 3238-3241. https://doi.org/10.1021/je9002256.
(5) Bagger, A.; Ju, W.; Varela, A. S.; Strasser, P.; Rossmeisl, J. Electrochemical CO_2 Reduction: A Classification Problem. *ChemPhysChem* **2017**, *18* (22), 3266-3273. https://doi.org/10.1002/cphc.201700736.
(6) Kuhl, K. P.; Cave, E. R.; Abram, D. N.; Jaramillo, T. F. New Insights into the Electrochemical Reduction of Carbon Dioxide on Metallic Copper Surfaces. *Energy & Environmental Science* **2012**, *5* (5), 7050-7059. http://dx.doi.org/10.1039/C2EE21234J.
(7) Scholten, F.; Sinev, I.; Bernal, M.; Roldan Cuenya, B. Plasma-Modified Dendritic Cu Catalyst for CO_2 Electroreduction. *ACS Catalysis* **2019**, *9* (6), 5496-5502. https://doi.org/10.1021/acscatal.9b00483.
(8) Biesinger, M. C. Advanced Analysis of Copper X-ray Photoelectron Spectra. *Surface and Interface Analysis* **2017**, *49* (13), 1325-1334. https://doi.org/10.1002/sia.6239.

CHAPTER 7. Outlook and future perspectives

View of the CO_2 electroreduction research field, summary of the Cu-Sn and Cu-S electrocatalysts study and importance of other electrocatalytic processes

The anthropogenic activities have caused continuous increase of the atmospheric CO_2 concentration leading to the climate change phenomenon. Therefore, the strive for independence of fossil fuels combustion for energy production as main source of this greenhouse gas, are urging for immediate actions toward mitigation of the CO_2 emissions, its conversion into industry/transport desirable fuels and chemicals and relying on renewable sources of energy. Hence, development of large-scale facilities for CO_2 capture from air/flue gas and its conversion into valuable products, or in more general terms integrated capture-conversion-utilization-storage systems, are required. A reasonable option is to integrate such capture-conversion-utilization-storage systems with CO_2 emission sources. For building a sustainable society in terms of energy and economy, such facilities should be powered using renewable sources of energy such as solar, wind, hydro, thermal etc. Focusing on the CO_2 conversion, it appears that the electrochemical reduction of CO_2 (CO_2ER) has many advantages over the other routes due to the direct utilization of electricity without requirements for its transformation into another type of energy e.g., heat, that can lead to energy loses and additional costs. Moreover, the electrochemically driven CO_2 conversion can be coupled with any renewable electricity sources regardless of their nature which makes this approach independent e.g., of the amount solar energy, wind, water level in hydroelectric power plants etc. Since CO_2ER is a cathodic process, an anodic counter reaction is required which in most laboratory research cases represents the oxygen evolution reaction (OER) as source of electrons and protons required for the CO_2ER itself. The development of efficient OER electrocatalyst is equally significant as the CO_2ER ones since coupling both reactions is one system that is driven by e.g., renewable solar produced electricity represents artificial photosynthesis, which by concept is mimicking the nature with ultimate goal of closing the carbon cycle. Focusing on research regarding the possibilities of coupling other oxidation reactions for electrosynthesis of valuable products is of great importance.

The electrochemical conversion of CO_2 approach, even though seriously developing in the last 35 years, suffers from challenges of various nature. The Cu electrocatalysts have been extensively studied since this metal has an intrinsic property to catalyze CO_2ER into various multi electron/H^+ products with industrial/transport value as chemical feedstocks and fuels, that is hydrocarbons, alcohols etc. Yet, the advantage of CO_2ER into various products is also a disadvantage that makes the Cu electrocatalysts generally nonselective and moreover the

issues with suppression of the competitive hydrogen evolution reaction (HER) in aqueous electrolytes require post-electrolysis separation steps for application in practice, thus leading to additional costs. In addition to the previously stated, catalysts stability issues, effect of impurities, problems with rescaling the experiments from laboratory electrolysis cells into reactors that are supposed to achieve high current densities i.e., industrial relevant CO_2 to product reaction rates, various parameters, experimental conditions, reactor configurations, designs and engineering challenges etc., indeed hamper and delay the full commercial application of the CO_2ER. Therefore, under the climate change circumstances requiring urgent large-scale CO_2 conversion application, it is important to emphasize that the two electron/H^+ CO_2ER into CO or $HCOO^-$ can reach significant selectivity for these products, thus avoiding the additional purification steps. Moreover, CO_2ER into CO or $HCOO^-$ under specific cost of electricity and industrially relevant current densities appears to be feasible, based on various techno- economic analyses. Thus, it is anticipated that most of the existing pilot-plant projects, are indeed focused on CO_2ER into CO and $HCOO^-$ or CO_2ER/HER to syngas. Furthermore, the efforts for production of the industry/transport valuable fuels and chemicals can be achieved via converting the CO_2ER produced CO into further reduced products in a second step(s), not necessarily electrochemical, for example in biochemical processes or hydrogenation using thermocatalysis approaches. On the other hand, the HCOOH/$HCOO^-$ are important chemical feedstocks in various industrial fields and moreover can possibly substitute H_2 in fuel cells. However, efficient, stable, cost-effective, earth abundant etc. electrocatalyst materials are prerequisite for feasible CO_2ER into CO and $HCOO^-$. Various electrocatalysts can be used for this purpose, yet considering the cost and abundance of the elements, it can be stated that the Cu-rich or Sn low Cu-Sn materials appear to be optimal solution for CO_2ER into CO, while the Cu-S based ones for production of $HCOO^-$, which makes these materials inspiring and significant to be more thoroughly examined for this purpose, especially under *in-situ* conditions.

Studying and understanding the composition-structure-CO_2ER activity relations on the Cu-Sn and Cu-S materials is important for the catalysts design and optimization of the experimental conditions and parameters in order to tackle the challenges for efficient CO_2ER, aiming towards future large-scale application. Therefore, in the scope of this thesis, the Cu-Sn electrocatalysts were studied using x-ray spectroscopy techniques under various conditions (*ex-situ* soft and *in-situ* hard x-ray XAS, and *quasi* in-situ XPS) and other characterization techniques, and computational modelling to reveal information regarding the catalytic processes relevant Cu:Sn surface composition, oxidation states and favourable reaction pathways. Regarding the challenges arising from the x-ray spectroscopy methods, it is important to summarize that even though the soft-ray XAS is able to probe the surface of the

Cu-Sn electrocatalysts, it is limited to *ex-situ* examination, while the hard x-rays XAS can be utilized under *in-situ* conditions but this technique is rather bulk sensitive. The significance of probing the electrocatalyst materials surface under operating conditions is important for preserving the oxidations states of the Cu and Sn active sites, having in mind that metallic or partially oxidized Cu and Sn are prone towards further surface oxidation when exposed to air, post-electrolysis, hence important electronic structure information can be lost. Therefore, the compromise was found in the surface sensitive technique XPS applied under the *quasi in-situ* conditions, that is electrolysis in inert atmosphere and sample transfer in vacuum, to preserve the oxidation states of the Cu and Sn active sites. After this technique was successfully utilized for studying the Cu-Sn composition-structure-activity relations, it was applied for the same purpose in the case of the Cu-S electrocatalysts.

The results from the study of the Cu-Sn electrocatalysts, synthesized with nanowires morphology, showed that the CO selective materials with low Sn content resemble metallic Cu and SnO_x surface species supporting the Sn to Cu charge redistribution from the fact that the surface Sn is oxidized and not metallic. These oxidized or partially oxidized Sn sites are found to destabilize *CO intermediate that is expected to be bound on the Cu sites hence, favouring its easier desorption and CO gas evolution, compared to the surface of pristine Cu where the *CO intermediate is bound stronger and can undergo subsequent reduction in multielectron/H^+ steps. The increase of the Sn content via synthesis of Sn rich Cu-Sn electrocatalysts and when examined under more negative applied potentials show that the SnO_x readily reduce hence, an increasement of the metallic Sn sites fraction can be observed. This increase of the metallic Sn sites is diminishing the charge redistribution effect, leading to altering the CO_2ER selectivity from CO into $HCOO^-$ production via the *OCHO* intermediate pathway. The enhancement of the $HCOO^-$ selectivity is accompanied with suppression of the HER due to stronger binding of the *OCHO* compared to *H intermediate on metallic Sn sites.

Even though both Cu rich (Sn low) and Sn rich (high) Cu-Sn nanowires electrocatalysts can reach high selectivity for CO and $HCOO^-$, respectively, the synthesis method for these materials in this study utilizes atomic layer deposition (ALD) which makes it rather sophisticated, moreover expensive and time consuming. Besides that, both Cu and Sn are endangered elements in terms of future supply, hence synthesizing CO selective Cu rich Cu-Sn electrocatalyst via recycling or repurposing waste materials that contain both Cu and Sn can be a feasible strategy for sustainable supply of these elements and for the sake of minimizing and hopefully terminating their extraction from Earth's crust. Yet, having knowledge about the optimal Cu:Sn composition for CO selective Cu rich Cu-Sn electrocatalysts, from the previous study and literature sources, a successful electrochemical deriving of such CO_2ER to CO catalyst material with foam morphology from waste technical grade purity Cu-Sn bronze was achieved, as described in the second study of this thesis. The CO_2ER to CO selectivity on

this waste bronze derived Cu-Sn catalyst is comparable with other CO selective electrocatalysts prepared from high purity precursors thus showing an example that recycling/repurposing wastes can be promising approach to prepare catalyst materials with avoiding purification costs.

Regarding CO_2ER to $HCOO^-$ selective catalysts, it was stated above that the Cu-S based materials appear to be the most optimal option for this purpose, even though the Sn rich Cu-Sn ones can attain equivalent activity under identical applied potentials. This is because both Cu and Sn are elements with jeopardized future supply, while S is not, and moreover Cu and S are cheaper and more abundant than Sn. Therefore, the last study of this thesis describes investigation of the relations between the composition-structure and CO_2ER to $HCOO^-$ activity on Cu-S catalysts with foam morphology that are prepared via simple, cheap and fast synthesis method. The synthesis method is composed of two steps including electrochemical deposition of Cu foam and its subsequent sulfidation with sulfur dissolved in toluene at room temperature. This method is avoiding utilization of extremely toxic precursors, long synthesis times and high temperatures, that in many cases can be typical for the methods for preparation of copper sulfides intended for specific application. The results from the electrocatalysts' Cu and S surface speciation with *quasi in-situ* XPS showed presence of Cu^+ sites that are stabilized by negatively charged residual sulfur species suggesting that complete reduction of the material does not occur even at the most negative applied potential of –0.9 V vs. RHE, while only metallic Cu was found when pristine Cu foam was studied under identical conditions. The Cu^+ sites resemble oxoplilic nature, hence supporting the mechanism that occurs via favourable binding of the *OCHO* intermediate formed in first electron/H^+, subsequently transforming into $HCOO^-$, in a second electron step. Furthermore, it is found that the $HCOO^-$ selectivity enhancement is affected by the Cu:S surface composition and somehow related with electrode-electrolyte interface effects such as local pH change when the materials are subjected to applied potential of –0.9 V vs. RHE. Under these conditions besides S^{2-}, presence of unexpected SO_4^{2-} surface species is observed. These effects are of dynamic nature and not fully understood which is indeed motivating for further studies using other surface and electrode-electrolyte interface sensitive techniques under *in-situ* conditions, such as Raman and infrared spectroscopies.

The CO_2ER activity on the waste bronze derived Cu-Sn and on the Cu-S foams catalysts were examined under laboratory scale conditions in which industrially relevant current densities cannot be achieved due to the limitations discussed in the introduction of this thesis. Namely, in order to achieve the current density requirements, the future challenges include adapting and optimizing the synthesis approaches for loading these electrocatalyst materials

on gas-diffusion electrodes (GDE) and performing electrolysis in gas-diffusion electrolyzers. Achieving this goal is far from trivial hence, enormous research efforts will be required.

A very important industrial process, that generates CO_2 as a by-product thus contributing to the greenhouse emissions is the synthesis of NH_3 as a basic and most important precursor of fertilizers (nitrates, ammonium salts, urea etc.) that support the global food production. Namely, NH_3 is still mainly produced by the unfortunately not so efficient and energy demanding Haber-Bosch process based on reaction between N_2 and H_2.[269] The industrial production of H_2 required for the NH_3 synthesis is based on reforming, pyrolysis and partial oxidation processes utilizing fossil oil, gas and coal, as precursors. Hence, full commercial development of technologies for production of `green` H_2 such as the renewable energy driven water splitting is one of the possible solutions for providing sustainable H_2 supply. Moreover, efficient renewable energy driven electrochemical reduction of nitrogen (N_2ER) into NH_3 could possibly emerge as an alternative for synthesis of this very important chemical feedstock.[269] Finally, tandem CO_2 conversion and nitrogen fixation via CO_2/N_2 co-electrolysis leading to urea synthesis[270] arises as an ideal concept that utilizes CO_2 for fertilizer production. If this concept develops as very efficient, hence large-scale applied in future, ultimately renewable energy driven and based on utilization of low-cost and recyclable catalyst materials prepared via cheap and simple synthesis methods, it could become one of greatest accomplishments in the pathway towards full sustainability of the human society.

List of abbreviations in alphabetical order

- ADP — adenosine diphosphate
- AFM — atomic force microscopy
- Ag/AgCl — silver/silver chloride reference electrode (filled with 3 $mol \cdot dm^{-3}$ KCl)
- ALD — atomic layer deposition
- ATP — adenosine triphosphate
- BAM — *German*: Bundesanstalt für Materialforschung und -prüfung, *English*: Federal institute for materials research and testing
- BE — binding energy
- BSE — backscattered electron(s)
- BESSY II — *German:* Berliner Elektronenspeicherring-Gesellschaft für Synchrotronstrahlung, *English*: Berlin electron storage ring – Society for synchrotron radiation
- CA — chronoamperometry
- CB — conduction band
- CE — counter electrode
- COR — electrochemical reduction of CO
- CO_2ER — electrochemical reduction of CO_2
- CuNW — copper nanowires
- CuNW-Sn — copper nanowires functionalized with Sn
- CuNW-Sn_{HIGH} — copper nanowires functionalized with 182 ALD cycles of SnO_2
- CuNW-Sn_{LOW} — copper nanowires functionalized with 15 ALD cycles of SnO_2
- CV — cyclic voltammetry
- DEMS — differential electrochemical mass spectrometry
- DFT — density functional theory
- DHBT — dynamic hydrogen (H_2) bubbling template
- DFFC — direct formate fuel cell
- DL — double layer
- DSC — differential scanning calorimetry
- EASA — electrochemically active surface area

- EC-MS electrolysis coupled with mass spectrometry
- EDX energy dispersive x-ray spectrometry
- EF-TEM energy filtered transmission electron microscopy
- EXAFS extended x-ray absorption fine structure
- FE faradaic efficiency
- FIB focused ion beam (ablation)
- FTIR Fourier-transform infrared spectroscopy
- GC gas chromatography
- GDE gas-diffusion electrode
- GI-XRD grazing-incidence x-ray diffraction
- HER hydrogen evolution reaction
- HR-TEM high resolution transmission electron microscopy
- HPLC high-performance (pressure) liquid chromatography
- ICP-OES inductively coupled plasma-optical emission spectrometry
- ILs ionic liquids
- KE kinetic energy
- LCA(F) linear combination analysis (fitting)
- LDPE low-density polyethylene
- LSV linear sweep voltammetry
- MOF metal organic frameworks
- MS mass spectrometry
- NADPH nicotinamide adenine dinucleotide phosphate in reduced form
- $NADP^+$ nicotinamide adenine dinucleotide phosphate in oxidized form
- N_2ER electrochemical reduction of nitrogen
- NW nanowires
- OD-Cu oxide-derived Cu
- OER oxygen evolution reaction
- PM particulate matter (PM_{10} and $PM_{2.5}$)
- PTFE polytetrafluoroethylene
- RDS rate determining step

- RE reference electrode
- RHE reversible hydrogen electrode
- RSF relative sensitivity factor
- RSRF relative surface roughness factor
- SAED selected area electron diffraction
- SE secondary electron(s)
- SHE standard hydrogen electrode
- SEM scanning electron microscopy
- SR scan rate
- TEM transmission electron microscopy
- TEY total electron yield
- TGA thermogravimetric analysis
- VB valence band
- vs. versus
- WE working electrode
- WF work function
- XANES x-ray absorption near edge structure
- XAS x-ray absorption spectroscopy
- XPS x-ray photoelectron spectroscopy
- XRD x-ray diffraction
- XRF x-ray fluorescence spectroscopy

List of published papers included in the thesis

- L.C. Pardo Pérez, A. Arndt, **S. Stojkovikj**, I.Y. Ahmet, J.T. Arens, F. Dattila, R. Wendt, A. Guilherme Buzanich, M. Radtke, V. Davies, K. Höflich, E. Köhnen, F. Tockhorn, R. Golnak, J. Xiao, G. Schuck, M. Wollgarten, N. López, M.T. Mayer, Determining Structure-Activity Relationships in Oxide Derived Cu–Sn Catalysts During CO_2 Electroreduction Using X-Ray Spectroscopy. *Adv. Energy Mater*. *12*, **2022**, 2103328. DOI: https://doi.org/10.1002/aenm.202103328

- **S. Stojkovikj**, G.A. El-Nagar**,** F. Firschke, L.C. Pardo Pérez, L. Choubrac, M. Najdoski, M.T. Mayer, Electrocatalyst Derived from Waste Cu–Sn Bronze for CO_2 Conversion into CO, *ACS Appl. Mater. Interfaces, 13(32)*, **2021**, 38161–38169. DOI: https://doi.org/10.1021/acsami.1c05015

Manuscript in preparation included in the thesis

- **S. Stojkovikj**, G. A. El-Nagar, S. Gupta, M. Najdoski, V. Koleva, T. Tzanoudakis, F. Firschke, P. Bogdanoff, M. T. Mayer, Facile method for synthesis of Cu_xS catalysts and study of various effects on the selectivity for electrochemical conversion of CO_2 into formate.

List of publications from the Doctoral period that are not in the scope of the thesis

- T. Boettcher, **S. Stojkovikj**, P. Khadke, U. Kunz, M.T. Mayer, C. Roth, W. Ensinger, F. Muench, Electrodeposition of Palladium-Dotted Nickel Nanowire Networks as a Robust Self-Supported Methanol Electrooxidation Catalyst. *J. Mater. Sci. 56*, **2021**, 12620–12633. https://doi.org/10.1007/s10853-021-06088-6

- Abouserie, G.A. El-Nagar, B. Heyne, C. Günter, U. Schilde, M.T. Mayer, **S. Stojkovikj**, C. Roth, A. Taubert, Facile Synthesis of Hierarchical CuS and $CuCo_2S_4$ Structures from an Ionic Liquid Precursor for Electrocatalysis Applications, *ACS Appl. Mater. Interfaces, 12(47)*, **2020**, 52560–52570. https://doi.org/10.1021/acsami.0c13927

Curriculum Vitae

Personal information

- First name and surname: Sasho Stojkovikj

- Languages: Macedonian (native), English, Serbian, Croatian, basic Slovenian and basic German.
- Private e-mail address: sashostojkovikj@gmail.com
- Helmholtz-Zentrum Berlin e-mail address: sasho.stojkovikj@helmholtz-berlin.de
- Freie Universität Berlin e-mail address: sashostojk91@zedat.fu-berlin.de
- Helmholtz-Zentrum Berlin Business card: https://www.helmholtz-berlin.de/pubbin/vkart.pl?v=nnazo
- Google Scholar: https://scholar.google.de/citations?user=FyQQhX8AAAAJ&hl=en
- ResearchGate: https://www.researchgate.net/profile/Sasho_Stojkovikj2
- ORCID: https://orcid.org/0000-0002-3346-2143

Education

- (1997-2006): Elementary, primary and secondary school ``Dimo Hadzi-Dimov`` - Skopje.
- (2006-2010): High School of Chemistry and Chemical technology ´´Marija Kiri - Sklodovska´´ - Skopje (as the best student).
- (2010-2014): **BSc in Chemistry - Applied Chemistry**, Institute of Chemistry, Faculty of Natural Sciences and Mathematics, Ss. Cyril and Methodius University – Skopje (best GPA 10.00/10.00 and the best student at the Faculty of Natural Sciences and Mathematics in Skopje).
  Title of the Diploma work in English: Chemical deposition and characterization of electrochromic potassium manganese oxide hydrate thin films and of manganese(II) carbonate thin films that are transformed into electrochromic materials. Supervisor: Prof. Dr. Metodija Najdoski.
- (2014-2016): **MSc in Chemistry - Applied Chemistry**, Institute of Chemistry, Faculty of Natural Sciences and Mathematics, Ss. Cyril and Methodius University – Skopje (GPA 10.00/10.00).
  Title of the Master thesis in English: Design of modified electrodes with $MnCO_3$ in the role of amperometric sensors for hydrogen peroxide. Supervisor: Prof. Dr. Metodija Najdoski.
  (2018-2022): Doctoral researcher at the Young Investigator Group Electrochemical Conversion, Helmholtz-Zentrum Berlin für Materialen und Energie GmbH. Enrolled as Doctoral student at the Institut für Chemie und Biochemie, Freie Universität Berlin. Supervisor: Dr. Matthew Mayer.

Field of research and interest

- Electrochemical conversion of CO_2 (Doctoral research).
- Other electrochemical processes: Oxygen evolution reaction (OER) and electrooxidation.
- Development of methods for chemical synthesis of thin solid films of inorganic compounds and application for electrochromic materials and sensors.
- Design of experiments and apparatuses for application in microscale experimentation.
- Design of chemical methods for visualization of latent fingerprints.
- Interested in development of methods for chemical synthesis with potential application in large scale industrial processes.

Career and work experience

- >15 years of experience in chemical laboratories (since the start of high school in 2006).
- Practical internship - one month in 2008 and one month in 2009 in OKTA Crude Oil Refinery – Skopje.
- Chemist at Promis Ltd. Skopje, Company for construction, trade, and services, import-export: (employed from 12.11.2014 to 20.07.2015).
- Chemical analyst at Euromak-Kontrol Ltd. Skopje, Macedonia, Company for chemical analysis, quality control, quantity control and inspection of goods (employed from 21.07.2015 to 14.03.2016).
- Chemical research analyst at PRG Ltd. Skopje, Metal refinery for tantalum and niobium in Gostivar, (employed from 15.03.2016 to 09.08.2016).
- Chemical analyst, Inspector of quality and quantity control of petroleum and petroleum derivates and Head of Team for measurements of emissions of air pollutant from point sources (stack emissions) at Euromak-Kontrol Ltd. Skopje, Company for chemical analysis, quality control, quantity control and inspection of goods (employed from 10.08.2016 to 31.10.2017).
- Doctoral researcher at the Young Investigator Group Electrochemical Conversion, Helmholtz-Zentrum Berlin für Materialen und Energie GmbH, Hahn-Meitner-Platz 1, D-14109, Berlin (Employed from 08.01.2018).
- Teaching assistant at the Freie Universität Berlin, Solids and interfaces course, Winter semester 2021/2022.

Membership in international projects (before starting the Doctoral research)

- Macedonian – Austrian bilateral project (2009-2013): Design of new, cheap methods for chemical deposition of inorganic thin films, their electrochemical characterization and application as biosensors and electrochromic devices, under supervision of Prof. Dr. Metodija Najdoski.
- Macedonian – Bulgarian bilateral project – collaboration between Macedonian Academy of Sciences and Arts and Bulgarian Academy of Sciences (2014-2016): Preparation and characterization of electrochromic thin films of vanadium oxides.

Awards

- Award from the Royal Society of Chemistry – Electrochemistry Group for One of the Best Poster Prizes, for the poster presentation ´´Repurposing Waste Cu–Sn Bronze for Selective CO_2 Electroreduction into CO´´, RSC Electrochemistry Group's Electrochemistry 2021 virtual conference, September 7-8th 2021.
- Several shared international awards including Golden and Silver Medals (in 2017) for the Patent titled ´´Production of a Simple Defoaming Agent´´, Application number: 2016/476, Registration number: 7473, State Office of Industrial Property of the Republic of North Macedonia.
- Award (in 2016): For winning the 1st Prize for an oral presentation at the Workshop: From Molecules to Functionalized Materials, 1-5th September 2016, Ohrid, Macedonia.
- Award-Certificate of Merit (in 2014): For the Best Faculty Student, with GPA 10.00/10.00, at the Institute of Chemistry and the Faculty of Natural Sciences and Mathematics, for achieved continued success during the study period from 2010 to 2014.
- Award (in 2014): For winning the 1st Prize for an oral presentation at the Workshop: From Molecules to Functionalized Materials, 7-9th September 2014, Ohrid, Macedonia.
- Award (in 2013): For Excellent poster presentation at the 15th International Workshop on Nanoscience and Nanotechnology, 21-23rd November 2013, Sofia, Bulgaria.
- Award (in 2010): For the Best High School Student – from the Mayor of the City of Skopje.
- Award Gold Medal (in 2009): „Ekonova 2009", at the VIIth International Exhibition of Inventions, Technical Improvements, New Products and Creation of Youth, for the innovation: ´´And another way to purify wastewater´´, 13-17th October 2009, Skopje, Macedonia.

Membership in science related societies

- Member of the Society of Chemists and Technologists of Macedonia (SCTM) since 2016.

Organization of science related meetings

- Co-organizer or the MatSEC Young Scientists Conference (within the MatSEC Graduate School at Helmholtz-Zentrum Berlin für Materialen und Energie) that took place in Chorin, Germany on February 11th, 2020.

Courses, workshops, seminars, colloquiums, tutoring of internship students and other activities during the Doctoral research period (2018-2022)

- Attended the 1st X-ray diffraction school, May 14-18th 2018, at the Helmholtz-Zentrum Berlin für Materialen und Energie, Lise Meitner Campus in Berlin-Wannsee.
- Talk at the MatSEC Colloquium (within the MatSEC Graduate School at Helmholtz-Zentrum Berlin für Materialen und Energie), November 8th 2018, HZB Lise Meitner Campus in Berlin-Wannsee.
- Attended German language courses in 2018 and 2019.
- Talk at the MatSEC Retreat (within the MatSEC Graduate School at Helmholtz-Zentrum Berlin für Materialen und Energie), January 14th and 15th 2019, Chorin, Germany.
- Attended the Applied Electrochemistry (Angewandte Elektrochemie) Course, Summer Semester 2019 at the Freie Universität Berlin. Lecturer: Dr. Matthew Mayer.
- Tutoring of Master student's internship project at the Young Investigator Group Electrochemical Conversion, Helmholtz-Zentrum Berlin für Materialen und Energie, Winter Semester 2019/2020.
- Student-assistant at the nanoGE Fall Meeting, November 4th-8th 2019, Berlin.
- Talk at the MatSEC Retreat (within the MatSEC Graduate School at Helmholtz-Zentrum Berlin für Materialen und Energie), February 12th and 13th 2020, Chorin, Germany.
- Talk at the Institute of Solar Fuels - General Institute Meeting, Helmholtz-Zentrum Berlin für Materialen und Energie, February 19th 2020.
- Tutoring of a second Master student's internship at the Young Investigator Group Electrochemical Conversion, Helmholtz-Zentrum Berlin für Materialen und Energie, Summer Semester 2020 and Winter Semester 2020/2021.
- Online talk at the Joint Seminar between the Young Investigator Group Electrochemical Conversion (Group leader: Dr. Matthew Mayer), Helmholtz-Zentrum Berlin für Materialen und Energie and the Group of Prof. Dr. Peter Broekmann, University of Bern, Switzerland, August 25th 2020.
- Attended the Online Good Scientific Practice Course, organized by the Helmholtz-Zentrum Berlin für Materialen und Energie and given by a certified trainer on October 8-9th 2020.

- Talk at the Online MatSEC Colloquium (within the MatSEC Graduate School at Helmholtz-Zentrum Berlin für Materialen und Energie), November 30th and December 1st 2020, HZB Lise Meitner Campus in Berlin-Wannsee.
- Attended the Online Transferable skills training: Career and Leadership, supported by the Helmholtz Association, March 2nd 2021.
- Involved in preparation and online presentation of the research conducted at the Young Investigator Group Electrochemical Conversion, at the Long Night of Sciences, organized by Helmholtz-Zentrum Berlin für Materialen und Energie, June 5th 2021. https://www.helmholtz-berlin.de/appimages/360/tour-de/hzb-elektrochemische_umwandlung/index.html
- Attended the Nanospectroscopy course at Helmholtz-Zentrum Berlin/Humboldt Universität zu Berlin (online), Sumer Semester 2021. Lecturer: Prof. Dr. Simone Raoux.
- Presentation of the research conducted at the Young Investigator Group Electrochemical Conversion, Helmholtz-Zentrum Berlin für Materialen und Energie in the scope of the Virtual Guided Tour for members from the Young German Physics Society (Junge Deutsche Physikalische Gesellschaft), August 27th 2021.
- Presentation of the research conducted at the Young Investigator Group Electrochemical Conversion, Helmholtz-Zentrum Berlin für Materialen und Energie in the scope of the Guided Tour for high school students, October 14th 2021.
- Online presentation of the research conducted at the Young Investigator Group Electrochemical Conversion, Helmholtz-Zentrum Berlin für Materialen und Energie, at the Berlin Science Week, Virtual Guided Tour: Electrifying Carbon, November 9th 2021.
- Responsible for instrument (gas chromatograph) at the Young Investigator Group Electrochemical Conversion, Helmholtz-Zentrum Berlin für Materialen und Energie since 2018 and involved in setting the laboratory since the start of the Doctoral research period.

Total list of publications (2010-2022)

1. L.C. Pardo Pérez, A. Arndt, **S. Stojkovikj**, I.Y. Ahmet, J.T. Arens, F. Dattila, R. Wendt, A. Guilherme Buzanich, M. Radtke, V. Davies, K. Höflich, E. Köhnen, F. Tockhorn, R. Golnak, J. Xiao, G. Schuck, M. Wollgarten, N. López, M.T. Mayer, Determining Structure-Activity Relationships in Oxide Derived Cu–Sn Catalysts During CO_2 Electroreduction Using X-Ray Spectroscopy. *Adv. Energy Mater*. *12*, **2022**, 2103328. https://doi.org/10.1002/aenm.202103328
2. **S. Stojkovikj**, G.A. El-Nagar**,** F. Firschke, L.C. Pardo Pérez, L. Choubrac, M. Najdoski, M.T. Mayer, Electrocatalyst Derived from Waste Cu–Sn Bronze for CO_2 Conversion into CO, *ACS Appl. Mater. Interfaces, 13(32)*, **2021**, 38161–38169. https://doi.org/10.1021/acsami.1c05015

3. T. Boettcher, **S. Stojkovikj**, P. Khadke, U. Kunz, M.T. Mayer, C. Roth, W. Ensinger, F. Muench, Electrodeposition of Palladium-Dotted Nickel Nanowire Networks as a Robust Self-Supported Methanol Electrooxidation Catalyst. *J. Mater. Sci. 56*, **2021**, 12620–12633. https://doi.org/10.1007/s10853-021-06088-6

4. А. Андоновски, **С. Стојковиќ**, С. Оклевски, М. Најдоски, Визуелизација на латентни отпечатоци од прсти на неиспукани куршуми со хемиска депозиција на олово(II) сулфид, Студентска конференција на младите уметници и научници СКУН, Скопје, 13ти-14ти октомври 2020, Зборник на трудови, **2021**, 31–43. (**Translated in English:** A. Andonovski, **S. Stojkovikj**, S. Oklevski, M. Najdoski, Visualization of Latent Fingermarks on Unfired Cartridge Cases via Chemical Deposition of Lead(II) Sulfide*, Student Conference of Young Artists and Scientists SKUN, 13th and 14th October 2020, Skopje*, *Proceedings*, **2021**, 31–43). http://www.tmf.ukim.edu.mk/Data/aktuelnosti/%d0%a1%d0%9a%d0%a3%d0%9d-%d0%97%d0%91%d0%9e%d0%a0%d0%9d%d0%98%d0%9a-2021.pdf

5. A. Abouserie, G.A. El-Nagar, B. Heyne, C. Günter, U. Schilde, M.T. Mayer, **S. Stojkovikj**, C. Roth, A. Taubert, Facile Synthesis of Hierarchical CuS and $CuCo_2S_4$ Structures from an Ionic Liquid Precursor for Electrocatalysis Applications, *ACS Appl. Mater. Interfaces, 12(47)*, **2020**, 52560–52570. https://doi.org/10.1021/acsami.0c13927

6. M. Najdoski, S. Oklevski, S. Demiri, S. **Stojkovikj**, Cuprous Sulfide Deposition Method for Visualization of Latent Fingermarks on Unfired Cartridge Cases, *Journal of the Chinese Chemical Society, 67(8)*, **2020**, 1415–1422. https://doi.org/10.1002/jccs.202000034

7. **S. Stojkovikj,** S. Oklevski, O.P. Jasuja, M. Najdoski, Visualization of Latent Fingermarks on Thermal Paper: A New Method based on Nitrogen Dioxide Treatment**,** *Forensic Chemistry*, 17, **2020**, 100196. https://doi.org/10.1016/j.forc.2019.100196 (**In addition to this article:** Corrigendum to "Visualization of Latent Fingermarks on Thermal Paper: A New Method based on Nitrogen Dioxide Treatment" [*Forensic Chem.* 17, **2020**, 100196], *Forensic Chemistry*, *18*, **2020**, 100220. https://doi.org/10.1016/j.forc.2020.100220).

8. **S. Stojkovikj,** M. Najdoski**,** B. Sefer, V. Mirčeski, Non–Enzymatic Amperometric Sensor for H_2O_2 based on $MnCO_3$ Thin Film Electrodes, *Croatica Chemica Acta*, *91(4)*, **2018**, 567–575. https://doi.org/10.5562/cca3424

9. M. Najdoski, **S. Stojkovikj**, S. Oklevski, Chemical Method for Processing of Sebaceous Fingerprints on Unfired Cartridge Cases by Potassium Birnessite Deposition, *Journal of Forensic Identification, 67(2)*, **2017**, 227–242.

10. M. Najdoski, V. Koleva, **S. Stojkovikj**, T. Todorovski, Electrochromic Thin Films of Sodium Intercalated Vanadium(V) Oxide Xerogels: Chemical Bath Deposition and Characterization, *Surface and Coatings Technology*, *277(15)*, **2015**, 308–317. https://doi.org/10.1016/j.surfcoat.2015.07.041

11. **S. Stojkovikj**, V. Koleva, M. Najdoski, Chemical Deposition of Nano-Sized Electrochromic Thin Films of $Na_{0.33}V_2O_5 \cdot H_2O$ Xerogels, *Nanoscience & Nanotechnology - Nanostructured materials, application, and innovation transfer*, *14*, **2014**, 67–69.
12. M. Najdoski, **S. Stojkovikj**, A Simple Microscale Gas Generation Apparatus (Sencillo aparato de generación de gas para los experimentos de microescala), *Journal of Science Education (Revista de Educación en Ciencias)*, *15(1)*, **2014**, 49–50.
13. **S. Stojkovikj**, M. Najdoski, V. Koleva, S. Demiri, Preparation of Electrochromic Thin Films by Transformation of Manganese(II) Carbonate, *Journal of Physics and Chemistry of Solids*, *74(10)*, **2013**, 1433–1438. https://doi.org/10.1016/j.jpcs.2013.05.001
14. M. Najdoski, V. Koleva, S. Demiri, **S. Stojkovikj**, A Simple Chemical Method for Deposition of Electrochromic Potassium Manganese Oxide Hydrate Thin Films, *Materials Research Bulletin*, *47(9)*, **2012**, 2239–2244. https://doi.org/10.1016/j.materresbull.2012.05.057
15. M. Najdoski, **S. Stojkovikj**, Cost Effective Microscale Gas Generation Apparatus, *Chemistry*, *19(6)*, **2010**, 444–449.
16. **С. Стојковиќ**, М. Томиќ, Б. Цекова, Синтеза на зеолит 4А од отпаден материјал, *Зборник на трудови, „МИТ Универзитет“- Скопје*, *1*, **2010**, 101–110. (**Translated in English: S. Stojkovikj**, M. Tomikj, B. Cekova, Synthesis of Zeolite 4A from Waste Material*, Proceedings, MIT University - Skopje*, *1*, **2010**, 101–110).
17. М. Томиќ, **С. Стојковиќ**, Б. Цекова, Структура на зеолити, *Зборник на трудови*, *„МИТ Универзитет“- Скопје*, *1*, **2010**, 315-323. (**Translated in English:** M. Tomikj, **S. Stojkovikj**, B. Cekova, Structure of Zeolites, *Proceedings, MIT University - Skopje*, *1*, **2010**, 315-323).

Total list of conference presentations/participations (2009-2021)

1. **S. Stojkovikj**, G.A. El-Nagar**,** F. Firschke, L.C. Pardo Pérez, L. Choubrac, M. Najdoski, M.T. Mayer, Repurposing Waste Cu-Sn Bronze for Selective CO_2 Electroreduction into CO, RSC Electrochemistry Group's Electrochemistry 2021 virtual conference, **September 7-8th 2021 (Presenting author – Poster presentation).**
2. **S. Stojkovikj**, G.A. El-Nagar, M.T. Mayer, Transformation of Industrial Waste Bronze Alloy into an Electrocatalyst for Selective Conversion of CO_2 into CO, GDCh Electrochemistry undercover 2020 - Berlin Online, **September 23-24th 2020 (Presenting author – Poster presentation).**
3. **S. Stojkovikj**, G.A. El-Nagar, F. Firschke, M. Najdoski, V. Koleva, M.T. Mayer, Novel and Facile Synthesis of $Cu_{2-x}S$-Based Electrocatalysts for Selective CO_2 Conversion into HCOOH, 71st Annual Meeting of the International Society of Electrochemistry "Electrochemistry towards Excellence"- Belgrade Online, **September 30th August-4th 2020 (Presenting author – Poster presentation).**
4. A. Arndt, L. Pardo-Perez, **S. Stojkovikj,** G. Schuck, L. Xi, M.T. Mayer, Investigating Synergetic Effects in SnO_x-Modified CuO_x Nanowire Array CO_2 Reduction Electrocatalysts by X-ray

Absorption Spectroscopy, Proceedings of Online Meetup: Structure-function Relationships in CO_2 Electrocatalysis (CO_2cat), nanoGE Online Meetup Conferences, **June 9-10th 2020 (Coauthor – Poster presentation).**

5. G.A. El-Nagar, **Sasho Stojkovikj,** A. Arndt, L.C. Pardo-Perez, M.T. Mayer, Gas-Diffusion Electrodes for Practical CO_2 Reduction: Challenges & Strategies, Symposium on Insights into Gas Diffusion Electrodes: From Fundamentals to Industrial Applications **September 23-25th, 2019,** Magdeburg, Germany **(Coauthor – Poster presentation).**
6. L.C. Pardo-Perez, **S. Stojkovikj**, A. Arndt, M.T. Mayer, Investigating Synergetic Effects in Cu-Sn Mixed Metal Oxide CO_2 Reduction Electrocatalysts by Hard and Soft X-ray Spectroscopy, E-MRS 2019 Fall Meeting, **September 16-19th 2019**, Warsaw. Poland **(Coauthor – Poster presentation).**
7. **S. Stojkovikj**, M. Najdoski, V. Koleva, M.T. Mayer, Study of Copper/Cuprous Sulfide Composites as Catalysts for Electrochemical Reduction of Carbon Dioxide, 17th International Conference on Carbon Dioxide Utilization - ICCDU 2019, **June 23-27th 2019**, Aachen, Germany **(Presenting author – Oral presentation).**
8. **S. Stojkovikj,** S. Oklevski, O.P. Jasuja, M. Najdoski, Thermal paper: An Overview of the Methods for Visualization of Latent Fingerprints, 3rd World Conference and Exhibition on Forensic Science, **June 3-4th, 2019**, Berlin, Germany **(Presenting author – Oral presentation).**
9. **S. Stojkovikj,** S. Oklevski, O.P. Jasuja, M. Najdoski, Design of a Novel Nitrogen Dioxide Method for Visualization of Latent Fingerprints on Thermal Paper, 3rd World Conference and Exhibition on Forensic Science, **June 3-4th, 2019**, Berlin, Germany **(Presenting author – Oral presentation).**
10. **S. Stojkovikj**, M.T. Mayer, Strategies and Problems during CO_2 Electrochemical Reduction Experiments, SurfCat Summer School 2018, ´´The Science of Sustainable Fuels and Chemicals´´, Danmarks Tekniske Universitet (DTU), **August 5-10th 2018**, Kysthusene, Gilleleje, Denmark **(Presenting author – Short oral + Poster presentation).**
11. **S. Stojkovikj**, V. Mircheski, B. Sefer, M. Najdoski, Design of Nonenzymatic Amperometric Sensor for H_2O_2 based on Electrodes Modified with Nanoscaled $MnCO_3$ Thin Films, 2nd International Congress of Chemists and Chemical Engineers of Bosnia and Herzegovina, **October 21-23rd 2016,** Sarajevo, Bosnia and Herzegovina **(Presenting author – Poster presentation).**
12. **S. Stojkovikj**, V. Mircheski, B. Sefer, M. Najdoski, Application of Potassium Birnessite Thin Film/FTO modified Electrodes as Nonenzymatic Sensors for Hydrogen Peroxide, 2nd International Congress of Chemists and Chemical Engineers of Bosnia and Herzegovina, **October 21-23rd 2016**, Sarajevo, Bosnia and Herzegovina **(Presenting author – Poster presentation).**
13. **S. Stojkovikj**, V. Mirčeski, B. Sefer, M. Najdoski, Design of Amperometric Sensors for H_2O_2 based on $K_{0.27}MnO_2 \cdot xH_2O$ Thin Films, MatCatNet Workshop - From Molecules to Functionalized Materials, **1-5th September 2016**, Ohrid, Macedonia **(Presenting author – Oral presentation).**

14. V. Koleva, M. Najdoski, **S. Stojkovikj**, Effects of the Structure on the Electrochromic Properties of Nano-Sized Vanadium(V) Oxide Thin Films, International Conference on Sustainable Materials, Science and Technology, **July 15-17th 2015**, Paris, France **(Coauthor – Poster presentation).**
15. V. Koleva, **S. Stojkovikj**, M. Najdoski, Electrochromism in Layered Vanadium-Based Thin Films, 16th International Workshop on Nanoscience and Nanotechnology, **November 7-8th 2014**, Sofia, Bulgaria **(Coauthor – Poster presentation).**
16. **S. Stojkovikj**, V. Koleva, M. Najdoski, Electrochromic Vanadium Oxide Thin Films: From a Layered to a Tunnel Structure, XXIIIrd Congress of Chemists and Technologists of Macedonia, **October 8-11th 2014**, Ohrid, Macedonia **(Presenting author – Poster presentation).**
17. **S. Stojkovikj**, M. Najdoski, B. Sefer, V. Mirčeski, Development of Nonenzymatic Amperometric Sensor for Detection of Hydrogen Peroxide Based on Manganese(II) Carbonate Thin Films, MatCatNet Workshop - From Molecules to Functionalized Materials, **September 5-10th 2014**, Ohrid, Macedonia **(Presenting author – Oral presentation).**
18. **S. Stojkovikj**, V. Koleva, M. Najdoski, Influence of Thermal Treatment on the Electrochromic Properties of Sodium Intercalated Vanadium(V) Oxide Xerogel Thin Films,15th International Workshop on Nanoscience and Nanotechnology, **November 21-23rd 2013**, Sofia, Bulgaria **(Presenting author – Poster presentation).**
19. **S. Stojkovikj**, V. Koleva, M. Najdoski, Chemical Deposition of Nano-Sized Electrochromic Thin Films of $Na_{0.33}V_2O_5{\cdot}H_2O$ Xerogels, 15th International Workshop on Nanoscience and Nanotechnology, **November 21-23rd 2013**, Sofia, Bulgaria **(Presenting author – Poster presentation).**
20. **S. Stojkovikj**, M. Najdoski, S. Demiri, Chemical Bath Coating and Characterisation of Electrochromic Manganese(II) Carbonate Thin Films, IXth Congress of Pure and Applied Chemistry of Students from Macedonia (with International participation), **October 6-8th 2011**, Skopje, Macedonia **(Presenting author – Oral presentation)**
21. **S. Stojkovikj**, M. Najdoski, S. Demiri, V. Koleva, Electrochromic $K_{0.27}MnO_2 \cdot 0.6H_2O$ Thin Films Deposition on Glass Substrates using Dip Coating Method, IXth Congress of Pure and Applied Chemistry of Students from Macedonia (with international participation), **October 6-8th 2011**, Skopje, Macedonia **(Presenting author – Oral presentation).**
22. M. Tomikj, B. Cekova, **S. Stojkovikj**, Structural Investigations of ´´Filter Bread´´ as a Byproduct of Water Glass Synthesis, 6th Symposium of Recycling Technologies and Sustainable Development, **September 18-21st 2011**, Soko Banja, Serbia **(Coauthor – Poster presentation).**
23. B. Cekova, S. Koevska - Maksimovska, **S. Stojkovikj**, Wastewater Treatment using Zeolite 4A, XXIst Congress of Chemists and Technologists of Macedonia, **September 23-26th 2010**, Ohrid, Macedonia **(Coauthor – Poster presentation).**

24. **S. Stojkovikj**, B. Cekova, Synthesis of Zeolites from Waste Materials, VIIIth Congress of Pure and Applied Chemistry of Students from Macedonia (with International participation), **October 8-10th 2009**, Skopje, Macedonia **(Presenting author – Oral presentation).**

Patents

1. F. Karafiljkovska, **S. Stojkovikj**, V. Solakova, Production of a simple defoaming agent, Patent Application number: 2016/476, Registration number: 7473, State Office of Industrial Property of the Republic of North Macedonia, **2017**.

Bibliography

(this list does not include the citations from the publications/manuscript embedded in the thesis as Chapters 4-6, they have separate lists of references)

(1) Hudson, P. *The Industrial Revolution*; Bloomsbury Publishing, 2014. https://books.google.de/books?id=5j5uBAAAQBAJ.
(2) Hahn, B. *Technology in the Industrial Revolution*; Cambridge University Press, 2020. DOI: https://doi.org/10.1017/9781316900864.
(3) Encyclopaedia, T. E. o. *Industrial Revolution. Encyclopedia Britannica.*; Encyclopædia Britannica, Inc., 2022. https://www.britannica.com/event/Industrial-Revolution.
(4) *Our World in Data. Global Change Data Lab*. https://ourworldindata.org/ (accessed 29.04.2022).
(5) *Population Dynamics: 2019 Revision of World Population Prospects. United Nations: Department of Economic and Social Affairs*. https://population.un.org/wpp/ (accessed 29.04.2022).
(6) Floud, R.; Fogel, R. W.; Harris, B.; Hong, S. C. *The Changing Body: Health, Nutrition, and Human Development in the Western World since 1700*; Cambridge University Press, 2011. https://books.google.de/books?id=eZLHQlX9S_MC.
(7) Mackenbach, J. P. The Rise and Fall of Diseases: Reflections on the History of Population Health in Europe since ca. 1700. *European Journal of Epidemiology* **2021**, *36* (12), 1199-1205. https://doi.org/10.1007/s10654-021-00719-7.
(8) Rodrigue, J.-P. Transportation and Geography. In *The Geography of Transport Systems*, 5th Edition ed.; https://doi.org/10.4324/9780429346323Routledge, 2020.
(9) Wrigley, E. A. Energy and the English Industrial Revolution. *Philosophical Transactions of the Royal Society A: Mathematical, Physical and Engineering Sciences* **2013**, *371* (1986), 20110568. https://doi.org/10.1098/rsta.2011.0568.
(10) *World Population. The World Counts.* 2022. https://www.theworldcounts.com/populations (accessed 29.04.2022).
(11) *The Consumer Economy. The World Counts.* 2022. https://www.theworldcounts.com/economies (accessed 29.04.2022).
(12) *Global Challenges. The World Counts.* 2022. https://www.theworldcounts.com/challenges (accessed 29.04.2022).
(13) Cheshmehzangi, A. From Transitions to Transformation: A Brief Review of the Potential Impacts of COVID-19 on Boosting Digitization, Digitalization, and Systems Thinking in the Built Environment. *Journal of Building Construction and Planning Research* **2021**, *9* (1), 26-39. https://www.scirp.org/journal/paperinformation.aspx?paperid=107749.
(14) Al-Nuaimi, M. N.; Al-Kabi, M. N.; Al-Emran, M. Digitizing Learning During the Outbreak of COVID-19 Pandemic: Lessons Learned from the Most Infected Countries. In *Emerging Technologies During the Era of COVID-19 Pandemic*, Arpaci, I., Al-Emran, M., A. Al-Sharafi, M., Marques, G. Eds.; https://doi.org/10.1007/978-3-030-67716-9_18Springer International Publishing, 2021; pp 291-303.
(15) Smil, V. Energy in the Twentieth Century: Resources, Conversions, Costs, Uses, and Consequences. *Annual Review of Energy and the Environment* **2000**, *25* (1), 21-51. https://doi.org/10.1146/annurev.energy.25.1.21.
(16) Smil, V. *Energy transitions: Global and National Perspectives*; ABC-Clio, 2017. https://vaclavsmil.com/2016/12/14/energy-transitions-global-and-national-perspectives-second-expanded-and-updated-edition/.
(17) Ritchie, H. How Have the World's Energy Sources Changed Over the Last Two Centuries? *Our World in Data* **2021**, https://ourworldindata.org/global-energy-200-years. https://ourworldindata.org/global-energy-200-years.
(18) Lewis, N. S.; Nocera, D. G. Powering the planet: Chemical Challenges in Solar Energy Utilization. *Proceedings of the National Academy of Sciences* **2006**, *103* (43), 15729-15735. https://www.pnas.org/doi/abs/10.1073/pnas.0603395103.
(19) Henckens, T. Scarce Mineral Resources: Extraction, Consumption and Limits of Sustainability. *Resources, Conservation and Recycling* **2021**, *169*, 105511. https://doi.org/10.1016/j.resconrec.2021.105511.
(20) *Endangered Elements. ACS Green Chemistry Institute*. https://www.acs.org/content/acs/en/greenchemistry/research-innovation/endangered-elements.html (accessed 29.04.2022).

(21) *Element Scarcity – EuChemS Periodic Table*. https://www.euchems.eu/euchems-periodic-table/ (accessed 29.04.2022).
(22) Rhodes, C. J. Endangered Elements, Critical Raw Materials and Conflict minerals. *Science Progress* **2019**, *102* (4), 304-350. https://doi.org/10.1177/0036850419884873.
(23) Ratner, P. *What do we do with all the chemical elements? This ingenious periodic table shows you. Big Think*. 2017. https://bigthink.com/hard-science/this-helpful-periodic-table-shows-you-how-to-use-all-the-elements/ (accessed 29.04.2022).
(24) *Global Total Material Use by Resource Type. European Environment Agency*. 2016. https://www.eea.europa.eu/data-and-maps/figures/global-total-material-use-by (accessed 29.04.2022).
(25) Ritchie, H.; Roser, M. Energy. *Our World in Data* **2020**, https://ourworldindata.org/fossil-fuels#citation. https://ourworldindata.org/fossil-fuels#citation.
(26) Höök, M.; Tang, X. Depletion of Fossil Fuels and Anthropogenic Climate Change-A Review. *Energy Policy* **2013**, *52*, 797-809. https://doi.org/10.1016/j.enpol.2012.10.046.
(27) *Waste. The World Counts.* 2022. https://www.theworldcounts.com/challenges/planet-earth/waste (accessed 29.04.2022).
(28) *Chemicals and Toxics Topics. EPA - U.S. Environmental Protection Agency.* 2021. https://www.epa.gov/environmental-topics/chemicals-and-toxics-topics (accessed 29.04.2022).
(29) Szafranko, E. H. Assessment of Direct and Indirect Effects of Building Developments on the Environment. *Open Engineering* **2019**, *9* (1), 109-114. https://doi.org/10.1515/eng-2019-0013.
(30) Yao, N.; Feng, B.; Zhang, M.; He, L.; Zhang, H.; Liu, Z. Impact of Industrial Production, Dam Construction, and Agriculture on the Z-IBI in River Ecosystems: A Case Study of the Wanan River Basin in China. *Water* **2021**, *13* (2), 123. https://doi.org/10.3390/w13020123.
(31) Pacheco-Torgal, F. 1 - Introduction to the Environmental Impact of Construction and Building materials. In *Eco-efficient Construction and Building Materials*, Pacheco-Torgal, F., Cabeza, L. F., Labrincha, J., de Magalhães, A. Eds.; https://doi.org/10.1533/9780857097729.1Woodhead Publishing, 2014; pp 1-10.
(32) Dobrowolska, K. *How Does Construction Affect The Environment?* 2021. https://archdesk.com/blog/how-does-construction-affect-the-environment/ (accessed 29.04.2022).
(33) Westing, A. H. The Impact of War on the Environment. In *War and Public Health*, Barry S. Levy, V. W. S. Ed.; https://books.google.de/books?id=aAUSDAAAQBAJOxford University Press, USA, 2008.
(34) Tiseo, I. *Municipal solid waste recycling rates worldwide in 2020, by select country. Statista.* 2022. https://www.statista.com/statistics/1052439/rate-of-msw-recycling-worldwide-by-key-country/ (accessed 29.04.2022).
(35) *Municipal Waste Recycling Rate, 1992 to 2015. Our World in Data.* https://ourworldindata.org/grapher/municipal-waste-recycling-rate?tab=chart&country=PRT~TUR~NOR~AUS~DEU~AUT~BEL~BRA~CAN~CRI~CZE~DNK~EST~FIN~FRA~GRC~HUN~GBR~USA~CHE~SWE~ESP~SVN~SVK~POL~OECD+-+Europe~OECD+-+Total~MEX~NLD~LUX~LTU~LVA~Korea~ISL~IRL~ISR~ITA~JPN (accessed 29.04.2022).
(36) Garside, M. *Lithium Mine Production Worldwide from 2010 to 2021. Statista.* 2022. (accessed 29.04.2022).
(37) Castelvecchi, D. *Electric Cars and Batteries: How will the World Produce Enough? News Feature. Nature.* 2021. https://www.nature.com/articles/d41586-021-02222-1 (accessed 29.04.2022).
(38) *What are Hazardous Air Pollutants? EPA - U.S. Environmental Protection Agency.* 2022. https://www.epa.gov/haps/what-are-hazardous-air-pollutants (accessed 29.04.2022).
(39) *Air Pollutants. CDC - Centers for Disease Control and Prevention.* 2021. (accessed 29.04.2022).
(40) Nathanson, J. A. *Air pollution. Encyclopedia Britannica.* 2020. https://www.britannica.com/science/air-pollution (accessed 29.04.2022).
(41) *Particulate Matter (PM) Basics. EPA - U.S. Environmental Protection Agency*. https://www.epa.gov/pm-pollution/particulate-matter-pm-basics (accessed 29.04.2022).
(42) *The Intergovernmental Panel on Climate Change* https://www.ipcc.ch/ (accessed 29.04.2022).
(43) *Global Warming of 1.5 ºC.The Intergovernmental Panel on Climate Change.* https://www.ipcc.ch/sr15/ (accessed 29.04.2022).
(44) Wu, J.; Huang, Y.; Ye, W.; Li, Y. CO_2 Reduction: From the Electrochemical to Photochemical Approach. *Advanced Science* **2017**, *4* (11), 1700194. https://doi.org/10.1002/advs.201700194.
(45) Durrani, J. *Can Catalysis Save Us from Our CO_2 Problem? Royal Society of Chemistry* 2019. https://www.chemistryworld.com/news/can-catalysis-save-us-from-our-co2-problem/3010555.article (accessed 29.04.2022).
(46) Kondratenko, E. V.; Mul, G.; Baltrusaitis, J.; Larrazábal, G. O.; Pérez-Ramírez, J. Status and Perspectives of CO_2 Conversion into Fuels and Chemicals by Catalytic, Photocatalytic and

Electrocatalytic Processes. *Energy Environ. Sci.* **2013**, *6* (11), 3112-3135. http://dx.doi.org/10.1039/C3EE41272E.
(47) Chen, W.-Y.; Suzuki, T.; Lackner, M. *Handbook of Climate Change Mitigation and Adaptation*; Springer International Publishing, 2017.
(48) Burkart, M. D.; Hazari, N.; Tway, C. L.; Zeitler, E. L. Opportunities and Challenges for Catalysis in Carbon Dioxide Utilization. *ACS Catal.* **2019**, *9* (9), 7937-7956. https://doi.org/10.1021/acscatal.9b02113.
(49) Lee, S.; Choi, M.; Lee, J. Looking Back and Looking Ahead in Electrochemical Reduction of CO_2. *Chem Rec.* **2020**, *20* (2), 89-101. DOI: https://doi.org/10.1002/tcr.201900048.
(50) Ritchie, H.; Roser, M.; Rosado, P. CO_2 and Greenhouse Gas Emissions. *Our World in Data* **2020**, https://ourworldindata.org/co2-and-other-greenhouse-gas-emissions#citation. https://ourworldindata.org/co2-and-other-greenhouse-gas-emissions#citation.
(51) *Global Greenhouse Gas Emissions Data. EPA - U.S. Environmental Protection Agency.* https://www.epa.gov/ghgemissions/global-greenhouse-gas-emissions-data (accessed 29.04.2022).
(52) Wei, P.-S.; Chiu, H.-H.; Hsieh, Y.-C.; Yen, D.-L.; Lee, C.; Tsai, Y.-C.; Ting, T.-C. Absorption Coefficient of Water Vapor Across Atmospheric Troposphere Layer. *Heliyon* **2019**, *5* (1), e01145. https://doi.org/10.1016/j.heliyon.2019.e01145.
(53) *Global Monitoring Laboratory. Trends in Atmospheric Carbon Dioxide. Global Monthly Mean CO_2.* https://gml.noaa.gov/ccgg/trends/global.html (accessed 19.05.2022).
(54) Nitopi, S.; Bertheussen, E.; Scott, S. B.; Liu, X.; Engstfeld, A. K.; Horch, S.; Seger, B.; Stephens, I. E. L.; Chan, K.; Hahn, C.; et al. Progress and Perspectives of Electrochemical CO_2 Reduction on Copper in Aqueous Electrolyte. *Chemical Reviews* **2019**, *119* (12), 7610-7672. https://doi.org/10.1021/acs.chemrev.8b00705.
(55) Davis, S. J.; Lewis, N. S.; Shaner, M.; Aggarwal, S.; Arent, D.; Azevedo, I. L.; Benson, S. M.; Bradley, T.; Brouwer, J.; Chiang, Y.-M.; et al. Net-Zero Emissions Energy Systems. *Science* **2018**, *360* (6396), eaas9793. https://www.science.org/doi/abs/10.1126/science.aas9793
(56) Encyclopaedia, T. E. o. *Biogeochemical Cycle. Encyclopedia Britannica.*; Encyclopædia Britannica, Inc., 2020. https://www.britannica.com/science/biogeochemical-cycle.
(57) *The Carbon Budget. Copernicus.* https://atmosphere.copernicus.eu/ghg-services/carbon-cycle (accessed 29.04.2022).
(58) Normile, D. Round and Round: A Guide to the Carbon Cycle. *Science* **2009**, *325* (5948), 1642-1643. https://www.science.org/doi/10.1126/science.325_1642.
(59) Bar-Even, A.; Noor, E.; Lewis, N. E.; Milo, R. Design and Analysis of Synthetic Carbon Fixation Pathways. *Proceedings of the National Academy of Sciences* **2010**, *107* (19), 8889-8894. https://doi.org/10.1073/pnas.0907176107.
(60) *Carbon Dioxide Levels are Rising: Is it really that Simple?. Copernicus.* 2019. https://atmosphere.copernicus.eu/carbon-dioxide-levels-are-rising-it-really-simple (accessed 29.04.2022).
(61) Agustí-Panareda, A.; Massart, S.; Chevallier, F.; Boussetta, S.; Balsamo, G.; Beljaars, A.; Ciais, P.; Deutscher, N. M.; Engelen, R.; Jones, L.; et al. Forecasting Global Atmospheric CO_2. *Atmospheric Chemistry and Physics* **2014**, *14* (21), 11959-11983. https://doi.org/10.5194/acp-14-11959-2014.
(62) Gibbs, H. K.; Ruesch, A. S.; Achard, F.; Clayton, M. K.; Holmgren, P.; Ramankutty, N.; Foley, J. A. Tropical Forests were the Primary Sources of new Agricultural Land in the 1980s and 1990s. *Proceedings of the National Academy of Sciences* **2010**, *107* (38), 16732-16737. https://doi.org/10.1073/pnas.0910275107.
(63) Gabrielli, P.; Gazzani, M.; Mazzotti, M. The Role of Carbon Capture and Utilization, Carbon Capture and Storage, and Biomass to Enable a Net-Zero-CO_2 Emissions Chemical Industry. *Industrial & Engineering Chemistry Research* **2020**, *59* (15), 7033-7045. https://doi.org/10.1021/acs.iecr.9b06579.
(64) van Sluisveld, M. A. E.; de Boer, H. S.; Daioglou, V.; Hof, A. F.; van Vuuren, D. P. A Race to Zero - Assessing the Position of Heavy Industry in a Global Net-Zero CO_2 Emissions Context. *Energy and Climate Change* **2021**, *2*, 100051. https://doi.org/10.1016/j.egycc.2021.100051.
(65) Hong, W. Y. A Techno-Economic Review on Carbon Capture, Utilisation and Storage Systems for Achieving a Net-Zero CO_2 Emissions Future. *Carbon Capture Science & Technology* **2022**, *3*, 100044. https://doi.org/10.1016/j.ccst.2022.100044.
(66) De Luna, P.; Hahn, C.; Higgins, D.; Jaffer, S. A.; Jaramillo, T. F.; Sargent, E. H. What Would it Take for Renewably Powered Electrosynthesis to Displace Petrochemical Processes? *Science* **2019**, *364* (6438). https://www.science.org/doi/10.1126/science.aav3506.

(67) DeAngelo, J.; Azevedo, I.; Bistline, J.; Clarke, L.; Luderer, G.; Byers, E.; Davis, S. J. Energy Systems in Scenarios at Net-Zero CO_2 emissions. *Nature Communications* **2021**, *12* (1), 6096. https://doi.org/10.1038/s41467-021-26356-y.
(68) Marques Mota, F.; Kim, D. H. From CO_2 Methanation to Ambitious Long-Chain Hydrocarbons: Alternative Fuels Paving the Path to Sustainability. *Chemical Society Reviews* **2019**, *48* (1), 205-259. http://dx.doi.org/10.1039/C8CS00527C.
(69) *Reutilization: Insights into the Circular Economy. Recovery.* 2019. https://www.recovery-worldwide.com/en/artikel/insights-into-the-circular-economy_3356579.html (accessed 29.04.2022).
(70) Gunnarsdottir, I.; Davidsdottir, B.; Worrell, E.; Sigurgeirsdottir, S. Sustainable Energy Development: History of the Concept and Emerging Themes. *Renewable and Sustainable Energy Reviews* **2021**, *141*, 110770. https://doi.org/10.1016/j.rser.2021.110770.
(71) *Paris Agreement. European Commission Website.* https://ec.europa.eu/clima/eu-action/international-action-climate-change/climate-negotiations/paris-agreement_en (accessed 29.04.2022).
(72) Sinha, R. K.; Chaturvedi, N. D. A Review on Carbon Emission Reduction in Industries and Planning Emission Limits. *Renewable and Sustainable Energy Reviews* **2019**, *114*, 109304. https://doi.org/10.1016/j.rser.2019.109304.
(73) Hannah Ritchie, M. R. a. P. R. Renewable Energy. *Our World in Data* **2020**, https://ourworldindata.org/renewable-energy#licence. https://ourworldindata.org/renewable-energy#licence.
(74) Sørensen, B. *Renewable Energy - Physics, Engineering, Environmental Impacts, Economics and Planning (Fifth Edition)*; Elsevier, 2017. https://www.sciencedirect.com/book/9780128045671/renewable-energy.
(75) Ghazouani, A.; Xia, W.; Ben Jebli, M.; Shahzad, U. Exploring the Role of Carbon Taxation Policies on CO_2 Emissions: Contextual Evidence from Tax Implementation and Non-Implementation European Countries. *Sustainability* **2020**, *12* (20), 8680. https://doi.org/10.3390/su12208680.
(76) Koytsoumpa, E. I.; Bergins, C.; Kakaras, E. The CO_2 Economy: Review of CO_2 Capture and Reuse Technologies. *The Journal of Supercritical Fluids* **2018**, *132*, 3-16. https://doi.org/10.1016/j.supflu.2017.07.029.
(77) Nanda, S.; Reddy, S. N.; Mitra, S. K.; Kozinski, J. A. The Progressive Routes for Carbon Capture and Sequestration. *Energy Science & Engineering* **2016**, *4* (2), 99-122. https://doi.org/10.1002/ese3.117.
(78) Ghiat, I.; Al-Ansari, T. A Review of Carbon Capture and Utilisation as a CO_2 Abatement Opportunity within the EWF Nexus. *Journal of CO2 Utilization* **2021**, *45*, 101432. https://doi.org/10.1016/j.jcou.2020.101432.
(79) Prajapati, A.; Singh, M. R. Assessment of Artificial Photosynthetic Systems for Integrated Carbon Capture and Conversion. *ACS Sustainable Chemistry & Engineering* **2019**, *7* (6), 5993-6003. https://doi.org/10.1021/acssuschemeng.8b04969.
(80) Yu, C.-H.; Huang, C.-H.; Tan, C.-S. A Review of CO_2 Capture by Absorption and Adsorption. *Aerosol and Air Quality Research* **2012**, *12* (5), 745-769. http://dx.doi.org/10.4209/aaqr.2012.05.0132.
(81) Fasihi, M.; Efimova, O.; Breyer, C. Techno-Economic Assessment of CO_2 Direct Air Capture Plants. *Journal of Cleaner Production* **2019**, *224*, 957-980. https://doi.org/10.1016/j.jclepro.2019.03.086.
(82) Bushuyev, O. S.; De Luna, P.; Dinh, C. T.; Tao, L.; Saur, G.; van de Lagemaat, J.; Kelley, S. O.; Sargent, E. H. What Should We Make with CO_2 and How Can We Make It? *Joule* **2018**, *2* (5), 825-832. https://doi.org/10.1016/j.joule.2017.09.003.
(83) Zou, L.; Sun, Y.; Che, S.; Yang, X.; Wang, X.; Bosch, M.; Wang, Q.; Li, H.; Smith, M.; Yuan, S.; et al. Porous Organic Polymers for Post-Combustion Carbon Capture. *Advanced Materials* **2017**, *29* (37), 1700229. https://doi.org/10.1002/adma.201700229.
(84) Song, C.; Pan, W.; Srimat, S. T.; Zheng, J.; Li, Y.; Wang, Y.-H.; Xu, B.-Q.; Zhu, Q.-M. Tri-Reforming of Methane over Ni Catalysts for CO_2 Conversion to Syngas With Desired H_2/CO Ratios Using Flue Gas of Power Plants Without CO_2 Separation. In *Studies in Surface Science and Catalysis*, Park, S.-E., Chang, J.-S., Lee, K.-W. Eds.; Vol. 153; Elsevier, 2004; pp 315-322.
(85) Zheng, C.; Duan, D.; Chang, Q.; Liu, S.; Yang, Z.; Liu, X.; Weng, W.; Gao, X. Experiments on Enhancing the Particle Charging Performance of an Electrostatic Precipitator. *Aerosol and Air Quality Research* **2019**, *19* (6), 1411-1420. http://dx.doi.org/10.4209/aaqr.2018.11.0400.
(86) Artz, J.; Müller, T. E.; Thenert, K.; Kleinekorte, J.; Meys, R.; Sternberg, A.; Bardow, A.; Leitner, W. Sustainable Conversion of Carbon Dioxide: An Integrated Review of Catalysis and Life Cycle Assessment. *Chemical Reviews* **2018**, *118* (2), 434-504. https://doi.org/10.1021/acs.chemrev.7b00435.

(87) *Hydrogen and Syngas Production and Purification Technologies*; Center for Chemical Process Safety of the American Institute of Chemical Engineers and John Wiley & Sons, Inc., 2009. https://onlinelibrary.wiley.com/doi/book/10.1002/9780470561256.
(88) *Hydrogen Production: Natural Gas Reforming. Office of Energy Efficiency & Renewable Energy*. https://www.energy.gov/eere/fuelcells/hydrogen-production-natural-gas-reforming (accessed 29.04.2022).
(89) *Direct Air Capture. International Energy Agency.* 2021. https://www.iea.org/reports/direct-air-capture (accessed 29.04.2022).
(90) Álvarez, A.; Borges, M.; Corral-Pérez, J. J.; Olcina, J. G.; Hu, L.; Cornu, D.; Huang, R.; Stoian, D.; Urakawa, A. CO_2 Activation over Catalytic Surfaces. *ChemPhysChem* **2017**, *18* (22), 3135-3141. https://doi.org/10.1002/cphc.201700782.
(91) Alam, M. I.; Cheula, R.; Moroni, G.; Nardi, L.; Maestri, M. Mechanistic and Multiscale Aspects of Thermo-Catalytic CO_2 Conversion to C_1 products. *Catalysis Science & Technology* **2021**, *11* (20), 6601-6629. http://dx.doi.org/10.1039/D1CY00922B.
(92) Hou, H. J. M.; Najafpour, M. M.; Moore, G. F.; Allakhverdiev, S. I. Photosynthesis: Structures, Mechanisms, and Applications. Springer Cham: 2017; https://doi.org/10.1007/978-3-319-48873-8.
(93) Hatch, M. D.; Boardman, N. K. The Biochemistry of Plants: A Comprehensive Treatise, Volume 8: Photosynthesis. Elsevier: 1981; https://doi.org/10.1016/C2013-0-07615-3.
(94) Pessarakli, M. Handbook of Photosynthesis Second Edition. CRC Press Taylor & Francis Group: 2005.
(95) Schmidt-Rohr, K. O_2 and Other High-Energy Molecules in Photosynthesis: Why Plants Need Two Photosystems. *Life* **2021**, *11* (11), 1191. https://doi.org/10.3390/life11111191.
(96) Mori, J. E. *Calvin Cycle*; BookPatch LLC, 2015. https://books.google.de/books?id=2NcdjgEACAAJ.
(97) Campbell, A. M.; Paradise, C. J. *Cellular Respiration*; Momentum Press, 2016. https://books.google.de/books?id=1djVCwAAQBAJ.
(98) Schmidt-Rohr, K. Oxygen Is the High-Energy Molecule Powering Complex Multicellular Life: Fundamental Corrections to Traditional Bioenergetics. *ACS Omega* **2020**, *5* (5), 2221-2233. https://doi.org/10.1021/acsomega.9b03352.
(99) Fu, Z.; Yang, Q.; Liu, Z.; Chen, F.; Yao, F.; Xie, T.; Zhong, Y.; Wang, D.; Li, J.; Li, X.; et al. Photocatalytic Conversion of Carbon dioxide: From Products to Design the Catalysts. *Journal of CO_2 Utilization* **2019**, *34*, 63-73. https://doi.org/10.1016/j.jcou.2019.05.032.
(100) Gao, Y.; Qian, K.; Xu, B.; Li, Z.; Zheng, J.; Zhao, S.; Ding, F.; Sun, Y.; Xu, Z. Recent Advances in Visible-Light-Driven conversion of CO_2 by Photocatalysts into Fuels or Value-Added Chemicals. *Carbon Resources Conversion* **2020**, *3*, 46-59. https://doi.org/10.1016/j.crcon.2020.02.003.
(101) White, J. L.; Baruch, M. F.; Pander, J. E.; Hu, Y.; Fortmeyer, I. C.; Park, J. E.; Zhang, T.; Liao, K.; Gu, J.; Yan, Y.; et al. Light-Driven Heterogeneous Reduction of Carbon Dioxide: Photocatalysts and Photoelectrodes. *Chemical Reviews* **2015**, *115* (23), 12888-12935. https://doi.org/10.1021/acs.chemrev.5b00370.
(102) Nandal, N.; Jain, S. L. A Review on Progress and Perspective of Molecular Catalysis in Photoelectrochemical Reduction of CO_2. *Coordination Chemistry Reviews* **2022**, *451*, 214271. https://doi.org/10.1016/j.ccr.2021.214271.
(103) Kan, M.; Wang, Q.; Hao, S.; Guan, A.; Chen, Y.; Zhang, Q.; Han, Q.; Zheng, G. System Engineering Enhances Photoelectrochemical CO_2 Reduction. *The Journal of Physical Chemistry C* **2022**, *126* (4), 1689-1700. https://doi.org/10.1021/acs.jpcc.1c10156.
(104) Zhang, H.; Long, J. Chapter 9 - Photoelectrochemical Reduction of Carbon Dioxide. In *Nanomaterials for CO_2 Capture, Storage, Conversion and Utilization*, Nguyen Tri, P., Wu, H., Nguyen, T. A., Barnabé, S., Bénard, P. Eds.; https://doi.org/10.1016/B978-0-12-822894-4.00008-3Elsevier, 2021; pp 197-210.
(105) Salehizadeh, H.; Yan, N.; Farnood, R. Recent Advances in Microbial CO_2 Fixation and Conversion to Value-Added Products. *Chemical Engineering Journal* **2020**, *390*, 124584. https://doi.org/10.1016/j.cej.2020.124584.
(106) Gonzales, J. N.; Matson, M. M.; Atsumi, S. Nonphotosynthetic Biological CO_2 Reduction. *Biochemistry* **2019**, *58* (11), 1470-1477. https://doi.org/10.1021/acs.biochem.8b00937.
(107) Antonovsky, N.; Gleizer, S.; Noor, E.; Zohar, Y.; Herz, E.; Barenholz, U.; Zelcbuch, L.; Amram, S.; Wides, A.; Tepper, N.; et al. Sugar Synthesis from CO_2 in *Escherichia coli*. *Cell* **2016**, *166* (1), 115-125. https://doi.org/10.1016/j.cell.2016.05.064.
(108) Haas, T.; Krause, R.; Weber, R.; Demler, M.; Schmid, G. Technical Photosynthesis Involving CO_2 Electrolysis and Fermentation. *Nat. Catal.* **2018**, *1* (1), 32-39. https://doi.org/10.1038/s41929-017-0005-1.

(109) Roider, H. *Artificial Photosynthesis for the Energy Transition*. 2020. https://www.bayern-innovativ.de/en/page/rheticus-test-facility-from-evonik-and-siemens-energy (accessed 29.04.2022).
(110) de Klerk, A. Fischer–Tropsch Process. In *Kirk-Othmer Encyclopedia of Chemical Technology*, https://doi.org/10.1002/0471238961.fiscdekl.a01Wiley-VCH Verlag GmbH & Co. KGaA, pp 1-20.
(111) *Methanation Process. HELMETH project*. http://www.helmeth.eu/index.php/technologies/methanation-process (accessed 29.04.2022).
(112) Wang, W.; Wang, S.; Ma, X.; Gong, J. Recent Advances in Catalytic Hydrogenation of Carbon Dioxide. *Chemical Society Reviews* **2011**, *40* (7), 3703-3727. http://dx.doi.org/10.1039/C1CS15008A.
(113) Wilson, R. B. Fundamental Investigation of the Bosch Reaction, Master Thesis, Massachusetts Institute of Technology. 1971. https://dspace.mit.edu/handle/1721.1/45746.
(114) Shetty, S. G.; Ciobîcă, I. M.; Hensen, E. J. M.; van Santen, R. A. Site Regeneration in the Fischer–Tropsch Synthesis Reaction: a Synchronized CO Dissociation and C–C coupling Pathway. *Chemical Communications* **2011**, *47* (35), 9822-9824. http://dx.doi.org/10.1039/C1CC11499A.
(115) Dincer, I. Green Methods for Hydrogen Production. *International Journal of Hydrogen Energy* **2012**, *37* (2), 1954-1971. https://doi.org/10.1016/j.ijhydene.2011.03.173.
(116) Sakakura, T.; Choi, J.-C.; Yasuda, H. Transformation of Carbon Dioxide. *Chemical Reviews* **2007**, *107* (6), 2365-2387. https://doi.org/10.1021/cr068357u.
(117) Liu, Q.; Wu, L.; Jackstell, R.; Beller, M. Using Carbon Dioxide as a Building Block in Organic Synthesis. *Nature Communications* **2015**, *6* (1), 5933. https://doi.org/10.1038/ncomms6933.
(118) Aresta, M.; Dibenedetto, A.; Nocito, F.; Pastore, C. Comparison of the behaviour of Supported Homogeneous Catalysts in the Synthesis of Dimethylcarbonate from Methanol and Carbon Dioxide: Polystyrene-Grafted Tin-Metallorganic Species versus Silesquioxanes linked Nb-Methoxo Species. *Inorganica Chimica Acta* **2008**, *361* (11), 3215-3220. https://doi.org/10.1016/j.ica.2007.11.005.
(119) Jessop, P. G. Homogeneous Hydrogenation of Carbon Dioxide. In *The Handbook of Homogeneous Hydrogenation*, https://doi.org/10.1002/9783527619382.ch172006; pp 489-511.
(120) Poormohammadian, S. J.; Bahadoran, F.; Vakili-Nezhaad, G. R. Recent Progress in Homogeneous Hydrogenation of Carbon Dioxide to Methanol. *Reviews in Chemical Engineering* **2022**, https://doi.org/10.1515/revce-2021-0036. https://doi.org/10.1515/revce-2021-0036.
(121) Garg, S.; Li, M.; Weber, A. Z.; Ge, L.; Li, L.; Rudolph, V.; Wang, G.; Rufford, T. E. Advances and Challenges in Electrochemical CO_2 Reduction Processes: An Engineering and Design Perspective Looking Beyond New Catalyst Materials. *Journal of Materials Chemistry A* **2020**, *8* (4), 1511-1544. http://dx.doi.org/10.1039/C9TA13298H.
(122) Liang, S.; Altaf, N.; Huang, L.; Gao, Y.; Wang, Q. Electrolytic Cell Design for Electrochemical CO_2 Reduction. *Journal of CO2 Utilization* **2020**, *35*, 90-105. https://doi.org/10.1016/j.jcou.2019.09.007.
(123) Kuhl, K. P.; Cave, E. R.; Abram, D. N.; Jaramillo, T. F. New Insights into the Electrochemical Reduction of Carbon Dioxide on Metallic Copper Surfaces. *Energy & Environmental Science* **2012**, *5* (5), 7050-7059. http://dx.doi.org/10.1039/C2EE21234J.
(124) Senthilkumar, P.; Mohapatra, M.; Basu, S. The Inchoate Horizon of Electrolyzer Designs, Membranes and Catalysts Towards Highly Efficient Electrochemical Reduction of CO_2 to Formic acid. *RSC Advances* **2022**, *12* (3), 1287-1309. http://dx.doi.org/10.1039/D1RA05062A.
(125) Cave, E. R.; Shi, C.; Kuhl, K. P.; Hatsukade, T.; Abram, D. N.; Hahn, C.; Chan, K.; Jaramillo, T. F. Trends in the Catalytic Activity of Hydrogen Evolution during CO_2 Electroreduction on Transition Metals. *ACS Catalysis* **2018**, *8* (4), 3035-3040. https://doi.org/10.1021/acscatal.7b03807.
(126) Long, C.; Li, X.; Guo, J.; Shi, Y.; Liu, S.; Tang, Z. Electrochemical Reduction of CO_2 over Heterogeneous Catalysts in Aqueous Solution: Recent Progress and Perspectives. *Small Methods* **2019**, *3* (3), 1800369. https://doi.org/10.1002/smtd.201800369.
(127) Zhang, Y.-J.; Sethuraman, V.; Michalsky, R.; Peterson, A. A. Competition between CO_2 Reduction and H_2 Evolution on Transition-Metal Electrocatalysts. *ACS Catalysis* **2014**, *4* (10), 3742-3748. https://doi.org/10.1021/cs5012298.
(128) König, M.; Vaes, J.; Klemm, E.; Pant, D. Solvents and Supporting Electrolytes in the Electrocatalytic Reduction of CO_2. *iScience* **2019**, *19*, 135-160. https://doi.org/10.1016/j.isci.2019.07.014.
(129) Li, L.; Li, X.; Sun, Y.; Xie, Y. Rational Design of Electrocatalytic Carbon Dioxide Reduction for a Zero-Carbon Network. *Chemical Society Reviews* **2022**, *51* (4), 1234-1252. http://dx.doi.org/10.1039/D1CS00893E.
(130) Birdja, Y. Y.; Pérez-Gallent, E.; Figueiredo, M. C.; Göttle, A. J.; Calle-Vallejo, F.; Koper, M. T. M. Advances and Challenges in Understanding the Electrocatalytic Conversion of Carbon Dioxide to Fuels. *Nature Energy* **2019**, *4* (9), 732-745. https://doi.org/10.1038/s41560-019-0450-y.

(131) Schreier, M.; Héroguel, F.; Steier, L.; Ahmad, S.; Luterbacher, J. S.; Mayer, M. T.; Luo, J.; Grätzel, M. Solar Conversion of CO_2 to CO using Earth-Abundant Electrocatalysts Prepared by Atomic Layer Modification of CuO. *Nature Energy* **2017**, *2* (7), 17087. https://doi.org/10.1038/nenergy.2017.87.
(132) Shen, H.; Gu, Z.; Zheng, G. Pushing the Activity of CO_2 Electroreduction by System Engineering. *Science Bulletin* **2019**, *64* (24), 1805-1816. https://doi.org/10.1016/j.scib.2019.08.027.
(133) Antipin, D.; Risch, M. Trends of Epitaxial Perovskite Oxide Films Catalyzing The Oxygen Evolution Reaction in Alkaline Media. *Journal of Physics: Energy* **2020**, *2* (3), 032003. http://dx.doi.org/10.1088/2515-7655/ab812f.
(134) Song, J.; Wei, C.; Huang, Z.-F.; Liu, C.; Zeng, L.; Wang, X.; Xu, Z. J. A Review on Fundamentals for Designing Oxygen Evolution Electrocatalysts. *Chemical Society Reviews* **2020**, *49* (7), 2196-2214. http://dx.doi.org/10.1039/C9CS00607A.
(135) Pérez-Gallent, E.; Turk, S.; Latsuzbaia, R.; Bhardwaj, R.; Anastasopol, A.; Sastre-Calabuig, F.; Garcia, A. C.; Giling, E.; Goetheer, E. Electroreduction of CO_2 to CO Paired with 1,2-Propanediol Oxidation to Lactic Acid. Toward an Economically Feasible System. *Industrial & Engineering Chemistry Research* **2019**, *58* (16), 6195-6202. https://doi.org/10.1021/acs.iecr.8b06340.
(136) Vass, Á.; Kormányos, A.; Kószó, Z.; Endrődi, B.; Janáky, C. Anode Catalysts in CO_2 Electrolysis: Challenges and Untapped Opportunities. *ACS Catalysis* **2022**, *12* (2), 1037-1051. https://doi.org/10.1021/acscatal.1c04978.
(137) Vass, Á.; Endrődi, B.; Janáky, C. Coupling Electrochemical Carbon Dioxide Conversion with Value-Added Anode Processes: An Emerging Paradigm. *Current Opinion in Electrochemistry* **2021**, *25*, 100621. https://doi.org/10.1016/j.coelec.2020.08.003.
(138) Royer, M. E. Réduction de l'acide carbonique en acide formique. *Comptes rendus de l'Académie des Sciences* **1870**, *70*, 731.
(139) Teeter, T. E.; Rysselberghe, P. V. Reduction of Carbon Dioxide on Mercury Cathodes. *The Journal of Chemical Physics* **1954**, *22* (4), 759-760. https://doi.org/10.1063/1.1740178.
(140) Rabinowitsch, M.; Maschowetz, A. Elektrochemische Gewinnung von Formiaten aus Kohlensäure. *Zeitschrift für Elektrochemie und angewandte physikalische Chemie* **1930**, *36* (10), 846-850. https://doi.org/10.1002/bbpc.19300361004.
(141) Yoshio, H.; Katsuhei, K.; Shin, S. Production of CO and CH_4 in Electrochemical Reduction of CO_2 at Metal Electrodes in Aqueous Hydrogencarbonate Solution *Chemistry Letters* **1985**, *14* (11), 1695-1698. https://doi.org/10.1246/cl.1985.1695.
(142) Frese, K. W.; Leach, S. Electrochemical Reduction of Carbon Dioxide to Methane, Methanol, and CO on Ru Electrodes. *Journal of The Electrochemical Society* **1985**, *132* (1), 259-260. http://dx.doi.org/10.1149/1.2113780.
(143) Yoshio, H.; Katsuhei, K.; Akira, M.; Shin, S. Production of Methane and Ethylene in Electrochemical Reduction if Carbon Dioxide at Copper Electrode in Aqueous Hydrogencarbonate Solution. *Chemistry Letters* **1986**, *15* (6), 897-898. https://doi.org/10.1246/cl.1986.897.
(144) Hori, Y.; Murata, A.; Takahashi, R. Formation of Hydrocarbons in the Electrochemical Reduction of Carbon Dioxide at a Copper Electrode in Aqueous Solution. *Journal of the Chemical Society, Faraday Transactions 1: Physical Chemistry in Condensed Phases* **1989**, *85* (8), 2309-2326. http://dx.doi.org/10.1039/F19898502309.
(145) Hori, Y. Electrochemical CO_2 Reduction on Metal Electrodes. In *Modern Aspects of Electrochemistry*, Vayenas, C. G., White, R. E., Gamboa-Aldeco, M. E. Eds.; Vol. 42; Springer, 2008; pp 89-189.
(146) Bagger, A.; Ju, W.; Varela, A. S.; Strasser, P.; Rossmeisl, J. Electrochemical CO_2 Reduction: A Classification Problem. *ChemPhysChem* **2017**, *18* (22), 3266-3273. https://doi.org/10.1002/cphc.201700736.
(147) Yoo, J. S.; Christensen, R.; Vegge, T.; Nørskov, J. K.; Studt, F. Theoretical Insight into the Trends that Guide the Electrochemical Reduction of Carbon Dioxide to Formic Acid. *ChemSusChem* **2016**, *9* (4), 358-363. https://doi.org/10.1002/cssc.201501197.
(148) Kortlever, R.; Shen, J.; Schouten, K. J. P.; Calle-Vallejo, F.; Koper, M. T. M. Catalysts and Reaction Pathways for the Electrochemical Reduction of Carbon Dioxide. *The Journal of Physical Chemistry Letters* **2015**, *6* (20), 4073-4082. https://doi.org/10.1021/acs.jpclett.5b01559.
(149) Zhang, W.; Hu, Y.; Ma, L.; Zhu, G.; Wang, Y.; Xue, X.; Chen, R.; Yang, S.; Jin, Z. Progress and Perspective of Electrocatalytic CO2 Reduction for Renewable Carbonaceous Fuels and Chemicals. *Advanced Science* **2018**, *5* (1), 1700275. https://doi.org/10.1002/advs.201700275.
(150) Goodpaster, J. D.; Bell, A. T.; Head-Gordon, M. Identification of Possible Pathways for C–C Bond Formation during Electrochemical Reduction of CO_2: New Theoretical Insights from an Improved

Electrochemical Model. *Journal of Physical Chemistry Letters* **2016**, *7* (8), 1471-1477. https://doi.org/10.1021/acs.jpclett.6b00358.
(151) Bui, J. C.; Kim, C.; King, A. J.; Romiluyi, O.; Kusoglu, A.; Weber, A. Z.; Bell, A. T. Engineering Catalyst–Electrolyte Microenvironments to Optimize the Activity and Selectivity for the Electrochemical Reduction of CO_2 on Cu and Ag. *Accounts of Chemical Research* **2022**, *55* (4), 484-494. https://doi.org/10.1021/acs.accounts.1c00650.
(152) Wang, L.; Nitopi, S. A.; Bertheussen, E.; Orazov, M.; Morales-Guio, C. G.; Liu, X.; Higgins, D. C.; Chan, K.; Nørskov, J. K.; Hahn, C.; et al. Electrochemical Carbon Monoxide Reduction on Polycrystalline Copper: Effects of Potential, Pressure, and pH on Selectivity toward Multicarbon and Oxygenated Products. *ACS Catalysis* **2018**, *8* (8), 7445-7454. https://doi.org/10.1021/acscatal.8b01200.
(153) Li, C. W.; Ciston, J.; Kanan, M. W. Electroreduction of Carbon Monoxide to Liquid Fuel on Oxide-Derived Nanocrystalline Copper. *Nature* **2014**, *508* (7497), 504-507. https://doi.org/10.1038/nature13249.
(154) Chang, X.; Li, J.; Xiong, H.; Zhang, H.; Xu, Y.; Xiao, H.; Lu, Q.; Xu, B. C−C Coupling Is Unlikely to Be the Rate-Determining Step in the Formation of C_{2+} Products in the Copper-Catalyzed Electrochemical Reduction of CO. *Angewandte Chemie International Edition* **2022**, *61* (2), e202111167. https://doi.org/10.1002/anie.202111167.
(155) Greenblatt, J. B.; Miller, D. J.; Ager, J. W.; Houle, F. A.; Sharp, I. D. The Technical and Energetic Challenges of Separating (Photo)Electrochemical Carbon Dioxide Reduction Products. *Joule* **2018**, *2* (3), 381-420. https://doi.org/10.1016/j.joule.2018.01.014.
(156) Ye, W.; Guo, X.; Ma, T. A Review on Electrochemical Synthesized Copper-Based Catalysts for Electrochemical Reduction of CO_2 to C_{2+} Products. *Chemical Engineering Journal* **2021**, *414*, 128825. https://doi.org/10.1016/j.cej.2021.128825.
(157) Wakerley, D.; Lamaison, S.; Wicks, J.; Clemens, A.; Feaster, J.; Corral, D.; Jaffer, S. A.; Sarkar, A.; Fontecave, M.; Duoss, E. B.; et al. Gas Diffusion electrodes, Reactor Designs and Key Metrics of Low-Temperature CO_2 Electrolysers. *Nature Energy* **2022**, *7* (2), 130-143. https://doi.org/10.1038/s41560-021-00973-9.
(158) Bard, A. J.; Faulkner, L. R. *Electrochemical Methods: Fundamentals and Applications, Second Edition*; John Wiley & Sons Inc., 2001.
(159) Luo, Y.; Zhang, K.; Li, Y.; Wang, Y. Valorizing Carbon Dioxide via Electrochemical Reduction on Gas-Diffusion Electrodes. *InfoMat* **2021**, *3* (12), 1313-1332. https://doi.org/10.1002/inf2.12253.
(160) Tan, Y. C.; Quek, W. K.; Kim, B.; Sugiarto, S.; Oh, J.; Kai, D. Pitfalls and Protocols: Evaluating Catalysts for CO_2 Reduction in Electrolyzers Based on Gas Diffusion Electrodes. *ACS Energy Letters* **2022**, https://doi.org/10.1021/acsenergylett.2c00763, 2012-2023. https://doi.org/10.1021/acsenergylett.2c00763.
(161) Faggion, D.; Gonçalves, W. D. G.; Dupont, J. CO_2 Electroreduction in Ionic Liquids. *Frontiers in Chemistry* **2019**, *7*, Mini Review. DOI: https://doi.org/10.3389/fchem.2019.00102.
(162) Dutta, A.; Rahaman, M.; Luedi, N. C.; Mohos, M.; Broekmann, P. Morphology Matters: Tuning the Product Distribution of CO_2 Electroreduction on Oxide-Derived Cu Foam Catalysts. *ACS Catalysis* **2016**, *6* (6), 3804-3814. https://doi.org/10.1021/acscatal.6b00770.
(163) Hyun, G.; Song, J. T.; Ahn, C.; Ham, Y.; Cho, D.; Oh, J.; Jeon, S. Hierarchically Porous Au Nanostructures with Interconnected Channels for Efficient Mass Transport in Electrocatalytic CO_2 Reduction. *Proceedings of the National Academy of Sciences* **2020**, *117* (11), 5680-5685. https://doi.org/10.1073/pnas.1918837117.
(164) Zeng, J.; Bejtka, K.; Ju, W.; Castellino, M.; Chiodoni, A.; Sacco, A.; Farkhondehfal, M. A.; Hernández, S.; Rentsch, D.; Battaglia, C.; et al. Advanced Cu-Sn foam for Selectively Converting CO_2 to CO in Aqueous Solution. *Applied Catalysis B: Environmental* **2018**, *236*, 475-482. https://doi.org/10.1016/j.apcatb.2018.05.056.
(165) Ju, W.; Zeng, J.; Bejtka, K.; Ma, H.; Rentsch, D.; Castellino, M.; Sacco, A.; Pirri, C. F.; Battaglia, C. Sn-Decorated Cu for Selective Electrochemical CO_2 to CO Conversion: Precision Architecture beyond Composition Design. *ACS Applied Energy Materials* **2019**, *2* (1), 867-872. https://doi.org/10.1021/acsaem.8b01944.
(166) Burdyny, T.; Graham, P. J.; Pang, Y.; Dinh, C.-T.; Liu, M.; Sargent, E. H.; Sinton, D. Nanomorphology-Enhanced Gas-Evolution Intensifies CO_2 Reduction Electrochemistry. *ACS Sustainable Chemistry & Engineering* **2017**, *5* (5), 4031-4040. https://doi.org/10.1021/acssuschemeng.7b00023.
(167) Vesztergom, S.; Dutta, A.; Rahaman, M.; Kiran, K.; Zelocualtecatl Montiel, I.; Broekmann, P. Hydrogen Bubble Templated Metal Foams as Efficient Catalysts of CO_2 Electroreduction. *ChemCatChem* **2021**, *13* (4), 1039-1058. https://doi.org/10.1002/cctc.202001145.

(168) Scholten, F.; Sinev, I.; Bernal, M.; Roldan Cuenya, B. Plasma-Modified Dendritic Cu Catalyst for CO_2 Electroreduction. *ACS Catalysis* **2019**, *9* (6), 5496-5502. https://doi.org/10.1021/acscatal.9b00483.
(169) Chen, C. S.; Wan, J. H.; Yeo, B. S. Electrochemical Reduction of Carbon Dioxide to Ethane Using Nanostructured Cu_2O-Derived Copper Catalyst and Palladium(II) Chloride. *The Journal of Physical Chemistry C* **2015**, *119* (48), 26875-26882. https://doi.org/10.1021/acs.jpcc.5b09144.
(170) Ma, S.; Sadakiyo, M.; Heima, M.; Luo, R.; Haasch, R. T.; Gold, J. I.; Yamauchi, M.; Kenis, P. J. A. Electroreduction of Carbon Dioxide to Hydrocarbons Using Bimetallic Cu–Pd Catalysts with Different Mixing Patterns. *Journal of the American Chemical Society* **2017**, *139* (1), 47-50. https://doi.org/10.1021/jacs.6b10740.
(171) Wan, L.; Zhang, X.; Cheng, J.; Chen, R.; Wu, L.; Shi, J.; Luo, J. Bimetallic Cu–Zn Catalysts for Electrochemical CO_2 Reduction: Phase-Separated versus Core–Shell Distribution. *ACS Catalysis* **2022**, *12* (5), 2741-2748. DOI: 10.1021/acscatal.1c05272.
(172) Keerthiga, G.; Chetty, R. Electrochemical Reduction of Carbon Dioxide on Zinc-Modified Copper Electrodes. *Journal of The Electrochemical Society* **2017**, *164* (4), H164-H169. http://dx.doi.org/10.1149/2.0421704jes.
(173) Su, X.; Sun, Y.; Jin, L.; Zhang, L.; Yang, Y.; Kerns, P.; Liu, B.; Li, S.; He, J. Hierarchically Porous Cu/Zn Bimetallic Catalysts for Highly Selective CO_2 Electroreduction to Liquid C_2 Products. *Applied Catalysis B: Environmental* **2020**, *269*, 118800. https://doi.org/10.1016/j.apcatb.2020.118800.
(174) Ren, D.; Gao, J.; Pan, L.; Wang, Z.; Luo, J.; Zakeeruddin, S. M.; Hagfeldt, A.; Grätzel, M. Atomic Layer Deposition of ZnO on CuO Enables Selective and Efficient Electroreduction of Carbon Dioxide to Liquid Fuels. *Angewandte Chemie International Edition* **2019**, *58* (42), 15036-15040. https://doi.org/10.1002/anie.201909610.
(175) Vasileff, A.; Zhi, X.; Xu, C.; Ge, L.; Jiao, Y.; Zheng, Y.; Qiao, S.-Z. Selectivity Control for Electrochemical CO_2 Reduction by Charge Redistribution on the Surface of Copper Alloys. *ACS Catalysis* **2019**, *9* (10), 9411-9417. https://doi.org/10.1021/acscatal.9b02312.
(176) He, J.; Dettelbach, K. E.; Huang, A.; Berlinguette, C. P. Brass and Bronze as Effective CO_2 Reduction Electrocatalysts. *Angewandte Chemie International Edition* **2017**, *56* (52), 16579-16582. https://doi.org/10.1002/anie.201709932.
(177) Pardo Pérez, L. C.; Arndt, A.; Stojkovikj, S.; Ahmet, I. Y.; Arens, J. T.; Dattila, F.; Wendt, R.; Guilherme Buzanich, A.; Radtke, M.; Davies, V.; et al. Determining Structure-Activity Relationships in Oxide Derived Cu-Sn Catalysts During CO_2 Electroreduction Using X-Ray Spectroscopy. *Advanced Energy Materials* **2022**, *12* (5), 2103328. https://doi.org/10.1002/aenm.202103328.
(178) Stojkovikj, S.; El-Nagar, G. A.; Firschke, F.; Pardo Pérez, L. C.; Choubrac, L.; Najdoski, M.; Mayer, M. T. Electrocatalyst Derived from Waste Cu–Sn Bronze for CO_2 Conversion into CO. *ACS Applied Materials & Interfaces* **2021**, *13* (32), 38161-38169. https://doi.org/10.1021/acsami.1c05015.
(179) Xie, H.; Chen, S.; Ma, F.; Liang, J.; Miao, Z.; Wang, T.; Wang, H.-L.; Huang, Y.; Li, Q. Boosting Tunable Syngas Formation via Electrochemical CO_2 Reduction on Cu/In_2O_3 Core/Shell Nanoparticles. *ACS Applied Materials & Interfaces* **2018**, *10* (43), 36996-37004. https://doi.org/10.1021/acsami.8b12747.
(180) Hoffman, Z. B.; Gray, T. S.; Moraveck, K. B.; Gunnoe, T. B.; Zangari, G. Electrochemical Reduction of Carbon Dioxide to Syngas and Formate at Dendritic Copper–Indium Electrocatalysts. *ACS Catalysis* **2017**, *7* (8), 5381-5390. https://doi.org/10.1021/acscatal.7b01161.
(181) Zhao, S.; Li, S.; Guo, T.; Zhang, S.; Wang, J.; Wu, Y.; Chen, Y. Advances in Sn-Based Catalysts for Electrochemical CO_2 Reduction. *Nano-Micro Letters* **2019**, *11* (1), 62. https://doi.org/10.1007/s40820-019-0293-x.
(182) Lee, C. W.; Yang, K. D.; Nam, D.-H.; Jang, J. H.; Cho, N. H.; Im, S. W.; Nam, K. T. Defining a Materials Database for the Design of Copper Binary Alloy Catalysts for Electrochemical CO_2 Conversion. *Advanced Materials* **2018**, *30* (42), 1704717. https://doi.org/10.1002/adma.201704717.
(183) Jia, Y.; Li, F.; Fan, K.; Sun, L. Cu-Based Bimetallic Electrocatalysts for CO_2 Reduction. *Advanced Powder Materials* **2022**, *1* (1), 100012. https://doi.org/10.1016/j.apmate.2021.10.003.
(184) Sarfraz, S.; Garcia-Esparza, A. T.; Jedidi, A.; Cavallo, L.; Takanabe, K. Cu–Sn Bimetallic Catalyst for Selective Aqueous Electroreduction of CO_2 to CO. *ACS Catalysis* **2016**, *6* (5), 2842-2851. https://doi.org/10.1021/acscatal.6b00269.
(185) Zhang, S.-N.; Li, M.; Hua, B.; Duan, N.; Ding, S.; Bergens, S.; Shankar, K.; Luo, J.-L. A Rational Design of Cu_2O−SnO2 Core-Shell Catalyst for Highly Selective CO_2-to-CO Conversion. *ChemCatChem* **2019**, *11* (16), 4147-4153. https://doi.org/10.1002/cctc.201900395.
(186) Ju, W.; Jiang, F.; Ma, H.; Pan, Z.; Zhao, Y.-B.; Pagani, F.; Rentsch, D.; Wang, J.; Battaglia, C. Electrocatalytic Reduction of Gaseous CO_2 to CO on Sn/Cu-Nanofiber-Based Gas Diffusion

Electrodes. *Advanced Energy Materials* **2019**, *9* (32), 1901514. https://doi.org/10.1002/aenm.201901514.
(187) Li, Q.; Fu, J.; Zhu, W.; Chen, Z.; Shen, B.; Wu, L.; Xi, Z.; Wang, T.; Lu, G.; Zhu, J.-j.; et al. Tuning Sn-Catalysis for Electrochemical Reduction of CO_2 to CO via the Core/Shell Cu/SnO_2 Structure. *J. Am. Chem. Soc.* **2017**, *139* (12), 4290-4293. https://doi.org/10.1021/jacs.7b00261.
(188) Vasileff, A.; Xu, C.; Jiao, Y.; Zheng, Y.; Qiao, S.-Z. Surface and Interface Engineering in Copper-Based Bimetallic Materials for Selective CO_2 Electroreduction. *Chem* **2018**, *4* (8), 1809-1831. https://doi.org/10.1016/j.chempr.2018.05.001.
(189) Luo, W.; Xie, W.; Mutschler, R.; Oveisi, E.; De Gregorio, G. L.; Buonsanti, R.; Züttel, A. Selective and Stable Electroreduction of CO_2 to CO at the Copper/Indium Interface. *ACS Catalysis* **2018**, *8* (7), 6571-6581. https://doi.org/10.1021/acscatal.7b04457.
(190) Wu, Y.; Iwase, K.; Harada, T.; Nakanishi, S.; Kamiya, K. Sn Atoms on Cu Nanoparticles for Suppressing Competitive H_2 Evolution in CO_2 Electrolysis. *ACS Applied Nano Materials* **2021**, *4* (5), 4994-5003. https://doi.org/10.1021/acsanm.1c00514.
(191) Chen, Y.; Chen, K.; Fu, J.; Yamaguchi, A.; Li, H.; Pan, H.; Hu, J.; Miyauchi, M.; Liu, M. Recent Advances in the Utilization of Copper Sulfide Compounds for Electrochemical CO_2 Reduction. *Nano Materials Science* **2020**, *2* (3), 235-247. https://doi.org/10.1016/j.nanoms.2019.10.006.
(192) Dou, T.; Qin, Y.; Zhang, F.; Lei, X. CuS Nanosheet Arrays for Electrochemical CO_2 Reduction with Surface Reconstruction and the Effect on Selective Formation of Formate. *ACS Applied Energy Materials* **2021**, *4* (5), 4376-4384. https://doi.org/10.1021/acsaem.0c03190.
(193) Luc, W.; Ko, B. H.; Kattel, S.; Li, S.; Su, D.; Chen, J. G.; Jiao, F. SO_2-Induced Selectivity Change in CO2 Electroreduction. *Journal of the American Chemical Society* **2019**, *141* (25), 9902-9909. https://doi.org/10.1021/jacs.9b03215.
(194) Pan, Z.; Wang, K.; Ye, K.; Wang, Y.; Su, H.-Y.; Hu, B.; Xiao, J.; Yu, T.; Wang, Y.; Song, S. Intermediate Adsorption States Switch to Selectively Catalyze Electrochemical CO_2 Reduction. *ACS Catalysis* **2020**, *10* (6), 3871-3880. https://doi.org/10.1021/acscatal.9b05115.
(195) Deng, Y.; Huang, Y.; Ren, D.; Handoko, A. D.; Seh, Z. W.; Hirunsit, P.; Yeo, B. S. On the Role of Sulfur for the Selective Electrochemical Reduction of CO_2 to Formate on CuS_x Catalysts. *ACS Applied Materials & Interfaces* **2018**, *10* (34), 28572-28581. https://doi.org/10.1021/acsami.8b08428.
(196) Huang, Y.; Deng, Y.; Handoko, A. D.; Goh, G. K. L.; Yeo, B. S. Rational Design of Sulfur-Doped Copper Catalysts for the Selective Electroreduction of Carbon Dioxide to Formate. *ChemSusChem* **2018**, *11* (1), 320-326. https://doi.org/10.1002/cssc.201701314.
(197) Wang, S.; Kou, T.; Varley, J. B.; Akhade, S. A.; Weitzner, S. E.; Baker, S. E.; Duoss, E. B.; Li, Y. Cu_2O/CuS Nanocomposites Show Excellent Selectivity and Stability for Formate Generation via Electrochemical Reduction of Carbon Dioxide. *ACS Materials Letters* **2021**, *3* (1), 100-109. https://doi.org/10.1021/acsmaterialslett.0c00520.
(198) Lim, J. W.; Dong, W. J.; Park, J. Y.; Hong, D. M.; Lee, J.-L. Spontaneously Formed CuS_x Catalysts for Selective and Stable Electrochemical Reduction of Industrial CO_2 Gas to Formate. *ACS Applied Materials & Interfaces* **2020**, *12* (20), 22891-22900. https://doi.org/10.1021/acsami.0c03606.
(199) Yang, Z.; Oropeza, F. E.; Zhang, K. H. L. P-Block Metal-Based (Sn, In, Bi, Pb) Electrocatalysts for Selective Reduction of CO_2 to Formate. *APL Materials* **2020**, *8* (6), 060901. https://doi.org/10.1063/5.0004194.
(200) Gálvez-Vázquez, M. d. J.; Moreno-García, P.; Guo, H.; Hou, Y.; Dutta, A.; Waldvogel, S. R.; Broekmann, P. Leaded Bronze Alloy as a Catalyst for the Electroreduction of CO_2. *ChemElectroChem* **2019**, *6* (8), 2324-2330. https://doi.org/10.1002/celc.201900537.
(201) Chen, Z.; Wang, N.; Yao, S.; Liu, L. The Flaky Cd Film on Cu Plate Substrate: An Active and Efficient Electrode for Electrochemical Reduction of CO_2 to Formate. *Journal of CO2 Utilization* **2017**, *22*, 191-196. https://doi.org/10.1016/j.jcou.2017.09.023.
(202) Li, H.; Yue, X.; Che, J.; Xiao, Z.; Yu, X.; Sun, F.; Xue, C.; Xiang, J. High Performance 3D Self-Supporting Cu−Bi Aerogels for Electrocatalytic Reduction of CO_2 to Formate. *ChemSusChem* **2022**, *15* (7), e202200226. https://doi.org/10.1002/cssc.202200226.
(203) Wang, Z.; Yuan, Q.; Shan, J.; Jiang, Z.; Xu, P.; Hu, Y.; Zhou, J.; Wu, L.; Niu, Z.; Sun, J.; et al. Highly Selective Electrocatalytic Reduction of CO_2 into Methane on Cu–Bi Nanoalloys. *The Journal of Physical Chemistry Letters* **2020**, *11* (17), 7261-7266. https://doi.org/10.1021/acs.jpclett.0c01261.
(204) Hietala, J.; Vuori, A.; Johnsson, P.; Pollari, I.; Reutemann, W.; Kieczka, H. Formic Acid. In *Ullmann's Encyclopedia of Industrial Chemistry*, https://doi.org/10.1002/14356007.a12_013.pub3pp 1-22.
(205) Sun, X.; Lou, Y.; He, Y.-L.; Li, Y. A Na-ion Direct Formate Fuel Cell Converting Solar Fuel to Electricity and Hydrogen. *Journal of Power Sources* **2021**, *499*, 229960. https://doi.org/10.1016/j.jpowsour.2021.229960.

(206) Li, Y.; Feng, Y.; Sun, X.; He, Y. A Sodium-Ion-Conducting Direct Formate Fuel Cell: Generating Electricity and Producing Base. *Angewandte Chemie International Edition* **2017**, *56* (21), 5734-5737. https://doi.org/10.1002/anie.201701816.
(207) Bienen, F.; Kopljar, D.; Löwe, A.; Aßmann, P.; Stoll, M.; Rößner, P.; Wagner, N.; Friedrich, A.; Klemm, E. Utilizing Formate as an Energy Carrier by Coupling CO_2 Electrolysis with Fuel Cell Devices. *Chemie Ingenieur Technik* **2019**, *91* (6), 872-882. https://doi.org/10.1002/cite.201800212.
(208) Jouny, M.; Luc, W.; Jiao, F. General Techno-Economic Analysis of CO_2 Electrolysis Systems. *Ind. Eng. Chem. Res.* **2018**, *57* (6), 2165-2177. https://doi.org/10.1021/acs.iecr.7b03514.
(209) Chang, Z.; Huo, S.; Zhang, W.; Fang, J.; Wang, H. The Tunable and Highly Selective Reduction Products on Ag@Cu Bimetallic Catalysts Toward CO_2 Electrochemical Reduction Reaction. *The Journal of Physical Chemistry C* **2017**, *121* (21), 11368-11379. https://doi.org/10.1021/acs.jpcc.7b01586.
(210) Nguyen, D. L. T.; Jee, M. S.; Won, D. H.; Jung, H.; Oh, H.-S.; Min, B. K.; Hwang, Y. J. Selective CO_2 Reduction on Zinc Electrocatalyst: The Effect of Zinc Oxidation State Induced by Pretreatment Environment. *ACS Sustainable Chemistry & Engineering* **2017**, *5* (12), 11377-11386. https://doi.org/10.1021/acssuschemeng.7b02460.
(211) Zong, X.; Jin, Y.; Li, Y.; Zhang, X.; Zhang, S.; Xie, H.; Zhang, J.; Xiong, Y. Morphology-controllable ZnO catalysts enriched with oxygen-vacancies for boosting CO_2 electroreduction to CO. *Journal of CO2 Utilization* **2022**, *61*, 102051. https://doi.org/10.1016/j.jcou.2022.102051.
(212) Rasul, S.; Anjum, D. H.; Jedidi, A.; Minenkov, Y.; Cavallo, L.; Takanabe, K. A Highly Selective Copper–Indium Bimetallic Electrocatalyst for the Electrochemical Reduction of Aqueous CO_2 to CO. *Angewandte Chemie International Edition* **2015**, *54* (7), 2146-2150. https://doi.org/10.1002/anie.201410233.
(213) Nguyen-Phan, T.-D.; Hu, L.; Howard, B. H.; Xu, W.; Stavitski, E.; Leshchev, D.; Rothenberger, A.; Neyerlin, K. C.; Kauffman, D. R. High Current Density Electroreduction of CO_2 into Formate with Tin Oxide Nanospheres. *Scientific Reports* **2022**, *12* (1), 8420. https://doi.org/10.1038/s41598-022-11890-6.
(214) Haxel, G. B.; Hedrick, J. B.; Orris, G. J. *Rare Earth Elements—Critical Resources for High Technology. U.S. Geological Survey Fact Sheet 087-02.* 2002. https://pubs.usgs.gov/fs/2002/fs087-02/ (accessed 15.06.2022).
(215) *Copper. Trading Economics.* 2022. https://tradingeconomics.com/commodity/copper (accessed 02.06.2022).
(216) *Sulfur Price. Sulfur Price in Germany.* 2022. https://sulfur-price.com/today/germany (accessed 02.06.2022).
(217) *Tin. Trading Economics.* 2022. https://tradingeconomics.com/commodity/tin (accessed 02.06.2022).
(218) Cao, X.; Tan, D.; Wulan, B.; Hui, K. S.; Hui, K. N.; Zhang, J. In Situ Characterization for Boosting Electrocatalytic Carbon Dioxide Reduction. *Small Methods* **2021**, *5* (10), 2100700. https://doi.org/10.1002/smtd.202100700.
(219) Adarsh, K. S.; Chandrasekaran, N.; Chakrapani, V. *In-situ* Spectroscopic Techniques as Critical Evaluation Tools for Electrochemical Carbon dioxide Reduction: A Mini Review. *Frontiers in Chemistry* **2020**, *8*, Mini Review. https://doi.org/10.3389/fchem.2020.00137.
(220) Jin, L.; Seifitokaldani, A. In Situ Spectroscopic Methods for Electrocatalytic CO_2 Reduction. *Catalysts* **2020**, *10* (5), 481. https://doi.org/10.3390/catal10050481.
(221) Clark, E. L.; Singh, M. R.; Kwon, Y.; Bell, A. T. Differential Electrochemical Mass Spectrometer Cell Design for Online Quantification of Products Produced during Electrochemical Reduction of CO_2. *Analytical Chemistry* **2015**, *87* (15), 8013-8020. https://doi.org/10.1021/acs.analchem.5b02080.
(222) Li, X.; Wang, S.; Li, L.; Sun, Y.; Xie, Y. Progress and Perspective for In Situ Studies of CO_2 Reduction. *Journal of the American Chemical Society* **2020**, *142* (21), 9567-9581. https://doi.org/10.1021/jacs.0c02973.
(223) Velasco-Velez, J.-J.; Mom, R. V.; Sandoval-Diaz, L.-E.; Falling, L. J.; Chuang, C.-H.; Gao, D.; Jones, T. E.; Zhu, Q.; Arrigo, R.; Roldan Cuenya, B.; et al. Revealing the Active Phase of Copper during the Electroreduction of CO_2 in Aqueous Electrolyte by Correlating *In Situ* X-ray Spectroscopy and *In Situ* Electron Microscopy. *ACS Energy Letters* **2020**, *5* (6), 2106-2111. https://doi.org/10.1021/acsenergylett.0c00802.
(224) Ranninger, J.; Nikolaienko, P.; Mayrhofer, K. J. J.; Berkes, B. B. On-line Electrode Dissolution Monitoring during Organic Electrosynthesis: Direct Evidence of Electrode Dissolution during Kolbe Electrolysis. *ChemSusChem* **2022**, *15* (5), e202102228. https://doi.org/10.1002/cssc.202102228.

(225) Zhang, W.; Wen, X.; Yang, S.; Berta, Y.; Wang, Z. L. Single-Crystalline Scroll-Type Nanotube Arrays of Copper Hydroxide Synthesized at Room Temperature. *Advanced Materials* **2003**, *15* (10), 822-825. https://doi.org/10.1002/adma.200304840.
(226) Tian, L.; Liu, B. Fabrication of CuO Nanosheets Modified Cu Electrode and its Excellent Electrocatalytic Performance towards Glucose. *Applied Surface Science* **2013**, *283*, 947-953. https://doi.org/10.1016/j.apsusc.2013.07.048.
(227) Singh, D. P.; Ojha, A. K.; Srivastava, O. N. Synthesis of Different $Cu(OH)_2$ and CuO (Nanowires, Rectangles, Seed-, Belt-, and Sheetlike) Nanostructures by Simple Wet Chemical Route. *The Journal of Physical Chemistry C* **2009**, *113* (9), 3409-3418. https://doi.org/10.1021/jp804832g.
(228) La, D.-D.; Park, S. Y.; Choi, Y.-W.; Kim, Y. S. Wire-like Bundle Arrays of Copper Hydroxide Prepared by the Electrochemical Anodization of Cu Foil. *Bulletin of the Korean Chemical Society* **2010**, *31* (8), 2283-2288. https://doi.org/10.5012/bkcs.2010.31.8.2283.
(229) Oviroh, P. O.; Akbarzadeh, R.; Pan, D.; Coetzee, R. A. M.; Jen, T.-C. New Development of Atomic Layer Deposition: Processes, Methods and Applications. *Science and Technology of Advanced Materials* **2019**, *20* (1), 465-496. https://doi.org/10.1080/14686996.2019.1599694.
(230) Nikolić, N. D. Influence of the Exchange Current Density and Overpotential for Hydrogen Evolution Reaction on the Shape of Electrolytically Produced Disperse Forms. *Journal of Electrochemical Science and Engineering* **2020**, *10* (2), 111-126. https://doi.org/10.5599/jese.707.
(231) Urbanová, M.; Kupčík, J.; Bezdička, P.; Šubrt, J.; Pola, J. Room-Temperature Sulfidation of Copper Nanoparticles with Sulfur Yielding Covellite Nanoparticles. *Comptes Rendus Chimie* **2012**, *15* (6), 511-516. https://doi.org/10.1016/j.crci.2012.03.014.
(232) Steudel, R.; Holz, B. Detection of Reactive Sulfur Molecules (S6, S7, S9, S∞) in Commercial Sulfur, in Sulfur Minerals, and in Sulfur Melts Slowly Cooled to 20 °C [1]. *Zeitschrift für Naturforschung B* **1988**, *43* (5), 581-589. DOI: doi:10.1515/znb-1988-0516.
(233) Epp, J. 4 - X-ray diffraction (XRD) Techniques for Materials Characterization. In *Materials Characterization Using Nondestructive Evaluation (NDE) Methods*, Hübschen, G., Altpeter, I., Tschuncky, R., Herrmann, H.-G. Eds.; https://doi.org/10.1016/B978-0-08-100040-3.00004-3Woodhead Publishing, 2016; pp 81-124.
(234) Murawski, C.; Elschner, C.; Lenk, S.; Reineke, S.; Gather, M. C. Investigating the Molecular Orientation of Ir(ppy)3 and Ir(ppy)2(acac) Emitter Complexes by X-ray Diffraction. *Organic Electronics* **2018**, *53*, 198-204. https://doi.org/10.1016/j.orgel.2017.11.036.
(235) Hou, X.; Amais, R. S.; Jones, B. T.; Donati, G. L. Inductively Coupled Plasma Optical Emission Spectrometry. In *Encyclopedia of Analytical Chemistry*, Meyers, R. A. Ed.; https://doi.org/10.1002/9780470027318.a5110.pub42021; pp 1-29.
(236) Khan, S. R.; Sharma, B.; Chawla, P. A.; Bhatia, R. Inductively Coupled Plasma Optical Emission Spectrometry (ICP-OES): a Powerful Analytical Technique for Elemental Analysis. *Food Analytical Methods* **2022**, *15* (3), 666-688. https://doi.org/10.1007/s12161-021-02148-4.
(237) Prime, R. B.; Bair, H. E.; Vyazovkin, S.; Gallagher, P. K.; Riga, A. Thermogravimetric Analysis (TGA). In *Thermal Analysis of Polymers*, https://doi.org/10.1002/9780470423837.ch32009; pp 241-317.
(238) de Hoffmann, E.; Stroobant, V. *Mass Spectrometry: Principles and Applications, 3rd Edition*; John Wiley & Sons, 2013.
(239) Höhne, G. W. H.; Hemminger, W. F.; Flammersheim, H.-J. *Differential Scanning Calorimetry - Second Edition*; Springer Berlin, Heidelberg, 2003. https://doi.org/10.1007/978-3-662-06710-9.
(240) Inkson, B. J. 2 - Scanning Electron Microscopy (SEM) and Transmission Electron Microscopy (TEM) for Materials Characterization. In *Materials Characterization Using Nondestructive Evaluation (NDE) Methods*, Hübschen, G., Altpeter, I., Tschuncky, R., Herrmann, H.-G. Eds.; https://doi.org/10.1016/B978-0-08-100040-3.00002-XWoodhead Publishing, 2016; pp 17-43.
(241) Shindo, D.; Oikawa, T. Energy Dispersive X-ray Spectroscopy. In *Analytical Electron Microscopy for Materials Science*, Shindo, D., Oikawa, T. Eds.; https://doi.org/10.1007/978-4-431-66988-3_4Springer Japan, 2002; pp 81-102.
(242) Phaneuf, M. W. FIB for Materials Science Applications - a Review. In *Introduction to Focused Ion Beams: Instrumentation, Theory, Techniques and Practice*, Giannuzzi, L. A., Stevie, F. A. Eds.; https://doi.org/10.1007/0-387-23313-X_8Springer US, 2005; pp 143-172.
(243) Whiteside, P. J. D.; Chininis, J. A.; Hunt, H. K. Techniques and Challenges for Characterizing Metal Thin Films with Applications in Photonics. *Coatings* **2016**, *6* (3), 35. https://www.mdpi.com/2079-6412/6/3/35.
(244) Williams, D. B.; Carter, C. B. *Transmission Electron Microscopy (A Textbook for Materials Science)*; Springer New York, NY, 2009. https://doi.org/10.1007/978-0-387-76501-3.

(245) Šatović, D.; Desnica, V.; Fazinić, S. Use of Portable X-ray Fluorescence Instrument for Bulk Alloy Analysis on Low Corroded Indoor Bronzes. *Spectrochimica Acta Part B: Atomic Spectroscopy* **2013**, *89*, 7-13. https://doi.org/10.1016/j.sab.2013.08.007.
(246) Haschke, M.; Flock, J.; Haller, M. *X-Ray Fluorescence Spectroscopy for Laboratory Applications*; Wiley-VCH Verlag GmbH & Co. KGaA, 2021. https://onlinelibrary.wiley.com/doi/book/10.1002/9783527816637.
(247) Stevie, F. A.; Donley, C. L. Introduction to X-ray Photoelectron Spectroscopy. *Journal of Vacuum Science & Technology A* **2020**, *38* (6), 063204. https://doi.org/10.1116/6.0000412.
(248) Greczynski, G.; Hultman, L. X-ray Photoelectron Spectroscopy: Towards Reliable Binding Energy Referencing. *Progress in Materials Science* **2020**, *107*, 100591. https://doi.org/10.1016/j.pmatsci.2019.100591.
(249) Pauly, N.; Tougaard, S.; Yubero, F. LMM Auger Primary Excitation Spectra of Copper. *Surface Science* **2014**, *630*, 294-299. https://doi.org/10.1016/j.susc.2014.08.029.
(250) *X-ray Photoelectron Spectroscopy (XPS) Reference Pages*. 2021. http://www.xpsfitting.com (accessed 29.04.2022).
(251) Biesinger, M. C. Advanced Analysis of Copper X-ray Photoelectron Spectra. *Surface and Interface Analysis* **2017**, *49* (13), 1325-1334. https://doi.org/10.1002/sia.6239(acccessed 2022/05/08).
(252) Brundle, C. R. *Photoionization Cross-sections, σ, and Relative Sensitivity Factors, RSF - A Tutorial*. https://xpslibrary.com/σ-sf-asf-and-rsf/ (accessed 29.04.2022).
(253) *Synchrotron Radiation at BESSY II. Helmholtz-Zentrum Berlin für Materialien und Energie GmbH.* https://www.helmholtz-berlin.de/forschung/oe/ps/synchrotron-radiation-research/synchrotron/photons/bessy_en.html (accessed 29.04.2022).
(254) *KMC-2 Beamline/End-station. Helmholtz-Zentrum Berlin für Materialien und Energie GmbH.* https://www.helmholtz-berlin.de/pubbin/igama_output?modus=einzel&sprache=en&gid=1615&typoid=75136 (accessed 29.04.2022).
(255) Többens, D. M.; Zander, S. KMC-2: an X-ray Beam-Line with dedicated Diffraction and XAS Endstations at BESSY II. *Journal of large-scale research facilities* **2016**, *2*, A49. http://dx.doi.org/10.17815/jlsrf-2-65.
(256) *BAMline. Helmholtz-Zentrum Berlin für Materialien und Energie GmbH.* https://www.helmholtz-berlin.de/pubbin/igama_output?modus=einzel&sprache=en&gid=1658&typoid=75136 (accessed 29.04.2022).
(257) Riesemeier, H.; Ecker, K.; Görner, W.; Müller, B. R.; Radtke, M.; Krumrey, M. Layout and First XRF Applications of the BAMline at BESSY II. *X-Ray Spectrometry* **2005**, *34* (2), 160-163. https://doi.org/10.1002/xrs.750.
(258) Aziz, E. F.; Xiao, J.; Golnak, R.; Tesch, M. Helmholtz-Zentrum Berlin für Materialien und Energie. LiXEdrom: High Energy Resolution RIXS Station dedicated to Liquid Investigation at BESSY II. *Journal of large-scale research facilities* **2016**, *2*, A80. http://dx.doi.org/10.17815/jlsrf-2-85.
(259) *UE56-2_PGM-2. Helmholtz-Zentrum Berlin für Materialien und Energie GmbH.* https://www.helmholtz-berlin.de/pubbin/igama_output?modus=einzel&sprache=en&gid=1633&typoid=75136 (accessed 29.04.2022).
(260) Evans, J. *X-Ray Absorption Spectroscopy for the Chemical and Materials Sciences*; John Wiley & Sons Ltd., 2017. https://onlinelibrary.wiley.com/doi/book/10.1002/9781118676165.
(261) Schnohr, C. S.; Ridgway, M. C. Introduction to X-Ray Absorption Spectroscopy. In *X-Ray Absorption Spectroscopy of Semiconductors*, Schnohr, C. S., Ridgway, M. C. Eds.; https://doi.org/10.1007/978-3-662-44362-0_1Springer Berlin Heidelberg, 2015; pp 1-26.
(262) Kowalska, J.; DeBeer, S. The Role of X-ray Spectroscopy in Understanding the Geometric and Electronic Structure of Nitrogenase. *Biochimica et Biophysica Acta (BBA) - Molecular Cell Research* **2015**, *1853* (6), 1406-1415. https://doi.org/10.1016/j.bbamcr.2014.11.027.
(263) *Long Night of Sciences 2021 Virtual Guided Tour at Helmholtz-Zentrum Berlin: Electrifying carbon.Long Night of Sciences 2021 Virtual Guided Tour at Helmholtz-Zentrum Berlin : Electrifying carbon.* 2021. https://www.helmholtz-berlin.de/appimages/360/tour-de/hzb-elektrochemische_umwandlung/index.html (accessed 29.04.2022).
(264) *CRC Handbook of Chemistry and Physics 95th Edition 2014-2015*; CRC Press Taylor & Francis Group, Boca Raton - London - New York, 2014.
(265) Morales, D. M.; Risch, M. Seven Steps to Reliable Cyclic Voltammetry Measurements for the Determination of Double Layer Capacitance. *Journal of Physics: Energy* **2021**, *3* (3), 034013. http://dx.doi.org/10.1088/2515-7655/abee33.

(266) Srinivasan, S. Electrode/Electrolyte Interfaces: Structure and Kinetics of Charge Transfer. In *Fuel Cells: From Fundamentals to Applications*, Srinivasan, S. Ed.; https://doi.org/10.1007/0-387-35402-6_2Springer US, 2006; pp 27-92.
(267) Khademi, M.; Barz, D. P. J. Structure of the Electrical Double Layer Revisited: Electrode Capacitance in Aqueous Solutions. *Langmuir* **2020**, *36* (16), 4250-4260. https://doi.org/10.1021/acs.langmuir.0c00024.
(268) Liu, T.; Liu, G. Block Copolymer-Based Porous Carbons for Supercapacitors. *Journal of Materials Chemistry A* **2019**, *7* (41), 23476-23488. http://dx.doi.org/10.1039/C9TA07770G.
(269) Qing, G.; Ghazfar, R.; Jackowski, S. T.; Habibzadeh, F.; Ashtiani, M. M.; Chen, C.-P.; Smith, M. R.; Hamann, T. W. Recent Advances and Challenges of Electrocatalytic N_2 Reduction to Ammonia. *Chemical Reviews* **2020**, *120* (12), 5437-5516. https://doi.org/10.1021/acs.chemrev.9b00659.
(270) Chen, C.; Zhu, X.; Wen, X.; Zhou, Y.; Zhou, L.; Li, H.; Tao, L.; Li, Q.; Du, S.; Liu, T.; et al. Coupling N_2 and CO_2 in H_2O to Synthesize Urea under Ambient Conditions. *Nature Chemistry* **2020**, *12* (8), 717-724. https://doi.org/10.1038/s41557-020-0481-9.